ISSN: 1411-9420 (print) 2460-1578 (online)

Indonesian Journal of Chemistry

Vol. 22, No. 1, February 2022

Indones. J. Chem. | Vol. 22 | No. 1 | pp. 1-302 | Yogyakarta February 2022

Adsorption and Inhibition Analysis of Aconitine and Tubocurarine Alkaloids as Eco-friendly Inhibitors of Pitting Corrosion in ASTM – A47 Low Carbon Steel in HCl Acid Environment

Benedict Ushaka Ugi[1*], Mbang Eze Obeten[2], Victoria Mfon Bassey[1], Louis Hitler[1], Stephen Adie Adalikwu[3], Chijioke Everistus Omaliko[1], Desmond Obi Nandi[1], and Ikama Edet Uwah[1]

[1]*Department of Pure & Applied Chemistry, University of Calabar, Calabar, Nigeria*

[2]*Department of Chemistry, Cross River State University of Technology, Calabar, Nigeria*

[3]*Department of Chemistry, College of Education Akamkpa, Nigeria*

* ***Corresponding author:***

tel: +234-7067921098
email: ugibenedict@gmail.com

Received: June 9, 2020
Accepted: November 2, 2020

DOI: 10.22146/ijc.56745

Abstract: *The research on the adsorption and inhibition analysis of aconitine alkaloid (ACA) and tubocurarine alkaloid (TBA) as eco-friendly inhibitors of pitting corrosion in ASTM – A47 low carbon steel in HCl acid was carried out under the following experimental and analytical methods: gravimetric method, gasometric method, electrochemical impedance spectroscopy, potentiodynamic polarization, and scanning electron microscopy method. Results revealed good inhibitors as inhibition efficiencies were recorded at 98.8% and 91.2% at a maximum inhibitor concentration of 1500 ppm for tubocurarine and aconitine alkaloids, respectively. The inhibition efficiency was found to increase with increasing inhibitor concentrations indicating a strong binding between inhibitor molecules and ASTM – A47 low carbon steel in HCl acid. Electrochemical data strongly supported the efficacy of both inhibitors as earlier presented by the chemical methods as a trend in values of charge transfer resistance, double layer capacitance, corrosion potential, and corrosion current density were in accordance with standards for a good inhibitor. The inhibitors were seen to be spontaneous, stabled, endothermic and physically adsorbed. Adsorption of the inhibitors on metal surface obeyed Langmuir, El-Awady, Freundlich, and Temkin adsorption isotherm as regression values were approximately unity. A monolayer physical adsorption was defined for the system.*

Keywords: *tubocurarine; aconitine; alkaloids; corrosion; polarization; adsorption; micrographs; Tafel; Nyquist; impedance*

INTRODUCTION

Corrosion generally is a serious social and economic disadvantage such that millions of dollars have been already spent by different countries in combatting its menace. On a normal day, corrosion can be defined from the instance of deterioration of a material, especially metal, when exposed to an aggressive environment, possible to cause anodic metal dissolution or cathodic hydrogen evolution [1-3]. Corrosion can be electrochemical or dry, depending on the medium of interaction. Disadvantages of corrosion irrespective of types have been long discovered in many areas ranging from leakages of oil crude at truck pipelines, leakages of food from cans, failure of bridges at different intervals, road accidents from wear and tears of bolts and nuts, the collapse of building in several occasions leading to loss of lives and properties, etc. [2-5]. Pitting corrosion is a localized form of corrosion that involves the formation of cavities and holes in a material (Fig. 1) [1-2,5-6]. For a defect-free perfect material, pitting corrosion could arise from the environment as a factor that may contain aggressive chemical species damaging to the passive film (oxide) hence initiate pitting at oxide breaks [1,4,7].

Ninety-five percent of all uniform corrosion occurs

just after the presence of pitting corrosion, and due to difficulties in early detection of pitting corrosion, it becomes so destructive [3,5-8]. The struggle against corrosion challenges has seen advances from both cathodic protection, anodization, galvanization, surface coating – paint coating, plastic coating, or powder coating, electroplating, and also the use of synthesized inorganic compounds, especially free radicals [4,7-8]. In all these advances, both organic and inorganic corrosion inhibitors have taken the lead in corrosion reduction research in all leading metal-dominant sectors of the economy. The interest in corrosion inhibitors came from their ready availability, non-toxic, eco-friendly nature, and cost-effectiveness, among others [1-3,5-9]. Very interestingly, their ability to adsorb on the metal surface forming protective films, strong ability to combine with corrosion product films to protect the metal surface and formation of precipitates which visibly coat and protect metal surfaces consequence upon the possession of hetero-compounds and atoms, double bonds, benzene rings, and pie-bond led to usage in testing corrosion inhibition of ASTM – A47 low carbon steel in HCl acid environment [3-9]. Tubocurarine is a benzylisoquinoline alkaloid and an active ingredient and naturally occurring curare alkaloid isolated from *Chondrodendron tomentosum* [10]. Meanwhile, aconitine is an alkaloid with a diterpenoid structure that occurs naturally in the roots of *Aconitum napellus* [11]. Structures and chemical formulas of the investigated inhibitors are presented in Fig. 2(a–b).

In line with growing research in the field of organic and eco-friendly corrosion inhibitors as control measures of metal anodic dissolution and cathodic hydrogen evolution, this research was carried out to investigate the adsorption and inhibition analysis of aconitine alkaloid and tubocurarine alkaloid as eco-friendly inhibitors of pitting corrosion in ASTM – A47 Low Carbon Steel in HCl acid.

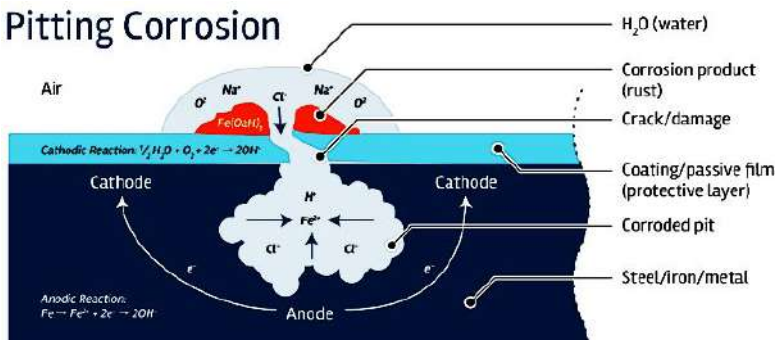

Fig 1. A typical pitting corrosion process

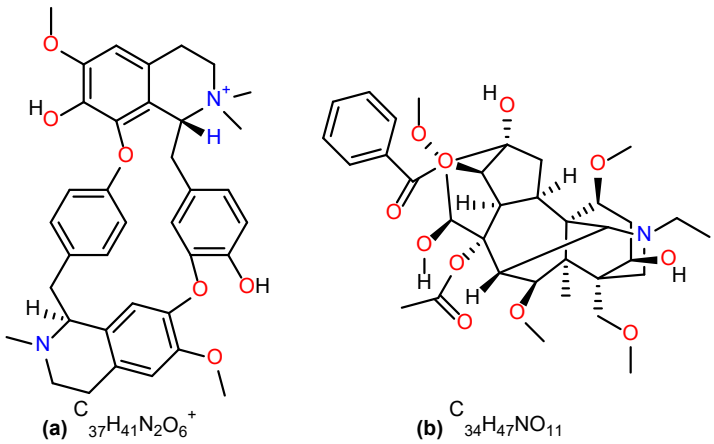

Fig 2. Structure and chemical formula for (a) Tubocurarine and (b) Aconitine alkaloids

■ EXPERIMENTAL SECTION

Materials

The materials used for this research are as follows: *Chondrodendron tomentosum* and *Aconitum napellus* plants, ethanol, diethyl ether, hydrochloric acid, ammonia, hydrobromic acid, tubocurarine alkaloid, tartaric acid, 1000 mL volumetric flask, electronic UNIPOL-820 metallographic polishing machine, ADAM PGW 253e electronic digital weighing balance, distilled water, emery paper, acetone.

Instrumentation

In the course of this research, the following instrumentations used were M36 MEMERY Oven, separating funnel of 500 mL, Soxhlet extraction (heat extraction) process, gravimetric method, gasometric method, electrochemical impedance spectroscopy, potentiodynamic polarization, and scanning electron microscopy.

Procedure

Preparation of stock solution, inhibitors, and metal dressing

The back of *Chondrodendron tomentosum* and the roots of *Aconitum napellus* plants were both obtained from the bush around the boundary between the Obudu local government area of Cross River State and Tsa Local government area of Benue State, Nigeria. Both plant parts were brought to the Ultra-modern Petroleum Trust Fund Laboratory at the University of Calabar – Nigeria, where they were washed thoroughly to remove sand and other external materials and dried in an M36 MEMERY Oven at 55 °C for 48 h. The dried parts were removed, ground to a powdered form, and sieved to attain a smaller surface area for better surface coverage and optimal extraction. Extraction of 200 g powdered form of the roots and stem separately was carried out using a Soxhlet extractor (heat extraction) for 72 h in ethanol as solvent. The crude ethanol extracts were then evaporated in a water bath for 3.5 h each to concentrate the crude through the removal of retained ethanol to at least one-tenth of the original concentration. In other to isolate each of the alkaloids from the crude extract, a separating funnel of 500 mL was used. Two hundred mL of 0.5 M HCl was measured into the separating funnel containing 50 g of the crude extract. This was followed immediately by 200 mL diethyl ether to wash and remove resins and fatty materials. The mixture was separated from the non-alkaloids contents while the diethyl ether content was made alkaline (to reduce the acidic content) with excess ammonia and another 150 mL diethyl ether plus 200 mL dilute hydrobromic acid solution to isolate the aconitine alkaloid. For the isolation of tubocurarine alkaloid, tartaric acid was used in place of hydrobromic acid, and the sample was collected in semi-solid form. Seven grams of each alkaloid was weighed into a 1000 mL volumetric flask and digested with 1 M HCl solution, allowed for 24 h for proper absorption and dissolution, then filtered and stored as inhibitors.

Gravimetric method

Gravimetric, or as it is called, weight loss analysis, was carried out on a 5.0 × 1.5 cm diameter low carbon steel every 24 h for 168 h. The resized metals earlier polished mechanically to mirror surface were weighed using ADAM PGW 253e electronic digital weighing balance. They were then immersed into 100 mL beakers containing different concentrations of each inhibitor (300, 500, 750, 1000, 1250, and 1500 ppm) by suspension and allowed for 24 h. After every 24 h, the metals were removed, washed with distilled water, degreased in ethanol, rinsed in acetone, and air-dried, then reweighed to obtain the different loss in weight of metals. The experiment was duplicated and mean taken to allow for accuracy. All reagents were of analytical grade. The corrosion rate of the low carbon steel in both the presence and absence of inhibitors was determined from the slope of the plot of weight loss against time; the surface coverage and inhibition efficiency were obtained from Eq. (1) and (2), respectively.

$$\theta = \frac{Wl_b - Wl_i}{Wl_b} \quad (1)$$

$$IE\% = \frac{Wl_b - Wl_i}{Wl_b} \times 100 \quad (2)$$

where θ is the surface coverage, Wl_b and Wl_i are the weight loss of blank and inhibitor respectively, and IE% is the percentage inhibitor efficiency.

Gasometric method

The gasometric assembly was used for the experiment. Polished resized metals of 2.5 × 0.05 cm were immersed in different concentrations of each inhibitor (300, 500, 750, 1000, 1250, and 1500 ppm) at different intervals with the initial paraffin oil level properly adjusted to the graduated mark and noted. The conical flask attached to the assembly carrying the metal was let into the water bath and experimental temperature adjusted to 30, 45, 55, and 60 °C, respectively, at different times. After each minute, the fall in the level of paraffin as a result of hydrogen gas evolution was recorded until 60 min. The assembly was stopped, and the experiment restarted for the remaining inhibitor concentrations with new metals. The corrosion rate of the low carbon steel in both the presence and absence of inhibitors was determined from the slope of the plot of weight loss against time; the surface coverage and inhibition efficiency were obtained from Eq. (1) and (2), respectively.

Electrochemical impedance method

The EIS was investigated at ambient temperature in a triple electrode cell compartment using Gamry Reference 600 potentiostat inclusive of a Gamry framework EIS300 system. Echem analyst software was used to analyze the fitting of the data. A saturated calomel (SCE) electrode was introduced as the reference electrode, and a 1 cm^2 platinum foil was introduced as a counter electrode. The working electrode with dimension 1 × 1 cm was dipped in 1 M HCl acid. Electrochemical tests were conducted within a frequency of 10–10,000 Hz within potentiodynamic conditions, with an amplitude of 5 mV, involving alternating current signals at E_{corr}. All experiments were conducted every 60 min with and without various concentrations of the inhibitors. From the R_{ct} obtained, the retardation efficiency was calculated using Eq. (3):

$$IE\% = \frac{R^{i}_{ct} - R^{0}_{ct}}{R^{i}_{ct}} \times 100 \quad (3)$$

where R^{0}_{ct} and R^{i}_{ct} represent the charge transfer resistance with and without the inhibitors.

Potentiodynamic polarization method

The potentiodynamic polarization curves were measured at a scan rate of 1 mV s^{-1}, from -500 to 0 mV versus SCE. The Tafel curves for the anode and cathode for low carbon steel dissolution were recorded in both the presence and absence of the inhibitor. Extrapolation of the linear segments of the anodic and cathodic curves gives useful parameters, including anodic and cathodic Tafel slopes, corrosion potential (E_{corr}), and corrosion current density (i_{corr}). The corrosion current density (i_{corr}) was used to calculate the inhibition efficiency of the inhibitors given by Eq. (4):

$$\%IE_{pdp} = \left(1 - \frac{I_{corr}}{I^{0}_{corr}}\right) \times 100 \quad (4)$$

Scanning electron microscope analysis

The Scanning electron microscopic study was conducted using the JSM-5600 LV instrument (Hitachi) at the accelerating voltage of 15 kV. For the SEM study, the ASTM – A47 low carbon steel resized metals were allowed to corrode in 1 M HCl solution in the presence and absence of the inhibitors (1 M HCl, 300 ppm, and 1500 ppm). After that, the surfaces of the coupons were examined for their morphological changes.

■ RESULTS AND DISCUSSION

Gravimetric Analysis/Result

Research findings from the gravimetric experimentation in Table 1 showed increasing inhibition efficiency for both alkaloids (aconitine and tubocurarine) as concentration was increased up to 1500 ppm. This effect has a contrary impact on the corrosion rate of the metal in various concentrations as corrosion rate values were found to be decreasing from 0.934 in 1 M HCl solutions to 0.083 and 0.011 ppm for aconitine and tubocurarine alkaloids, respectively, as earlier observed in a similar work [12-15]. This observation could generally be attributed to the strong binding power, large surface area coverage of both inhibitors on the low carbon steel surface due to adsorption, and significant water molecules substitution at the metal arena [12,16-19]. Comparing inhibition

Table 1. Gravimetric analysis data revealing corrosion rate of metal, surface coverage, and inhibition efficiency of inhibitors on ASTM – A47 low carbon steel in 1 M HCl

Inhibitor Conc. (ppm)	Aconitine alkaloid			Tubocurarine alkaloid		
	Corrosion Rate ($mg/cm^2/h$)	Surface Coverage	Inhib. Efficiency (%)	Corrosion Rate ($mg/cm^2/h$)	Surface Coverage	Inhib. Efficiency (%)
1 M HCl	0.934			0.934	-	-
300 ppm + 1 M HCl	0.457	0.51	51.1	0.310	0.67	66.8
500 ppm + 1 M HCl	0.296	0.68	68.3	0.162	0.83	82.6
750 ppm + 1 M HCl	0.205	0.78	78.1	0.095	0.90	89.8
1000 ppm + 1 M HCl	0.158	0.83	83.1	0.029	0.97	96.9
1250 ppm + 1 M HCl	0.110	0.88	88.2	0.022	0.98	97.7
1500 ppm + 1 M HCl	0.083	0.91	91.2	0.011	0.99	98.8

efficiencies of both aconitine and tubocurarine alkaloids, it was observed that low carbon steel was less inhibited in aconitine alkaloids (91.2%) compared to tubocurarine alkaloids (98.8%). This could be due to the presence of more hetero-atoms (2N), pi bonds from double bonds, and benzene rings, including proper orientation of the molecular structure on metal during adsorption [15,20-22].

Gasometric Analysis and Result

To ascertain the effectiveness of the inhibitors when exposed to a relative amount of heat, a gasometric analysis was done, and the data obtained and analyzed are presented in Tables 2 and 3. It was noticed, just as in the case of the gravimetric analysis, inhibition efficiency was found to increase with a corresponding increase in inhibitor concentration. This showed that the inhibitors

Table 2. Gasometric analysis revealing corrosion rate of metal, surface coverage, and inhibition efficiency of tubocurarine on ASTM – A47 low carbon steel in 1 M HCl

Inhibitor Conc. (ppm)	Corrosion Rate ($mg/cm^2/h$)				Surface coverage				Inhibition efficiency (%)			
	30 °C	45 °C	55 °C	60 °C	30 °C	45 °C	55 °C	60 °C	30 °C	45 °C	55 °C	60 °C
1 M HCl	1.028	1.136	1.771	2.085	-	-	-	-	-	-	-	-
300 ppm	0.254	0.351	0.751	0.968	0.75	0.69	0.58	0.54	75.3	69.1	57.6	53.6
500 ppm	0.200	0.313	0.547	0.753	0.81	0.72	0.69	0.64	80.6	72.4	69.1	63.9
750 ppm	0.169	0.254	0.418	0.594	0.84	0.78	0.76	0.72	83.6	77.6	76.4	71.5
1000 ppm	0.091	0.230	0.376	0.529	0.91	0.80	0.79	0.75	91.2	79.8	78.8	74.6
1250 ppm	0.048	0.205	0.359	0.527	0.95	0.82	0.80	0.75	95.3	82.0	79.7	74.7
1500 ppm	0.016	0.174	0.348	0.501	0.98	0.85	0.80	0.76	98.5	84.7	80.4	76.0

Table 3. Gasometric analysis revealing corrosion rate of metal, surface coverage, and inhibition efficiency of aconitine alkaloid on ASTM – A47 low carbon steel in 1 M HCl

Inhibitor Conc. (ppm)	Corrosion Rate ($mg/cm^2/h$)				Surface coverage				Inhibition efficiency (%)			
	30 °C	45 °C	55 °C	60 °C	30 °C	45 °C	55 °C	60 °C	30 °C	45 °C	55 °C	60 °C
1 M HCl	1.028	1.136	1.771	2.085	-	-	-	-	-	-	-	-
300 ppm	0.477	0.558	0.887	1.107	0.54	0.51	0.50	0.47	53.6	50.9	49.9	46.9
500 ppm	0.453	0.517	0.835	1.027	0.56	0.54	0.53	0.51	56.0	54.5	52.9	50.7
750 ppm	0.389	0.466	0.786	0.951	0.62	0.59	0.56	0.54	62.2	59.0	55.6	54.4
1000 ppm	0.213	0.382	0.719	0.905	0.79	0.66	0.59	0.57	79.3	66.4	59.4	56.6
1250 ppm	0.174	0.265	0.527	0.658	0.83	0.77	0.70	0.68	83.1	76.7	70.2	68.4
1500 ppm	0.096	0.174	0.386	0.546	0.91	0.85	0.78	0.74	90.7	84.7	78.2	73.8

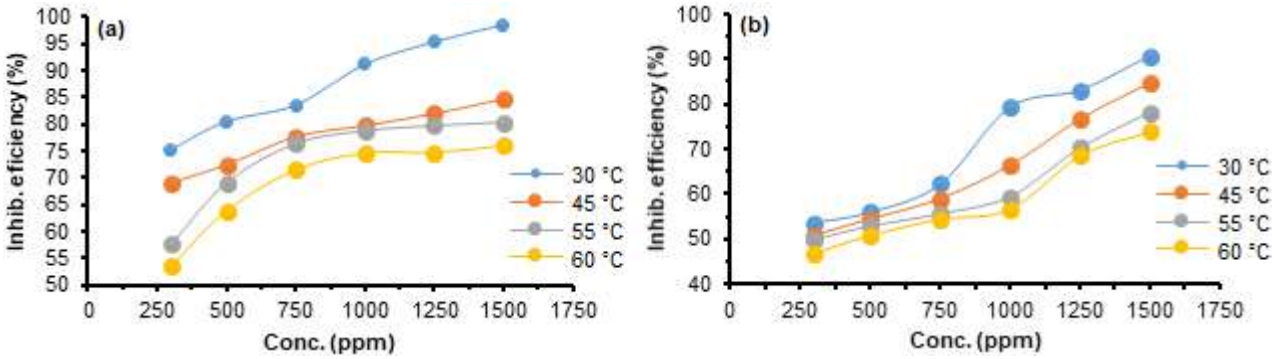

Fig 3. Plots revealing the inhibition efficiency of inhibitors against concentration for (a) tubocurarine and (b) aconitine alkaloids on ASTM – A47 low carbon steel in 1 M HCl

had a good performance on the metal due to proper molecular orientation, size of the inhibitor molecule, and increase adsorption of the inhibitor molecules or its ions on anodic and/or cathodic sites of the low carbon steel Fig. 3(a–b) [17,19,23-28]. However, both inhibitors were seen to be very active in their performance at lower temperatures (30 °C) with an efficiency of 98.5 and 90.7% for tubocurarine and aconitine alkaloids, respectively (Table 2 and 3). In contrary to the result of the corrosion rate of metal at ambient temperature in the gravimetric analysis, the gasometric analysis showed increased corrosion rate and a slight decrease in inhibition efficiency as the temperature was increased accordingly. This is due to the high-temperature effects that bring about agitation and desorption of weakly bounded inhibitor molecules held on the low carbon steel surface by van der Waals forces of attraction rather than ionic bonding [13,22,27-30]. This can also be possible because of the migration of segments of molecules or individual molecules (inhibitors) in jumps, from one place in a site to a vacant hole of the site [17,25,31].

Electrochemical Impedance Spectroscopy

The electrochemical methods allow us to determine the relationship between the ionic, molecular, or charge transfer between the inhibitors and the metal surface in a conducting medium. In this experimental procedure, important information relating to the metal/inhibitor interaction like charge transfer resistance, double layer capacitance, surface coverage, and inhibition efficiency are unraveled. However, data for the double-layer capacitance for the semicircles and inhibition efficiency were calculated using Eq. (5) and (6).

$$C_{dl} = \frac{1}{\omega Z''} \quad (5)$$

where Z" is an imaginary component of impedance at any frequency inside the semicircle, and ω is the angular frequency.

$\omega = 2 * \pi * f_{max}$ (in Hz used for measurement of EIS).

Hence,

$$C_{dl} = \frac{1}{2\pi f_{max} Z''} \quad (6)$$

where f_{max} describes the maximum frequency of the semicircle, and the π is 3.142.

However, the data for the IE_R % were obtained from the fitting of the charge transfer resistance values into Eq. (7).

$$IE_R\,\% = \frac{R_{ct}^0 - R_{ct}^i}{R_{ct}^0} \times 100 \quad (7)$$

Fig. 4(a–b) reveals a Nyquist plot with only one capacitive loop, and this may be due to the presence of just a single charge transfer [17-21,32-35]. It was also observed that the size of the loops increased with the rise of both tubocurarine and aconitine alkaloid concentration up to 1500 ppm, which indicates that both inhibitors were adsorbed on the low carbon steel surface, and the surface area exposed to the 1 M HCl was reduced [14-16,22,36-37]. This was analyzed in Table 4 as the charged transfer resistance values were seen increasing with increasing inhibitor concentration up to 1500 ppm. The double-layer capacitance found decreases with increasing inhibitor concentration, and inhibition efficiency increases

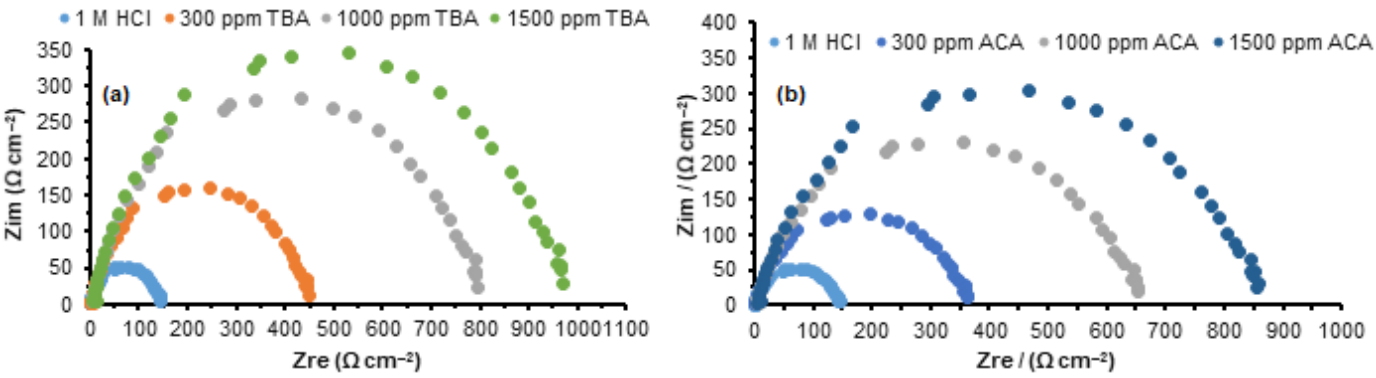

Fig 4. Nyquist plots for the corrosion inhibition of metal by (a) tubocurarine and (b) aconitine alkaloids on ASTM – A47 low carbon steel in 1 M HCl

Table 4. Electrochemical impedance data revealing charge transfer resistance of the metal, double layer capacitance, surface coverage, and inhibition efficiency of inhibitors on ASTM – A47 low carbon steel in 1 M HCl

	Inh. Conc.	R_{ct}	C_{dl}	θ	%IE
TBA	1 M HCl	122	1.3×10^{-5}	-	-
	300 ppm	338	4.7×10^{-6}	0.639	63.9
	1000 ppm	683	2.3×10^{-6}	0.821	82.1
	1500 ppm	923	1.7×10^{-6}	0.868	86.8
ACA	300 ppm	268	5.9×10^{-6}	0.545	54.5
	1000 ppm	674	2.4×10^{-6}	0.819	81.9
	1500 ppm	770	2.1×10^{-6}	0.842	84.2

with the concentration increment. This proved strong adsorption of the inhibitor molecules on the metal surface due to the flow type and flow rate of the inhibitors [28-30,36-40]. It can also be said that the strong adsorption help the system to overcome electron transfer from the positive electrode (anodic site) to the hydrogen ions in the solution phase and subsequent reduction in cathodic hydrogen gas evolution, hence blocking the corrosion reaction [15,27,39-45].

Potentiodynamic Polarization

The corrosion rate is directly proportional to the corrosion current density [33,35]. The plots and values obtained from the potentiodynamic polarization experiment are presented in Table 4. Values are seen to increase with increasing inhibitor concentration, an indication that depicts decreasing diffusion rate for reactants to the surface of the metal and decreasing electrical resistance of metal surface due to strength of bonding to the substrate, cross-linking ability of the inhibitors, and solubility of the 1 M HCl environment [19,24,46-48]. In addition, as shown in Fig. 5 and Table 5, the addition of tubocurarine and aconitine alkaloid molecules shifted the corrosion potential (E_{corr}) values away from the non-inhibited solution and also showed changes in both the cathodic and anodic polarization branches and values. These results indicate that the added inhibitors acted as mixed-type inhibitors [26-27,39,48-50].

Thermodynamics

Fig. 6 shows plots drawn from the temperature dependence data obtained from the gasometric methods. Values analyzed from the plots of ln CR against 1/T, as shown in Table 6.

$$CR = A\exp\left(\frac{-Ea}{RT}\right) \quad (8)$$

By taking the log of Eq. (8), Eq. (9) was obtained.

$$\ln CR = \ln A - \frac{Ea}{RT} \quad (9)$$

where CR is the rate of corrosion, A is the collision constant, R is the universal gas constant, T is the temperature (in kelvin), and Ea is the amount of energy

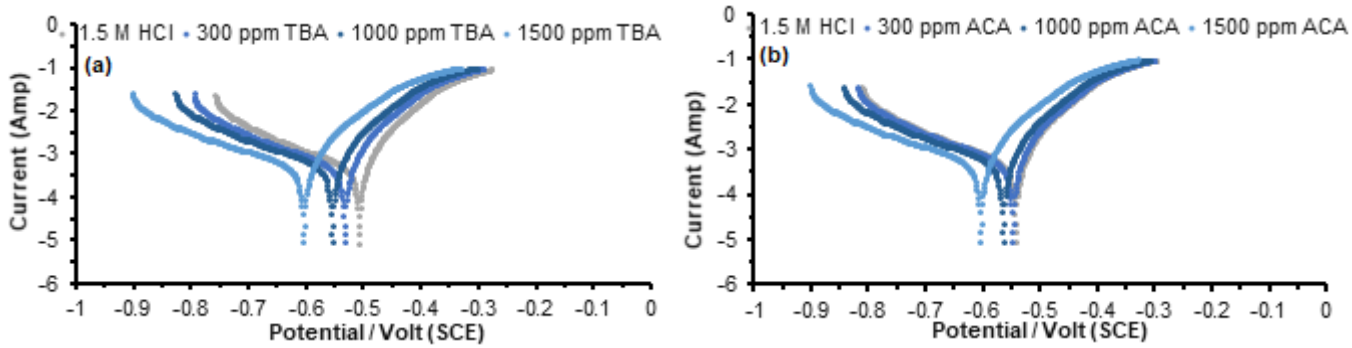

Fig 5. Tafel plots for ASTM – A47 low carbon steel corrosion in 1 M HCl acid solution with and without (a) tubocurarine and (b) aconitine alkaloids

Table 5. Potentiodynamic polarization data revealing corrosion current density, corrosion potential, Tafel slopes, and inhibition efficiency of inhibitors on ASTM – A47 low carbon steel in 1 M HCl

	Inh. Conc.	I_{corr} (mA cm^{-2})	E_{corr} (mV)	βc (mV/dec)	βa (mV/dec)	θ	IE_i (%)
	1 M HCl	2.106	-625	427	550	-	-
TBA	300 ppm	0.847	-419	308	316	0.598	59.8
	1000 ppm	0.414	-295	274	173	0.803	80.3
	1500 ppm	0.269	-174	216	85	0.872	87.2
ACA	300 ppm	0.911	-743	357	319	0.567	56.7
	1000 ppm	0.524	-585	291	236	0.751	75.1
	1500 ppm	0.348	-321	200	170	0.835	83.5

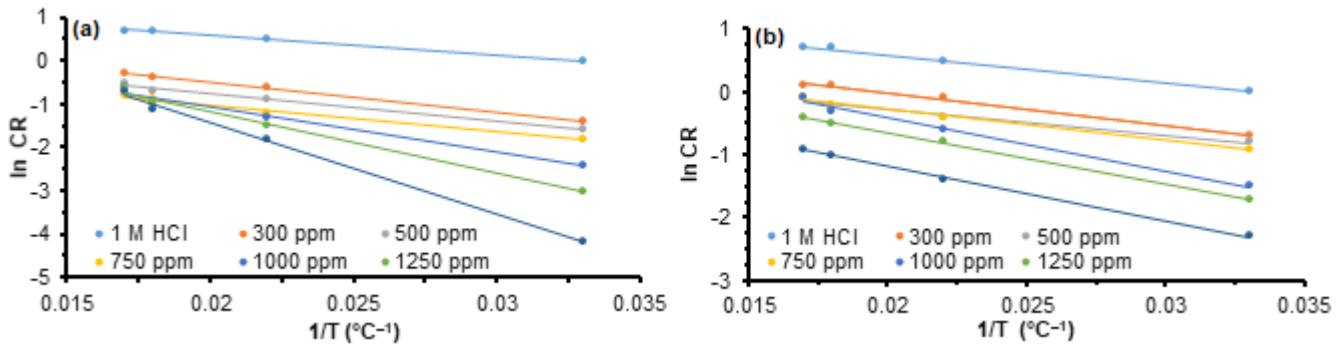

Fig 6. Arrhenius plots revealing the kinetics of corrosion reaction in the presence of (a) tubocurarine and (b) aconitine alkaloids inhibitors on ASTM – A47 low carbon steel in 1 M HCl

required to ensure that a reaction happens [16,19,22,31-37]. The collision coefficient or binding constant derived from Eq. (9) was found to decrease with inhibitor concentration but with a sudden increase from 1250 to 1500 ppm concentration. This is an indication that the inhibitors, especially that of tubocurarine alkaloid, had a stronger binding tendency at higher concentrations. However, activation energy values were seen to be higher in the inhibited solution compared to the non-inhibiting solution (1 M HCl). This is apparently due to the strong adsorption of molecules of inhibitors onto the ASTM – A47 low carbon steel resized metals and decreasing diffusion rate of corrosion reactants to the metal surfaces, including a possible in situ application advantage consequence to the higher energy barrier required for the corrosion reactants to overcome [20-22,41-43,50-51]. This tendency can also be due to the physical adsorption mechanism of the inhibitor reaction. This has been seen as the activation energy values being less than 20 kJ/mol [15,17-19,42-44,51-53].

Table 6. Thermodynamic data revealing corrosion inhibition of (a) tubocurarine and (b) aconitine alkaloids on ASTM – A47 low carbon steel in 1 M HCl

	Inh. Conc.	A	Ea (kJ/mol)	ΔH (kJ/mol)	ΔS (kJ/mol)
Tubocurarine alkaloid	1 M HCl	1.5	3.74	28.267	49.72
	300 ppm	0.9	5.65	29.68	51.14
	500 ppm	0.5	5.39	24.27	45.73
	750 ppm	0.2	5.08	21.94	43.40
	1000 ppm	1.0	8.64	54.22	75.68
	1250 ppm	1.7	11.85	83.55	105.01
	1500 ppm	2.9	17.76	142.27	163.73
Aconitine alkaloid	300 ppm	1.0	4.29	28.40	49.86
	500 ppm	0.6	3.49	28.40	49.86
	750 ppm	0.7	4.02	82.56	104.02
	1000 ppm	1.3	6.99	34.86	56.32
	1250 ppm	1.0	6.71	29.69	51.15
	1500 ppm	0.6	7.23	50.87	72.33

The Eyring transition state equation is given in Eq. (10) was adopted for the graphical determination of both the enthalpy and entropy of adsorption using the gasometric data that evolved from the experimental analysis.

$$\ln\frac{k}{T} = -\frac{\Delta H\dagger}{R}\frac{1}{T} + \ln\frac{kB}{h} + \frac{\Delta S\ddagger}{R} \quad (10)$$

The values for ΔH‡ and Δ*S*‡ can be determined from kinetic data obtained from a plot of $\ln\frac{k}{T}$ vs. $\frac{1}{T}$, as seen in Fig. 7(a–b). The straight line with a negative slope, $-\frac{\Delta H\dagger}{R}$, and a y-intercept, $\ln\frac{kB}{h} + \frac{\Delta S\ddagger}{R}$ from the equation gives the two major thermodynamic parameters investigated. From Table 6, values of the enthalpy of adsorption were seen to be positive, an indication of endothermic reaction in the inhibitor-metal interface and possible absorption of energy (heat) by the inhibitor reacting system, leading to increase inhibitor reaction and limiting ionic transference at the anodic site of the metal [13-16,29-34,44]. The values were also found to be less than 80 kJ mol^{-1} claiming that the inhibitors were physically adsorbed on the metal surface [39,43-48]. This is in agreement with the inhibition efficiency result that shows decreasing efficiency while the temperature was increased. The values for the entropy of adsorption, as presented still in Table 6, show that the system was less disordered as values were negative. This situation will allow for the orderly and stable coverage of the inhibitors on the metal surface hence higher activation complex and advancement in the corrosion inhibition reaction [17-25,31,52-54]. The adsorption energy values are presented in Table 6. The values showed that the inhibitors

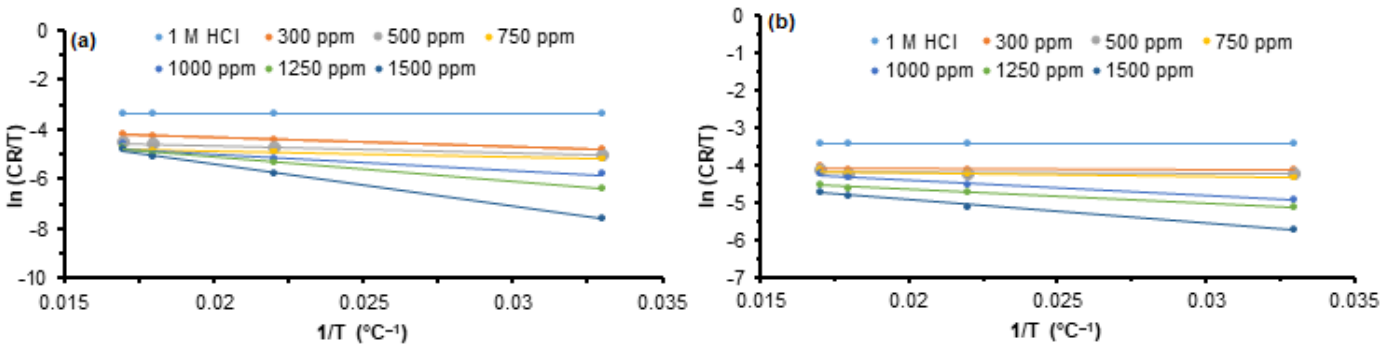

Fig 7. Transition state plots the corrosion inhibition of (a) tubocurarine and (b) aconitine alkaloids on ASTM – A47 low carbon steel in 1 M HCl

presented negative free energy of adsorption, indicating that the inhibitors were stable ones, and their reaction was spontaneous in the forward direction. The inhibitors also influenced the reaction to having the free energy values less negative than 20 kJ mol^{-1}, an indication that the reaction followed a physical adsorption mechanism [19-25,35-39,50,52], and this had been already confirmed from the data obtained for activation energy (Ea) and adsorption enthalpy (ΔH).

Adsorption Evaluation

In an attempt to study the adsorption characteristics of the inhibitor molecules on the metal surface, the Langmuir, El-Awady, Freundlich, and Temkin adsorption isotherms as presented in Fig. 8–11 were studied constructed from Eq. (11), (12), (13), and (14), respectively.

$$\frac{C}{q_e} = \frac{1}{k} + C \quad (11)$$

$$\log\left(\frac{\theta}{1-c}\right) = \log b + y \log C \quad (12)$$

$$\ln q_e = \frac{1}{n}\ln C + \ln K_F \quad (13)$$

$$q_e = \frac{RT}{b}\ln C + \frac{RT}{b}\ln K_T \quad (14)$$

where C is the concentration of inhibitors, q_e is the amount of adsorbate adsorbed per unit mass, k is the equilibrium constant, y is the number of inhibitor molecules occupying one active site, b is the heat of sorption, K_T is the equilibrium binding constants and K_F maximum adsorption capacity, while the R and T take their usual meanings.

Generally, it was observed from Table 7–10 that the correlation coefficient values for the isotherms were approximately unity when fitted to the isotherms, and their isotherm equilibrium binding constants were decreasing with temperature. This implies that both

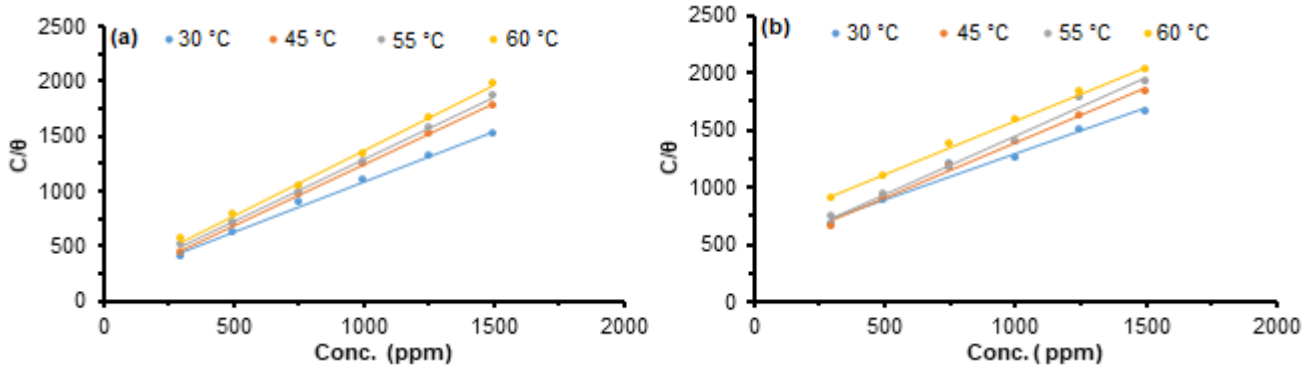

Fig. 8. Langmuir adsorption isotherm plots for (a) tubocurarine and (b) aconitine alkaloids on ASTM – A47 low carbon steel in 1 M HCl

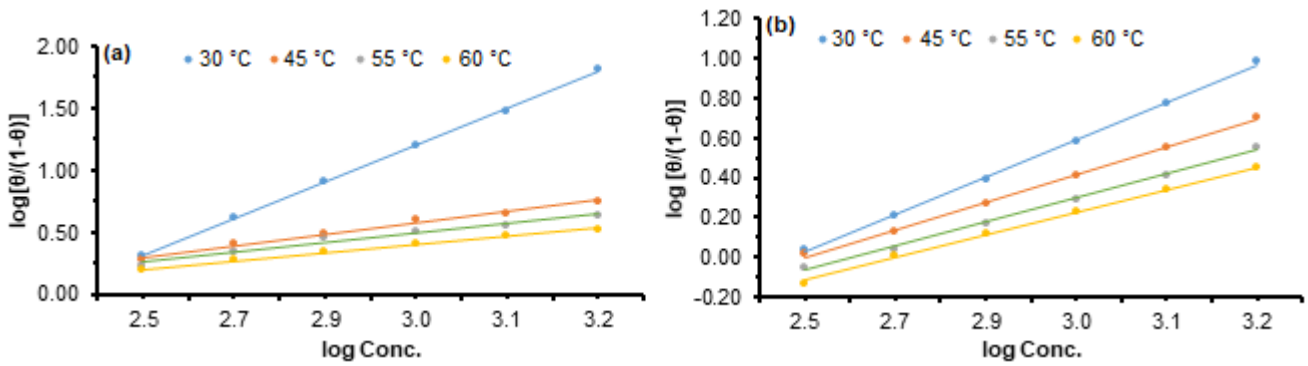

Fig 9. El – Awady adsorption isotherm for (a) tubocurarine and (b) aconitine alkaloids on ASTM – A47 low carbon steel in 1 M HCl

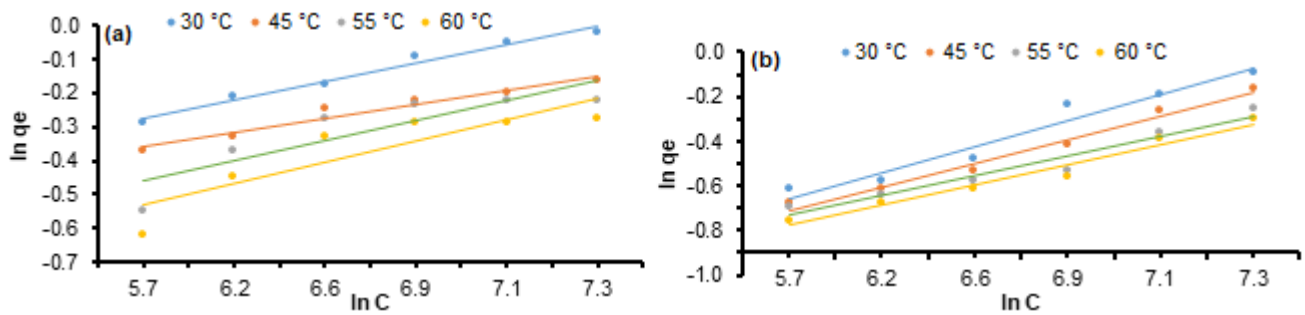

Fig 10. The Freundlich adsorption isotherm showing corrosion inhibition of (a) Tubocurarine and (b) Aconitine alkaloids on ASTM – A47 low carbon steel in 1 M HCl

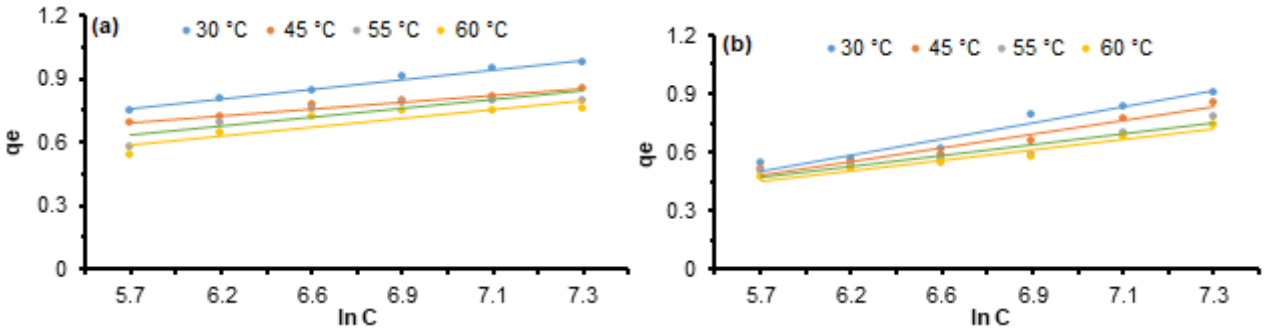

Fig 11. The Temkin adsorption isotherm for (a) tubocurarine and (b) aconitine alkaloids on ASTM – A47 low carbon steel in 1 M HCl

isotherms were obeyed, and a physical adsorption process was eminent [14-18,21-30,39]. However, the Langmuir isotherm was very well obeyed comparatively. The values of k for the Langmuir isotherm were found to be relatively large (> 1) for both inhibitors, an indication that there is a strong interaction between the inhibitors and the surface and a physical adsorption process [21-29,55]. The El-Awady isotherm characterizes the adsorption sites on the metal surface. The plots in Fig. 9 were obtained from Eq. (12). From the result in Table 8, values

Table 7. Langmuir data for the corrosion inhibition of (a) tubocurarine and (b) aconitine alkaloids on ASTM – A47 low carbon steel in 1 M HCl

Temp.	Aconitine alkaloid				Tubocurarine alkaloid			
(°C)	k	R	slope	ΔG (kJ/mol)	k	R	slope	ΔG (kJ/mol)
30	4.92	0.9713	0.7986	-13.99	1.55	0.9953	0.9272	-11.11
45	4.14	0.9943	0.9712	-13.56	1.22	0.9988	1.1141	-10.51
55	4.26	0.9899	1.0160	-13.63	1.61	0.9987	1.1246	-11.21
60	6.42	0.9980	0.9399	-14.66	1.86	0.9986	1.1814	-11.57

Table 8. El-Awardy adsorption data for tubocurarine and aconitine alkaloids on ASTM – A47 low carbon steel in 1 M HCl

Temp.	Aconitine alkaloid				Tubocurarine alkaloid			
(°C)	1/y	R	y	ΔG (kJ/mol)	1/y	R	y	ΔG (kJ/mol)
30	0.01	0.9996	0.30	-14.69	0.16	0.9985	0.19	-5.45
45	0.20	0.9889	0.09	-9.01	0.13	0.9987	0.14	-7.39
55	0.19	0.9721	0.08	-10.77	0.19	0.9966	0.12	-10.77
60	0.14	0.9915	0.07	10.23	0.22	0.9980	0.11	-12.48

Table 9. Freundlich adsorption isotherm data for tubocurarine and aconitine alkaloids on ASTM – A47 low carbon steel in 1 M HCl

Temp.	Tubocurarine alkaloid				Aconitine alkaloid			
(°C)	K_F	R	1/n	ΔG (kJ/mol)	K_F	R	1/n	ΔG (kJ/mol)
30	0.469	0.9817	0.054	-8.13	0.171	0.9522	0.115	-5.61
45	0.397	0.9588	0.042	-11.6	0.153	0.9812	0.107	-8.00
55	0.301	0.7738	0.055	-12.9	0.151	0.9454	0.089	-9.72
60	0.254	0.7795	0.064	-13.2	0.136	0.9625	0.091	-10.08

Table 10. Temkin adsorption isotherm data for tubocurarine and aconitine alkaloids on ASTM – A47 low carbon steel in 1 M HCl

Temp.	Tubocurarine alkaloid				Aconitine alkaloid			
(°C)	K_T (L/mol)	R	b (kcal/mol)	ΔG (kJ/mol)	K_T (L/mol)	R	b (kcal/mol)	ΔG (kJ/mol)
30	2.21	0.9869	1.1×10^{-5}	-12.00	1.53	0.9512	1.9×10^{-5}	-11.09
45	1.94	0.9669	7.7×10^{-6}	-17.53	1.50	0.9634	1.7×10^{-5}	-16.56
55	1.81	0.7986	1.0×10^{-6}	-21.08	1.52	0.9206	1.3×10^{-5}	-20.29
60	1.73	0.8028	1.0×10^{-6}	-24.68	1.47	0.9424	1.2×10^{-5}	-23.87

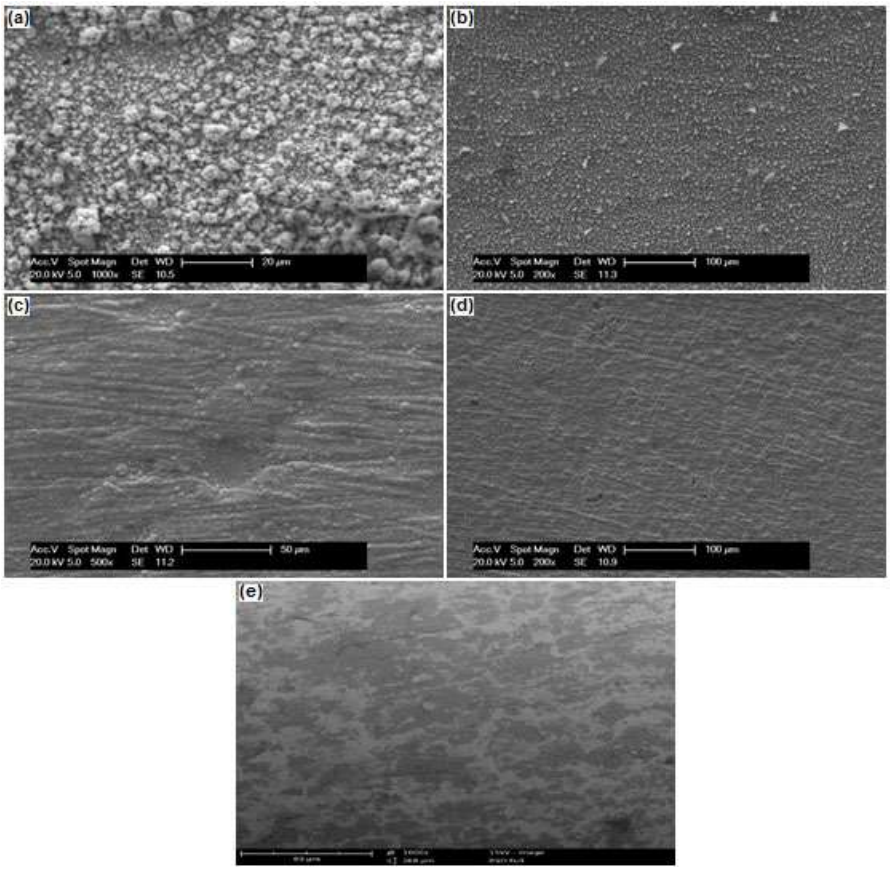

Fig 12. SEM micrographs of ASTM – A47 low carbon steel in (a) 1 M HCl, (b) 300 ppm ACA, (c) 300 ppm TBA, (d) 1500 ppm ACA and (e) 1500 ppm TBA

of 1/y are less than 1, confirming that both inhibitors occupied more than one active site, making them good inhibitors in 1 M HCl. However, y values were found to decrease with temperature, indicating that the inhibitors

were bounded to the metal surface by weak Van der Waal forces of attraction [39,51-53], and this had been confirmed from the physical adsorption nature of the inhibitors. The 1/n value derived from the Freundlich equation serves to describe the linearity of adsorption [54-55]. Normally, when 1/n values range from 0.7–10, it implies that the relative adsorption decreases as inhibitor concentration increases and values less than 0.7 implies increased relative adsorption [55-56]. From Table 9, it is observed that the inhibitors proffered increased relative adsorption on the metal surface. It was also observed that the "b" (kcal/mol) values (adsorption energy) in Table 10 were positive and less than unity. This implies an endothermic reaction as already observed with the enthalpy of adsorption (Table 6) and a physical adsorption process, as indicated in the thermodynamic evaluation [54-57].

Surface Morphology

Micrographs drawn from the scanning electron microscopic study are presented in Fig. 12(a-e). A close observation on the slides shows a very rough surface for the metal immersed directly in the 1 M HCl solution. This is an indication of a direct acid attack on the surface, leading to the formation and possible evolution of hydrogen gas, giving rise to corrosion [39,51,29]. It was evident from the micrographs of metals immersed in inhibitor solution that the inhibitor molecules adsorbed strongly on the metal surface, hence blocking all anodic sites from further corrosion as it were with those of the free solution [39,56-60]. However, the micrographs for the inhibition of metal by tubocurarine alkaloid at both inhibitor concentrations (300 ppm and 1500 ppm) presented better adsorption compared to those from aconitine alkaloid, and this confirmed the earlier assertions from other experimental results.

■ CONCLUSION

The research work presents the following findings. Tubocurarine and aconitine alkaloids inhibited at 98.9 and 91.2%, respectively, in the presence of 1 M HCl, indicating that they are good inhibitors of ASTM – A47 low carbon steel. Temperature dependence of the inhibitors revealed strong adsorption of inhibitors at lower temperatures, but however, inhibition was found increasing with the concentration of inhibitors at different temperatures. Thermodynamic data presented the inhibitors as stabled, spontaneous, physically adsorbed, and with a little or no degree of disorderliness. Electrochemical results revealed good adsorption performance by the inhibitors as charge transfer resistance was found increasing, double-layer capacitance and polarization resistance were decreasing, and mixed–type inhibition was recorded. Adsorption consideration revealed that both inhibitors occupied more than one active site and as well as obeyed more of the Langmuir adsorption assumptions, hence monolayer. The surface morphology of the metals was smooth enough in both inhibitor concentrations hence strong bonding and large surface coverage.

■ REFERENCES

[1] Bardal, E., 2004, *Corrosion and Protection*, Springer-Verlag, London.

[2] Davis, J.R., 2000, *Corrosion: Understanding the Basics*, ASM International, USA.

[3] Gergely, A., 2019, *Phenomenal and Theories in Corrosion Science: Methods of Prevention*, Nova Science Publishers Inc., USA.

[4] McCafferty, E., 2010, *Introduction to Corrosion Science*, Springer-Verlag, New York.

[5] Ohtsuka, T., Nishikata, A., Sakari, M., and Fushimi, K., 2018, *Electrochemistry for Corrosion Fundamentals*, Springer, Singapore.

[6] Perez, N., 2016, *Electrochemistry and Corrosion Science*, 2nd Ed., Springer, Cham, Switzerland.

[7] Rajendran, S., Nguyen, T.A., Kakooei, S., Li, Y., and Yeganeh, M., 2020, *Corrosion Protection of the Nanoscale*, 1st Ed., Elsevier UK.

[8] Roberge, P.R., 2008, *Corrosion Engineering: Principle and Practices*, McGraw Hill Professional, Canada.

[9] Talbot, D.E.J., and Talbot, J.D.R., 2018, *Corrosion Science and Technology*, 3rd Ed., CRC Press, Boca Raton, US.

[10] Tang, W.T., Wong, S.K., Law, T.Y., Pang, K.C., Sin, D., and Tam, Y.K., 2006, Method for the determination of *Aconitum* alkaloids in dietary

supplements and raw materials by reversed phased liquid chromatography with ultraviolet detection and conformation by tandem mass spectrometry: Single-laboratory validation, *J. AOAC Int.*, 89 (6), 1496–1514.

[11] Paech, K., and Tracey, M.K., 1955, *Modern Methods of Plant Analysis*, Springer-Verlag, Berlin Heidelberg.

[12] Akalezi, C.O., and Oguzie, E.E., 2018, Evaluation of anticorrosion properties of *Chrysophyllum albidum* leaves extract for mild steel protection in acidic media, *Int. J. Ind. Chem.*, 7 (1), 81–92.

[13] Ali, I.H., and Suleiman, M.H.A., 2018, Effects of acid extract of leaves of *Juniperus procera* on corrosion inhibition of carbon steel in HCl solution, *Int. J. Electrochem. Sci.*, 13, 3910–3922.

[14] Al-Shehri, D.A., 2019, Oil and gas wells: Enhanced wellbore casing integrity management through corrosion rate prediction using an augmented intelligent approach, *Sustainability*, 11 (3), 818.

[15] Al-Sodani, K.A.A., Al-Amoudi, O.S.B., Maslehuddin, M., and Shameem, M., 2018, Efficiency of corrosion inhibitors in mitigating corrosion of steel under elevated temperature and chloride concentration, *Constr. Build. Mater.*, 163, 97–112.

[16] Ameh, P.O., and Eddy, N.O., 2018, Experimental and computational chemistry studies on the inhibition efficiency of phthalic acid (PHA) for the corrosion of aluminum in hydrochloric and tetraoxosulphate(VI) acids, *Prot. Met. Phys. Chem. Surf.*, 54 (6), 1169–1181.

[17] Ammal, P.R., Prajila, M., and Joseph, A., 2018, Effective inhibition of mild steel corrosion in hydrochloric acid using EBIMOT, a 1, 3, 4-oxadiazole derivative bearing a 2-ethylbenzimidazole moiety: Electro analytical, computational and kinetic studies, *Egypt. J. Pet.*, 27 (4), 823–833.

[18] Bharatiya, U., Gal, P., Agrawal, A., Shah, M., and Sircar, A., 2019, Effect of corrosion on crude oil and natural gas pipeline with emphasis on prevention by ecofriendly corrosion inhibitors: A comprehensive review, *J. Bio- Tribo-Corros.*, 5 (2), 35.

[19] Boumhara, K., Harhar, H., Tabyaoui, M., Bellaouchou, A., Guenbour, A., and Zarrouk, A., 2019, Corrosion inhibition of mild steel in 0.5 M H_2SO_4 solution by *Artemisia herba-alba* oil, *J. Bio-Tribo-Corros.*, 5 (1), 8.

[20] Zaher, A., Chaouiki, A., Salghi, R., Boukhraz, A., Bourkhiss, B., and Ouhssine, M., 2020, Inhibition of mild steel corrosion in 1M hydrochloric medium by the methanolic extract of *Ammi visnaga* L. Lam seeds, *Int. J. Corros.*, 2020, 9764206.

[21] Chaubey, N., Savita, Singh, V.K., and Quraishi, M.A., 2017, Corrosion inhibition performance of different bark extracts on aluminium in alkaline solution, *J. Assoc. Arab Univ. Basic Appl. Sci.*, 22, 38–44.

[22] Cookey, G.A., Tambari, B.L., and Iboroma, D.S., 2018, Evaluation of corrosion inhibition potentials of green tip forest lily (*Clivia nobilis*) leaves extract on mild steel in acid media, *J. Appl. Sci. Environ. Manage.*, 22 (1), 90–94.

[23] Dagdag, O., El Harfi, A., Cherkaoui, O., Safi, Z., Wazzan, N., Guo, L., Akpan, E.D., Verma, C., Ebenso, E.E., and Jalgham, R.T.T., 2019, Rheological, electrochemical, surface, DFT and molecular dynamics simulation studies on the anticorrosive properties of new epoxy monomer compound for steel in 1 M HCl solution, *RSC Adv.*, 9 (8), 4454–4462.

[24] Lavanya, D.K., Priya, F.V., and Vijaya, D.P., 2020, Green approach to corrosion inhibition of mild steel in hydrochloric acid by 1-[morpholin-4-yl(thiophen-2-yl)methyl]thiourea, *J. Fail. Anal. Prev.*, 20 (2), 494–502.

[25] Es'haghi, M., Amjad, A., Asghari, S., and Lotfi, A., 2018, Studying effect of plantain extract behavior as an eco-friendly corrosion inhibitor on the mild steel in 1 M HCl solution, *Anti-Corros. Methods Mater.*, 65 (3), 310–316

[26] Essien, E.A., Kavaz, D., Ituen, E.B., and Umoren, S.A., 2018, Synthesis, characterization and anticorrosion property of olive leaves extract-titanium nanoparticles composite, *J. Adhes. Sci. Technol.*, 32 (16), 1773–1794.

[27] Faiza, M., Zahari, A., Awang, K., and Hussin, H., 2020, Corrosion inhibition on mild steel in 1 M HCl

solution by *Cryptocarya nigra* extracts and three of its constituents (alkaloids), *RSC Adv.*, 10 (11), 6547–6562.

[28] Feng, L., Yang, H., Cui, X., Chen, D., and Li, G., 2018, Experimental and theoretical investigation on corrosion inhibitive properties of steel rebar by a newly designed environmentally friendly inhibitor formula, *RSC Adv.*, 8 (12), 6507–6518.

[29] Fouda, A.S., El-Abbasy, H.M., and El-Sherbini, A.A., 2018, Inhibitive effect of *Artemisia judaica* herbs extract on the corrosion of carbon steel in hydrochloric acid solutions, *Int. J. Corros. Scale Inhib.*, 7 (2), 213–235.

[30] Go, L.C., Depan, D., Holmes, W.E., Gallo, A., Knierim, K., Bertrand, T., and Hernandez, R., 2020, Kinetic and thermodynamic analyses of the corrosion inhibition of synthetic extracellular polymeric substances, *PeerJ Mater. Sci.*, 2, e4.

[31] Go, L.C., Holmes, W., and Hernandez, R., 2019, Sweet corrosion inhibition on carbon steel using waste activated sludge extract, *2019 IEEE Green Technologies Conference (GreenTech)*, 3-6 April 2019, Lafayette, LA, USA.

[32] He, T., Emori, W., Zhang, R.H., Okafor, P.C., Yang, M., and Cheng, C.R., 2019, Detailed characterization of *Phellodendron chinense* Schneid and its application in the corrosion inhibition of carbon steel in acidic media, *Bioelectrochemistry*, 130, 107332.

[33] Idouhli, R., Koumya, Y., Khadiri, M., Aityoub, A., Abouelfida, A., and Benyaich, A., 2019, Inhibitory effect of *Senecio anteuphorbium* as green corrosion inhibitor for S_{300} steel, *Int. J. Ind. Chem.*, 10 (2), 133–143.

[34] Wang, Q., Tan, B., Bao, H., Xie, Y., Mou, Y., Li, P., Chen, D., Shi, Y., Li, X., and Yang, W., 2019, Evaluation of *Ficus tikoua* leaves extract as an eco-friendly corrosion inhibitor for carbon steel in HCl media, *Biochemistry*, 128, 49–55.

[35] Loto, R.T., and Loto, C.A., 2018, Anti-corrosion properties of the symbiotic effect of *Rosmarinus officinalis* and trypsin complex on medium carbon steel, *Results Phys.*, 10, 99–106.

[36] Majd, M.T., Ramezanzadeh, M., Ramezanzadeh, B., and Bahlakeh, G., 2020, Production of an environmentally stable anti-corrosion film based on *Esfand* seed extract molecules-metal cations: Integrated experimental and computer modeling approaches, *J. Hazard. Mater.*, 382, 121029.

[37] Ngobiri, N.C., Oguzie, E.E., Oforka, N.C., and Akaranta, O., 2019, Comparative study on the inhibitive effect of Sulfadoxine–Pyrimethamine and an industrial inhibitor on the corrosion of pipeline steel in petroleum pipeline water, *Arabian J. Chem.*, 12 (7), 1024–1034.

[38] Ngobiri, N.C., and Okorosaye-Orubite, K., 2018, Corrosion pattern of pipeline steel in petroleum pipeline water in the presence of bio-mass derived extracts of *Brassica oleracea* and *Citrus paradise* mesocarp, *Mater. Sci. Appl.*, 9 (1), 216–141.

[39] Obot, I.B., Umoren, S.A., and Ankah, N.K., 2019, Pyrazine derivatives as green oil field corrosion inhibitors for steel, *J. Mol. Liq.*, 277, 749–761.

[40] Ogunleye, O.O., Arinkoola, A.O., Eletta, O.A., Agbede, O.O., Osho, Y.A., Morakinyo, A.F., and Hamed, J.O., 2020, Green corrosion inhibition and adsorption characteristics of *Luffa cylindrica* leaf extract on mild steel in hydrochloric acid environment, *Heliyon*, 6 (1), e03205.

[41] Ahmed, M.H.O., Al-Amiery, A.A., Al-Majedy, Y.K., Kadhum, A.A.H., Mohamad, A.B., and Gaaz, T.S., 2018, Synthesis and characterization of a novel organic corrosion inhibitor for mild steel in 1 M hydrochloric acid, *Results Phys.*, 8, 728–733.

[42] Othman, N.K., Yahya, S., and Ismail, M.C., 2019, Corrosion inhibition of steel in 3.5% NaCl by rice straw extract, *J. Ind. Eng. Chem.*, 70, 299–310.

[43] Qiang, Y., Zhang, S., Tan, B., and Chen, S., 2018, Evaluation of *Ginkgo* leaf extract as an eco-friendly corrosion inhibitor of X70 steel in HCl solution, *Corros. Sci.*, 133, 6–16.

[44] Radwan, A.B., Sliem, M.H., Yusuf, N.S., Alnuaimi, N.A., and Abdullah, A.M., 2019, Enhancing the corrosion resistance of reinforcing steel under aggressive operational conditions using behentrimonium chloride, *Sci. Rep.*, 9 (1), 18115.

[45] Rodič, P., and Milošev, I., 2019, The influence of additional salts on corrosion inhibition by

cerium(III) acetate in the protection of AA 7075-T6 in chloride solution, *Corros. Sci.*, 149, 108–122.

[46] Sangeetha, C., Chinnakani, C., and Selvaraj, S., 2020, *Jatropha gossyfolia* – A green inhibitor act as anticorrosive agent on carbon steel, *J. Adv. Sci. Res.*, 11 (1), 180–186.

[47] Sanni, O., Popoola, A.P.I., and Fayomi, O.S.I., 2018, Enhanced corrosion resistance of stainless steel type 316 in sulphuric acid solution using eco-friendly waste product, *Results Phys.*, 9, 225–230.

[48] Shahzad, K., Sliem, M., Shakoor, R.A., Radwan, A.B., Kahraman, R., Umer, M.A., Manzoor, U., and Abdullah, A.M., 2020, Electrochemical and thermodynamic study on the corrosion performance of API X120 steel in 3.5% NaCl solution, *Sci. Rep.*, 10 (1), 4314.

[49] Singh, D.K., Ebenso, E.E., Singh, M.K., Behera, D., Udayabhanu, G., and John, R.P., 2018, Non-toxic Schiff bases as efficient corrosion inhibitors for mild steel in 1 M HCl: Electrochemical, AFM, FE-SEM and theoretical studies, *J. Mol. Liq.*, 250, 88–99.

[50] Ikeuba, A.I., Ita, B.I., Okafor, P.C., Ugi, B.U., and Kporokpo, E.B., 2015, Green corrosion inhibitors for mild steel in H_2SO_4 solution: Comparative study of flavonoids extracted from *Gongronema latifolium* with crude extract, *Prot. Met. Phys. Chem*, 51 (6), 1043–1049.

[51] Solomon, M.M., Umoren, S.A., Quraishi, M.A., Tripathi, D.B., and Abai, E.J., 2020, Effect of akyl chain length, flow, and temperature on the corrosion inhibition of carbon steel in a simulated acidizing environment by an imidazoline-based inhibitor, *J. Pet. Sci. Eng.*, 187, 106801.

[52] Tamalmani, K., and Husin, H., 2020, Review on corrosion inhibitors for oil and gas corrosion issues, *Appl. Sci.*, 10 (10), 3389.

[53] Tian, H., Li, W., Liu, A., Gao, X., Han, P., Ding, R., Yang, C., and Wang, D., 2018, Controlled delivery of multi-substituted triazole by metal-organic framework for efficient inhibition of mild steel corrosion in neutral chloride solution, *Corros. Sci.*, 131, 1–16.

[54] Khayyun, T.S., and Mseer, A.H., 2019, Comparison of the experimental results with the Langmuir and Freundlich models for copper removal on limestone adsorbent, *Appl. Water Sci.*, 9 (8), 170.

[55] Umoren, S.A., and Ebenso, E.E., 2008, Studies of the anti-corrosive effect of *Raphia hookeri* exudate gum-halide mixtures for aluminium corrosion in acidic medium, *Pigm. Resin Technol.*, 37 (3), 173–182.

[56] Tian, Y., and Zheng, M., 2019, Inhibition effect of silicate and molybdate on the corrosion of SS 316 in neutral corrosive solution at high temperature, *Mater. Res. Express*, 6, 096569.

[57] Wang, C., Chen, J., Han, J., Wang, C., and Hu, B., 2019, Enhanced corrosion inhibition performance of novel modified polyaspartic acid on carbon steel in HCl solution, *J. Alloys Compd.*, 771, 736–746.

[58] Wang, X., Jiang, H., Zhang, D., Hou, L., and Zhou, W., 2019, *Solanum lasiocarpum* extract as green corrosion inhibitor for A3 steel in 1 M HCl solution, *Int. J. Electrochem. Sci.*, 14, 1178–1196.

[59] Zeino, A., Abdulazeez, I., Khaled, M., Jawich, M.W., and Obot, I.B., 2018, Mechanistic study of polyaspartic acid (PASP) as eco-friendly corrosion inhibitor on mild steel in 3% NaCl aerated solution, *J. Mol. Liq.*, 250, 50–62.

[60] Ugi, B.U., Bassey, V.M., Obeten, M.E., Adalikwu, S.A., and Nandi, D.O., 2020, Secondary plant metabolites of natural product origin-*Strongylodon macrobotrys* as pitting corrosion inhibitors of steel around heavy salt deposits in Gabu, Nigeria, *J. Mater. Sci. Chem. Eng.*, 8 (5), 38–60.

Synthesis of SO_4^{2-}/ZrO_2 Solid Acid and Na_2O/ZrO_2 Solid Base Catalysts Using Hydrothermal Method for Biodiesel Production from Low-Grade Crude Palm Oil

Sri Setyaningsih[1], Maisari Utami[2], Akhmad Syoufian[3], Eddy Heraldy[4], Nasih Widya Yuwono[5], and Karna Wijaya[3*]

[1]*Department of Science Education, Faculty of Teacher Training and Education, Universitas Islam Lamongan, Jl. Veteran No. 53A, Lamongan 62211, Indonesia*

[2]*Department of Chemistry, Faculty of Mathematics and Natural Sciences, Universitas Islam Indonesia, Jl. Kaliurang km. 14, Yogyakarta 55584, Indonesia*

[3]*Department of Chemistry, Faculty Mathematics and Natural Science, Universitas Gadjah Mada, Sekip Utara, PO BOX BLS 21, Yogyakarta 55281, Indonesia*

[4]*Department of Chemistry, Faculty of Mathematics and Natural Sciences, Sebelas Maret University, Jl. Ir. Sutami 36A, Surakarta 57126, Central Java, Indonesia*

[5]*Department of Soil Science, Faculty of Agriculture, Universitas Gadjah Mada, Jl. Flora, Bulaksumur, Yogyakarta 55281, Indonesia*

* ***Corresponding author:***

email: karnawijaya@ugm.ac.id

Received: April 20, 2021
Accepted: October 18, 2021

DOI: 10.22146/ijc.65404

Abstract: *Biodiesel is a renewable energy source that can be produced through esterification as well as transesterification reactions. This work presents a series of zirconia catalysts synthesized by hydrothermal method on various concentrations in acidic (H_2SO_4 0.3, 0.5, and 0.7 M) and basic (NaOH 1, 2, 3, and 4 M) solution to get a catalyst with the highest acidity or basicity. Characterizations of the catalysts were performed by FTIR, XRD, SEM-EDX, surface area analysis, acidity, and basicity test. The most active acid catalyst activity was evaluated for the esterification of low-grade crude palm oil (LGCPO), while the solid base catalyst was utilized for the transesterification reaction. The solid acid catalyst of 0.7 M SO_4^{2-}/ZrO_2 60 °C; 24 h was denoted as the most active acid catalyst with a total acidity of 1.86 mmol g^{-1}, while 4 M Na_2O/ZrO_2 60 °C; 24 h catalyst was considered as the solid base catalyst with the highest total basicity of 3.75 ± 0.12 mmol g^{-1}. The optimized acid catalyst exhibited a 31 times higher acidity than commercial ZrO_2. The concentration of free fatty acids (FFA) decreased to 68.87% in the esterification reaction. The solid base catalyst of 4 M Na_2O/ZrO_2 60 °C; 24 h successfully converted LGCPO into biodiesel by 68.55% through a transesterification reaction.*

Keywords: *SO_4^{2-}/ZrO_2 solid acid catalyst; Na_2O/ZrO_2 solid base catalyst; esterification; transesterification; biodiesel*

■ INTRODUCTION

More than 90% of the consumption of energy sources in the world is currently based on fossil fuels [1]. Fossil fuels are a limited source of energy. One effort to tackle the scarcity of fossil fuels is creating alternative fuels. Biodiesel is a monoalkyl ester compound that has the potential to be an alternative renewable fuel. Biodiesel has been widely accepted in the market because of its low sulfur content and higher octane number than petrodiesel [1]. The presence of 11–15% oxygen in biodiesel can accelerate the combustion process and reduce the number of particulates, soot, and CO gas. Therefore, greenhouse gas emissions are low [2-3].

Biodiesel is formed from the conversion of free fatty acids and triglycerides to methyl esters. The source of triglycerides (TG) and free fatty acids (FFA) are

generally contained in vegetable and animal oils [4]. Low Grade Crude Palm Oil (LGCPO) produced by the oil industry as a waste containing triglycerides and FFA can be used as raw material for forming methyl esters [5]. LGCPO has been used as raw material for low grade soap and boiler fuel. Therefore, processing LGCPO into biodiesel can increase its value. LGCPO raw materials are high abundance and inexpensive, so they have the potential to be developed on a large scale with low production costs [6].

In general, biodiesel is produced through a transesterification reaction by adding a base catalyst when the FFA number in the raw material is < 2 wt.%. Highly FFA will affect the formation of biodiesel. The concentration of FFA exceeds more than 1%, causing saponification when catalyzed using base catalysts such as NaOH [7]. The soap formation will complicate the separation process and cause a low yield. A two-step process through esterification reaction using an acid catalyst followed by transesterification using a base catalyst is employed to overcome this problem [8]. The acid catalyst is needed to reduce the concentration of FFA in the raw material by the esterification reaction [9]. Esterification is a reversible reaction that aims to reduce the concentration of FFA using an acid catalyst, where one mole of FFA will react with one mole of alcohol to form one mole of biodiesel and one mole of water [10-11].

Most methyl ester formation reactions are catalyzed by homogeneous base catalysts such as NaOH and KOH [1,8]. However, the application of homogeneous catalysts causes the separation process to be complicated, reactor corrosion, and an increasing amount of pollutants [12]. On the other hand, heterogeneous catalysts have advantages such as being easily separated and having low pollutants [8,13]. Therefore, the method of heterogeneous catalyst synthesis that is safe for the environment with low production costs is being developed [4]. The ideal characteristic of heterogeneous catalysts is a strong acid or base site, hydrophobic surface area, large pores interconnected, high activity, selective, stable to pressure and temperature [14-15]. For example, zirconia dioxide (ZrO_2) can be used as a catalyst and supporting material because it has redox activity and bifunctionality for both acidity and basicity properties [16-17]. Research using heterogeneous acid and base catalysts from ZrO_2 to produce biodiesel has evolved today [18-19].

Sulfated zirconia as a catalyst has been successfully synthesized using the sol-gel method, precipitation, and wet impregnation. The weakness of the sol-gel method is the difficulties of the preparation process on pH control, composition, and temperature that affect the synthesized material. In addition, the precursors are expensive. The route of material synthesis using the precipitation method is easier, but the shape of the particles is irregular, and the size distribution is wide. The material synthesized using the hydrothermal method has a lower crystallization temperature and agglomeration rate. The resulted powder is good without calcination. The shape and distribution of particle size are controlled [20]. However, no previous publication has developed a hydrothermal method to investigate the activity of monoclinic zirconia as an acid and base catalyst.

Sulfated zirconia (SO_4^{2-}/ZrO_2) has been reported to have super acidic properties [21]. The strong acid character is caused by the presence of sulfate ions which bind to the substrate [22]. Its high acid strength and combination of acid sites (Brønsted and Lewis) are the most significant factors in enhancing selectivity and activity [11]. The superiority of this catalyst is its high activity at relatively low temperatures [23]. SO_4^{2-}/ZrO_2 has a catalytic activity that can convert hydrocarbons at low temperatures [24]. The lack of SO_4^{2-}/ZrO_2 catalysts are the limited surface area that affects the acidity, so some modifications are developed to increase the acidity of the catalyst. The physical and chemical properties of this catalyst are determined by the sulfation method [25]. Synthesis in hydrothermal conditions offers significant advantages, such as easily controlling particle size and morphology by optimizing synthesis parameters and conditions [26]. Catalytic activities of SO_4^{2-}/ZrO_2 can be improved by optimizing the preparation conditions to enhance the zirconia framework's acidic strength [27].

The catalytic activity of ZrO_2 in the transesterification reaction is not great because of its

weak basic properties. On the other hand, the existence of empty sites on the surface of ZrO_2 facilitates molecular dispersion to be used as an excellent supporting material [28]. The prospect of supporting basic species on metal oxide supports is expected to tune the basicity and redox properties, leading to a more active and selective catalytic system [29]. The common method used to increase the basic strength of the catalyst is by modifying a supporting material using alkali and alkaline earth metals [30]. It is well-known that alkali metals (such as Li, Na, and K) or alkaline earth have good interactions for transesterification reactions and can be applied to supporting materials such as bentonite, Al_2O_3, SiO_2, and activated carbon. The metals loading on a supporting material produces heterogeneous catalysts that can increase the transesterification reaction's activity [31]. Modifying the ZrO_2 matrix with NaOH to synthesize heterogeneous base catalysts with high catalytic activity becomes challenging to develop.

Catalyst synthesis using the hydrothermal method is expected to increase the dispersion of SO_4^{2-} or Na^+ in the ZrO_2 matrix and strengthen the acidity or basicity of the catalyst. This research led to synthesizing SO_4^{2-}/ZrO_2 solid acid and Na_2O/ZrO_2 solid base catalyst by hydrothermal method for converting LGCPO to biodiesel. The method is highlighted to enhance the catalytic performance of both catalysts by providing more acid and base sites for the potential applications of biodiesel production. The solid catalysts and the catalytic activities of the obtained product are optimized to obtain the best results.

■ EXPERIMENTAL SECTION

Materials

Commercial zirconium dioxide (ZrO_2) was acquired from Jiaozou Huasu Chemical Co., Ltd (Henan, China). LGCPO was obtained from one of the palm oil factories in Kabupaten Lampung Selatan, Lampung, Indonesia. The analytical reagents were sulfuric acid (H_2SO_4 98%), sodium hydroxide (NaOH), ammonium hydroxide (NH_4OH 25%), methanol (CH_3OH), hydrochloric acid (HCl), potassium hydroxide (KOH), sodium sulfate anhydrous (Na_2SO_4), oxalic acid ($C_2H_2O_4$) and phenolphthalein indicators purchased from Merck.

Instrumentation

The catalysts were characterized using Fourier Transform Infrared Spectrophotometer (FTIR, Shimadzu Prestige-21), Scanning Electron Microscope (SEM, JEOL JSM-6510) combined with Energy Dispersive X-Ray (EDS, JED-2300 Analysis Station) and Surface Area Analyzer (SAA, Quadrasorb EVO Model QDS-30). The transesterification products were analyzed using Gas Chromatography-Mass Spectrometer (GC-MS, Shimadzu QP2010S), Fourier Transform Infrared Spectrophotometer (FTIR, Shimadzu Prestige-21), and Proton Nuclear Magnetic Resonance Spectrometer (^{1}H-NMR, NMR JEOL NMR 500 MHz).

Procedure

Synthesis of SO_4^{2-}/ZrO_2 solid acid and Na_2O/ZrO_2 solid base catalysts

The SO_4^{2-}/ZrO_2 catalysts were synthesized from 5 g of ZrO_2 and 75 mL of H_2SO_4 with various concentrations of 0.3, 0.5, and 0.7 M using the hydrothermal method. After being mixed perfectly, it was put into an autoclave and heated at a temperature of 60 °C for 24 h. The solid mixture and solution were separated by centrifugation at 2500 rpm for 15 min. Finally, the separate solids were heated at a temperature of 105 °C for 24 h [32]. Catalysts that have been synthesized were labeled as 0.3 M SO_4^{2-}/ZrO_2 60 °C; 24 h, 0.5 M SO_4^{2-}/ZrO_2 60 °C; 24 h, and 0.7 M SO_4^{2-}/ZrO_2 60 °C; 24 h. The catalysts were then characterized using FTIR and acidity tests.

The Na_2O/ZrO_2 catalysts were synthesized by a similar method using NaOH 1, 2, 3, and 4 M. The mixture was then heated at a temperature of 60 °C for 12 h in an autoclave. The catalysts were denoted as 1 M Na_2O/ZrO_2 60 °C; 12 h, 2 M Na_2O/ZrO_2 60 °C; 12 h, 3 M Na_2O/ZrO_2 60 °C; 12 h, and 4 M Na_2O/ZrO_2 60 °C; 12 h then characterized using FTIR and basicity test.

Characterization of SO_4^{2-}/ZrO_2 solid acid and Na_2O/ZrO_2 solid base catalysts

Each catalyst was characterized using Fourier Transform Infrared Spectrophotometer (FTIR, Shimadzu Prestige-21). Catalyst powder was diluted to an appropriate concentration of dry KBr with a ratio of 1:10 (catalyst:KBr) and pressed into a pellet using a

compressor. The infrared spectrum was collected at 400–4000 cm^{-1}.

The acidity test of the acid catalyst was carried out using the gravimetric method. First, the empty crucible was weighed as W_0. Next, a sample of 0.1 g was put into a crucible, heated at a temperature of 105 °C for one hour, then cooled and weighed as W_1. The crucible containing the sample was placed into a desiccator and then vacuumed. Ammonia was heated then flowed the vapor into a desiccator. The sample was allowed to stand for 24 h and then weighed as W_2 [17]. The acidity test was determined using NH_3 as a basic probe molecule. The total amount of adsorbed ammonia was calculated using the following equation:

$$\text{Total acidity (mmol g}^{-1}) = \frac{W_2 - W_1}{(W_1 - W_0) \times \text{Mr NH}_3} \times 1000 \quad (1)$$

The catalyst basicity test was carried out using an acid-base titration method. A sample of 0.1 g was mixed with 10 mL of distilled water. The mixture was stirred using a magnetic stirrer for one hour. 3–5 drops of phenolphthalein indicator were added and titrated using 0.01 M HCl. The titration was carried out until it reached the equivalence point and was repeated three times. The total volume of HCl in mL has been obtained was entered into Eq. (2) to obtain the total basicity of the catalyst [33].

$$\text{Total basicity (mmol g}^{-1}) = \frac{V_{HCl}(\text{mL}) \times M_{HCl}(\text{M})}{\text{mass of catalyst (g)}} \quad (2)$$

The SO_4^{2-}/ZrO_2 catalyst with the highest total acidity and the Na_2O/ZrO_2 catalyst with the highest total basicity calcined at various temperatures of 400, 500, 600, 700, and 800 °C, then characterized using X-Ray Diffractometer (XRD, X PHILIPS XPert MPD). The catalyst was ground to a fine powder then placed into a sample holder. Diffractogram was recorded at 2θ = 10–45° using XRD with an X-ray source of Cu Kα radiation (λ = 1.5406 Å).

The calcined catalyst with the highest total acidity and basicity was characterized using SEM combined with EDX and Surface Area Analyzer (SSA). The analysis of surface topography and composition of the catalyst was carried out with SEM (JEOL JSM-6510) equipped with an EDS (JED-2300 Analysis Station) spectrometer. Carbon tape was attached on the sample stage, and the catalyst powder was placed on the carbon tape then vacuumed. The energy resolution was 200 eV. The pressure of the SEM chamber was about 10^{-3} Pa. The accelerating voltage was set to 15 kV. The probe current was set to 10 nA. The SEM-EDX analysis was set to 300 sec. The specific surface area and pore size analysis were performed using Quadrasorb EVO Model QDS-30. The catalyst was loaded into analysis stations. The catalyst was degasified to free surfaces from contaminants such as water and oils under a vacuum. The sample was brought to a constant temperature. Then, nitrogen gas flowed to the sample chamber.

The esterification reaction using SO_4^{2-}/ZrO_2 solid acid catalyst

The raw material of LGCPO was heated at 105 °C to vaporize water and filtered to remove impurities. The molecular weight of LGCPO was determined by saponification, while the concentration of FFA in LGCPO was determined by titration method using a KOH solution [34-35]. The SO_4^{2-}/ZrO_2 solid acid catalyst has the highest total acidity applied in the esterification reaction.

Optimization of esterification conditions was carried out on three different parameters on wt.% catalyst, the molar ratio of LGCPO to methanol, and reaction time. The SO_4^{2-}/ZrO_2 solid acid catalyst on 1, 3, 5, and 7 wt.% of the total mass of LGCPO and methanol with the molar ratio of LGCPO: methanol = 1:9 inserted into a three-necked round-bottom flask, followed by methanol at the molar ratio LGCPO: methanol = 1:9. The mixture was magnetically stirred at 600 rpm in an oil bath, maintaining a constant temperature of 45 °C for 10 min. Then 25 g LGCPO was added to the mixture, and the reaction was continued at 55 °C for 20 min. The study of the effect of the molar ratio of LGCPO to methanol on %FFA LGCPO was conducted on ratios of 1:3, 1:6, and 1:12, and reaction times varied for 40 and 60 min. Free Fatty Acid concentrations contained in esterified oil were determined, and the reduction of FFA (%) was calculated using Eq. (3) [36].

$$\text{FFA Reduction (\%)} = \frac{\text{\%FFA LGCPO} - \text{\%FFA esterified oil}}{\text{\%FFA LGCPO}} \times 100\% \quad (3)$$

Transesterification reaction using Na_2O/ZrO_2 solid base catalyst

The Na_2O/ZrO_2 solid base catalyst with 7 wt.% of the total mass of LGCPO and methanol with the molar ratio of LGCPO: methanol = 1:24 inserted into a three-necked round-bottom flask, followed by methanol at the molar ratio LGCPO: methanol = 1:24. The mixture was magnetically stirred at 600 rpm in an oil bath, maintaining a constant temperature of 45 °C for 10 min. Then, 20 g esterified oil was added to the mixture, and the reaction was continued at 55 °C for 20 min.

The transesterification compound was characterized using FTIR and analyzed using Gas Chromatography-Mass Spectrometer (GC-MS, Shimadzu QP2010S). The formed methyl ester was analyzed using Proton Nuclear Magnetic Resonance Spectrometer (^{1}H-NMR, NMR JEOL NMR 500 MHz) to identify the %conversion of methyl ester (C_{ME}), which was calculated based on the proton integration of proton between triglycerides (I_{TAG}) with a methoxy (I_{ME}) using Eq. (4) [37].

$$C_{ME} = 100 \times \frac{5 \times I_{ME}}{5 \times I_{ME} + 9 \times I_{TAG}} \quad (4)$$

■ RESULTS AND DISCUSSION

Synthesis and Characterization of SO_4^{2-}/ZrO_2 Solid Acid Catalysts

Catalyst synthesis studies on various H_2SO_4 concentrations were conducted to determine the effect of the concentration of H_2SO_4 on the acidity properties of the catalyst. Characterization using FTIR explains the existence of a functional group owned by a material. Fig. 1 gives information on the differences in the absorption peaks for each catalyst. The absorption of the functional sulfate group belongs to the wavenumber of 750–1350 cm^{-1}. Absorption at that wavenumber is characteristic of inorganic chelate formation where sulfate ions bidentate coordinate with metal cation [38].

The sharpness of the peak for the three catalysts at wavenumbers between 1000–1300 cm^{-1} looks fluctuating. The absorption peak of catalyst at a concentration of 0.5 M H_2SO_4 looks sharper than the others, but the decline in transmittance is followed by a decrease in transmittance at other wavenumbers. These indications do not show the catalyst acidity with a concentration of H_2SO_4 0.5 M greater than 0.7 M due to decreased transmittance on the spectra. On the other hand, the absorption of ZrO_2 catalyst with a concentration of H_2SO_4 0.7 M appears blunter than other catalysts. It can be analyzed that the vibrations which tend to be detected are sulfate groups dispersed on ZrO_2. Pavia et al. [39] explained that the vibration of the S–O bond of the sulfonate group was in the absorption band 1000–750 cm^{-1}, which was marked by the appearance of several peaks, whereas the S=O bond had asymmetric and symmetry stretch vibrations detected at 1350 and 1175 cm^{-1}, respectively.

The results of the acidity test on various H_2SO_4 concentrations are listed in Table 1 to strengthen the analysis. The total acidity is obtained from the number of ammonia bases absorbed in the catalyst. Total acidity is defined as the total number of sites of Brønsted and Lewis acids in mmol g^{-1}. Catalysts synthesized using

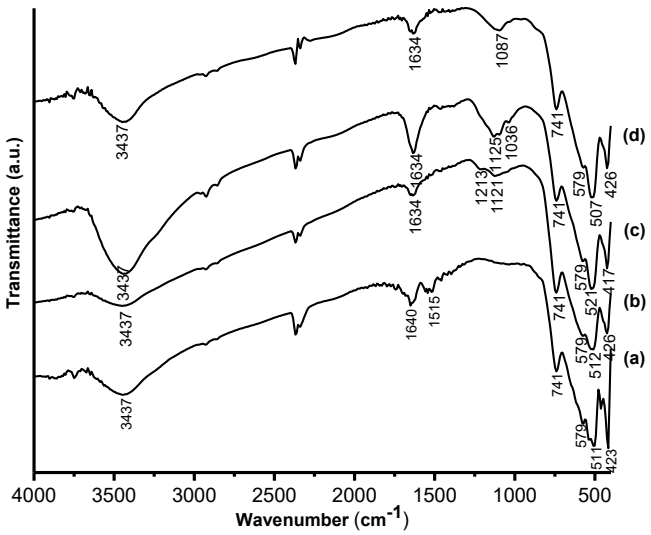

Fig 1. FTIR spectra of (a) ZrO_2 and SO_4^{2-}/ZrO_2 60 °C; 24 h catalyst on various H_2SO_4 concentration (b) 0.3 M, (c) 0.5 M, and (d) 0.7 M

Table 1. The result of the acidity test of SO_4^{2-}/ZrO_2 catalyst on various H_2SO_4 concentrations

Catalyst	Total acidity (mmol g^{-1})
0.3 M SO_4^{2-}/ZrO_2 60 °C; 24 h	0.68
0.5 M SO_4^{2-}/ZrO_2 60 °C; 24 h	1.35
0.7 M SO_4^{2-}/ZrO_2 60 °C; 24 h	1.86

H_2SO_4 0.7 M has a total acidity of 1.86 mmol g^{-1}. That acidity value is higher than ZrO_2, with a total acidity of 0.06 mmol g^{-1}. The results show that a greater concentration of sulfuric acid increases the total acidity. Increased total acidity correlated with the formation of the number of acid sites. The addition of H_2SO_4 will initiate the formation of sulfate ion coordination to the Zr site. The coordination of sulfate groups on ZrO_2 adds acidic sites to the surface. The super acidic properties of this material can be related to the formation of S=O, which is naturally formed in the complex due to the interaction between ZrO_2 and sulfate ions so that the S=O group provides a strong induction effect [21].

The study of the effect of calcination temperature aims to determine the ZrO_2 crystal phase transformation. The results of FTIR characterization of 0.7 M SO_4^{2-}/ZrO_2 60 °C; 24 h catalyst on various calcination temperatures are shown in Fig. 2. The absorption bands at the wavenumbers of 429, 518, 585, 740, 1633, and 3426 cm^{-1} are detected on each catalyst. The FTIR spectra of the catalyst after sulfonation can be observed with the appearance of an absorption band at the wavenumber 1045 cm^{-1}, which is the vibration of the O=S=O group [40]. The vibration of the $-SO_3H$ group is detected at 1149 cm^{-1}. The absorption band at 1237 cm^{-1} is the vibration of S–O [41]. The appearance of absorption at 3426 cm^{-1} is suspected of the vibration from the $-SO_2OH$ group [42]. The absorption bands at 990, 1050-1060, 1130–1140, and 1220–1230 cm^{-1} indicate the coordination of sulfate bidental ion in Zr^{4+}. The FTIR spectra do not show that the existence of that group significantly changes after being calcined.

The results of the acidity test of the catalysts in various calcination temperatures are displayed in Table 2. The total acidity of the catalyst decreases as the calcination temperature increases. These changes indicate a strong interaction between sulfate anion with ZrO_2 [43]. Sulfur is estimated to reach the highest oxidation level of S^{6+} as SO_4^{2-} as the main species when heated. The increase in heat energy will break the bond between sulfate and ZrO_2, so catalyst acidity decreases.

The catalyst phase structure influences the selectivity of chemical reactions. Zirconium dioxide in the tetragonal phase is more sensitive than ZrO_2 in the monoclinic phase. In addition, the specific surface area and appropriate pore size also affect the performance of catalysts in reaction. Sulfate anions that enter the zirconia framework can increase the thermal stability of the material. Incorporating a functional acid group can improve the catalytic acid site to be used as a catalyst in biodiesel production [16].

Adsorption of oxygen ions on the surface of ZrO_2 can trigger phase transformation [23]. Shi et al. [38] explained that the monoclinic crystal phase is very influential in impregnating sulfate groups on the zirconia surfaces. This influence is related to the inhibition of Zr^{3+} formation in the monoclinic phase. The formation of Zr^{3+} can occur in the presence of an oxygen vacancy in the tetragonal phase. Thus, more sulfate groups can bind to the surface of the zirconia. The more sulfate groups that can be impregnated, the acidity site will increase along with the increased catalysis activity [38].

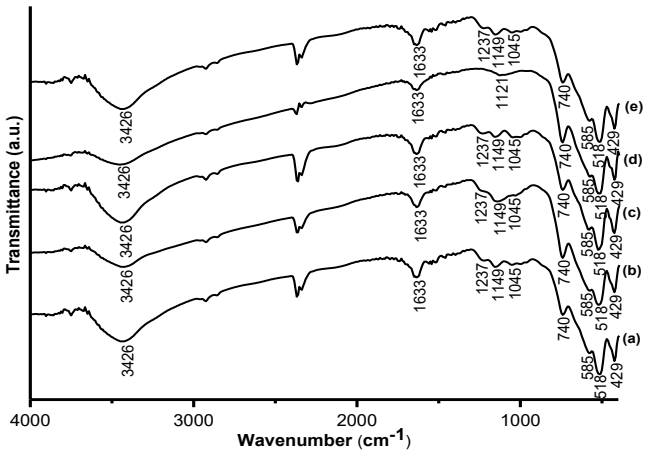

Fig 2. FTIR spectra of 0.7 M SO_4^{2-}/ZrO_2 60 °C; 24 h catalyst on various calcination temperature (a) 400, (b) 500, (c) 600, (d) 700, and (e) 800 °C

Table 2. The result of the acidity test of 0.7 M SO_4^{2-}/ZrO_2 60 °C; 24 h catalyst on the various calcination temperature

Catalyst	Total acidity (mmol g^{-1})
0.7 M SO_4^{2-}/ZrO_2-400	0.67
0.7 M SO_4^{2-}/ZrO_2-500	0.46
0.7 M SO_4^{2-}/ZrO_2-600	0.24
0.7 M SO_4^{2-}/ZrO_2-700	0.12
0.7 M SO_4^{2-}/ZrO_2-800	0.11

The result of the catalyst characterization using the XRD is shown in Fig. 3. Based on PDF 01-089-9066, the entire peaks appear on the XRD patterns showing a monoclinic ZrO_2. Increasing temperature up to 800 °C does not change the catalyst phase 0.7 M SO_4^{2-}/ZrO_2. No significant changes can be observed at 2θ = 28.21° and 31.46° [44].

Morphology of ZrO_2 and 0.7 M SO_4^{2-}/ZrO_2 60 °C; 24 h catalyst are shown in Fig. 4. ZrO_2 has an irregular shape. The size of the material becomes smaller and uniform, with an imperfect round shape after sulfation. Spherical particles tend to have good reactant transport properties. The use of strong acids triggers framework shrinkage and damage some bonds, resulting in smaller particle sizes and changes in passageways between materials. Based on the results of the EDS compiled in Table 3, the sulfur on the surface of ZrO_2 reached 1.07%. The dot mapping results show that the sulfur element is evenly distributed and does not show clumping on any particular side.

The performance of this catalyst is determined by the strength and accessibility of the active acid site to large compounds such as triglycerides and FFA [45]. The physical properties of the catalyst obtained using N_2 adsorption and pore size analysis of the catalyst are summarized in Table 3. Based on these results, it can be seen that the incorporation of sulfuric acid groups in

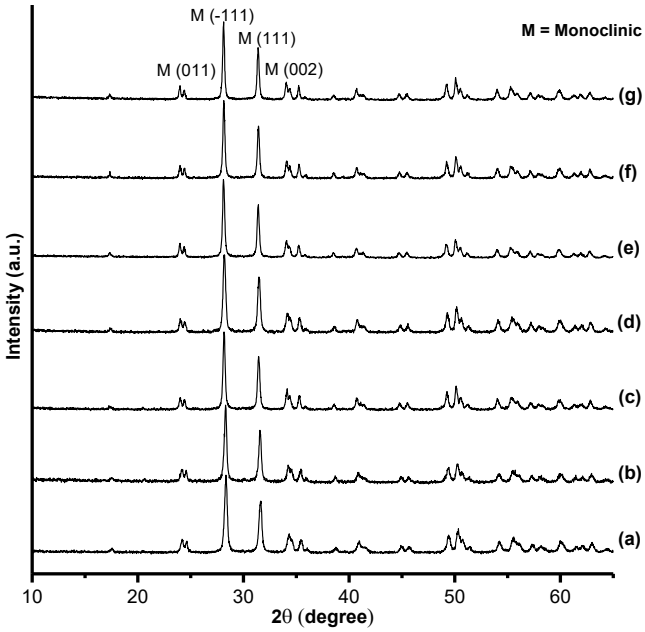

Fig 3. The XRD patterns of catalyst (a) ZrO_2, (b) 0.7 M SO_4^{2-}/ZrO_2 60 °C; 24 h at the calcination temperature (c) 400, (d) 500, (e) 600, (f) 700, and (g) 800 °C

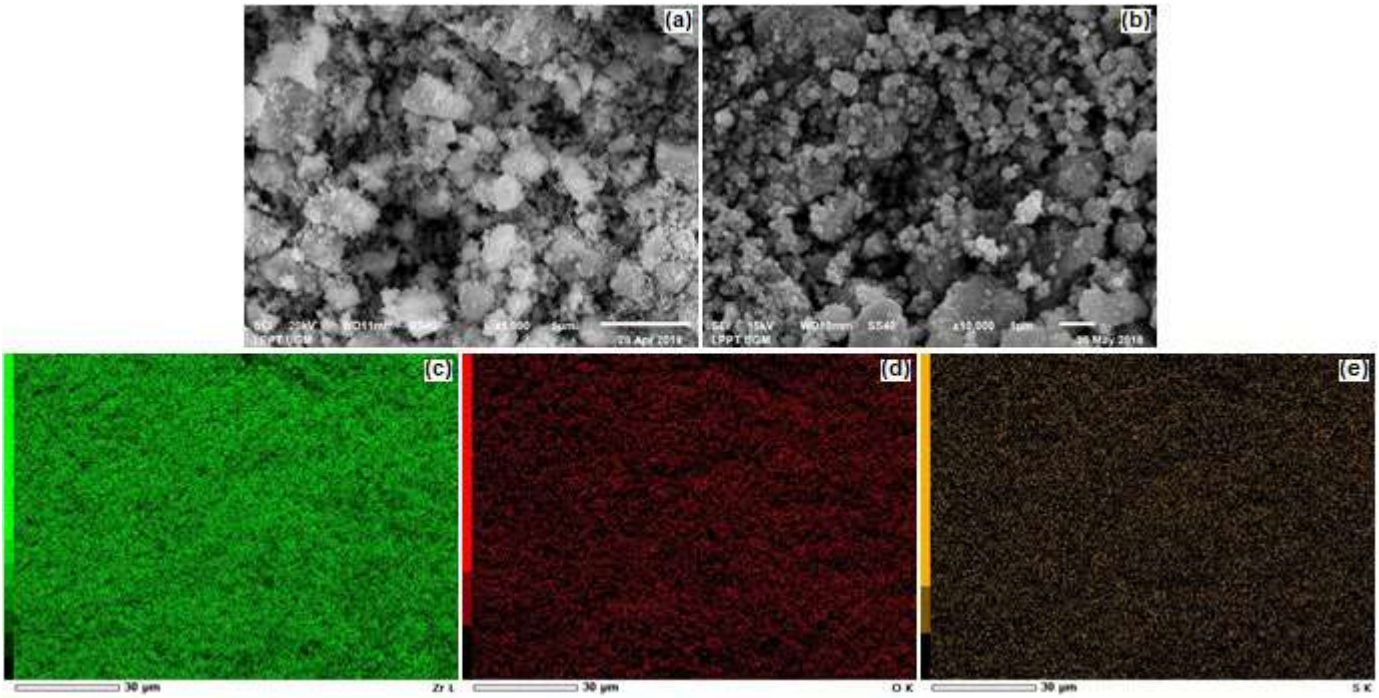

Fig 4. SEM images of catalyst (a) ZrO_2 at magnification 5000×, (b) 0.7 M SO_4^{2-}/ZrO_2 60 °C; 24 h at magnification 10.000×, the dot mapping element of (c) zirconium (d) oxygen and (e) sulfur

Table 3. The elemental composition and surface area analysis of the acid catalyst

Catalyst	% of Element mass			Properties		
	Zr	O	S	S_{BET} [a] ($m^2\ g^{-1}$)	V_p [b] ($cm^3\ g^{-1}$)	D_p [c] (Å)
ZrO_2	69.67	25.20	-	13.95	1.74×10^{-2}	25.02
0.7 M SO_4^{2-}/ZrO_2 60 °C; 24 h	64.52	28.48	1.07	9.21	1.25×10^{-2}	27.19

[a] Specific surface area
[b] Pore diameter
[c] Pore volume taken at $P/P_o = 0.90$

zirconia decreases the pore volume and surface area of the sulfated zirconia catalyst. The surface area of the catalyst decreased to 9.21 $m^2\ g^{-1}$. The sulfur element has a diameter of 1.02 Å. An increase in pore diameter is possible due to damage to the structure by acids and the formation of bonds between S and ZrO_2. The interaction between sulfate ions and ZrO_2 protects the catalyst from sintering [21].

The pore size of the synthesized catalyst is around 27.19 Å. Triglyceride molecules have a dimension of 2.5 nm and can easily fit into the internal surface of the catalyst so that the reaction can take place on the entire catalyst's active site. Large reactants such as triglycerides are not restricted to access catalytic sites. Catalytic activity occurs on external and internal surfaces [31].

Application of SO_4^{2-}/ZrO_2 Solid Acid Catalyst on Esterification Reactions

Esterification is part of an organic reaction that aims to form an ester of a mixture of acid and alcohol. In this research, biodiesel was made from the raw material of LGCPO. LGCPO was produced from the palm oil industry, so it needs to be filtered and evaporated. A heterogeneous catalyst is easily degraded by H_2O [3]. The presence of water acts as an impurity. Water will block the active site of the catalyst, which causes its catalytic activity to diminish. Triglycerides will be hydrolyzed to form glycerol and FFA. FFA in LGCPO will react with a basic catalyst to form soap which deactivates the catalyst and makes the separation process more difficult. The scheme of triglycerides hydrolysis is illustrated in Fig. 5.

Effect of wt.% catalyst on %FFA LGCPO

The concentration of FFA is denoted in %FFA. The FFA concentration in the LGCPO is 1.40%. %FFA of each reaction at various conditions is presented in Table 4. There

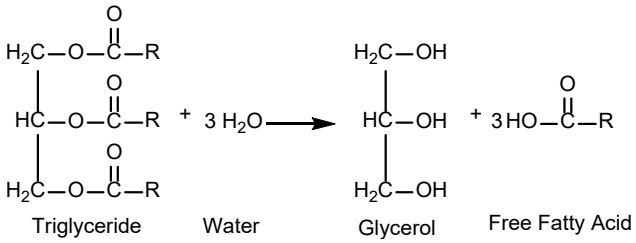

Fig 5. Schematic of triglycerides hydrolysis

is a tendency that shows an increase in wt.% of the catalyst inversely with %FFA. The more amount of catalysts used, the lower the acidity of the oil. The lowest %FFA is obtained when the wt.% of catalyst used is 7%. The esterification reaction that took place using 7 wt.% of catalyst can reduce acidity by 58.01%. Decreasing oil acidity can be attributed to the conversion of FFA to ester. The greater the number of catalysts, the more catalytic's active sites are available for the reaction.

Effect of the molar ratio of LGCPO to methanol on %FFA LGCPO

The molar ratio of LGCPO to methanol is a factor that influences the reduction of FFA concentration. The addition of excess alcohol can accelerate the reaction and is preferred in the formation of biodiesel. Theoretically, the formation of one mole Fatty Acid Methyl Esters (FAME) and one mole of water requires one mole of methanol and one mole of FFA. Excess methanol is needed so the reaction equilibrium shifts towards the product, updating the catalyst surface by removing water molecules from surfaces and regenerating catalytic sites [10,31].

The reduction of %FFA is directly proportional to the molar ratio of methanol. A significant reduction in %FFA is observed at a molar ratio of 1:6. At larger ratios, the FFA decreases until it reaches a maximum reduction

Table 4. The results of %FFA LGCPO in the esterification reaction on various parameters

Catalyst type	Reaction parameters			FFA concentration (%)
	wt.% Catalyst (%)	Molar ratio LGCPO:methanol	Reaction time (min)	
Without catalyst	-	1:12	20	1.24
ZrO_2	7	1:12	20	1.08
0.7 M SO_4^{2-}/ZrO_2 60 °C; 24 h	1	1:9	20	1.10
0.7 M SO_4^{2-}/ZrO_2 60 °C; 24 h	3	1:9	20	0.85
0.7 M SO_4^{2-}/ZrO_2 60 °C; 24 h	5	1:9	20	0.81
0.7 M SO_4^{2-}/ZrO_2 60 °C; 24 h	7	1:3	20	1.24
0.7 M SO_4^{2-}/ZrO_2 60 °C; 24 h	7	1:6	20	0.68
0.7 M SO_4^{2-}/ZrO_2 60 °C; 24 h	7	1:9	20	0.59
0.7 M SO_4^{2-}/ZrO_2 60 °C; 24 h	7	1:12	20	0.44
0.7 M SO_4^{2-}/ZrO_2 60 °C; 24 h	7	1:12	40	0.58
0.7 M $SO_4^{2-}/ZrO_2$60 °C; 24 h	7	1:12	60	0.58
0.7 M SO_4^{2-}/ZrO_2 60 °C; 24 h-500	7	1:12	20	1.01

of 68.87% when the molar ratio was 1:12. The more methanol used, the more the formation of methoxy species will be, the reaction will eventually shift towards the product. At low ratios, the produced methoxy ions are also low, so the yield is slight. If the molar ratio is too low, the oil volume fraction in the mixture is high. Then it greatly allows the catalyst to be at the oil phase. The oil covers the catalyst surface then reduces the formation of methoxy ions so that the yield decreases. The oil and methanol interface areas depend on the dispersion of these solutions with each other [46]. Improved interface area makes it easier to transfer methoxy ions faster from the aqueous phase to the organic phase.

Effect of reaction time on %FFA LGCPO

The influence of time reaction was carried out for 20, 40, and 60 min. The addition of reaction time does not give a significant reduction. The best reduction of %FFA lasts for 20 min, giving a decline of 68.87%. Mass transfer between oil and alcohol will increase when the given residence time is longer [10]. The optimum time needed in this reaction is 20 min. The mixture is sufficiently dispersed during this time. Increasing the reaction time will shift the equilibrium towards the reactants because the reaction is reversible and triggers the deactivation of the $-SO_3H$ acid site due to bonds with a polar molecule from reaction mixtures such as H_2O [42]. The prediction of the mechanism of esterification reaction on SO_4^{2-}/ZrO_2 solid acid catalyst are shown in Fig. 6 and 7.

The esterification reaction is carried out under different conditions to examine the performance of the catalyst [47]. The reaction within 20 min without a catalyst resulted in an 11.24% reduction. Sulfated zirconia can reduce FFA up to 68.87%. This value shows that SO_4^{2-}/ZrO_2 catalyst has better performance than ZrO_2. Therefore, it can be confirmed that modification using H_2SO_4 improves catalyst performance. The %FFA test results show that the performance of the SO_4^{2-}/ZrO_2 catalyst calcined at 500 °C decreased. This data supports that the acidity of the catalyst greatly influences the catalyst performance.

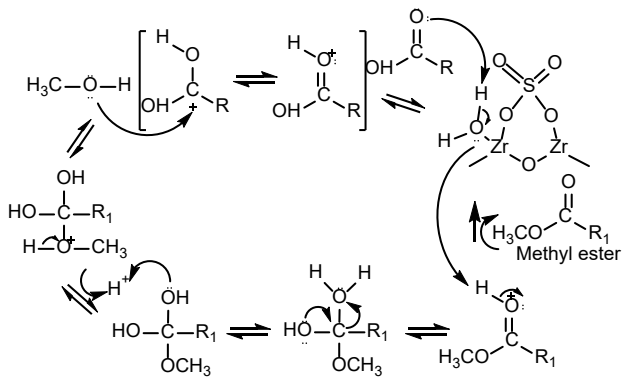

Fig 6. Prediction of the esterification reaction mechanism on Brønsted acid site of SO_4^{2-}/ZrO_2 solid acid catalyst

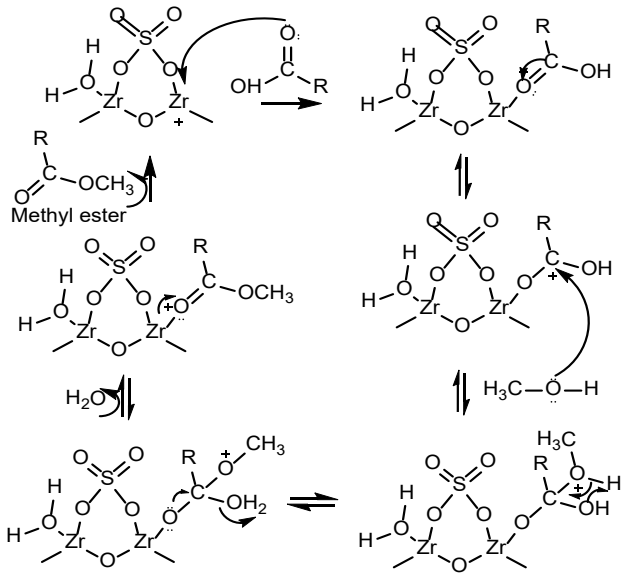

Fig 7. Prediction of the esterification reaction mechanism on Lewis acid site of SO_4^{2-}/ZrO_2 solid acid catalyst

Synthesis and Characterization of Na_2O/ZrO_2 Solid Base Catalysts

Characterization of the catalyst using FTIR on various NaOH concentrations is shown in Fig. 8. This study is carried out to determine the effect of the amount of NaOH on the basic properties of the base catalyst. The FTIR spectra show that each catalyst has absorption at wavenumbers 422, 500, 583, 745, 871, 1455, 1637, and 3432 cm^{-1}. The Na_2O/ZrO_2 catalyst can absorb CO_2 from the environment. The greater concentration of base that is given in the reaction, the more CO_2 will be absorbed. As a result, the CO_3^{2-} absorption band appears even sharper. There are several changes observed in Fig. 8. The sharpness of the vibration of Zr–O–Na asymmetry detected at 1637 cm^{-1} decreases with the increasing concentration of NaOH. This is possibly due to the large addition of Na covering the substrate surface. Based on Table 5, the catalyst that uses NaOH 4 M has the highest total basicity value. The addition of sodium ions triggers the formation of strong basic sites. Active sites increase with the increasing number of alkali metals on ZrO_2 [28].

The FTIR spectra of 4 M Na_2O/ZrO_2 60 °C; 12 h catalyst on various calcination temperatures are shown in Fig. 9. Absorption bands at wavenumbers 423, 500, 576, 750, 865, 1446, 1577, 2852, 2918, and 3420 cm^{-1} are detected on each catalysts. In general, there is a tendency that shows a decrease in the sharpness of vibration CO_3^{2}. These results are confirmed by the basicity test results given in Table 6, which show that the basicity of the

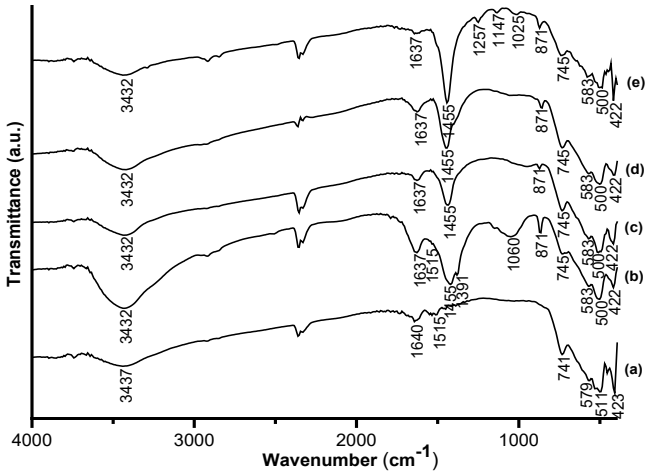

Fig 8. FTIR spectra of (a) ZrO_2 and Na_2O/ZrO_2 60 °C; 12 h catalyst on various NaOH concentration (b) 1 M, (c) 2 M, (d) 3 M, and (e) 4 M

Table 5. The result of basicity test of Na_2O/ZrO_2 catalyst on various NaOH concentrations

Catalyst	Total basicity (mmol g^{-1})
1 M Na_2O/ZrO_2 60 °C; 12 h	0.56 ± 0.01
2 M Na_2O/ZrO_2 60 °C; 12 h	1.43 ± 0.04
3 M Na_2O/ZrO_2 60 °C; 12 h	1.83 ± 0.02
4 M Na_2O/ZrO_2 60 °C; 12 h	3.75 ± 0.12

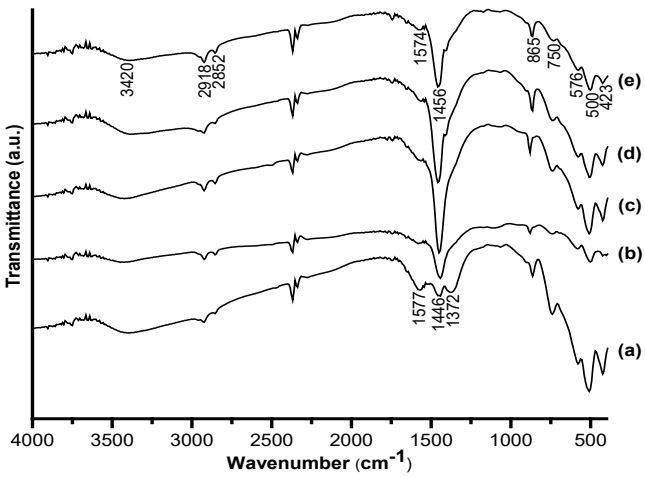

Fig 9. FTIR spectra of 4 M Na_2O/ZrO_2 60 °C; 12 h catalyst on various calcination temperature (a) 400, (b) 500, (c) 600, (d) 700, and (e) 800 °C

catalyst tends to decrease after calcination. The result of catalyst characterization using XRD is shown in Fig. 10. The existence of the monoclinic ZrO_2 phase is characterized by the appearance of peaks at 2θ = 28.21° and 31.46°. Temperature rising to 800 °C does not change the catalyst phase.

Fig. 11 shows the SEM image of 4 M Na_2O/ZrO_2 60 °C; 12 h at a magnification of 1000× and 3000×. The size of the material becomes smaller and uniform with the forms of granules that overlap each other. Based on the results of EDS compiled in Table 7, Na dispersed on the surface of ZrO_2 reached 8.41%. The results of the physical properties characterization of catalysts are reported in Table 7. Based on these results, it can be seen that modified zirconia has decreased pore volume and surface area. The surface area of the modified catalyst has decreased to 10.38 m^2 g^{-1}. These changes are related to changes in the surface of the catalyst. Na covers the surface of the pore of the catalyst [48]. The detected pores are pseudo pores.

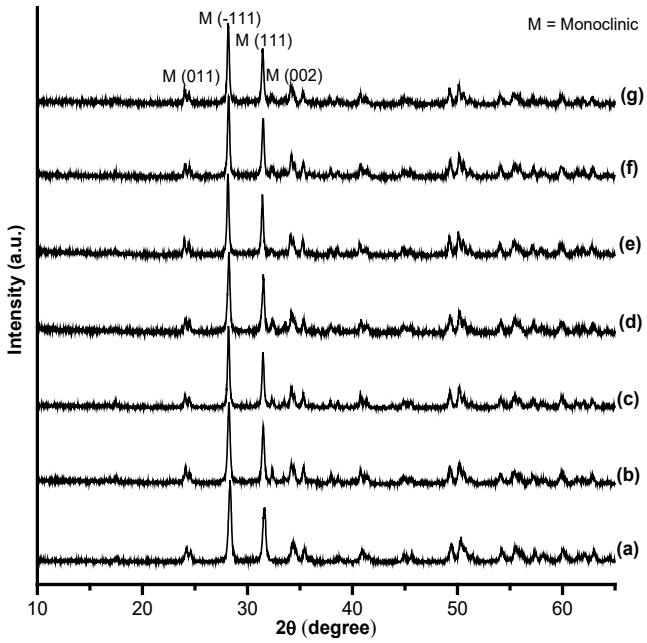

Fig 10. The XRD patterns of catalyst (a) ZrO_2, (b) 4 M Na_2O/ZrO_2 60 °C; 12 h at the calcination temperature (c) 400, (d) 500, (e) 600, (f) 700, and (g) 800 °C

Application of Na_2O/ZrO_2 Solid Base Catalyst for Transesterification Reaction

At this stage, the esterified LGCPO with the lowest FFA concentration is used as a source of triglycerides. The reaction temperature is chosen at the optimum temperature of 55 °C. The optimum temperature is the temperature that closes to the boiling point of methanol, where methanol is

Table 6. The result of basicity test of 4 M Na_2O/ZrO_2 60 °C; 12 h catalyst on the various calcination temperature

Catalyst	Total basicity (mmol g^{-1})
4 M Na_2O/ZrO_2-400	3.07 ± 1.06
4 M Na_2O/ZrO_2-500	3.03 ± 0.06
4 M Na_2O/ZrO_2-600	2.98 ± 0.05
4 M Na_2O/ZrO_2-700	2.68 ± 0.49
4 M Na_2O/ZrO_2-800	2.58 ± 0.07

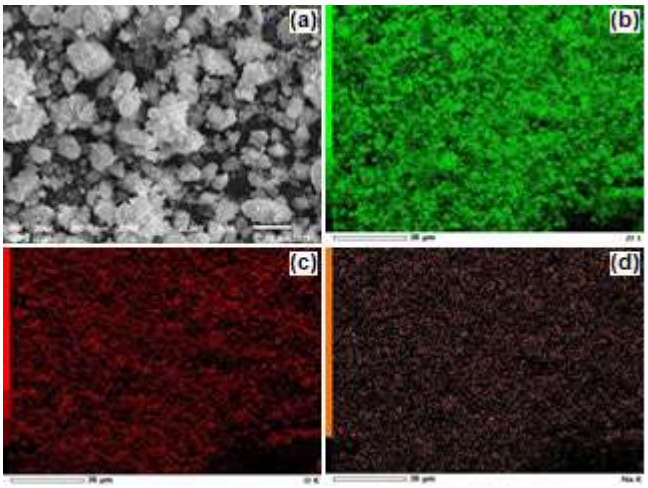

Fig 11. (a) SEM image of 4 M Na_2O/ZrO_2 60 °C; 12 h catalyst at magnification 3000×, the dot mapping element of (b) zirconium (c) oxygen and (d) sodium

Table 7. The elemental composition and surface area analysis of the base catalyst

Catalyst	% of Element mass			Properties		
	Zr	O	Na	S_{BET} [a] (m^2 g^{-1})	V_p [b] (cm^3 g^{-1})	D_p [c] (Å)
ZrO_2	69.67	25.20	-	13.95	1.74×10^{-2}	25.02
4 M Na_2O/ZrO_2 60 °C; 12 h	42.65	38.28	8.41	10.38	1.35×10^{-2}	25.97

[a] Specific surface area
[b] Pore diameter
[c] Pore volume taken at P/P_o = 0.90

in the liquid phase. At temperatures above the boiling point, the methanol is evaporated to reduce the contact interface [46]. Fig. 12 presents the results of FTIR characterization of LGCPO and transesterification compound. According to Pavia et al. [39], C–O vibrations in esters are indicated by strong absorption at 1300–1000 cm^{-1}, while C=O is at 1850–1650 cm^{-1}. This shift is affected by the dipole moment. Oxygen on the ester triggers an increase in frequency in that area. The results of the interpretation of functional groups are summarized in Table 8. The biodiesel content is determined using gas chromatography. The chromatogram of the transesterified compound is presented in Fig. 13. The results of the transesterified compound are listed in Table 9.

Transesterification and LGCPO compounds analyzed by a ^{1}H-NMR spectrometer are shown in Fig. 14 and 15. The results of the analysis are used to confirm the presence of compounds based on the proton environment. An indication that shows the success of transesterification is the appearance of an ester group from triglycerides or FFA.

Based on the results of the LGCPO ^{1}H-NMR in Fig. 15, there is a peak that appears in the chemical shift δ = 4.3 ppm indicating the presence of triglycerides [49]. The characteristic chemical shift of esters compound shows at 2.1 to 2.5 ppm and 3.5 to 4.8 ppm [39]. The presence of peak with triplet integrated at 0.88 ppm indicates the proton of methyl groups. The peak is in the most upfield area, which shows the proton in the least protected environment and is not affected by the induction of other protons.

The methoxy group shows a peak at 3.66 ppm with a singlet pattern. The peak is in a shifting area that is more downfield than the other peaks. The shift is influenced by the pull of electron clouds of carbonyl groups and induction of methoxy groups (–OCH_3 δ = 3.66 ppm is 2.59), while triglycerides in LGCPO have integration of 0.66. Methyl ester conversion is calculated from the integration of triglycerides and methyl esters [37]. The

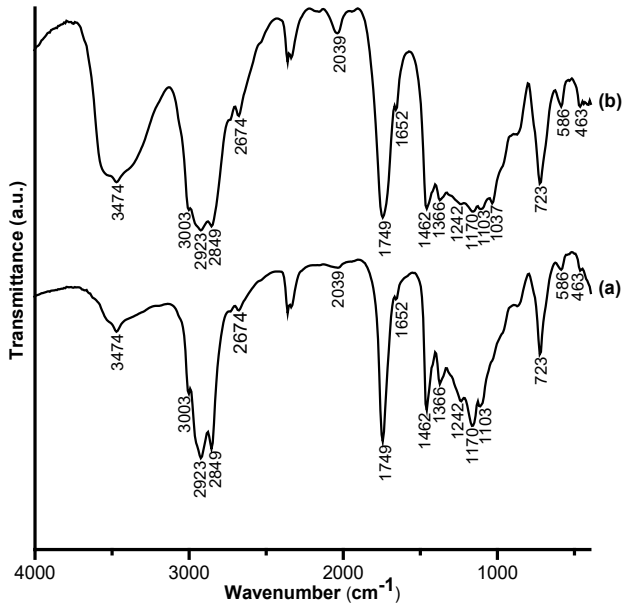

Fig 12. FTIR spectra of (a) LGCPO dan (b) transesterified compound

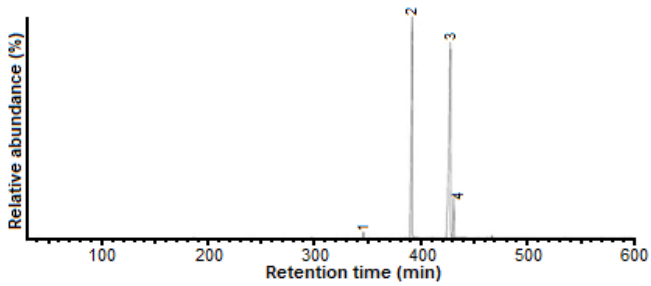

Fig 13. Chromatogram of transesterified compounds

Table 8. Interpretation of FTIR spectra of LGCPO and transesterified compound

Functional group	Vibration type	Wavenumber (cm^{-1})	
		LGCPO	Transesterified compound
–OH	Stretching	3474	3474
–CH_2	Asymmetry stretching	2923	2923
–CH_2	Symmetry stretching	2849	2849
–C=O	Stretching	1749	1749
–CH_2	Shear-type	1462	1462
–CH_3	Bending	1366	1366
C–O–C	Symmetry stretching	1170	1170
–CH_2	Plane rocking	723	723

Table 9. The interpretation of the chromatogram of transesterified compound

Peak	Retention time (min)	Compound	Molecular formula	Molecular weight (g mol^{-1})	Selectivity (%)
1	34.6	Methyl Miristate	$C_{15}H_{30}O_2$	242	0.56
2	39.2	Methyl Palmitate	$C_{17}H_{34}O_2$	270	43.36
3	42.7	Methyl Oleate	$C_{19}H_{36}O_2$	296	51.51
4	43.1	Methyl Stearate	$C_{19}H_{38}O_2$	298	4.57

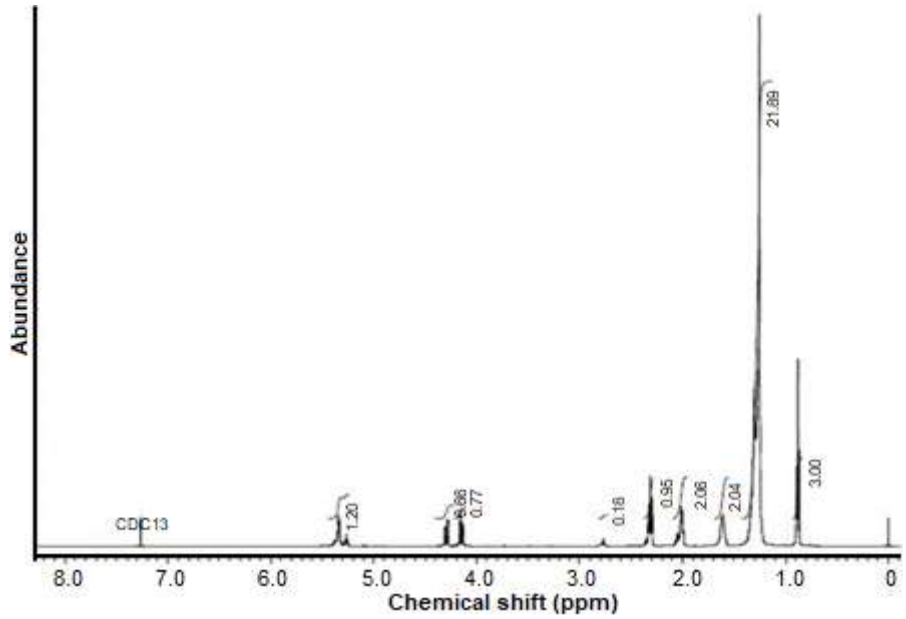

Fig 14. ^{1}H-NMR spectra of LGCPO

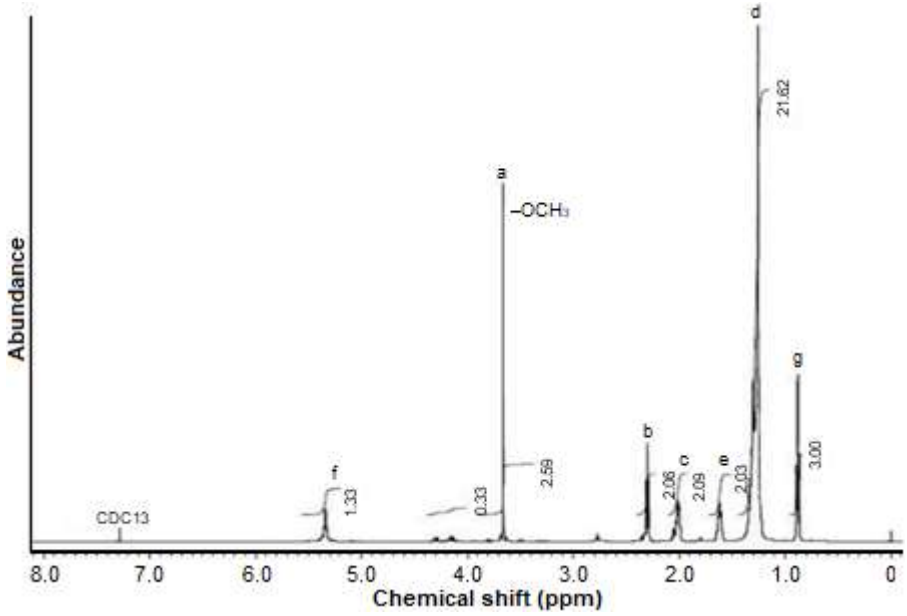

Fig 15. ^{1}H-NMR spectra of transesterified compound

Table 10. Calculation of methyl esters conversion

Integration of triglycerides (I_{TAG})	Integration of methyl esters (I_{ME})	% of Methyl ester conversion (C_{ME})
0.66	2.59	68.55%

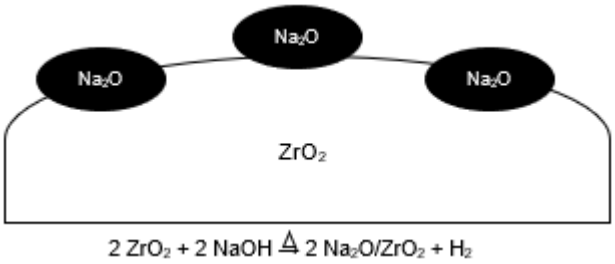

Fig 16. The design of Na_2O/ZrO_2 solid base catalyst formation as a composite material

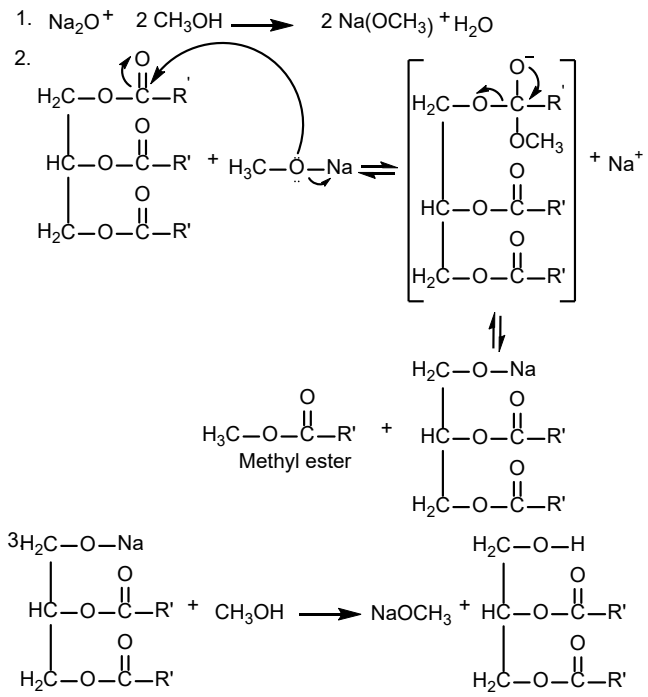

Fig 17. The prediction of the mechanism of transesterification reaction on Na_2O/ZrO_2 solid base catalyst

conversion of methyl ester was 68.55%. After being calculated using the Knotee equation referring to Table 10, the conversion of methyl ester is 68.55%.

Base catalysts that were synthesized have characteristics as composite materials. The composition design of the composite material of Na_2O/ZrO_2 is illustrated in Fig. 16. Zirconia dioxide has a function as supporting material. The prediction of the mechanism of transesterification reaction on Na_2O/ZrO_2 solid base catalyst is shown in Fig. 17. Na_2O tends to be in the aqueous phase (methanol) because it is hydrophilic. Na_2O polarized CH_3OH to form methoxide ions ($^-OCH_3$) [50]. Sodium methoxide ($NaOCH_3$) is on the surface of Na_2O. $NaOCH_3$ transfers the methoxy group to carbonyl triglycerides to form insoluble organic salts. The alkoxy triglyceride group binds to sodium to form sodium alkoxy and methyl ester. Alkoxy sodium with excess methanol produces sodium methoxide and glycerol (after all stages have been reached).

■ CONCLUSION

This work demonstrates the synthesis of a solid acid-base catalyst based on ZrO_2 for biodiesel conversion. In summary, the design concept of this catalyst synthesis is to maintain a mixture of ZrO_2 with NaOH or H_2SO_4 under a certain temperature and pressure. The focus is to understand the influence of several parameters in this reaction system on the catalyst's acidity/basicity properties. The evidence has demonstrated the successful preparation of catalysts. The solid acid catalyst of SO_4^{2-}/ZrO_2 60 °C; 24 h had the highest total acidity of 1.86 mmol g^{-1} using 0.7 M H_2SO_4. The solid base catalyst of Na_2O/ZrO_2 60 °C; 12 h has the highest total basicity of 3.75 ± 0.12 mmol g^{-1} using 4 M NaOH. The acidity and basicity of the catalyst increase with the increasing concentration of H_2SO_4 or NaOH. The total acidity of the 0.7 M SO_4^{2-}/ZrO_2 60 °C; 24 h solid acid catalyst and the basicity of 4 M Na_2O/ZrO_2 60 °C; 24 h solid base catalyst decreases with increasing calcination temperature. The release of functional groups on the catalyst causes the acidity and basicity of the catalyst to decrease.

Since we are interested in investigating the performance of these catalysts, some important parameters for biodiesel conversion are conducted. The

concentration of FFA decreased to 68.87% after being processed using an optimized acid catalyst. The solid base catalyst of 4 M Na_2O/ZrO_2 60 °C; 24 h successfully converted LGCPO into biodiesel by 68.55% through a transesterification reaction. The spectroscopic analysis helped to investigate the product. ^{1}H-NMR revealed the presence of triglycerides (δ = 4.3 ppm) and methoxy groups (δ = 3.66 ppm). The conversion of methyl ester that was obtained is 68.55%. Methyl oleate is the major product, accompanied by other methyl ester compounds, including methyl palmitate, methyl stearate, and a small amount of methyl myristate.

■ ACKNOWLEDGMENTS

The authors are grateful for financial support from the Ministry of Research, Technology and Higher Education of Republic Indonesia through STRANAS Research Grant (contract number 001/SP2H/LT/DRPM/IV/2017) and World Class Research (WCR) 2019 (contract number 1980/UN1.DITLIT/DIT-LIT/LT/2019).

■ REFERENCES

[1] Hajjari, M., Tabatabaei, M., Aghbashlo, M., and Ghanavati, H., 2017, A review on the prospects of sustainable biodiesel production: A global scenario with an emphasis on waste-oil biodiesel utilization, *Renewable Sustainable Energy Rev.*, 72, 445–464.

[2] Muanruksa, P., and Kaewkannetra, P., 2020, Combination of fatty acids extraction and enzymatic esterification for biodiesel production using sludge palm oil as a low-cost substrate, *Renewable Energy*, 146, 901–906.

[3] Atadashi, I.M., Aroua, M.K., Aziz, A.R.A., and Sulaiman, N.M.N., 2013, The effects of catalysts in biodiesel production: A review, *J. Ind. Eng. Chem.*, 19 (1), 14–26.

[4] Li, Y., Ye, B., Shen, J., Tian, Z., Wang, L., Zhu, L., Ma, T., Yang, D., and Qiu, F., 2013, Optimization of biodiesel production process from soybean oil using the sodium potassium tartrate doped zirconia catalyst under Microwave Chemical Reactor, *Bioresour. Technol.*, 137, 220–225.

[5] Hasanudin, H., Rachmat, A., Said, M., and Wijaya, K., 2020, Kinetic model of crude palm oil hydrocracking over Ni/Mo ZrO_2–pillared bentonite catalyst, *Period. Polytech., Chem. Eng.*, 64 (2), 238–247.

[6] Hayyan, A., Mjalli, F.S., Hashim, M.A., Hayyan, M., AlNashef, I.M., Al-Wahaibi, T., and Al-Wahaibi, Y.M., 2014, A solid organic acid catalyst for the pretreatment of low-grade crude palm oil and biodiesel production, *Int. J. Green Energy*, 11 (2), 129–140.

[7] Min Oo, Y., Prateepchaikul, G., and Somnuk, K., 2021, Continuous acid-catalyzed esterification using a 3D printed rotor–stator hydrodynamic cavitation reactor reduces free fatty acid content in mixed crude palm oil, *Ultrason. Sonochem.*, 72, 105419.

[8] Pua, F., Fang, Z., Zakaria, S., Guo, F., and Chia, C., 2011, Direct production of biodiesel from high-acid value *Jatropha* oil with solid acid catalyst derived from lignin, *Biotechnol. Biofuels*, 4 (1), 56.

[9] Qu, T., Niu, S., Zhang, X., Han, K., and Lu, C., 2021, Preparation of calcium modified Zn-Ce/Al_2O_3 heterogeneous catalyst for biodiesel production through transesterification of palm oil with methanol optimized by response surface methodology, *Fuel*, 284, 118986.

[10] Chuah, L.F., Bokhari, A., Yusup, S., Klemeš, J.J., Abdullah, B., and Akbar, M.M., 2016, Optimisation and kinetic studies of acid esterification of high free fatty acid rubber seed oil, *Arabian J. Sci. Eng.*, 41 (7), 2515–2526.

[11] Rattanaphra, D., Harvey, A.P., Thanapimmetha, A., and Srinophakun, P., 2012, Simultaneous transesterification and esterification for biodiesel production with and without a sulfated zirconia catalyst, *Fuel*, 97, 467–475.

[12] Ropero-Vega, J.L., Aldana-Pérez, A., Gómez, R., and Niño-Gómez, M.E., 2010, Sulfated titania [TiO_2/SO_4^{2-}]: A very active solid acid catalyst for the esterification of free fatty acids with ethanol, *Appl. Catal., A*, 379 (1-2), 24–29.

[13] Johnson, M., Ren, J., Lefler, M., Licht, G., Vicini, J., Liu, X., and Licht, S., 2017, Carbon nanotube wools

made directly from CO_2 by molten electrolysis: Value-driven pathways to carbon dioxide greenhouse gas mitigation, *Mater. Today Energy*, 5, 230–236.

[14] Chouhan, A.P.S., and Sarma, A.K., 2011, Modern heterogeneous catalysts for biodiesel production: A comprehensive review, *Renewable Sustainable Energy Rev.*, 15 (9), 4378–4399.

[15] Devyatkov, S.Y., Zinnurova, A.A., Aho, A., Kronlund, D., Peltonen, J., Kuzichkin, N.V., Lisitsyn, N.V., and Murzin, D.Y., 2016, Shaping of sulfated zirconia catalysts by extrusion: understanding the role of binders, *Ind. Eng. Chem. Res.*, 55 (23), 6595–6606.

[16] Pan, Y., Zhang, J., Xu, Y., Gao, Y., Chen, Z., and Wang, J., 2016, A facile one-pot hydrothermal process to synthesize sulfonated mesoporous ZrO_2, *J. Porous Mater.*, 23 (2), 489–495.

[17] Utami, M., Trisunaryanti, W., Shida, K., Tsushida, M., Kawakita, H., Ohto, K., Wijaya, K., and Tominaga, M., 2019, Hydrothermal preparation of a platinum-loaded sulfated nanozirconia catalyst for the effective conversion of waste low density polyethylene into gasoline-range hydrocarbons, *RSC Adv.*, 9 (71), 41392–41401.

[18] Li, Y., He, D., Zhu, Q., Zhang, X., and Xu, B., 2004, Effects of redox properties and acid-base properties on isosynthesis over ZrO_2-based catalysts, *J. Catal.*, 221 (2), 584–593.

[19] Rabee, A.I.M., Manayil, J.C., Isaacs, M.A., Parlett, C.M.A., Durndell, L.J., Zaki, M.I., Lee, A.F., and Wilson, K., 2018, On the impact of the preparation method on the surface basicity of Mg–Zr mixed oxide catalysts for tributyrin transesterification, *Catalysts*, 8 (6), 228.

[20] Noh, H.J., Seo, D.S., Kim, H., and Lee, J.K., 2003, Synthesis and crystallization of anisotropic shaped ZrO_2 nanocrystalline powders by hydrothermal process, *Mater. Lett.*, 57 (16-17), 2425–2431.

[21] Sohn, J.R., Kim, H.W., Park, M.Y., Park, E.H., Kim, J.T., and Park, S.E., 1995, Highly active catalyst of NiO-ZrO_2 modified with H_2SO_4 for ethylene dimerization, *Appl. Catal., A*, 128 (1), 127–141.

[22] Saravanan, K., Tyagi, B., and Bajaj, H.C., 2012, Esterification of caprylic acid with alcohol over nano-crystalline sulfated zirconia, *J. Sol-Gel Sci. Technol.*, 62 (1), 13–17.

[23] Srinivasan, R., Sparks, D.E., and Davis, B.H., 1996, State of platinum in zirconia and sulfated zirconia catalysts, *Catal. Lett.*, 40 (3), 167–173.

[24] Zhang, C., Miranda, R., and Davis, B.H., 1994, Platinum-sulfated-zirconia. Infrared study of adsorbed pyridine, *Catal. Lett.*, 29 (3), 349–359.

[25] Popova, M., Szegedi, Á., Lazarova, H., Dimitrov, M., Kalvachev, Y., Atanasova, G., Ristić, A., Wilde, N., and Gläser, R., 2017, Influence of the preparation method of sulfated zirconia nanoparticles for levulinic acid esterification, *React. Kinet., Mech. Catal.*, 120 (1), 55–67.

[26] Sayılkan, F., Asiltürk, M., Burunkaya, E., and Arpaç, E., 2009, Hydrothermal synthesis and characterization of nanocrystalline ZrO_2 and surface modification with 2-acetoacetoxyethyl methacrylate, *J. Sol-Gel Sci. Technol.*, 51 (2), 182–189.

[27] Devulapelli, V.G., and Weng, H.S., 2009, Esterification of 4-methoxyphenylacetic acid with dimethyl carbonate over mesoporous sulfated zirconia, *Catal. Commun.*, 10 (13), 1711–1717.

[28] Qiu, F., Li, Y., Yang, D., Li, X., and Sun, P., 2011, Heterogeneous solid base nanocatalyst: Preparation, characterization and application in biodiesel production, *Bioresour. Technol.*, 102 (5), 4150–4156.

[29] El-Desouki, D.S., Ibrahim, A.H., Abdelazim, S.M., Aboul-Gheit, N.A.K., and Abdel-Hafizar, D.R., 2021, The optimum conditions for methanol conversion to dimethyl ether over modified sulfated zirconia catalysts prepared by different methods, *J. Fuel Chem. Technol.*, 49 (1), 63–71.

[30] Pratap, S.R., Shamshuddin, S.Z.M., and Shyamprasad, K., 2020, Microwave assisted synthesis of propyl esters over modified versions of zirconia: Kinetic study, *Chem. Data Collect.*, 30, 100579.

[31] Essamlali, Y., Amadine, O., Larzek, M., Len, C., and Zahouily, M., 2017, Sodium modified hydroxyapatite: Highly efficient and stable solid-

base catalyst for biodiesel production, *Energy Convers. Manage.*, 149, 355–367.

[32] Abedin, M.A., Kanitkar, S., Bhattar, S., and Spivey, J.J., 2021, Methane dehydroaromatization using Mo supported on sulfated zirconia catalyst: Effect of promoters, *Catal. Today*, 365, 71–79.

[33] Marinković, D.M., Stanković, M.V., Veličković, A.V., Avramović, J.M., Miladinović, M.R., Stamenković, O.O., Veljković, V.B., and Jovanović, D.M., 2016, Calcium oxide as a promising heterogeneous catalyst for biodiesel production: Current state and perspectives, *Renewable Sustainable Energy Rev.*, 56, 1387–1408.

[34] Helmiyati, H., Budiman, Y., Abbas, G.H., Dini, F.W., and Khalil, M., 2021, Highly efficient synthesis of biodiesel catalyzed by a cellulose@hematite-zirconia nanocomposite, *Heliyon*, 7 (3), e06622.

[35] dos Santos, L.K., Hatanaka, R.R., de Oliveira, J.E., and Flumignan, D.L., 2019, Production of biodiesel from crude palm oil by a sequential hydrolysis/esterification process using subcritical water, *Renewable Energy*, 130, 633–640.

[36] Chong, Y.Y., Thangalazhy-Gopakumar, S., Gan, S., Lee, L.Y., and Ng, H.K., 2020, Esterification and neutralization of bio-oil from palm empty fruit bunch fibre with calcium oxide, *Bioresour. Technol. Rep.*, 12, 100560.

[37] Knothe, G., 2000, Monitoring a progressing transesterification reaction by fiber-optic near infrared spectroscopy with correlation to ^{1}H nuclear magnetic resonance spectroscopy, *J. Am. Oil Chem. Soc.*, 77 (5), 489–493.

[38] Shi, G., Yu, F., Wang, Y., Pan, D., Wang, H., and Li, R., 2016, A novel one-pot synthesis of tetragonal sulfated zirconia catalyst with high activity for biodiesel production from the transesterification of soybean oil, *Renewable Energy*, 92, 22–29.

[39] Pavia, D.L., Lampman, G.M., Kriz, G.S., and Vyvyan, J.A., 2009, Introduction to Spectroscopy, 4th Ed., Brooks/Cole, Cengage Learning, Belmont, CA.

[40] Liu, N., Ma, Z., Wang, S., Shi, L., Hu, X., and Meng, X., 2020, Palladium-doped sulfated zirconia: Deactivation behavior in isomerization of *n*-hexane, *Fuel*, 262, 116566.

[41] Navio, J.A., Colón, G., Sánchez-Soto, P.J., and Macias, M., 1997, Effects of H_2O_2 and SO_4^{2-} species on the crystalline structure and surface properties of ZrO_2 processed by alkaline precipitation, *Chem. Mater.*, 9 (5), 1256–1261.

[42] Tuong, T., Tran, V., Kaiprommarat, S., Kongparakul, S., Reubroycharoen, P., Guan, G., Huan, M., and Samart, C., 2016, Green biodiesel production from waste cooking oil using an environmentally benign acid catalyst, *Waste Manage.*, 52, 367–374.

[43] El-Dafrawy, S.M., Hassan, S.M., and Farag, M., 2020, Kinetics and mechanism of Pechmann condensation reaction over sulphated zirconia-supported zinc oxide, *J. Mater. Res. Technol.*, 9 (1), 13–21.

[44] Vannucci, J.A., Nichio, N.N., and Pompeo, F., 2021, Solketal synthesis from ketalization of glycerol with acetone: A kinetic study over a sulfated zirconia catalyst, *Catal. Today*, 372, 238–245.

[45] Pirez, C., Reche, M.T., Lee, A.F., Manayil, J.C., dos-Santos, V.C., and Wilson, K., 2015, Hydrothermal saline promoted grafting of periodic mesoporous organic sulfonic acid silicas for sustainable FAME production, *Catal. Lett.*, 145 (7), 1483–1490.

[46] Colombo, K., Ender, L., and Barros, A.A.C., 2017, The study of biodiesel production using CaO as a heterogeneous catalytic reaction, *Egypt. J. Pet.*, 26 (2), 341–349.

[47] Zhang, H., Luo, X., Shi, K., Wu, T., He, F., Yang, H., Zhang, S., and Peng, C., 2019, Nanocarbon-based catalysts for esterification: Effect of carbon dimensionality and synergistic effect of the surface functional groups, *Carbon*, 147, 134–145.

[48] Chang, A., Pan, J.H., Lai, N.C., Tsai, M.C., Mochizuki, T., Toba, M., Chen, S.Y., and Yang, C.M., 2020, Efficient simultaneous esterification/transesterification of non-edible Jatropha oil for biodiesel fuel production by template-free synthesized nanoporous titanosilicates, *Catal. Today*, 356, 56–63.

[49] Shah, K.A., Parikh, J.K., and Maheria, K.C., 2014, Optimization studies and chemical kinetics of silica sulfuric acid-catalyzed biodiesel synthesis from waste cooking oil, *Bioenergy Res.*, 7 (1), 206–216.

[50] Saravana Sathiya Prabhahar, R., Benitha, V.S., and Nagarajan, J., 2021, Improved yield of palm oil biodiesel through nano catalytic transesterification, *Mater. Today: Proc.*, 46, 8433–8437.

Novel Benzo[*f*]coumarin Derivatives as Probable Acetylcholinesterase Inhibitors: Synthesis, In Vitro, and In Silico Studies for Evaluation of Their Anti-AChE Activity

Zaizafoon Nabeel[1], Qassim Abdul-Hussein Jaber[2*], and Nabeel Abed Abdul-Rida[3]

[1]*Department of Chemistry, College of Science, Mustansiriyah University, Baghdad, Iraq*

[2]*Department of Chemistry, General Directorate of Education in Babylon, Hilla, Iraq*

[3]*Department of Chemistry, College of Science, University of Qadisiyah, Diwanyiah, Iraq*

* ***Corresponding author:***

email: qassimjaber99@gmail.com

Received: May 4, 2021
Accepted: August 26, 2021

DOI: 10.22146/ijc.65663

Abstract: *Novel benzo[f]coumarin derivatives bearing pyrimidine unit were successfully synthesized. The target is to develop novel acetylcholinesterase inhibitors. The benzo[f]coumarin chalcone **4** was prepared via Claisen-Schmidt condensation between 3-acetyl-5,6-benzocoumarin and 4-hydroxybenzaldehyde in the alkaline medium. Then, the cyclocondensation of chalcone **4** with urea, thiourea, and guanidine HCl in the presence of glacial acetic acid led to the formation of various pyrimidines. Structures of the newly synthesized compounds were characterized by FT-IR, ^{1}H-NMR, ^{13}C-NMR spectra, and elemental analysis. The acetylcholinesterase (AChE) inhibitory activity tests were carried out using Ellman's assay and donepezil as a reference drug. The biological activity results revealed that the derivatives **6** and **7** inhibit AChE activity in healthy samples showed that the greater inhibition percentage was found respectively at concentrations of 10^{-4} and 10^{-10} M while low inhibition percentage was obtained at 10^{-12} and 10^{-4} M. AChE showed inhibition constant Ki in the range of 10^{-4}–10^{-12} M in the presence of maximum and minimum inhibitor concentrations, probably due to variant types of inhibition from non and uncompetitive. In addition, molecular modeling simulations of targeted compounds revealed their mechanism of action as potent inhibitors for the AChE enzyme.*

Keywords: *benzo[f]coumarin; pyrimidine; chalcone; acetylcholinesterase*

INTRODUCTION

Alzheimer's disease (AD) is known as a neurodegenerative disorder, which appears in older adults with symptoms as loss of memory, a decline in cognitive functions and language skills [1]. According to the cholinergic hypothesis, AD is mainly related to the level decrease of acetylcholine (AChE) in the brain because of the damage of cholinergic neurons, thus raising the AChE via inhibition of acetylcholinesterase is one of the effective approaches to treatment AD's symptoms [2-3]. In this context, several AChE inhibitors such as umbelliferone, hymecromone, and ensaculin (**I**, **II**, Fig. 1), which belong to the coumarin family, were used as approved therapeutic by the FDA to curb the progression of AD in early stages [4-6]. In addition, coumarin derivatives have been studied extensively due to their biological activities such as antimicrobial [7], anticancer [8-11], anticoagulant [12], analgesic [13], ulcerogenic [14], antiviral [15], antimalarial [16], anti-inflammatory [17-18], antidepressant [19], and antioxidant [20-21] activities, as well as anti-HIV protease [22], acetylcholinesterase [23-24], and mono-amine oxidase B (MAO-B) [25] inhibitors. It was worth mentioning that many coumarin derivatives were designed and found to be successful as significant organic fluorescent materials for potential applications in biochemical and biological imaging due to their light emission properties [23]. This work reports the synthesis of new series of benzocoumarin derivatives conjugated with various pyrimidines and their anti-cholinesterase activity evaluation.

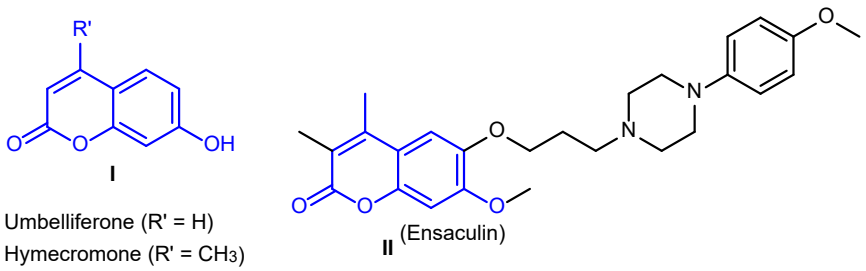

Fig 1. Structures of coumarin derivatives used as acetylcholinesterase inhibitors

EXPERIMENTAL SECTION

Materials

The reagents, including 2-hydroxynaphthal-dehyde, ethyl acetoacetate, piperidine, 4-hydroxy benzaldehyde, urea, thiourea, guanidine HCl, ethanol, and glacial acetic acid, were purchased from Merck and TCI. At the same time, the materials used in the biological evaluation include 5,5-dithio-bis-(2-nitro benzoic acid) (DTNB), serum-blood, sodium phosphate, acetyl thiocholineiodide, and dimethyl sulfoxide (DMSO).

Instrumentation

Melting points were measured on a Stuart melting point apparatus SMP30 (Büchi Labortechnik AG, Switzerland) and are uncorrected. Infrared (FT-IR) spectra were recorded (KBr discs) on a Shimadzu FT-IR 8201 PC spectrophotometer. NMR data were obtained on Varian INOVA (^{1}H, 500 MHz; ^{13}C, 125.65 MHz) spectrometers used TMS as internal standard and DMSO-d_6 solvent on the δ scale in ppm. Analytical silica gel TLC plates 60 F254 were purchased from Merck. Elemental analyses (CHN) were carried out using Vario Elemental Analyzer 3000 (Shimadzu, Japan). All reagents were obtained from commercial suppliers and were used without further purification.

Procedure

Synthesis

Preparation of 3-acetyl-5,6-benzocoumarin (3). To a stirred solution of 2-hydroxynaphthaldehyde **1** (1.722 g, 0.01 mol) in absolute EtOH (15 mL) containing tree drops of piperidine, ethyl acetoacetate **2** (1.30 g, 0.01 mol) was added and the mixture was refluxed until formed the precipitate. The solid result was collected by filtration, washed with water, dried, and recrystallized from EtOH to get compound **3**. Physical state: yellow crystals, yield: 93%, m.p. 186–188°C, R_f = 0.59 (Hexane:Ethyl acetate 7:3). FT-IR (KBr, cm^{-1}): ν 1211 (C–O), 1450, 1558, 1612 (C=C), 1735, 1681 (C=O), 3031, 2931 (C–H). ^{1}H-NMR (DMSO-d_6, δ, ppm): δ 8.10 (s., 1H, H-4), 7.89 (d, *J* = 7.9 Hz, 1H, H-5), 7.84 (d, *J* = 7.7 Hz, 1H, H-8), 7.68 (m, 1H, H-6), 7.49 (m, 1H, H-7), 7.39 (d, *J* = 8.4 Hz, 1H, H-9), 7.04 (d, *J* = 7.9 Hz, 1H, H-10), 2.21 (s, 3H, Me). ^{13}C-NMR (DMSO-d_6): δ 172.0 (C=O_{ketone}), 161.7 (C=$O_{coum.}$-2), 155.5 ($C_{coum.}$-10a), 137.6 ($C_{coum.}$-4), 135.1, 134.1, 131.1, 130.7, 130.2, 129.0, 128.3, 120.6, 120.4, 116.8, 113.4 ($C_{coum.}$), 29.5 (Me). Anal. calculated for $C_{15}H_{10}O_3$: C, 75.62; H, 4.23; Found; C, 74.35; H, 4.06.

Preparation of 2-(3-(4-hydroxyphenyl)acryloyl)-3H-benzo[*f*]chromen-3-one (4). A solution of compound **3** (1.191 g, 0.005 mol) in ethanol and 4-hydroxybenzaldehyde (0.61 g, 0.005 mol) was stirred at 50 °C for 6 h in the presence of piperidine (0.5 mL) (TLC check). After cooling, the reaction mixture was stirred for 1 h and then kept in the refrigerator for 24 h, the formed solid was filtered and crystallized from ethanol to get compound **4**. Brown crystals, yield: 73%, m.p. 203–205 °C, R_f = 0.58 (Hexane:Ethyl acetate 8:2). IR spectrum, ν, cm^{-1}: 1218 (C–O), 1604 (C=C), 1675 (C=O), 1738 (C=O), 3471 (OH). ^{1}H-NMR spectrum, δ, ppm: 9.80 (s., 1H, OH), 8.42 (s., 1H, H-4), 8.07 (d, *J* = 7.2 Hz, 1H, H-5), 8.04 (d, *J* = 7.6 Hz, 1H, H-8), 7.86 (d, *J* = 8.4 Hz, 1H, H-13), 7.20 (d, *J* = 5.8 Hz, 1H, H-12), 7.68–6.76 (8H, $H_{coum.+}H_{arom.}$). ^{13}C-NMR spectrum, δC, ppm: 171.1 (C=$O_{chalcone}$), 159.5 (C=$O_{coum.}$-2), 157.8 (C–OH), 149.1 ($C_{coum.}$-10a), 138.5 ($C_{coum.}$-4), 135.1, 134.1, 131.1, 130.7, 130.2, 129.5, 128.7, 126.7, 125.1, 124.8, 121.0, 120.0, 119.2 ($C_{coum.+}C_{arom.}$). Anal. calculated for $C_{22}H_{14}O_4$:

C, 77.18; H, 4.12; Found; C, 77.56; H, 4.29.

Synthesis of 2-(2-oxo-6-(4-hydroxyphenyl)pyrimidin-4-yl)-3H-benzo[*f*]chromen-3-one (5). A mixture of chalcone **4** (4.74 g, 0.01 mol), urea (0.72 g, 0.012 mol) in 20 mL of absolute ethanol containing glacial acetic acid (0.5 mL) was refluxed for 7 h (TLC check). After cooling, the reaction mixture was poured onto ice-water (50 mL) with continuous stirring. The solid obtained was filtered and crystallized from dry ethanol to get compound **5**. White crystals, yield: 68%, m.p. 223–225 °C, R_f = 0.54 (Hexane:Ethyl acetate 7:3). IR spectrum, ν, cm^{-1}: 1218 (C–O), 1635 (C=N), 1728, 1679 (C=O), 3240 (NH), 3397 (OH). ^{1}H-NMR spectrum, δ, ppm: 10.54 (s., 1H, NH), 9.76 (s., 1H, OH), 8.40 (s., 1H, H-4), 8.08 (d, *J* = 7.1 Hz, 1H, H-5), 7.87 (d, *J* = 7.7 Hz, 1H, H-8), 7.86–6.76 (8H, $H_{coum.+}H_{arom.}$). ^{13}C-NMR spectrum, δC, ppm: 166.8 (C=N), 164.0 (C-$4_{Pyrim.}$), 161.4 (C=$O_{coum.}$-2), 160.3 (C=$O_{Pyrim.}$), 157.9 (C–OH), 153.9 (C-10a $_{coum.}$), 143.1 (C-$4_{coum.}$), 134.9, 134.2, 130.6, 130.3, 128.6, 127.7, 126.6, 125.1, 124.0, 118.4, 116.1, 115.2, 115.0 ($C_{coum.+}C_{arom.}$), 101.0 (C-$5_{Pyrim.}$). Anal. calculated for $C_{23}H_{14}N_2O_4$:C, 72.25; H, 3.69; N, 7.33. Found; C, 71.62; H, 3.24; N, 7.02.

Synthesis of 2-(6-(4-hydroxyphenyl)-2-thioxo-1,2-dihydropyrimidin-4-yl)-3H-benzo[*f*]chromen-3-one (6). A mixture of chalcone **4** (4.74 g, 0.01 mol), thiourea (0.84 g, 0.011 mol) in 20 mL absolute ethanol containing glacial acetic acid (0.5 mL) was refluxed for 8 h (TLC check). After cooling, the reaction mixture was poured onto ice-water (50 mL) with continuous stirring. The solid obtained was filtered and crystallized from dry ethanol to get compound **6**. White crystals, yield: 62%, m.p. 214–216 °C, R_f = 0.65 (Hexane:Ethyl acetate 8:2). IR spectrum, ν, cm^{-1}: 1232 (C–O), 1636 (C=N), 1745 (C=O), 3178 (NH), 3387 (OH). ^{1}H-NMR spectrum, δ, ppm: 10.65 (s., 1H, NH), 9.58 (s., 1H, OH), 8.32 (s., 1H, H-4), 8.01 (d, *J* = 6.8 Hz, 1H, H-5), 7.94 (d, *J* = 7.1 Hz, 1H, H-8), 7.68–6.89 (8H, $H_{coum.+}H_{arom.}$), 6.37 (s., 1H, H-$5_{Pyrim.}$). ^{13}C-NMR spectrum, δC, ppm: 176.3 (C=S), 169.3 (C=N), 161.0 (C-$4_{Pyrim.}$), 160.4 (C=$O_{coum.}$), 155.9 (C–OH), 153.8 (C-10a $_{coum.}$), 147.5 (C-$4_{coum.}$), 134.4, 134.0, 130.2, 125.1, 124.8, 118.6, 117.7, 116.1 ($C_{coum.+}C_{arom.}$), 101.5 (C-$5_{Pyrim.}$). Anal. calculated for $C_{23}H_{14}N_2O_4S$: C, 69.33; H, 3.54; N, 7.03. Found; C, 68.56; H, 3.29; N, 6.78.

Synthesis of 2-(2-amino-6-(4-hydroxyphenyl) pyrimidin-4-yl)-3H-benzo[*f*]chromen-3-one (7). A mixture of chalcone **4** (4.74 g, 0.01 mol), guanidine HCl (1.05 g, 0.011 mol) in 20 mL absolute ethanol containing glacial acetic acid (0.5 mL) was refluxed for 5 h (TLC check). After cooling, the reaction mixture was poured onto ice-water (50 mL) with stirring. The resulting solid was filtered and crystallized from ethanol to get the compound **7**. White crystals, yield: 55%, m.p. 231–233 °C, R_f = 0.58 (Hexane:Ethyl acetate 8:2). IR spectrum, ν, cm^{-1}: 1211 (C–O), 1638 (C=N), 1743 (C=O), 3256, 3235 (NH_2), 3391 (OH). ^{1}H-NMR spectrum, δ, ppm: 9.42 (s., 1H, OH), 8.29 (s., 1H, H-4), 7.97 (d, *J* = 7.3 Hz, 1H, H-5), 7.93 (d, *J* = 7.5 Hz, 1H, H-8), 7.88–6.65 (8H, $H_{coum.+}H_{arom.}$), 6.45 (s., 2H, NH_2). ^{13}C-NMR spectrum, δC, ppm: 165.2 (C=N), 163.2 (C-$2_{Pyrim.}$), 161.3 (C-$4_{Pyrim.}$), 160.3 (C=$O_{coum.}$), 157.9 (C–OH), 153.9 ($C_{coum.}$-10a), 147.9(C-$4_{coum.}$), 134.2, 130.3, 129.6, 128.6, 128.0, 127.9, 127.8, 125.1, 116.3, 116.1 ($C_{coum.+}C_{arom.}$), 108.7 (C-$5_{Pyrim.}$). Anal. calculated for $C_{23}H_{15}N_3O_3$: C, 72.43; H, 3.96; N, 11.02. Found; C, 71.26; H, 3.79; N, 10.55.

Determination of AChE activity

Human serum AChE activity was determined using Ellman et al. [26] method. 50 μL of DTNB solution 0.001 M is added to 2.25 mL of sodium phosphate buffer solution (pH = 7.3, 0.2 M), then 10 μL of serum was added and mixed well. Two milliliters of the mixture were transferred to a measuring cell (1 cm). Then, 34 μL of acetyl thiocholineiodide (ASChI, 0.06 M) is added. The changes in absorbency are measured before and after adding the substrate at 430 nm for 3 min. The enzyme activity is calculated as a concentration in μmol of the substrate hydrolyzed to every 1 mL of samples in 3 min and expressed as μmol/3 min/mL.

Determination of the biological activity of newly prepared derivatives

A stock concentration solution of 0.01 M concentration of each **6** and **7** in Fig. 1 has been prepared. Then, each complex's different concentrations (10^{-2}, 10^{-3}, 10^{-5}, 10^{-7}, 10^{-9}, and 10^{-11} M) were prepared by diluting it with DMSO as a solvent. ChE activity is measured in human serum as follows:

DTNB solution (50 μL, 0.001 M) is added to 2.25 mL of sodium phosphate buffer solution (pH = 7.3, 0.2 M), 0.25 mL of inhibitor was mixed with 2 mL of the same buffer 10 μL of serum is added and mixed well. Two milliliters of the mixture were transferred to a measuring cell (1 cm), then 34 μL of AChI (0.06 M) was added. The changes in absorbency changes are measured after adding the substrate at 430 nm for 3 min. The inhibition percentage was calculated by comparing the activity between with and without inhibitor under the same conditions according to the equation:

$$\%\ \text{Inhibition} = 100 - \left(\frac{\text{The activity in the presence of inhibitor}}{\text{The activity in the absence of inhibitor}} \times 100 \right)$$

Determination of the type of inhibition

Constant concentrations of inhibitors (second higher inhibition and lower inhibition) were used with different concentrations (0.02, 0.04, 0.06, and 0.08 M) to study the type of inhibition. These concentrations were prepared using the stock solution of AChI 0.1 M. The enzyme activity was determined with and without the inhibitors using the Lineweaver-Burk-equation by plotting 1/V vs. 1/[s] following values were then calculated as follows: 1) K_i, 2) Apparent V_{max} (V_{mapp}), 3) Apparent K_m (K_{mapp}), and 4) type of inhibition.

Molecular docking

A molecular docking study was carried out using the Autodock 4.2 program [27], while Discovery Studio Visualizer was used to select the best binding mode with the receptor and 3D interaction poses. The 3D structures of AChE (PDB 2ACE) were obtained from the Protein Data Bank (www.rcsb.org), followed by separating the co-crystallized ligands and water molecules. Then polar hydrogens were added. Finally, the 3D structures of the tested coumarin analogs were optimized using Gaussian 03 software with the semi-empirical AM1 method.

■ RESULTS AND DISCUSSION

Chemical Structure

3-Acetyl-5,6-benzocoumarin **3** were successfully prepared from a reaction of 2-hydroxynaphthal-dehyde **1** with ethyl acetoacetate **2** and few drops of piperidine under reflux conditions. Next, condensation of benzocoumarin derivative **3** with 4-hydroxybenzaldehyde using piperidine as a catalyst was done via reflux to form benzocoumarin chalcone **3**. Later, cyclocondensation of chalcone **4** with urea, thiourea, and guanidine HCl was done by reflux and using glacial acetic acid as a catalyst to produce various pyrimidine rings. The synthetic methods to the novel compounds are shown in the following Scheme 1.

The structures of compounds **3**–**7** were confirmed on the basis of elemental analyses as well as spectral data (FT-IR, ^{1}H-NMR, and ^{13}C-NMR spectra). The FT-IR spectra of the synthesized compounds exhibited absorption bands at 1728–1745 cm^{-1} due to lactone carbonyl stretching, whereas compounds 3 and 4 showed two bands at 1675 and 1681 cm^{-1} assignable to carbonyl group stretching of chalcone and ketone, respectively. In addition, hydroxyl group stretching bands were exhibited in the range of 3387–3471 cm^{-1}, other absorption bands assignable to substituents were comprehensively analyzed.

In ^{1}H-NMR spectra of the compounds **3**–**7**, the protons of the benzocoumarin moiety appeared almost similar pattern. The C4-H of the benzocoumarin moiety was resonated as singlets at δ = 8.20–8.42 ppm. Meanwhile, the range of resonance at δ = 9.42–9.80 ppm is due to the O–H bond. The spectrum of compound **4** exhibited two doublets at 7.20 ppm and 7.86 ppm, indicating that the ethylene group in the enone linkage is in a trans-conformation in the chalcone. In addition, the aromatic and other substituents protons were comprehensively analyzed.

In the ^{13}C-NMR spectra of the compounds **3**–**7**, the carbon atom of the C=N group was resonated at the regions δ = 169.3–165.2 ppm, while carbonyl group of benzocoumarin and were resonated at the regions δ = 161.7–159.5 ppm. The resonances at the regions δ = 155.0–149.1 ppm and δ = 147.5–137.6 ppm were assigned to carbon atoms C-10a and C-4 of the benzocoumarin, respectively. In addition, the carbon atoms of the C–OH group in the phenol ring was resonated at the regions δ = 157.9–155.9. Other aromatic and benzocoumarin atoms and the other substituted were comprehensively analyzed.

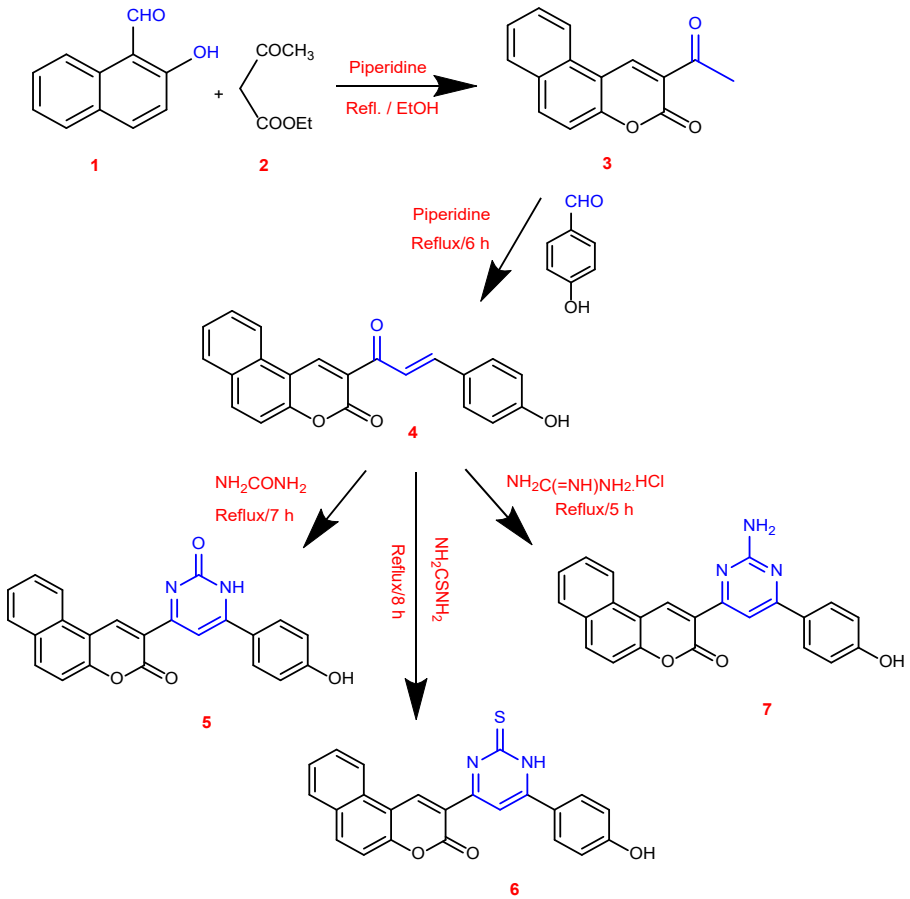

Scheme 1. The experimental steps for synthesizing benzo[*f*]coumarin derivatives (**3**–**7**)

Molecular Docking Results

In the present work, *in silico* study was performed using molecular docking simulation in order to test the capability of some synthesized compounds as potential AChE inhibitors. The targeted compounds (**5**–**7**) and Donepezil were docked as ligands with the active pocket of AChE (PDB ID: 2ACE) to attain favorable conformation, with the maximum number of interactions and minimal free energy, as shown in Fig. 2–5. The findings of the study, which include binding energies and types of interactions, are shown in Table 1.

Fig. 4 shows 2D and 3D Donepezil's interactions as ligand with the target 2ACE, including H-bond, π-π and van der Waal's interactions with residues of His398, Cys402, Tyr524, Phe284, and Pro361 amino acids in the active site of AChE with binding energy -10.6 kcal/mol

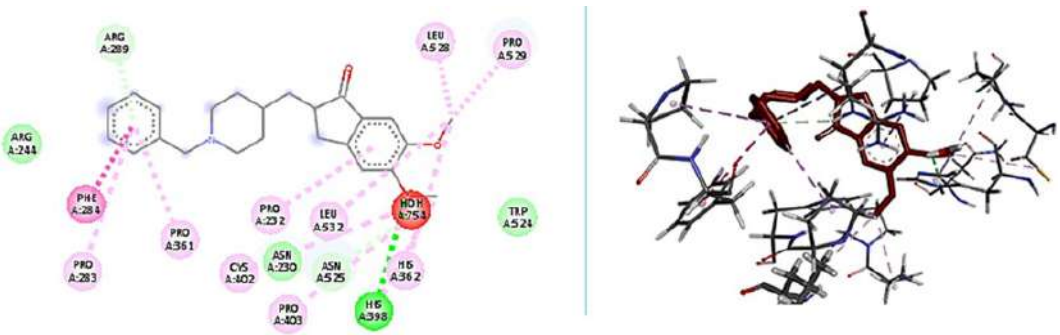

Fig 2. The docking interactions of Donepezil with the catalytic site of AChE enzyme

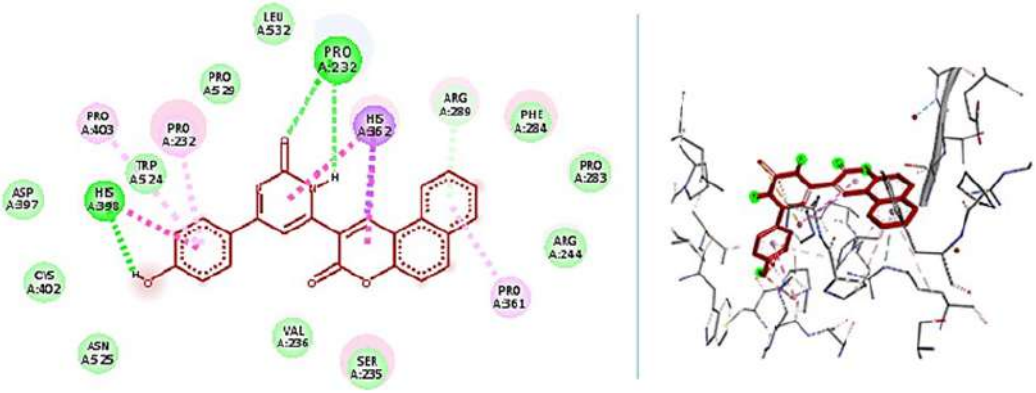

Fig 3. The docking interactions of compound 5 with the catalytic site of AChE enzyme

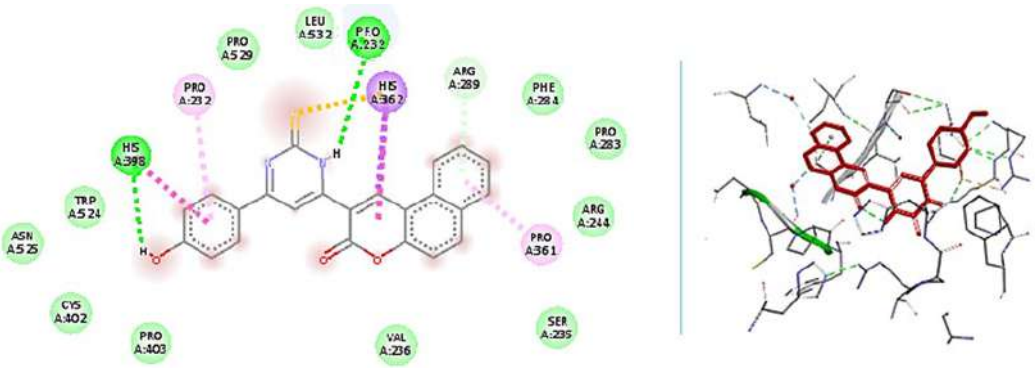

Fig 4. The docking interactions of compound 6 with the catalytic site of AChE enzyme

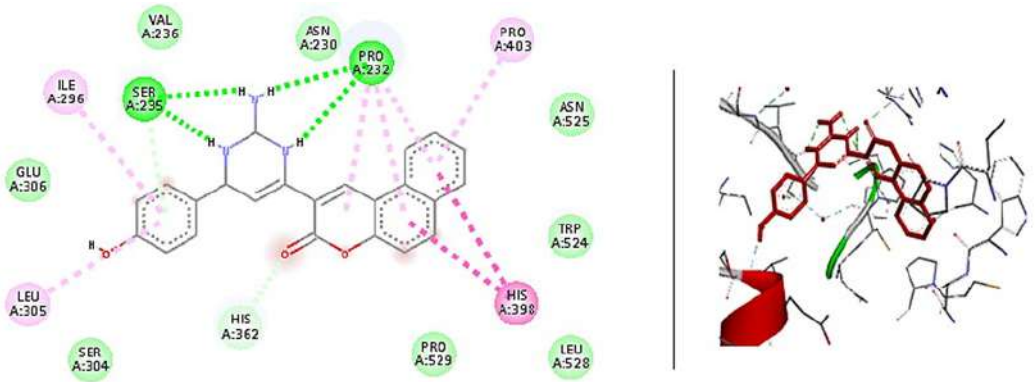

Fig 5. The docking interactions of compound 7 with the catalytic site of AChE enzyme

and distances varying from 2.68 to 3.23 Å. The docking simulation of compounds **5**–**7** had demonstrated stronger electrostatic interactions (van der Waal's, π–π stacking, and H-bond) with lower docking energies -17.4, 13.6, and -11.3 kcal/mol, respectively, when compared to the docking score of Donepezil -10.6 kcal/mol, as shown in Fig. 3–5. Among the other derivatives, derivative **7** formed four H-bond interactions with key amino acids residues: Ser235, Asn230, Pro232, and His398, whereas the other electrostatic interactions formed with His362, Arg289, Arg244, Pro361, Pro232, Pro403, Val236, Leu532, and Phe284. In derivatives **5** and **6**, similar binding interactions with active pockets of 2ACE were observed due to the high homology of binding site residues and other electrostatic interactions formed with residues Cys402, Trp524, and Ala234 amino acids. The huge number of various binding interactions with amino acid residues of the active pocket in the target protein and

Table 1. Docking results obtained for synthesized coumarin derivatives with acetylcholinesterase (PDB ID: 2ACE)

Compound	Ligand moiety	Site	Interaction	E (kcal/mol)
5	OH	N HIS 398 (A)	H- acceptor	-11.3
	NH	O PRO 232(A)	H- acceptor	
	C=O	N PRO 232(A)	H- donor	
	6-ring	ARG 289(A)	π–H	
	C=C	HIS 362(A)	π–π, π-Si	
6	OH	N HIS 398 (A)	H- acceptor	-13.6
	NH	O PRO 232(A)	H- acceptor	
	C=S	N HIS 362(A)	π–Sulfur	
	6-ring	ARG 289(A)	π–H	
	C=C	HIS 362(A)	π–π	
7	NH_2	O SER 235 (A)	H- acceptor	-17.4
	NH	O PRO 232(A)	H- acceptor	
	C=O	N HIS 362(A)	π–H	
	6-ring	SER 235(A)	π–H	
	C=C	HIS 398(A)	π–π	
Donepezil	$-OCH_3$	NH HIS 398 (A)	H- acceptor	-10.6
		O PRO 232(A)	H- acceptor	
	6-ring	N PHE 284(A)	H- donor	
		ARG 289(A)	π–H	
	C=C	HIS 362(A)	π–π, π-Si	
		PRO 361(A)	π–π	

favorable binding energies suggests that these compounds could be used as clinically effective inhibitors for the AChE enzyme.

Biological Evaluation

Acetylcholinesterase inhibition assay

Inhibitory activity of the newly synthesized compounds was screened in vitro for their anti-AChE activity. Electric eel AChE was used as the target enzyme. Meanwhile, donepezil hydrochloride was used as a reference compound. The obtained data are listed in Table 1. The first test tried to study the effect of DMSO solvent, which no longer exhibited any inhibitory effect [28]. Then examine the **6**, **7** in the mixture at exceptional concentrations (10^{-4}, 10^{-6}, 10^{-8}, 10^{-10}, and 10^{-12} M). Before every set of inhibition experiments was conducted, the AChE activity was measured using four distinct concentrations of acetylthiocholineiodide substrate (0.02, 0.04, 0.06, and 0.08 M) in a healthy subject in Fig. 6.

The impact of distinct concentrations of every inhibitor at acetylcholine concentrations on AChE undertaking is illustrated in Fig. 7. As clear in Fig. 3, the **6** and **7** compounds had low inhibition effect on AChE activity at low concentrations (10^{-12} M), but at high concentrations (10^{-6} and 10^{-4} M) and middle concentrations (10^{-10} and 10^{-8} M) of two compounds had high inhibition effect on AChE. The biochemical tests indicated that two prepared compounds have caused noticed inhibitory effects on enzyme activity compared with the measured control values of 2.5 μmol/2 min/mL, see Table 2.

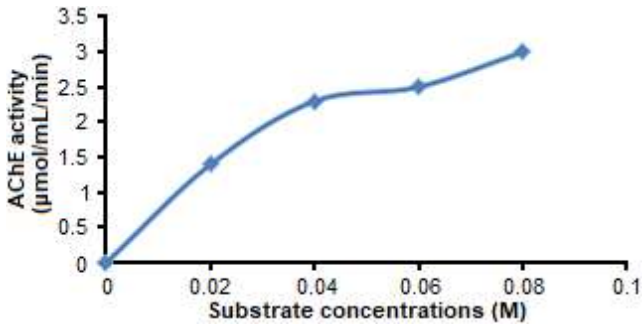

Fig 6. The hyperbolic curve of AChE at variant concentrations of AChTI and in the absence of inhibitor

From these results, it is clear that **6** and **7** inhibited AChE activity in healthy samples. Table 2 showed that the more significant inhibition percent was found at 10^{-4} and 10^{-10} M concentrations, and low inhibition was obtained at 10^{-12} and 10^{-4} M in **6** and **7**, respectively. These can be attributed to the presence of six common interactions. First, the benzocumarin ring interacts with the phenyl of the Trp286 indole by a π–π interaction—the nitrogen atom of pyrimidine forms a hydrogen bond with the hydroxy of Tyr124. Second, the carbonylphenyl ring creates a π–π interaction with the indole of Trp86. This carbonyl substituent is also essential for polar interactions. Third, the phenoxy group forms two hydrogen bonds with the carbonyl of Gly120 by acting as a hydrogen donor. Finally, the hydroxy of the Tyr133 acts as a hydrogen acceptor or may create another hydrogen bond with the carbonyl of Glu202.

Our work could not be compared exactly to other work because, as far as we know, this is the only study that demonstrates the effects of new prepared coumarins derivatives on the activities of AChE enzyme activity. However, Abdul-Rida et al. [23] concluded that the tested coumarin derivatives are potential candidates as leads for potent and efficacious ChEs inhibitors. The assayed compounds exhibited moderate inhibitory activity against AChE, with IC_{50} values ranging from 1.828–8.252 mM.

Study Type of Inhibition

The second part of this study is to decide the type of inhibition and kinetic parameters (K_m, V_{max}, and K_i) at extraordinary substrate concentrations and beneath the same stipulations. Lineweaver-Burk's graph showed that (**6** and **7** inhibit AChE by different types of inhibition and gave a different value of K_i. The results are summarized in Table 3 and Fig. 8.

The study indicated that K_m was varied from same or less in the presence of prepared compounds compared with the non-inhibiting system. A low K_m means the higher affinity of the substrate toward enzyme

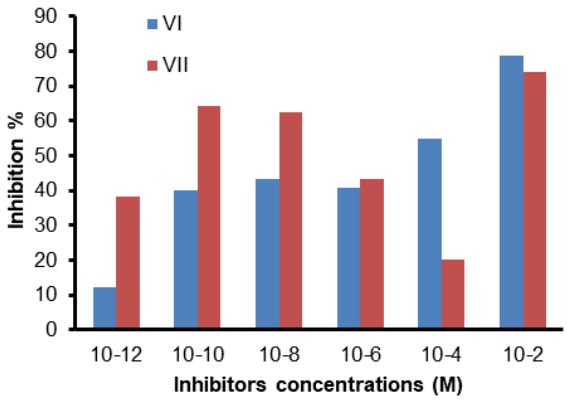

Fig 7. Effect of different concentrations of 6 and 7 compounds on AChE activity represented as a percent of inhibition

Table 2. Effect of different concentrations of 6 and 7 in sera of normal subjects on the AChE activity

Samples	Inhibitor conc. (M)	AChE activity (μmol/2 min/mL)	% Inhibition
control	zero	2.5	-
6	10^{-2}	0.533	78.68*
	10^{-4}	1.128	54.88
	10^{-6}	1.48	40.8
	10^{-8}	1.42	43.2
	10^{-10}	1.5	40
	10^{-12}	2.199	12.04
7	10^{-2}	0.652	73.92*
	10^{-4}	2	20
	10^{-6}	1.42	43.2
	10^{-8}	0.937	62.52
	10^{-10}	0.89	64.41
	10^{-12}	1.54	38.4

* Excluded in the kinetic study due to turbid solution

Table 3. The kinetic parameters of AChE with and without inhibitors in sera of healthy subjects

Sample		Inhibitor conc. (M)	K_m (M)	V_{max} (μmol/2 min/mL)	K_i (M)	Inhibition type
Control		Zero	0.05	5	-	-
6	Maximum inhibition	10^{-4}	0.05	2.77	1.25×10^{-4}	Non-comp
	Minimum inhibition	10^{-12}	0.041	3.33	1.99×10^{-12}	Un-comp
7	Minimum inhibition	10^{-4}	0.04	3.44	2.2×10^{-4}	Un-comp
	Maximum inhibition	10^{-10}	0.033	2.63	1.1×10^{-10}	Un-comp

*Non-comp: noncompetitive inhibition
Un-comp: uncompetitive inhibition

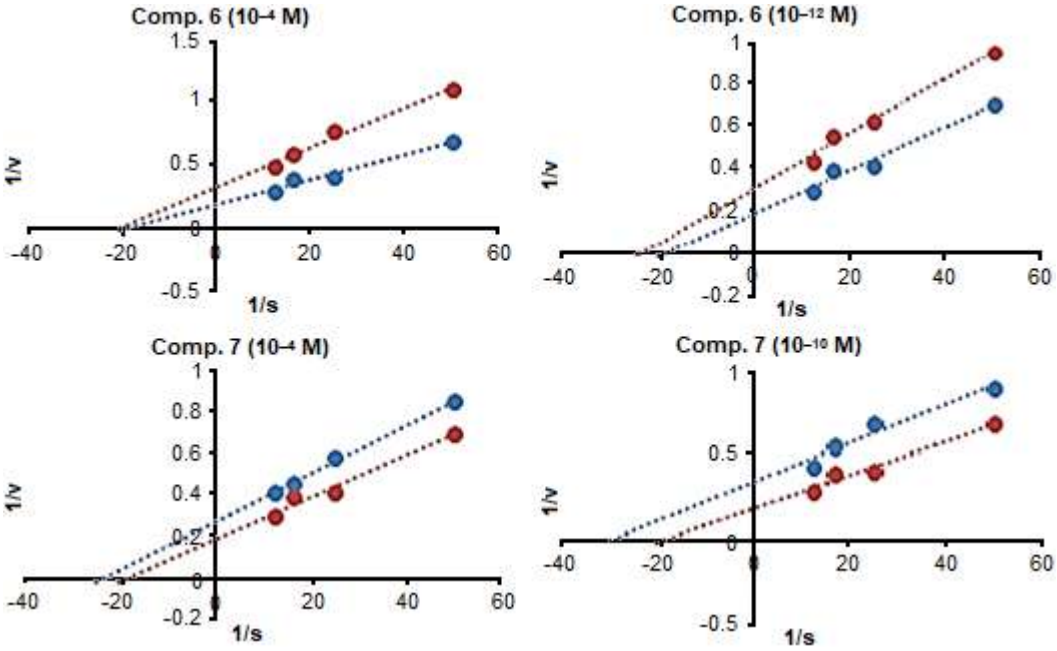

Fig 8. Lineweaver-Burk graphs at four different AChTI concentrations at maximum and minimum inhibition concentrations of 6 and 7 in healthy and patient samples

and the lower affinity of inhibitors to fits into the active-site cleft of the enzyme, which is present in **6** at concentrations of 10^{-12} M and in **7** at concentrations of 10^{-4} and 10^{-10} M (uncompetitive inhibition). On the other hand, 10–4 M concentrations do not compute with a substrate on the enzyme's active site (noncompetitive inhibition). The affinity is influenced by several factors, such as size, three-dimensional structure, and the presence of metals imidazole complexes that easily bind non-covalently to the active site. AChE showed inhibition constant K_i in the range of 10^{-4}–10^{-12} M in the presence of maximum and minimum inhibitors concentrations, probably due to variant types of inhibition from non and uncompetitive.

Table 3 clearly showed that the V_{max} value for the control sample (5 KU/L) was higher than in inhibited samples. So, it is clear that the amount of active enzyme V_{max} is present in the non-inhibited system. Ilkay et al. [29] showed AChE inhibitory activities of seven coumarin derivatives (umbelliferone (1), 4-methylumbelliferone (2), 4-hydroxycoumarin (3), scopoletin (4), 8-methoxy psoralen (5), bergapten (6), and iso-bergapten (7)). A furanocoumarin mixture obtained from *Heracleum crenatifolium* Boiss (Umbelliferae), as well as two anthraquinone derivatives (rhein (8) and aloe-emodine (9)) and one stilbene, rhapontin (10), were tested by the spectrophotometric method of Ellman using an ELISA microplate-reader at

1 mg/mL. Among them, the furanocoumarin mixture (68.8 ± 0.76%), bergapten (62.4 ± 0.74%), aloe-emodine (57.2 ± 1.32%), scopoletin (53.1 ± 0.83%), and 4-methyl umbelliferone (62.3 ± 1.03%) showed over 50% inhibition against AChE. The distinction in K_i values allows us to conclude that no longer all of the assumptions underlying basic Michaelis–Menten equations are being obeyed and that the facts are steady with the kinetics of a tight-binding inhibitor. Also, the outcomes demonstrated that **6** and **7** exhibit different sorts of inhibition at maximum and minimum concentration. The combined inhibition by using **6** and **7** in most inhibition can explain for to inhibitors structure that makes conformational modifications after binding to –SH, –COOH, imidazole groups of Ser, His, and Glu in AChE, which is both localized in the active core or is essential in deciding the energetic conformation of the enzyme molecule.

On the other hand, noncompetitive inhibition can be defined according to the classical models described that the inhibitor binds to the allosteric site that reasons conformational trade lock the enzyme and prevents the substrate binding or lowering substrate affinity to AChE. Baruah et al. [30] found that inhibit AChE in an anon-competitive manner with Chromenyl Coumarate showing the highest inhibition potency. Sequestration of the inhibitors by human serum albumin rendered the reduction in AChE inhibition activity. Therefore, a potential AChEI is expected to bind with AChE strongly but with a lower tendency to be confiscated in HSA.

CONCLUSION

In conclusion, novel benzo[*f*]coumarin derivatives bearing various pyrimidines were synthesized with good yields via cyclocondensation of chalcone **4** with urea, thiourea, and guanidine HCl in the presence of glacial acetic acid. The synthesized compounds were screened against Acetylcholinesterase activity. The obtained results revealed that the benzocoumarin derivatives conjugated with various pyrimidines contain substituted groups (–OH, –S, and –NH). It showed that **6** and **7** inhibit AChE activity in healthy samples. The more significant inhibition percent was found at 10^{-4} and 10^{-10} M concentrations, while the low inhibition was obtained at 10^{-12} and 10^{-4} M in **6** and **7**, respectively.

ACKNOWLEDGMENTS

The authors are very thankful and gratefully to Department of Chemistry, College of Education, University of Al-Qadisiyah for support in providing necessary facilities. We also wish to thank Dr. Najim A. Al-Masoudi for his sustain guidance to complete this work.

REFERENCES

[1] Tran, L., and Ha-Duong, T., 2015, Exploring the Alzheimer amyloid-β peptide conformational ensemble: A review of molecular dynamics approaches, *Peptides*, 69, 86–91.

[2] Terry, A.V., and Buccafusco, J.J., 2003, The cholinergic hypothesis of age and Alzheimer's disease-related cognitive deficits: Recent challenges and their implications for novel drug development, *J. Pharmacol. Exp. Ther.*, 306 (3), 821–827.

[3] Knopman, D.S., Petersen, R.C., and Jack, C.R., 2019, A brief history of "Alzheimer disease": Multiple meanings separated by a common name, *Neurology*, 92 (22), 1053–1059.

[4] Alipour, M., Khoobi, M., Moradi, A., Nadri, H., Moghadam, F.H., Emami, S., Hasanpour, Z., Foroumadi, A., and Shafiee, A., 2014, Synthesis and anti-cholinesterase activity of new 7-hydroxycoumarin derivatives, *Eur. J. Med. Chem.*, 82, 536–544.

[5] Ali, M.Y., Jannat, S., Jung, H.A., Choi, R.J., Roy, A., and Choi, J.S., 2016, Anti-Alzheimer's disease potential of coumarins from *Angelica decursiva* and Artemisia capillaris and structure-activity analysis, *Asian Pac. J. Trop. Med.*, 9 (2), 103–111.

[6] Anand, P., and Singh, B., 2013, A review on cholinesterase inhibitors for Alzheimer's disease, *Arch. Pharm. Res.*, 36 (4), 375–399.

[7] Sahoo, C.R., Sahoo, J., Mahapatra, M., Lenka, D., Sahu, P.K., Dehury, B., and Paidesetty, S.K., 2021, Coumarin derivatives as promising antibacterial agent(s), *Arabian J. Chem.*, 14 (2), 102922.

[8] Chen, Z., Bi, J., and Su, W., 2013, Synthesis and antitumor activity of novel coumarin derivatives via a three-component reaction in water, *Chin. J. Chem.*, 31 (4), 507–514.

[9] Hassan, A.Y., Sarg, M.T., El Deeb, M.A., Bayoumi, A.H., and El Rabeb, S.I., 2018, Facile synthesis and anticancer activity study of a novel series of substituted and fused coumarin derivatives, *J. Heterocycl. Chem.*, 55 (6), 1426–1443.

[10] Sairam, K.V., Gurupadayya, B.M., Vishwanathan, B.I., Chandan, R.S., and Nagesha, D.K., 2016, Cytotoxicity studies of coumarin analogs: Design, synthesis and biological activity, *RSC Adv.*, 6 (101), 98816–98828.

[11] Jaber, Q.A.H., Abdul-Rida, N.A., and Adnan, S., 2020, Boosting 3*H*-benzo[*f*]chromen-3-one chalcone with anti-inflammatory drugs: Synthesis, characterization, and evaluation of cytotoxicity and antimicrobial activity, *Russ. J. Org. Chem.*, 56 (9), 1622–1627.

[12] Lei, L., Xue, Y., Liu, Z., Peng, S., He, Y., Zhang, Y., Fang, R., Wang, J., Luo, Z., Yao, G., Zhang, J., Zhang, G., Song, H., and Zhang, Y., 2015, Coumarin derivatives from *Ainsliaea fragrans* and their anticoagulant activity, *Sci. Rep.*, 5 (1), 13544.

[13] Ghate, M., Kusanur, R.A., and Kulkarni, M.V., 2005, Synthesis and in vivo analgesic and anti-inflammatory activity of some bi heterocyclic coumarin derivatives, *Eur. J. Med. Chem.*, 40 (9), 882–887.

[14] Basanagouda, M., Jadhav, V.B., Kulkarni, M.V., and Rao, R.N., 2011, Computer aided prediction of biological activity spectra: Study of correlation between predicted and observed activities for coumarin-4-acetic acids, *Indian J. Pharm. Sci.*, 73 (1), 88–92.

[15] Hassan, M.Z., Osman, H., Ali, M.A., and Ahsan, M.J., 2016, Therapeutic potential of coumarins as antiviral agents, *Eur. J. Med. Chem.*, 123, 236–255.

[16] Hu, X.L., Gao, C., Xu, Z., Liu, M.L., Feng, L.S., and Zhang, G.D., 2018, Recent development of coumarin derivatives as potential antiplasmodial and antimalarial agents, *Curr. Top. Med. Chem.*, 18 (2), 114–123.

[17] Chen, L.Z., Sun, W.W., Bo, L., Wang, J.Q., Xiu, C., Tang, W.J., Shi, J.B., Zhou, H.P., and Liu, X.H., 2017, New arylpyrazoline-coumarins: Synthesis and anti-inflammatory activity, *Eur. J. Med. Chem.*, 138, 170–181.

[18] Chougala, B.M., Samundeeswari, S., Holiyachi, M., Naik, N.S., Shastri, L.A., Dodamani, S., Jalalpure, S., Dixit, S.R., Joshi, S.D., and Sunagar, V.A., 2018, Green, unexpected synthesis of bis-coumarin derivatives as potent anti-bacterial and anti-inflammatory agents, *Eur. J. Med. Chem.*, 143, 1744–1756.

[19] Wang, S.B., Liu, H., Li, G.Y., Li, J., Li, X.J., Lei, K., Wei, L.C., Quan, Z.S., Wang, X.K., and Liu, R.M., 2019, Coumarin and 3,4-dihydroquinolinone derivatives: Synthesis, antidepressant activity, and molecular docking studies, *Pharmacol. Rep.*, 71 (6), 1244–1252.

[20] Bai, Y., Li, D., Zhou, T., Qin, N., Li, Z., Yu, Z., and Hua, H., 2016, Coumarins from the roots of Angelica dahurica with antioxidant and antiproliferative activities, *J. Funct. Foods*, 20, 453–462.

[21] Al-Amiery, A.A., Al-Majedy, Y.K., Kadhum, A.A.H., Mohamad, A.B., 2014, New coumarin derivatives as an eco-friendly inhibitor of corrosion of mild steel in acid medium, *Molecules*, 20 (1), 366–383.

[22] Xu, Z., Chen, Q., Zhang, Y., and Liang, C., 2021, Coumarin-based derivatives with potential anti-HIV activity, *Fitoterapia*, 150, 104863.

[23] Yusufzai, S.K., Khan, M.S., Sulaiman, O., Osman, H., and Lamjin, D.N., 2018, Molecular docking studies of coumarin hybrids as potential acetylcholinesterase, butyrylcholinesterase, monoamine oxidase A/B and β-amyloid inhibitors for Alzheimer's disease, *Chem. Cent. J.*, 12 (1), 128.

[24] Abdul-Rida, N.A., Adnan, S., and Jaber, Q.A.H., 2020, Development of novel imaging fluorescent agents bearing anti-inflammatory drugs: Synthesis, structural characterization and evaluation of biological activity, *Russ. J. Bioorg. Chem.*, 46 (4), 620–626.

[25] Matos, M.J., Vilar, S., Gonzalez-Franco, R.M., Uriarte, E., Santana, L., Friedman, C., Tatonetti,

N.P., Viña, D., and Fontenla, J.A., 2013, Novel (coumarin-3-yl)carbamates as selective MAO-B inhibitors: Synthesis, *in vitro* and *in vivo* assays, theoretical evaluation of ADME properties and docking study, *Eur. J. Med. Chem.*, 63, 151–161.

[26] Ellman, G.L., Courtney, K.D., Andres, V., and Featherstone, R.M., 1961, A new and rapid colorimetric determination of acetylcholinesterase activity, *Biochem. Pharmacol.*, 7 (2), 88–95.

[27] Rizvi, S.M.D., Shakil, S., and Haneef, M., 2013, A simple click by click protocol to perform docking: AutoDock 4.2 made easy for non-bioinformaticians, *EXCLI J.*, 12, 831–857.

[28] Nabil, Z., 2015, Kinetics for the inhibition of serum acetylthiocholin esterase activity by some prepared phenobarbital derivatives, *Int. J. Biochem. Res. Rev.*, 7 (2), 100–111.

[29] Ilkay, O., Fatma, T., and Bilge, S., 2008, Coumarin, anthroquinone and stilbene derivatives with anticholinesterase activity, *Z. Naturforsch., C: Biosci.*, 63 (5-6), 366–370.

[30] Baruah, P., Basumatary, G., Yesylevskyy, S.O., Aguan, K., Bez, G., and Mitra, S., 2018, Novel coumarin derivatives as potent acetylcholinesterase inhibitors: Insight into efficacy, mode and site of inhibition, *J. Biomol. Struct. Dyn.*, 37 (7), 1–52.

Supplementary Data

This supplementary data is a part of paper entitled "Development of an Analytical Method for Kasugamycin Residue in Herbal Medicine, *Achyranthes japonica* Nakai".

Table S1. Recovery rate (%) according to the difference in extraction solvents

Compound	Recovery rate (%)[1)]		
	Methanol	Methanol:water (50:50, v/v)	Water
Kasugamycin	58.4 ± 2.6	90.2 ± 2.1	96.3±2.7

[1)] Triplicate recovery average ± RSD

Table S2. Recovery rate (%) by loading volume of SCX SPE cartridge after matrix application

Loading volume	Recovery rate (%				
	Loading	Water 10 mL[1]	Methanol 10 mL[1]	5% NH_4OH in methanol 10 mL[2]	Total
1 mL	-	-	-	95.5	95.5
2 mL	-	-	-	101.2	101.2
3 mL	-	-	-	97.4	97.4
4 mL	-	24.5	-	69.5	94.0

[1)] Washing

[2)] Elution

"-" means that the target compound was not eluted from the column and therefore no recovery

Table S3. LC/MS/MS calibration curve of working solution at various concentrations range

	STD #1	STD #2	STD #3	STD #4	STD #5	STD #6
Concentration (μg/mL) at volume 500 μL	0.005	0.008	0.01	0.05	0.08	0.1
Matrix (μL)	500	500	500	500	500	500

Table S4. Recovery rate and MLOQ for chlorantraniliprole in *Achyranthes japonica Nakai* root

Herbal medicine	Fortification (mg/L)	Recovery (%)[a)]	C.V. (%)[b)]	MLOQ (mg/kg)
Achyranthes japonica Nakai	0.04	97.2	8.8	0.04
	0.4	86.3	2.8	

[a)] Mean values of triplicate samples with standard deviations

[b)] CV (coefficient of variation, %) = standard deviation/average × 100

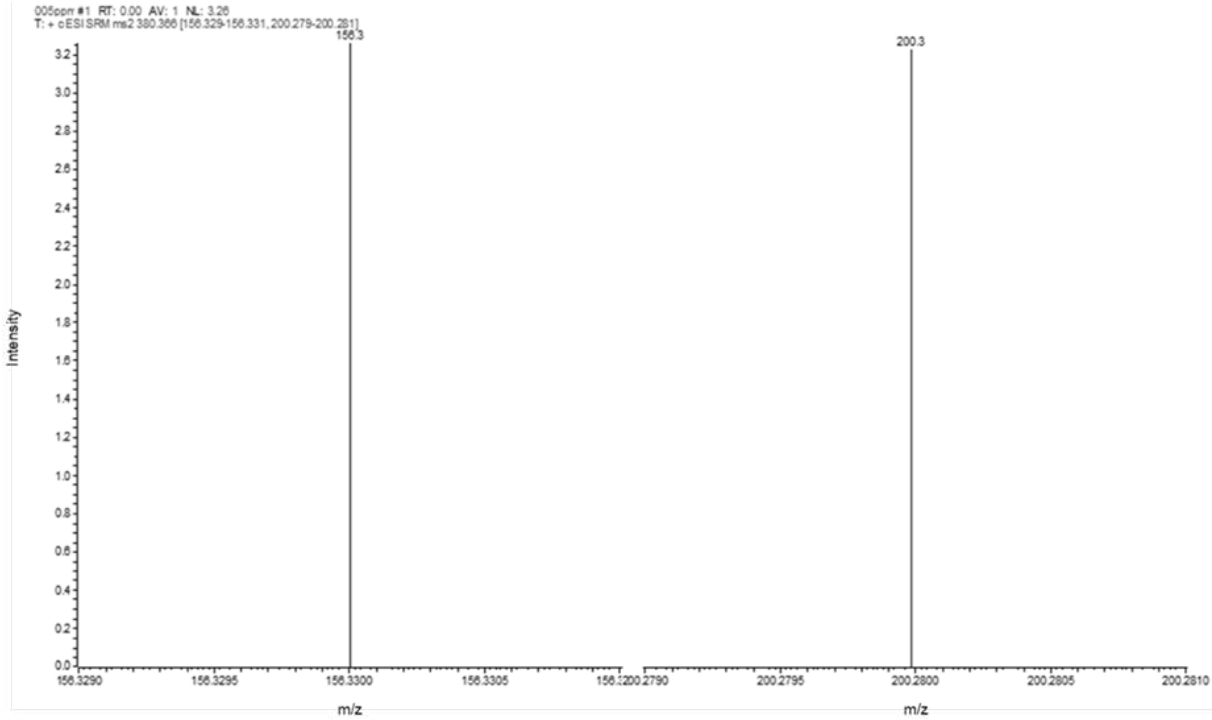

Fig S1. The MS-MS iron scan and fragmentation of kasugamycin

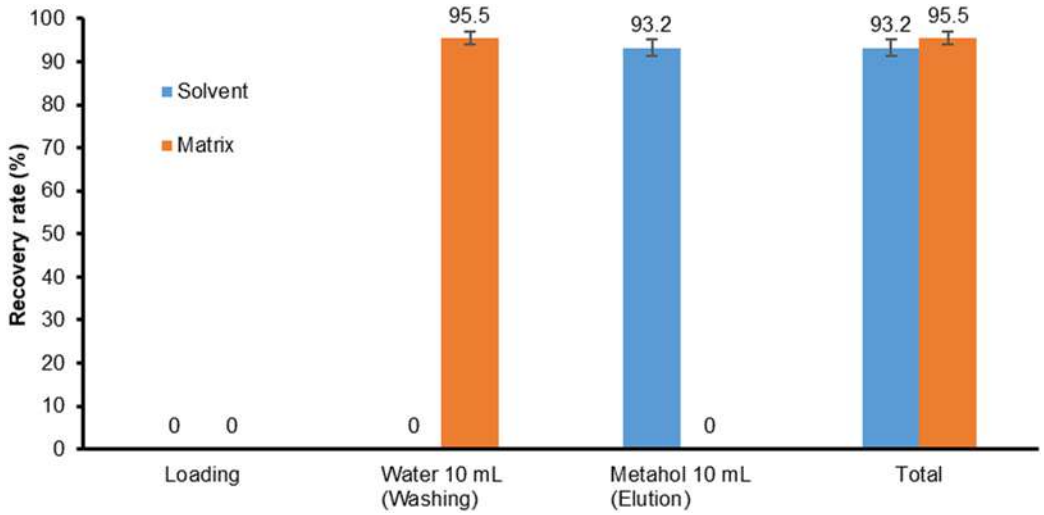

Fig S2. Recovery rate (%) elution purified by silica SPE cartridge

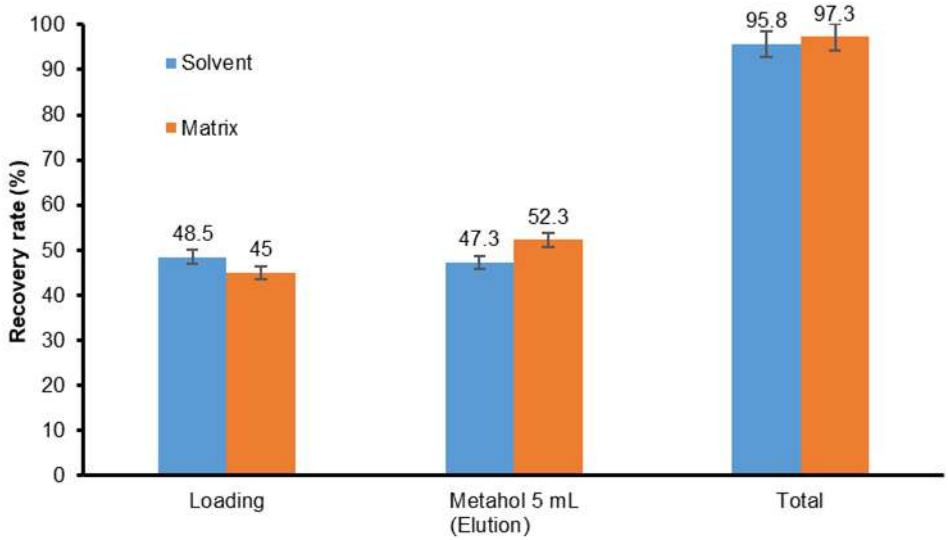

Fig S3. Recovery rate (%) of elution purified by HLB SPE cartridge

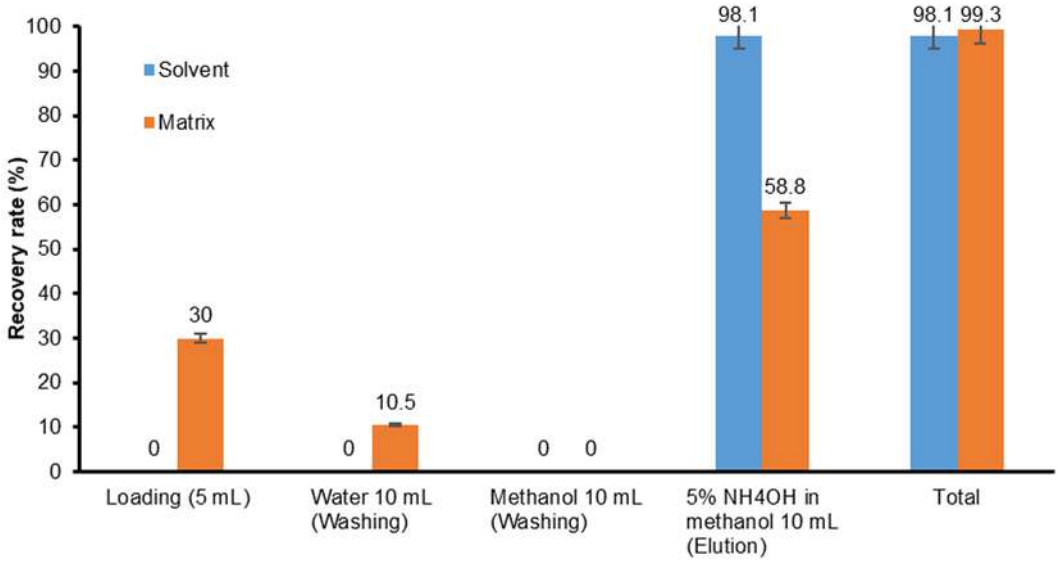

Fig S4. Recovery rate (%) of elution purified by SCX SPE cartridge

Development of an Analytical Method for Kasugamycin Residue in Herbal Medicine, *Achyranthes japonica* Nakai

Jeong Yoon Choi[1], Hun Ju Ham[2], Min-woo Kim[1], Abd Elaziz Sulieman Ahmed Ishag[1,3], and Jang-Hyun Hur[1*]

[1]*Department of Biological Environment, Kangwon National University, Chuncheon 24341, Republic of Korea*

[2]*Environment Friendly Agricultural Products Safety Center, Chuncheon 24341, Republic of Korea*

[3]*Department of Crop Protection, University of Khartoum, Khartoum North, Shambat 13314, Sudan*

* ***Corresponding author:***

email: hurpub303@gmail.com

Received: May 19, 2021
Accepted: October 12, 2021

DOI: 10.22146/ijc.65970

Abstract: *This study developed a suitable analytical method for kasugamycin residues in* Achyranthes japonica *using LC/MS/MS equipped with an amide column for polar substances. Extraction and cleanup processes were done at pH 4.5–5. Purification efficiency was assessed and confirmed step by step by selecting silica, hydrophilic-lipophilic balance (HLB), strong cation exchange (SCX), and double (HLB and SCX) cleanup SPE cartridges. The results indicated that silica SPE cartridge exhibited overloading tendency, while HLB SPE cartridge had low cleaning efficiency. Among SPE cartridges used, double cleanup and SCX were found sufficient with respective matrix effects of –15% and +14%, respectively. The LOD and LOQ were 0.008 ng and 0.04 mg/kg, respectively. The correlation coefficient (R^2) was higher than 0.99, recovery rate ranges were 86.3–97.2%, and the RSD was below 8.8%. All methods are consistent with the Codex guidelines criteria. This study developed an appropriate LC/MS/MS analytical method for kasugamycin residue analysis in A. japonica with optimized, efficient extraction and purification conditions using a single SCX SPE cartridge, which is simple and time-efficient. In addition, the HLB and SCX SPE cartridges of the double cleanup methods were identified as primary methods that can be applied for the cleanup of other medicinal herbs.*

Keywords: *LC-MS/MS analysis; Kasugamycin residues;* Achyranthes japonica*; SPE-cartridges*

■ INTRODUCTION

Herbal medicine uses medicinal crops' dried roots and leaves for various purposes such as health promotion and disease treatment [1]. The herbal medicine *Achyranthes japonica* Nakai (Japanese chaff flower) is a perennial herb belonging to the Amaranthaceae family. *A. japonica* contains saponin and a large amount of inflammation-relieving ingredients; thus, it is widely used for arthritis and as a diuretic and tonic [2]. However, in the fall, *A. japonica* is frequently affected by a powdery mildew disease caused by *Albugo achyranthis* (P. Henn.). This disease could be controlled using a fungicide of copper sulfate basic, copper oxychloride with metalaxyl-m, and copper oxychloride with kasugamycin [3]. Among these, kasugamycin of the aminoglycoside family is a subject of social interest because it can have a potentially adverse effect on the treatment of diseases in humans and livestock due to the occurrence of antibiotic-resistant bacteria [4].

Kasugamycin, developed as an agricultural fungicide, is a highly polar substance with a Log P_{ow} value of –5.75 and is a dissociative compound with carboxy and amino groups in the molecule [5]. The pKa of the carboxylic acid (pKa1), primary cyclic amine (pKa2), and secondary amine (pKa3) are 3.23, 7.73, and 11.0, respectively, which is characterized by ionization of certain areas in various pH ranges [6]. The solubility of

kasugamycin is 228 g/L in water (pH 7, 25 °C) and 7.44 mg/L in methanol (25 °C). However, it is hardly soluble in most organic solvents. Moreover, kasugamycin is non-volatile and is physically and chemically unstable in heat; thus, its analysis process is difficult due to its low sensitivity during analysis [5]. According to previous studies, biological potency assays (cup, standard strain *Pseudomonas fluorescens*) and capillary electrophoresis (CE) were performed, but there were disadvantages in that the analysis time was long, and there were poor precision and selectivity [7]. Also, in the case of HPLC and GLC, which are often used for residual analysis, HPLC/UV showed low absorbance because there was no chromophore for ultraviolet or fluorescence, so there was a sensitivity problem. In addition, it has been reported that the time required for pretreatment is long, and reproducibility is low [5-6,8]. In particular, it has been reported that aminoglycoside-based components are challenging to analyze using GLC without the derivatization of amino and hydroxyl groups due to the hydrophilicity and non-volatile nature of the molecule [9].

On the other hand, studies that analyze kasugamycin on agricultural samples using LC/MS/MS have been conducted steadily recently, with excellent selectivity and sensitivity. Several reports confirmed using various SPE methods to remove interfering substances from samples and improve the sensitivity of kasugamycin. Many authors reported the purification of peppers and soil extracts using an MCX SPE cartridge [7,10]. A study of simultaneous analysis of agricultural fungicides using an HLB SPE cartridge and MCX SPE cartridge was reported. The simultaneous analysis of kasugamycin and validamycin-A through a consecutive cleanup process combined HLB SPE cartridge and SCX SPE cartridge as described in previous studies [8], and simultaneous analysis of kasugamycin and streptomycin in five vegetables was reported [11].

Furthermore, research conducted by the Korean Ministry of Food and Drug Safety (MFDS) to extract kasugamycin with methanol (pH 13) for five representative agricultural products, namely brown rice, soybeans, peppers, potatoes, and tangerines, purify it with an HLB SPE cartridge, and conduct analysis using LC/MS/MS was reported [12]. As described above, there are various established methods for analyzing kasugamycin residues in agricultural products in the previous studies; however, there is no report of residual analysis for kasugamycin in herbal medicines containing complex active ingredients. Therefore, this study aims to establish a residual analysis method for the kasugamycin in herbal medicine for the first time in this field by selecting *A. japonica* Nakai among herbal medicines with various pharmacological components. In particular, to minimize the interference effect that may occur due to the complex matrix in herbal medicine (*A. japonica* Nakai); by systematically comparing and analyzing the purification efficiency of various SPE cartridges, including extraction and distribution processes. Furthermore, the analysis method also was intended to confirm whether it conforms to the analysis criteria of pesticide residues of the International Food Standards Commission (Codex Alimentarius Commission, CAC/GL 40) and the Guideline on Standard Procedure for Preparation of Test Methods for Food [13] of the Korean MFDS.

■ EXPERIMENTAL SECTION

Reagents and Instruments

The standard product for the analysis of kasugamycin was bought from Sigma-Aldrich (USA) and had a purity of 98.7% or higher. The HPLC grade solvents used in the analysis process were water, dichloromethane, acetonitrile, and methanol, purchased from Thermo Fisher Scientific (USA). Formic acid (98.0%) and ammonia solution were purchased from Sigma-Aldrich (USA) and Daejeonghwageum (Korea), respectively. Also, other organic solvents and reagents were purchased and used for residue analysis. For purification, SPE cartridges, silica ((55 µm, 70 Å), 1 g) and SCX ((55 µm, 70 Å), 1 g) obtained from Phenomenex (USA), and HLB ((60 µm, 80 Å), 500 mg) purchased from Waters (USA) were used. For uniform extraction, a sonicator (Jeio Tech. Co. Ltd., Korea) was used for sample extraction, and a centrifuge (Allegra X-1R, Beckman Coulter Life Sciences, USA) was used for

centrifugation. In the purification process, a vacuum manifold (Visiprep SPE vacuum manifold, Supelco, USA) and vacuum pump (DOA-P704-AC, Gast, USA) were used for the SPE cartridge. Kasugamycin is highly soluble in water or methanol and ionized in wide pH ranges. The physicochemical properties and chemical structural formulas of kasugamycin are shown in Table 1 [12,14].

Procedure

Preparation of standard solution

A stock solution was prepared by accurately taking 10.13 mg of the standard compound (98.7%) of kasugamycin, placing it in a 100 mL volumetric flask, and then dissolving it in water to make 100 μg mL^{-1}. In the same way, the working solution was diluted stepwise to concentrations of 0.005, 0.008, 0.01, 0.05, 0.08, and 0.1 μg mL^{-1}. For the standard calibration curve for quantification, the matrix was included in a 1:1 ratio of the standard solution and the extraction solution to create a matrix-matched calibration curve. Since the target component is an aminoglycoside-based fungicide that has the property of adsorbing to glass, all containers used in the analysis were made of polypropylene [12].

Herbal medicine sample

The herbal medicine, *Achyranthes japonica* Nakai, was purchased from a pharmaceutical company (Iksan, Jeollabuk-do) that applied distribution according to the drug specifications and was used after verification and a sensory evaluation a herbal medicine expert. Since the roots are used as medicinal herbs, the dried roots were ground and passed through a 2 mm sieve, and then a 5 g sample was weighed and used for analysis.

Extraction and distribution

Ten mL of distilled water was added to 5 g of the dried roots sample, and the wetting process was performed for 1 h. The extraction solvent was used after adjusting the pH to 4.5–5 by adding 0.1% formic acid to methanol, methanol/water (5/5, v/v), and water. Sample extraction was performed by ultrasonic extraction using a sonicator for 30 min, followed by centrifugation for 10 min at 4 °C and 4,000 G. The liquid-liquid distribution process was carried out by taking 5 mL of the supernatant when using water in the extraction solvent and then adding 5 mL of dichloromethane.

Purification conditions using SPE cartridge

In this study, a comparative experiment was conducted using various SPE cartridges to establish the optimal purification conditions for kasugamycin in *A. japonica*. The SPE cartridges used during the experiment were silica, HLB, and SCX SPE cartridges. The purification conditions are as follows: In the SPE cartridge refining process, a vacuum manifold device equipped with a vacuum pump was used to allow elution at a flow rate of one to two drops per second to maintain a constant flow rate and shorten the time required.

Silica SPE cartridge purification conditions. After activating the filler, 3 mL of methanol and water was

Table 1. Physicochemical properties of kasugamycin

	Kasugamycin
IUPAC name	2-amino-2-[(2R,3S,5S,6R)-5-amino-2-methyl-6-[(2R,3S,5S,6S)-2,3,4,5,6-pentahydroxycyclohexyl]oxyoxan-3-yl]iminoacetic acid
Chemical structure	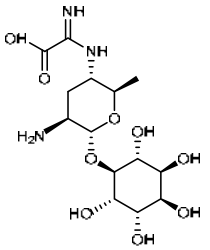
Mol. wt.	379.4
V.p. (mPa)	< 1.3 × 10^{-4} mm Hg (25 °C)
K_{ow} logP	-5.75

added to the silica SPE cartridge (1 g), 1 mL of the extraction supernatant was adsorbed onto the cartridge. After that, 10 mL of water was sequentially discharged, and kasugamycin was eluted using 10 mL of methanol.

HLB SPE cartridge purification conditions. Hydrophilic lipophilic balance (HLB) was used after activating the filler with 3 mL of methanol and water in the SPE cartridge (500 mg). Then, 5 mL of the extraction supernatant was loaded into the cartridge; 5 mL of methanol was added and combined with the previously fractionated eluate to obtain a sample.

SCX SPE cartridge purification conditions. After activating the filler using 5 mL of water and methanol in the SCX SPE cartridge (1 g), 2 mL of the extracted supernatant was adsorbed to the cartridge. After that, 10 mL of water and 10 mL of methanol were sequentially discharged, and kasugamycin was eluted using 10 mL of methanol, to which 5% NH_4OH was added.

LC/MS/MS instrument analysis

The LC-20AXR series (Shimadzu, Japan) was used as an analytical instrument for HPLC, and the TSQ Quantum Ultra (Thermo Scientific, USA) was used for mass spectrometry. The columns used included an Imtakt C18 column (2 mm ID × 100 mm, 3.0 μm, USA), Waters Hydrophilic Interaction Liquid Chromatography (HILIC) column (3.0 mm i.d. × 100 mm, 3.5 μm, USA), and Xbridge amide column (3.0 mm i.d. × 100 mm, 3.5 μm, USA). The oven temperature was fixed at 35 °C. The mobile phase solvents were 0.1% formic acid in water (A) and 0.1% formic acid in acetonitrile (B). The flow rate was 0.4 mL/min, and the injection volume was 5.0 μL. The gradient conditions were set as the following: (1) 20% A and 80% B held for 1.0 min, (2) 60% A and 40% B for 4.0 min, (3) 90% A and 10% B for 2.0 min, (4) 20% A and 80% B for 0.5 min, and finally, (5) 20% A and 80% B for 2.5 min. The overall running time was 10.0 min. The MS/MS was analyzed by the multiple reactions monitoring (MRM) method using electrospray ionization (ESI) positive mode, a spray voltage of 4.0 kV, and capillary and vaporizer temperatures of 280 and 300 °C, respectively. The Ion sweep gas pressure was set to 1.5 Arb. Sheath gas pressure was 40 units, and Aux gas pressure was 30.0 units. The precursor and product ions were monitored (Table 2).

Test method validation

The established test method for kasugamycin was verified using the detection and quantitation limits of the device, the quantitative limit of the test method, linearity, accuracy, and repeatability. As for the instrument's detection limit, a concentration in which the signal-to-noise ratio (signal/noise, S/N) of the peak detected on the chromatogram was 3 or more, and the quantitative limit was 10 or more. The limit of quantification of the test method was calculated by taking into account the minimum detection amount, sample amount, test solution amount, and dilution ratio in instrument analysis (Eq. (1)). Linearity was evaluated by making a blank line using a matrix-matched standard solution and calculating the correlation of determination (R^2). The suitability, precision, and repeatability of the

Table 2. LC/MS/MS operating parameters for the analysis of kasugamycin

HPLC	LC-20AXR series (Shimadzu, Japan)		
Detector	TSQ Quantum Ultra (Thermo Science, USA)		
Column	① Imtakt C_{18} column (2 mm I.D. × 100 mm, 3.0 μm, USA) ② Waters HILIC column (3.0 mm I.D. × 100 mm, 3.5 μm, USA) ③ Xbridge amide column (3.0 mm I.D. × 100 mm, 3.5 μm, USA)		
Oven temp.	35 °C		
Scan events	Precursor ion	Product ions	CE
	380.093	111.993	32
		156.002	33
		199.963	33

above method were analyzed after adding a standard solution equivalent to the limit of quantification (0.04 mg/L) and the limit of quantitation 10 times (0.4 mg/L) to the untreated sample. The recovery rate and analysis error of three repetitions were verified.

$$A(ng)\times\frac{B(mL)}{C(g)}\times\frac{D(mL)}{E(mL)}\times\frac{F}{G(\mu L)}=MLQQ(mg/kg) \quad (1)$$

whereas A is the minimum amount of detection, B is the volume of extraction solvent, C is sample amount, D is the final volume, E is the supernatant amount taken from the extracted solvent, F is dilution factor, and G is injection quantity.

Matrix effect (ME) of the purification method

Matrix effect refers to suppressing or enhancing the component's ionization by affecting the analyte component's instrumental sensitivity due to the target sample [15]. Matrix effect calculation is determined by comparing the calibration curve of the standard solution with the calibration curve of the matrix-matched standard solution, and the formula is shown in Eq. (2). This study calculated the matrix effect after preparing a matrix-matched standard solution of 0.005, 0.008, 0.01, 0.05, 0.08, and 0.1 mg/kg using untreated samples extracted through each SPE purification process.

$$\text{Matric effect }(\%)=\left(\frac{\text{Slope of calibration curve matrix}}{\text{Slope of calibration curve solvent}}-1\right)\times 100 \quad (2)$$

■ RESULTS AND DISCUSSION

Establishment of LC/MS/MS Analysis Conditions

In this study, analysis conditions using LC/MS/MS with high sensitivity and high selectivity were established to analyze kasugamycin. For the LC/MS/MS instrument analysis, electrospray ionization (ESI) positive mode was selected, and precursor ion and collision energy were optimized using multiple reaction monitoring (MRM) mode. The parent compound was detected as $[M+H]^+$ in positive mode, and the precursor ion was selected as m/z 380.072. The product ion was selected as m/z 111.994, m/z 156.003, and m/z 199.964. The high intensity (m/z 156.003 and m/z 199.964) was selected for quantitation (Fig. S1).

Kasugamycin is a polar compound with a log P_{ow} value of –5.75 and high solubility in water or methanol. Besides that, this compound is ionized in a wide range of pH values [16-17]. Therefore, in this study, water and acetonitrile, commonly used to analyze aminoglycoside antibiotics, were selected as the mobile phase solvent, and 0.1% formic acid solution was added to improve the sensitivity and resolution efficiency of the target component [5,18]. Previous studies found that the sensitivity of the analyte is increased when a 0.1% formic acid solution is added to the mobile phase, while the sensitivity of the signal decreases when a concentration lower than 0.1% is added [8,19].

As a result of comparing and analyzing the resolution and sensitivity of kasugamycin through C18, HILIC, and amide columns for HPLC analysis, the C18 column was rapidly eluted without staying in the column due to the amino group of kasugamycin, and it was not easy to separate it from the interfering material, as shown in Fig. 1(a) [11,19]. The HILIC column acts effectively on polar basic compounds and aminoglycosides, but its retention time was short, and peak tailing was confirmed, which required improvement, as seen in Fig. 1(b) [20-21]. An amide column is a form in which polar amide groups are bound [7]. Nevertheless, it was reported that the retention time and sensitivity were excellent, and because of confirming this, sufficient retention time and sensitivity were secured, as shown in Fig. 1(c) [7,10,19]. Therefore, in this study, an amide column highly effective for kasugamycin was selected and analyzed.

Establishment of Extraction and Distribution Process

Dried samples showed low extraction efficiency in aqueous organic solvents, so the wetting process was essential. Thus, 10 mL of distilled water was added to the dried sample during analysis [22]. The extraction solvent was reported to increase the recovery rate when a small amount of acid was added during the extraction of kasugamycin; accordingly, the pH of the extraction solvent was maintained between about 4.5–5.5 using a formic acid solution [8]. Therefore, the recovery rates of

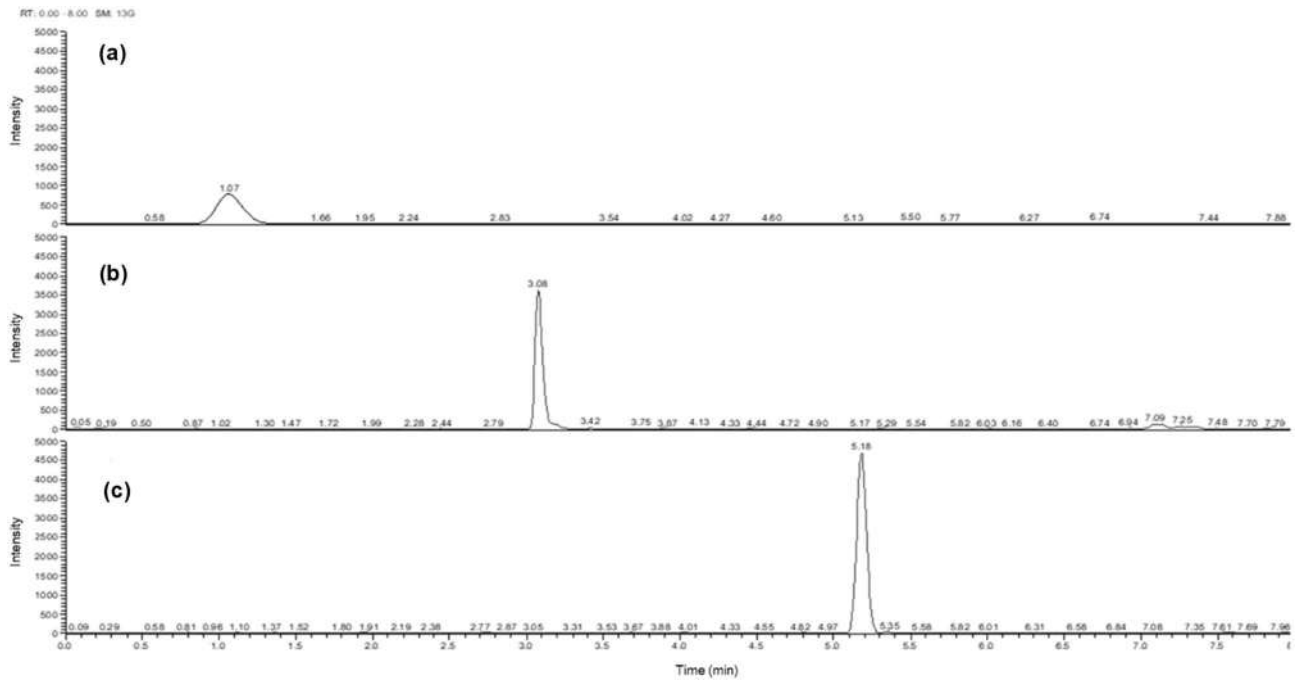

Fig 1. Chromatogram of 0.1 mg kg^{-1} kasugamycin standard solution compared by columns ((a): 0.1 mg kg^{-1} of kasugamycin using a C_{18} column, (b): 0.1 mg kg^{-1} of kasugamycin using HILIC column, (c): 0.1 mg kg^{-1} of kasugamycin using amide column)

methanol, methanol/water (5:5, v/v), and water were compared to select the optimal extraction solvent when the pH was maintained at 4.5–5. The recovery rates were 58.4%, 90.2%, and 96.3%, respectively. Water was selected as the final extraction solvent in% with the highest recovery rate (Table S1). The extraction of kasugamycin from dried samples using methanol and water was previously reported, and the recovery rate found increased as the water content increased [7]. Therefore, in this study, 10 mL of distilled water was added to the sample (5 g), followed by a wetting process for 1 h, and then extracted with 40 mL of water adjusted to pH 4.5-5 by adding 0.1% formic acid solution. After 30 min of ultrasonic extraction using a sonicator, centrifugation was performed at 4 °C and 4,000 G for 10 min. Even after the extraction process, a liquid-liquid distribution process using dichloromethane, an organic solvent with high specific gravity, was added to remove the non-polar interfering substances contained in the sample extracts. It was visually confirmed that suspended matter or precipitates in the actual extract were removed. In addition, since dichloromethane effectively removes a large amount of non-polar substances and substances of fat components, the above analysis method was determined to be effective in removing non-polar substances and interference substances fat components [7]. However, the results in Fig. 2 show that the effect of removing interference substances on the chromatogram was insufficient, so various types of SPE purification methods were attempted for further purification.

Solid-Phase Extraction (SPE) Cartridge Purification

Interfering substances continued to appear on the chromatogram even after the extraction and distribution process, and based on previous studies, a suitable SPE cartridge of kasugamycin was selected and compared. In this study, a silica SPE cartridge representing the adsorption principle as a normal cartridge was selected and analyzed for the smooth separation and analysis of the large amount of pharmacologically active substances contained in *A. japonica* and kasugamycin, and the HLB SPE cartridge analyzed for agricultural products by the

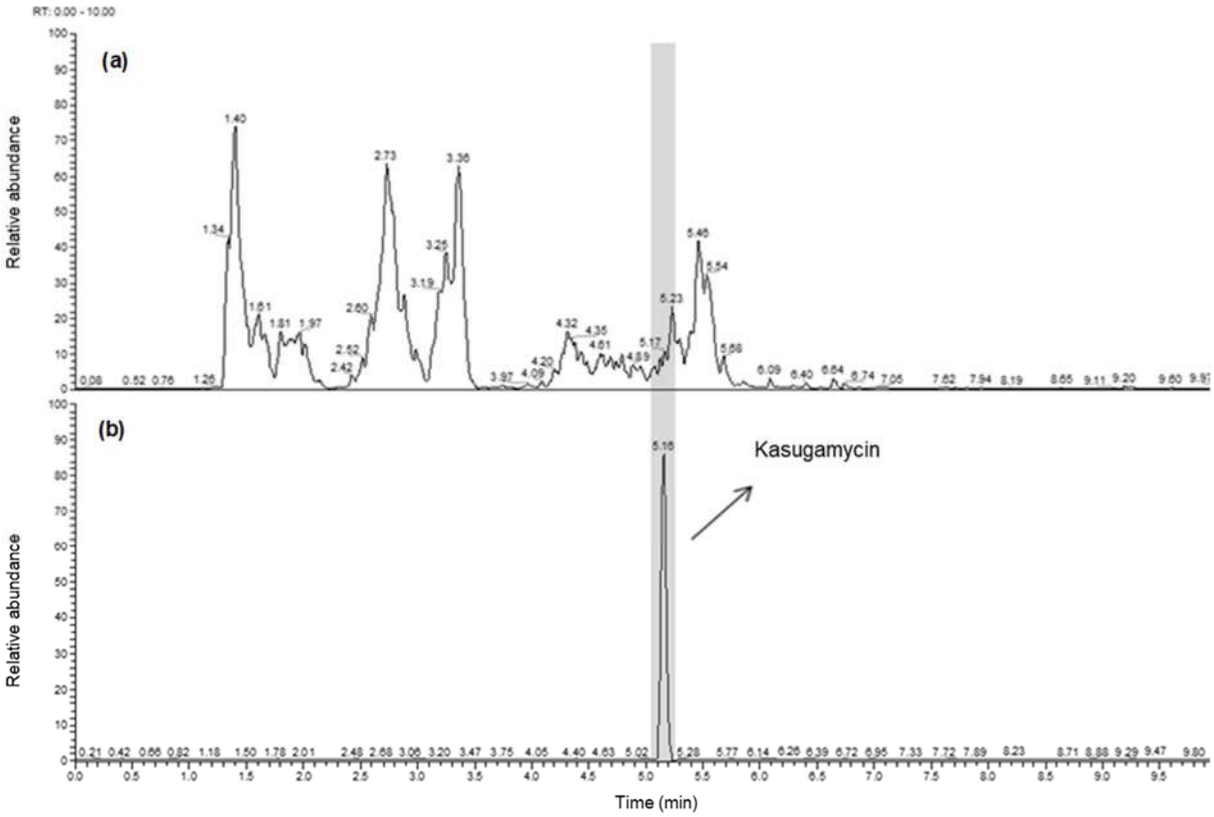

Fig 2. Chromatogram of liquid-liquid partitioning of kasugamycin in *Achyranthes japonica* Nakai and kasugamycin standard ((a): control, (b): kasugamycin 0.1 mg kg^{-1})

MFDS. As a result, it was confirmed that it could be applied to the herbal medicine *A. japonica* [12]. In addition, when analyzing kasugamycin, the SCX and SCE SPE cartridges were selected and analyzed as recommended by Zhang et al. [8].

Silica SPE cartridge

The current study is intended to check whether the silica SPE cartridge normally used in the cleanup process during the analysis of pesticide residues can be used to clean kasugamycin, a bio-pesticide used in herbal medicine. The main problem in kasugamycin residue analysis in herbal medicine is the matrix's interference effect, continuously observed after extraction. Therefore, complete removal of *A. Japonica* roots matrix effect is important and required by the national MRLs [8]. The removal of the matrix effect during kasugamycin residue analysis in herbal medicine is determined using the elution conditions. Therefore, the current study focused on optimizing the elution conditions of kasugamycin residue analysis. The effect of the loading volume of the extract and the volume and type of the eluting solvent indicated that using 1 mL fortified elution volume with 10 mL methanol as an eluting solvent on silica SPE cartridge could result in a 93.2% dissolution rate of kasugamycin (Fig. S2). However, the dissolution rate of kasugamycin was increased to 95.5% when using 10 mL of pure water. The lost amount of kasugamycin residue in both cases is attributed to the interfering substances of the matrix causing the overloading of the cartridge and consequently the loss of the target compound (kasugamycin). Several trials were done to minimize the influence of the matrix of the *A. Japonica* roots of the purification method using a silica SPE cartridge without success. Therefore, another set of trials were done to replace the silica SPE cartridge with HLB SPE and SCX SPE cartridges which were reported to have better efficiency [5,23].

HLB SPE cartridge

The HLB SPE cartridge is known to have high purification efficiency in analyzing aminoglycoside antibiotics. Previous studies reported the analysis of kasugamycin among agricultural products by using an HLB SPE cartridge [12,5]. When using the kasugamycin standard solution, only the HLB SPE cartridge purification gave a recovery rate of 95.8%. When applying 5 mL of the sample extract to the standard condition, a 97.3% recovery rate of kasugamycin was obtained (Fig. S3). However, quantification of the minimum concentration was not possible due to the interference substances in the *A. japonica* roots extract co-eluted with kasugamycin on the chromatogram (Fig. 3). The current result is similar to the results reported by previous authors that the HLB SPE cartridge has low purification efficiency and high ion suppression [7-8]. Therefore, another purification condition was tested using the SCX SPE cartridge, a strong cationic SPE cartridge that exhibits an efficient purification effect for polar substances with many amino and hydroxy groups [8].

SCX SPE cartridge

The SCX SPE cartridge (1 g), a strong ion exchange cartridge, has been reported to effectively purify basic amine compounds from materials with complex matrices [24-25]. In particular, kasugamyacin has various pKa values, so the purification efficiency is higher when an ion exchange cartridge is used, rather than the florisil or silica SPE cartridge generally used [5]. In addition, the optimal purification method with SCX SPE cartridges has been widely reported. It can sufficiently separate the matrix interfering substance during kasugamycin and validamycin A analysis [18]. The purification conditions with the SCX SPE cartridge were tested using the standard solution, and the target component was not eluted in the loading and washing section. Kasugamycin showed a 98.1% dissolution rate when 10 mL of 5% NH_4OH in methanol was used. However, when the sample was applied, the recovery rate was 58.8%, which indicates a section lost before the elution section. Therefore, a recovery rate test was performed for each section to solve this problem by applying an *A. japonica* sample. As a result, about 40.5% was eluted in the loading and washing sections (Fig. S4).

The overloading phenomena may explain these results due to the matrix effect in the test cartridge as

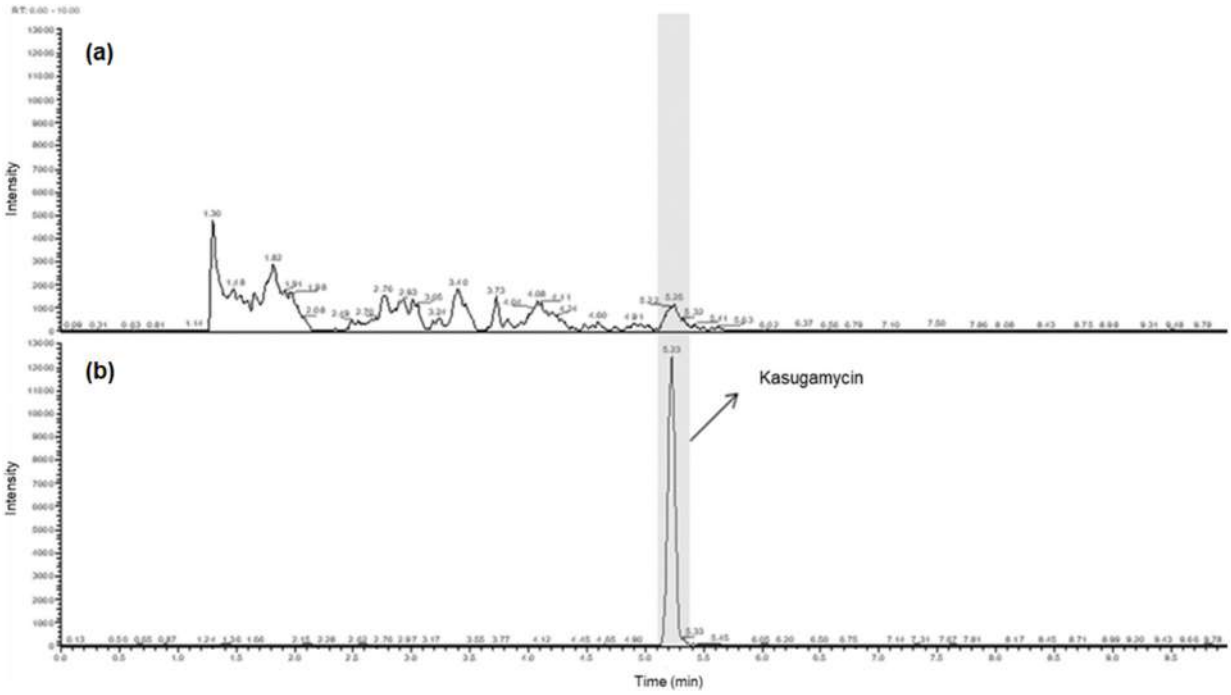

Fig 3. Chromatogram of HLB SPE cartridge test of kasugamycin in *Achyranthes japonica* Nakai and kasugamycin standard ((a): control, (b): kasugamycin 0.1 mg kg^{-1})

reported for the silica SPE cartridge [26]. Therefore, a test was conducted using a loading range of 1–4 mL sample extract. The results of the loading capacity experiment showed that the target component was not eluted in the loading and washing sections when 1–3 mL was used, and the entire amount was eluted in 10 mL of 5% NH_4OH in methanol from the elution section (Table S2). Based on this result, 2 mL was selected as the optimal loading capacity, and the elution solvent was established under purification conditions using 10 mL of 5% NH_4OH in methanol. The above purification conditions gave a recovery rate of 101.2%, and the interfering substances continuously appearing near the retention time of kasugamycin were removed, and quantification was possible even at the minimum concentration (Fig. 4). Further experiments were done using a consecutive cleanup process combining the HLB SPE cartridge and the SCX SPE cartridge, which was reported to have more efficiency [8].

Double cleanup using HLB SPE cartridge + SCX SPE cartridge

Based on previous studies, the double cleanup method using the HLB and SCX SPE cartridge was performed. The result indicated a recovery rate in the elution section of 93.7% using the standard solution (Fig. S3). However, the recovery rate was reduced to 48.5%. Therefore, a second purification was performed using 5 mL of the sample extract. Overloading is reported to be caused by the difference in sample matrix type used and the cartridge capacity. Therefore, the overloading phenomenon observed in this study may be due to the overwhelming capacity limit of the SCX SPE cartridge by the *A. japonica* roots extract [27].

Unlike agricultural products, herbal extracts contain various and considerable pharmacological ingredients that saturate the cartridge's adsorption sites. As a result, the normal adsorption and desorption of the analyte components are impossible. Therefore, to overcome overloading from the sample, an additional cleanup process was performed by applying the improved SCX SPE cartridge purification method in which the volume of the extract was reduced from 5 to 2 mL. The result of the improved purification conditions gave a recovery rate in the elution section of 88.4%, and

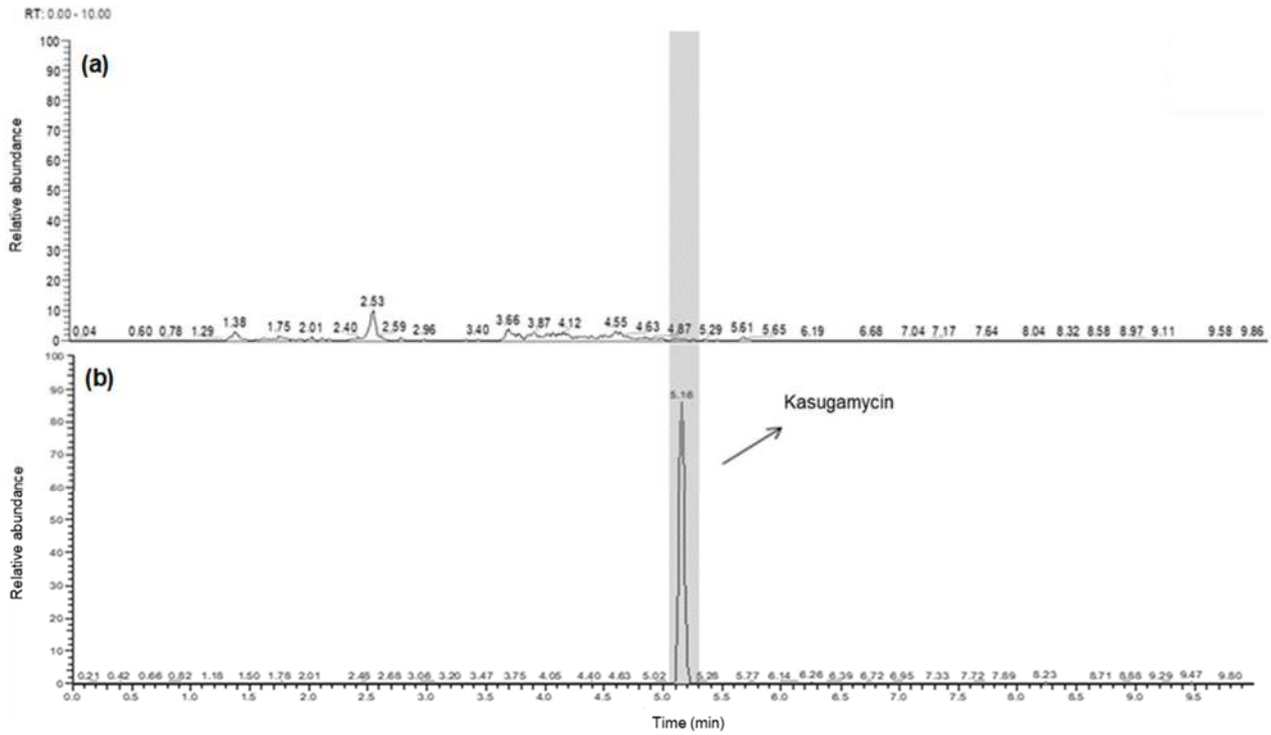

Fig 4. Chromatogram of SCX SPE cartridge test of kasugamycin in *Achyranthes japonica* Nakai and kasugamycin standard ((a): control, (b): kasugamycin 0.1 mg kg^{-1})

after double clean-up, the interfering substances eluted around the retention time of kasugamycin disappeared, and therefore that the minimum concentration could be quantified (Fig. 5). Thus, the current results indicated that the SCX SPE cartridge with the double clean-up method, and reduced loading to 2 mL, effectively prevents overloading and removes the herbal extract's interference effects. However, the reduction in loading volume could reduce the representativeness of the sample, therefore not recommended.

Comparison of Matrix Effect (ME) of the Purification Methods

The matrix effect of each purification method developed for kasugamycin analysis in *A. japonica* gave different results depending on the cartridge. The matrix effect of the HLB SPE cartridge was –36%, while those of the SCX SPE cartridge alone and the double clean up with HLB and SCX SPE cartridges were –15% and +14%, respectively (Table 3). The two analytical methods of the SCX SPE cartridge were matrix-matched in 1:1 ratio of the standard substance and the extract solution with the lowest possible effect of the interfering substance in the LC/MS/MS analysis at the lowest possible quantitative level. Since there were no differences in the matrix effect value from the presence or absence of the HLB SPE cartridge, it was assumed that the purification through a non-retentive filter was insufficient, and therefore most of the purification was performed in the SCX SPE cartridge. The consecutive cleanup process that directly connects HLB and SCX SPE cartridges gave excellent superior results. Nevertheless, since purification with a single SCX SPE cartridge gave sufficient purification efficiency and saved time, effort, and the method's simplicity, the current investigation recommends using a single SCX SPE cartridge for the purification of kasugamycin in herbal medicine [8].

Overview of the Method Established for Kasugamycin in Herbal Medicine

The sample should be wetted for one hour by adding 10 mL of water to the dry sample and adjusting the pH to 4.5 to 5.0 using 40 mL of 0.1% formic acid in the water extraction solvent. Then, ultrasonic extraction should be performed for 30 min. Then the extract should be centrifuged for 10 min, 5 mL of the supernatant should

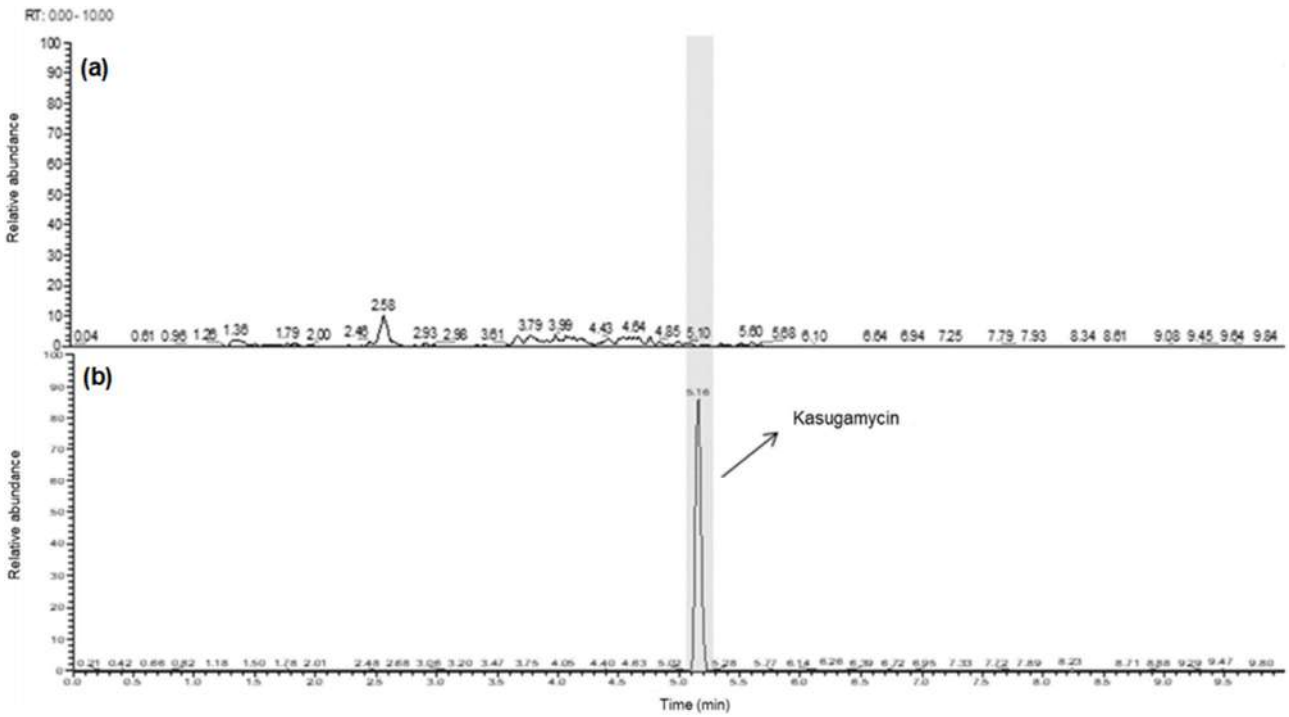

Fig 5. Chromatogram of HLB & SCX SPE cartridge test of kasugamycin in *Achyranthes japonica* Nakai and kasugamycin standard ((a): control, (b): kasugamycin 0.1 mg kg^{-1})

Table 3. Results of matrix effect (%) of kasugamycin in *Achyranthes japonica* Nakai

Sorbent	Regression equation	Linearity (r^2)	Matrix effect (%)
Solvent	y = 265136.035x - 473.3349723	0.9964	-
HLB	y = 168547.8359x + 6578.965386	0.9951	-36
SCX	y = 225862.6871x - 36.41891167	0.9968	-15
HLB + SCX	y = 301291.8221x + 422.1827966	0.9923	+14

be taken and centrifuged after liquid-liquid partitioning at the same ratio as dichloromethane, then 2 mL of the supernatant should be used as a loading sample for purification. Purification conditions should be done on the SCX SPE cartridge (1 g), a strong ion exchange cartridge. First, the filter should be activated by adding 5 mL of water and methanol, then loaded with 2 mL of the sample extract, followed by washing with 10 mL of water and methanol, and eluting with 10 mL of 5% NH_4OH in methanol. Next, the elution solution should be concentrated completely under a gentle stream of nitrogen, then reconstituted in 1 mL of water, filtered with a 0.2 µm membrane filter, and subject to LC/MS/MS analysis (Fig. 6).

Test Method Validation

The established method eliminated the effect of the interfering substance co-eluting with kasugamycin and therefore allowed accurate estimation of levels close to the quantification level. As a result of evaluating the selectivity of the test method, when the established analysis method was applied, the effect of interference near the kasugamycin retention time was minimized, and the quantitative limit level was quantifiable. Therefore, it could be said that it was a preferable analysis method. The reliability of the results of residue analysis in *A. japonica* was by a matrix-matched calibration curve done by diluting the standard solution

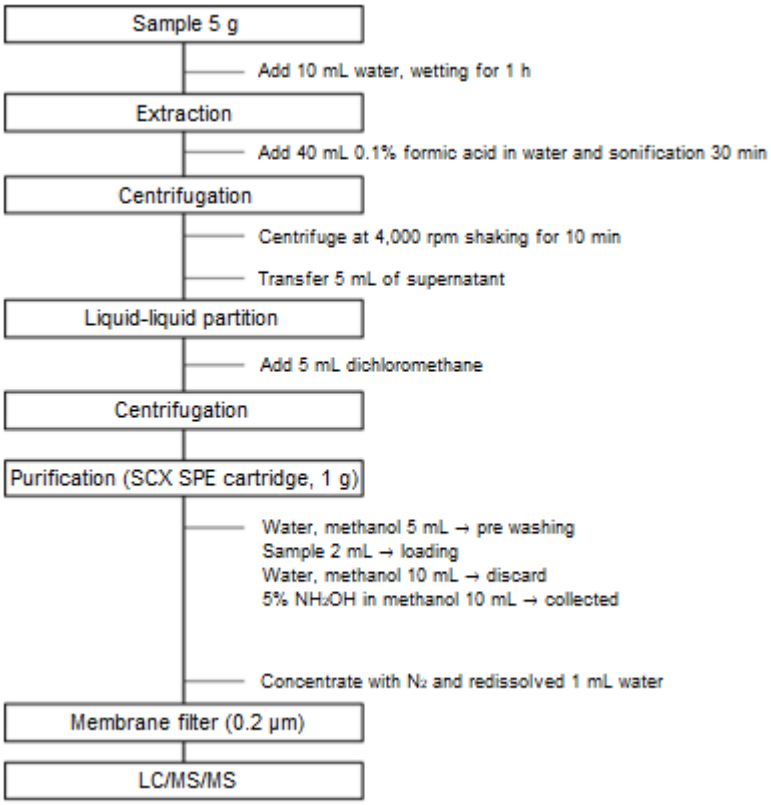

Fig 6. Improved analytical method of kasugamycin residue in *Achyranthes japonica* Nakai

of kasugamycin to 0.02, 0.05, 0.1, 0.2, 0.5, 1.0, and 2.0 mg/L. The results gave a matrix-matched calibration curve of 0.996 or higher (Fig. 7 and Table S3).

The detection limit (LOD) of the device used in the current study was 0.008 ng, while the quantification limit (LOQ) of the test method was 0.04 mg/kg (Eq. (3)). The LOQ obtained by the current method satisfies the minimum quantification limit of less than 0.05 mg/kg or less or 1/2 of the residual tolerance standard, the pesticide residues analysis standard in the international standard Codex [28], and the Pesticide Residue Analysis Standard in the MFDA [21]. The analytical quantitation limit calculated in the current method was consistent with the minimum quantification limit of less than 0.05 mg/kg or less set by FAO codex Alimentarius or 1/2 of the residual tolerance standard set by MFDS [21,28]. To evaluate the accuracy, precision, and repeatability of the tested method standard solution containing the limit of quantitation (0.04 mg/L) and 10 times the limit of quantification (0.4 mg/L) was added to the untreated samples. The average recovery rates were 88.8–106.3% and 83.1–88.4%, and the RSD was generally good at a maximum of 8.8%, indicating that the current method is sensitive and selective. Furthermore, the ranges of the recovery rate and analysis error satisfy the 70–120% of the single component analysis method of the MFDS, and the result satisfies the value within 10% of the RSD (Table S4).

$$0.04(\text{ng}) \times \frac{50(\text{mL})}{5(\text{g})} \times \frac{1(\text{mL})}{2(\text{mL})} \times \frac{1}{5(\mu\text{L})} = 0.04(\text{mg/kg}) \quad (3)$$

The improved analysis method was used to analyze kasugamycin residues (Fig. 8) in *A. japonica* and agricultural products. The kasugamycin analysis method developed in this study is expected to be applied to the

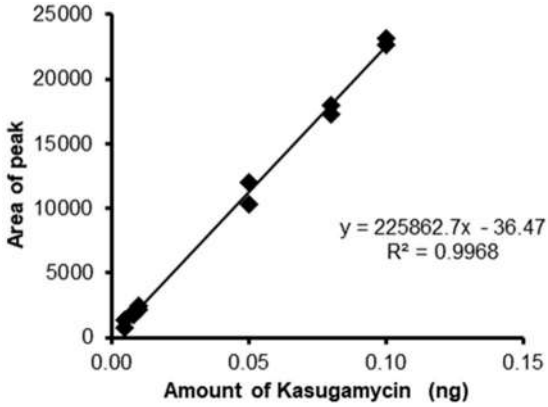

Fig 7. Calibration curve of kasugamycin matrix-matched standard by LC/MS/MS

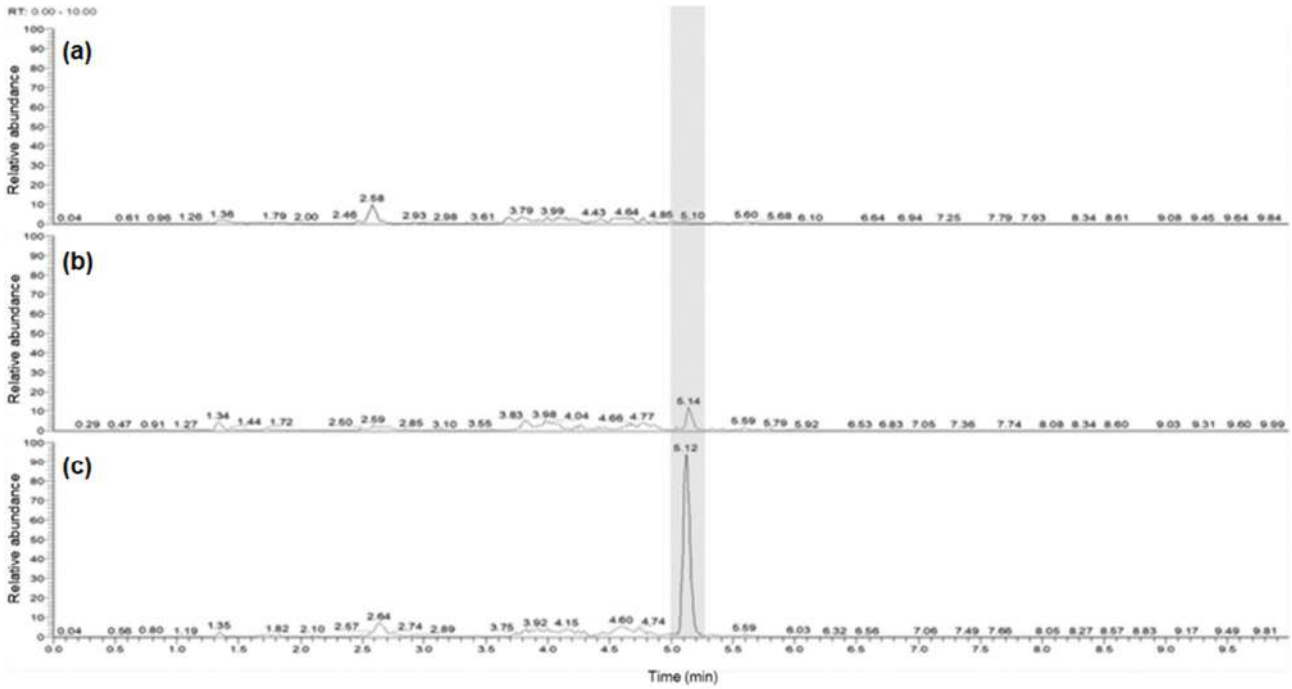

Fig 8. Chromatograms of kasugamycin residue analysis in *Achyranthes japonica* Nakai ((a): control, (b): 1 MLOQ (0.04 mg kg^{-1}), (c): 10 MLOQ (0.4 mg kg^{-1}))

aminoglycoside-based agricultural fungicides and bactericides in various herbal medicines. Furthermore, it could also be applied to analyze the residues of other fungicides and bactericides in agricultural, livestock, and aquatic products, which are major food sources in the Republic of Korea and other countries. Therefore, this method may contribute to human safety.

■ CONCLUSION

A suitable analytical method for the determination of the trace residue of kasugamycin in *A. japonica* was developed. The developed method involved using LC/MS/MS equipped with an amide column for polar substances with efficient extraction and purification processes optimized using a single SCX SPE cartridge, which is simple and time-efficient. The developed purification and cleanup method showed high efficiency in removing interferences with respective matrix effects while maintaining a high recovery rate of kasugamycin. The current results are consistent with the criteria ranges indicated in the guidelines of the Codex (CAC/GL 40-1993, 2003) and MFDS (2016). Furthermore, currently developed kasugamycin analysis could be applied to the aminoglycoside-based agricultural fungicides and bactericides and also the residues of other fungicides and bactericides. Therefore, this method may contribute to human safety.

■ ACKNOWLEDGMENTS

This research was conducted with the Ministry of Food and Drug Safety funding in 2020 (19172 herbal medicines 196), and the authors are grateful for this.

■ AUTHOR CONTRIBUTIONS

Jang Hyun is the team leader who proposed the work and designed the experiment. Jeong Yoon, Min-woo, and Hun Ju executed the experiments and analyzed the results. Jang Hyun and Abd Elaziz wrote the experiment. The first author (Jeong Yoon Choi) and the second author (Hun Ju Ham) have equal contributions. All authors read and approved the manuscript.

■ REFERENCES

[1] Na, E.S., Kim, S.S., Hong, S.S., Kim, K.J., Lee, Y.J., Lee, B.C., and Lee, K.S., 2020, Development of Multi-residue analytical method for 261 pesticides in herbal medicines using GC-MS/MS and LC-MS/MS, *Korean J. Environ. Agric.*, 39 (2), 142–169.

[2] Kang, M.Y., Lee, S.H., Lee, S.W., Cha, S.W., Song, J.L., and Lee, S.C., 2015, Effect of *Achyranthis radix* and *Drynariae rhizoma* extracts on antioxidant activity and antioxidant enzymes, *Korean J. Plant Resour.*, 28 (5), 600–607.

[3] Rural Development Administration, 2021, *Pesticide Safety Information System (PSIS)*, Rural Development Administration, Jeonju, Korea, http://psis.rda.go.kr/psis/agc/res/agchmRegistStusLst.ps.

[4] Kim, S.H., and Park, Y.H., 2008, Antimicrobial resistance and food safety, *Safe Food*, 3 (1), 30–36.

[5] Park, J.S., Do, J.A., Lee, H. S., Park, S.M., Cho, S.M., Shin, H.S., Jang, D.E., Cho, M.S., Jung, Y.H., and Lee, K., 2019, Development of analytical method for detection of fungicide validamycin A residues in agricultural products using LC-MS/MS, *J. Food Hyg. Saf.*, 34 (1), 22–29.

[6] Kim, T.J., Kim, K.S., Yoon, C.H., Joo, J.B., and Kim, C.H., 1997, Analysis of kasugamycin in pesticides formulations by reversed-phase ion pair liquid chromatography, *Anal. Sci. Technol.*, 10 (5), 343–349.

[7] Li, W., Dai, X., Pu, E., Bian, H., Chen, Z., Zhang, X., Guo, Z., Li, P., Li, H., Yong, Y., Wang, C., Zhang, Y., and Han, L., 2020, HLB-MCX-based solid-phase extraction combined with liquid chromatography-tandem mass spectrometry for the simultaneous determination of four agricultural antibiotics (kasugamycin, validamycin A, ningnanmycin, and polyoxin b) residues in plant-origin foods, *J. Agric. Food Chem.*, 68 (47), 14025–14037.

[8] Zhang, H., Wang, C., Li, H., Nie, Y., Fang, L., and Chen, Z., 2017, Simultaneous determination of kasugamycin and validamycin-A residues in cereals by consecutive solid-phase extraction combined with liquid chromatography-tandem mass spectrometry, *Food Addit. Contam., Part A*, 35 (3), 487–497.

[9] Isoherranen, N., and Soback, S., 1999, Chromatographic methods for analysis of aminoglycoside antibiotics, *J. AOAC Int.*, 82 (5), 1017–1045.

[10] Lu, L., Zhao, S., Deng, L., Chen, Y., Liu, X., and Li., D., 2012, Residues and dynamics of kasugamycin in chilli and soil, *Bull. Environ. Contam. Toxicol.,* 89 (3), 649–653.

[11] Alechaga, É., Moyano, E., and Galceran, M.T., 2015, Simultaneous analysis of kasugamycin and streptomycin in vegetables by liquid chromatography-tandem mass spectrometry, *Anal. Methods*, 7 (8), 3600–3607.

[12] Lee, H.S., Do, J.A., Park, J.S., Cho, S.M., Shin, H.S., Jang, D.E., Jung, Y.H., and Lee, K., 2019, Development of analytical method for kasugamycin in agricultural products using LC-MS/MS, *J. Food Hyg. Saf.*, 34 (3), 235–241.

[13] Ministry of Food and Drug Safety Guidelines (MFDSG), 2016, *Standard Procedure for Preparing Testing Methods for Food, etc. Test Guidelines*, South Korea's Ministry of Food and Drug Safety.

[14] Turner, J.A., 2015, *The Pesticide Manual*, 17th Ed., BPC Publications, Alton, Hampshire, UK.

[15] Zhou, W., Yang, S., and Wang, P.G., 2017, Matrix effects and application of matrix effect factor, *Bioanalysis*, 9 (23), 1839–1844.

[16] Ministry of Food and Drug Safety (MFDS), 2013, *Pesticide Analytical Residues Manual in Food Code*, 13–14.

[17] Chemicalize, 2021, *Kasugamycin*, https://chemicalize.com/#/calculation, accessed on 23 August 2021.

[18] Arsand, J.B., Jank, L., Martins, M.T., Hoff, R.B., Barreto, F., Pizzolato, T.M., and Sirtori., C., 2016, Determination of aminoglycoside residues in milk and muscle based on a simple and fast extraction procedure followed by liquid chromatography coupled to tandem mass spectrometry and time of flight mass spectrometry, *Talanta*, 154, 38–45.

[19] Wang, C., Li, H., Wang, N., Li, H., Fang, L., Dong, Z., Du, H., Guan, H., Zhu, Q., Chen, Z., and Yang, G., 2017, Simultaneous analysis of kasugamycin and validamycin-1 A in fruits and vegetables using liquid chromatography-tandem mass spectrometry and consecutive solid-phase extraction, *Anal. Methods*, 9 (4), 634–642.

[20] New, L.S. and Chan, E.C.Y., 2008, Evaluation of BEH C_{18}, BEH HILIC, and HSS T3 (C_{18}) column chemistries for the UPLC–MS–MS analysis of glutathione, glutathione disulfide, and ophthalmic acid in mouse liver and human plasma, *J. Chromatogr. Sci.*, 46 (3), 209–214.

[21] Asakawa, D., Uemura, M., Sakiyama, T., and Yamano, T., 2017, Sensitivity enhancement of aminoglycosides in hydrophilic interaction liquid chromatography with tandem mass spectrometry by post-column addition of trace sodium acetate in methanol, *Food Addit. Contam., Part A*, 35 (6), 1116–1126.

[22] Ministry of Food and Drug Safety (MFDS), 2017, *Guideline for Pesticide Residue Analysis Practice in the Korean Food Public Code*, 4th Ed, Osong, Republic of Korea.

[23] Kim, J.H., Moon, S.E., Kim, K.Y., Jung, Y.J., Lee, C.H., Ku, E.J., Yoon, M.H., and Lee, J.B., 2016, Simultaneous analysis for veterinary drug residues in honey by HPLC/MS/MS, *J. Food Hyg. Saf.*, 31 (2), 94–98.

[24] Fontanals, N., Zohar, J., Borrull, F., Ronka, S., and Marcé, R.M., 2021, Development of a maleic acid-based material to selectively solid-phase extract basic compounds from environmental samples, *J. Chromatogr. A*, 1647, 462165.

[25] Fontanals, N., Marcé, R.M., and Borrull, F., 2019, Materials for solid-phase extraction of organic compounds, *Separations*, 6 (4), 56.

[26] Choi, J.Y., Lee, Y.J., Ham, H.J., Ishag, A.E.S.A., and Hur, J.H., 2021, A study on improvement of the analytical method of chlorantraniliprole residue in herbal medicine (*Rehmannia glutinosa* Libosch) using HPLC-UVD, *Korean J. Pestic. Sci.*, 25 (3), 196–211.

[27] Bierman, S., and Campognone, M.V., 2009, Simplifying solid-phase extraction method development: exploring the use of software, *LCGC*, 27 (8), 24–26.

[28] Joint FAO/WHO Codex Alimentarius Commission, 2003, *Codex Alimentarius: Guidelines on Good Laboratory Practice in Pesticide Residue Analysis*, World Health Organization: Food and Agriculture Organization of the United Nations, Rome, CAC/GL 40-1993, 1–36.

Preparation and Characterization of New Tetra-Dentate N_2O_2 Schiff Base with Some of Metal Ions Complexes

Naser Shaalan[1*], Waleed Madhloom Khalaf[2], and Shatha Mahdi[3]

[1]*Department of Chemistry, College of Science for Women, University of Baghdad, Baghdad 10071, Iraq*

[2]*Ministry of Interior, Iraqi Police College, Baghdad, Iraq*

[3]*Ministry of Education, Al-Karkh Second Education Directorate, Baghdad, Iraq*

* ***Corresponding author:***

email: naserds_chem@csw.uobaghdad.edu.iq

Received: May 5, 2021
Accepted: August 19, 2021

DOI: 10.22146/ijc.66118

Abstract: *This study describes the preparation of a new series tetra-dentate N_2O_2 dinuclear complexes Cr(III), Co(II)and Cu(II) of the Schiff base 2-[5-(2-hydroxy-phenyl)-1,3,4-thiadiazol-2-ylimino]-methyl-naphthalen-1-ol], (LH_2) derived from 1-hydroxy-naphthalene-2-carbaldehyde with 2-amino-5-(2-hydroxy-phenyl)-1,3,4-thiadiazole. These ligands were characterized by FT-IR, UV-Vis, Mass spectra, elemental analysis, and ^{1}H-NMR. All prepared complexes have been characterized by conductance measurement, magnetic susceptibility, electronic spectra, infrared spectrum, thermal Analysis (TGA), and metal analysis by atomic absorption. The stoichiometry of metal to ligand, magnetic susceptibility, and electronic spectra measurements show an octahedral geometry for all (Cr^{3+}, Co^{2+}, Cu^{2+}) complexes. Conductivity measurement shows that the prepared Co^{2+} and Cu^{2+} complexes were nonelectrolytes except for Cr^{3+}. Studying the extraction efficiency such as ligand concentration, temperature and incubation time, centrifuge time, amount of surfactant were evaluated and optimized. The linear range of ions Cr(III), Co(II) and Cu(II) with ligand is 0.2–3, 0.2–4, 0.2–3, μg mL^{-1}, with the relative standard deviation of 0.15%, 0.34%, 0.46%, respectively. The successful method was applied for the determination of trace metal ions in the wastewater.*

Keywords: *tetradentate N_2O_2; naphthaldehyde; thiadiazole; cloud point*

INTRODUCTION

Multiple or tetra-dentate Schiff bases contain N_2O_2 coordination, and their mineral complexes have gained significant interest due to their excellent complexity. They are used in extracting many metallic ions from water due to their ability to form stable metal chelates complexes. They are widely studied in coordination chemistry, especially those which contains heterocyclic compounds with the azomethene group, as it has basic properties due to the presence of an electron pair on the nitrogen atom azomethene (–C=N) and often pentagonal or hexagonal rings with the metal ion [1-3]. Heavy metal pollutions are released into the environment by industrial activities affecting the ecosystem. The metal content determination is necessary for controlling purposes because there is an active procedure for simultaneous enrichment and separation species from matrices of various analytical applications and separation procedures [4]. Cloud point extraction has become one of the most popular methods used to separate and enrich metal ions. Due to their low cost, simplicity, safety, and high capacity for pre-concentration, the metals can be collected in small volumes (0.2–0.5 mL) of the surfactant phase [5-6]. Cloud point extraction has been used for extractive pre-concentration, separation, and/or purification of metallic species, metal chelates, biomaterials, and organic compounds [7]. The present study describes the coordination behavior of Schiff base (LH2) towards some transition elements, and we report on the results obtained in a study of the CPE of Cr(III), Co(II), and Cu(II) after the formation of a complex with (LH_2) using

Triton X-114 as surfactant followed by analysis by UV-Vis.

■ EXPERIMENTAL SECTION

Materials

All chemicals were obtained from Sigma- Aldrich companies such as phosphorus(V) oxide chloride 99%, thiosemicarbazide 98%, salicylic acid 99%, 1-hydroxy-naphthalene-2-carbaldehyde technical grade, potassium hydroxide 90%, $CrCl_3{\cdot}6H_2O$ 98%, $CoCl_2{\cdot}6H_2O$ 99%, and $CuCl_2{\cdot}2H_2O$ 99%.

Instrumentation

The electronic spectra were collected by using Shimadzu 160 A- Spectrophotometer. Mass analysis of ligand has been performed with LC-Mass 100P Shimadzu. The IR spectra of ligand and complexes have been obtained using the KBr method in the range of 4000–400 cm^{-1}. Using the Faraday Method, a Bruker BM6 device was used to conduct magnetic sensitivity measurements at room temperature. Thermal analysis studies of the compounds were performed on the Mettler instrument TGA. Conductivity measurements were performed with a conductivity meter of Model PCM 3 - JENWAY. The analysis of CHN was carried out using analyzer model 5500 Carlo-Erba. AAS. Spectrophotometer model Double-beam atomic Absorption spectrometer, model: AA400 Analytic Jeana. Centrifuge model PLC-03, Electro-thermal bath model AA-00267.

Procedure

Preparation of compound [A] [8]

The melting point (M.p.), yield, and CHNO analysis are listed in Table 1.

Synthesis of 2-[5-(2-Hydroxy-phenyl)-1,3,4-thiadiazol-2-ylimino]-methyl-naphthalen-1-ol] LH_2 [9-10]. A mixture with the same stoichiometric (0.02 mol) ratio of compound [A] with 1-hydroxy-naphthalene-2-carbaldehyde was added in a crucible. It was then put in microwave irradiation of 230 W for 3 min. After the reaction was complete, the obtained solid was recrystallized by absolute ethanol. Some properties of the product are listed in Table 1.

Preparation of metal complexes

A stoichiometric reaction of the corresponding LH_2 ligand (0.02 mol in 20 mL methanol) was added to a few drops of Triethylamine before mixing in 50 mL round bottom flask with (0.02 mol) metal(II) chlorides molar ratio (M:L) of 1:1. The mixture was put in an ultrasonic bath at 60 °C. After 60 min, crystalline-colored precipitates formed after cooling at room temperature. The resulting solids were filtered off, washed with distilled water and ether, and then dried in a desiccator. Some properties are summarized in Table 1.

Stoichiometric determination of complexes [11]

The continuous variation (JOB) method ensured the correlation ratio between ions and ligand in equilibrium media.

Analytical procedure

Metal ions Cr(III), Co(II), Cu(II) Chloride (3×10^{-4} mol L^{-1}) and LH_2 (3×10^{-4} mol L^{-1}) were put in 10 mL centrifuge tubes containing Triton X-114 (10% w/v) each individually. The mixture was shacked for 3 min then put and heated in an oil bath at 65 °C for 20 min. After that, heating was transferred to centrifuged late at 20 min and then cooled in an ice bath for 10 min. The

Table 1. LH_2 and metal yield percentages and CHNO analysis

Compound	Yield%	Analysis (calculated)					
		C%	H%	N%	O	Cl	M
LH_2 $C_{19}H_{13}N_3O_2S$	67%	65.45 (65.69)	3.82 (3.77)	12.24 (12.10)	19.27 (9.21)	--	--
$[Cr_2 (LH_2)_2 (H_2O)_4]Cl$	%73	48.83 (48.67)	3.18 (3.22)	8.83 (8.96)	13.55 (13.65)	7.63 (7.56)	10.97 (11.09)
$[Co_2 (LH_2)_2(H_2O)_4]$	%77	51.69 (51.82)	3.49 (3.43)	9.67 (9.54)	14.65 (14.53)	--	13.23 (13.38)
$[Cu_2 (LH_2)_2(H_2O)_4]$	%71	51.13 (51.29)	3.47 (3.40)	9.53 (9.44)	14.29 (14.38)	--	14.45 (14.28)

final step was taking the Triton X-114 rich phase and diluting it in 1 mL of ethanol. The eluent solution was transferred to a UV-VIS device, and the absorbance was measured. Titrations were performed using different solutions for any of the solutions Cr(III), Co(II), and Cu(II). The same method was used to determine the metal ions Cr(III), Co(II), and Cu(II) in the wastewater.

■ RESULTS AND DISCUSSION

FT-IR Spectra of LH_2

The method for synthesis of LH_2 is illustrated in Scheme 1. The FT-IR spectra of the ligand showed the emergence of new beams, which are the bundles of the right group (C=N). The absorption beams of the imine group of the prepared ligand were in the range of 1623 cm^{-1}, which belongs to the azomethene group, and the frequencies of the thiadiazole ring appeared at 1053–1239 cm^{-1} [10]. Fig. 1 and Table 2 contain the values of the infrared spectra of the prepared ligand.

Mass Spectral Data and ^{1}H-NMR

The mass spectral data of Schiff base ligand have been observed to give molecular ion peaks at *m/z* 348.0 (M+), which is in good agreement with the expected values at *m/z* = 347.39. This value refers to ($C_{19}H_{13}N_3O_2S$), *m/z* = 191 ($C_8H_5N_3OS$), *m/z* = 156 ($C_{11}H_8O$), and *m/z* = 94 (C_6H_6O).

^{1}H-NMR Spectroscopy

The peaks of the ^{1}H-NMR spectra of ligand are shown in Fig. 2. ^{1}H-NMR ($CDCl_3$ – 400 MHz) of LH_2 exhibited two singlet peaks at 13.687 and 11.506 ppm corresponding to OH proton. The signals at 8.756 ppm were attributed to the azomethine proton peak (CH=N). The doublets and multiplets were observed in the range of 6.155–7.504 ppm due to benzene rings' aryl protons.

FT-IR Spectra of Complexes

The all FT-IR spectra bands assignment of the compounds are presented in Table 2. The imine group ν(C=N) band in the LH_2 (1623) cm^{-1} complexes shifted to lower frequencies in all the complexes. The shifting indicates linked by the nitrogen atom of C=N in coordination with the metal [12]. As shown in the tables, the disappearance of the bands in the range 3419–3481 cm^{-1} belonging to the hydroxyl phenolic (O) complexes is evidence of its chelation by the phenolic oxygen atom [13]. The bending (Wagging and twisting) of the coordination water complexes appears by about 623–757 cm^{-1} [14]. The linked nitrogen atom of thiadiazol

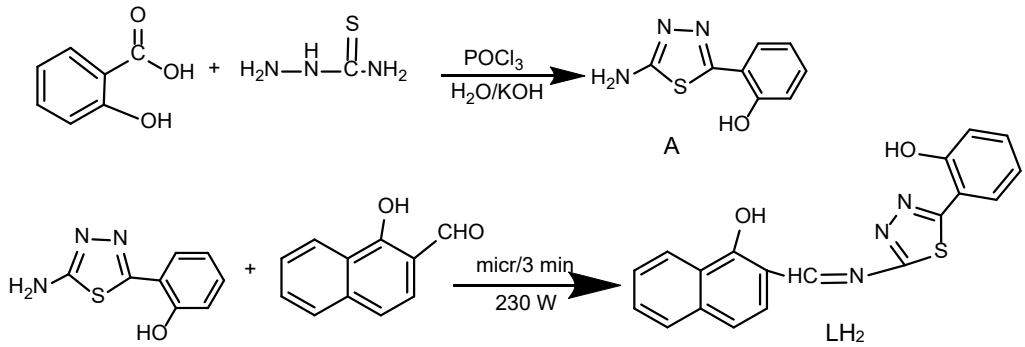

Scheme 1. Synthesis of ligand

Table 2. FT-IR data of ligand and its metal complexes (cm^{-1})

Compound	ν(C=N)	ν(H-O)	ν(C-N=N-C)	Wagging ν H_2O	Twisting ν H_2O	ν(H_2O)	ν(M-N)	ν(M-O)
LH_2	1623(s)	3419–3481	1156–1354	-	-	3441	-	-
$[Cr_2 (LH_2)_2 (H_2O)_4] Cl_2$	1606(s)	-	1155–1301	623	757	3375	493	586
$[Co_2 (LH_2)_2(H_2O)_4]$	1598(s)	-	1159–1311	683	748	3345	458	590
$[Cu_2 (LH_2)_2(H_2O)_4]$	1613(s)	-	1117–1299	692	749	3387	495	587

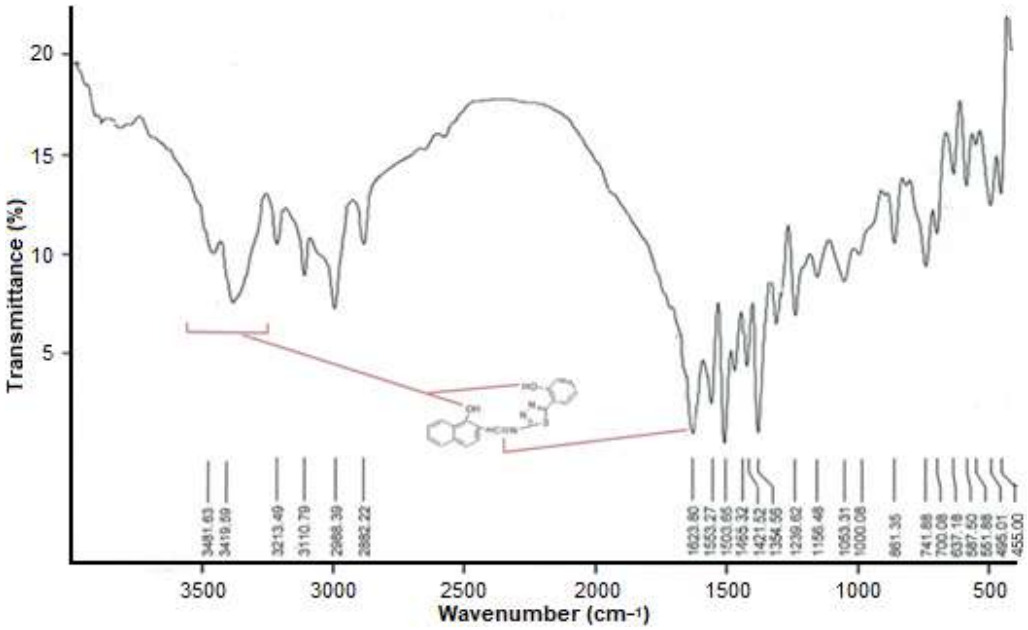

Fig 1. FT-IR for LH_2 ligand

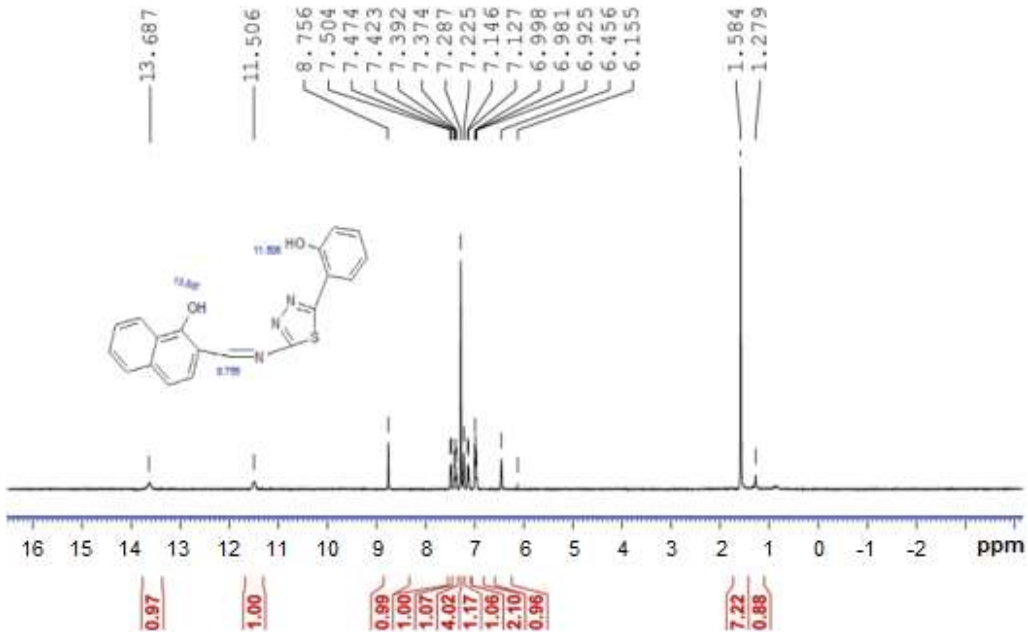

Fig 2. ^{1}H-NMR for LH_2 ligand

ring shows shifted absorption bands of ligand at 1174–1303 cm^{-1} in complexes confirming the metal's binding to the by group =N–N= [15]. For all complexes, a new beam appeared in the range of 586–590 cm^{-1} due to the vibrations of the group stretch (M–O) [16] and showed a stretching of the group (M–N) of the prepared complexes in the bounded region between 458 and 495 cm^{-1}. This confirms the metal's association via the N atom [17]. All the infrared spectrum values for the complexes are shown in Table 2.

Electronic Spectra, Magnetic Moments, and Molar Conductance of Complexes

Most of the complexes of the transition elements show absorbance at certain wavelengths of the spectrum because most of these complexes are colored. The

electronic spectrum of the prepared complexes was recorded in the range of 200–1100 nm using DMF solvent [18].

The spectra of the chromium complex observed two (428 nm, 608 nm) in Table 3, attributed to the allowed transfer $^4A_2g \rightarrow {}^4T_1g$ (F) and $^4A_2g \rightarrow {}^4T_1g$ (F) respectively [19]. It has been observed that the electron spectrum is complex cobalt(II) low spin octahedral ($t_2g^6eg^1$), one permissible transition 500 nm, which is $^2Eg\ {}^2T_2g$ (20). The spectrum of the copper(II) complexes showed an absorption peak at the region of 722 nm, as shown in Table 3, which attributed to$^2B_1g \rightarrow {}^2B_2g$. It agrees with the published research in this regard [21].

The UV–Vis spectra of a ligand with complexes show a displacement in the range between 5 and 20 nm. There is a difference between the spectra of the ligand and the metal ion solution and the clear difference in the colors of the mixing solutions from the solutions of the ligand and the metal ion before mixing, which is clear evidence of coordination between them [22]. Table 3 gives the prepared compounds' electronic spectral, magnetic moments, and Molar Conductance data. The magnetic susceptibility results gave values for the magnetic moment, which correspond to the suggested shape. From the electronic spectra, infrared spectrum, and magnetic measurements, it indicates that most of Cr(III), Co(II), and Cu(II) complexes contain hexacoordinate and have octahedral geometry, as illustrated in Scheme 2.

Continuous Variation Method

The absorbance of the complexes was measured at λ_{max} = 483, 500, and 413 nm. The stoichiometric ratio between the Cr(III), Co(II), Cu(II) and ligand was 1:1.

Table 3. Some physical data electronic spectra for LH_2 and complexes in DMF

Compound	Dec. Point °C	Conductivity ohm^{-1} cm^2 mol^{-1} 25 °C	Magnetic Moment (B.M)	Color	Absorption Bands (nm)	Assigned Transition
LH_2	206–207	8	-	Yellow	235	$\pi \rightarrow \pi^*$
					345	$N \rightarrow \pi^*$
$[Cr_2 (LH_2)_2 (H_2O)_4]Cl_2$	268d	142	3.9	Violet	608	$^4A_2g \rightarrow {}^4T_2g$ (F)
					452	$^4A_2g \rightarrow {}^4T_1g$ (F)
					374	Charge Transfer
$[Co_2 (LH_2)_2(H_2O)_4]$	281	19	2.39	Dark brown	500	$^2E_1g \rightarrow {}^2T_2g$
					375	Charge Transfer
$[Cu_2 (LH_2)_2(H_2O)_4]$	255d	23	1.89	brown	722	$^2B_1g \rightarrow {}^2B_2g$
					483	Charge Transfer

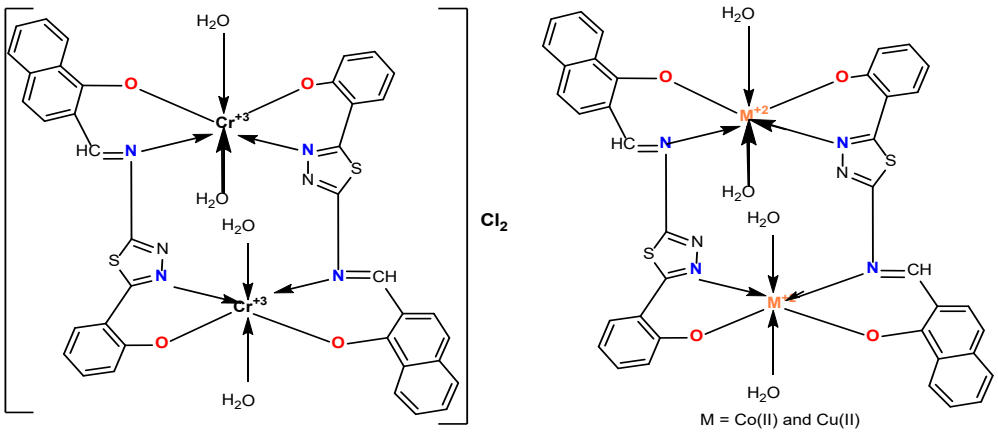

Scheme 2. Suggested structure for complexes

Extraction Metal Ions in Water Sample

The spectrum of ligand LH_2 and complexes

The general relative standard deviation was the absorbance of Cr(III), Co(II), and Cu(II) complexes' highest absorption. Surfactant-rich phases against blank prepared under similar conditions were recorded. Triton X-114 was good as an extracting agent [23].

Effect of ligand amount

As shown in Fig. 3, increasing the concentration of LH2 inclines the absorbance of the complexes, but at a higher concentration, the absorbance declines for all metal ions investigated. The ligand concentration of 3×10^{-4} mol L^{-1} was chosen as the optimum condition for other variables. The effects of the ligand on relative standard deviation efficiency were investigated as 55×10^{-4} mol L^{-1}. Obaid et al. reported that the best ligand concentration for extracting metal ions from water by cloud point extraction (CPE) was 55×10^{-4} mol L^{-1}. At a higher concentration (excess of LH_2), competition with a complexing agent (Triton X-114) reduces the metal ion concentration in complexes and decreases absorbance [24].

Effect of surfactant

The correct choice of Triton X-114 as a surfactant is fundamental for obtaining an optimal extraction process, separating the metal-ligand complex from the aqueous phase surfactants, and assisting quantitative extraction of the metal chelate complex. Furthermore, among the nonionic surfactants used, Triton X-114 gave a higher absorbance value to the samples Cr(III), Co(II), and Cu(II) complexes (0.103, 0.198, 0.210) highest absorption when compared with other surfactants; hence, Triton X-114 was preferred as an extracting solvent [25].

Calibration graph

The linear calibration graph of Cr(III), Co(II), and Cu(II) with agent LH_2 ligand was obtained as given in Fig. 4 for each ion. The Beer law was obeyed over the concentration range of 0.2–3, 0.2–4, and 0.2–3 μg L^{-1}.

The methods were applied to the determination of Cr(III), Co(II), and Cu(II) ions in Water of Marshlands (Mesan/Iraq) and wastewater of Industrial sewage of Tannery Factories in Nahrawan (Bagdad /Iraq). It gave good accuracy and precision, as shown in Table 4. In addition, the good method was compared with other literature methods.

Thermal Analysis

As shown in Fig. 5, the complex showed three well-defined steps. The first step represents the loss of four

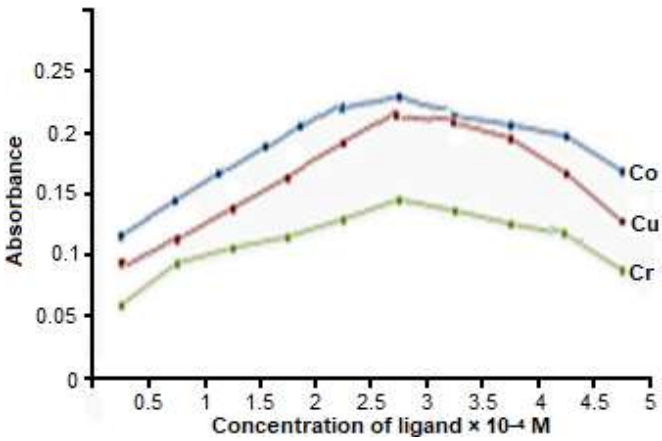

Fig 3. Effect of ligand concentration on complex absorbance; Cr(III), Co(II), Cu(II) = 3×10^{-4} mol L^{-1} (each 1 mL) and 10% (V/V) Triton X-114

Table 4. Application of the proposed method for determination of Cr(III), Co(II), and Cu(II) by LH_2

Metal ions	Real sample	Found	RSD%*	RSD% average	Recovery%	Recovery% Average
Cr^{+3}	Wastewater of Tannery Factories	2.95	0.49%	1.609%	99.3%	98.7%
	Water of Marshlands	1.92	0.110%	0.431%	97.2%	96.95%
Co^{+2}	Wastewater of Tannery Factories	3.979	0.82%	0.55%	99.3%	99.08%
	Water of Marshlands	2.81	0.16%	0.57%	96.2%	97.15%
Cu^{+2}	Wastewater of Tannery Factories	1.94	0.37%	0.41%	97.9%	97.65%
	Water of Marshlands	1.99	0.12%	0.62%	99.1%	97.44%

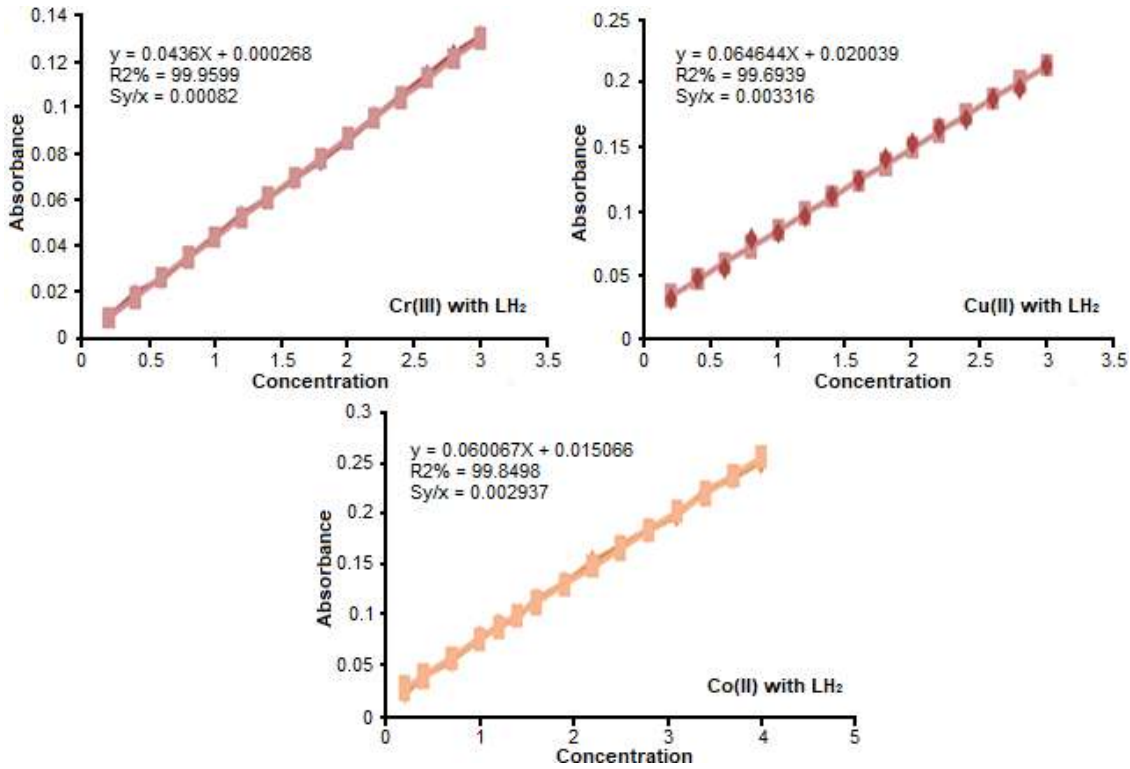

Fig 4. The calibration curves showing the correlation between absorbance and concentration of the complexes

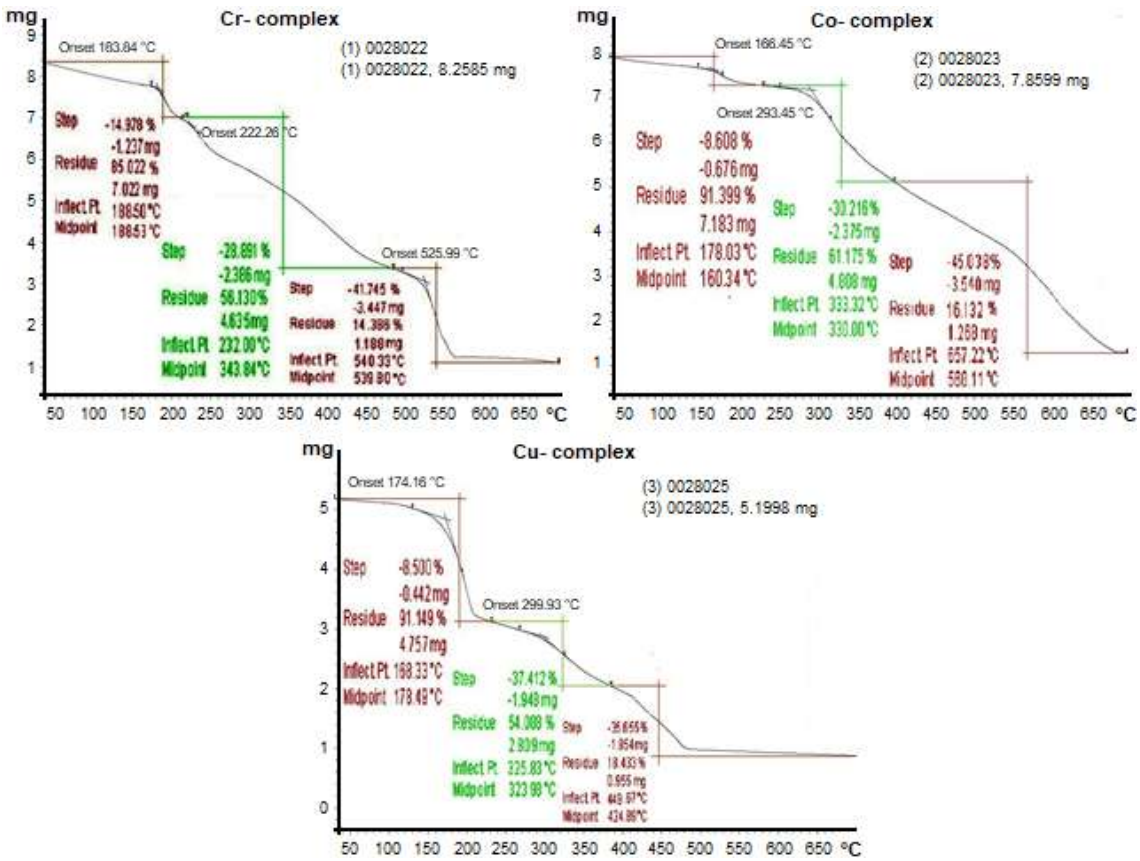

Fig 5. Thermal analysis of the complexes

Table 5. TGA analysis data of complexes

Sample (step)	T. range °C	Weight mass loss (calc) found%	Reaction
Cr(1)	37–188	(14.97) 15.26	($4H_2O$+2Cl)
Cr(2)	188–343	(29.980) 28.891	$C_{14}H_{10}O_2$
Cr(3)	343–540	(41.75) 40.95	$C_{16}H_{12}N_6O_2S_2$
Final residual		(14.50) 14.38	$2CrO^+$
Co(1)	37–178	(8.17) 8.60	$4H_2O$
Co(2)	140–272	(31.83) 30.22	$C_{20}H_{10}O_2$
Co(3)	272–462	(46.09) 45.04	$C_{18}H_{10}N_6O_2S_2$
Final residual		(17.84) 17.13	2CoO
Cu(1)	37–178	(8.10) 8.50	4H2O
Cu(2)	178–325	(38.02) 37.42	$C_{22}H_{14}N_2O_2$
Cu(3)	325–449	(35.10) 35.65	$C_{16}H_{12}N_4S_4$
Final residual		(17.87) 18.36	2CuO

H_2O molecules from Co(II) and Cu(II) but Cr(III) loses $2H_2O$ and 2Cl as evidence of the coordinated water molecules in complexes [26]. The second, third, and fourth steps are explained in Table 5. These steps are due to the loss of mass in the form of gases. The final step's large weight drop can be explained by considering that the residue is a 1:1 mixture of 2 (Metal oxide).

CONCLUSION

We have observed new ligand compounds and complexes from the first series of transitional metals by examining their physical properties using various analyses. The collected data demonstrated that the ligand behaves as a tetradentate ligand of N_2O_2 and forms binuclear stable complexes. Molar conductivity measurements indicate that complexes with the formula $[M_2(LH_2)_2(H_2O)_4]$ with M(II) = Co, Cu were neutral (a nonelectrolyte), while the other complexes with the formula $[Cr_2(LH_2)_2(H_2O)_4]Cl_2$ were electrostatic type (1:2). The determination trace of Cr(III), Co(II), and Cu(II) in water samples performed well by using cloud point extraction by applying Schiff (LH_2) as extracting reagent because it is a stable and selective complexing reagent. The cloud point extraction method is good, fast, and inexpensive to use compared to other methods for quantifying metal ions. The method gives a very low limit of detection and good relative standard deviation values.

REFERENCES

[1] Radoske, T., Kloditz, R., Fichter, S., März, J., Kaden, P., Patzschke, M., Schmidt, M., Stumpf, T., Walter, O., and Ikeda-Ohno, A., 2019, Systematic comparison of the structure of homoleptic tetradentate N_2O_2-type Schiff base complexes of tetravalent f-elements (M(IV) = Ce, Th, U, Np, and Pu) in solid-state and in solution, *Dalton Trans.*, 48 (9), 17559–17570.

[2] Barwiolek, M., Kędziera, A.K., Muziol, T.M., Jankowska, D., Jezierska, J., and Bieńko, A., 2020, Dinuclear copper(II) complexes with Schiff bases derived from 2-hydroxy-5-methylisophthalaldehyde and histamine or 2-(2-aminoethyl)pyridine and their application as magnetic and fluorescent materials in thin film deposition, *Int. J. Mol. Sci.*, 21 (13), 4587.

[3] Maher, K., 2018, Schiff bases derived from 2-hydroxynaphthalene-1-carbaldehyde and their metal complexes, *Asian J. Chem.*, 30 (6), 1171–1182.

[4] Althobiti, S.A., and Zabin, S.A., 2020, New Schiff bases of 2-(quinolin-8-yloxy)acetohydrazide and their Cu(II), and Zn(II) metal complexes: Their *in vitro* antimicrobial potentials and *in silico* physicochemical and pharmacokinetic properties, *Open Chem.*, 18 (1), 591–607.

[5] Soylak, M., Ghaedi, M., and Niknam, K., 2017, Cloud point extraction and flame atomic absorption spectrometric determination of lead, cadmium, and palladium in some food and biological samples, *Pak. J. Anal. Environ. Chem.*, 12 (1-2), 42–48.

[6] Alfahdawi, A.S., Al-Sorchee, S.M., Saleh, S.E., and Saleh, M.M., 2021, Synthesis and study of N,N`-(ethane-1,2-diyl)bis(1-phenyl methanimine) and their complex derivative with *in-vivo* and *in-vitro* bacterial biological study, *Egypt. J. Chem.,* 64 (6), 2879–2888.

[7] Shaalan, N., Abed, A.Y., Alkubaisi, H.M., and Mahde, S., 2019, Synthesis, spectroscopy, biological activities and thermodynamic studies for new complexes of some lanthanide metals with Schiff's bases derived from [2-acetylthiophene] with [2,5-dihydrazino-1,3,4-thiadiazole], *Res. J. Chem. Environ.*, 23, 181–187.

[8] Al Zoubi, W., Kim, M.J., Al-Hamdani, A.A.S., Kim, Y.G., and Ko, YG, 2019, Phosphorus-based Schiff bases and their complexes as nontoxic antioxidants: Structure-activity relationship and mechanism of action, *Appl. Organomet. Chem.*, 33 (11), 11–16.

[9] Ji, Y., Wu, L., Lv, R., Wang, H., Song, S., and Cao, M., 2021, Facile cloud point extraction for the separation and determination of phenolic acids from dandelion, *ACS Omega*, 6 (20), 13508–13515.

[10] Shaalan, N., Fadel, Z.H., Mahmood, W.A., and Al-Hamdani, A.A.S., 2016, Synthesis and characterization studies of metal complexes with Schiff base derived from 4-[5-(2-hydoxy-phenyl)-[1,3,4-oxadiazol-2-ylimino methyl]-1,5-dimethyl-2-phenyl-1,2-dihydro-pyrazol-3-one, *Baghdad Sci. J.*, 13 (2), 19–28.

[11] Ismael, M., Hmood, A.B., Shaalan, N., Al-Taa'y, W.A., Hasan, A., Ali, M., Al Ahmed, A., and Yousif, E., 2016, Study on optical properties of PVC-2,5di (2-pyrrole hydrazone) 1,3,4-thiadiazole complexes, *Res. J. Pharm., Biol. Chem. Sci.*, 7 (5), 2347–2355.

[12] Akram, E., Shaalan, N., Rashad., A.A., Hasan, A., Al-Amiery, A., and Yousif, E., 2016, Study of structural and optical properties of new films derived PVC-2-[5-phenyl-1,3,4-thiadiazol-2-ylimino-methyl]-benzoic acid, *Res. J. Pharm., Biol. Chem. Sci.*, 7 (5), 2836–2844.

[13] Ntoi, L.L.A., and von Eschwege, K.G., 2017, Spectrophotometry mole ratio and continuous variation experiments with dithizone, *Afr. J. Chem. Educ.*, 7 (2), 59–92.

[14] Obaid, S.M.H., Sultan, J.S., and Al-Hamdani, A.A.S., 2020, Synthesis, characterization and biological efficacies from some new dinuclear metal complexes for base 3-(3,4-dihydroxy-phenyl)-2-[(2-hydroxy-3-methylperoxy-benzylidene)-amino]-2-methyl pro pionic acid, *Indones. J. Chem.*, 20 (6), 1311–1322.

[15] Rasyda, Y.A., Widowati, M.K., Marliyana, S.D., and Rahardjo, S.B., 2021, Synthesis, characterization and antibacterial properties of nickel(II) complex with 4-aminoantipyrine ligand, *Indones. J. Chem.*, 21, (2), 391–399.

[16] Shalan, N., and Hussein, Y., 2018, Preparation, spectral characterization, structural study, and evaluation of antibacterial activity of metal complexes with Schiff base derived from (N,Ń-bis(1,5-dimethyl-2-phenyl-1,2-dihydro-pyrazolidine-3-one) -1,2-diamino ethane), *Res. J. Pharm., Biol. Chem. Sci.*, 9 (1), 376–385.

[17] Shalan, N., Balkhi, A, Hamo, S., and Falah, A., 2014, Synthesis, spectroscopic, thermodynamic and biological activity studies of Schiff base and metal complexes derived from 2-[(1H-pyrrol-2-ylimino methyl)]-5-(2-hydoxy-phenyl)-[1,3,4-thiadiazol], *J. Al-Nahrain Univ.*, 17 (3), 1–8.

[18] Srivastava, A.K., Pandey, O.P., and Sengupta, S.K., 2005, Synthesis, spectral and antimicrobial studies of bis(cyclopentadienyl)titanium(IV) derivatives with Schiff bases derived from 2-amino-5-phenyl-l,3,4-thiadiazole, *Bioinorg. Chem. Appl.*, 3, 702657.

[19] Shaalan, N, Hassan, S.S., and Al-Hamdani, A.A.S., 2015, Synthesis, spectroscopic and thermodynamic studies of metal complexes with Schiff bases derived from 2-[5-(pyridin-2-ylmethylene)-amino] 1,3,4-oxadiazol-2-yl-phenol, *J. Al-Nahrain Univ.*, 18 (4), 13–21.

[20] AL-Mukhtar, S.E., and Mustafa I.A., 1988, *Inorganic and Coordination Chemistry*, 1st Ed. Arabic Version, Mosul University Press, Mosul.

[21] Fan, X., Zhang, G., and Zhu, C., 1998, Synthesis of 2-[2-(5-methylbenzolyl)azo]-5-dimethylaminobenzoic acid and its application to the spectrophotometric

determination of nickel, *Analyst*, 123, 109–112.

[22] Nicholls, D., 1973, *The Chemistry of Iron, Cobalt, and Nickel*, 1st Ed., Pergamon Press, Oxford, 1037, 1087–1088,1090–1091,1093, 1151, 1154.

[23] Al-Hamdani, A.A.S., Al-Khafaji, N.R., and Shaalan, N., 2017, Preparation, spectral, thermal and bio activity studies of azo dyes complexes, *Res. J. Pharm., Biol. Chem. Sci.*, 8 (3), 740–750.

[24] Obaid, S.M.H., Jarad, A.J., and Al-Hamdani, A.A.S., 2020, Synthesis, characterization and biological activity of mixed ligand metal salts complexes with various ligands, *J. Phys.: Conf. Ser.*, 1660, 012028.

[25] Shaalan, N., and Abdulwahhab, S., 2021, Synthesis, characterization and biological activity study of some new metal complexes with Schiff's bases derived from [*O*-vanillin] with [2-amino-5-(2-hydroxy-phenyl)-1,3,4-thiadiazole], *Egypt. J. Chem.*, 64 (8), 4059–4067.

[26] Al Zoubi, W., Al-Hamdani, A.A.S., and Ko, Y.G., 2017, Schiff bases and their complexes: Recent progress in thermal analysis, *Sep. Sci. Technol.*, 52 (6), 1052–1069.

Physicochemical Properties, Chemical Compositions and Antioxidant Activities of Rhizome Oils from Two Varieties of *Kaempferia galanga*

I Wayan Muderawan*, I Wayan Mudianta, and Ni Wayan Martiningsih

Department of Chemistry, Faculty of Mathematics and Natural Sciences, Ganesha University of Education, Singaraja 81117, Bali, Indonesia

** Corresponding author:*

email: wayan.muderawan@undiksha.ac.id

Received: June 4, 2021
Accepted: October 12, 2021

DOI: 10.22146/ijc.66348

Abstract: Kaempferia galanga *is a tropical plant with an impressive range of food and medicinal uses. This study, therefore, investigated the variation in yields, physicochemical properties, chemical compositions, and antioxidant activities of rhizome oils from two* K. galanga *varieties,* K. galanga *bigger rhizomes (V1) and* K. galanga *smaller rhizomes (V2), isolated by steam distillation (S) and maceration (M) techniques. The air-dried rhizomes' oil contents were found to be 2.81±0.09% (SV1O), 7.93±0.20% (MV1O), 3.60±0.10% (SV2O), and 8.76±0.22% (MV2O), respectively. From the GC-MS analysis, the SV1O, MV1O, SV2O, and MV2O samples contain 49, 48, 61, and 56 compounds, respectively. Furthermore, ethyl trans-*p*-methoxycinnamate was the most prevalent chemical constituent in four oils with a percentage contribution of 43.37% (SV1O), 60.62% (MV1O), 24.92% (SV2O), and 57.17% (MV2O). Several long-chain alcohols (6Z,9Z-pentadeca-6,9-dien-1-ol, 9E,12E-octadeca-9,12-dien-1-ol, heptadecan-1-ol), aldehyde (Z-octadec-9-enal), carboxylic acids (4-(4-methoxyphenyl)oxane-4-carboxylic acid, hexadecanoic acid), diterpene sandaracopimaradiene, steroid ergosterol, and alkaloid 2-imino-3-(3-nitrophenyl)-1,3-thiazolidin-4-one, were also identified in* K. galanga *rhizome oils isolated by maceration method. In addition, all oils showed high antioxidant activities with the* IC_{50} *values of 86.10±1.51, 85.24±1.48, 89.19±1.72, and 86.49±2.03 μg/mL for SV1O, MV1O, SV2O, and MV2O, respectively.*

Keywords: Kaempferia galanga*; rhizome oil; physicochemical properties; chemical compositions; antioxidant activities*

INTRODUCTION

Kaempferia galanga Linn, known in Indonesia as '*kencur*', is an aromatic plant belonging to the Zingiberaceae family, with broadly ovate and pale green leaves. This aromatic ginger leaves and rhizomes are commonly used as food flavoring agents and perfumery and prescribed as a traditional treatment against asthma, hypertension, malaria, and bronchitis [1-2]. In Traditional Chinese Medicines (TCM), the plant treats cholera, contusion, constipation, and stomachache. Meanwhile, the Indian *Ayurvedic* formulation suggested the plant's use for muscular swelling and rheumatism treatments [3]. Furthermore, the leaves have higher phenolic content, antioxidant activity, and metal ion-chelating ability than *K. galanga* rhizomes [4]. The rhizomes are also used to prepare '*Jamu beras kencur*' in Indonesia, as a local tonic frequently consumed for beneficial health effects [5].

Srivastava et al. [6] recently reported on the physicochemical values and nutritional composition of *K. galanga* rhizomes. However, the rhizome oil's detailed chemical composition is scarce, especially oils obtained from the Indonesian cultivars. Also, reports on the plant's chemical and bioactivities are dominated by specimens collected from India [6], Bangladesh [7], Thailand [8-9], and Malaysia [10]. Most studies also investigated the rhizomes' polar extracts, using methanol and ethanol as major solvents. For instance, the ethanolic extract of *K. galanga* from Thailand

displayed moderate cytotoxic activity against human tumor cell lines [8]. In contrast, the methanolic rhizome extract of the plant collected in India was effective against acute inflammation in rats.

Interestingly, ethyl-*p*-methoxycinnamate was discovered to be the extracts' major phytoconstituents [11]. Thus, only a few studies have investigated the rhizome extracts' non-polar fraction, including the report by Othman et al. [10], on organic extract preparation, using Soxhlet extractor, with petroleum ether and dichloromethane. Recently, Srivastava et al. [6] isolated a *K. galanga* rhizome oil using the hydrodistillation method, and ethyl *trans-p*-methoxycinnamate was purified as the major volatile component.

Currently, there are 10 different *K. galanga* cultivars domesticated in Indonesia. However, these are simply grouped into two types: the bigger rhizome, usually with wide leaves, dark brown skin, and the smaller counterpart, with narrow leaves and light brown skin [12]. The bigger rhizomes are widely cultivated in West Java, while the smaller counterparts are mostly grown in Central and East Java regions. Also, larger rhizomes have higher productivity (12-16 tons/ha) compared to small counterparts (6-8 tons/ha) but lower essential oil content [13].

Methanolic extracts of *K. galanga* rhizomes have been reported to have antioxidant activities [4,7]. Antioxidants are secondary metabolites produced by plants to protect against oxidative damage. Thus, they are completely essential for maintaining optimal cellular and systemic health and well-being. In the family Zingiberaceae, it is generally believed that antioxidants produced by the plant are transported to the rhizomes, where they are accumulated [4]. This study, therefore, reports the physicochemical properties, chemical compositions, and antioxidant activities of bigger and smaller rhizomes varieties of *K. galanga* rhizome essential oils.

■ EXPERIMENTAL SECTION

Materials

For this experiment, two *Kaempferia galanga*, L. varieties, bigger (a) and smaller (b) rhizomes, were collected from Bali. Fig. 1(a) shows variety-1 (V1) has broad leaves, bigger rhizomes with a dark-brown epidermis, 5.5–10.3 cm in length and 1.73–2.24 cm in diameter. Fig. 1(b) shows variety-2 (V2) has narrow leaves, a smaller rhizome with a light-brown epidermis, 4.0–7.2 cm length, and 1.5–1.7 cm diameter. The plant materials were then identified, and voucher specimens (KGR.01 and KGR.02) were deposited at the Herbarium of Biology Laboratory, Faculty of Mathematics and Natural Sciences, Ganesha University of Education, Singaraja Bali. Subsequently, the rhizomes were washed with water, cut into small pieces, air-dried at room temperature for 7 days, and ground to powder form. The powders were then stored in an air-tight container protected from light until further use.

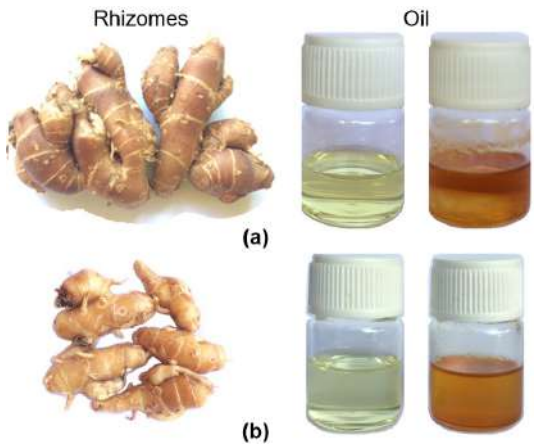

Fig 1. Two varieties of *K. galanga,* L. (a) bigger rhizomes with dark brown epidermis and the oils (SV1O and MV1O), and (b) smaller rhizomes with light brown epidermis and the oils (SV2O and MV2O)

Procedure

Isolation of the rhizome oil

Steam distillation. In this study, the steam distillation of essential oil from the *K. galanga* rhizomes employed a modified reported procedure [14]. First, the air-dried *K. galanga* rhizome powder (50 g) was steam distilled in Clevenger apparatus for 4 h. Subsequently, the distillate was extracted with *n*-hexane (3 × 50 mL), and the organic layer was dried with anhydrous sodium sulfate, left to stand overnight, filtered, as well as evaporated with a rotary vacuum evaporator. The essential oil obtained was then weighed to determine the mass, labeled SV1O and SV2O for the varieties 1 and 2, respectively, and stored to preserve freshness until use.

Maceration. A modified reported procedure was used to maceration of oil from the *K. galanga* rhizomes [14]. For this process, air-dried *K. galanga* rhizome powder (50 g) was immersed in *n*-hexane (250 mL) for 3 days, and the mixture was separated by filtration. Subsequently, the residue was washed with *n*-hexane (100 mL) and combined with the filtrate. The light-yellow filtrate was then dried with sodium sulfate anhydrous, left overnight, filtered again, and evaporated using a rotary vacuum evaporator. It was followed by weighing the rhizome essential oil obtained, labeled as MV1O and MV2O for the varieties 1 and 2, respectively, and storage to preserve freshness until use.

Determination of physicochemical properties

Physicochemical characteristics provide a baseline for the suitability of oils [6,14-15]. The oil's physicochemical properties determined were percentage yield based on oil weight per weight of material used, color based on physical observation in daylight and under UV radiation using UV chamber, odor on organoleptic evaluation, solubility in water, hexane. Other properties include solubility, specific gravity on the pycnometer, refractive index on a refractometer, and optical activity on a polarimeter were also examined [14]. Meanwhile, the oils' acid value (AV), saponification value (SV), ester value (EV), and iodine value (IV) were determined according to standard methods [15].

Gas chromatography-mass spectrometry analysis

Essential oil analysis was performed by gas chromatography coupled with mass spectrometry (GC/MS) in a GCMS-QP2010 Ultra, Shimadzu, equipped with an autosampler, AOC-20s, Shimadzu, auto-injector, AOC-20i, Shimadzu, and RTX-5MS (30 m × 0.25 mm ID and 0.25 μm film thickness) columns. The injector temperature was set at 200 °C. The oven temperature was initially at 70 °C for 2 min, programmed to reach 180 °C at the rate of 20 °C/min and held at 180 °C for 3 min, then increased to 250 °C at the rate of 20 °C/min, and finally kept constant at 250 °C for 16 min. Helium was used as the carrier gas with a 35.2 mL/min flow and 100 kPa pressure. The sample (0.2 μL) was neatly injected with a 20:1 split ratio, and the mass spectrometer was operated in the electron impact (EI) mode at 70eV. Thus, the mass scanning range was varied over 35-500 m/z. Also, the ion source and quadrupole temperatures were set at 230 and 150 °C, respectively. The essential oil components were identified based on their mass spectral fragmentation using the Wiley 9 GC/MS libraries. Subsequently, the identified compound's percentage was computed from a total ion chromatogram [16].

Antioxidant activity

The free radical scavenging activity of the rhizome oil of *K. galanga* was determined spectrophotometrically. First, the rhizome oils' hydrogen atom or electron donation abilities were measured from the bleaching of purple-colored methanol solution of stable 2,2-diphenyl-1-picrylhydrazyl radical (DPPH•) according to the reported procedure [17-18]. For this process, 0.5 mL of rhizome oil solution in 99.9% methanol, in the final concentration range of 0.025–0.250 mg/mL, or 0.5 mL of methanol (control), were mixed with 3.5 mL of 100 μM DPPH solution (0.0039 g in 100 mL 99.9% methanol prepared daily). Then, the mixture was vortexed thoroughly for a minute and left at room temperature for 30 min, and the absorbance was read against control at 517 nm, using a UV-2600 spectrophotometer (Shimadzu). The control probe contained all components except for the radicals. Subsequently, the oils' abilities to scavenge DPPH radicals, (DPPH• scavenging activity ($SA_{DPPH\bullet}$)), was calculated using the equation:

$$SA_{DPPH\bullet}(\%) = 100 \times \left(A_{Control} - A_{Sample}\right) / A_{Control}$$

where $A_{Control}$ is the control reaction's absorbance (containing all reagents except the rhizome oil), and A_{Sample} is the absorbance in the rhizome oil's presence. The oils' radical-scavenging ability was calculated as IC_{50} (g/mL) from the graph of the percentage of radical scavenging activity against the oil concentration.

Statistical analysis

All measurements were carried out in triplicate, and results were reported as mean±SD, except for GC-MS analysis. Furthermore, statistical analysis was performed using analysis of variance (ANOVA), and significant difference between sample averages ($p < 0.05$)

was calculated using IBM SPSS Statistics software package version 23.

■ RESULTS AND DISCUSSION

Physicochemical Properties of the Oils

Studies of various physicochemical characteristics identify the practical importance and provide bases for the suitability and utility of various oils of plants origin in daily life. The physicochemical properties of the oil, including color, odor, solubility in water and organic solvents, specific gravity, refractive index, optical rotation, acid value, iodine value, and saponification value, indirectly affect the essential oil's quality.

In this study, oils obtained from two *K. galanga* varieties' rhizomes, isolated by steam distillation and maceration extraction, were evaluated for their physicochemical characteristics (Table 1). The oils isolated by steam distillation (SOs) were light yellow, transparent in physical state, and pleasant aromatic odor. At the same time, the maceration (MOs) counterparts were yellow, viscous, and had a pleasant aromatic odor. However, the oils had no difference in color and were both soluble in organic solvents, including *n*-hexane, ethanol, and diethyl ether, but insoluble in water.

The percent yields of oils obtained in this study were 2.81±0.09, 7.93±0.20, 3.60±0.10, and 8.76±0.22 for SV1O, MV1O, SV2O, and MV2O, respectively. The varieties and isolation methods affected these yields significantly ($p < 0.05$). Furthermore, the bigger rhizomes, SV2O and MV2O, produced higher yields than the smaller counterparts, while maceration gave higher yields than the steam distillation. The study reports higher SV1O and SV2O oil yields than the previous study from Indian counterparts (1.30%) [6] and (3.50%) [11]. The differences are possibly due to physiological variations as well as environmental conditions. Similarly, MV1O and MV2O showed variations yield, with extraction by maceration technique, using *n*-hexane solvent. These yields were higher than those extracted using ethanol 95% (3.21–5.98%) as reported by Huda et al. [19].

Specific gravity is the ratio of a substance's density, respective to the density of water. Generally, essential oils have specific gravity values below 1, except for a few containing oxygenated aromatic compounds. In this study, MV1O and MV2O have higher specific gravity than SV1O and SV2O from the two rhizome varieties. MV1O has the highest value of 0.90±0.01 g/mL, followed by MV2O (0.88±0.01), SV1O (0.86±0.01), and SV2O (0.83±0.01), at 30 °C. These findings agreed with the values obtained for the essential oils of *K. galanga* rhizomes from Java (0.87–0.88 g/mL). However, the results are inconsistent with the report by Srivastava et al. [6],

Table 1. Yields and physicochemical properties of *K. galanga,* L rhizome oil

Properties	SV1O	MV1O	SV2O	MV2O
Yield (%)	2.81±0.09	7.93±0.20	3.60±0.10	8.76±0.22
Physical state	Transparent liquid	Viscous	Transparent liquid	Viscous
Color	Light yellow	Yellow	Light yellow	Yellow
Odor	Aromatic	Aromatic	Aromatic	Aromatic
Solubility in water	Immiscible	Immiscible	Immiscible	Immiscible
Solubility in hexane	Miscible	Miscible	Miscible	Miscible
Solubility in ethanol	Miscible	Miscible	Miscible	Miscible
Specific density (g/mL) at 30 °C	0.86±0.01	0.90±0.01	0.83±0.01	0.88±0.01
Refractive index at 30 °C	1.48±0.00	1.49±0.00	1.48±0.00	1.49±0.00
Optical rotation at 30 °C	-2.45	-2.56	-3.26	-3.31
Acid value (mg KOH/g)	1.23±0.01	1.35±0.01	1.82±0.02	1.98±0.01
Saponification value (mg KOH/g)	103.50±0.67	104.73±0.84	106.85±1.02	107.56±0.69
Ester value (mg KOH/g)	179.75±3.35	180.55±3.30	190.25±5.10	191.35±4.20
Iodine value (g/100g)	97±0.20	99±0.21	105±0.35	104±0.33

showing the essential oil of *K. galanga* rhizome from India isolated by hydrodistillation has a specific gravity of 1.03 g/mL, at 25 °C.

Based on the table above, SV2O and MV2O were discovered to have higher optical rotation (-3.26° and -3.31°), compared to SV1O and MV1O (-2.45° and -2.56°). The oils isolated by maceration with *n*-hexane (MV1O and MV2O) also have higher optical activity than the steam distillation counterparts. Furthermore, the study samples have similar refractive index values, ranging from 1.4771 to 1.4855, indicating the samples are rich in terpenes and oxygenated terpenes.

The acid value measures the amount of acids present in the oil and is expressed as a number of KOH milligrams required to neutralize the acid present in one gram of oil. This method is an indirect method for determining the acid amount in oil samples and, consequently, the oil's edibility. The acid values (AV) recorded in this study were 1.23±0.01, 1.35±0.01, 1.82±0.02, and 1.98±0.01 mg KOH/g, for SV1O, MV1O, SV2O, and MV2O, respectively. The acid value was significantly ($p < 0.05$) different for all oils and affected by varieties and isolation methods. These values are higher, compared to the results reported for Indian rhizome counterparts by Kumar (1.12 mg KOH/g) [15], but lower, compared to the report by Srivastava et al. (2.24 mg KOH/g) [6]. The lower the acid value, the better the oil quality.

Meanwhile, the number of KOH milligrams required to saponify one gram of oil completely is called saponification value (SV). In this study, the SVs were greater for oils from smaller *K. galanga* rhizomes than the bigger counterparts and were significantly different ($p < 0.05$). The saponification values were found to be 103.50±0.67, 104.73±0.84, 106.85±1.02, and 107.56±0.69 mg KOH/g, for SV1O, MV1O, SV2O, and MV2O, respectively. The values were lower, compared to the report by Kumar (190.7 mg KOH/g) [15], and had similar values with the report by Srivastava et al. (106.59 mg KOH/g) [6]. The lower the saponification value, the better the oil quality.

The ester values (EV) were high in all oils and found 179.75±3.35, 180.55±3.30, 190.25±5.10, and 191.35±4.20 mg KOH/g for SV1O, MV1O, SV2O, and MV2O, respectively, that probably due to the high content of cinnamic esters in oils. The values were comparable with the results reported by Kumar (189.65 mg KOH/g) [15]. In addition, the EVs were found to be greater for oils from smaller *K. galanga* rhizomes than the bigger counterparts and were significantly ($p < 0.05$) different.

Iodine value (IV) refers to the number of iodine grams absorbed per 100 grams of fat or oil. This qualitative parameter denotes the oil sample's degree of unsaturation. The high iodine value of oils indicates the high content of unsaturation and the high quality of the oil. In this study, the samples had IVs of 97±0.20, 99±0.21, 105±0.35, and 104±0.33 g/100 g of oil for SV1O, MV1O, SV2O, and MV2O, respectively. The value was significantly ($p < 0.05$) different for all oils and affected by varieties and isolation methods. These values were slightly lower than a previous report (107 g/100 g oil) [6].

Chemical Constituent of the Oils

Fig. 2 shows the GC-MS chromatograms of four oils, SV1O, MV1O, SV2O, and MV2O, from two *K. galanga* rhizome varieties isolated by steam distillation and maceration. Meanwhile, Table 2 shows the oils' chemical constituents, determined based on mass fragmentation patterns and comparison with mass spectra of Wiley library.

The total number of compounds identified in oils isolated by steam distillation and maceration from both *K. galanga* rhizome varieties were 48 (SV1O), 46 (MV1O), 59 (SV2O), and 53 (MV2O), representing 99.88, 99.95, 99.94, and 99.95% of the total oil, respectively. These show that the chemical components of oils from both varieties differ significantly in number and quantities. However, oils' chemical constituents from the isolation methods, steam distillation, and maceration were almost identical, which means the chemical constituents of oils from *K. galanga* rhizomes cultivated in Indonesia strongly depend on varieties rather than isolation methods. The oils contain monoterpenes, oxygenated monoterpenes, sesquiterpenes, oxygenated sesquiterpenes, long-chain alkane hydrocarbons, compounds derived from shikimic

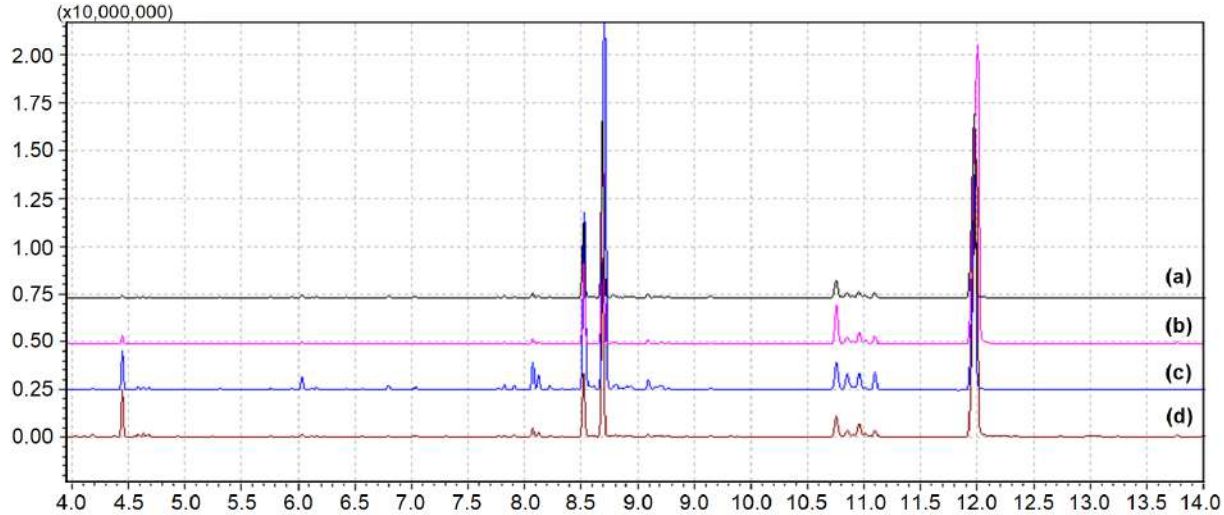

Fig 2. An overlay of *K. galanga*, L. rhizome oils chromatograms. (a) SV1O, (b) MV1O, (c) SV2O, and (d) MV2O

Table 2. Chemical composition of *K. galanga,* L. rhizome oils

No	RT	Common Name	Molecular Formula	MW (g/mol)	% Area			
					SV1O	MV1O	SV2O	MV2O
1	3.629	(-)-α-Pinene	$C_{10}H_{16}$	136.23	-	0.02	0.09	0.25
2	3.806	Camphene	$C_{10}H_{16}$	136.23	-	0.04	0.13	0.30
3	3.928	Benzaldehyde	C_7H_6O	106.12	-	-	0.02	-
4	4.108	(-)-β-Pinene	$C_{10}H_{16}$	136.23	-	-	-	0.05
5	4.185	7-Methyl-3-methylene-1,6-octadiene	$C_{10}H_{16}$	136.23	-	0.03	0.15	0.23
6	4.377	(-)-Phelandrene	$C_{10}H_{16}$	136.23	-	-	0.06	0.08
7	4.445	Δ-3-Carene	$C_{10}H_{16}$	136.23	0.22	0.64	2.34	3.97
8	4.582	1-Methyl-3-(1-methylethyl)-benzene	$C_{10}H_{14}$	134.22	0.04	0.05	-	-
9	4.586	1-Methyl-4-(1-methylethyl)-benzene	$C_{10}H_{14}$	134.22	-	-	0.22	0.28
10	4.632	(-)-Limonene	$C_{10}H_{16}$	136.23	0.07	0.05	0.22	0.27
11	4.687	1,8-Cineole	$C_{10}H_{18}O$	154.25	0.04	0.04	0.16	0.18
12	4.937	γ-Terpinene	$C_{10}H_{16}$	136.23	-	-	0.03	0.03
13	5.245	α-Terpinolene	$C_{10}H_{16}$	136.23	-	-	0.05	0.04
14	5.313	*(E)*-Farnesene epoxide	$C_{15}H_{24}O$	220.35	0.04	-	0.07	0.03
15	5.758	Ipsdienol	$C_{10}H_{16}O$	152.23	0.08	0.03	0.09	0.04
16	5.946	*p*-Mentha-1,5-dien-8-ol	$C_{10}H_{16}O$	152.23	0.08	-	0.14	0.03
17	6.033	*endo*-Borneol	$C_{10}H_{18}O$	154.25	0.43	0.15	0.87	0.27
18	6.122	4-Acetoxy-tricyclo[4.3.1.0(3,8)]-dec-10-yl acette	$C_{14}H_{20}O_4$	252.31	0.10	-	-	-
19	6.162	α,α,4-Trimethyl-benzenemethanol	$C_{10}H_{14}O$	150.22	0.09	0.04	0.18	0.06
20	6.229	β-Fenchyl alcohol	$C_{10}H_{18}O$	154.25	0.04	-	0.05	0.03
21	6.424	Eucarvone	$C_{10}H_{14}O$	150.22	0.06	-	0.09	-
22	6.566	2-Methyl-6-methylene-2,7-octadien-4-ol	$C_{10}H_{16}O$	152.23	-	-	0.06	0.03
23	6.799	4-Methoxy benzaldehyde	$C_8H_8O_2$	136.15	0.25	0.04	0.32	0.06
24	7.040	Tridecane	$C_{13}H_{28}$	184.36	0.20	0.12	0.29	0.13
25	7.304	Verbenone	$C_{10}H_{14}O$	150.22	-	-	0.07	0.08
26	7.373	Cyclofenchene	$C_{10}H_{16}$	136.23	-	-	0.03	-
27	7.560	α-Cubebene	$C_{15}H_{24}$	204.35	-	-	0.02	-
28	7.768	α-Ylangene	$C_{15}H_{24}$	204.35	0.12	0.05	0.19	0.05

Table 2. Chemical composition of *K. galanga,* L. rhizome oils (*Continued*)

No	RT	Common Name	Molecular Formula	MW (g/mol)	% Area			
					SV1O	MV1O	SV2O	MV2O
29	7.822	Tetradecane	$C_{14}H_{30}$	198.39	0.25	0.13	0.35	0.12
30	7.911	(-)-β-Elemene	$C_{15}H_{24}$	204.35	0.12	0.06	0.31	0.15
31	8.074	β-Patchoulene	$C_{15}H_{24}$	204.35	0.70	0.48	1.87	0.76
32	8.121	(+)-α-Gurjunene	$C_{15}H_{24}$	204.35	0.30	0.21	1.02	0.41
33	8.224	*trans*-Caryophyllene	$C_{15}H_{24}$	204.35	0.14	0.06	0.35	0.11
34	8.327	α-Guaiene	$C_{15}H_{24}$	204.35	0.13	0.03	0.14	0.08
35	8.380	(-)-Aristolene	$C_{15}H_{24}$	204.35	0.06	-	0.11	-
36	8.432	Selina-3,7(11)-diene	$C_{15}H_{24}$	204.35	-	-	0.20	-
37	8.524	Ethyl *trans*-cinnamate	$C_{11}H_{12}O_2$	176.21	12.54	7.06	14.44	6.97
38	8.610	(+)-Sativen	$C_{15}H_{24}$	204.30	-	0.09	0.38	0.13
39	8.607	α-Amorphene	$C_{15}H_{24}$	204.35	0.20	-	-	-
40	8.696	Pentadecane	$C_{16}H_{34}$	226.44	28.67	19.16	37.21	18.78
41	8.785	Germacrene D	$C_{15}H_{24}$	204.35	0.73	0.32	-	-
42	8.810	2-Isopropenyl-4a,8-dimethyl-1,2,3,4,4a,5,6,7-octahydro-naphthalene	$C_{15}H_{24}$	204.35	-	-	0.77	0.31
43	8.855	(-)-β-Silnene	$C_{15}H_{24}$	204.35	0.08	0.04	0.16	0.05
44	8.898	(+)-Valencene	$C_{15}H_{24}$	204.35	0.16	0.07	0.34	0.11
45	8.935	α-Salinene	$C_{15}H_{24}$	204.35	0.16	0.07	-	-
46	8.938	β-Chamigrene	$C_{15}H_{24}$	204.35	-	-	0.36	-
47	8.965	2,6-Bis(1,1-dimethylethyl)-4-methyl-phenol	$C_{15}H_{24}O$	220.30	0.08	-	-	-
48	9.003	(-)-Sinularene	$C_{15}H_{24}$	204.35	-	-	0.06	-
49	9.090	(-)-γ-Cadinene	$C_{15}H_{24}$	204.35	0.73	0.41	0.82	0.30
50	9.152	(+)-Δ-Cadinene	$C_{15}H_{24}$	204.35	0.19	0.08	0.33	
51	9.155	(-)-Valencene	$C_{15}H_{24}$	204.35	-	-	-	0.10
52	9.206	(+)-γ-Gurjunene	$C_{15}H_{24}$	204.35	0.27	0.17	-	0.21
53	9.210	Δ-Guaiene	$C_{15}H_{24}$	204.35	-	-	0.57	-
54	9.267	(-)-Isoledene	$C_{15}H_{24}$	204.35	0.27	0.20	0.17	0.16
55	9.433	Elemol	$C_{15}H_{26}O$	222.37	0.04	-	0.06	0.03
56	9.585	(-)-Isoledene	$C_{15}H_{24}$	204.35	0.04	-	-	-
57	9.649	Germacrene B	$C_{15}H_{24}$	204.35	0.44	0.13	0.17	0.06
58	9.755	Hexadecane	$C_{16}H_{34}$	226.44	-	-	0.07	-
59	9.882	Spathulenol	$C_{15}H_{24}O$	220.35	0.04	-	0.07	-
60	9.984	2,4,6-Tris(1,1-dimethylethyl)-phenol	$C_{18}H_{30}O$	262.40	0.07	-	-	-
61	9.987	(-)-Caryophyllene oxide	$C_{15}H_{24}O$	220.35	-	-	0.09	-
62	10.247	Veridiflorol	$C_{15}H_{26}O$	222.37	-	-	0.06	-
63	10.333	Cubenol	$C_{15}H_{26}O$	222.37	0.07	0.04	0.08	-
64	10.411	Azulene	$C_{10}H_8$	128.17	0.06	-	-	-
65	10.755	Ethyl *trans-m*-methoxycinnamate	$C_{12}H_{14}O_3$	206.24	3.87	4.53	2.92	2.90
66	10.848	(*E*)-9-Eicosene	$C_{20}H_{40}$	280.50	1.22	1.02	1.81	0.97
67	10.905	7-Decen-2-one	$C_{10}H_{18}O$	154.25	0.33	-	0.28	-
68	10.906	1-Cyclododecyl-ethanone	$C_{14}H_{26}O$	210.36	-	0.32	-	0.24
69	10.956	(*Z*6, *Z*9)-Pentadecadien-1-ol	$C_{15}H_{28}O$	224.38	1.21	1.30	1.55	1.61
70	11.008	Methyl *trans-p*-methoxycinnamate	$C_{11}H_{12}O_3$	192.21	0.50	0.53	0.24	0.36
71	11.096	Eicosane	$C_{20}H_{42}$	282.55	0.98	0.90	1.54	0.76

Table 2. Chemical composition of *K. galanga,* L. rhizome oils (*Continued*)

No	RT	Common Name	Molecular Formula	MW (g/mol)	% Area			
					SV1O	MV1O	SV2O	MV2O
72	11.988	Ethyl *trans-p*-methoxycinnamate	$C_{12}H_{14}O_3$	206.24	43.37	60.62	24.92	57.17
73	12.737	4-(4-Methoxyphenyl)oxane-4-carboxylic acid	$C_{13}H_{16}O_4$	236.26	-	-	-	0.04
74	12.739	Methyl *trans*-3,4- dimethoxycinnamate	$C_{12}H_{14}O_4$	222.24	-	0.03	-	-
75	12.960	9,12-Octadecadien-1-ol/(Z)-9,17-Octadecadienal	$C_{18}H_{34}O$	266.50	-	0.06	-	0.02
76	13.011	1-Heptadecanol	$C_{17}H_{36}O$	256.50	-	-	-	0.03
77	13.013	(*Z*)-9-Octadecenal	$C_{18}H_{34}O$	266.50	-	0.14	-	-
78	13.648	Hexadecanoic acid	$C_{16}H_{32}O_2$	256.42	-	0.03	-	-
79	13.766	2-Imino-3-(3-nitrophenyl)-tetrahydrothiazol-4-one	$C_9H_7N_3O_3S$	237.20	-	0.21	-	0.17
80	13.999	Sandaracopimaradiene	$C_{20}H_{32}$	272.50	-	0.08	-	0.07
81	17.457	Ergosterol	$C_{28}H_{44}O$	396.65	-	0.04	-	0.08
		Total			99.88	99.95	99.94	99.95

acid, and other miscellaneous components. Table 2 shows the oils' constituents in detail.

The air-dried rhizome oils of both *K. galanga* varieties, isolated by steam distillation and maceration, consisted of compounds derived from shikimic acid, 60.53% (SV1O), 72.81% (MV1O), 42.86% (SV2O), and 67.46% (MV2O), respectively with ethyl *trans-p*-methoxycinnamate (43.37% in SV1O, 60.62% in MV1O, 24.92% in SV2O, and 57.17% in MV2O) as the major components. Meanwhile, the total *trans*-cinnamic acid derivatives contents, including ethyl *trans-p*-methoxycinnamate, ethyl *trans*-cinnamate, ethyl *trans-m*-methoxycinnamate, methyl *trans-p*-methoxycinnamate, and methyl *trans-m,p*-dimethoxycinnamate, were 59.78, 72.21, 42.28, and 67.04% in SV1O, MV1O, SV2O, and MV2O, respectively. In addition, ethyl *trans-p*-methoxycinnamate and ethyl-*trans*-cinnamate show monoamine oxidase inhibiting and larvicidal effects [20]. Also, the cinnamate derivatives are responsible for the spicy aromatic odor [21].

The higher alkane hydrocarbons with a percentage contribution of 31.32% in SV1O, 21.33% in MV1O, 39.46% in SV2O, and 19.79 % in MV2O, were the second major constituent compound in oils from bigger *K. galanga* rhizome varieties, isolated by steam distillation and maceration. This result shows that steam distillation obtains more alkane hydrocarbons compared to maceration. In these oils, pentadecane (28.67% in SV1O, 19.16% in MV1O, 37.21% in SV2O, and 18.78% MV2O) was the main higher alkane hydrocarbons detected. Meanwhile, the sesquiterpene hydrocarbons and oxygenated sesquiterpenes contributed 5.11, 2.51, 8.83, and 3.22%, respectively, as the oil's third major constituents. Similarly, the steam distillation method obtained more sesquiterpenes and oxygenated sesquiterpenes content than the maceration method. In addition, the important sesquiterpenes and oxygenated sesquiterpenes identified in all oil samples (SV1O, MV1O, SV2O and MV2O) were α-ylangene (0.12, 0.05, 0.19, 0.05%), (-)-β-elemene (0.12, 0.06, 0.31, and 0.15%), β-patchoulene (0.70, 0.48, 1.87, and 0.76%), α-gurjunene (0.30, 0.21, 1.02, 0.41%), *trans*-caryophyllene (0.14, 0.06, 0.35, and 0.11%), and α-guaiene (0.13, 0.03, 0.14, and 0.08%).

The essential oils from smaller rhizomes were discovered to have higher and oxygenated monoterpene contents (4.81 and 5.95%), compared to oils from bigger rhizomes (1.15 and 1.09%), isolated by both methods. Furthermore, the important and oxygenated monoterpenes present in all oil samples (SV1O, MV1O, SV2O and MV2O) were Δ-3-carene (0.22, 0.64, 2.34 and 3.97%), (-)-limonene (0.07, 0.05, 0.22 and 0.27%), 1,8-cineole (0.04, 0.04, 0.16, and 0.18%), ipsdienol (0.08, 0.03, 0.09, and 0.04%) and *endo*-borneol (0.43, 0.15, 0.87, and 0.27%).

Fig. 3 shows the *K. galanga* rhizome oils also contained three saturated- and unsaturated long-chain alcohols (6*Z*,9*Z*-pentadeca-6,9-dien-1-ol, 9*E*,12*E*-

octadeca-9,12-dien-1-ol, and heptadecan-1-ol), one long-chain aldehyde (*Z*-octadec-9-enal), as well as two long-chain carboxylic acids (4-(4-methoxyphenyl)oxane-4-carboxylic acid, hexadecanoic acid). It is interesting to note that the rhizome oils from both *K. galanga* varieties isolated by maceration were found to contain one diterpene compound (sandaracopimaradiene), one steroid (ergosterol), and one alkaloid (2-imino-3-(3-nitrophenyl)-1,3-thiazolidin-4-one), in small quantities, Fig. 3. No other studies have never reported this finding. Meanwhile, sandaracopimaradiene is a diterpene derived from pimarane by dehydrogenation across the C(8)-C(14) and C(15)-C(16) bonds with a role as a metabolite and derived from an isopimarane hydride [21-22]. Furthermore, ergosterol is a phytosterol consisting of ergostane, with double bonds at the 5,6-, 7,8- and 22,23-positions and a 3-beta-hydroxy group. The compound has a role as a fungal metabolite and a *Saccharomyces cerevisiae* metabolite [23] and is also a biological precursor of vitamin D_2, called ergocalciferol. Exposure to ultraviolet light causes a photochemical reaction, converting ergosterol to ergocalciferol [24]. The essential oils were also contained some miscellaneous compounds as minor components.

Based on the results, numerous previously unreported compounds were not only identified in the rhizome oils from *K. galanga*, but the two varieties were also found to differ remarkably. The oils from variety-2 (the plant with smaller rhizomes) contained more compounds than variety-1 (the plant with bigger rhizomes). A previous study reported only eight components identified in the essential oil of *K. galanga* rhizome from East Java, Indonesia, isolated by maceration using methanol as solvent [25]. Meanwhile, twenty five different compounds in *K. galanga* essential oil, representing 95.98% of the total oil were identified by Yang et al. [26] and fourty one components by Li et al. [27] in Chinese samples. In addition, Wong et al. [20] successfully identified 53 compounds in a Malaysian sample, with 34 compounds identified through the OV-101 column and 19 through Carbowax 20M column, including indole, vanillin, and other compounds. Raina et al. [28] reported over 38 constituents in oil from South Indian samples, while Srivastava et al. [29] reported fifty four constituents identified from Hamirpur India which amounting to 92.77% of the *Kaempferia galanga* rhizome volatile organic compounds (VOCs). VOCs were ethyl *trans-p*-methoxycinnamate (52.54%), ethyl

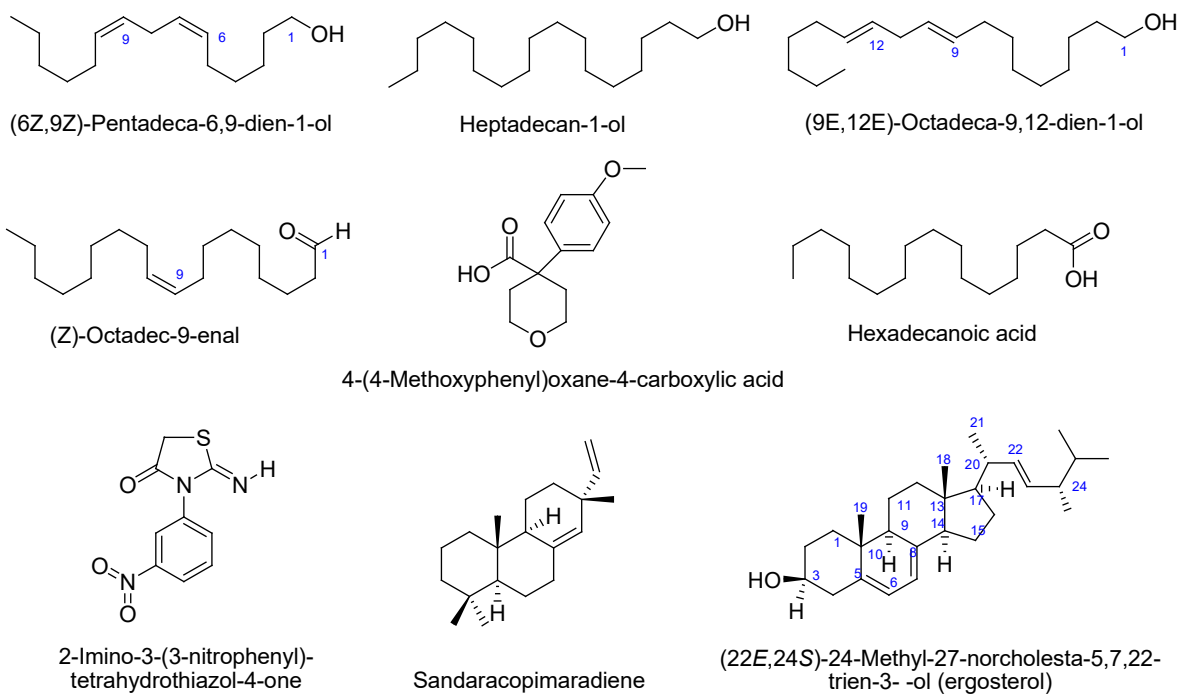

Fig 3. Structures of selected metabolites identified in the *K. galanga* rhizome oils

trans-cinnamate (24.98%), 1,8-cineole (4.14%), 3-carene (3.94%), dihydroterpineol (1.84%), α-terpineol (1.64%), and camphene (1.02%).

This study identified 48 and 46 compounds in the bigger *K. galanga* rhizome oils isolated by steam distillation and maceration. The two oils contained 36 similar compounds. However, 12 compounds were identified in SV1O but not in MV1O. Meanwhile, 59 and 53 compounds were identified in the smaller rhizome oils, isolated by steam distillation and maceration, respectively. However, 43 compounds were common to both oils, while 16 were present in SV2O but not in MV2O. A total of 81 compounds were identified in all oils, with 28 similar compounds, including ethyl *trans-p*-methoxycinnamate (24.92–60.64%), ethyl *trans*-cinnamate (6.97–14.44%), ethyl *trans-m*-methoxycinnamate (2.90–4.53%) and methyl *trans-p*-methoxycinnamate (0.24–0.53%). Other important chemical compounds identified in all oil samples were δ-3-carene (0.22–3.97%), (-)-limonene (0.05–0.27%), 1,8-cineole (0.04–0.18%), borneol (0.15–0.87%), and pentadecane (18.78–37.21%).

As seen in Fig. 4, the analyzed rhizome essential oils from two *K. galanga* varieties isolated by steam distillation and maceration contained major compounds derived from shikimic acid, phenylpropanoids, with contributions of 42.86–72.81%, followed by higher alkanes hydrocarbon (19.79–39.46%), sesquiterpenes hydrocarbons (2.47–8.34%), miscellaneous compounds (1.89–4.04%), monoterpenes hydrocarbons (0.76–5.49%), oxygenated monoterpenes (0.11–0.84%), and oxygenated sesquiterpenes (0.04–0.43%). Furthermore, ethyl *trans-p*-methoxycinnamate (24.92–60.62%) was discovered to be the most prevalent chemical compound derived from shikimic acid in oils.

The quantitative data, especially on the main chemical component of *K. galanga* oils tested, were quite comparable with the counterparts reported in the literature from other regions of the world. However, in some cases, a notable variation in the oils' composition was also observed, which agrees with previous studies stating a considerable variation in the rhizome oils' main chemical composition (18.42–63.36%) for varieties and isolation methods. Wong et al. [20] reported the constituent of steam-distilled essential oil from fresh *K. galanga*, L. rhizomes growing in Malaysia to be ethyl *trans-p*-methoxycinnamate (51.6%), ethyl cinnamate (16.5%), pentadecane (9.0%), 1,8-cineole (5.7%), 6-car-3-ene (3.3%) and borneol (2.7%). Meanwhile, Baharudin et al. [30] identified ethyl *trans-p*-methoxycinnamate (57.2%) and ethyl cinnamate (39.1%) as the major constituents of essential oils of *K. galanga* from Pahang, Malaysia. In addition, the chemical components of volatile

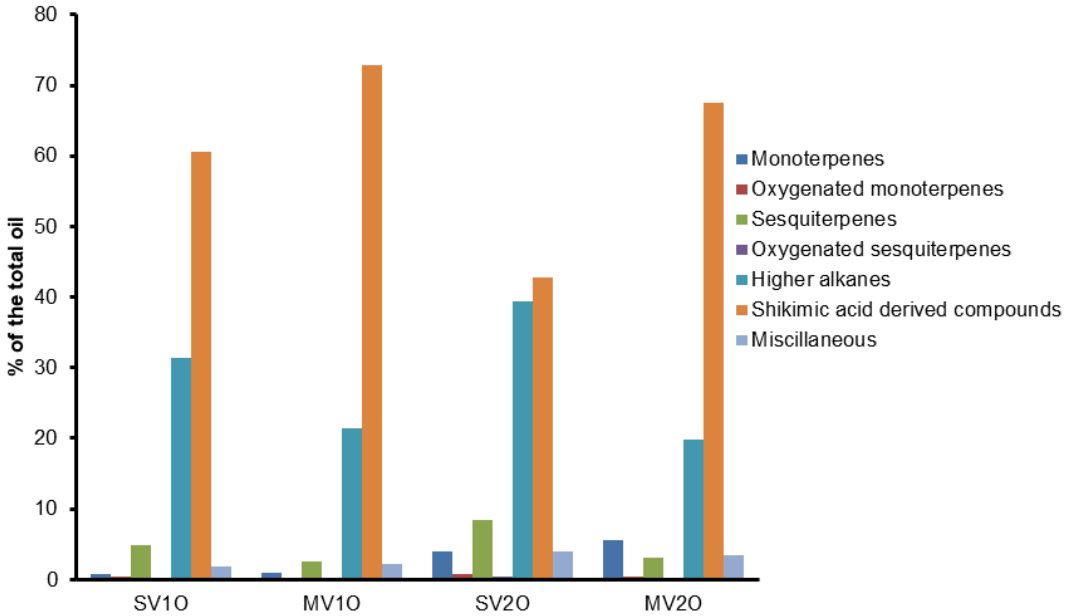

Fig 4. The proportion of different compound classes in *K. galanga* rhizome essential oils

K. galanga dried rhizome oil from Amphur Chana, Songkhla Province, Thailand, obtained by steam distillation, were reported to be ethyl *trans-p*-methoxycinnamate (31.77%), methyl *trans*-cinnamate (23.23%), carvone (11.13%), eucalyptol (9.59%), pentadecane (6.41%), borneol (2.87%), camphene (2.24%), benzene (1.33%), and pinene (1.23%) [31]. A separate study reported that essential oil from *K. galanga* obtained from Chiang Mai province, Thailand, isolated by steam distillation, contained ethyl *trans-p*-methoxycinnamate (25.96%), pentadecane (26.10%), and eucalyptol (2.12%) [32]. Meanwhile, the Bangladesh counterpart obtained by hydrodistillation was reported to contain ethyl *trans-p*-methoxycinnamate (63.36%), ethyl cinnamate (6.31%), 4-cyclooctene-1-methanol (4.61%), caryophyllene oxide (4.37%), and limonene (3.22%) [33]. Also, the essential oils from two *K. galanga* Linn varieties, 'Kasthuri' and 'Rajani' from India, were reported to contain ethyl *trans-p*-methoxycinnamate (39 and 35%, respectively) [29]. In addition, essential oil from dried *Kaempferia galanga* L. rhizome, from Herbal Garden Rishikesh, India, isolated by steam distillation, was reported to contain ethyl *trans*-cinnamate (29.48%), ethyl *trans-p*-methoxycinnamate (18.42%), γ-cadinene (9.81%), 1,8-cineole (6.54%), δ-carene (6.19%), borneol (5.21%), ethyl *trans-m*-methoxycinnamate (2.15%), camphene (1.58%), linoleoyl chloride (1.35%), and α-pinene (1.32%) [15].

In this study, the analyzed air-dried rhizome essential oils, isolated by steam distillation and maceration, using *n*-hexane as the solvent, contained mainly ethyl *trans-p*-methoxycinnamate, although significantly varying concentration, compared to other *K. galanga* varieties and isolation methods employed. The highest oil yield was obtained from smaller rhizome varieties isolated by maceration (MV2O), while the highest ethyl *trans-p*-methoxycinnamate content was obtained from bigger counterparts isolated by maceration (MV1O).

Antioxidant Activities

Antioxidants can either delay or inhibit oxidation processes occurring under atmospheric oxygen or reactive oxygen species. Thus, these compounds are involved in an organism's defense mechanism against pathologies associated with free radical attacks. In the Zingiberaceae family, antioxidants produced by the plant are generally believed to be transported and accumulated in the rhizomes, implying that rhizomes are bound to have higher antioxidant activity than other plant parts. In this present study, antioxidant activities of four oils from two *K. galanga* rhizome varieties were assessed for comparison purposes, and all samples exhibited high antioxidant activities. The antioxidant activity in DPPH free radical-scavenging assay of all oil samples expressed as IC_{50} values were found to be 86.10±1.51, 85.24±1.48, 89.19±1.72, and 86.49±2.03 μg/mL, for SV1O, MV1O, SV2O, and MV2O, respectively. These values did not differ significantly ($p>0.05$), which means the *K. galanga* rhizome oils' antioxidant activities are high and not dependent on the variety and isolation method.

Chan et al. [4] reported weak antioxidant activity exhibited by methanol extract of *K. galanga* from Selangor Malaysia. According to the study, the antioxidant activity expressed as ascorbic acid equivalent (AAE) was 17±1 mg AA/100 g for the rhizomes. However, Ali et al. [18] reported high antioxidant activity exhibited by methanolic extract of *K. galanga* plant. The antioxidant activity represented as IC_{50} of DPPH radical scavenging activity of *K. galanga* plant from Chittagong Bangladesh dried in an air was 16.58 μg/mL. Sahoo et al. also evaluated this property in essential oil isolated by hydrodistillation from conventionally propagated (CP) and *in vitro* propagated (IVP) *K. galanga* L rhizomes [34]. The antioxidant activity IC_{50} values assessed by DPPH radical scavenging were 26.0 and 19.5 μg/mL for CP and IVP oils, respectively. These results the oils' antioxidant activities are very high compared to this study.

■ CONCLUSION

Generally, the high rhizome essential oil yield from selected *K. galanga* varieties was obtained by the maceration method. The tested oils comprise mainly compounds derived from shikimic acid, phenylpropanoid and exhibited high antioxidant

activity with IC_{50} values, in the range of 85.24 to 89.19 μg/mL. Furthermore, the oils' major chemical component was ethyl *trans-p*-methoxycinnamate, and the most prevalent chemical constituents varied for varieties and isolation methods employed. Therefore, additional bioassays would be necessary to be done soon to uncover the biomedical of the oil. Furthermore, the complexation of the oil with cyclodextrin is expected to boost the complex's physicochemical properties and eventually increase the versatility of its applications.

■ AUTHOR CONTRIBUTIONS

IWM conceived, designed, performed the experiments, and drafted the manuscript; IWM performed the GCMS analysis and corrected manuscript draft; NWM performed the antioxidant activities.

■ REFERENCES

[1] Kumar, A., 2020, Phytochemistry, pharmacological activities and uses of traditional medicinal plant *Kaempferia galanga* L. – an Overview, *J. Ethnopharmacol.*, 253, 112667.

[2] Preetha, T.S., Hemanthakumar, A.S., and Krishnan, P.N., 2016, A comprehensive review of *Kaempferia Galanga* L. (Zingiberaceae): A high sought medicinal plant in Tropical Asia, *J. Med. Plants Stud.*, 4 (3), 270–276.

[3] Maurya, S.K., and Seth, A., 2014, Potential medicinal plants and traditional Ayurvedic approach towards Urticaria, an allergic skin disorder, *Int. J. Pharm. Pharm. Sci.*, 6 (5), 172–177.

[4] Chan, E.W.C., Lim, Y.Y., Wong, L.F., Lianto, F.S., Wong, S.K., Lim, K.K., Joe, C.E., and Lim, T.Y., 2008, Antioxidant and tyrosinase inhibition properties of leaves and rhizomes of ginger species, *Food Chem.*, 109 (3), 477–483.

[5] Elfahmi, Woerdenbag, H.J., and Kayser, O., 2014, Jamu: Indonesian traditional herbal medicine towards rational phytopharmacological use, *J. Herb. Med.*, 4 (2), 51–73.

[6] Srivastava, N., Ranjana, Singh, S., Gupta, A.C., Shanker, K., Bawankule, D.U., and Luqman, S., 2019, Aromatic ginger (*Kaempferia galanga* L.) extracts with ameliorative and protective potential as a functional food, beyond its flavor and nutritional benefits, *Toxicol. Rep.*, 6, 521–528.

[7] Ali, H., Yesmin, R., Satter, M.A., Habib, R., and Yeasmin, T., 2018, Antioxidant and antineoplastic activities of methanolic extract of *Kaempferia galanga* Linn. rhizome against Ehrlich ascites carcinoma cells, *J. King Saud Univ., Sci.*, 30 (3), 386–392.

[8] Amuamuta, A., Plengsuriyakarn, T., and Na-Bangchang, K., 2017, Anticholangiocarcinoma activity and toxicity of the *Kaempferia galanga* Linn. rhizome ethanolic extract, *BMC Complementary Altern. Med.*, 17 (1), 213.

[9] Plengsuriyakarn, T., Viyanant, V., Eursitthichai, V., Picha, P., Kupradinun, P., Itharat, A., and Na-Bangchang, K., 2012, Anticancer activities against cholangiocarcinoma, toxicity and pharmacological activities of Thai medicinal plants in animal models, *BMC Complementary Altern. Med.*, 12, 23.

[10] Othman, R., Ibrahim, H., Mohd, M.A., Mustafa, M.R., and Awang, K., 2006, Bioassay-guided isolation of a vasorelaxant active compound from *Kaempferia galanga* L., *Phytomedicine*, 13 (1-2), 61–66.

[11] Jagadish, P.C., Latha, K.P., Mudgal, J., and Nampurath, G.K., 2016, Extraction, characterization and evaluation of *Kaempferia galanga* L. (Zingiberaceae) rhizome extracts against acute and chronic inflammation in rats, *J. Ethnopharmacol.*, 194, 434–439.

[12] Rostiana, O., Abdulah, A., Martono, B., Haryudin, W., and Aisyah, S., 1993, Pengaruh rimpang utama dan rimpang cabang terhadap pertumbuhan dan produksi tiga tipe kencur di kp. Citayam, *Bul. Littro*, 8 (2), 89–93.

[13] Rostiana, O.S.M., Rosita, H., Wawan, Supriadi, and Aisyah, S., 2003, Status pemuliaan tanaman kencur, *Perkembangan Teknologi Tanaman Rempah dan Obat*, 15 (2), 25–38.

[14] Barkatullah, Ibrar, M., Rauf, A., and Ur-Rahman, I., 2012, Physicochemical characterization of essential and fixed oils of *Skimmia laureola* and

Zanthoxylum armatum, *Middle-East J. Med. Plants Res.*, 1 (3), 51–58.

[15] Kumar, A., 2014, Physico-chemical and natural products investigations of essential oil from the rhizomes of *Kaempferia galanga* L., *Chem. Sin.*, 5 (2), 91–94.

[16] Fan, S., Chang, J., Zong, Y., Hu, G., and Jia, J., 2018, GC-MS analysis of the composition of the essential oil from *Dendranthema indicum* Var. Aromaticum using three extraction methods and two columns, *Molecules*, 23 (3), 576.

[17] Shekhar, T.C., and Anju, G., 2014, Antioxidant activity by DPPH radical scavenging method of *Ageratum conyzoides* Linn. leaves, *Am. J. Ethnomed.*, 1 (4), 244–249.

[18] Ali, H., Yesmin, R., Satter, M.A., Habib, R., and Yeasmin, T., 2018, Antioxidant and antineoplastic activities of methanolic extract of *Kaempferia galanga* Linn. rhizome against Ehrlich ascites carcinoma cells, *J. King Saud Univ., Sci.*, 30 (3), 386–392.

[19] Huda, M.I., Daryon, E.D., and Muyassaroh, 2013, Minyak kencur dari rimpang kencur dengan variabel jumlah pelarut dan waktu maserasi, *Jurnal Teknik Kimia*, 8 (1), 1–6.

[20] Wong, K.C., Ong, K.S., and Lim, C.L., 1992, Composition of the essential oil of rhizomes of *Kaempferia galanga* L., *Flavour Fragrance J.*, 7 (5), 263–266.

[21] Reveglia, P., Cimmino, A., Masi, M., Nocera, P., Berova, N., Ellestad, G., and Evidente, A., 2018, Pimarane diterpenes: Natural source, stereochemical configuration, and biological activity, *Chirality*, 30 (10), 1115–1134.

[22] Swapana, N., Tominaga, T., Elshamy, A.I., Ibrahim, M.A., Hegazy, M.E.F., Singh, C.B., Suenaga, M., Imagawa, H., Noji, M., and Umeyama, A., 2018, Kaemgalangol A: Unusual seco-isopimarane diterpenoid from aromatic ginger *Kaempferia galanga*, *Fitoterapia*, 129, 47–53.

[23] Jordá, T., and Puig, S., 2020, Regulation of ergosterol biosynthesis in *Saccharomyces cerevisiae*, *Genes*, 11 (7), 795.

[24] Hirsch, A.L., 2011, "Industrial Aspects of Vitamin D" in *Vitamin D*, 3rd Ed., Eds. Feldman, D., Pike, J.W., and Adams, J.S., Academic Press, San Diego, 73–93.

[25] Adianingsih, O.R., Widaryanto, E., Saitama, A., and Zaini, A.H., 2021, Analysis of bioactive compounds present in *Kaempferia galanga* rhizome collected from different regions of East Java, Indonesia, *IOP Conf. Ser.: Earth Environ. Sci.*, 913, 012074.

[26] Yang, Y., Tian, S., Wang, F., and Li, Z., 2018, Chemical composition and antibacterial activity of *Kaempferia galanga* essential oil, *Int. J. Agric. Biol.*, 20 (2), 457–462.

[27] Li, Y.C., Ji, H., Li, X.H., Zhang, H.X., and Li, H.T., 2017, Isolation of nematicidal constituents from essential oil of *Kaempferia galanga* L rhizome and their activity against *Heterodera avenae* Wollenweber, *Trop. J. Pharm. Res.*, 16 (1), 59–65.

[28] Raina, A.P., Abraham, Z., and Sivaraj, N., 2015, Diversity analysis of *Kaempferia galanga* L. germplasm from South India using DIVA-GIS approach, *Ind. Crops Prod.*, 69, 433–439.

[29] Srivastava, N., Ranjana, Singh, S., Gupta, A.C., Shanker, K., Bawankule, D.U., and Luqman, S., 2019, Aromatic ginger *(Kaempferia galanga* L.) extracts with ameliorative and protective potential as a functional food, beyond its flavor and nutritional benefits, *Toxicol. Rep.*, 6, 521–528.

[30] Baharudin, M.K.A., Hamid, S.A., and Susanti, D., 2015, Chemical composition and antibacterial activity of essential oils from three aromatic plants of the Zingiberaceae family in Malaysia, *J. Phys. Sci.*, 26 (1), 71–81.

[31] Tewtrakul, S., Yuenyongsawad, S., Kummee, S., and Atsawajaruwan, L., 2005, Chemical components and biological activities of volatile oil of *Kaempferia galanga* Linn, *Songklanakarin J. Sci. Technol.*, 27 (Suppl. 2), 503–507.

[32] Wang, S.Y., Zhao, H., Xu, H.T., Han, X.D., Wu, Y.S., Xu, F.F., Yang, X.B., Göransson, U., and Liu, B., 2021, *Kaempferia galanga* L.: Progresses in phytochemistry, pharmacology, toxicology and

ethnomedicinal uses, *Front. Pharmacol.,* 12, 675350.

[33] Bhuiyan, M.N.I., Begum, J., and Anwar, M., 2013, Essential oils of leaves and rhizomes of *Kaempferia galanga* Linn, *Chittagong Univ. J. Biol. Sci.*, 3 (1-2), 65–76.

[34] Sahoo, S., Parida, R., Singh, S., Padhy, R.N., and Nayak, S., 2014, Evaluation of yield, quality and antioxidant activity of essential oil of in vitro propagated *Kaempferia galanga* Linn, *J. Acute Dis.*, 3 (2), 124–130.

Influence of Different Kinds of Plant Fibers on the Curing Kinetics of Epoxy Resin

Yeng-Fong Shih[1], Jia-Yi Xu[1], Nian-Yi Wu[1], Ting-Yuan Ou[1], and Saprini Hamdiani[1,2*]

[1]*Department of Applied Chemistry, Chaoyang University of Technology, No. 168, Jifeng E. Rd., Wufeng District, Taichung 41349, Taiwan*

[2]*Department of Chemistry, Faculty of Mathematics and Natural Sciences, University of Mataram, Majapahit Street No. 62, NTB 83115, Indonesia*

* ***Corresponding author:***

tel: +886-973068465
email: saprini.h@unram.ac.id

Received: June 18, 2021
Accepted: November 19, 2021

DOI: 10.22146/ijc.66771

Abstract: *The curing kinetics of the epoxy resin crosslinked by an anhydride hardener with and without plant fibers was investigated. The epoxy composites containing modified pineapple leaf fiber (EASF), banana fiber (EBSF), and bamboo chopsticks fibers (ECSF) were analyzed by non-isothermal differential scanning calorimetry (DSC) technique. Dynamic methods were used to predict the total heat of reaction of the epoxy resin and its activation energy based on the methods of Kissinger and Ozawa. The results showed that, at a low heating rate (5 °C/min), the ΔH of the pure epoxy, EASF, EBSF, and ECSF were 326.2, 307.6, 295.6, and 366.6 J/g, respectively. The curing rate increased, and the activation energy was decreased due to the catalytic role of hydroxyl groups of plant fibers. Based on Kissinger and Ozawa methods, the calculation of activation energy for pure epoxy was 70.08 kJ/mol and 73.21 kJ/mol, EBSF was 68.07 kJ/mol and 71.41 kJ/mol, ECSF was 60.11 kJ/mol and 63.87 kJ/mol, and EASF was 58.71 kJ/mol and 62.49 kJ/mol. The activation energy for the three kinds of epoxy composite modified fibers was less than pure epoxy resin due to the gel effect resulting from the higher viscosity, faster curing rate, and steric hindrance.*

Keywords: *epoxy; curing kinetics; plant fiber; activation energy*

■ INTRODUCTION

Epoxy resin can be cured at room or elevated temperature by adding hardeners, resulting in a three-dimensional structure. After cross-linking, epoxy resin is a thermoset polymer, with some different characteristics from the general resin, such as low volume shrinkage, dimensional stability, superior mechanical properties, excellent chemical resistance, corrosion resistance, thermal stability, good electrical insulation, and other excellent properties. Therefore, epoxy resin is widely used in electronic components substrates, structural adhesives, composite materials, the aviation industry, sports equipment, and military engineering [1].

Recently, plant fibers have replaced glass fibers and are widely used to reinforce polymers concerning environmental aspects. The advantages of plant fibers over glass fibers include low density, low cost, recyclability, and biodegradability [2-4]. Many researchers have investigated the reinforcing effects on the plant fiber-reinforced epoxy and various polymer composites [5-9]. Sapuan et al. (2006) used woven banana fibers, water bamboo husk, palm fiber, fruit bunches/jute fibers, and untreated Phormium Tenax leaf fibers. The addition of woven banana fibers to *Musaceae*/epoxy resulted in the composite with the maximum stress of 26.181 MN/m^2 and Young's modulus of 2.685 GN/m^2 [5]. Bamboo husk increased the storage moduli of PLA 50–200% [6]. Palm fiber added to the polyester resin increased the composite's interfacial relaxation strength (Δε) to 85.743 at 130 °C [7]. Oil palm empty fruit bunches (EFB)/jute fiber reinforced the epoxy hybrid composite's flexural properties. The flexural strength and modulus of jute/EFB/jute were 49.0 MPa and 3.07 GPa, respectively, higher than the pure epoxy, which was 33.5 MPa and 1.04 GPa [8]. In the research proposed by Rosa et al. (2010), the use of untreated Phormium Tenax leaf fibers

to epoxy composites showed the increment of modulus and strength both in tensile and flexural loading compared to pure epoxy resin [9]. Many researchers discuss the reinforcement effect of plant fiber. However, only a few kinds of literature explained the reaction kinetics of epoxy resin [10-11].

Achilias et al. [12] performed isothermal scanning by differential scanning calorimetry (DSC) and observed the curing reaction between the epoxy resin and the cycloaliphatic diamine. They obtained the relationship between the hardening temperature and the reaction order. In addition, they found that the results analyzed by Fourier Transform Infrared (FT-IR) spectroscopy were consistent with those by DSC. Yeo [13] used DSC to investigate the curing behavior and obtain the reaction rate constant and reaction activation energy of liquid crystalline 4,4′-diglycidyloxybiphenyl epoxy with various diamines. Ren et al. [14] studied the curing kinetics of the epoxy resin hardened by phthalide-containing aromatic diamine. They calculated the reaction activation energy of epoxy resins with different structures through a secondary self-catalytic reaction mechanism. The results showed that the increased rigidity of the chain and reduced symmetry would increase the activation energy of the curing reaction. Bessa et al. [10] extracted *Arundo donax* L. cellulosic fibers (RF) from giant reed cane and investigated the effect of raw and treated RF on the curing kinetics of bisphenol A-based benzoxazine (BA-a) by DSC technique under non-isothermal conditions. RF was subjected to different chemical treatments, including alkaline, silane, or combining treatments. The results revealed a decrease in the heat of curing and activation energy (Ea).

In this study, three kinds of agricultural wastes (pineapple leaf fibers, banana fibers, and bamboo chopsticks fibers) [15-18] were incorporated into epoxy resin to prepare the plant fiber-reinforced epoxy composites. The waste was found in a huge abundant agricultural waste in Taiwan. Every year more than 5 million tons of waste is produced. Plant waste can be a severe problem and pollute the environment. Such waste requires proper treatment to increase its commercial utilization. In addition, the influence of different plant fibers on the curing kinetics of epoxy resin was investigated by the non-isothermal DSC technique. Ozawa [19-21] and Kissinger [22-24] methods were used to predict the curing behavior of the epoxy resin. The kinetic studies are critical to provide general information, especially if a large industrial-scale composite will be manufactured. The kinetic prediction can reduce the process, cost, and time-consuming in commercialization.

■ EXPERIMENTAL SECTION

Materials

Bisphenol F-epoxy resin (ML3564) with a density of 1.1 g/cm^3, polyaminoanhydride (curing agent), and benzyldimethylamine (accelerator) were supplied by Golden-Gate Chem. Co., Taiwan. Silane coupling agent (3-aminopropyltriethoxysilane) (Sigma Aldrich) was supplied by Dow Corning Co. The banana plant and pineapple leaves were kindly supplied by Taiwan Agricultural Research Institute.

Instrumentation

Polarizing optical microscopy (POM) (Carl Zeiss, Axio Scope A1) was used to analyze the morphology of fibers. The curing behavior was analyzed by a differential scanning calorimeter (TA Instruments DSC Q20).

Procedure

Fibers treatment and preparation of composites

The raw pineapple leaf fiber (ASF), banana fiber (BSF), and recycled disposable chopsticks fibers (CSF) were alkaline treated, washed with distilled water, and dried in an oven. The fibers were then chopped and screened to obtain an average length of 2 to 4 mm, and subsequently treated by a silane coupling agent (3-aminopropyltriethoxysilane) (Fig. 1) to obtain the modified pineapple leaf fiber, banana fiber, and recycled disposable chopsticks fiber. Next, the epoxy, curing agent, accelerator (100:90:2), and different kinds of modified fibers (20 wt.%) were mixed to obtain the modified fiber-reinforced epoxy composites (EASF, EBSF, and ECSF). The composites sample with a mass of 5–10 mg was kept in a sealed aluminum pan in DSC equipment. The heating program was set to 30–250 °C

at different heating rates of 5, 10, 15, and 20 °C/min under a constant nitrogen atmosphere.

Kinetic analysis

The degree of curing reaction (or cross-linking conversion rate), α, can be calculated by using the concentration of epoxy before and after the reaction or the change in the heat of the reaction as follow [25-27]:

$$\alpha = \frac{[E]_o - [E]_t}{[E]_o} \quad (1)$$

$$\text{or } \alpha = \frac{H_t}{\Delta H} \quad (2)$$

where $[E]_o$ and $[E]_t$ are the concentrations of epoxide at the beginning of curing and after curing time t, respectively. H_t is the enthalpy at a determined time and temperature, whereas ΔH is the total enthalpy of the curing reaction. The reaction rate equation for epoxy curing reactions can be expressed as:

$$\frac{d\alpha}{dt} = kf(\alpha) \quad (3)$$

$$\text{or } g(\alpha) = \int \frac{d\alpha}{f(\alpha)} = \int k dt \quad (4)$$

where α is the conversion of epoxy, k is the total reaction rate constant, and f(α) is the function of conversion rate, which is related to the reaction mechanism. The Arrhenius equation can be described as the relationship between reaction rate constant k and temperature T. A, Ea, and R are the pre-exponential factor, the activation energy, and the universal gas constant, respectively.

$$k = A\exp^{(-Ea/RT)} \quad (5)$$

There are two methods to study the kinetics of the curing reaction of epoxy resin by DSC: dynamic method and isothermal method (or static method). The dynamic method is used to record the relationship between the heat change of the reaction and the temperature at a fixed heating rate. The isothermal method is used to carry out the curing reaction at a fixed temperature and record the reaction heat versus time curve. The results obtained by the DSC measurement can be analyzed by Ozawa Method [19-21], Kissinger Method [22-24], or Barrett Method [28] to calculate the kinetic parameters such as total reaction rate constant, frequency factor, total reaction order, and reaction activation energy.

Kissinger method [22]. Assuming that the curing conversion is a function of time and temperature, the reaction rate (r) of the curing reaction can be expressed as:

$$r = \frac{d\alpha}{dt} = \left(\frac{\partial\alpha}{\partial t}\right)_T + \left(\frac{\partial\alpha}{\partial T}\right)_t \frac{dT}{dt} \quad (6)$$

When the reaction is a first-order reaction, and the temperature is fixed, dT/dt = 0, so the above formula can be rewritten as:

$$\frac{d\alpha}{dt} = k(1-\alpha) \quad (7)$$

When the reaction rate reaches the maximum at the peak temperature T_p, the differential value of the reaction rate concerning time $\frac{d}{dt}(\frac{d\alpha}{dt})$ is zero. Substituting the Arrhenius equation in Eq.7 and letting the heating rate dT/dt = β, the following equation can be obtained:

$$-\ln\left(\frac{\beta}{T_p^2}\right) = -\ln\left(\frac{AR}{E_a}\right) + \frac{E_a}{RT_p} \quad (8)$$

By plotting ln $(\frac{\beta}{T_p^2})$ versus $1/T_p$, the activation energy (E_a) and the frequency factor (A) can be obtained from the slope and the intercept.

Ozawa method [19-21,29]. Different integration methods for Eq. (3) can be used. One example is the Ozawa method. Flynn and Wall [30] and Ozawa [19-21,29] have shown that at a constant degree of conversion, the activation energy of a reaction is related to the heating rate, β, and the peak temperature of the reaction, T_p, by the following equation:

$$E_a = \frac{-R}{1.052} \frac{\Delta \ln\beta}{\Delta(1/T_p)} \quad (9)$$

where R is the ideal gas constant (8.314 J/mol K). The activation energy can be estimated from the slope of the plot of ln β versus $1/T_p$.

■ RESULTS AND DISCUSSION

Synthesis of Modified Fibers-Crosslinked Epoxy Composites

The synthesis process of modified fibers began with the delignification process. Delignification for

pineapple, banana, and recycled disposable chopsticks fibers in alkaline conditions aims to remove lignin and hemicellulose content. The removal of lignin and hemicellulose will improve the performance and surface properties of the fibers [31-33]. The chemical composition of pineapple, banana, and recycled disposable chopsticks fibers is ~98.63% cellulose [34-36]. Cellulose contained a hydroxyl group that will react with –Si–O– groups in 3-aminopropyltriethoxysilane to produce modified fibers. The formation of modified fibers will increase the stability of the epoxy composite [37-38]. Thus, the amine groups in modified fibers provide free electrons by nucleophilic addition process to open the oxirane rings in epoxy. The reaction forced the curing reaction process. An illustration of the curing reaction of the epoxy resin and modified fiber (MF) is shown in Fig. 1.

Morphology of Fibers

Fig. 2(a), (b), and (c) showed the morphology of modified pineapple leaf fiber, banana fiber, and recycled disposable chopsticks fiber analyzed by polarized optical microscopy (POM). The diameters of modified pineapple leaf fiber, banana fiber, and recycled disposable chopsticks fiber were about 50, 30, and 60 μm, respectively. The difference in diameter of the modified fibers affects the composite's physical properties, which affects the curing process's heat (ΔH) and activation energy. Sivasubramanian et al. (2020) used pineapple leaf fiber with diameters of 50, 100, and 150 μm as natural rubber composites fillers [39]. Researchers found that fibers with a diameter of more than 100 μm will decrease filler distribution in the composite. The filler function will be practical if the filler fibers fragment into smaller sizes, which will increase their distribution in the composite [39-40]. In this study, the diameter of the fiber less than 100 μm would be better to improve the physical properties of the composite. The effect of fiber diameter on the curing process will be explained in the kinetics analysis.

Kinetics Analysis

DSC thermograms of pure epoxy and the composites containing modified pineapple leaf, banana, or recycled disposable chopsticks fiber (EASF, EBSF, and ECSF) at a different heating rate (5, 10, 15, and 20 °C/min) are shown in Fig. 3–6. It is found that the

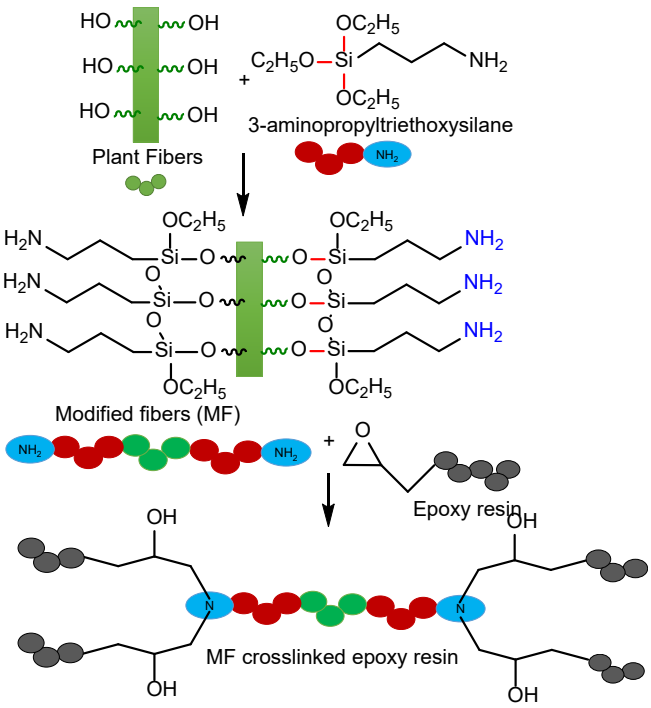

Fig 1. Illustration of curing reaction of the epoxy resin and modified fiber (MF)

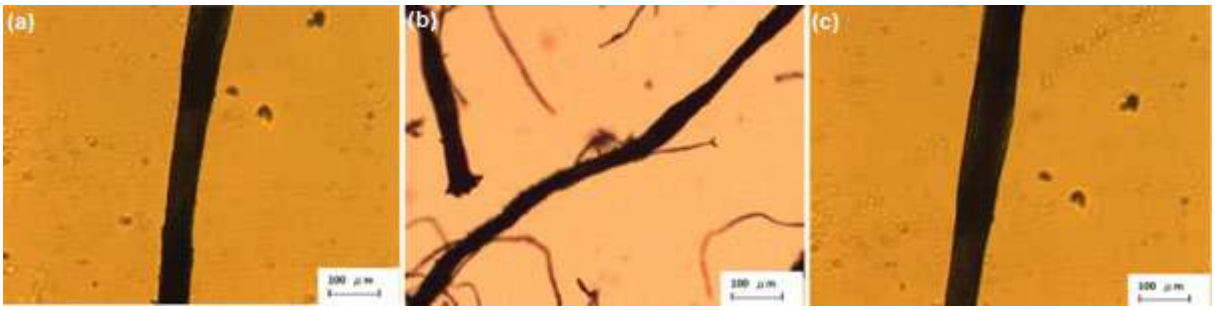

Fig 2. POM micrographs of (a) ASF (b) BSF (c) CSF

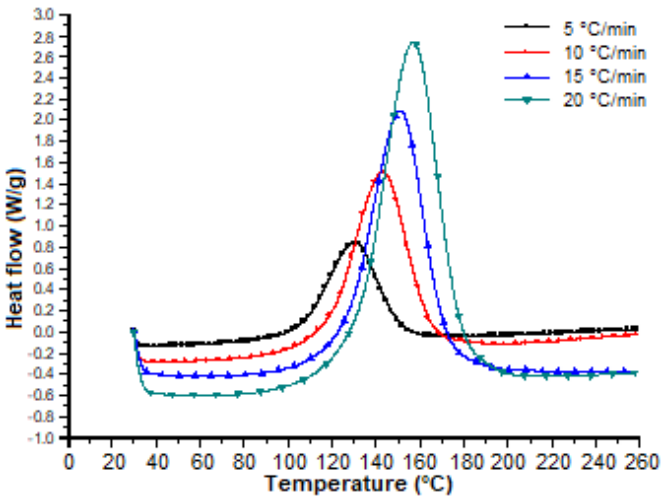

Fig 3. DSC thermograms of pure epoxy at a different heating rate

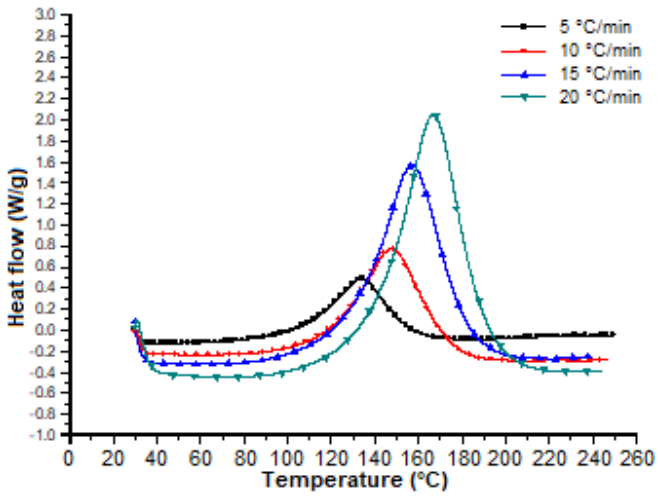

Fig 4. DSC thermograms of EASF composite at a different heating rate

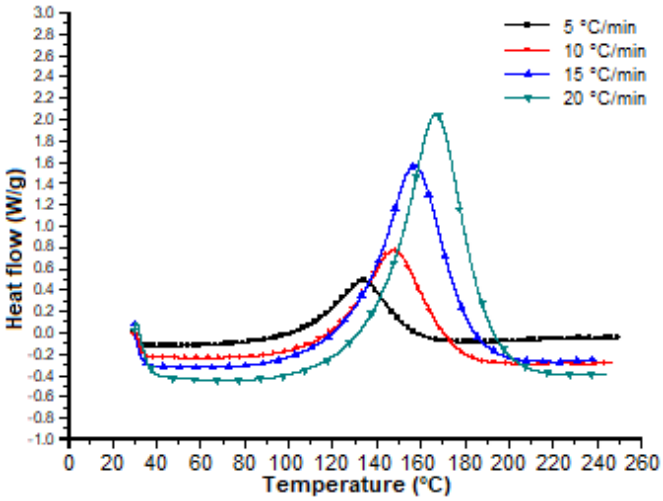

Fig 5. DSC thermograms of EBSF composite at a different heating rate

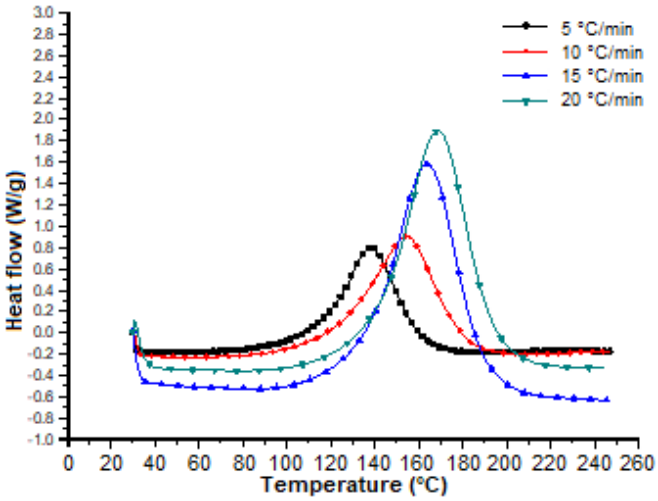

Fig 6. DSC thermograms of ECSF composite at a different heating rate

initial curing temperature (T_i) and the peak temperature (T_p) were all increased with the increasing heating rate. In addition, the exothermic peak was getting sharper with the increasing heating rate. The results of DSC analysis, including heating rate (β), initial curing temperature (T_i), peak temperature (T_p), final curing temperature (T_f), and the heat of curing (ΔH), are shown in Table 1.

The degree of crosslinking of epoxy can be evaluated by the heat of curing (ΔH). The results showed that the ΔH (307.6 and 295.6 J/g) of the EASF and EBSF at a low heating rate (5 °C/min) was smaller than that of pure epoxy (326.2 J/g). It is speculated that the smaller diameter of modified pineapple leaf fiber and banana fiber makes its volume fraction larger, which leads to higher viscosity and steric hindrance. The fibers with smaller diameters contained a considerable amount of particles. The increase of particle density thus hinders the curing process cause of the higher viscosity. In the banana fibers, the fiber diameter is only 50–60% of the other two fibers, so its volume fraction is substantial, leading to a higher viscosity and steric hindrance. Therefore, its heat of curing (ΔH) is the smallest, which means that the degree of cross-linking is low. The illustration of the fibers particle density in the composites system is shown in Fig. 7.

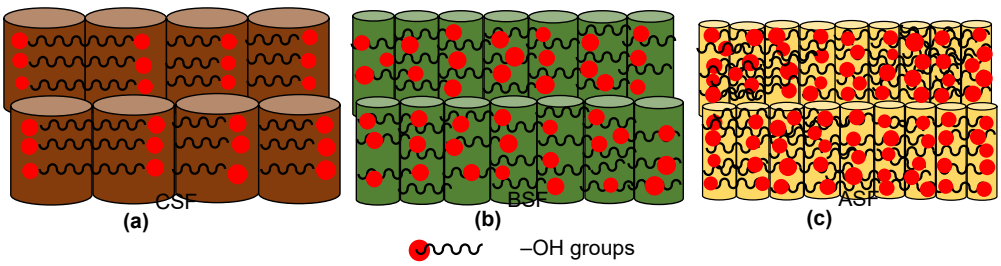

Fig 7. The illustration of fibers with different diameter sizes and the appearance of hydroxyl groups on the surface

Table 1. The results of DSC analysis

Sample	B (°C/min)	T_i (°C)	T_p (°C)	T_f (°C)	ΔH (J/g)
Pure epoxy	5	42.6	131.1	176.9	326.2
	10	55.4	143.2	190.1	313.1
	15	73.5	151.4	215.7	314.8
	20	76.7	157.1	217.2	321.2
EASF	5	50.1	134.7	180.9	307.6
	10	68.7	148.1	204.9	335.0
	15	78.0	157.3	215.1	352.8
	20	87.4	166.7	220.1	340.8
EBSF	5	44.7	138.6	182.4	295.6
	10	53.0	152.8	205.8	311.6
	15	73.4	160.8	211.4	324.3
	20	87.9	166.1	215.6	290.3
ECSF	5	56.6	138.6	184.8	366.6
	10	68.1	154.6	210.3	333.4
	15	87.1	164.4	232.2	328.6
	20	89.4	169.1	233.1	318.9

At the same time, the results of DSC analysis were used to calculate the reaction activation energy of pure epoxy resin and three kinds of fiber-reinforced composites through Kissinger and Ozawa methods. After importing from the formula, the analysis diagram of pure epoxy resin and various composites drawn in the Kissinger model is obtained and shown in Fig. 8, while the analysis diagram of pure epoxy resin and various composites in the Ozawa model is shown in Fig. 9. In addition, the activation energy and linear regression values obtained are sorted as shown in Table 2. It was found that the linear regression values were all larger than 0.993, indicating that both models were appropriate for describing the curing reactions, and the predicted curves from the calculated kinetic parameters fit well with the experimental data.

The results in Table 2 show that the order of activation energy is pure epoxy (Kissinger: 70.08 kJ/mol,

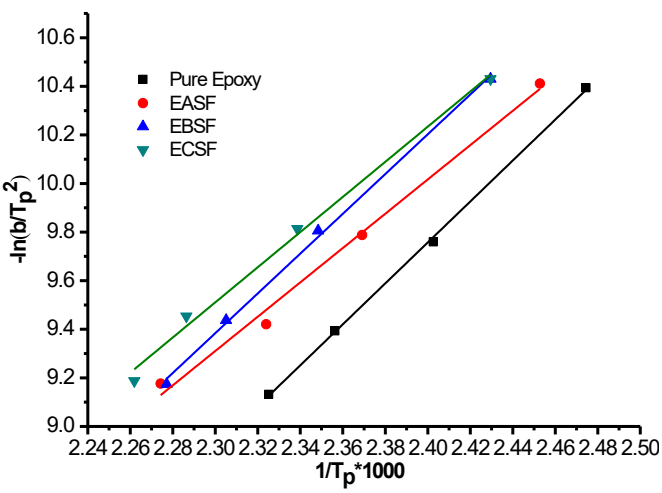

Fig 8. Analysis diagram of pure epoxy resin and composites drawn in Kissinger model

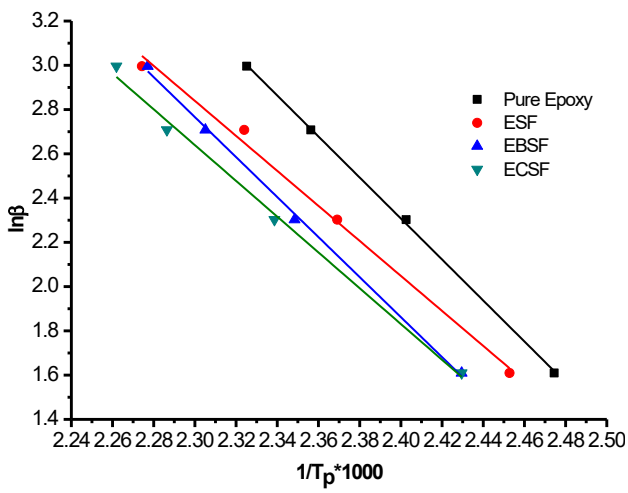

Fig 9. Analysis diagram of pure epoxy resin and composites drawn in Ozawa model

Table 2. Activation energy and regression value obtained by Kissinger and Ozawa model

Sample	Kissinger method		Ozawa method	
	E_a (kJ/mol)	Regression	E_a (kJ/mol)	Regression
Pure epoxy	70.08	0.999	73.21	0.999
EASF	58.71	0.993	62.49	0.994
EBSF	68.07	0.998	71.41	0.999
ECSF	60.11	0.995	63.87	0.996

Table 3. Comparison of activation energy value with similar studies of other systems

Type of polymer	Type of reinforced materials/fibers	E_a (kJ/mol)	Ref.
Bisphenol A-based benzoxazine	• No fibers	95.81	[10]
	• Giant reed cellulosic fibers (Arundo donax L/AF) alkali-treated	95.09	
	• AF silane treated	86.42	
	• AF alkali silane treated	88.19	
Epoxy	• No fibers	72.63	[11]
	• Curauá fibers alkaline treated	61.57	
Bisphenol A/triethylenetetramine (DGEBA/TETA) epoxy	• No fibers	58.97	[41]
	• 20% v Mallow fibers	44.54	
Bisphenol A (BPA)-based epoxy	• No fibers	48.40	[42]
	• 25% de-polymerized Kraft/organosolv lignins (softwood)	48.30	
	• 25% de-polymerized Kraft/organosolv lignins (hardwood)	45.10	

Ozawa: 73.21 kJ/mol) > EBSF (Kissinger: 68.07 kJ/mol, Ozawa: 71.41 kJ/mol) > ECSF (Kissinger: 60.11 kJ/mol, Ozawa: 63.87 kJ/mol) > EASF (Kissinger: 58.71 kJ/mol, Ozawa: 62.49 kJ/mol). These results reveal that the activation energy required for the reaction of the three kinds of fiber-reinforced composites is less than that of pure epoxy resin. Presumably, the hydroxyl groups on the fiber surface can promote the reaction. Moreover, the amine groups on the surface of the modified fiber will also participate in the reaction, thus accelerating the curing reaction. It can be found that the activation energy of the composite containing modified banana fiber (EBSF) is larger than those of the other two composites. Banana fibers have the smallest diameters with the highest activation energy value. As explained previously, the fibers with smaller diameters contained a huge particle density. The massive fiber density contained more hydroxyl groups on the banana fiber surface than the other fiber. Although the hydroxyl groups promote the curing reaction, in this case, too crowded hydroxyl groups on the surface cause the increment of steric hindrance in banana leaf (BSF) fibers (see Fig. 7). This result is consistent with that obtained from heat of curing. It is due to that the diameter of the modified banana fiber is small so that its volume fraction is larger, resulting in a larger viscosity and stereoscopic barriers, and leads to the larger activation energy. Our results were in good agreement with the previously reported work [10-11,41-43], where the value of activation energy decreases by the addition of fibers/modified fibers, as summarized in Table 3.

■ CONCLUSION

The results showed that the hydroxyl groups on the plant fiber and the amine groups on the modified fiber could accelerate the cross-linking reaction and reduce the activation energy of the epoxy resin. The calculation by Kissinger and Ozawa method showed the reduction of activation energy was 2.8% and 2.4%, 14.2% and 12.8%, and 16.2% and 14.6% for EBSF, ECSF, and EASF, respectively. However, the final degree of cross-linking for pure epoxy resin was more significant than the composites containing fibers. This is because the higher viscosity of the composite and the accelerating effects of

the hydroxyl groups on the plant fiber and amine groups on the modified fiber resulted in greater viscosity and steric hindrance, leading to the lower final degree of cross-linking. EASF and ECSF have a similar degree of cross-linking and activation energy among the three fiber-containing composites. The degree of cross-linking of EBSF is the lowest due to the smallest diameter of banana fiber, leading to a large volume fraction, higher viscosity, and steric hindrance so that the degree of cross-linking is relatively tiny with great activation energy.

■ AUTHOR CONTRIBUTIONS

Author Contributions: Y.F. Shih conceived and designed the original idea and methodology; Y.F. Shih, J.Y. Xu, and N.Y. Wu fabricated the sample, data collection, and curation; Y.F. Shih prepared the original draft; T.Y. Ou revised the draft; S. Hamdiani wrote the review and editing. All authors have read and agreed to the published version of the manuscript.

■ REFERENCES

[1] Saba, N., Jawaid, M., Alothman, O.Y., Paridah, M., and Hassan, A., 2016, Recent advances in epoxy resin, natural fiber-reinforced epoxy composites and their applications, *J. Reinf. Plast. Compos.*, 35 (6), 447–470.

[2] Kumar, R., Kumar, K., Sahoo, P., and Bhowmik, S., 2014, Study of mechanical properties of wood dust reinforced epoxy composite, *Procedia Mater. Sci.*, 6, 551–556.

[3] Rohit, K., and Dixit, S., 2016, A review - Future aspect of natural fiber reinforced composite, *Polym. Renewable Resour.*, 7 (2), 43–59.

[4] Mahmud, S., Hasan, K.M.F., Jahid, M.A., Mohiuddin, K., Zhang, R., and Zhu, J., 2021, Comprehensive review on plant fiber-reinforced polymeric biocomposites, *J. Mater. Sci.*, 56 (12), 7231–7264.

[5] Sapuan, S.M., Leenie, A., Harimi, M., and Beng, Y.K., 2006, Mechanical properties of woven banana fibre reinforced epoxy composites, *Mater. Des.*, 27 (8), 689–693.

[6] Wang, K.H., Wu, T.M., Shih, Y.F., and Huang, C.M., 2008, Water bamboo husk reinforced poly(lactic acid) green composites, *Polym. Eng. Sci.*, 48 (9), 1833–1839.

[7] Amor, I.B., Ghallabi, Z., Kaddami, H., Raihane, M., Arous, M., and Kallel, A., 2010, Experimental study of relaxation process in unidirectional (epoxy/palm tree fiber) composite, *J. Mol. Liq.*, 154 (2-3), 61–68.

[8] Jawaid, M., Abdul Khalil, H.P.S., and Abu Bakar, A., 2010, Mechanical performance of oil palm empty fruit bunches/jute fibres reinforced epoxy hybrid composites, *Mater. Sci. Eng., A*, 527 (29-30), 7944–7949.

[9] De Rosa, I.M., Santulli, C., and Sarasini, F., 2010, Mechanical and thermal characterization of epoxy composites reinforced with random and quasi-unidirectional untreated *Phormium tenax* leaf fibers, *Mater. Des.*, 31 (5), 2397–2405.

[10] Bessa, W., Trache, D., Derradji, M., Ambar, H., Tarchoun, A.F., Benziane, M., and Guedouar, B., 2020, Characterization of raw and treated *Arundo donax* L. cellulosic fibers and their effect on the curing kinetics of bisphenol A-based benzoxazine, *Int. J. Biol. Macromol.*, 164, 2931–2943.

[11] Libera, V.D., Teixeira, L.A., Leão, R.M., and Luz, S.M., 2019, Evaluation of thermal behavior and cure kinetics of a curauá fiber prepreg by the non-isothermal method, *Mater. Today: Proc.*, 8, 839–846.

[12] Achilias, D.S., Karabela, M.M., Varkopoulou, E.A., and Sideridou, I.D., 2012, Cure kinetics study of two epoxy systems with Fourier transform infrared spectroscopy (FTIR) and differential scanning calorimetry (DSC), *J. Macromol. Sci., Part A: Pure Appl. Chem.*, 49 (8), 630–638.

[13] Yeo, H., 2019, Curing kinetics of liquid crystalline 4,4′-diglycidyloxybiphenyl epoxy with various diamines, *Polymer*, 168, 209–217.

[14] Ren, R., Xiong, X., Ma, X., Liu, S., Wang, J., Chen, P., and Zeng, Y., 2016, Isothermal curing kinetics and mechanism of DGEBA epoxy resin with phthalide-containing aromatic diamine, *Thermochim. Acta*, 623, 15–21.

[15] Shih, Y.F., Cai, J.X., Kuan, C.S., and Hsieh, C.F., 2012, Plant fibers and wasted fiber/epoxy green composites, *Composites, Part B*, 43 (7), 2817–2821.

[16] Boopalan, M., Niranjanaa, M., and Umapathy, M.J., 2013, Study on the mechanical properties and thermal properties of jute and banana fiber reinforced epoxy hybrid composites, *Composites, Part B*, 51, 54–57.

[17] Jain, J., Jain, S., and Sinha, S., 2019, Characterization and thermal kinetic analysis of pineapple leaf fibers and their reinforcement in epoxy, *J. Elastomers Plast.*, 51 (3), 224–243.

[18] Shih, Y.F., Chang, W.C., Liu, W.C., Lee, C.C., Kuan, C.S., and Yu, Y.H., 2014, Pineapple leaf/recycled disposable chopstick hybrid fiber-reinforced biodegradable composites, *J. Taiwan Inst. Chem. Eng.*, 45 (4), 2039–2046.

[19] Ozawa, T., 1971, Kinetics of non-isothermal crystallization, *Polymer*, 12 (3), 150–158.

[20] Zheng, T., Xi, H., Wang, Z., Zhang, X., Wang, Y., Qiao, Y., Wang, P., Li, Q., Li, Z., Ji, C., and Wang, X., 2020, The curing kinetics and mechanical properties of epoxy resin composites reinforced by PEEK microparticles, *Polym. Test.*, 91, 106781.

[21] Kumar, S., Samal, S.K., Mohanty, S., and Nayak, S.K., 2017, Study of curing kinetics of anhydride cured petroleum-based (DGEBA) epoxy resin and renewable resource based epoxidized soybean oil (ESO) systems catalyzed by 2-methylimidazole, *Thermochim. Acta*, 654, 112–120.

[22] Kissinger, H.E., 1956, Variation of peak temperature with heating rate in differential thermal analysis, *J. Res. Nat. Bur. Stand.*, 57 (4), 217–221.

[23] Ferdosian, F., Zhang, Y., Yuan, Z., Anderson, M., and Xu, C.C., 2016, Curing kinetics and mechanical properties of bio-based epoxy composites comprising lignin-based epoxy resins, *Eur. Polym. J.*, 82, 153–165.

[24] Tikhani, F., Moghari, S., Jouyandeh, M., Laoutid, F., Vahabi, H., Saeb, M.R., and Dubois, P., 2020, Curing kinetics and thermal stability of epoxy composites containing newly obtained nano-scale aluminum hypophosphite ($AlPO_2$), *Polymers*, 12 (3), 644.

[25] Saeb, M.R., Rastin, H., Nonahal, M., Ghaffari, M., Jannesari, A., and Formela, K., 2017, Cure kinetics of epoxy/MWCNTs nanocomposites: Nonisothermal calorimetric and rheokinetic techniques, *J. Appl. Polym. Sci.*, 134 (35), 45221.

[26] Wu, F., Zhou, X., and Yu, X., 2018, Reaction mechanism, cure behavior and properties of a multifunctional epoxy resin, TGDDM, with latent curing agent dicyandiamide, *RSC Adv.*, 8 (15), 8248–8258.

[27] Thanki, J.D., and Parsania, P.H., 2017, Dynamic DSC curing kinetics and thermogravimetric study of epoxy resin of 9,9′-bis(4-hydroxyphenyl) anthrone-10, *J. Therm. Anal. Calorim.*, 130 (3), 2145–2156.

[28] Barrett, K.E.J., 1967, Determination of rates of thermal decomposition of polymerization initiators with a differential scanning calorimeter, *J. Appl. Polym. Sci.*, 11 (4), 1617–1626.

[29] Tripathi, M., Kumar, D., Rajagopal, C., and Roy, P.K., 2015, Curing kinetics of self-healing epoxy thermosets, *J. Therm. Anal. Calorim.*, 119 (1), 547–555.

[30] Flynn, J.H., and Wall, L.A., 1966, A quick, direct method for the determination of activation energy from thermogravimetric data, *J. Polym. Sci., Part B: Polym. Lett.*, 4 (5), 323–328.

[31] Buitrago, B., Jaramillo, F., and Gómez, M., 2015, Some properties of natural fibers (sisal, pineapple, and banana) in comparison to man-made technical fibers (aramide, glass, carbon), *J. Nat. Fibers*, 12 (4), 357–367.

[32] Sari, N.H., Wardana, I.N.G., Irawan, Y.S., and Siswanto, E., 2018, Characterization of the chemical, physical, and mechanical properties of NaOH-treated natural cellulosic fibers from corn husks, *J. Nat. Fibers*, 15 (4), 545–558.

[33] Wahyuningsih, K., Iriani, E.S., and Fahma, F., 2016, Utilization of cellulose from pineapple leaf fibers as nanofiller in polyvinyl alcohol-based film, *Indones. J. Chem.*, 16 (2), 181–189.

[34] Asim, M., Abdan, K., Jawaid, M., Nasir, M., Dashtizadeh, Z., Ishak, M.R., and Hoque, M.E., 2015, A review on pineapple leaves fibre and its composites, *Int. J. Polym. Sci.*, 2015, 950567.

[35] Radoor, S., Karayil, J., Rangappa, S.M., Siengchin, S., and Parameswaranpillai, J., 2020, A review on the extraction of pineapple, sisal and abaca fibers and their use as reinforcement in polymer matrix, *eXPRESS Polym. Lett.*, 14 (4), 309–335.

[36] Padam, B.S., Tin, H.S., Chye, F.Y., and Abdullah, M.I., 2014, Banana by-products: An under-utilized renewable food biomass with great potential, *J. Food Sci. Technol.*, 51 (12), 3527–3545.

[37] Lu, T., Jiang, M., Jiang, Z., Hui, D., Wang, Z., and Zhou, Z., 2013, Effect of surface modification of bamboo cellulose fibers on mechanical properties of cellulose/epoxy composites, *Composites, Part B*, 51, 28–34.

[38] Parbin, S., Waghmare, N.K., Singh, S.K., and Khan, S., 2019, Mechanical properties of natural fiber reinforced epoxy composites: A review, *Procedia Comput. Sci.*, 152, 375–379.

[39] Sivasubramanian, P., Mayandi, K., Santulli, C., Alavudeen, A., and Rajini, N., 2020, Effect of fiber length on curing and mechanical behavior of pineapple leaf fiber (PALF) reinforced natural rubber composites, *J. Nat. Fibers*, 0 (0), 1–12.

[40] Chandra Sekhar, V., Sreedhar, C., and Rajesh, P., 2018, Effect of fiber loading and fiber length on tensile properties of fiber reinforced epoxy composites, *Mater. Today: Proc.*, 5 (13), 27149–27154.

[41] Nascimento, L.F.C., da Luz, F.S., Costa, U.O., Braga, F.O., Lima Júnior, É.P., and Monteiro, S.N., 2019, Curing kinetic parameters of epoxy composite reinforced with mallow fibers, *Materials*, 12 (23), 3939.

[42] Zhu, L., Wang, Z., Rahman, M.B., Shen, W., and Zhu, C., 2021, The curing kinetics of E-glass fiber/epoxy resin prepreg and the bending properties of its products, *Materials*, 14, 4673.

[43] Ferdosian, F., Yuan, Z., Anderson, M., and Xu, C.C., 2016, Thermal performance and thermal decomposition kinetics of lignin-based epoxy resins, *J. Anal. Appl. Pyrolysis*, 119, 124–132.

Synthesis of Mn-Doped Fe-MOFs with Different Ratios and Its Application for Photocatalytic Degradation of Rhodamine B Dye

Kim Ngan Thi Tran[1,2*], Thuy Bich Tran[3], Sy Trung Do[4], Kim Oanh Thi Nguyen[1,2], and Tan Van Lam[1,2]**

[1]*Institute of Environmental Sciences, Nguyen Tat Thanh University, Ho Chi Minh City, Vietnam*

[2]*Faculty of Environmental and Food Engineering, Nguyen Tat Thanh University, Ho Chi Minh City, Vietnam*

[3]*Institute of Environmental Science, Engineering and Management, Industrial University of Ho Chi Minh City, Vietnam*

[4]*Institute of Chemistry, Vietnam Academy of Science and Technology (VAST), Hanoi City, Vietnam*

* ***Corresponding author:***

email: nganttk@ntt.edu.vn; lvtan@ntt.edu.vn***

Received: July 19, 2021
Accepted: September 27, 2021

DOI: 10.22146/ijc.67742

Abstract: *Recent trends in environmental remediation have shifted to the use of metal-organic framework (MOF) composites due to their unique structural properties. It is still challenging to diversify MOFs photocatalysts to fulfill application to treat toxic organic pigments. In this study, Fe-MOF bimetallic materials were synthesized by doping Mn^{2+} ions at different ratios. The structural and morphological characteristics of the materials were analyzed by XRD, UV-Vis, FT-IR, SEM, and UV-Vis DRS methods. Mn/Fe-MOF bimetallic organic framework materials were used to evaluate the photocatalytic degradation of Rhodamine B (RhB) dyes. The results show that, under the same experimental conditions, the RhB degradation efficiency of Mn/Fe-MOF is enhanced than that of the pristine Fe-MOF catalyst under the influence of visible light. After 120 min, the RhB solution was decomposed to 91.78% by combining 0.1 Mn/Fe-MOF, H_2O_2, and visible light irradiation. At the same time, the presence of H_2O_2 in the reaction system also showed a strong impact on the efficiency of RhB degradation. The activity from the two metal centers of Mn/Fe-MOF contributes to the formation of a unique structure and composition that can be used as a photocatalyst for colored wastewater treatment.*

Keywords: *synthesis; bimetallic-organic framework; photocatalytic dye degradation*

■ INTRODUCTION

Behind the development, environmental pollution and pollution of toxic organic pigments are some of the urgent problems. Pollution of organic pigments directly affects people's life, health, and activities. Therefore, the treatment of wastewater right at factories and industrial parks is extremely necessary and requires a research investment. In treating toxic pigments, a low-cost catalyst, especially a high-efficiency and reusable one, is an effective and potential method.

In new material technology, Metal-Organic Frameworks (MOFs) are considered as one of the potential materials because of their stable structure, ability to contain functional groups essential for adsorption, porosity, large surface area, specificity, simple material fabrication process [1-3]. Currently, it is attracting much attention from researchers because of its potential application in the field of adsorption [4], catalysis [5-6], sensors [7], and drug delivery [8-9]. Recently, several MOFs with novel structures have been synthesized from two different metal centers and possess interesting photocatalytic properties. Some recent research results also indicate that small changes in the synthesis process can lead to different crystal structures. Specifically, Wang et al. (2020) carried out the synthesis of Fe_xCo_yP based on the change in the molar ratio of Co/Fe. As a result, the $FeCo_2P$ polyhedra have a controllable composition and morphology hollow structure and exhibits high electrocatalytic activity for the oxygen evolution reaction (OER) [10]. In another publication in 2020, Wu and co-workers significantly improved the adsorption and Fenton photodegradation

for dyes (methylene blue, MB, and methyl orange, MO) of pristine Fe-BDC by doping Ni into the $FeNi_x$-BDC frames at various ratios different [11].

The decrease in surface charges or pore volume and increased specific surface area is caused by secondary metal doping. For example, Kirchon et al. (2020) demonstrated markedly degraded removal efficiency of toxic organic compounds by partial substitution of Mn and Co for Fe in Fe-based MOFs. In which, 100% of MB was decomposed by Fenton photocatalysis in the presence of PCN-250 (Fe_2Mn) catalyst in less than 300 min [12].

Methods for synthesizing MOFs include precipitation, sol-gel, heat transfer, solvothermal, direct oxidation, physical or chemical evaporation, and ultrasonic methods [13-15]. However, these methods often exhibit limitations, such as high energy costs, many by-products, or low crystallinity of the resulting materials. In this study, we propose a solvothermal synthesis method with high efficiency and productivity.

Fe-based MOF materials with Mn were synthesized by the solvothermal method using DMF solvent and linked together by terephthalic acid as the organic ligand. The properties of Mn/Fe-MOF, such as their size and porosity, change significantly when the synthesis rate is changed, leading to the change in the photocatalytic properties of the decomposition of the organic compounds. Furthermore, the difference in the material structure under the influence of different solvents leads to the change in the light absorption properties and affects the photocatalytic mechanism of the material. Thus, this study provides new insight into the enhanced photocatalytic activity of organic compounds' degradation of Mn/Fe-MOF.

■ EXPERIMENTAL SECTION

Materials

In this study, all chemicals used were supplied by the commercial company and are commercially available. Those include Iron(III) nitrate nonahydrate $Fe(NO_3)_3{\cdot}9H_2O$ (98.5%, China), Manganese Chloride $MnCl_2{\cdot}6H_2O$ (China 99%), Terephthalic acid H_2BDC (Sigma Aldrich 98%), *N,N*-dimethylformamide DMF (China 99.5%), Acetonitrile CH_3CN (Merck, Germany 99.5%), Methanol CH_3OH (China), Rhodamine B $C_{28}H_{31}ClN_2O_3$ (Sigma Aldrich), and Hydrogen peroxide (H_2O_2, 30%). The chemicals were used without further purification.

Instrumentation

The composites' formation and crystal phase change were determined by X-ray diffraction on D8 Advanced (Hitachi, Germany), with a wavelength λ of 1.5406 Å. Infrared spectroscopy (FT-IR) method was used to determine the presence of functional groups on the surface of materials by Nicolet 6700 (Thermo Fisher Scientific, USA) instrument with the wavelength in the range of 500–4000 cm^{-1}. Scanning electron microscopy (SEM) method to determine the morphology and size of the material particles by S4800 series (JEOL, Japan). Diffuse reflectance spectroscopy can determine the absorption peaks of the catalysts and evaluate the change in bandgap energy (Eg) values based on the Shimazu UV-2450 instrument with wavelengths from 200 nm to 1400 nm. UV-Vis instrument (Aligent Cary 60, Malaysia) was used to determine the concentration of organic pigment solution during the photocatalytic activity assay of the material.

Procedure

The synthesis of Fe-MOF was carried out based on a previously published paper [16]. Specifically, a mixture of $Fe(NO_3)_3{\cdot}9H_2O$ (0.16 mmol) and H_2BDC (0.18 mmol) was dissolved in 40 mL of *N,N*-dimethylformamide (DMF). Next, 40 mL of CH_3CN was added to the homogenizing stirring solution for 30 min at room temperature. The reaction was carried out in a 100 mL Teflon sample container with a stainless steel protective cover and heated at 150 °C for 12 h in the reactor. After the reaction was completed, the reaction mixture was allowed to cool naturally to room temperature. Then wash the reaction mixture with DMF (3 times) and methanol (3 times), respectively. Finally, the obtained material was dried at 150 °C under vacuum for 12 h. Similarly, samples of Fe-MOF bimetallic materials were further synthesized by doping Mn^{2+} ions at the selected Mn^{2+}/Fe^{3+} molar ratios of 0.05, 0.1, 0.3, and 0.5. The appropriate proportion of denatured samples was

selected based on the structure and morphology to carry out the photocatalytic degradation of Rhodamine B (RhB).

The photocatalytic reaction was carried out through the ability to decompose RhB under a 40 W LED irradiation, and the solution was stirred continuously at 500 rpm. RhB concentrations were analyzed using a UV-Vis spectrophotometer at a maximum absorption wavelength λ = 554 nm. All Mn/Fe-MOF doped samples at different molar ratios were photoactivated through a reaction system in a heat-resistant beaker (250 mL) containing 100 mL of RhB solution with concentrations of 3×10^{-5} M and 5 mg of the adsorbent [17]. The reaction mixture was stirred on a magnetic stirrer for 60 min until adsorption equilibrium was reached. Then, 4 mL of the mixture was taken out, centrifugated the solids, and measured the absorbance (t = 0). Next, 1 mL of H_2O_2 (1 mM) was added, and the solution began to be illuminated. After a certain period, 4 mL of sample solution will be taken out until the 120 min is up. Finally, UV-Vis absorption analysis was conducted to evaluate the concentration of the RhB solution through the decrease in color concentration, expressed by the change in the maximum absorption peak intensity under the effect of light.

■ RESULTS AND DISCUSSION

Characterization

XRD was used to examine the composition and crystal phase growth of samples of Fe-MOFs modified with Mn at different Mn: Fe molar ratios of 0.05, 0.1, 0.3, and 0.5. The XRD results showed that the Fe-MOF sample showed characteristic diffraction peaks at 2θ of 11.42°; 18.13°; 19.38° corresponded to the study of Sun et al. and compared with simulated spectrum (CCDC 1892483) [18]. In addition, the crystalline characteristics of the three samples of Mn/Fe-MOF bimetallic materials are shown more specifically in Fig. 1. X-ray diffraction (XRD) analysis of the three Mn-modified Fe-MOF samples all shows similar characteristic peaks, indicating that they have nearly identical crystal structures, although with some slight differences in the peak intensity. However, magnifying at about 10°–20°, the diffraction peak of about

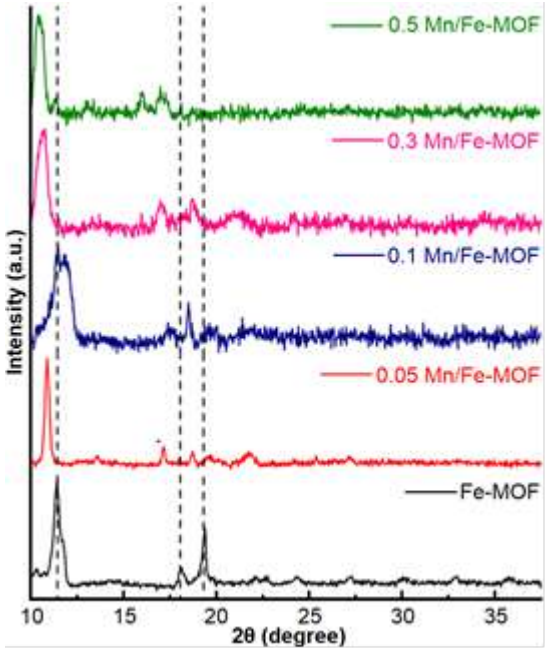

Fig 1. XRD spectrum of Mn/Fe-MOF at different ratios

11.42° is slightly shifted to a lower angle as the molar ratio of Mn/Fe increases, while the opposite trend with 0.1 Mn/Fe-MOF molar ratio has a clear shift towards a higher angle. The modified sample with Mn^{2+} broke the structure of Fe-MOF, the diffraction peaks characteristic of the Fe-MOF frame almost disappeared. The competition for electron affinity between the two ions and the significant difference in ionic radii between Mn^{2+} and Fe^{3+} (Fe^{3+} = 0.64 Å, Mn^{2+} = 0.75 Å) lead to the deformation of the original material structure. On the other hand, due to the flexibility or breathing effect of the Fe-MOF construct [19-20].

The infrared spectrum of Fe-MOF materials is presented in Fig. 2. It can be seen that the absorption bands with wavenumbers of 1594, 1390, 1396, and 750 cm^{-1} are typical for the vibrations of the carboxylate group of Fe-MOF. The absorption band at a wavenumber of 3093.3 cm^{-1} (strong) indicates the O–H group's existence in the structure's water molecules. The absorption band at wavenumbers of 1593.8 and 1389.5 cm^{-1} are typical for the symmetric and asymmetric valence vibrations of the carboxylic group of BDC coordinated with the central metal, demonstrating that, in the sample, there is a formation into a dicarboxylate group bond. The absorption band at a wavenumber of

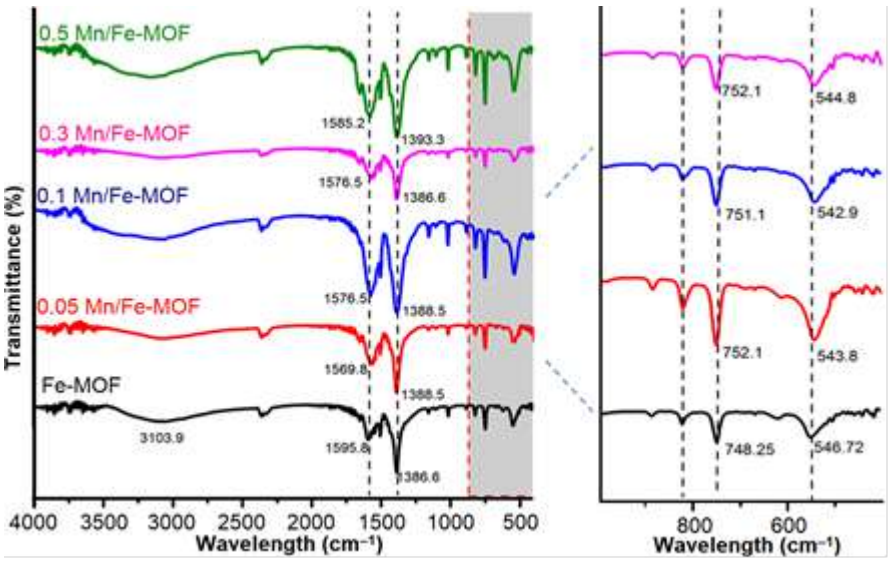

Fig 2. FTIR spectrum of Mn/Fe-MOF at different ratios

750 cm^{-1} confirms the benzene ring's C–H bond vibration. The absorption band at wave number 552 cm^{-1} is characteristic of the Fe–O bond covalent vibration. When modifying Fe-MOF with Mn, the FTIR spectrum of the material still shows the characteristic peaks of Fe-MOF, no apparent change in the structure of the material is observed on the FTIR spectrum.

Fig. 3 surface morphology of Fe-MOFs observed by SEM shows that the typical grain size of Fe-MOFs is mainly the formation of well-defined homogeneous hexagonal bars with pointed tips. However, the shape and size of the Fe-MOF modified materials are highly dependent on the Mn/Fe molar ratio. The increased Mn doping makes the morphology of bimetallic MOFs more

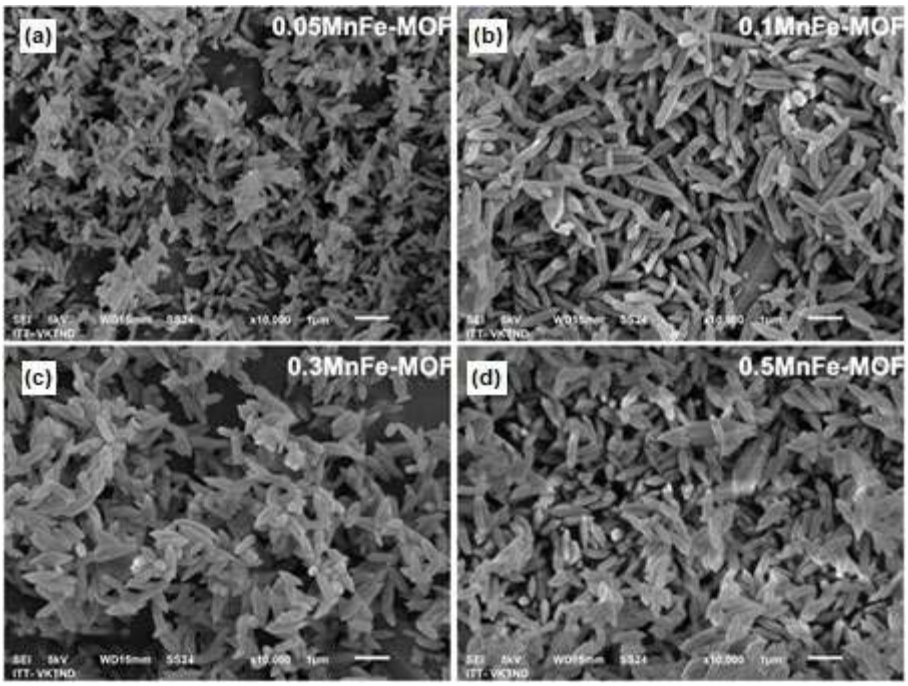

Fig 3. SEM images of Mn/Fe-MOF materials: (a) 0.05 Mn/Fe-MOF, (b) 0.1 Mn/Fe-MOF, (c) 0.3 Mn/Fe-MOF and (d) 0.5 Mn/Fe-MOF

regular but significantly different. The surface morphology and shape of the Mn/Fe-MOF materials were studied through SEM images. The results show a clear change in the shape and size of the material when changing the ratio of Mn^{2+}/Fe^{3+}. In the sample of 0.05 Mn/Fe-MOF, heterogeneous particles with different shapes and sizes appeared. When increasing the ratio of 0.1 Mn/Fe-MOF, the particles are uniform in size and shape. However, as the ratio increases, the size uniformity decreases, the grain shape begins to lengthen and stick together. Hence, the size of the crystals is larger at the ratio of 0.3 Mn/Fe-MOF and 0.5 Mn/Fe-MOF.

The UV-Vis diffuse reflectance spectroscopy (DRS) method was used to determine the light absorption characteristics of the bimetallic Mn/Fe-MOF, and the corresponding results are depicted in Fig. 4. The UV-Vis DRS results demonstrate the successful doping of Mn into the Fe-MOF lattice of the materials. Samples of composites at different scales give different bandgap energy values. The bandgap energy of Fe-MOF narrowed after Mn doping in the ratio of Fe-MOF, from 2.81 to 2.79 eV of 0.05 Mn/Fe-MOF, 2.77 eV of 0.1 Mn/Fe-MOF, 2.67 eV of 0.3 Mn/Fe-MOF eV, and 2.66 eV of 0.5 Mn/Fe-MOF samples, respectively. This difference is explained by the more efficient separation of the excited electron pairs supported by the second metal ion in the MOF lattice. Some previously published results indicate a helical d-d transition ([6A1g → 4A1g + 4Eg(G)]) of Fe^{3+} in MOFs [21-22]. However, the presence of a second metal ion, in addition to helping to disperse the Fe-MOF crystals evenly, creates small-sized particles. The second metal ion plays a crucial role in receiving electrons from the conduction band of MOFs photocatalysts, reducing and limiting the recombination between electrons and the h^+ hole, thus effectively increasing the catalytic activity.

Photocatalytic Activity

The photocatalytic activity of the material was evaluated on the decomposition reaction of RhB organic pigment using visible light through experiments [23]. Experimental conditions were fixed at RhB concentration of 3×10^{-5} M, catalyst weight of 5 mg, solution pH 5, and H_2O_2 concentration of 10^{-3} M. The results of photocatalytic degradation reaction of RhB on Fe-MOF samples and samples modified with Mn^{2+} at different ratios are presented in Fig. 5(a). The RhB dye was removed up to 85% in 120 min by the presence of Fe-MOF/H_2O_2. However, the decrease in RhB concentration was evident when using Fe-MOF modified with Mn at different nMn^{2+}/nFe^{3+} ratios. The results showed that the sample denatured at the ratio Mn^{2+}/Fe^{3+} of 0.1 results in the best catalytic activity with

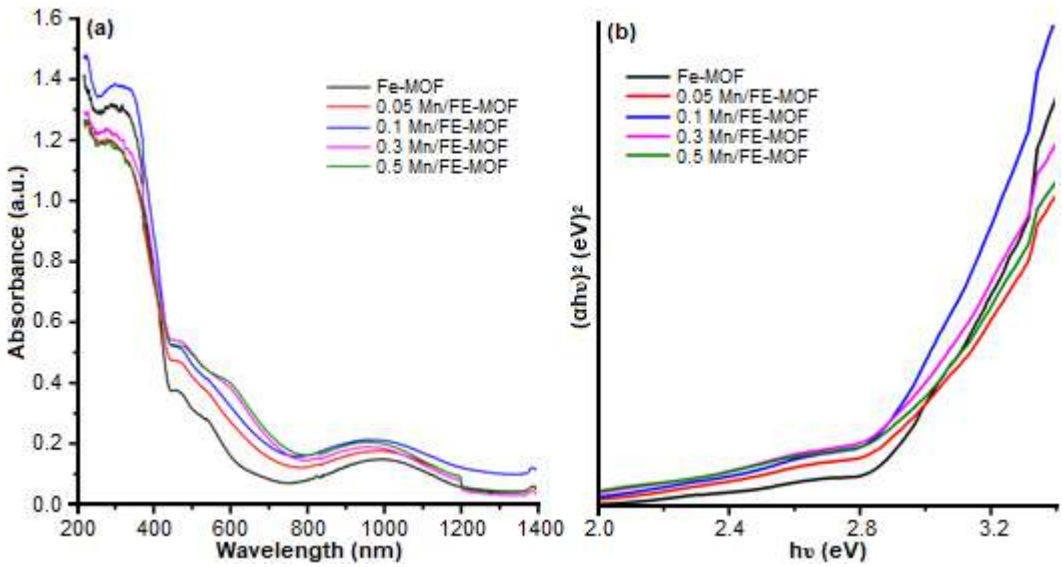

Fig 4. UV-Vis DRS plot (a) and bandgap energy (b) of Mn/Fe-MOF at different ratios

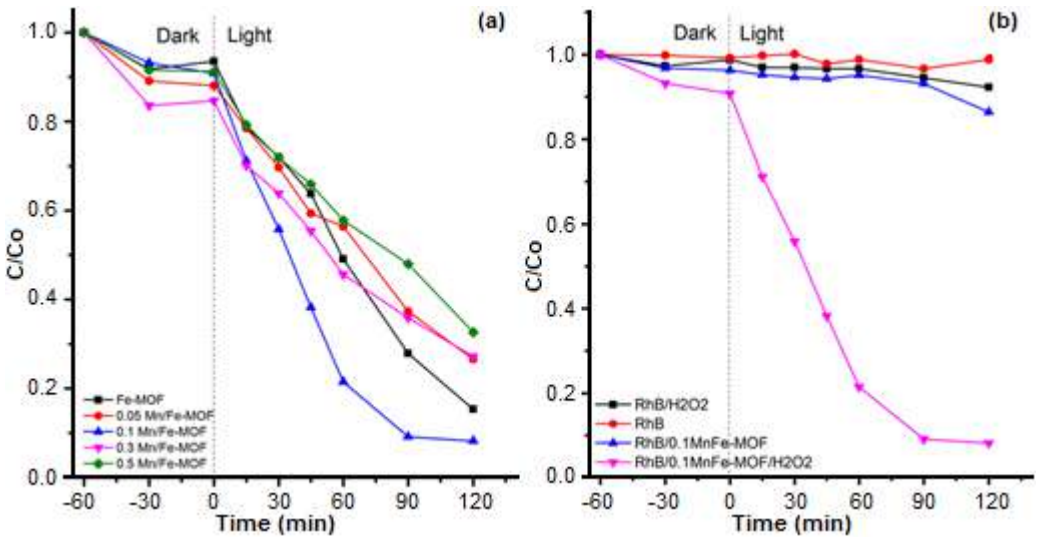

Fig 5. Photocatalysis of RhB decomposition of Mn/Fe-MOF at different rates

91.78% after 120 min of illumination. Then it followed by Mn^{2+}/Fe^{3+} of 0.05 (73.41%), and Mn^{2+}/Fe^{3+} of 0.3 (72.82%). Meanwhile, the lowest sample was Mn^{2+}/Fe^{3+} of 0.5 (67.38%).

Partial substitution of the metal center of MOFs can enhance the photocatalytic activity under visible light, introducing new energy levels leading to metal-to-metal charge transfer, which will improve MOF photocatalytic activity. Recently, the study by Wu et al. (2020) showed that in a heterogeneous Fenton-like system, the catalytic performance of $FeNi_x$-BDC is derived from the active sites of Fe in the lattice framework, determining oxidation capacity and reaction rate of the system. Therefore, the more Ni replaces Fe in the lattice framework, the worse the catalytic performance of bimetallic MOFs [11]. In addition, Sun et al. (2016) describe the partial isomer substitution of iron in the Fe metal-organic framework (BDC) with Mn, Co, and Ni. The catalytic performance of these materials was examined in the decomposition of phenol at 35 °C and a near-neutral pH of 6.2. The results show that the degradation efficiency can be clearly improved by incorporating Mn. Furthermore, the n(Fe)/n(Mn) ratio in bimetallic MOFs has a strong impact on the decomposition process [18].

Fig. 5(b) shows that H_2O_2 affects the degradation of RhB dye. When adding H_2O_2 to the reaction, combined with the catalyst under lamp irradiation, the RhB decomposition reached 92% within 120 min, and the RhB decomposition took place faster. The photocatalytic activities were carried out under conditions containing only (RhB and light) or (RhB, H_2O_2, and light). The RhB color degradation efficiency was only less than 5%, and the efficiency reached 10% in the presence of 0.1 Mn/Fe-MOF catalyst but without the support of hydrogen peroxide. It can be explained by the fact that $OH^{\bullet}$ radicals from H_2O_2 are generated much, promoting the reaction process, leading to an increase in the rate and efficiency of decomposition.

The efficiency of RhB removal in photochemical reaction by 0.1 Mn/Fe-MOF catalyst is shown by the light absorption intensity in the UV-Vis spectrum in Fig. 6. When the irradiation time was increased, the intensity of the characteristic peaks of RhB at 554 nm decreased suddenly. The pink color of the solution completely disappeared after 120 min of irradiation, indicating that the irradiation process photocatalytic effect destroyed the chromophoric structure of the RhB dye. The RhB color degradation of 0.1 Mn/Fe-MOF gives a high efficiency of Fe-MOF in 120 min of illumination. During RhB degradation, the absorption peak of RhB decreases in intensity or shifts to a lower wavelength (hypsochromic) or can remain at the same wavelength (554 nm) with increasing irradiation time. On the other hand, the *N*-deethylation degradation mechanism and the formation of a series of *N*-deethylated intermediates lead to a peak left-shift (blueshift) of the absorption peak

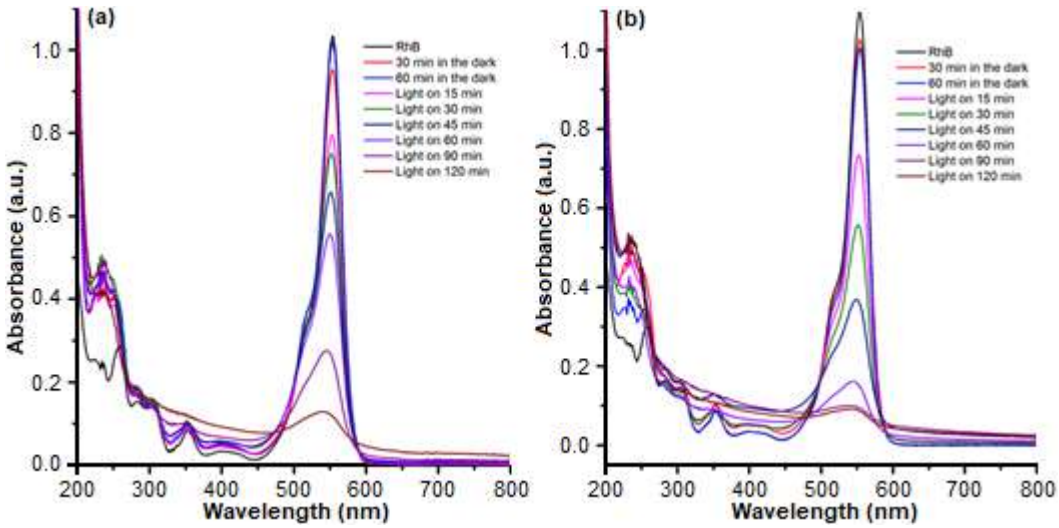

Fig 6. The absorption spectrum of RhB on Fe-MOF (a) and 0.1 Mn/Fe–MOF (b) catalyst

of RhB. The results show that the 0.1 Mn/Fe-MOF material has strong activity and can be used as a photocatalyst for potential practical applications [24].

CONCLUSION

In summary, we have successfully synthesized Fe-MOF bimetallic materials with doped molar ratios of Mn/Fe by the solvothermal method. The material characteristics of SEM, UV-Vis DRS, XRD, FT-IR, and UV-Vis materials have shown that the material has a very high order. The crystals have a uniform octahedral morphology and high crystallinity. The results indicated that the molar ratio of 0.1 Mn/Fe showed excellent photocatalytic activities and durability when removing organic pollutants under visible light irradiation. The 0.1 Mn/Fe-MOF material gave the highest catalytic activity with RhB conversion of 91.78% after 120 min of illumination in the following conditions: initial RhB concentration was 3×10^{-5} M; catalyst amount is 5 mg; 1 mL H_2O_2 (1 mM) and pH 5. The doping of the second metal in the lattice framework of MOF significantly improved the photocatalytic degradation activity, and the reaction was also more stable than that of the catalyst pristine Fe-MOF. This result opens the possibility of applying photocatalytic decomposition in the treatment of the toxic organic matter.

ACKNOWLEDGMENTS

This study was supported by grants from Nguyen Tat Thanh University, Ho Chi Minh City, Vietnam.

REFERENCES

[1] Furukawa, H., Cordova, K.E., O'Keeffe, M., and Yaghi, O.M., 2013, The chemistry and applications of metal-organic frameworks, *Science*, 341 (6149), 1230444.

[2] Shekhah, O., Wang, H., Zacher, D., Fischer, R.A., and Wöll, C., 2009, Growth mechanism of metal-organic frameworks: Insights into the nucleation by employing a step-by-step route, *Angew. Chem. Int. Ed.*, 48 (27), 5038–5041.

[3] Dey, C., Kundu, T., Biswal, B.P., Mallick, A., and Banerjee, R., 2014, Crystalline metal-organic frameworks (MOFs): Synthesis, structure and function, *Acta Crystallogr., Sect. B: Struct. Sci., Cryst. Eng. Mater.*, 70, 3–10.

[4] Akhbari, K., and Morsali, A., 2015, Needle-like hematite nano-structure prepared by directed thermolysis of MIL-53 nano-structure with enhanced methane storage capacity, *Mater. Lett.*, 141, 315–318.

[5] George, P., Dhabarde, N.R., and Chowdhury, P., 2017, Rapid synthesis of Titanium-based metal-organic framework (MIL-125) via microwave route

and its performance evaluation in photocatalysis, *Mater. Lett.*, 186, 151–154.

[6] Yu, B., Wang, F., Dong, W., Hou, J., Lu, P., and Gong, J., 2015, Self-template synthesis of core-shell ZnO@ZIF-8 nanospheres and the photocatalysis under UV irradiation, *Mater. Lett.*, 156, 50–53.

[7] Liu, J., Hou, J.X., Gao, J.P., Liu, J.M., Jing, X., Li, L.J., and Du, J.L., 2019, Stable Cd(II)-MOF as a fluorescent sensor for efficient detection of uranyl ions, *Mater. Lett.*, 241, 184–186.

[8] Jiang, K., Zhang, L., Hu, Q., Yang, Y., Lin, W., Cui, Y., Yang, Y., and Qian, G., 2018, A biocompatible Ti-based metal-organic framework for pH-responsive drug delivery, *Mater. Lett.*, 225, 142–144.

[9] Gao, X., Cui, R., Zhang, M., and Liu, Z., 2017, Metal-organic framework nanosheets that exhibit pH-controlled drug release, *Mater. Lett.*, 197, 217–220.

[10] Wang, J., Wang, J., Zhang, M., Li, S., Liu, R., and Li, Z., 2020, Metal-organic frameworks-derived hollow-structured iron-cobalt bimetallic phosphide electrocatalysts for efficient oxygen evolution reaction, *J. Alloys Compd.*, 821, 153463.

[11] Wu, Q., Siddique, M.S., and Yu, W., 2021, Iron-nickel bimetallic metal-organic frameworks as bifunctional Fenton-like catalysts for enhanced adsorption and degradation of organic contaminants under visible light: Kinetics and mechanistic studies, *J. Hazard. Mater.*, 401, 123261.

[12] Kirchon, A., Zhang, P., Li, J., Joseph, E.A., Chen, W., and Zhou, H. C., 2020, Effect of isomorphic metal substitution on the Fenton and photo-Fenton degradation of methylene blue using Fe-based metal-organic frameworks, *ACS Appl. Mater. Interfaces,* 12 (8), 9292–9299.

[13] Cai, X., Lin, J., and Pang, M., 2016, Facile synthesis of highly uniform Fe-MIL-88B particles, *Cryst. Growth Des.*, 16 (7), 3565–3568.

[14] Ma, M., Bétard, A., Weber, I., Al-Hokbany, N.S., Fischer, R.A., and Metzler-Nolte, N., 2013, Iron-based metal-organic frameworks MIL-88B and NH_2-MIL-88B: High-quality microwave synthesis and solvent-induced lattice 'breathing', *Cryst. Growth Des.*, 13 (6), 2286–2291.

[15] Hou, S., Wu, Y.N., Feng, L., Chen, W., Wang, Y., Morlay, C., and Li, F., 2018, Green synthesis and evaluation of an iron-based metal-organic framework MIL-88B for efficient decontamination of arsenate from water, *Dalton Trans.*, 47 (7), 2222–2231.

[16] Choi, S., Cha, W., Ji, H., Kim, D., Lee, H.J., and Oh, M., 2016, Synthesis of hybrid metal-organic frameworks of $\{Fe_xM_yM'_{1-x-y}\}$-MIL-88B and the use of anions to control their structural features, *Nanoscale*, 8 (37), 16743–16751.

[17] Nguyen, H.T.T., Dinh, V.P., Phan, Q.A.N., Tran, V.A., Doan, V.D., Lee, T., and Nguyen, T.D., 2020, Bimetallic Al/Fe metal-organic framework for highly efficient photo-Fenton degradation of rhodamine B under visible light irradiation, *Mater. Lett.*, 279, 128482.

[18] Sun, Q., Liu, M., Li, K., Han, Y., Zuo, Y., Chai, F., Song, C., Zhang, G., and Guo, X., 2017, Synthesis of Fe/M (M = Mn, Co, Ni) bimetallic metal-organic frameworks and their catalytic activity for phenol degradation under mild conditions, *Inorg. Chem. Front.*, 4 (1), 144–153.

[19] Ahmed, M.A., Rady, K.S., El-Shokrofy, K.M., Arais, A.A., and Shams, M.S., 2014, The influence of Zn^{2+} ions substitution on the microstructure and transport properties of Mn-Zn nanoferrites, *Mater. Sci. Appl.*, 5 (13), 932–942.

[20] Zhang, S., Gao, H., Li, J., Huang, Y., Alsaedi, A., Hayat, T., Xu, X., and Wang, X., 2017, Rice husks as a sustainable silica source for hierarchical flower-like metal silicate architectures assembled into ultrathin nanosheets for adsorption and catalysis, *J. Hazard. Mater.*, 321, 92–102.

[21] Vuong, G.T., Pham, M.H., and Do, T.O., 2013, Direct synthesis and mechanism of the formation of mixed metal Fe_2Ni-MIL-88B, *CrystEngComm*, 15 (45), 9694–9703.

[22] Zhang, C., Ai, L., and Jiang, J., 2015, Solvothermal synthesis of MIL-53(Fe) hybrid magnetic composites for photoelectrochemical water oxidation and organic pollutant photodegradation under visible light, *J. Mater. Chem. A*, 3 (6), 3074–3081.

[23] Saigl, Z.M., 2021, Various adsorbents for removal of

rhodamine B dye: A review, *Indones. J. Chem.*, 21 (4), 1039–1056.
[24] Chiu, Y.H., Chang, T.F.M., Chen, C.Y., Sone, M., and Hsu, Y.J., 2019, Mechanistic insights into photodegradation of organic dyes using heterostructure photocatalysts, *Catalysts*, 9 (5), 430.

Synthesis and Docking Study of 2–Aryl-4,5-diphenyl-1*H*-imidazole Derivatives as Lead Compounds for Antimalarial Agent

Ika Septiana[1], Bambang Purwono[1*], Chairil Anwar[1], Beta Achromi Nurohmah[1], and Jufrizal Syahri[2]

[1]*Department of Chemistry, Faculty Mathematics and Natural Sciences, Universitas Gadjah Mada, Sekip Utara, PO BOX BLS 21, Yogyakarta 55281, Indonesia*

[2]*Department of Chemistry, Faculty of Mathematics and Natural Sciences, Universitas Muhammadiyah Riau, Pekanbaru 28156, Indonesia*

* ***Corresponding author:***

email: purwono.bambang@ugm.ac.id

Received: July 20, 2021
Accepted: September 7, 2021

DOI: 10.22146/ijc.67777

Abstract: *Series of 2-aryl-4,5-diphenyl-1*H*-imidazole derivatives of 2-(4-hydroxy-3-methoxyphenyl)-4,5-diphenyl-1*H*-imidazole (**1**), 2-(4,5-dimethoxyphenyl)-4,5-diphenyl-1*H*-imidazole (**2**) and 2-(4-methoxyphenyl)-4,5-diphenyl-1*H*-imidazole (**3**) were produced and evaluated for their* in vitro *antimalarial activities against the chloroquine-sensitive* Plasmodium falciparum *3D7 strain. A molecular docking study was also carried out against the crystal protein of* Plasmodium falciparum *dihydrofolate reductase-thymidylate synthase (PfDHFR-TS) (PDB ID: 1J3I.pdb) to predict the interaction between the compounds and protein. The physicochemical and pharmacokinetic parameters were computationally performed to predict the parameters of the absorption, distribution, metabolism, excretion, and toxicity (ADMET). Imidazoles were synthesized from aryl aldehyde derivatives with benzyl and ammonium acetate in glacial acetic acid using microwave-assisted-organic synthesis. Compounds **1**, **2**, and **3** were produced in 64.33, 50.56, and 70.55% yields, respectively. The IC_{50} of compounds **1**, **2**, and **3** against chloroquine-sensitive* Plasmodium falciparum *3D7 strain was found to be 1.14, 5.28, and 2.42 μM, respectively. The molecular docking study agreed with the* in vitro *data by showing the lowest CDOCKER energy for compound **1** (-47.48 kcal/mol), followed by **3** (-43.79 kcal/mol) and **2** (-41.47 kcal/mol). The physicochemical and pharmacokinetic parameters showed that imidazoles **1**, **2**, and **3** obeyed Lipinski rules of five to propose as lead compounds for the antimalarial agents.*

Keywords: *antimalarial; imidazole; 3D7 strain; molecular docking*

INTRODUCTION

Malaria is a parasitic infectious disease transmitted by the Anopheles mosquito. In 2019, World Health Organization reported that malaria was a threat to approximately half of the world's population [1]. Malaria is produced by the infection of five parasites of the genus of *Plasmodium*, where most of the mortality are caused by *Plasmodium falciparum* and *Plasmodium vivax* [2]. Some effective drugs to treat malaria have been developed, including quinoline, quinine, mefloquine, and artemisinin. Quinoline was used for malaria treatment triggered by *P. falciparum*. However, the resistance of the parasite to this drug has been reported [2]. The resistance parasite has also been developed to other drugs [3]. Different approaches which involve combination therapy of two or more antimalarials have been evaluated and reported to overcome drug resistance of antimalarials.

Imidazoles are members of heterocyclic compounds with various biological activities such as anti-allergic [4], anti-inflammatory [5], antibacterial and antiviral [6], as well as cancer [7]. Imidazoles combined with some heterocycle compounds have also been reported with wide range of antimalarial activity [8-9]. As a part of our search for novel antimalarial agents from theoretical and chemical synthesis, we prepared several imidazoles substituted with methoxy

and hydroxy groups using a one-step reaction from aryl aldehydes with benzyl and ammonium acetate in glacial acetic acid using microwave-assisted-synthesis. The methoxy and hydroxyl groups have been reported to increase antimalarial activities in compounds of chalcone [10-11], benzimidazoles [12], and coumarins [13].

This study presented the synthesis of simple methoxy imidazoles using the green chemistry technique and their potential as an antimalarial drug (Scheme 1). The activity of antimalaria was determined using *P. falciparum* parasite. The computational methods were performed to predict the interaction formed between the compounds with the co-crystal ligand of Plasmodium falciparum dihydrofolate reductase-thymidylate synthase (PfDHFR-TS) protein (PDB ID: 1J3I.pdb). Furthermore, it was also to predict the physicochemical and pharmacokinetic parameters such as absorption, distribution, metabolism, excretion, and toxicity (ADMET) to support the discovery of lead compounds of antimalaria. The results based on the *in vitro* assay, molecular docking study, prediction of the physicochemical and pharmacokinetic parameters indicated the good potential of the prepared imidazole derivatives for antimalarial agents and can be used for further modification.

■ EXPERIMENTAL SECTION

Materials

The materials used in this study were vanillin (3-methoxy-4-hydroxybenzaldehyde) (99% purity Merck, Germany), ammonium acetate (98% purity Merck, Germany), veratraldehyde (3,4-dimethoxybenzaldehyde) (99% purity Merck, Germany), anisaldehyde (4-methoxybenzaldehyde) (98% purity Merck, Germany), benzyl (99% purity Merck, Germany), glacial acetic acid (99% purity Merck, Germany), methanol (99% purity Merck, Germany), and ethanol (99% purity Merck, Germany). All reagents and solvents were analytical grade and used without further purification.

Instrumentation

The IR spectra were investigated from potassium bromide (KBr) pellet with FT-IR Spectrophotometer Shimadzu Prestige-21. ^{1}H Nuclear Magnetic Resonance (NMR) was recorded in JEOL JNM ECA 500 MHz with DMSO-d_6 as a solvent and tetramethylsilane (TMS) as the internal standard. ^{13}C Nuclear Magnetic Resonance (NMR) was recorded in JEOL JNM ECA 125 MHz with DMSO-d_6 solvent. In addition, mass spectra were performed on GC-MS Shimadzu QP-2010S, and the melting points were measured in open capillary tubes using Electrothermal-9100 (uncorrected).

Procedure

Synthesis of imidazoles 1-3

Imidazole derivatives **1**-**3** were synthesized according to the previous method in Singh et al. [14] with modification. A mixture of the appropriate aldehyde (1 mmol), benzyl (1 mmol), ammonium acetate (10 mmol) was dissolved in glacial acetic acid (5 mL) and irradiated in a microwave oven for 2 × 30 s. After the reaction mixture reached room temperature, it was dissolved in ethanol and then poured into distilled water afterward. The solid obtained was then filtered and washed with distilled water. Finally, the crude product was recrystallized from appropriate solvents (methanol or ethanol).

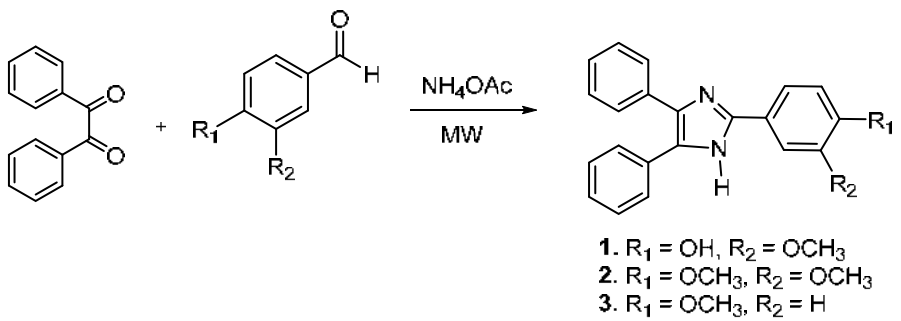

Scheme 1. Synthetic route to targeted imidazole derivatives (**1**, **2**, and **3**)

2-(4-hydroxy-3-methoxyphenyl)-4,5-diphenyl-*1*H-imidazole (1). Yield: 64.33%, m.p. 258–262 °C (Lit[20]. 255–256 °C) ^{1}H–NMR (DMSO-d_6, 500 MHz) δ (ppm): 3.86 (*s*, 3H, –OCH_3), 6.87 (d, 1H, H–Ar), 7.53 (*s*, 1H, Ar), 7.30 (t, 4H, H–Ar), 7.55 (d, *J* = 2 Hz, 4H, H–Ar), 7.43 (t, 2H, H–Ar), 7.65 (d, *J* = 2 Hz, 1H, H–Ar), 9.28 (*s*, 1H, –OH), 12.43 (*s*, 1H, –NH). ^{13}C–NMR (DMSO-d_6, 125 MHz) δ (ppm): 55.07 (–OCH_3), 109.12 (C–Ar), 115.60 (C–Ar), 118.35 (C–Ar), 121.94 (C–Ar), 126.35 (C–Ar), 127.02 (C–Ar), 127.57 (C–Ar), 128.38 (C–Ar), 131.34 (C–Ar), 146.06 (C–Ar), 147.04 (C–Ar), 147.07 (C–Ar). IR (cm^{-1}): 3435 (N–H), 1604 (C=N), 1496 (C=C) and 1459 (Ar). MS (*m/z*): 342 (M^+).

2-(3,4-Dimethoxyphenyl)-4,5-diphenyl-*1*H-imidazole (2). Yield: 50.56%, m.p. 224–225 °C (Lit[21], 220–221 °C), ^{1}H-NMR (DMSO-d_6, 500 MHz) δ (ppm): 3.81 (3, 3H, –OCH_3), 3.85 (*s*, 3H, OCH_3), 7.07 (d, 1H, Ar), 7.68 (*s*, 1H, Ar), 7.55 (t, 4H, H–Ar), 7.44 (t, 4H, H–Ar), 7.30 (t, 1H, H–Ar), 7.23 (d, 2H, H–Ar), 7.39 (d, 2H, H–Ar), 12.53 (*s*, 1H, –NH). ^{13}C-NMR (DMSO-d_6, 125 MHz) δ (ppm): 55.58 (–OCH_3), 55.53 (–OCH_3), 149.05 (C–Ar), 148.79 (C–Ar), 111.83 (C–Ar), 108.80 (C–Ar), 126.41 (C–Ar), 128.43 (C–Ar), 145.68 (C–Ar), 135.38 (C–Ar), 136.75 (C–Ar), 131.28 (C–Ar), 128.66 (C–Ar), 127.04 (C–Ar), 117.90 (C–Ar), 123.23 (C–Ar), 128.15 (C–Ar). IR (cm^{-1}): 3448 (N–H), 1604 (C=N), 1458 (C=C) and 1504 (Ar). MS (*m/z*): 356 (M^+).

2-(4-methoxyphenyl)-4,5-diphenyl-*1*H-imidazole (3). Yield: 70.55%, m.p. 230–232 °C (Lit[21], 228–230 °C) ^{1}H-NMR (DMSO-d_6, 500 MHz) δ (ppm): 3.86 (*s*, 3H, –OCH_3), 7.05 (d, 2H, H–Ar), 8.04 (d, 2H, H–Ar), 7.29 (t, 2H, H–Ar), 7.36 (t, 4H, H–Ar), 7.54 (d, 4H, H–Ar), 12.53 (*s*, 1H, –NH). ^{13}C-NMR (DMSO-d_6, 125 MHz) δ (ppm): 55.19 (–OCH_3), 114.09 (C–Ar), 159.41(C–Ar), 127.14 (C–Ar), 145.64 (C–Ar), 136.85 (C–Ar), 128.38 (C–Ar), 126.71 (C–Ar), 123.15 (C–Ar), 127.38 (C–Ar), 131.20 (C–Ar). IR (cm^{-1}): 3410 (N–H), 1604 (C=N), 1496 (C=C) and 1450 (Ar). MS (*m/z*): 326 (M^+).

Antimalarial activity assay

Antimalaria activity of imidazole derivatives was determined against chloroquine-sensitive *Plasmodium falciparum* 3D7 strain and conducted according to the previous procedure of Syahri et al. [11]. The IC_{50} of antimalarial activity was classified according to the following criteria: excellent (< 1 μM); good (1–20 μM); moderate (20–100 μM); low (100–200 μM); and inactive (> 200 μM) [15].

Molecular docking study

A molecular docking study was performed according to previous work by Syahri et al. [16]. The crystal structure of wild-type *Plasmodium falciparum* dihydrofolate reductase-thymidylate synthase (*Pf*DHFR-TS) protein (PDB ID: 1J3I.pdb) was chosen as the protein target. Discovery Studio Visualizer software was used to visualize the interaction.

Prediction of the ADMET parameters

The physicochemical and pharmacokinetic (ADMET) parameters were predicted using an online webserver admetSAR 2.0 (http://lmmd.ecust.edu.cn/admetsar2/admetopt/) [17] and ADMETlab webserver http://admet.scbdd.com/ [18]. Drug-like properties were assessed base on the prediction of Lipinski's 'rule of 5', including molecular weight, logP value, number of hydrogen bonds donor, and acceptor.

The absorption of drugs was generated from some factors, including human intestinal absorption (HIA), membrane permeability [showed by colon cancer cell line (Caco-2)], and human oral bioavailability (HOB). The distribution of drugs varies on parameters such as the plasma protein binding (PBB), P-glycoprotein inhibitor, and blood-brain barrier (BBB). Metabolism was predicted based on the CYP models for substrate or inhibitor (CYP2D6, CYP3A4, CYP1A2, CYP2C19, CYP2C9, CYP2D6, and CYP3A4). Excretion was expected based on the half-life (t ½) and the total clearance. The toxicity of drugs is calculated based on acute oral toxicity, hepatotoxicity, human *Ether-à go-go*-related gene (hERG) inhibition, AMES mutagenesis, and carcinogenesis. These factors were predicted and checked by the standard ranges.

Generally, the predicted ADMET parameters were labeled in positive and negative except for plasma protein binding (PPB), excretion (half-life (t ½) and the total clearance), and acute oral toxicity. The plasma protein binding was presented in percentage. The LD_{50} of acute oral toxicity was categorized into four

categories, i.e., I (≤ 50 mg/kg), II (> 50 mg/kg), III (> 500 mg/kg), and IV (> 5000 mg/kg) with label I and II as positive and III and IV as negative [19]. The half-life factor was classified as low ($t_{1/2}$ < 3h), moderate (3h < $t_{1/2}$ < 8h), and high ($t_{1/2}$ > 8h). Meanwhile, the predicted clearance factor was determined by following the classification of low clearance (< 5 mL/min/kg), moderate clearance (5–15 mL/min/kg), and high clearance (> 15 mL/min/kg) [18].

■ RESULTS AND DISCUSSION

Synthesis of Imidazole 1-3

Synthesis of compounds **1**, **2**, and **3** were conducted by reacting benzyl with aryl aldehydes in glacial acetic acid as a solvent in the presence of ammonium acetate (NH_4OAc) (Fig. 1). The IR spectra of compound **1**, **2** and **3** showed the sharp band at 1604 cm^{-1} that indicate the C=N functional group and the disappearance of C=O aldehydes band. The ^{1}H-NMR spectra showed one signal of protons –NH (12.43–12.59 ppm) from the five-membered heterocyclic ring with the integration of one proton, which is described as imidazole. The mass spectroscopy showed the molecular ion was confirmed in a good arrangement with the proposed structures of imidazole **1**, **2**, and **3**. The comparison with some literatures indicated that imidazole **1**, **2**, and **3** agreed with previous data in the literatures [20-21].

Antimalarial Activity Assay

From the IC_{50} value, *in vitro* antimalarial activity of imidazoles **1**–**3** against chloroquine-sensitive *Plasmodium falciparum* 3D7 strain are presented in Table 1. The IC_{50} value of compounds **1**–**3** showed good antimalarial activity in the range of 1–20 μM. The best activity was dominated by compound **1**, possessing a hydroxy and a methoxy group, with IC_{50} of 1.139 μM. Modification of one hydroxyl (at a *para* position from the imidazole ring) to methoxy groups (compound **2**) showed a significant decrease of the IC_{50} to 5.275 μM. These results showed that hydroxy and methoxy are positively affect the antimalarial activity of the imidazole products in the *para* and *meta* position from the imidazole ring, respectively. Moreover, one methoxy substituent at a *para* position from the imidazole ring still maintains better activity to 2.420 μM (compound **3**). However, the activities of imidazole **1** and **3** are still lower than the activity of chloroquine as a positive control (0.063 μM).

Molecular Docking Study

Molecular docking study toward wild-type of *Plasmodium falciparum* dihydrofolate reductase-thymidylate synthase (*Pf*DHFR-TS) protein (PDB ID: 1J3I.pdb) was performed to predict the interaction of the prepared compounds as antimalarial agents. Interactions formed by imidazoles **1**–**3** were presented in Table 2. The validation of the molecular docking was performed according to the previous work by redocking the co-crystal ligand to the protein [16]. The result showed an RMSD value of 0.6578 Å.

Table 1. IC_{50} of imidazoles **1**–**3** against *P. falciparum* 3D7 strain

Compound	IC_{50} (μg/mL)	IC_{50} (μM)
1	0.39	1.14
2	1.88	5.28
3	0.79	2.42
CQ	0.02	0.06

Table 2. Interactions of imidazole **1**–**3** based on the molecular docking

Ligands	CDOCKER (kcal/mol)	Interactions
1	-47.4844	Hydrogen bonds: GLY44 (2), SER108, SER111, SER167 π bonds: ALA16, LEU40, LEU46, PHE 58, ILE112
2	-41.4696	Hydrogen bonds: SER108, GLY166 π bonds: ALA16, LEU46, MET55, ILE112
3	-43.7887	Hydrogen bonds: GLY166, SER108 π bonds: PRO113, LEU46 (3), MET55, ILE112 (2)
WR99210	-54.3200	Hydrogen bonds: ALA16, ASP54, CYS15, ILE164, ILE 14, PHE58, SER108, TYR170 π bonds: LEU164, MET55

Imidazole **1** was found to form five hydrogen bonding to amino acids of GLY44, SER108, SER111, and SER167, also five π interactions to ALA16, LEU40, LEU46, PHE 58, and ILE112. Meanwhile, imidazole **3** displayed two hydrogen bonding to GLY166 and SER108, besides seven π interactions to PRO113, LEU46, MET55, and ILE112. On the other hand, imidazole **2** only have two hydrogen bonds to SER108 and GLY166 as well as four π interaction to ALA16, LEU46, MET55, and ILE112.

The ligand-protein docking showed a correlation between the CDOCKER energy (kcal/mol) with the number of hydrogen bonds and hydrophobic bonds. It can be seen that the increasing number of H-bonds at the active site of the receptor was suggested could improve the stability. This result emphasizes that hydrogen bonding interactions are mainly key interactions that affect the stability of the docking poses. As the result, compound **1** has the most stable interaction with the crystal protein 1J3I.pdb with the lowest CDOCKER energy of -47.4844 kcal/mol. Increasing CDOCKER energy was found for **3** (-43.7887 kcal/mol) and compound **2** (-41.4696 kcal/mol) with a smaller number of hydrogen bonds. On the other hand, the number of hydrophobic interactions also influences the stability of compound **3** compared to compound **2**. The low docking energy suggested the more stable the interaction of the ligand-protein and might lead to increase activity. Therefore, the interactions formed by imidazoles **1–3** were in agreement with the finding of the *in vitro* antimalarial assay.

The docking result (Table 3) proposed the significance of the hydroxyl group to determine the antimalarial activity of imidazole derivative **1** by forming hydrogen bonding to the SER167 that leads to an increase in the stability (lower docking energy). In addition, the presence of hydroxyl group in the *ortho* position to methoxy group in compound **1** would lead to the formation of hydrogen bonds from the methoxy group to GLY44 and SER111. It has been reported that the presence of the H-bonds to GLY44 could positively

Table 3. 2D and 3D interactions of imidazole **1–3**

Comp.	2D	3D
1	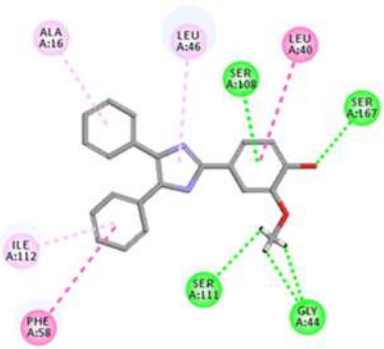	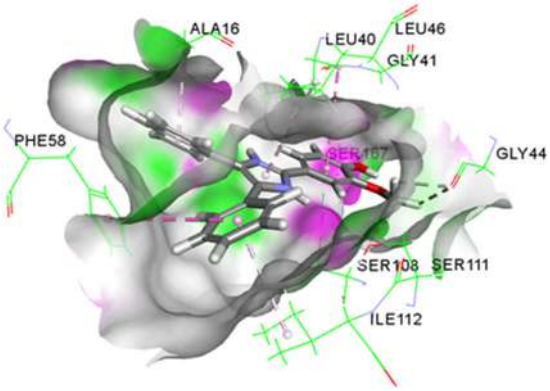
2	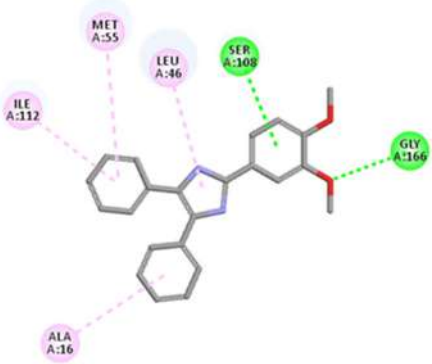	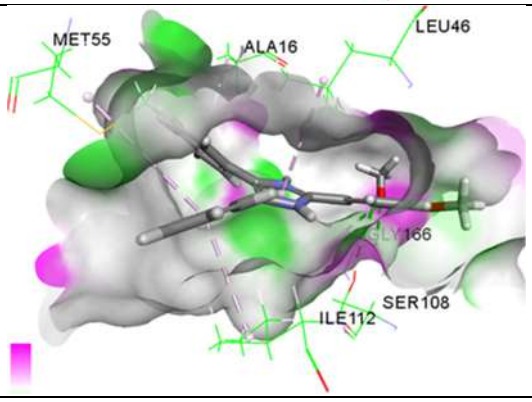

Table 3. 2D and 3D interactions of imidazole **1**–**3** (*Continued*)

Comp.	2D	3D
3	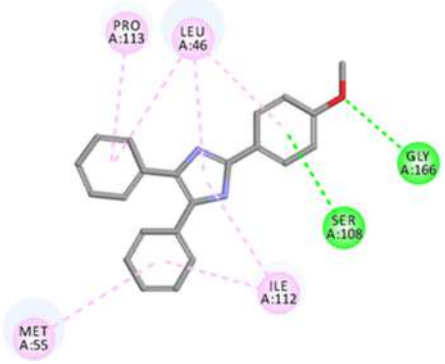	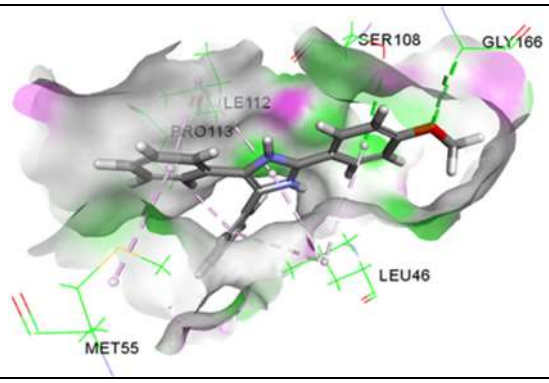

affect the stability of the interaction to PfDHFR-TS [12,22]. Furthermore, only one methoxy group in *meta* position from the imidazole ring of compound **2** contributes to the formation of a hydrogen bonding to GLY166, leading to the decreasing of antimalarial activity of imidazole **2**. However, when only one methoxy is present in *para* position from the imidazole ring (compound **3**), it leads to the formation of a greater number of hydrophobic interactions by the benzene rings than the compound **2**. Thus, the docking pose of imidazole **3** was more stable than imidazole **2**.

Prediction of ADMET Parameters

Lipinski's 'rule of 5' can be used to illustrate the drug-like properties for small molecules that are related to the oral bioavailability characteristic, including logP value (< 5), molecular weight (less than 500), number of hydrogen bonds for the donor (≤ 5) and acceptor (≤ 10). The defiance of two or more of the guidelines is proposed could produce the poor solubility and permeability of the molecules. Table 4 revealed the drug-likeness parameters of the prepared imidazole **1**–**3** according to Lipinski's 'rule of 5'. Imidazoles **1**–**3** followed the rules, implying for being probably orally bioavailable but have relatively poor water solubility with the logP higher than 5.

The ADMET properties of imidazoles **1**–**3** are presented in Table 4. Imidazoles **1**–**3** were predicted to have good (positive) human intestinal absorption and membrane permeability (Caco-2 permeability) but have poor oral bioavailability (negative). The poor oral bioavailability might be related to the lipophilicity (logP) of the molecules. Regarding the distribution parameters, imidazoles **1**–**3** were predicted to have good distribution (positive) where they can cross the blood-brain barrier easily and have a good plasma protein binding. It also can be noticed that all of the prepared compounds were a non-substate for P-glycoprotein, while imidazoles **1** and **2** were found to act as P-glycoprotein inhibitors. The induction of P-glycoprotein might reduce the bioavailability [23]. On the contrary, inhibition of these drug transporters could increase the bioavailability of the susceptible drug and might lead to an increased risk of adverse side effects [23-24].

Cytochrome P450s is an important enzyme system that metabolizes more than 90% of drugs in the liver with the main subtypes of CYP1A2, CYP2C9, CYP2C19, CYP2D6, and CYP3A4 [25]. Therefore, inhibition of CYP450 enzymes might decrease the elimination or change metabolic pathways of the substrates. This condition is the main cause of adverse drug-drug interactions [25]. The result showed that imidazoles **1**–**3** were predicted to be non-substrates for the subtypes of cytochrome CYP2C9, CYP2D6, and CYP3A4 with a probability value above 0.5. On the other hand, imidazoles **1** and **2** were predicted to be CYP1A2, CYP2C19, and CYP3A4 inhibitors, while imidazole **3** was an inhibitor for CYP1A2, CYP2C19, CYP3A4, and CYP2D6. This result suggested that imidazoles **1**–**3** might not be metabolized in the liver.

The excretion parameters were assessed by predicting the half-life ($t_{1/2}$) and the clearance rate. The

Table 4. Prediction of physicochemical and ADMET parameters

Parameters	Compounds		
	1	2	3
Drug-likeness			
Molecular weight	342.40	356.43	326.40
AlogP	5.12	5.43	5.42
H-bond acceptor	3	3	2
H-bond donor	2	1	1
A (Absorption)			
Human intestinal absorption (HIA)	+ (0.9897)	+ (0.9914)	+ (0.9914)
Human oral bioavailability (HOB)	- (0.5143)	- (0.5143)	- (0.5429)
Caco-2 permeability	+ (0.6144)	+ (0.7747)	+ (0.7613)
D (Distribution)			
Plasma protein binding (PPB)	1.067(100%)	0.933 (100%)	0.947 (100%)
P-glycoprotein inhibitor	+ (0.6154)	+ (0.8269)	+ (0.7470)
Blood-brain barrier penetration (BBB)	+ (0.9695)	+ (0.9801)	+ (0.9830)
M (Metabolism)			
CYP450 2C9 substrate	- (0.8058)	- (0.8078)	- (0.8078)
CYP450 2D6 substrate	- (0.7542)	- (0.7623)	- (0.7623)
CYP450 3A4 substrate	- (0.5493)	- (0.5479)	- (0.5574)
CYP450 1A2 inhibition	+ (0.8896)	+ (0.9538)	+ (0.9710)
CYP450 2D6 inhibition	- (0.6718)	- (0.6320)	- (0.5186)
CYP450 2C9 inhibition	- (0.7695)	- (0.7720)	- (0.6667)
CYP450 2C19 inhibition	+ (0.8710)	+ (0.8907)	+ (0.9226)
CYP450 3A4 inhibition	+ (0.5480)	+ (0.7257)	+ (0.7074)
E (Excretion)*			
Half time ($t_{1/2}$) (h)	1.739	1.736	2.007
Renal clearance (mL/min/kg)	1.939	1.915	1.899
T (Toxicity)			
Organ toxicity			
Hepatotoxicity	+ (0.8500)	+ (0.8000)	+ (0.8000)
hERG inhibition	- (0.5057)	+ (0.7353)	- (0.6940)
Acute oral toxicity	III (0.5713)	III (0.6426)	III (0.6793)
Genomic toxicity			
Ames mutagenesis	+ (0.9100)	+ (0.9900)	+ (0.8500)
Carcinogenesis	- (0.9143)	- (0.8714)	- (0.8714)

*Generated using ADMETlab web server (http://admet.scbdd.com/)

half-life of molecules is classified as long ($t_{1/2}$ > 3h) and short half-life ($t_{1/2}$ < 3h). The probability value of compounds **1**, **2**, and **3** for a long half-life was 0.701, 0.588, and 0.297, respectively. This result indicated that imidazole **3** was likely to have a shorter half-life than imidazoles **1** and **2**. Table 4 shows that imidazoles **1–3** were classified to have a moderate clearance rate (5–15 mL/min/kg), which was an excellent result. The excretion or drug elimination parameters are reported to be correlated with molecular weight and hydrophilicity [26].

The carcinogenicity of all of the tested imidazoles **1–3** was labeled as inactive compounds (negative). Furthermore, the acute oral toxicity was classified into negative (scale of III) [19]. On the other hand, the Ames mutagenesis was positive for all tested compounds, and

hERG inhibition was only negative for imidazole **1**. This result means that imidazoles **1**–**3** were predicted to be relatively toxic [19]. In conclusion, all of the prepared imidazoles **1**–**3** have the potential to be developed as antimalarial agents with further modification by lowering the lipophilicity properties (logP) and toxicity parameters.

CONCLUSION

This study presented the antimalarial assay of imidazole derivates **1**–**3** by assessing the *in vitro* assay against chloroquine-sensitive *Plasmodium falciparum* 3D7 strain, molecular docking, and prediction of pharmacokinetic parameters (ADMET). The *in vitro* assay indicated that compounds **1**–**3** could be considered to have good antimalarial activity with IC_{50} of 1.14, 5.28, and 2.42 μM, respectively. The molecular docking study supported the *in vitro* result by showing the lowest CDOCKER energy by compound **1** (-47.4844 kcal/mol), followed by **3** (-43.7887 kcal/mol) and **2** (-41.4696 kcal/mol). According to the prediction of ADMET parameters, imidazole **1**, **2**, and **3** have the potential as antimalarial drug candidates through further modification.

ACKNOWLEDGMENTS

This work was funded by The RTA Grant from Universitas Gadjah Mada for the fiscal year 2019 contract number: 2129/UN1/DITLIT/DIT-LIT/LT/2019.

AUTHOR CONTRIBUTIONS

Ika Septiana performed chemical synthesis and formal analysis. Jufrizal Syahri designed the molecular docking and data analysis. Beta Achromi Nurohmah prepared original draft and ADMET analysis. Bambang Purwono designed conceptualization, writing-review, editing and supervision. Chairil Anwar contributed to writing-review.

REFERENCES

[1] WHO, 2020, *World Malaria Report: 20 Years of Global Progress and Challenges*, World Health Organization, Geneva, Switzerland, CC BY-NC-SA 3.0 IGO.

[2] Milner Jr., D.A., 2018, Malaria Pathogenesis, *Cold Spring Harb. Perspect. Med.*, 8 (1), a025569.

[3] Cui, L., Mharakurwa, S., Ndiaye, D., Rathod, P.K., and Rosenthal, P.J., 2015, Antimalarial drug resistance: Literature review and activities and findings of the ICEMR network, *Am. J. Trop. Med. Hyg.*, 93 (3 Suppl.), 57–68.

[4] Kumar, M., Kumar, D., and Raj, V., 2017, Studies on Imidazole and its derivatives with particular emphasis on their chemical/biological applications as bioactive molecules/intermediated to bioactive molecule, *Curr. Synth. Syst. Biol.*, 5 (1), 1000135.

[5] dos Santos Nascimento, M.V.P., Mattar Munhoz, A.C., De Campos Facchin, B.M., Fratoni, E., Rossa, T.A., Mandolesi Sá, M., Campa, C.C., Ciraolo, E., Hirsch, E., and Dalmarco, E.M., 2019, New pre-clinical evidence of anti-inflammatory effect and safety of a substituted fluorophenyl imidazole, *Biomed. Pharmacother.*, 111, 1399–1407.

[6] Abrigach, F., Rokni, Y., Takfaoui, A, Khoutoul, M., Doucet, H., Asehraou, A., and Touzan, R., 2018, In vitro screening, homology modeling and molecular docking studies of some pyrazole and imidazole derivatives, *Biomed. Pharmacother.*, 103, 653–661.

[7] Guda, R., Kumar, G., Korra, R., Balaji, S., Dayakar, G., Palabindela, R., Myadaraveni, P., Yellu, N.R., and Kasula, M., 2017, EGFR, HER2 target based molecular docking analysis, in vitro screening of 2, 4, 5-trisubstituted imidazole derivatives as potential antioxidant and cytotoxic agents, *J. Photochem. Photobiol., B*, 176, 69–80.

[8] Le Manach, C., Gonzàlez Cabrera, D., Douelle, F., Nchinda, A.T., Younis, Y., Taylor, D., Wiesner, L., White, K.L., Ryan, E., March, C., Duffy, S., Avery, V.M., Waterson, D., Witty, M.J., Wittlin, S., Charman, S.A., Street, L.J., and Chibale, K., 2014, Medicinal chemistry optimization of antiplasmodial imidazopyridazine hits from high throughput screening of a SoftFocus kinase library: Part 1, *J. Med. Chem.*, 57 (6), 2789–2798.

[9] Kondaparla, S., Manhas, A., Dola, R.V., Srivastava, K., Puri, S.K., and Katti, S.B., 2018, Design, synthesis and antiplasmodial activity of novel imidazole derivatives based on 7-chloro-4-aminoquinoline, *Bioorg. Chem.*, 80, 204–211.

[10] Sharma, K., Shrivastava, A., Mehra, R.N., Deora, G.S., Alam, M.M., Zaman, M.S., and Akhter, M., 2017, Synthesis of novel benzimidazole acrylonitriles for inhibition of *Plasmodium falciparum* growth by dual target inhibition, *Arch. Pharm.*, 351 (1), e1700251.

[11] Syahri, J., Nasution, H., Nurohmah, B.A., Purwono, B., and Yuanita E., 2020, Aminoalkylated chalcone: Synthesis, biological evaluation, and docking simulation as potent antimalarial agents, *J. Appl. Pharm. Sci.*, 10 (6), 001–005.

[12] Purwono, B., Nurohmah, B.A., Fathurrohman, P.Z., and Syahri, J., 2021, Some 2-arylbenzimidazole derivatives as an antimalarial agent: Synthesis, activity assay, molecular docking and pharmacological evaluation, *Rasayan J. Chem.*, 14 (1), 94–100.

[13] Patel, K., Karthikeyan, C., Moorthy, N.S.H.N., Deora, G.S., Solomon, V.R., Lee, H., and Trivedi, P., 2012, Design, synthesis and biological evaluation of some novel 3-cinnamoyl-4-hydroxy-2H-chromen-2-ones as antimalarial agents, *Med. Chem. Res.*, 21 (8), 1780–1784.

[14] Singh, R.K., Bhatt, A., and Kant, R., 2016, Design and synthesis of some novel imidazole derivatives as potent antimicrobial & antimalarial agents, *Pharm. Lett.*, 8 (7), 188–194.

[15] Batista, R., De Jesus Silva Júnior A., and De Oliveira, A.B., 2009, Plant-derived antimalarial agents: new leads and efficient phytomedicines. Part II. Non-alkaloidal natural products, *Molecules*, 14 (8), 3037–3072.

[16] Syahri, J., Nasution, H., Nurohmah, B.A., Purwono, B., Yuanita, E., Zakaria, N.H., and Hassan, I., 2020, Design, synthesis and biological evaluation of aminoalkylated chalcones as antimalarial agent, *Sains Malays.*, 49 (11), 2667–2677.

[17] Yang, H., Lou, C., Sun, L., Li, J., Cai, Y., Wang, Z., Li, W., Liu, G., and Tang, Y., 2019, admetSAR 2.0: Web-service for prediction and optimization of chemical ADMET properties, *Bioinformatics*, 35 (6), 1067–1069.

[18] Xiong, G., Wu, Z., Yi, J., Fu, L., Yang, Z., Hsieh, C., Yin, M., Zeng, X., Wu, C., Lu, A., Chen, X., Hou, T., and Cao, D., 2021, ADMETlab 2.0: An integrated online platform for accurate and comprehensive predictions of ADMET properties, *Nucleic Acids Res.*, 49 (W1), W5–W14.

[19] Yang, H., Sun, L., Wang, Z., Li, W., Liu, G., and Tang, Y., 2018, ADMETopt: A web server for ADMET optimization in drug design via scaffold hopping, *J. Chem. Inf. Model.*, 58 (10), 2051–2056.

[20] Li, J.T., Chen, B.H., Li, Y.W., and Sun, X.L., 2012, Efficient improved synthesis of 2–aryl-4,5-diphenylimidazole by heating, *Int. J. Adv. Pharm., Biol. Chem.*, 1 (3), 287–292.

[21] Shelke, K.F., Sapkal, S.B., Sonal, S.S., Madje, B.R., Shingate, B.B., and Shingare, M.S., 2009, An efficient synthesis of 2,4,5-Triaryl-1*H*-Imidazole derivatives catalyzed by boric acid in aqueous media under ultrasound-irradiation, *Bull. Korean Chem. Soc.*, 30 (5), 1057–1060.

[22] Hadni, H., and Elhallaoui, M., 2019, Molecular docking and QSAR studies for modeling the antimalarial activity of hybrids 4-anilinoquinoline-triazines derivatives with the wild-type and mutant receptor *pf*-DHFR, *Heliyon*, 5 (8), e02357.

[23] Finch, A., and Pillans, P., 2014, Importance of P-glycoprotein and its role in drug-drug interactions, *Aust. Prescr.*, 37 (4), 137–139.

[24] Glaeser, H., 2011, "Importance of P-glycoprotein for drug-drug interactions" in *Drug Transporters. Handbook of Experimental Pharmacology*, Eds. Fromm, M., and Kim, R., Springer, Berlin, Heidelberg, 201, 285–297.

[25] Wu, Z., Lei, T., Shen, C., Wang, Z., Cao, D., and Hou, T., 2019, ADMET evaluation in drug discovery. 19. Reliable prediction of human Cytochrome P450 inhibition using artificial intelligence approaches, *J. Chem. Inf. Model.*, 59 (11), 4587–4601.

[26] Han, Y., Zhang, J., Hu, C.Q., Zhang, X., Ma, B., and Zhang, P., 2019, *In silico* ADME and toxicity prediction of ceftazidime and its impurities, *Front. Pharmacol.*, 10, 434.

On the Mechanical and Thermal Properties of Poly(Vinyl Alcohol) – Alginate Composite Yarn Reinforced with Nanocellulose from Oil Palm Empty Fruit Bunches

Ainul Maghfirah[1], Farah Fahma[2*], Nurmalisa Lisdayana[3], Muchammad Yunus[4], Ahmad Kusumaatmaja[5], and Grandprix Thomryes Marth Kadja[6,7,8]**

[1]*Department of Applied Chemistry, Graduate School of Engineering, Kyushu University, 744 Motooka, Nishi-ku, Fukuoka 819-0395, Japan*

[2]*Department of Agroindustrial Technology, Faculty of Agricultural Engineering and Technology, Bogor Agricultural University, Gedung Fateta, Jl. Raya Dramaga, Kampus IPB Dramaga, Bogor 16680, West Java, Indonesia*

[3]*Department of Agroindustrial Technology, Institut Teknologi Sumatera, Jl. Terusan Ryacudu, Way Hui Jati Agung, South Lampung 35365, Indonesia*

[4]*Department of Veterinary Parasitology, Faculty of Veterinary Medicine, Airlangga University, Campus C, Jl. Mulyorejo, Surabaya 60115, Indonesia*

[5]*Department of Physics, Faculty of Mathematics and Natural Sciences, Universitas Gadjah Mada, Sekip Utara, Yogyakarta 55281, Indonesia*

[6]*Division of Inorganic and Physical Chemistry, Faculty of Mathematics and Natural Sciences, Institut Teknologi Bandung, Jl. Ganesha No. 10, Bandung 40132, Indonesia*

[7]*Research Center for Nanosciences and Nanotechnology, Institut Teknologi Bandung, Jl. Ganesha No. 10, Bandung 40132, Indonesia*

[8]*Center for Catalysis and Reaction Engineering, Institut Teknologi Bandung, Jl. Ganesha No. 10, Bandung 40132, Indonesia*

**** Corresponding author:***

email: farah_fahma@apps.ipb.ac.id; kadja@chem.itb.ac.id***

Received: July 24, 2021
Accepted: October 25, 2021

DOI: 10.22146/ijc.67881

Abstract: *PVA-alginate hydrogel is a promising material for use in biomedical applications due to its desirable characteristics: biocompatible, durable, non-toxic, and low cost. However, the low gel strength of this composite limits its use in biomedical applications. This study aims to develop enhanced mechanical and thermal properties of poly(vinyl alcohol) PVA-alginate composite yarn by adding nanocellulose isolated from the sustainable oil palm empty fruit bunches (OPEFBs). The PVA-alginate composite yarns reinforced with nanocellulose were prepared with various nanocellulose contents (1 wt.%, 2 wt.%, and 5 wt.%). The composite's tensile strength exhibited an increasing trend with the addition of nanocellulose, while the elongation at break showed the opposite trend. Moreover, it was demonstrated that the composite's thermal degradation shifts to higher temperatures with the addition of nanocellulose. The observed activation energies for the thermal degradation calculated using the Coats-Redfern method exhibited a significant increment for the composites reinforced with nanocellulose. These results show that the addition of nanocellulose into the PVA-alginate matrix enhances the chemical and thermal properties of the resulting hydrogel. All these improvements have resulted from more abundant and robust hydrogen bonds generated by the nanocellulose presence.*

Keywords: *nanocellulose; OPEFBs; PVA-alginate; mechanical stability; thermal stability*

■ INTRODUCTION

Recently, the utilization of sustainable resources to produce new biodegradable materials has been intensively pursued as an alternative to the continuously declining raw material from non-renewable resources. In this sense, palm oil has emerged as one of the most potent

resources. From 1962 to 2012, palm oil plantation across the globe has expanded exponentially to around 13 million hectares establishing them as the global fastest-growing monoculture [1-2]. Indonesia is the largest palm-oil producing country globally, with a national annual yield of 17 tons of fresh fruit bunches per hectare [3]. However, the massive production is surely followed by a large number of wastes. The waste in palm oil plantations is dominated by biomass, such as oil palm empty fruit bunches (OPEFBs), fronds, trunks, and mesocarps. For example, OPEFBs are the solid-waste biomass produced after the stripping process of fresh fruit bunches. OPEFBs are composed of crystalline cellulose (41.3–46.5%), which is embedded in an amorphous matrix of lignin (27.6–32.5%) and hemicellulose (25.3–33.8%) [4].

Nowadays, many researchers have focused on the use and recycling of OPEFBs because of their exceptional potential as an organic carbon source and sustainability in producing high value-added materials, such as activated carbon [5-8], bioethanol [9-12], and nanocellulose [13-16]. Among them, nanocellulose has been an up-and-coming class of materials, which has a broad spectrum of applications, including food packaging [17], tissue engineering [18], pharmaceutics [19], and wound treatment [20-21]. These are possible due to their high surface area, hydrophilicity, mechanical strength, biocompatibility, biodegradability, and lack of toxicity. It becomes more interesting with the strong artificial adhesion and dispersion capability of nanocellulose in various host materials/matrices, leading to the potential use as reinforcement in polymer composite materials [13,15,22].

Many polymers have been studied as a system to be reinforced with nanocellulose, e.g., polyvinyl alcohol (PVA) [23], polyacrylamide [24], chitosan [25], and alginate [26]. These reports have shown the increased higher mechanical properties of the system after the incorporation of nanocellulose. Moreover, Poonguzhali et al. [27] reported that nanocellulose incorporation up to 10% into chitosan/poly(vinyl pyrrolidone) matrix improved wound healing yarn with a tensile strength of 39.7 ± 6.9 MPa. Similar nanocellulose reinforcements in various blend polymers have also been demonstrated [13,15,28]. In addition, Li et al. [29] also found that adding a small amount of long filamentous nanocellulose fibrils (NCFs) into PVA films increased the maximum degradation temperature around 4 to 16.9 °C indicating that nanocellulose addition also could enhance the thermal stability of the PVA films.

PVA-alginate is a hydrogel system that has attracted much attention, especially for its biomedical application. However, as it is highly hydrophilic, the mechanical strength is usually low, limiting its use in certain applications. Therefore, many efforts have been devoted to improving the properties of the PVA-based composite system. For example, by immersing PVA-alginate composite in the saturated NaCl aqueous solution, Jiang et al. [30] produced PVA-alginate with an improved mechanical strength (maximum tensile strength of 1.34 MPa). On the other hand, Islam and Karim [31] also reported a better tensile property of PVA-alginate blend nanofiber up to 35 MPa using the electrospinning method. Meanwhile, cross-linking PVA and sodium alginate using glutaraldehyde and calcium sulfate with the presence of nanocellulose showed compressive stress of up to 79.5 ± 2.35 kPa, which was 3.2 times higher than the pristine PVA/alginate hydrogel.

Herein, we report the preparation of PVA-alginate nanocomposite yarn modified with nanocellulose isolated from OPEFBs. The thermal stability of PVA-alginate with various nanocellulose content is investigated in detail resulting in the observed activation energies for their decomposition. Moreover, the tensile strength of PVA-alginate-nanocellulose yarn is thoroughly studied at different temperatures. Finally, the improved mechanical and thermal stabilities are correlated to the interaction between nanocellulose and PVA-alginate systems. Our results may provide valuable insights into the versatile design of polymer systems reinforced with nanocellulose.

■ EXPERIMENTAL SECTION

Materials

The fibers of OPEFBs for the production of nanocellulose were obtained from PTPN VIII, Kertajaya, Lebak, West Java, Indonesia. PVA (Celvol TM Sekisui Chemical Co., Ltd, Jakarta, Indonesia), sodium hydroxide

(NaOH, Merck), and hydrogen peroxide (H_2O_2, Merck) used were the commercial-grade products. All chemicals were used as received without further purification.

Instrumentation

X-ray diffraction (XRD) patterns were collected on a Bruker D8 Advance diffractometer using a Cu-Kα radiation beam (λ = 1.54 Å) from 2θ of 3° to 50° with a step size of 0.02°. The samples were placed on a 3 cm-diameter sample holder, and the measurement started under operating conditions of 40 kV and 40 mA. The morphologies of the materials were observed on a Hitachi SU-3500 scanning electron microscope (SEM) with a secondary electron (SE) mode at an accelerating voltage of 10 kV. The isolated nanocellulose was observed on a JEOL JEM 1010 transmission electron microscope (TEM). A Shimadzu Prestige spectrometer was employed to record the Fourier-transform infrared (FTIR) spectra of the samples with a spectral resolution of 4 cm^{-1}. Each spectrum was resulted from 64 scans. The thermal properties of the samples were analyzed using a Hitachi simultaneous thermal analyzer (STA) 7000 using N_2 (80 vol%) and O_2 (20 vol%) as the carrier gas with a flow rate of 50 mL min^{-1}. The temperature was increased to 600 °C at a fixed heating rate of 20 °C min^{-1}. The mechanical properties of the samples were analyzed using a Universal Testing Machine (Instron 3369) at a rate of 6 mm min^{-1}. Five measurements were carried out for each sample.

Procedure

Isolation of cellulose fibers from OPEFBs

The dried OPEFBs fibers were soaked in a 10 wt.% NaOH solution with a ratio of solution/fibers = 20/1 (v/w) at 95 °C for 1 h. In this step, the black solution was resulted due to the leaching of lignin. Subsequently, the fibers were separated from the black solution, washed, and filtered using distilled water until the neutral filtrate pH. After that, the obtained fibers were dried at 55 °C for 24 h. Furthermore, the bleaching was performed by immersing the delignified OPEFBs in 30 wt.% hydrogen peroxide solution with a solution/fibers ratio of 15/1 (v/w) at 95 °C for 1.5 h. The cellulose fibers were filtered and washed to neutral. The second stage of bleaching was performed using alkaline peroxide solution, obtained by mixing 30 wt.% H_2O_2 and 10 wt.% NaOH solutions, with a volume ratio of 2/1. The cellulose fibers were then immersed in this solution with a solution/fibers ratio of 15/1 (v/w) at 95 °C for 1.5 h. The cellulose fibers were filtered and washed to neutral. After the two-step bleaching treatment, the white cellulose fibers are obtained.

Isolation of nanocellulose from cellulose fibers

The cellulose fibers were diluted using distilled water to a concentration of 2 wt.%. Subsequently, the mixture was treated with an ultrafine grinder (Masuko Co., Ltd, Kawaguchi, Japan) at 1500 rpm with several gap levels, i.e., +5 (15 times), 0 (15 times), –5 (15 times), –10 (15 times), –15 (15 times) and –18 (15 times) [32], performed gradually. After the ultrafine grinding, a thick suspension was obtained and mixed with distilled water with a suspension/water ratio of 1:2 (v/v). Finally, the mixture underwent ultrasonication treatment ((20 kHz, 40 W, Q Sonica, Newtown, CT, USA) for 1 h to produce nanocellulose.

Production of nanocellulose composite yarn by wet spinning

The nanocellulose was dispersed in distilled water, followed by the addition of sodium alginate under stirring for 40 min under vigorous stirring. Subsequently, PVA was added, and the stirring was continued for 40 min at 200 °C. The final mixture has a PVA/alginate weight ratio of 1/1 and the PVA-alginate-nanocellulose to water weight ratio of 25. The content nanocellulose was varied, i.e., 0 wt.%, 1 wt.%, 2 wt.%, and 5 wt.%, relative to the total weight of PVA-alginate-nanocellulose. Then, the mixture was subsequently spun using a 2.5 mm needle with a spinning speed of 20 mL min^{-1}. The dope was coagulated in a 9 wt.% $CaCl_2$ solution followed by washing with distilled water. The resulting filament was then dried at room temperature for 4–6 h followed by soaking in distilled water for 15 min and dried in the oven at 55 °C for 30 min.

■ RESULTS AND DISCUSSION

The Structural Properties

Fig. 1 shows the TEM image of the isolated nanocellulose from the OPEFBs. The isolated nanocellulose exhibits thin, dendritic fibrous morphology

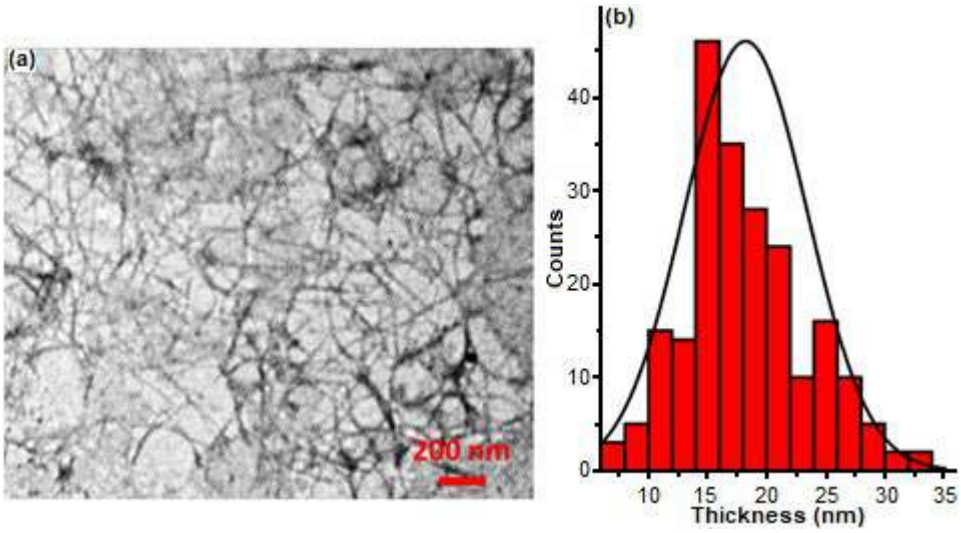

Fig 1. (a) TEM image and (b) the corresponding thickness distribution of the nanocellulose isolated from OPEFBs

with single and connected frameworks of filaments. This characteristic morphology of nanocellulose was rendered from strong hydrogen bonds amount the filaments [33]. The thickness distribution of the isolated nanocellulose is centered at around 20 nm, as depicted in Fig. 1(b).

The XRD patterns of all studied materials are shown in Fig. 2. All materials exhibit a dominant peak at 2θ of 19.6°, attributed to the strong intermolecular and intramolecular hydrogen bonding within the PVA structure [13,31]. No other peaks appear at 2θ of 13.7° and 23° [34], which should belong to the alginate structure. It indicates that the alginate structure might be distorted due to hydrogen bonding interaction between hydroxyl (–OH) and carbonyl (C=O) groups of alginate with hydroxyl groups of PVA. Meanwhile, the characteristic peak of nanocellulose appeared at 2θ of 22.5°, corresponding to cellulose's (200) crystal plane [35-36] with the PVA-alginate structure. The intensity of this peak increases along with the addition of nanocellulose. This result shows that the nanocellulose is successfully incorporated into the PVA-alginate composite structure. The nanocellulose addition up to 5 wt.% does not disturb the structure of the PVA-alginate composite. Moreover, a slight increase of crystallinity was observed with nanocellulose addition up to 2 wt.%. These results are similar to the work performed by Uddin et al. [37], where the addition of a small amount of cellulose whisker (CW) into PVA increased the degree of crystallinity of the fiber,

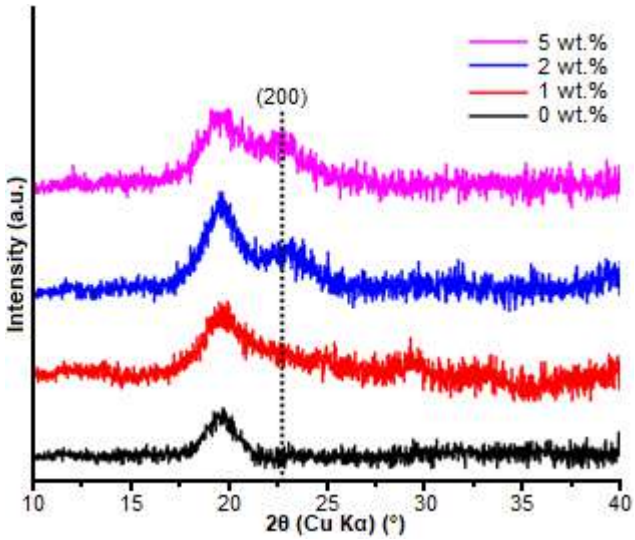

Fig 2. XRD patterns of PVA-alginate composites with different amounts of nanocellulose addition

while a higher concentration of CW, the ratio of CW and PVA weight > 5%, resulted in a lower degree of crystallinity. It was confirmed by wide-angle X-ray diffraction (WAXD) analysis that PVA-CW composite with CW/PVA weight ratio of 5% showed more enhanced crystal orientation of PVA component. Thus, the broader peak at 19.6° of PVA-alginate with 5 wt.% addition of nanocellulose is probably due to the impeded orientation of the PVA component caused by a large amount of nanocellulose network [15,38].

The effect of nanocellulose addition on the structural change and the molecular interaction was

further analyzed using FTIR spectroscopy, as depicted in Fig. 3. The vibrational bands at around 1418 and 1630 cm^{-1} are assigned to symmetric and asymmetric stretching of $-COO^-$ from alginate, respectively, [31], while bands at around 2920 cm^{-1} correspond to C–H asymmetric stretching from the alkyl group [39]. In addition, the hydroxyl (O–H) group is shown by the broadband centered at around 3448 cm^{-1}. This peak is attributed to all types of hydrogens bonded to hydroxyl groups. Furthermore, with the addition of nanocellulose, the O–H stretching vibration band undergoes a redshift to the lower wavenumber (Fig. 3(c)). This trend correlates to the stronger hydrogen bond within the composite with the addition of nanocellulose. The relationship between hydrogen bond strength and the stretching vibration redshift has been discussed in previous publications [40-41]. The added nanocellulose may likely penetrate between PVA and alginate backbones; thus, resulting in stronger interaction through hydrogen bonds. The molecular interactions of the present PVA-alginate composites yarn reinforced with nanocellulose are schematically illustrated in Fig. 4. The alginates form ionically cross-linking interactions to Ca-dicarboxylate chelate triplets since the composites were immersed in $CaCl_2$ solution during the preparation. Meanwhile, hydrogen bonds arise from hydroxyl bonds in PVA and nanocellulose.

The Morphological Analysis

Fig. 5 displays SEM images of PVA-alginate composite yarn with various amounts of nanocellulose at the same magnification and their corresponding 3D surface reconstruction. The morphology of the PVA-alginate composite without the addition of nanocellulose shows a relatively smooth surface with several folds (Fig. 5(a)). Nevertheless, some tears are observed as indicated by red arrows in Fig. 5(a), which might be due to the relatively weak interaction. On the other hand, tears do not appear in the samples with the

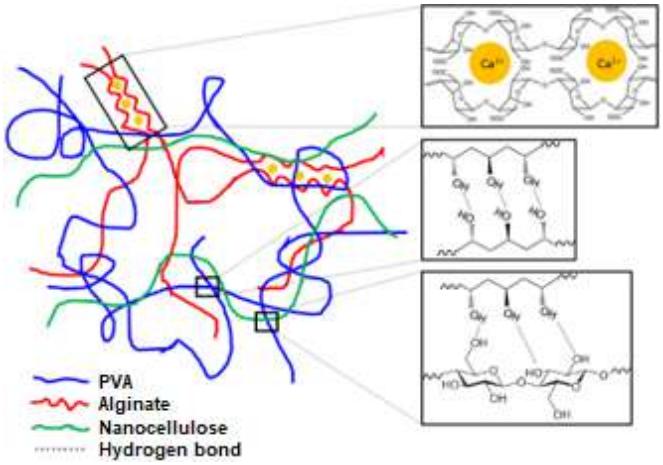

Fig 4. Schematic illustration of molecular interactions within PVA-alginate composites reinforced with nanocellulose

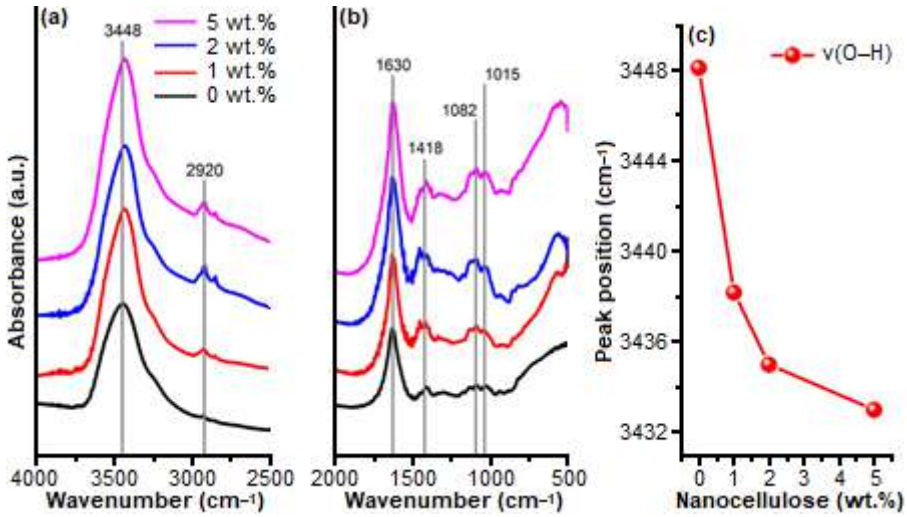

Fig 3. (a, b) FTIR spectra of PVA-alginate composites with different amounts of nanocellulose addition, and (c) the shift of O–H stretching vibration position as a function of nanocellulose addition

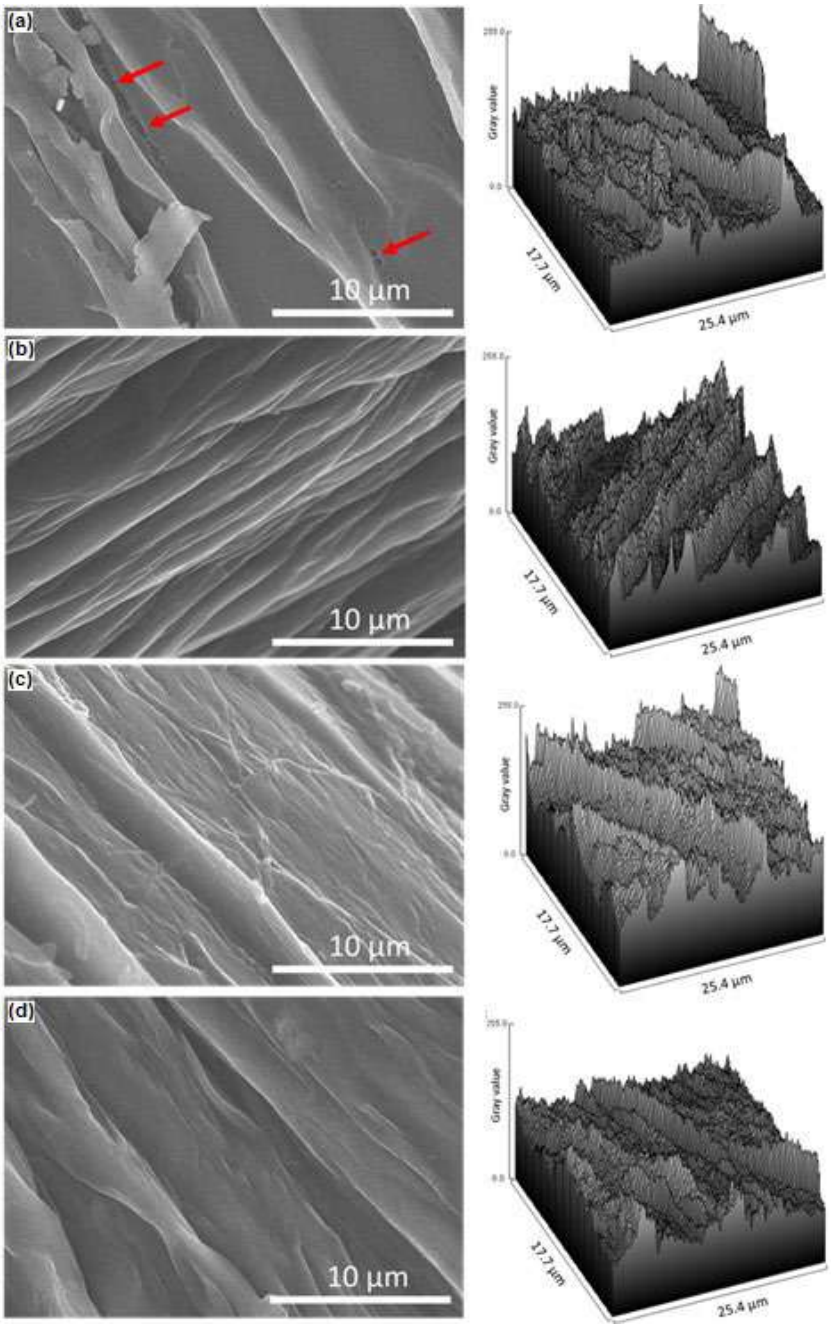

Fig 5. SEM images of PVA-alginate composites with nanocellulose addition of (a) 0 wt.% (b) 1 wt.%, (c) 2 wt.%, and (d) 5 wt.%

presence of nanocellulose. The addition of nanocellulose somewhat alters the surface morphology of the composite into rougher and filamentous, as also indicated by 3D surface construction. These observations are likely to be generated by the presence of nanocellulose. It appears that the nanocellulose is well-dispersed and a compatible nanofiller to the polymer matrices.

The Mechanical Properties

The tensile strength and elongation at break of PVA-alginate composites with different nanocellulose content are provided in Fig. 6. As more cellulose is added to the PVA–alginate, the tensile strength is enhanced. This phenomenon is associated with the effective

interfacial adhesion of PVA-alginate matrices with nanocellulose generated by the more and stronger hydrogen bonds. Li et al. [42] reported that the tensile strength of PVA-alginate hydrogels resulted from the ionically cross-linked structure of alginate due to the immersion ion $CaCl_2$ aqueous solution the hydrogen bonds among PVA networks. The former was broken upon initial stretched while the latter survived more stress, which shows the significant contribution of hydrogen bonds to the mechanical properties of the polymer matrices. The elongation at break tends to decline with the increase of nanocellulose content since nanocellulose can raise the stiffness effect originated from the more rigid structures due to the more abundant and robust hydrogen bond. Interestingly, a sharp decrease of elongation at break was observed at nanocellulose of 1 wt.%. It is probably because of the weak interaction between nanocellulose and the PVA-alginate matrix. However, this hypothesis merits further investigation. Our results agree with the work performed by Cho and Park [43]. They reported that the tensile modulus and strength of PVA nanocomposite were enhanced with the nanocellulose addition. Their nanocellulose was extracted from the microcrystalline cellulose through sulfuric acid hydrolysis. Similar trends of tensile strength and elongation at break to our study were reported by El Miri et al. [44] for carboxymethyl cellulose–starch composite reinforced with nanocellulose.

The Thermal Properties

The thermal properties of all studied materials are assessed using thermogravimetric analysis (TGA) and shown in Fig. 7(a). As the temperature increases, the mass of the samples decreases. This fact indicates the conversion, α, according to the following equation,

$$\alpha = \frac{m_o - m_t}{m_o - m_f} \quad (1)$$

where m_o and m_f are the initial and final mass of the samples, respectively, while m_t is the mass of the samples at a certain time, t. The initial stage is observed from around 50 to 200 °C, attributed to the evaporation of water molecules. Above 200 °C, the conversion increases dramatically, which can be classified into several stages, as shown by the first derivative of the thermogravimetric curve (Fig. 7(b)). Around 230 to 330 °C, the conversion is due to the dehydration and the formation of polyene. Moreover, a more intense conversion occurs from around 330 to 420 °C attributed to the polyene decomposition resulting in oxygen-containing molecules. Holland and Hay reported [45] that the thermal degradation of PVA may lead to the formation of aldehyde and alkene end molecules, and subsequently rearranged into vinyl ester molecules. Ultimately, the conversion stage from around 420 to 510 °C corresponds to the formation of polyaromatics. It is worth noting that the higher content of nanocellulose results in the shift toward higher conversion temperature, showing improved thermal stability.

The relative thermal stability is analyzed from the initial degradation of the composite, i.e, at 200–300 °C. As shown in Fig. 7(a), distinct shifts of initial degradation to higher temperature were observed for samples with higher amount of nanocellulose. Samples with 0 and 1 wt.% of nanocellulose start to degrade at around 250 °C. Meanwhile, samples with nanocellulose content > 1% initially degrade at temperature around 270 °C. Furthermore, the relative thermal stability is also described as T_{50}, the temperature when a half fraction of the samples has been converted (α = 0.5). The sample with a lower T_{50} exhibits better thermal stability. As seen

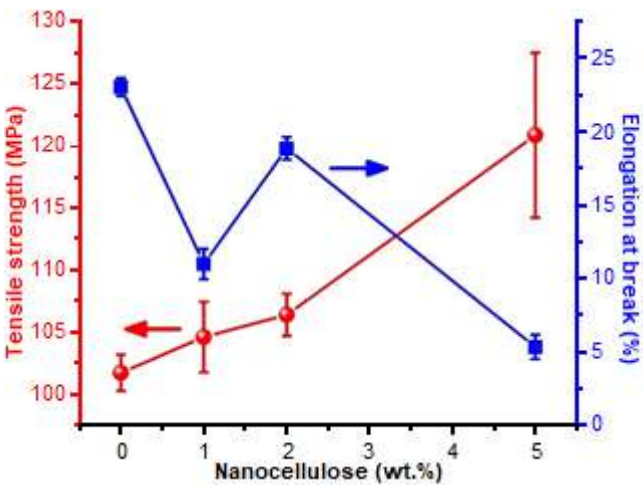

Fig 6. Mechanical properties of PVA-alginate composites with different amounts of nanocellulose addition

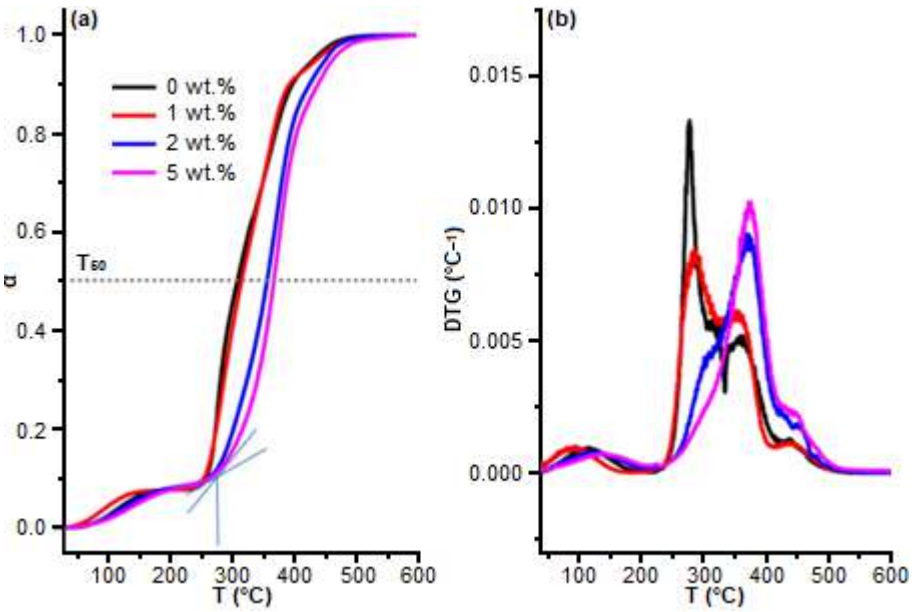

Fig 7. (a) TGA and (b) DTG curves of PVA-alginate composites with different amounts of nanocellulose addition

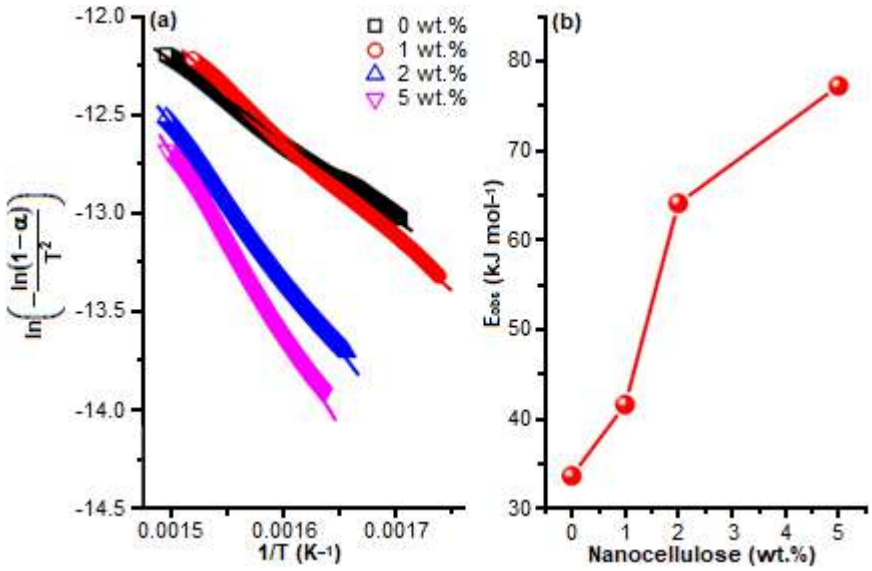

Fig 8. (a) Coats-Redfern plots and (b) E_{obs} of PVA-alginate composites with different amount of nanocellulose addition

in Fig. 7(a), the T_{50} shifts gradually to a higher value when a higher content of nanocellulose is added, based on the following order, 0 wt.% (308 °C) < 1 wt.% (315 °C) < 2 wt.% (355 °C) < 5 wt.% (367 °C). This result clearly demonstrates the usability of nanocellulose to reinforce the thermal stability of PVA-alginate composite yarn. The TGA curves can be further analyzed to determine the observed activation energy (E_{obs}) through the Coats-Redfern method since the thermal degradation of polymer is a first-order reaction. This model is a multi-heating rate that has been widely used for kinetic analysis of thermal decomposition [46-48]. Shukla et al. [49] also used this model for the multi-stage decomposition of epoxidized resole resin. This Coats-Redfern method is expressed as Eq. (2) [50-52],

$$\frac{da}{dT} = k(T)f(\alpha) = A\exp\left(-\frac{E_{obs}}{RT}\right)(1-\alpha) \quad (2)$$

where T is the temperature, A is the pre-exponential factor, and R is the ideal gas constant. Under the non-isothermal heating with a constant ramping, β = dT/dt,

Eq. (2) can be rearranged and integrated, resulting in the following equation,

$$\ln\left(-\frac{\ln(1-\alpha)}{T^2}\right)=\ln\left(\frac{AR}{\beta E_{obs}}\left(1-\frac{2RT}{E_{obs}}\right)\right)-\frac{E_{obs}}{RT} \quad (3)$$

Plotting ln $\left(-\frac{\ln(1-\alpha)}{T^2}\right)$ against $\frac{1}{T}$ will result in a linear correlation with a slope of $-\frac{E_{obs}}{R}$ as shown in Fig. 8(a). Thus, the observed activation energy can be calculated by multiplying the slope with R (8.314 J mol^{-1} K^{-1}). The calculation results are provided in Fig. 8(b). It is clearly demonstrated that the composite with higher nanocellulose content possesses enhanced observed activation energy. This is possible since the presence of nanocellulose strengthens the interaction within the composite through hydrogen bonds; hence, greater energy consumption is necessary to thermally degrade the composite.

CONCLUSION

PVA-alginate composite yarns reinforced with nanocellulose isolated from OPEFBs were successfully prepared *via* a wet spinning method with improved mechanical and thermal properties. The isolated nanocellulose displays well compatibility as the nanofiller within PVA – alginate matrices. Moreover, the peculiar structure of nanocellulose with an abundant presence of hydroxyl groups enables more and strong hydrogen bonds with the functional groups of PVA and alginate, leading to more robust interfacial adhesion. The addition of nanocellulose, i.e., 1 wt.%, 2 wt.%, and 5 wt.% gives rise to the mechanical properties of PVA-alginate composite yarn from 101.7 MPa to 104.6 MPa, 106.4 MPa, and 120.1 MPa, respectively. On the other hand, the trend of elongation at break shows the opposite trend since the more and stronger hydrogen bond increases the composite stiffness. The same molecular interaction also takes responsibility for the higher energy consumption for the composite to undergo degradation. As the nanocellulose content increases, the initial stage degradation, T_{50}, and E_{obs} are enhanced, demonstrating the upgrading of the thermal stability. Our result shows that the nanocellulose isolated from OPEFBs possesses an up-and-coming potential as sustainable materials for effectively reinforcing the polymer composites.

ACKNOWLEDGMENTS

We acknowledge a collaborative RKI program from the Indonesian World Class University Research scheme.

REFERENCES

[1] Brad, A., Schaffartzik, A., Pichler, M., and Plank, C., 2015, Contested territorialization and biophysical expansion of oil palm plantations in Indonesia, *Geoforum*, 64, 100–111.

[2] Gatto, M., Wollni, M., and Qaim, M., 2015, Oil palm boom and land-use dynamics in Indonesia: The role of policies and socioeconomic factors, *Land Use Policy*, 46, 292–303.

[3] Varkkey, H., Tyson, A., and Choiruzzad, S.A.B., 2018, Palm oil intensification and expansion in Indonesia and Malaysia: Environmental and socio-political factors influencing policy, *For. Policy Econ.*, 92, 148–159.

[4] Kim, S., and Kim, C.H., 2013, Bioethanol production using the sequential acid/alkali-pretreated empty palm fruit bunch fiber, *Renewable Energy*, 54, 150–155.

[5] Alam, M.Z., Muyibi, S.A., Mansor, M.F., and Wahid, R., 2007, Activated carbons derived from oil palm empty-fruit bunches: Application to environmental problems, *J. Environ. Sci.*, 19 (1), 103–108.

[6] Osman, N.B., Shamsuddin, N., and Uemura, Y., 2016, Activated carbon of oil palm empty fruit bunch (EFB); Core and shaggy, *Procedia Eng.*, 148, 758–764.

[7] Ooi, C.H., Cheah, W.K., Sim, Y.L., Pung, S.Y., and Yeoh, F.Y., 2017, Conversion and characterization of activated carbon fiber derived from palm empty fruit bunch waste and its kinetic study on urea adsorption, *J. Environ. Manage.*, 197, 199–205.

[8] Loo, W.W., Pang, Y.L., Lim, S., Wong, K.H., Lai, C.W., and Abdullah, A.Z., 2021, Enhancement of photocatalytic degradation of malachite green using iron doped titanium dioxide loaded on oil palm empty fruit bunch-derived activated carbon, *Chemosphere*, 272, 129588.

[9] Derman, E., Abdulla, R., Marbawi, H., and Sabullah, M.K., 2018, Oil palm empty fruit bunches as a promising feedstock for bioethanol production in Malaysia, *Renewable Energy*, 129, 285–298.

[10] Sudiyani, Y., Styarini, D., Triwahyuni, E., Sudiyarmanto, Sembiring, K.C., Aristiawan, Y., Abimanyu, H., and Han, M.H., 2013, Utilization of biomass waste empty fruit bunch fiber of palm oil for bioethanol production using pilot–scale unit, *Energy Procedia*, 32, 31–38.

[11] Pangsang, N., Rattanapan, U., Thanapimmetha, A., Srinopphakhun, P., Liu, C.G., Zhao, X.Q., Bai, F.W., and Sakdaronnarong, C., 2019, Chemical-free fractionation of palm empty fruit bunch and palm fiber by hot-compressed water technique for ethanol production, *Energy Rep.*, 5, 337–348.

[12] Suhartini, S., Rohma, N.A., Mardawati, E., Kasbawati, Hidayat, N., and Melville, L., 2022, Biorefining of oil palm empty fruit bunches for bioethanol and xylitol production in Indonesia: A review, *Renewable Sustainable Energy Rev.*, 154, 111817.

[13] Lisdayana, N., Fahma, F., Sunarti, T.C., and Iriani, E.S., 2020, Thermoplastic starch-PVA nanocomposite films reinforced with nanocellulose from oil palm empty fruit bunches (OPEFBs): Effect of starch type, *J. Nat. Fibers*, 17 (7), 1069–1080.

[14] Huang, S., Zhao, Z., Feng, C., Mayes, E., and Yang, J., 2018, Nanocellulose reinforced P(AAm-*co*-AAc) hydrogels with improved mechanical properties and biocompatibility, *Composites, Part A*, 112, 395–404.

[15] Fahma, F., Lisdayana, N., Abidin, Z., Noviana, D., Sari, Y.W., Mukti, R.R., Yunus, M., Kusumaatmaja, A., and Kadja, G.T.M., 2019, Nanocellulose-based fibers derived from palm oil by-products and their in vitro biocompatibility analysis, *J. Text. Inst.*, 111 (9), 1354–1363.

[16] Septevani, A.A., Rifathin, A., Sari, A.A., Sampora, Y., Ariani, G.N., Sudiyarmanto, and Sondari, D., 2020, Oil palm empty fruit bunch-based nanocellulose as a super-adsorbent for water remediation, *Carbohydr. Polym.*, 229, 115433.

[17] Sawar, M.S., Niazi, M.B.K., Jahan, Z., Ahmad, T., and Hussain, A., 2018, Preparation and characterization of PVA/nanocellulose/Ag nanocomposite films for antimicrobial food packaging, *Carbohydr. Polym.*, 184, 453–464.

[18] Jorfi, M., and Foster, E.J., 2015, Recent advances in nanocellulose for biomedical applications, *J. Appl. Polym. Sci.*, 132 (14), 41719.

[19] Salimi, S., Sotudeh-Gharebagh, R., Zargami, R., Chan, S.Y., and Yuen, K.H., 2019, Production of nanocellulose and its applications in drug delivery: A critical review, *ACS Sustainable Chem. Eng.*, 7 (19), 15800–15827.

[20] Liu, J., Chinga-Carrasco, G., Cheng, F., Xu, W., Willför, S., Syverud, K., and Xu, C., 2016, Hemicellulose-reinforced nanocellulose hydrogels for wound healing application, *Cellulose*, 23, 3129–3143.

[21] Basu, A., Lindh, J., Ålander, E., Strømme, M., and Ferraz, N., 2017, On the use of ion-crosslinked nanocellulose hydrogels for wound healing solutions: Physicochemical properties and application-oriented biocompatibility studies, *Carbohydr. Polym.*, 174, 299–308.

[22] Savadekar, N.R., and Mhaske, S.T., 2012, Synthesis of nano cellulose fibers and effect on thermoplastics starch based films, *Carbohydr. Polym.*, 89 (1), 146–151.

[23] Cataldi, A., Rigotti, D., Nguyen, V.D.H., and Pegoretti, A., 2018, Polyvinyl alcohol reinforced with crystalline nanocellulose for 3D printing application, *Mater. Today Commun.*, 15, 236–244.

[24] Chen, C., Wang, H., Li, S., Fang, L., and Li, D., 2017, Reinforcement of cellulose nanofibers in polyacrylamide gels, *Cellulose*, 24 (12), 5487–5493.

[25] Khalil, H.P.S.A., Saurabh, C.K., Adnan, A.S., Nurul Fazita, M.R., Syakir, M.I., Davoudpour, Y., Rafatullah, M., Abdullah, C.K., Haafiz, M.K.M., and Dungani, R., 2016, A review on chitosan-cellulose blends and nanocellulose reinforced chitosan biocomposites: Properties and their applications, *Carbohydr. Polym.*, 150, 216–226.

[26] Abdollahi, M., Alboofetileh, M., Rezaei, M., and Behrooz, R., 2013, Comparing physico-mechanical and thermal properties of alginate nanocomposite

films reinforced with organic and/or inorganic nanofillers, *Food Hydrocolloids*, 32 (2), 416–424.

[27] Poonguzhali, R., Basha, S.K., and Kumari, V.S., 2017, Synthesis and characterization of chitosan-PVP-nanocellulose composites for in-vitro wound dressing application, *Int. J. Biol. Macromol.*, 105, 111–120.

[28] Mandal, A., and Chakrabarty, D., 2015, Characterization of nanocellulose reinforced semi-interpenetrating polymer network of poly(vinyl alcohol) & polyacrylamide composite films, *Carbohydr. Polym.*, 134, 240–250.

[29] Li, W., Wu, Q., Zhao, X., Huang, Z., Cao, J., Li, J., and Liu, S., 2014, Enhanced thermal and mechanical properties of PVA composites formed with filamentous nanocellulose fibrils, *Carbohydr. Polym.*, 113, 403–410.

[30] Jiang, X., Xiang, N., Zhang, H., Sun, Y., Lin, Z., and Hou, L., 2018, Preparation and characterization of poly(vinyl alcohol)/sodium alginate hydrogel with high toughness and electric conductivity, *Carbohydr. Polym.*, 186, 377–383.

[31] Islam, M.S., and Karim, M.R., 2010, Fabrication and characterization of poly(vinyl alcohol)/alginate blend nanofibers by electrospinning method, *Colloids Surf., A*, 366 (1-3), 135–140.

[32] Fahma, F., Sapoan, M., Lisdayana, N., Iskandar, A., Sunarti, T.C., and Sugiarto, 2021, Release property of red ginger essential oil in silica-nanocellulose composite based sachet, *IOP Conf. Ser.: Earth Environ. Sci.*, 749, 012045.

[33] Zuluaga, R., Putaux, J.L., Restrepo, A., Mondragon, I., and Gañán, P., 2007, Cellulose microfibrils from banana farming residues: Isolation and characterization, *Cellulose*, 14, 585–592.

[34] Wang, Q., Hu, X., Du, Y., and Kennedy, J.F., 2010, Alginate/starch blend fibers and their properties for drug controlled release, *Carbohydr. Polym.*, 82 (3), 842–847.

[35] French, A.D., and Cintrón, M.S., 2013, Cellulose polymorphy, crystallite size, and the Segal crystallinity index, *Cellulose*, 20 (1), 583–588.

[36] Zhao, Y., Moser, C., Lindström, M.E., Henriksson, G., and Li, J., 2017, Cellulose nanofibers from softwood, hardwood, and tunicate: Preparation-structure-film performance interrelation, *ACS Appl. Mater. Interfaces*, 9 (15), 13508–13519.

[37] Uddin, A.J., Araki, J., and Gotoh, Y, 2011, Toward "strong" green nanocomposites: Polyvinyl alcohol reinforced with extremely oriented cellulose whiskers, *Biomacromolecules*, 12 (3), 617–624.

[38] Peng, J., Ellingham, T., Sabo, R., Turng, L.S., and Clemons, C.M., 2014, Short cellulose nanofibrils as reinforcement in polyvinyl alcohol fiber, *Cellulose*, 21 (6), 4287–4298.

[39] Yue, Y., Han, J., Han, G., French, A.D., Qi, Y., and Wu, Q., 2016, Cellulose nanofibers reinforced sodium alginate-polyvinyl alcohol hydrogels: Core-shell structure formation and property characterization, *Carbohydr. Polym.*, 147, 155–164.

[40] Rozenberg, M., Loewenschuss, A., and Marcus, Y., 2000, An empirical correlation between stretching vibration redshift and hydrogen bond length, *Phys. Chem. Chem. Phys.*, 2 (12), 2699–2702.

[41] Joseph, J., and Jemmis, E.D., 2007, Red-, Blue-, or No-shift in hydrogen bond: A unified explained, *J. Am. Chem. Soc.*, 129 (15), 4620–4632.

[42] Li, X., Shu, M., Li, H., Gao, X., Long, S., Hu, T., and Wu, C., 2018, Strong, tough and mechanically self-recoverable poly(vinyl alcohol)/alginate dual-physical double-network hydrogels with large cross-link density contrast, *RSC Adv.*, 8 (30), 16674–16689.

[43] Cho, M.J., and Park, B.D., 2011, Tensile and thermal properties of nanocellulose-reinforced poly(vinyl alcohol) nanocomposites, *J. Ind. Eng. Chem.*, 17 (1), 36–40.

[44] El Miri, N., Abdelouahdi, K., Barakat, A., Zahouily, M., Fihri, A., Solhy, A., and El Achaby, M., 2015, Bio-nanocomposite films reinforced with cellulose nanocrystals: Rheology of film-forming solutions, transparency, water vapor barrier and tensile properties of films, *Carbohydr. Polym.*, 129, 156–167.

[45] Holland, B.J., and Hay, J.N., 2001, The thermal degradation of poly(vinyl alcohol), *Polymer*, 42 (16), 6775–6783.

[46] Al-Bayaty, S.A., Al-Uqaily, R.A.H., and Jubier, N.J., 2020, Using the Coats-Redfern method during thermogravimetric analysis and differential scanning calorimetry analysis of the thermal stability of epoxy and epoxy/silica nanoparticle nanocomposites, *J. Southwest Jiaotong Univ.*, 55 (4), 1–12.

[47] Cai, J., and Bi, L., 2008, Precision of the Coats and Redfern method for the determination of the activation energy without neglecting the low-temperature end of the temperature integral, *Energy Fuels*, 22 (4), 2172–2174.

[48] Ge, J., Wang, R.Q., and Liu, L., 2016, Study on the thermal degradation kinetics of the common wooden boards, *Procedia Eng.*, 135, 72–82.

[49] Shukla, S.K., Srivastava, D., and Srivastava, K., 2015, Synthesis, spectral and thermal degradation kinetics of the epoxidized resole resin derived from cardanol, *Adv. Polym. Technol.*, 34 (1), 21469.

[50] Huang, S., Zhou, L., Li, M.C., Wu, Q., and Zhou, D., 2017, Cellulose nanocrystals (CNCs) from corn stalk: Activation energy analysis, *Materials*, 10 (1), 80.

[51] Wardani, M.K., Kadja, G.T.M., Fajar, A.T.N., Subagjo, Makertihartha, I.G.B.N., Gunawan, M.L., Suendo, V., and Mukti, R.R., 2019, Highly crystalline mesoporous SSZ-13 zeolite obtained *via* controlled post-synthetic treatment, *RSC Adv.*, 9 (1), 77–86.

[52] Kadja, G.T.M., Suprianti, T.R., Ilmi, M.M., Khalil, M., Mukti, R.R., and Subagjo, 2020, Sequential mechanochemical and recrystallization methods for synthesizing hierarchically porous ZSM-5 zeolites, *Microporous Mesoporous Mater.*, 308, 110550.

Molecular interactions of *Andrographis paniculata* Burm. f. Active Compound with Nuclear Receptor (CAR and PXR): An In Silico Assessment Approach

Elza Sundhani[1,2], Agung Endro Nugroho[3*], Arief Nurrochmad[3], and Endang Lukitaningsih[4]

[1]*Doctoral Program in Pharmaceutical Science, Faculty of Pharmacy, Universitas Gadjah Mada, Yogyakarta 55281, Indonesia*

[2]*Department of Pharmacology and Clinical Pharmacy, Faculty of Pharmacy, Universitas Muhammadiyah Purwokerto, Jl. KH. Ahmad Dahlan Dukuhwaluh, Purwokerto 53182, Central Java, Indonesia*

[3]*Department of Pharmacology and Clinical Pharmacy, Faculty of Pharmacy, Universitas Gadjah Mada, Sekip Utara, Yogyakarta 55281, Indonesia*

[4]*Department of Pharmaceutical Chemistry, Faculty of Pharmacy, Universitas Gadjah Mada, Yogyakarta 55281, Indonesia*

**** Corresponding author:***

tel: +62-85643929723
email: nugroho_ae@ugm.ac.id

Received: July 27, 2021
Accepted: October 10, 2021

DOI: 10.22146/ijc.67981

Abstract: *The study aims to analyze the potential Herb-Drug Interactions (HDIs) of the chemical compound in* Andrographis paniculate *Burm. f. against Constitutive Androstane Receptor (CAR) and Pregnane X Receptor (PXR). The 1XVP and 1SKX obtained from the Protein Data Bank (PDB) were used as the targeted protein. The molecular docking analysis was done using the Molecular Operating Environment (MOE) and molecular dynamics simulation using Gromacs. The results of the docking analysis showed that 14-Deoxy-11,12-didehydroandrographolide had the strongest binding energy (1XVP-21.0998 Å) with the Arene-H binding type on Tyr326 and Andrographidine A had the strongest binding energy (1SKX-24.7363 Å) with the Arene-H binding type on Trp299. While Andrographolide is the major component, it also has a high affinity for the two PDB IDs (1XVP-17.4044 Å and 1SKX-21.8881 Å). Based on the RMSD value, the radius of gyration (Rg), and MM/PBSA on molecular dynamic simulations, it shows that the ligand and protein complex as a whole can bind strongly to amino acid residues at the active site. The complex also has sufficient stability and good affinity. Therefore, this study can predict the mechanism in HDIs, especially in CYP 450 expression through the activation pathways of CAR and PXR receptors.*

Keywords: Andrographis paniculata*; CAR; PXR; 1XVP; 1SKX*

■ INTRODUCTION

Herb-drug interaction (HDI) is one type of interaction that can cause problems in therapy. Herbal products contain secondary metabolites that have several pharmacological activities. Therefore, the concurrent use of herbal products with conventional drugs can cause Herb-Drug pharmacodynamic and pharmacokinetic interactions at risk of causing adverse effects [1-2]. Interactions between herbs and drugs in the pharmacokinetics phase, particularly metabolism, have been shown to have a substantial impact. For example, plasma, tissue, and urine drug levels can be affected by interactions with herbs with drug-metabolizing enzyme complexes (cytochrome P450) [3-4].

Constitutive Androstane Receptor (CAR) and Pregnane X Receptor (PXR) are a group of nuclear receptors (orphan nuclear receptor subfamily) that play a role in the expression of several metabolizing enzymes [5]. CAR and PXR have several cytochrome P450 gene targets such as CYP3A1, CYP3A4, CYP3A5, CYP3A7, CYP2A6, CYP2B6, CYP2C8, CYP2C9, CYP2C19, CYP4F12, CYP27A1, as well as phase 2 conjugate enzymes (UGT-UG1, UGT1, UGT1A4, UGT1A6, and UGT1A9), sulfotransferases (Sult2a1), glutathione S-transferases (Gsta2 and GSTA4), and carboxylesterases

which play an essential role in the process of drug metabolism [6-7]. Thus, changes in the expression of drug metabolism genes mediated by CAR/RXR and PXR/RXR heterodimers can cause serious drug-drug/herb-drug interactions by enhancing the metabolism of other drugs [8].

Sambiloto (*Andrographis paniculata* Burm. f.) is a widely used plant as traditional medicinal in Asian countries such as China, Japan, Malaysia, Bangladesh, India, Thailand, and Indonesia [9]. The pharmacological effects of this plant include anti-inflammatory, antimalarial, antiviral, antibacterial, immune-suppressive, cardio and hepatoprotective, antidiabetic, antiobesity, and anticancer [10-12]. Herb-drug interactions have been observed when Sambiloto is used as a supplementary therapy with medicinal components. Based on previous studies, several characteristics of pharmacokinetics and pharmacological activities of several drugs such as theophylline, etoricoxib, and naproxen experienced significant changes after being combined with Sambiloto extract [13-15]. Sambiloto extracts and Andrographolide have proven to inhibit the kinetics of the CYP2E1 enzyme and reduce the expression of CYP2C and CYP3A proteins [16-19]. In contrast, the content of 14-Deoxy-11,12-didehydroandro-grapholide in Sambiloto was also reported to inhibit the expression of CYP3A4 protein [20].

Scientific evidence based on *in vitro* and *in vivo* test results from the active compounds of the Sambiloto plant shows that it has the potential to cause interactions if used together with drugs, especially in the metabolic phase involving the CYP 450 enzyme. The chemical compound in Sambiloto includes Andrographolide, Neoandrographolide, 14-Deoxyandrographolide, 14-Deoxy-11,12-didehydro-andrographolide, Andrographiside, Andrographidine A, and derivatives of other compounds are thought to play a role in determining its pharmacological activity and herb-drugs interaction [12,21-22]. The secondary metabolite in Sambiloto is thought to have the potential to cause interactions with several drugs considering their high use in the community. Still, it is not known as the mechanism of involvement of the CAR and PXR receptors. Based on the literature study, there was no study of the mechanism of chemical substances in Sambiloto on the activation of CAR and PXR receptors. The *in silico* study using molecular docking will predict the binding energy between chemical constituents of Sambiloto with CAR and PXR receptors.

In silico studies using CAR and PXR receptor targets have been widely used to predict drug-drug interactions or herb-drug interactions. Several isolated compounds from Chinese herbal medicines have been proven to activate the regulation of PXR (2QNV) and CYP3A4 through an *in silico* docking molecular study similar to the results of in vitro studies on HepG2 and Huh7 cells [23]. The metabolic mechanisms in CAR and PXR receptor activation pathways using molecular docking studies can predict molecular mechanisms on the animal study [6,24,25]. The results from molecular docking were then evaluated using molecular dynamics simulations to investigate stability, hydrogen bond occupancy, and binding free energy of ligands and proteins in an aqueous system. The results of this study are expected to be used to predict the mechanism of herb-drug interaction through the CAR-PXR receptor activation pathway.

■ EXPERIMENTAL SECTION

Materials

The target CAR (Constitutive Androstane Receptor) PDB IDs in the study are 1XVP (Complex of Human CAR/RXR heterodimer bound with CITCO) and 1XV9 (Complex of Human CAR/RXR heterodimer bound with SRC1 peptide, fatty acid, and 5b-pregnane-3,20-dione).

The PDB IDs are PXR (Pregnane X Receptor) receptors such as 1SKX (Complex of Human PXR and the Macrolide Antibiotic Rifampicin); 2QNV (Pregnane X Receptor bound to Colupulone); 3R8D (Human Nuclear Xenobiotic Receptor PXR by the Reverse Transcriptase-Targeted Anti-HIV Drug PNU-142721); 4NY9 (Human PXR-LBD In Complex with N-{(2R)-1-[(4S)-4-(4-chloro phenyl)-4-hydroxy-3,3-dimethylpiperidin-1-yl]-3-methyl -1-oxobutan-2-yl}-3-hydroxy-methyl butanamide). All of the PDB IDs were obtained from the protein data bank website (https://www.rcsb.org/).

The ligands used in this study were 11 chemical constituents from Sambiloto (Table 1), agonist ligand

1XVP (Phenytoin) dan agonist ligand 1SKX (hyperforin) collected from Pubchem, then drawn on Chemdraw Ultra 12.0.

Instrumentation

In silico molecular docking studies using Molecular Operating Environment (MOE) version 2010.10 (developed by Chemical Computing Group Inc, Canada), operated using HP 13-AN1033TU Notebook Windows 10 Home with an Intel® Core ™ i3-1005G1 processor with 512 GB SSD storage capacity and 8 GB memory. Molecular dynamics simulation to the molecular docking the result used AnteChamber PYthon Parser interfacE (ACPYPE), Gromacs 2016.3, g_mmpbsa package, and VMD 1.9.3 [26,27], which is operated using a computer with Intel (R) Core i5-8500 CPU@4.30GHz (6 CPUs) processor, 4096 MB RAM, 2 TB hard drive, 120 GB solid-state drive, NVIDIA GeForce GTX 1080 Ti.

Procedure

Ligands preparation

The chemical structures from Phenytoin (Agonist CAR receptor), Hyperforin (Agonist PXR receptor), and chemical constituents of *Andrographis paniculata* Burm. f. were drawn using the builder feature in MOE. First, the hydrogen atom was added with protonate 3D and charged with partial charges, and then the energy was minimized to give the most stable conformation.

Preparation of CAR and PXR receptor

All crystal structures for molecular docking were prepared using MOE software. The protein structure was prepared by removing the water molecule and adding hydrogen atoms with protonate 3D, being charged with partial charges, and correcting errors by quick-prep on the structure of each protein ID.

Validation of docking method

The validation of the docking method was begun by finding the binding target in the specific area of the CAR and PXR receptor target proteins, respectively. The validation process was based on the Root Mean Square Deviation (RMSD) value. The RMSD value is < 2 Å to ensure the best docking position between the ligand and the protein. Each CAR and PXR receptor ID obtained from PDB validity was tested by using the native ligand from each receptor at different positions. Each position was replicated ten times to get RMSD values less than 2 Å. Placement methods from the molecular docking with MOE software using *Triangle Mather*, refinement method using *forcefield*, and scoring method using *London DG* are selected to optimize the docking method that produces the best RMSD value.

Molecular docking analysis

Molecular docking of constituents of *Andrographis paniculata* Burm. f. (Table 1) and the receptor agonist was carried out at proper binding positions of target receptors. Observation of the ligand poses to predict interactions, binding modes, and overlapping structures and the docking score to estimate affinity was used in the research. The molecular docking score describes the strength of the interaction between the ligand and the receptor and can predict the quantity of bond energy. The lower the binding energy value from the molecular docking results, the more stable and more robust the bond between the ligand and the receptor can describe the higher affinity for the ligand to its target receptor [28-29].

Molecular dynamics simulation

The AMBER14SB force field was used to describe the protein in this molecular dynamics study. The ligand parameterization and calculation of the long-range electrostatic force employed the AnteChamber PYthon Parser interface (ACPYPE) and Particle Mesh Ewald method, respectively [27]. The system from molecular dynamics was neutralized by adding $Na^+$and Cl^- ions. These systems were solvated in explicit TIP3P water model.

Berendsen thermostats and barostats are used during the heating stage, with the pressure being maintained at 1 bar. The simulation steps included minimization until 500000 steps, heating until 310 K, temperature equilibration (NVT) in 500 ps, pressure equilibration (NPT) in 500 ps, and a production run with a 2 fs time step for 100 ns. Data analysis has been carried out in the form of Root Mean Square Deviation (RMSD), Root Mean Square Fluctuation (RMSF), Radius

Table 1. Chemical constituents of *Andrographis paniculata* taken by ChemDraw Ultra 12.0.2.1076 [9]

No	Compound	Structure	No	Compound	Structure
1	14-Deoxy-11,12-didehydroandrographolide	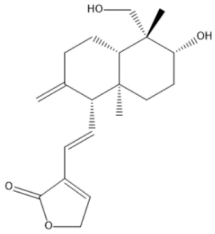	7	Andrographidine A	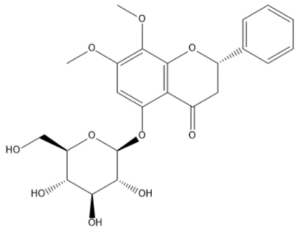
2	14-Deoxy-11-hydroxyandrographolide	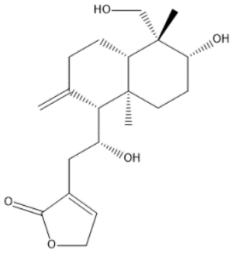	8	Andrographidine C	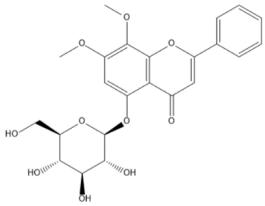
3	14-Deoxy-12-hydroxyandrographolide	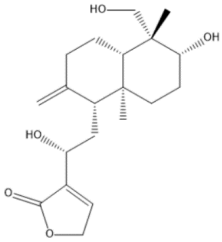	9	Andrographolactone	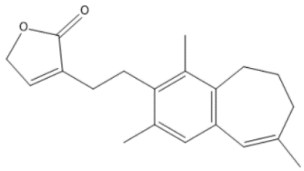
4	14-Deoxyandrographolide	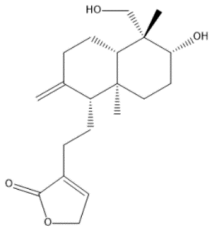	10	Andrographolide	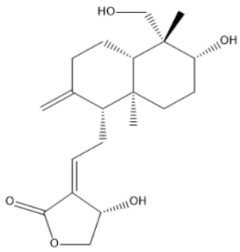
5	8,17-Epoxy-14-Deoxyandrographolide	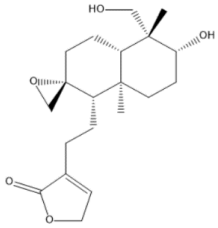	11	Neoandrographolide	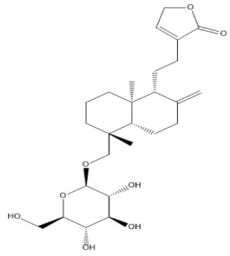
6	Andrograpanin	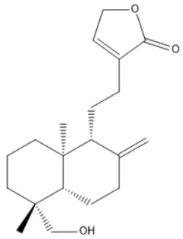			

of Gyration (Rg), Solvent-Accessible Surface Area (SASA), Radial Distribution Function (RDF), and hydrogen bond analysis (HBond).

MM/PBSA calculation

MM/PBSA calculation was performed using the g_mmpbsa within the Gromacs 2016.3 software [26]. Polar desolvation energy was calculated with the Poisson-Boltzmann equation with a grid size of 0.5 Å. The dielectric constant of the solvent was set to 80 to represent water as the solvent. The non-polar contribution was determined by calculating the solvent-accessible surface area (SASA) with the radii of the solvent as 1.4 Å. Finally, the binding free energy of the complex was determined based on 50 snapshots taken from the beginning to the end of the molecular dynamics simulation trajectories of the complex.

■ RESULTS AND DISCUSSION

The docking results of several PDB IDs for the CAR (1XVP & 1XV9) and PXR (1SKX, 2QNV, 3R8D, & 4NY9) receptors showed that 1XVP, 1SKX, and 4NY9 had the criteria for the RSMD value < 2 Å. The RMSD value according to these criteria indicated that the ligand position did not change significantly after the docking procedure. Based on the docking score, 1XVP and 1SKX have the best scores. The negative value shows intense binding energy and describes the greater affinity between the ligand and protein (Table 2). Thus, there are 1XVP and 1SKX, which have been selected for molecular docking studies with the chemical compounds in Sambiloto.

CITCO (native ligand of 1XVP) is the activator of human CAR. CITCO induce the expression of several phases 1 metabolizing enzymes (CYP2B6, CYP3A4, CYP2B6) and Phase II conjugation genes such as (SULT1A1, GSTA2, MDR1) [30]. Rifampicin is the native ligand of the ID 1SKX Protein, PXR receptor agonist, and an activator of some genes phase I and II metabolizing enzymes. Rifampicin targets the activation of the metabolizing enzyme gene through the PXR pathway, including CYP2B6, CYP2C8, CYP2C9, CYP2C19, CYP3A4, UGTs, and GSTs [31]. The macrolide ring in Rifampicin binds via several amino acids 178–209 and 229–235 on PXR ligand-binding pockets [32]. These amino acids are appropriate with the docking analysis for validating Rifampicin as a native ligand bound to the amino acids Phe 288 and Trp299 from 1SKX.

The molecular docking of Sambiloto chemical compounds on 1XVP and 1SKX proteins (Table 3) indicates that all compounds have an affinity for one or both proteins, as indicated by the more negative values of binging energy. Binging energy or docking score shows the strength of the bond between the ligand and the macromolecule or protein. The negative value binding energy indicates the solid and stability of the binding

Table 2. Result of the docking procedures validation for several PDB IDs of CAR and PXR receptor with native ligand

Receptor	PDB ID	Co-crystallized Ligand (native ligand)	Docking Score	RMSD (Å)	Ligand Atom	Amino Acid	Binding type	Distance (Å)
CAR	1XVP	CITCO	-29.3242	1.3640	C	Phe234	Arene-H	3.96
					C	Phe217	Arene-H	3.91
	1XV9	5b-pregnane-3,20-dione	-	-	-	-	-	-
PXR	1SKX	Rifampicin	-33.9689	1.2470	C	Phe288	Arene-H	4.10
					C	Trp 299	Arene-H	3.88
					C	Trp 299	Arene-H	3.60
	2QNV	Colupulone	-17.7709	5.4224	-	-	-	-
	3R8D	PNU-142721	-22.5619	6.9041	C	Phe288	Arene-Arene	3.85
	4NY9	N-{(2R)-1-[(4S)-4-(4-chlorophenyl)-4-hydroxy-3,3-dimethylpiperidin-1-yl]-3-methyl-1-oxobutan-2-yl}-3-hydroxy-methylbutanamide	-24.7378	1.1088	C	Leu240	Arene-H	4.48

Table 3. Molecular docking results of *Andrographis paniculata* chemical compound against protein 1XVP and 1SKX

No	Compound	1XVP					
		Docking Score	RMSD-Refine (Å)	Ligand Atom	Amino Acid	Binding type	Distance (Å)
1	14-Deoxy-11,12-didehydroandrographolide	-21.0998	1.4344	C	Tyr326	Arene-H	4.40
2	14-Deoxy-11-hydroxyandrographolide	-13.5205	0.5966	C	Tyr326	Arene-H	3.95
3	14-Deoxy-12-hydroxyandrographolide	-15.6392	0.8061	C	Tyr224	Arene-H	3.48
4	14-Deoxyandrographolide	-11.5683	1.4049	C	Phe234	Arene-H	4.14
5	8,17-Epoxy-14-Deoxyandrographolide	-15.9161	1.5090	C	Tyr224	Arene-H	3.48
6	Andrograpanin	-12.3822	1.1631	C	Phe234	Arene-H	3.96
7	Andrographidine A	-9.9899	1.0956	C	Leu206	Arene-H	3.82
8	Andrographidine C	-9.1853	1.8843	C	Phe161	Arene-H	4.34
				O	Phe161	Arene-H	3.99
9	Andrographolactone	-17.3880	1.7166	C	His203	Arene-H	3.92
10	Andrographolide	-17.4044	1.6933	C	Tyr326	Arene-H	4.61
11	Neoandrographolide	15.3878	1.1199	C	Tyr 224	Arene-H	3.82
12	Agonist ligand	-18.6943	1.2352	N	Phe217	Arene-H	4.15
				C	Phe161	Arene-H	3.97

Table 3. Molecular docking results of *Andrographis paniculata* chemical compound against protein 1XVP and 1SKX (*Continued*)

No	Compound	1SKX					
		Docking Score	RMSD-Refine (Å)	Ligand Atom	Amino Acid	Binding type	Distance (Å)
1	14-Deoxy-11,12-didehydroandrographolide	-19.1904	1.5274	C	Phe288	Arene-H	4.32
				C	Trp299	Arene-H	4.39
2	14-Deoxy-11-hydroxyandrographolide	-22.7215	1.7104	C	Trp 299	Arene-H	3.88
				C	Phe288	Arene-H	3.71
3	14-Deoxy-12-hydroxyandrographolide	-19.8710	2.3171	C	Trp 299	Arene-H	4.27
				C	Phe288	Arene-H	4.46
4	14-Deoxyandrographolide	-21.6525	1.8951	C	Phe288	Arene-H	4.43
				C	Phe288	Arene-H	3.67
				C	Trp299	Arene-H	3.88
5	8,17-Epoxy-14-Deoxyandrographolide	-20.9802	3.7858	C	Trp 299	Arene-H	3.88
				C	Phe288	Arene-H	3.84
6	Andrograpanin	-19.1204	3.4365	C	Trp 299	Arene-H	4.00
				C	Phe288	Arene-H	4.37
7	Andrographidine A	-24.7363	1.8460	O	Trp 299	Arene-H	3.11
8	Andrographidine C	-24.4739	2.8105	O	Phe420	Arene-H	3.91
				C	Phe288	Arene-H	3.78
				C	Leu324	Arene-H	4.11
9	Andrographolactone	-21.0887	2.0251	C	Trp299	Arene-H	3.70
				C	Tyr306	Arene-H	3.60
10	Andrographolide	-21.8881	1.9172	C	Trp299	Arene-H	3.79
11	Neoandrographolide	-21.6999	1.9530	C	Phe288	Arene-H	3.47
				C	Tyr 306	Arene-H	3.74
12	Agonist ligand	-15.5579	1.5085	C	Trp 299	Arene-H	4.35

formed between the ligand and the receptor on the macromolecule [26,33].

Each compound has explicitly binding sites on the amino acid target protein on Phe 234; Phe217 (1XVP), and the binding site on Phe288; Trp 299; Trp 299 (1SKX). 14-Deoxyandrographolide and Andrograpanin have bonded to Phe 234, such as the 1SKX native ligand on the C atom (Arene-H), while the Agonist ligand (Phenytoin) binds explicitly to N-Phe217 and Phe 161 (Arene-H) (Fig. 1 and 2). The compound 14-Deoxy-11,12-didehydro-andrographolide and Andrographolide had the most potent binding energy value against 1XVP. The lactone rings present in these two compounds play a role in determining the bond with Tyr326 in the 1XVP protein.

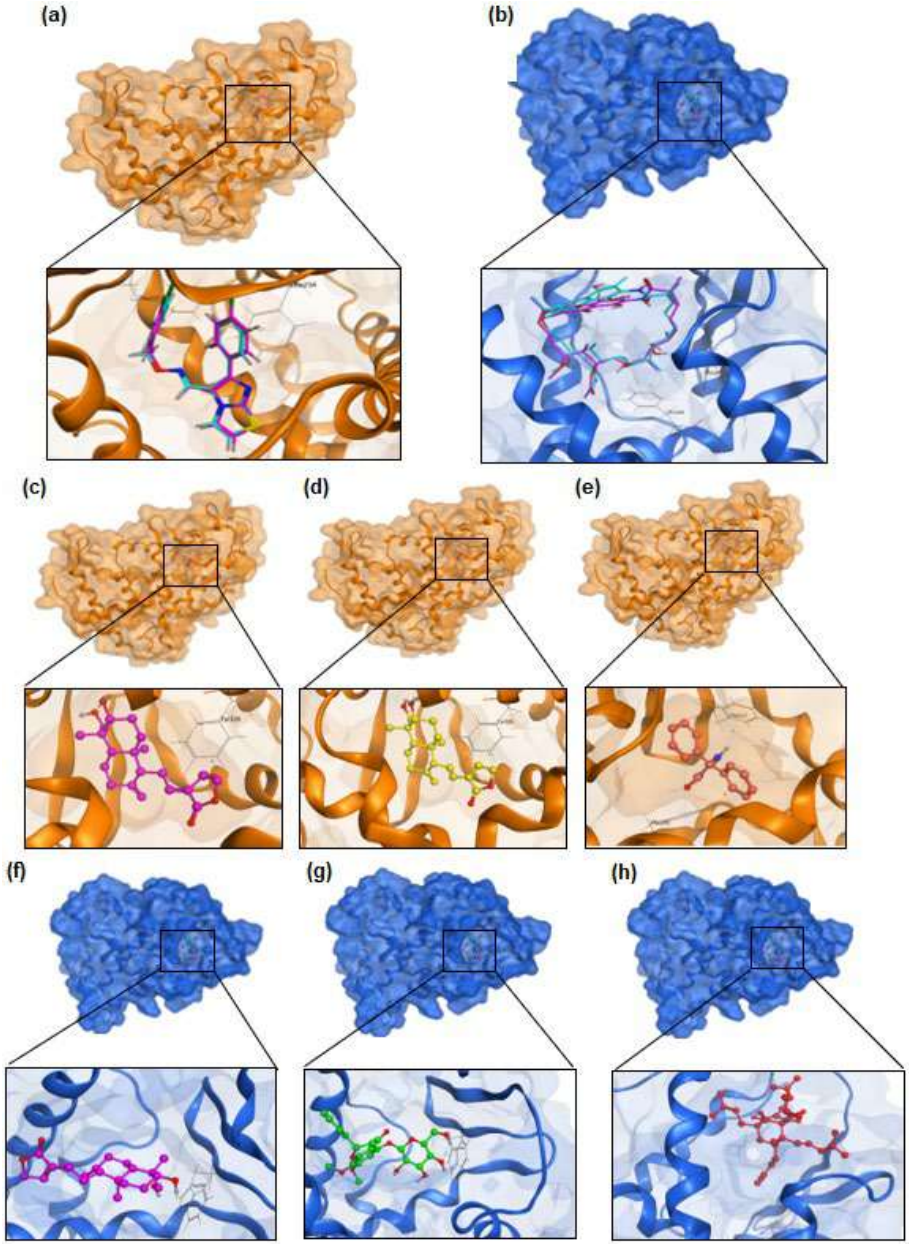

Fig 1. 3D-Conformation ligand position redocking with the proposed procedure: (a) 1XVP with CITCO (RMSD:1.364 Å) and; (b)1SKX with Rifampicin (RMSD: 1.247 Å) and ligand interaction Sambiloto chemical constituent to 1XVP and 1SKX using MOE. 1XVP-Andrographolide (c); 1XVP- 14-Deoxy-11,12-didehydroandrographolide (d); 1XVP agonist (e); 1SKX-Andrographolide (f); 1SKX- Andrographidine A (g); 1SKX-Agonist (h)

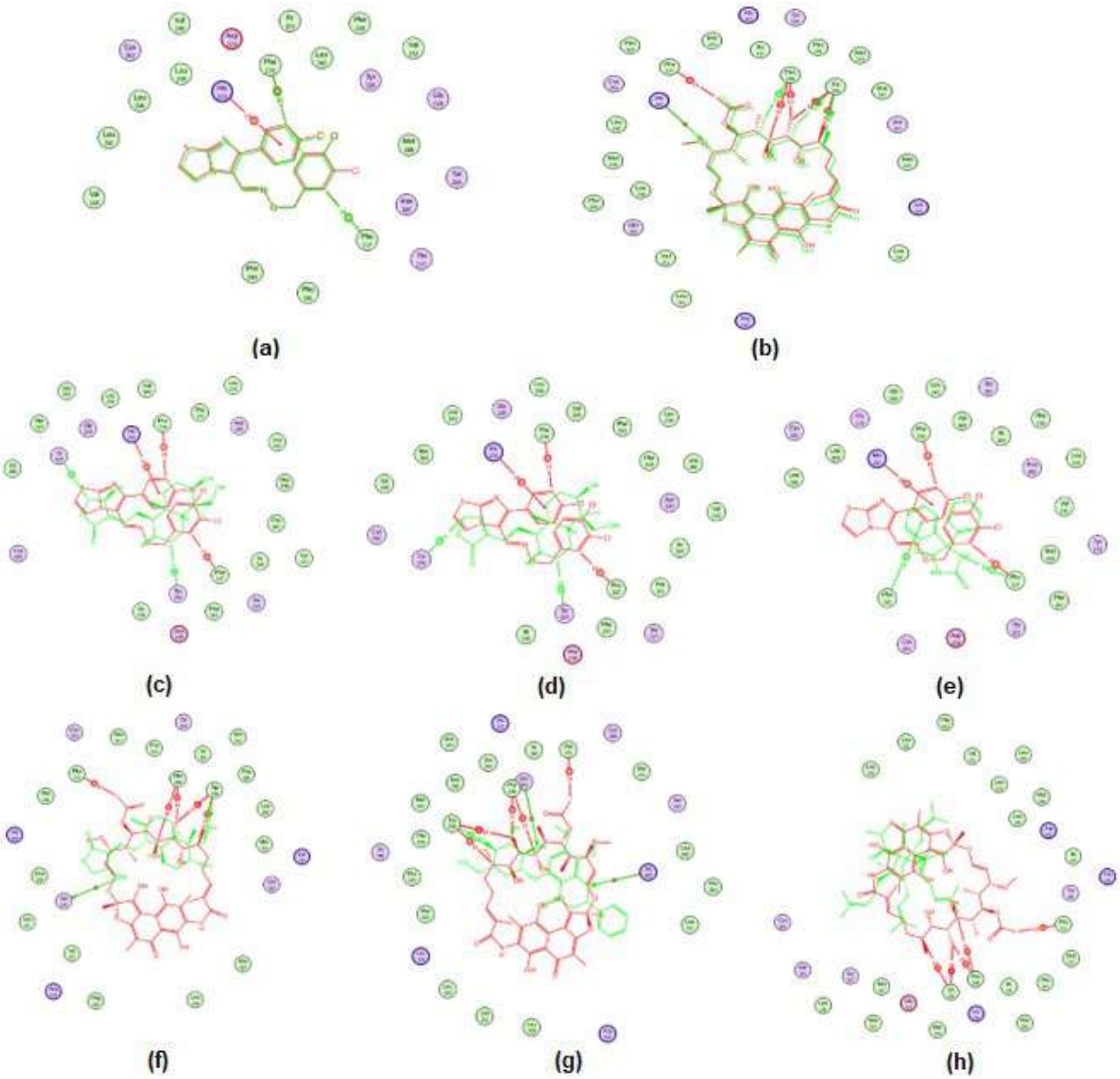

Fig 2. 2D-Conformation Ligand Position redocking with the proposed procedure: (a) 1XVP CITCO and; (b) 1SKX with Rifampicin, and ligand Interaction Sambiloto Chemical Constituent to 1XVP and 1SKX using MOE. 1XVP-Andrographolide (c); 1XVP- 14-Deoxy-11,12-didehydroandrographolide (d); 1XVP agonist (e) 1SKX-Andrographolide (f)1SKX- Andrographidine A (g) 1SKX-Agonist (h)

Even though it binds to the same amino acid residue, the binding energy of the Andrographolide is weaker than that of 14-Deoxy-11,12-didehydroandrographolide. Adding a hydroxyl group (–OH) to the lactone ring causes a decrease in the amount of Andrographolide binding energy in the protein.

14-Deoxyandrographolide and Andrograpanin compounds have lower bond energies compared to the two previous compounds. However, both bind to the same amino acid as the native 1XVP ligand, namely the amino acid Phe234. In contrast, 14-Deoxy-11,12-didehydroandrographolide and Andrographolide do not attach to amino acids bound by native ligands. The different types of amino acids in 1XVP that bind to the compound structure of the Sambiloto plant indicate a difference in the binding sites between these compounds

and the native ligand. However, the affinity with 1XVP is quite strong, considering that the binding energy value is different from the native ligand. The chemical compound of the Sambiloto plant has been shown to have an affinity for the PXR receptor, especially for the 1SKX protein, which is indicated by its strong binding energy value and binds to one or two of the same amino acids as the native ligand, namely Phe288 and Trp299. Furthermore, Andrographidine A is proven being the most potent binding energy against 1SKX in Trp299 amino acid. Andrographolide, the main compound in the Sambiloto plant, also binds to the same amino acid as the native ligand, Trp299.

Molecular dynamics simulation aims to identify the stability of the molecular interactions of each complex system by using the initial conformation of the molecular docking simulation results. Molecular dynamics captures the position and mobility of each atom at every second of time, allowing it to describe the behavior of proteins and other biomolecules in atomic detail. In addition, molecular dynamics simulations can be carried out under controlled conditions (initial protein

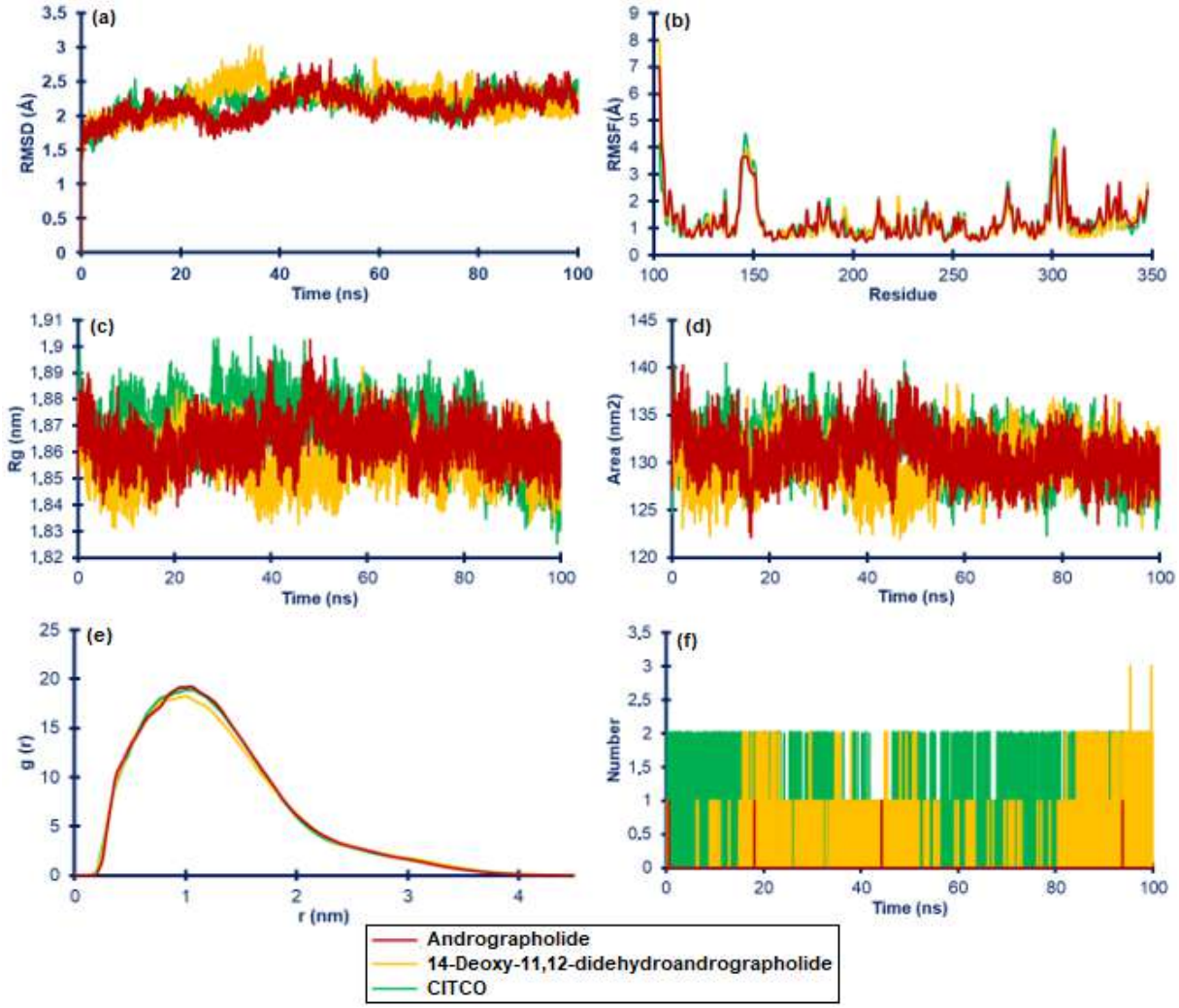

Fig 3. The molecular dynamics simulation results of complex Andrographolide, 14-Deoxy-11,12-didehydroandrographolide, and CITCO as native ligand with 1XVP. Root Mean Square Deviation (RMSD) (a); Root Mean Square Fluctuation (RMSF) (b); Radius of Gyration (Rg) (c); Solvent-Accessible Surface Area (SASA) (d); Radial Distribution Function (RDF) (e); and hydrogen bond analysis (HBond) (f)

conformation, bound ligand, post-translational mutation or modification, protonation state, temperature, and the voltage across the membrane) [34-35]. Based on snapshots taken at the beginning complex simulation with 1XVP and 1SKX (simulation), all compounds are rotated and translated during the simulation. Still, significant changes were shown by the 14-Deoxy-11.12-didehydroandrographolide-1XVP and Andrographolide-1SKX. These two compounds fluctuated and began to move away from the area of the active site of binding to the receptor macromolecule. The interaction dynamics between the compound and the target macromolecule were studied using molecular dynamics simulation in an explicit solvent. Strong affinity tends to reduce the movement of bound atoms and will generally stabilize the active site of the receptor macromolecule [34,36]. This phenomenon can be analyzed by calculating the RMSD value of the target macromolecule during a 100 ns simulation to ensure the stability and rationality of the selected conformation. The RMSD graphs in Fig. 3 and 4 show that 14-Deoxy-11,12-didehydroandrographolide-1XVP (2.22 Å); Andrographolide-1XVP (2.19 Å) and Andrographolide-1SKX (3.80 Å); Andrographidine A-1SKX (3.13 Å) experienced significant fluctuations during the simulation. However, the RMSF graph shows a difference in results with the RMSD graph; the average

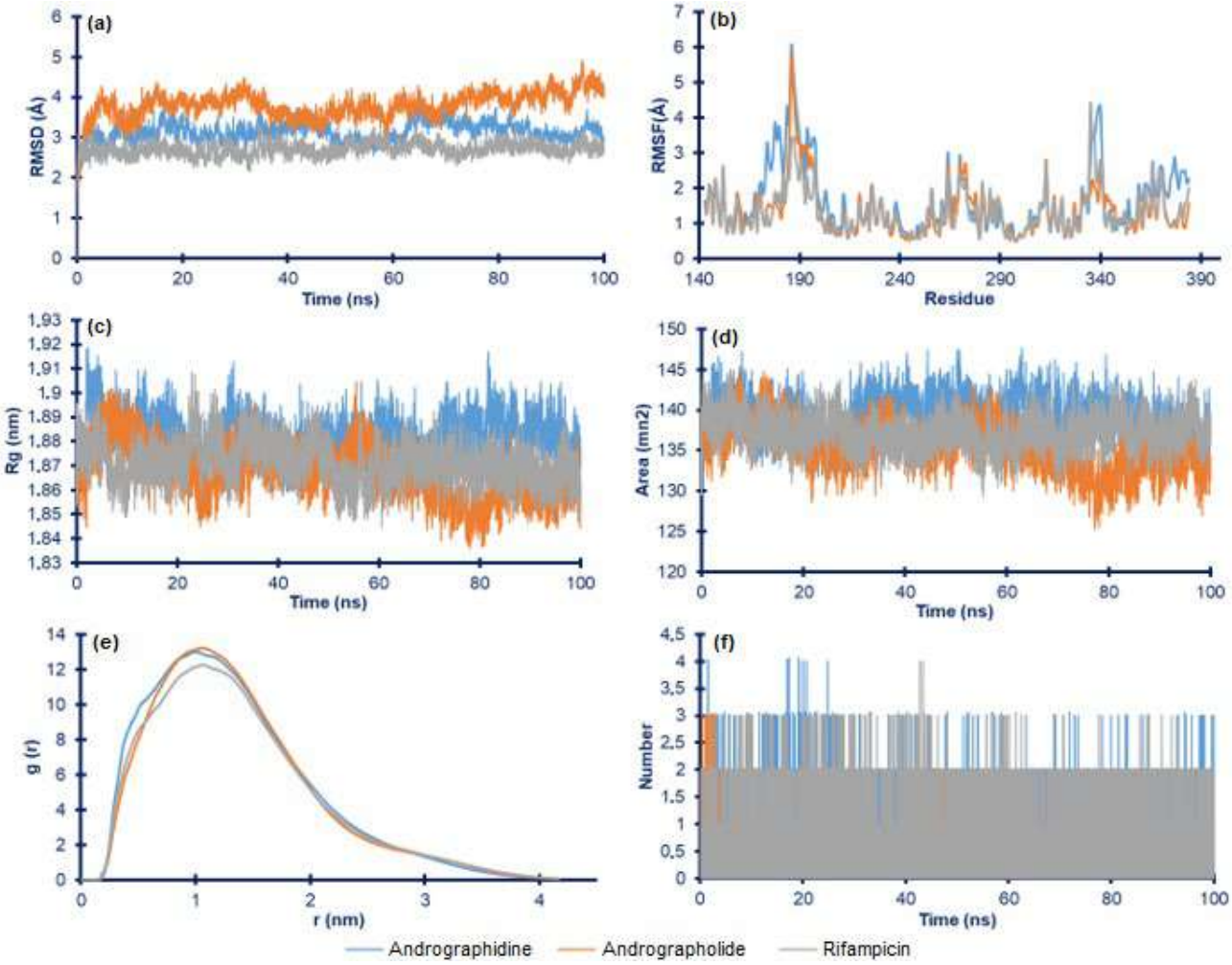

Fig 4. The molecular dynamics simulation results of complex Andrographidine A, Andrographolide, and Rifampicin as native ligand with 1SKX. Root Mean Square Deviation (RMSD) (a); Root Mean Square Fluctuation (RMSF) (b); Radius of Gyration (Rg) (c); Solvent-Accessible Surface Area (SASA) (d); Radial Distribution Function (RDF) (e); and hydrogen bond analysis (HBond) (f)

RMSF value of Andrographolide-1XVP (1.26 Å) and Andrographidine A-1SKX (1.64 Å) indicated the stability of the protein-ligand complex interaction, and the average value of the entire complex system can bind strongly with amino acid residues at the active site of binding of the receptor macromolecule [37].

Furthermore, identification of the radius of gyration (Rg) is carried out to determine the stability of the complex, whether the complex system is stable in folded or unfolded form during the simulation. The Rg value indicates an insignificant difference from the overall complex system. Observations on solvent-accessible surface area (SASA) were also carried out to predict the extent to which receptor macromolecules undergo conformational changes during simulations that are accessible to water molecules [38-39]. The results of the SASA analysis showed that Andrographolide-1XVP had a fairly high value of 131.21 nm^2, and Andrographidine A-1SKX had a higher average SASA value than other compounds, which was 139.44 nm^2. Then evaluation was carried out on the effect of each parameter variation on atomic density or probability at a certain radius using the radial distribution factor (RDF) (Fig. 3 and 4), which will illustrate the distribution of a molecule around another molecule giving the possibility of finding atomic pairs located at a distance of "r" [40-42]. The RDF value from 14-Deoxy-11,12-didehydroandrographolide-1XVP (6.27 g(r)) and Andrographolide-1XVP (6.23 g(r)) not much different with native ligand CITCO (6.26 g(r)). These results also occur in 1SKX complex (Andrographolide-1SKX (4.87 g(r)); Andrographidine A-1SKX (5.03 g(r)); and Rifampicin (4.73 g(r)). The results of H-bond calculations during the simulation showed fluctuations around amino acid residues located at the active binding site of receptor macromolecules. Then calculate the number of hydrogen bonds between the test compound and receptor macromolecules during the molecular dynamics simulation. The high percentage of hydrogen bonds and hydrogen bond occupancy from this study indicates stability (Table 4). Total hydrogen bond and hydrogen bond occupancy determine the stability of each system and are the keys to the interaction stabilization of the protein-ligand complex [43].

Based on the MM/PBSA calculations results, all complexes with 1XVP and 1SKX showed good affinity. However, CITCO and Rifampicin as native ligands of each protein still had the best affinity, as indicated by the high value of total binding energy (ΔGbind) represented in Table 5. The energies that contribute the most during the simulation are van der Waals, electrostatic, and non-polar interactions. This phenomenon is because the MM/PBSA approach allows the observation of van der Waals effects, electrostatic contributions, and changes in ligand-receptor affinity that are affected by the solvation process in complex systems [27,34,43].

Sambiloto chemical compound is a substrate of CYP450, which can act as an enzyme inductor or inhibitor. The inductor or inhibitor of the CYP450 enzyme can lead to potential herb-drug interactions when used in conjunction with conventional drugs. Based on *in silico* absorption, distribution, metabolism, and excretion (ADMET) analysis, Andrographolide, Neoandrographolide, 14-Deoxyandrographolide, and Andrographiside are substrates of CYP450, and most of them are absorbed through intestinal/positive HIA (Human Intestinal Absorption) scores [44]. Meanwhile, the SwissADME prediction study results show that deoxyandrographolide is a CYPD6 inhibitor, and Andrographolactone is an inhibitor of CYP2C9 [45]. Furthermore, *in vitro* studies show that Andrographolide

Table 4. Hydrogen bond occupancy

PDB ID	Active Compound	Occupancy (%)
1XVP	Andrographolide	59.14 %
	14-Deoxy-11,12-didehydroandrographolide	34.48 %
	CITCO	0.04 %
1SKX	Andrographidine A	76.67 %
	Andrographolide	24.34 %
	Rifampicin	74.97 %

Table 5. Free bonding energy during molecular dynamics simulation

PDB ID	Active Compound	ΔE_{vdw} (kJ/mol)	ΔE_{ele} (kJ/mol)	ΔG_{PB} (kJ/mol)	ΔG_{NP} (kJ/mol)	ΔG_{Bind} (kJ/mol)
1XVP	Andrographolide	−217.66	−26.69	125.72	−19.31	−137.94
	14-Deoxy-11,12-didehydroandrographolide	−211.21	−16.92	98.93	−18.80	−147.99
	CITCO	−228.58	−8.41	107.43	−20.36	−149.93
1SKX	Andrographidine A	−224.45	−53.52	161.16	−22.54	−159.35
	Andrographolide	−108.34	−32.49	119.40	−18.44	−108.86
	Rifampicin	−335.15	−46.52	172.72	−31.16	−240.11

ΔE_{vdw} = van der Waals contribution
ΔE_{ele} = electrostatic contribution
ΔG_{PB} = polar contribution of desolvation
ΔG_{NP} = non-polar contribution of desolvation

Table 6. *In vitro* activity of cytochrome P450s expression from *Andrographis paniculata* Burm. f. active compound

No	Active Compound	Expression Cytochrome P450s		Reference
		Increased	Decreased	
1	Andrographolide	nd	(CYP1A2, CYP2D6, CYP3A4)[*1]	[20]
		nd	(CYP3A4)[*2]	[19]
		nd	(CYP3A, CYP2C)[*3]	[17]
2	14-Deoxy-11,12-didehydroandrographolide	nd	(CYP1A2, CYP2D6, CYP3A4)[*1]	[20]
3	Andrographidine A	nd	nd	

[*1] protein expressions of cytochrome P450s in HepG2 hepatoma cells
[*2] protein expressions of cytochrome P450s in modified Caco-2 cells
[*3] hepatic cytochrome P450 mRNA expression on human hepatocyte cultures
[nd] means no data

plays a significant role in herb-drug interactions by inhibiting several CYP450 enzyme families (Table 6). This fact is consistent with the results of molecular docking analyses on CAR and PXR that Andrographolide has high binding energy in the two target proteins.

As the primary compound in Sambiloto, Andrographolide is known to play a role in determining pharmacological activity and potential herb-drug interaction. This interaction is widely evidenced in the antidiabetic activity of the bitter herb extract and Andrographolide which has been shown to have antihyperglycemic activity in a rat model of type 2 diabetes by repairing pancreatic beta cells and increasing GLUT-4 translocation [46-47]. The combination of Andrographolide with several oral antidiabetic drugs such as metformin, glimepiride, and glyburide can increase the antihyperglycemic effect compared to a single administration, which is in line with the increase in pharmacokinetic parameters C_{max} and AUC [48]. In addition, Andrographolide can change the pharmacokinetic parameters of other drugs such as etoricoxib by lowering C_{max}, AUC, TT values and increasing Vd and CL, which affect the anti-inflammatory activity of etoricoxib [14]. The pharmacokinetic profile and pharmacological action of Naproxen and Warfarin also changed due to co-administration with Andrographolide [13,49].

■ CONCLUSION

Based on *in silico* studies, it is proven that the compounds in Sambiloto (*Andrographis paniculata* Burm. f.), especially 14-Deoxy-11,12-didehydroandrographolide, Andrographidine A, and Andrographolide had the most potent binding energy for the nuclear receptors (CAR and PXR). Furthermore, molecular dynamics simulations show that all complexes of these compounds and receptors have good affinity and are sufficient stability. Therefore, although

it must be proven through *in vitro* and *in vivo* studies, this study is adequate to predict the mechanism of herb-drug interactions (HDIs) from Sambiloto to several drug metabolism via CYP450 through the activation pathways of CAR and PXR receptors.

ACKNOWLEDGMENTS

The author would like to acknowledge the funding support for molecular docking analysis from UGM No. 49.01.02/UN1/FFA1/SET.PIM/PT/2021 and molecular dynamics simulation from UGM No. 3143/UN1.P.III/DIT-LIT/PT/2021.

AUTHOR CONTRIBUTIONS

Elza Sundhani, Agung Endro Nugroho, Arief Nurrochmad, Endang Lukitaningsih conducted the experiment. Elza Sundhani wrote the manuscript and conducted the scoring docking analysis and simulation of dynamical molecules. Agung Endro Nugroho, Arief Nurrochmad, and Endang Lukitaningsih supervision of the experimental and revised the manuscript. All authors agreed to the final version of this manuscript.

REFERENCES

[1] Awortwe, C., Makiwane, M., Reuter, H., Muller, C., Louw, J., and Rosenkranz, B., 2018, Critical evaluation of causality assessment of herb-drug interactions in patients, *Br. J. Clin. Pharmacol.*, 84 (4), 679–693.

[2] Fasinu, P.S., Bouic, P.J., and Rosenkranz, B., 2012, An overview of the evidence and mechanisms of herb-drug interactions, *Front. Pharmacol.*, 3, 69.

[3] Showande, S.J., Fayeke, T.O., Kajula, M., Hokkanen, J., and Tolonen, A., 2018, Potential inhibition of major human cytochrome P450 isoenzymes by selected tropical medicinal herbs-Implication for herb-drug interactions, *Food Sci. Nutr.*, 7 (1), 44–55.

[4] Bo, L., Baosheng, Z., Yang, L., Mingmin, T., Beiran, L., Zhiqiang, L., and Huaqiang, Z., 2016, Herb-drug enzyme-mediated interactions, and the associated experimental methods: A review, *J. Tradit. Chin. Med.*, 36 (3), 392–408.

[5] Buchman, C.D., Chai, S.C., and Chen, T., 2018, A current structural perspective on PXR and CAR in drug metabolism, *Expert Opin. Drug Metab. Toxicol.*, 14 (6), 635–647.

[6] Daujat-Chavanieu, M., and Gerbal-Chaloin, S., 2020, Regulation of CAR and PXR expression in health and disease, *Cells*, 9 (11), 2395.

[7] Wang, Y.M., Ong, S.S., Chai, S.C., and Chen, T., 2012, Role of CAR and PXR in xenobiotic sensing and metabolism, *Expert Opin. Drug Metab. Toxicol.*, 8 (7), 803–817.

[8] Lynch, C., Mackowiak, B., Huang, R., Li, L., Heyward, S., Sakamuru, S., Wang, H., and Xia, M., 2018, Identification of modulators that activate the constitutive androstane receptor from the Tox21 10K compound library, *Toxicol. Sci.*, 167 (1), 282–292.

[9] Hossain, M.S., Urbi, Z., Sule, A., and Rahman, K.M.H., 2014, *Andrographis paniculata* (Burm. f.) Wall. ex Nees: A Review of ethnobotany, phytochemistry, and pharmacology, *Sci. World J.*, 2014, 274905.

[10] Kumar, S., Singh, B., and Bajpai, V., 2021, *Andrographis paniculata* (Burm.f.) Nees: Traditional uses, phytochemistry, pharmacological properties and quality control/quality assurance, *J. Ethnopharmacol.*, 275, 114054.

[11] Dai, Y., Chen, S.R., Chai, L., Zhao, J., Wang, Y., and Wang, Y., 2019, Overview of pharmacological activities of *Andrographis paniculata* and its major compound andrographolide, *Crit. Rev. Food Sci. Nutr.*, 59 (Suppl. 1), S17–S29.

[12] Kandanur, S.G.S., Tamang, N., Golakoti, N.R., and Nanduri, S., 2019, Andrographolide: A natural product template for the generation of structurally and biologically diverse diterpenes, *Eur. J. Med. Chem.*, 176, 513–533.

[13] Balap, A., Lohidasan, S., Sinnathambi, A., and Mahadik, K., 2017, Herb-drug interaction of *Andrographis paniculata* (Nees) extract and andrographolide on pharmacokinetic and pharmacodynamic of naproxen in rats, *J. Ethnopharmacol.*, 195, 214–221.

[14] Balap, A., Atre, B., Lohidasan, S., Sinnathambi, A., and Mahadik, K., 2016, Pharmacokinetic and

pharmacodynamic herb-drug interaction of *Andrographis paniculata* (Nees) extract and andrographolide with etoricoxib after oral administration in rats, *J. Ethnopharmacol.*, 183, 9–17.

[15] Chien, C.F., Wu, Y.T., Lee, W.C., Lin, L.C., and Tsai, T.H., 2010, Herb–drug interaction of *Andrographis paniculata* extract and andrographolide on the pharmacokinetics of theophylline in rats, *Chem. Biol. Interact.*, 184 (3), 458–465.

[16] Pan, Y., Abd-Rashid, B.A., Ismail, Z., Ismail, R., Mak, J.W., Pook, P.C.K., Er, H.M., and Ong, C.E., 2011, In vitro determination of the effect of *Andrographis paniculata* extracts and andrographolide on human hepatic cytochrome P450 activities, *J. Nat. Med.*, 65 (3-4), 440–447.

[17] Pekthong, D., Blanchard, N., Abadie, C., Bonet, A., Heyd, B., Mantion, G., Berthelot, A., Richert, L., and Martin, H., 2009, Effects of *Andrographis paniculata* extract and andrographolide on hepatic cytochrome P450 mRNA expression and monooxygenase activities after *in vivo* administration to rats and *in vitro* in rat and human hepatocyte cultures, *Chem. Biol. Interact.*, 179 (2-3), 247–255.

[18] Pekthong, D., Martin, H., Abadie, C., Bonet, A., Heyd, B., Mantion, G., and Richert, L., 2008, Differential inhibition of rat and human hepatic cytochrome P450 by *Andrographis paniculata* extract and andrographolide, *J. Ethnopharmacol.*, 115 (3), 432–440.

[19] Qiu, F., Hou, X.L., Takahashi, K., Chen, L.X., Azuma, J., and Kang, N., 2012, Andrographolide inhibits the expression and metabolic activity of cytochrome P450 3A4 in the modified Caco-2 cells, *J. Ethnopharmacol.*, 141 (2), 709–713.

[20] Ooi, J.P., Kuroyanagi, M., Sulaiman, S.F., Tengku Muhammad, T.S., and Tan, M.L., 2011, Andrographolide and 14-Deoxy-11,12-didehydroandrographolide inhibit cytochrome P450s in HepG2 hepatoma cells, *Life Sci.*, 88 (9-10), 447–454.

[21] Hafid, A.F., Rifai, B., Tumewu, L., Widiastuti, E., Dachliyati, L., Primaharinastiti, R., and Widyawaruyanti, A., 2015, Andrographolide determination of *Andrographis paniculata* extracts, ethyl acetate fractions and tablets by thin-layer chromatography, *J. Chem. Pharm. Res.*, 7 (12), 557–561.

[22] Wang, J., Yang, W., Wang, G., Tang, P., and Sai, Y., 2014, Determination of six components of *Andrographis paniculata* extract and one major metabolite of andrographolide in rat plasma by liquid chromatography-tandem mass spectrometry, *J. Chromatogr. B*, 951-952, 78–88.

[23] Liu. Y.H., Mo, S.L., Bi, H.C., Hu, B.F., Li, C.G., Wang, Y.T., Huang, L., Huang, M., Duan, W., Liu, J.P., Wei, M.Q., and Zhou, S.F., 2011, Regulation of human pregnane X receptor and its target gene cytochrome P450 3A4 by Chinese herbal compounds and a molecular docking study, *Xenobiotica*, 41 (4), 259–280.

[24] Küblbeck, J., Niskanen, J., and Honkakoski, P, 2020, Metabolism-disrupting chemicals and the constitutive androstane receptor CAR, *Cells*, 9 (10), 2306.

[25] Borse, S.P., Singh, D.P., and Nivsarkar, M., 2019, Understanding the relevance of herb-drug interaction studies with special focus on interplays: A prerequisite for integrative medicine, *Porto Biomed. J.*, 4 (2), e15.

[26] Pitaloka, D.A.E. Ramadhan, D.S.F., Arfan, A., Chaidir, L., and Fakih, T.M., 2021, Docking-based virtual screening and molecular dynamics simulations of quercetin analogs as enoyl-acyl carrier protein reductase (InhA) inhibitors of *Mycobacterium tuberculosis*, *Sci. Pharm.*, 89 (2), 20.

[27] Pitaloka, D.A.E., Damayanti, S., Artarini, A.A., and Sukandar, E.Y., 2019, Molecular docking, dynamics simulation, and scanning electron microscopy (SEM) examination of clinically isolated *Mycobacterium tuberculosis* by ursolic acid: A pentacyclic triterpenes, *Indones. J. Chem.*, 19, (2), 328–336.

[28] Shivanika, C., Deepak Kumar, S., Ragunathan, V., Tiwari, P., Sumitha, A., and Devi, P.B, 2020, Molecular docking, validation, dynamics simulations, and pharmacokinetic prediction of natural compounds against the SARS-CoV-2 main-protease, *J. Biomol. Struct. Dyn.*, 0 (0), 1–27.

[29] Lee, H.S., Jo, S., Lim, H.S., and Im, W., 2012, Application of binding free energy calculations to prediction of binding modes and affinities of MDM2 and MDMX inhibitors, *J. Chem. Inf. Model.*, 52 (7), 1821–1832.

[30] Maglich, J.M., Parks, D.J., Moore, L.B., Collins, J.L., Goodwin, B., Billin, A.N., Stoltz, C.A., Kliewer, S.A., Lambert, M.H., Willson, T.M., and Moore., J.T., 2003, Identification of a novel human constitutive androstane receptor (CAR) agonist and its use in the identification of CAR target genes, *J. Biol. Chem.*, 278 (19), 17277–17283.

[31] Chen, J., and Raymond, K., 2006, Roles of Rifampicin in drug-drug interactions: underlying molecular mechanisms involving the nuclear pregnane X receptor, *Ann. Clin. Microbiol. Antimicrob.*, 5 (1), 3.

[32] Chrencik, J.E., Orans, J., Moore, L.B., Xue, Y., Peng, L., Collins, J.L., Wisely, G.B., Lambert, M.H., Kliewer, S.A., and Redinbo, M.R., 2005, Structural disorder in the complex of human pregnane X receptor and the macrolide antibiotic Rifampicin, *Mol. Endocrinol.*, 19 (5), 1125–1134.

[33] Damayanti, S., Martak, N.A.S., Permana, B., Suwandi, A., Hartati, R., and Wibowo, I., 2020, *In silico* study on interaction and preliminary toxicity prediction of *Eleutherine Americana* components as an antifungal and antitoxoplasmosis candidate, *Indones. J. Chem.*, 20 (4), 899–910.

[34] Hollingsworth, S.A., and Dror, R.O., 2018, Molecular dynamics simulation for all, *Neuron*, 99 (6), 1129–1143.

[35] Bao, L., Wang, J., and Xiao, Y., 2019, Molecular dynamics simulation of the binding process of ligands to the add adenine riboswitch aptamer, *Phys. Rev. E*, 100 (2), 022412.

[36] Ravi, S., Priya, B., Dubey, P., Thiruvenkatam, V., and Kirubakaran, S., 2021, Molecular docking and molecular dynamics simulation studies of quinoline-3-carboxamide derivatives with DDR kinases–selectivity studies towards ATM kinase, *Chemistry*, 3 (2), 511–524.

[37] Bai, B., Zou, R., Chan, H.C.S., Li, H., and Yuan, S., 2021, MolADI: A web server for automatic analysis of protein-small molecule dynamic interactions, *Molecules*, 26 (15), 4625.

[38] Dash, R., Ali, M.C., Dash, N., Azad, M.A.K., Hosen, S.M.Z., Hannan, M.A., and Moon, I.S., 2019, Structural and dynamic characterizations highlight the deleterious role of SULT1A1 R213H polymorphism in substrate binding, *Int. J. Mol. Sci.*, 20 (24), 6256.

[39] Dewi, M.L., Fakih, T.M., and Sofyan, R.I., 2021, The discovery of tyrosinase enzyme inhibitors activity from polyphenolic compounds in red grape seeds through in silico study, *J. Pure Appl. Chem. Res.*, 10 (2), 104–112.

[40] Khanal, S.P., Koirala, R.P., Mishra, E., and Adhikari, N.P., 2021, Molecular dynamics study of structural properties of γ-aminobutyric acid (GABA), *BIBECHANA*, 18 (1), 67–74.

[41] Zhang, X., Liu, X., He, M., Zhang, Y., Sun, Y and Lu, X, 2020, A molecular dynamics simulation study of KF and NaF ion pairs in hydrothermal fluIDs, *Fluid Phase Equilib.*, 518, 112625.

[42] Levine, B.G., Stone, J.E., and Kohlmeyer, A., 2011, Fast analysis of molecular dynamics trajectories with graphics processing units—Radial distribution function histogramming, *J. Comput. Phys.*, 230 (9), 3556–3569.

[43] Zikri, A.T., Pranowo, H.D., and Haryadi, W., 2020, Stability, hydrogen bond occupancy analysis and binding free energy calculation from flavonol docked in DAPK1 active site using molecular dynamics simulation approaches, *Indones. J. Chem.*, 21 (2), 383–390.

[44] Subash, K.R., 2020, *In silico* pharmacokinetic and toxicological properties prediction of bioactive compounds from *Andrographis paniculata*, *Natl. J. Physiol., Pharm. Pharmacol.*, 10 (7), 537–542.

[45] Julaiha, J., Widodo, G.P., and Herowati, R., 2019, Predicting ADME and molecular docking analysis of *Andrographis paniculata* and *Strobilanthes crispus* chemical constituents against antidiabetic molecular targets, *J. Idn. Chem. Soc.*, 2 (2), 66–125.

[46] Lindawati, N.Y., Nugroho, A.E., and Pramono, S., 2015, Pengaruh kombinasi ekstrak terpurifikasi

herba sambiloto (*Andrographis paniculata* (Burm. f.) Nees) dan herba pegagan (*Centella asiatica* (L.) Urban) terhadap translokasi protein GLUT-4 pada tikus diabetes mellitus tipe 2 resisten insulin, *Trad. Med. J.*, 19 (2), 62–69.

[47] Nugroho, A.E., Rais, I.R., Setiawan, I., Pratiwi, P.Y., Hadibarata, T., Maulana, T., and Pramono, S., 2014, Pancreatic effect of andrographolide isolated from *Andrographis paniculata* (Burm. f.) Nees, *Pak. J. Biol. Sci.*, 17 (1), 22–31.

[48] Samala, S. and Veeresham, C., 2015, Andrographolide pretreatment enhances the bioavailability and hypoglycemic action of glimepiride and metformin, *Int. J. Phytomed.*, 7 (3), 254–264.

[49] Zhang, X., Zhang, X., Wang, X., and Zhao, M., 2018, Influence of andrographolide on the pharmacokinetics of warfarin in rats, *Pharm. Biol.*, 56 (1), 351–356.

NiAl Layered Double Hydroxide/Rice Husk Composite for the Efficient Removal of Malachite Green

Neza Rahayu Palapa[1], Tarmizi Taher[2], Normah Normah[3], and Aldes Lesbani[1,3*]

[1]*Graduate School of Mathematics and Natural Sciences, Faculty of Mathematics and Natural Sciences, Universitas Sriwijaya, Jl. Palembang Prabumulih Km. 32, Ogan Ilir 30662, Indonesia*

[2]*Department of Environmental Engineering, Faculty of Infrastructure and Regional, Institut Teknologi Sumatera, Jl. Terusan Ryacudu, Way Hui, Lampung Selatan 35365, Indonesia*

[3]*Research Center of Inorganic Materials and Coordination Complexes, Faculty of Mathematics and Natural Sciences, Universitas Sriwijaya, Jl. Palembang Prabumulih Km. 32, Ogan Ilir 30662, Indonesia*

**** Corresponding author:***

email: aldeslesbani@pps.unsri.ac.id

Received: July 28, 2021
Accepted: September 30, 2021

DOI: 10.22146/ijc.68021

Abstract: *Rice husk biochar (BC) loaded NiAl layered double hydroxide (LDH) has been synthesized to form NiAl LDH/BC composite through a co-precipitation method. NiAl LDH/BC has been used as an adsorbent to remove malachite green from water efficiently. The specific surface area analysis revealed that the surface area of NiAl LDH/BC composite increased five times, from 92.6 to 438.9 m²/g, compared to the original NiAl LDH. The adsorption studies revealed that NiAl LDH/BC composite followed the pseudo-second-order kinetic adsorption model while the isotherm followed the Langmuir monolayer adsorption model. The maximum adsorption capacity of NiAl LDH/BC composite prepared with a ratio of 1:1 and 1:0.5 achieved 185.1 mg/g and 142.9 mg/g, respectively, which is twice higher than the pristine ones (NiAl LDH). The thermodynamic parameters, determined at 303, 313, 323, and 333 K, revealed that the adsorption process was spontaneous and endothermic. The NiAl LDH/BC composite was tested for three consecutive adsorption-desorption cycles to investigate its reusability performance. It is found that their adsorption performance slightly decreased to 71.8% and 68.3% for NiAl LDH/BC composite 1:0.5 and 1:1, respectively. Therefore, it could be considered that the synthesized NiAl LDH/BC exhibited a good and efficient adsorbent for malachite greed removal.*

Keywords: *NiAl LDH; biochar; adsorption; kinetic study; thermodynamic study; malachite green*

INTRODUCTION

Synthetic dyes have been widely utilized in many industries such as textile, cosmetics, printing, and paints. It was reported that the annual worldwide production of synthetic dyes had achieved 7×10^5 tons [1]. Unfortunately, around 20% of dyes used during processing operations are discharged into wastewater [2]. The most provenance of dye wastewater is textile industries, which dispose of up to a hundred thousand tons for a year. The existence of dyes on fresh, natural water has detrimental impacts and is hazardous to the environment and aquatic life because of their mutagenic, allergenic, and carcinogenic effects [3-4]. Moreover, the presence of metals, chloride and aromatic structure in synthetic dyes further enhances their toxicities [5-6].

Among synthetic dyes, malachite green (MG) is one of the most used dyes in various industrial applications, including dyeing wool, silk, leather, and paper [7-8]. Malachite green is a cationic dye, which belongs to the triphenylmethane category [9]. Many studies have been investigated the hazards of MG for human and mammalians cells. According to Matpang et al. [10], MG in a concentration of less than 1 mg/L has been reported as toxic to fish, crab, and prawns.

Therefore, MG was already banned in Europe, the USA, and several countries globally. It is essential to remove MG from industrial wastewater before it is discarded into the aquatic environment due to the detrimental effect on ecological systems and public health [11-12].

The removal of MG from wastewater is difficult because MG's structure is hard to oxidize, low efficiency [13] on nature bio-precipitation and chemistry-precipitation [14]. Several methods have been studied to remove MG from an aqueous solution, such as electrochemical [15], flocculation [16], and adsorption [17]. Other traditional methods include reverse osmosis, electrodialysis, and ion exchange, with limitations such as incomplete removal, high cost, and high energy generation [18]. Among all these methods, adsorption is very effective due to its easy operation, low cost, and efficient removal of pollutants [19-20].

Recently, various adsorbents ranging from organic to inorganic materials have been reported to remove dyes from wastewater such as chitosan [3], zeolite [21], biochar [22], and layered double hydroxide [23-24]. Layered double hydroxide (LDH) is a double dimensional and negative charge inorganic layered material that exhibits brucite structure. Chemical composition of LDH is given by general formula of $[M^{2+}_{1-x}M^{3+}_{x}(OH)_2]^{x+}(An^-)_{x/n}]_nH_2O$; where, composting from bivalent (i.e., Ni^{2+}, Fe^{2+}, Zn^{2+} Cu^{2+} and Mg^{2+}), trivalent metal ions (Al^{3+}, Fe^{3+}, and Cr^{3+}), and anion in interlayer (Cl^-, SO_4^{2-}, NO_3^- and CO_3^-) [25]. Many researchers have been studying dye removal using LDHs. Shan et al. [26] used MgAl LDH to remove the reactive red dye in an aqueous solution with maximum uptake of 59.49 mg/g. Zhu et al. [27] reported MgAl LDH for adsorption methyl orange in an aqueous solution and obtained adsorption capacity up to 0.453 mol/kg. Starukh et al. [28] investigated the adsorption ability of ZnAl LDH toward methyl orange and obtained that the adsorption process was spontaneous and endothermic, and a possible mechanism for MO adsorption was proposed. Therefore, due to its excellent properties, LDH is a promising material to enhance the adsorptive performance of dye with the modification through intercalation [29] and combination to form composite [30].

Recently, Biochar (BC) has been studied as a support agent to increase the surface area of the prepared supported materials [31]. BC, a pyrogenic activated black carbon made from biomass [32], has been widely reported in dyes removal due to its high adsorption capacity and a large surface area [33]. The utilization of BC to improve material characteristics has been widely reported. The modification of LDH structure using BC can enhance its surface area, stability, adsorption capacity, and regeneration effectivity [34]. The resulting composite is used as an adsorbent to remove contaminants from wastewater by the adsorption method. Meili et al. [35] reported that MgAl hydrotalcite loaded bone BC as an adsorbent to remove methylene blue. Wan et al. [36] also reported that MgFe LDH composites with bamboo BC were applied as adsorbents to remove organic pollutants such as phosphate from an aqueous solution.

In this work, we investigated NiAl LDH modified with BC because Ni^{2+} and Al^{3+} could form as highly stable LDH with high surface area specific. Based on the literature mentioned earlier, to the best of our knowledge, the development of NiAl LDH loaded rice husk BC as an adsorbent for MG adsorption is rarely investigated. Furthermore, in this study, NiAl LDH contained different ratios of composite NiAl LDH, and BC was employed to enhance the effectiveness of removing MG in an aqueous system. NiAl LDH loaded rice husk BC were applied as adsorbent of MG from an aqueous solution. The effect of various adsorption conditions, including contact time, initial concentration, temperature adsorption, and reusability adsorbent, was investigated in detail. The kinetic and thermodynamic adsorption parameters were also calculated based on a variation of contact time, dye's initial concentration, and temperature adsorption.

■ EXPERIMENTAL SECTION

Materials

The materials used in the experiment were nickel nitrate trihydrate ($Ni(NO_3)_2{\cdot}3H_2O$, 98%, Merck Darmstadt, Germany), aluminum nitrate nonahydrate

($Al(NO_3)_3{\cdot}9H_2O$, 99.9%, Merck Darmstadt, Germany), sodium hydroxide (NaOH, 99%, Merck Darmstadt, Germany) and MG ($C_{23}H_{25}N_2{\cdot}C_2HO_4{\cdot}0.5C_2H_2O_4$, 90%, Sigma Aldrich). All those chemicals were purchased from Merck and Sigma Aldrich (purified/p.a. grade) without further purification. The rice husk as the BC source was obtained from the local rice field.

Instrumentation

X-ray diffraction pattern of the prepared adsorbent was recorded using XRD Rigaku Miniflex-600 (Japan). The sample was scanned at scan speed 1°/min from the 2theta range 5–70°. The specific surface area was calculated by using the Multipoint BET method based on data collected by ASAP Micromeritics 2020 Accelerated Surface Area and Porosimetry System (USA) at 77 K. Infrared spectra obtained from FTIR Shimadzu Prestige-21 (Japan) that measured by KBr disc method and scanned at wavenumber range of 400–4000 cm^{-1}. The surface morphology of materials was characterized using the SEM Quanta-650 Oxford instrument (Germany). Thermal analysis was conducted using TG-DTA Analyzer Shimadzu DTG-60H (Japan). The concentration of dye was analyzed using UV-Visible spectrophotometer Bio-Base BK-UV1800 (China) at wavelength 619 nm.

Procedure

Preparation of BC from rice husk

BC was produced through thermal treatment of the rice husk; the thermal treatment was carried out in a furnace at 300 °C under nitrogen flow (10 °C/min) for 2 h. Thereafter, the reactor was cooled down, and the prepared BC was characterized.

Preparation of NiAl LDH/BC composite

NiAl LDH was prepared by co-precipitation method according to Ravuru et al. [37] with slight modification. Meanwhile, NiAl LDH/BC composite preparation is similar to Meili et al. [35] with slight modification. NiAl LDH/BC composite was prepared using a co-precipitation method: Nickel nitrate (10.9 g; 0.750 M) and aluminum nitrate (4.6 g; 0.250 M) with ratio molar metal solutions 3:1 were mixed under vigorous stirring for an hour until the complete dissolution of the starting materials. The resulting mixtures were added to a solution of 1 g and 0.5 g BC with continuous stirring. The amount of BC is shown in Table 1. As much as 4 M sodium hydroxide solution was added dropwise until the settlement formed at pH 10. The mixing solution was kept at 80 °C for 3 d. NiAl LDH/BC composites were washed and dried at 40 °C for 24 h.

Adsorption study

The adsorption study was carried out using a batch system. The contact time to determine the kinetics experiments and temperature and concentration on the adsorption process were investigated. The kinetic study was conducted by adding 0.05 g of adsorbent to 0.05 L MG solution at room temperature in different initial concentrations. The kinetic parameters were evaluated based on pseudo-first-order (PFO) and pseudo-second-order (PSO) approaches as reported [38]. A similar procedure investigated the isotherm and thermodynamic study as a kinetic study in various temperatures and initial concentrations. The isotherm models have been investigated in the previous report [39].

Reusability study

The reusability test was aimed to examine the longevity of NiAl LDH/BC composites after a long period of application. In this study, several reagents such as ethylenediaminetetraacetic acid, sodium chloride, water, sodium hydroxide, hydrochloride acid were used in the desorption process. Reusability evaluation was conducted by adding 0.05 g of adsorbents to 0.05 L MG 100 mg/L. The mixture was shaken for 2 h, followed by filtration to separate the adsorbent from the adsorbate. Then, the adsorbent dried in the oven while the adsorbate had its absorbance read. The dried adsorbent (NiAl LDH/BC-MG LDH) was reused by adding it in 0.025 L of HCl followed by stirring for 2 h and then dried

Table 1. Composites of BC and NiAl in NiAl LDH/BC composites

Samples	BC (g	Ni:Al solution (g (0.750:0.250 M
NiAl LDH/BC composite 1:0.5	0.5	10.9:4.6
NiAl LDH/BC composite 1:1	1.0	10.9:4.6

at room temperature. Finally, the material was used in another adsorption test in a similar procedure, in which this procedure repeated three cycles of operations.

■ RESULTS AND DISCUSSION

Fig. 1(a) shows the IR spectra of NiAl LDH/BC composites that show both LDH and BC characteristics. The characteristic band at 3448 and 1635 cm^{-1} assigned to OH stretching vibrations and bending vibrations of the hydroxyl groups from water molecules. The band at 1000 cm^{-1} belongs to the vibration of metal-oxygen, while the bending vibration of nitrate appeared at 1381 cm^{-1} on LDH pristine and composite materials. The absorption band at 1095 cm^{-1} denotes the stretching vibration of C–O. The intensity of nitrate vibration was decreased after composite formed, and the presence of new vibration at 1095 cm^{-1} denotes carbon assumed that the successful preparation of the composite materials. Fig. 1(b) shows the diffractogram NiAl LDH/BC composite resembles the characteristic diffraction pattern of NiAl LDH and BC, as a similar finding by Palapa et al. [23]. The composite of NiAl LDH/BC composites showed the peaks at 10°, 22°, 28°, 35°, and 60° corresponding to reflections of (003), (002), (006), (012), and (110), respectively, which indicated the materials have layer structure and carbon reflection from BC characteristic [36]. The composite materials showed the characteristic peaks of raw materials (NiAl LDH and BC) with a reduced crystallinity. These phenomena, also supported by the LDH (003) reflections was shifted to lower 2theta. The strong reflections of NiAl LDH observed at a BC content of 0.5 g were observed at 1 g with a slight reduction in peak intensities, which indicates that the crystalline structure of the composites slightly deviated with the incorporation of increased BC.

Fig. 2 shows the textural properties of N_2 adsorption-desorption, and the results are presented in Table 2. Table 2 shows that the surface area of LDH increased after being supported by BC along with the decreases in pore size and increased surface area because pores of BC are supported in LDH's surface, decreasing the pore size, thus increasing the surface area. This finding assumed that NiAl LDH occupied the pore of BC with forming NiAl LDH/BC composite, increasing the composites' surface area. The adsorption isotherms of

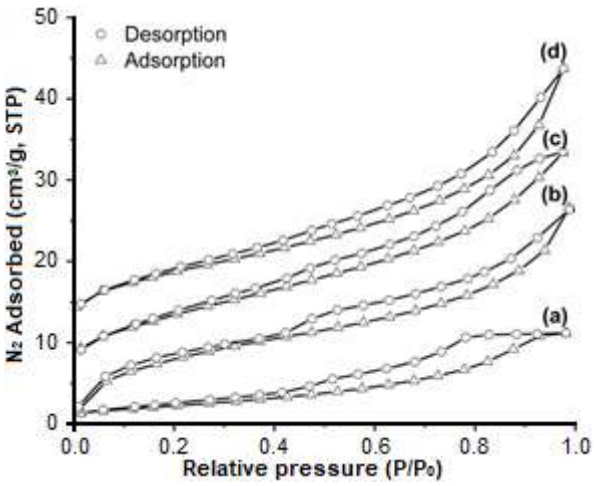

Fig 2. Nitrogen adsorption-desorption curve of materials NiAl LDH (a), BC (b), NiAl LDH/BC composite 1:0.5 (c) and 1:1 (d)

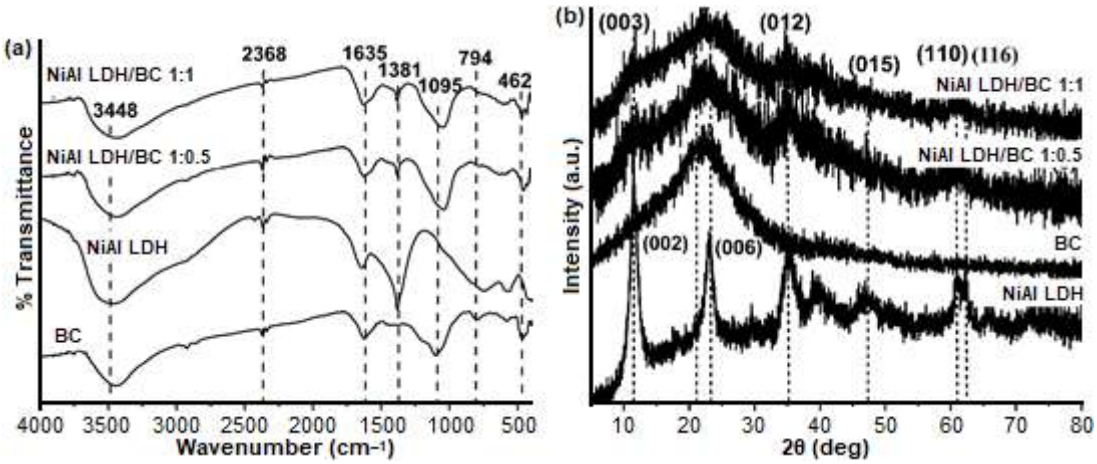

Fig 1. Spectrum FTIR (a) and PXRD pattern (b)

Table 2. Surface area and pore size of materials

Materials	Surface Area (m^2/g)	Pore Size (nm)
NiAl LDH	92.6	10.2
BC	50.9	12.0
NiAl LDH/BC composites 1:0.5	220.9	11.2
NiAl LDH/BC composites 1:1	438.9	11.3

each material are shown in Fig. 3. The isotherm curve showed the isotherms type IV characteristics of mesoporous materials according to the classification BDDT. The hysteresis of most materials is type H3 and H4 for BC. According to IUPAC classification, type H4 indicated that materials have not well-defined mesoporous structures, whereas the H3 type implies the presence of slit-shaped pores created by an aggregate particle as mesoporous material characteristic [40].

Fig. 3 exhibits thermogravimetric with divergent thermal analysis (TG-DTA) of the composite materials executed to show the thermal stabilities of materials. As shown in Fig. 3(a), the TG-DTA of NiAl LDH exhibits a two-stage weight loss from water molecules at 80–210 °C and breaking out of a layered structure of LDH at around 300 °C. The previous reported also confirm that the endothermic peak at 150–200 °C indicates the weight loss of water molecule in surface and interlayer [41]. The peak is around 350–560 °C which show in Fig. 3(b-d). presents the devolatilized and decomposed cellulose and lignin in materials. As similarly reported by James and Rao [42], the stage from 300–600 °C indicated that the decomposition of cellulose, lignin, and other organic material with strong bonds occurred.

Fig. 3(b) shows two steps of weight loss from BC. The steps included loss of water molecules and evaporation caused that the carbon material was oxidized. According to Mohapatra et al. [43], the BC's DTA showed that the broad and exotherm of the curve

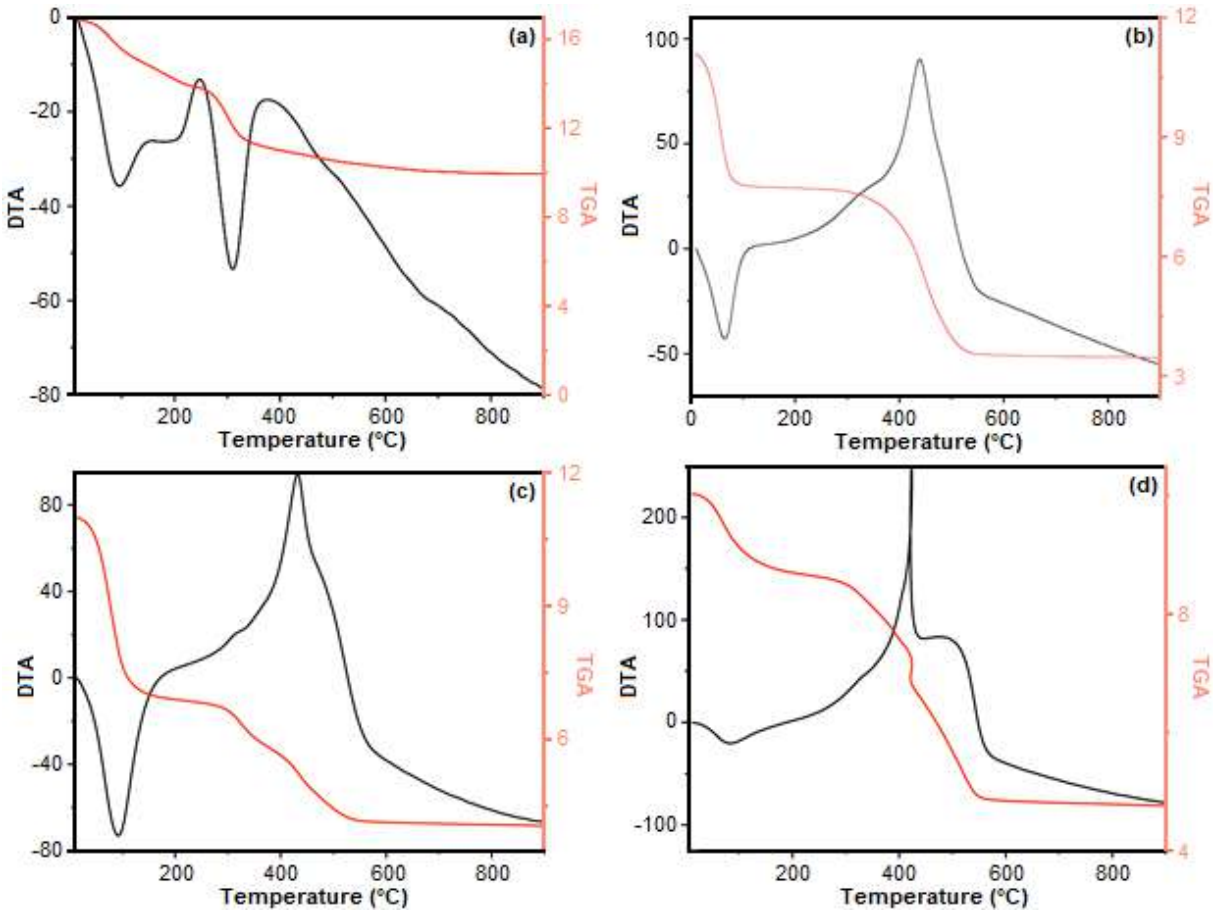

Fig 3. Thermograms of NiAl LDH (a), BC (b), NiAl LDH/BC composites 1:0.5 (c) and 1:1 (d)

as natural with two peaks, which is the first peaks denotes decay of organic compounds and the second peak is assigned to the decay of cellulose and bonded by organic molecules. Therefore, the NiAl LDH/BC composites have similar weight loss. Fig. 3(c) and 3(d) show the first step is weight loss of water molecules of composite materials, and slight decreases of weight loss from carbon and LDH interlayer was disappeared.

Fig. 4(a) shows the surface structure of NiAl LDH. The structure of NiAl LDH shows the agglomeration with large particles, which is caused by adjusting pH and temperature due to the synthesis co-precipitation process [44]. Fig. 4(b) shows the BC structure with large pore materials. This phenom is also confirmed by Table 1, which is the BC has a larger pore size than NiAl LDH and NiAl LDH/BC composites. Fig. 4(c) shows the NiAl LDH/BC composite with a ratio of 1:1. The NiAl LDH/BC composites 1:1 shows the agglomeration with predominantly reveals the presence of LDH phase.

The results effect of contact time was calculated by kinetic parameter. Fig. 5 shows the kinetic model fitted using PFO and PSO kinetic models in various contact times. The results showed that the NiAl LDH/BC composites were more adsorbed than NiAl LDH and BC. Furthermore, Fig. 5 presented the equilibrium of MG reached after 150 min for BC and 120 min for others. The equilibrium MG uptake using NiAl composite 1:0.5 was 79 mg/L, and NiAl composite 1:1 was 86 mg/L from 100 mg/L. The PFO and PSO curve is shown in Fig. 5, and the results of a kinetic parameter are presented in Table 3.

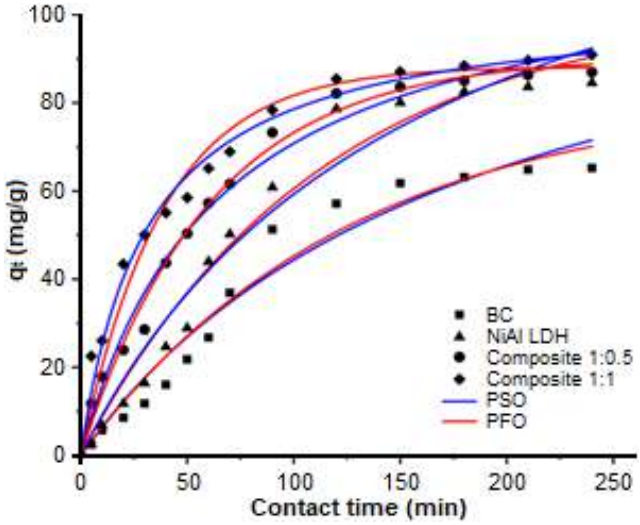

Fig 5. Kinetic curve parameter adsorption of NiAl LDH, BC, NiAl LDH/BC composite 1:0.5 and 1:1

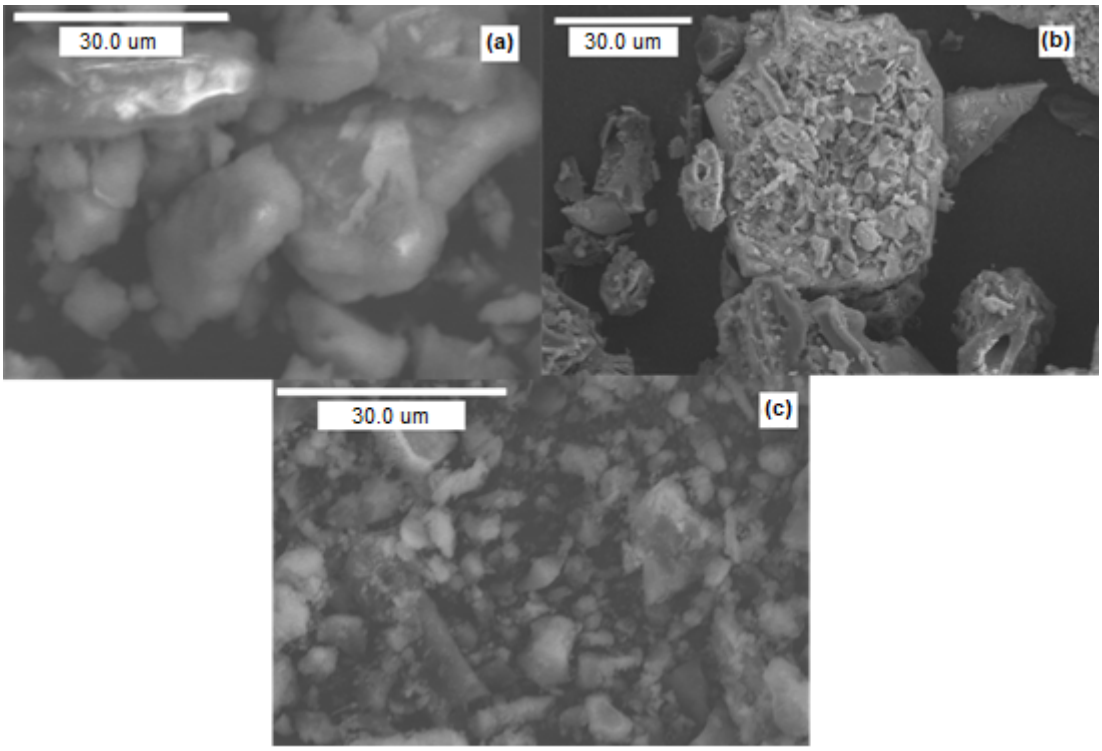

Fig 4. Morphologies of NiAl LDH (a), BC (b), NiAl LDH/BC composite 1:1 (c)

Table 3. Kinetic parameter adsorption results of materials

Adsorbent	Qe_{exp}	PFO		PSO				IPD		
		Qe_{Calc}	R^2	Qe_{Calc}	R^2	k_2	k_1	k_i	C	R^2
NiAl LDH	42.2	60.8	0.971	60.6	0.957	0.0001	0.022	2.964	1.677	0.913
BC	32.6	46.2	0.908	44.2	0.962	0.0003	0.020	2.967	1.614	0.908
NiAl LDH/BC 1:0.5	43.5	44.0	0.944	56.1	0.975	0.0003	0.020	3.462	1.809	0.904
NiAl LDH/BC 1:1	45.4	39.5	0.992	51.2	0.995	0.0006	0.019	5.197	2.713	0.926

Table 3 shows the kinetic parameter of MG adsorption obtained from the PFO and PSO equation calculation as reported by Lesbani et al. [45] based on experimental data. All materials follow PSO kinetic model based on coefficient correlation (R^2) which was higher than 0.95. The value of adsorption capacity of the adsorbent based on the PSO model was also indicated closer to the real experimental value and the graph in Fig. 5. This phenomenon suggested that the adsorption process can be assumed by chemical interaction or chemisorption. A similar phenomenon was also reported by Harizi et al. [46], in which the adsorption kinetics more fitted PSO than PFO indicated the chemisorption mechanism. Furthermore, to identify the importance of diffusion in the adsorption process, mathematical expression of intraparticle diffusion (IPD) model was used

$$q_t = k_i t^{0.5} + C \quad (1)$$

where k_i is the IPD constant (mg/g $min^{0.5}$) and the intercept (C) reflects the boundary layer effect. The values of k_i were calculated from slopes (k_i) of the plots of q_t vs. $t^{0.5}$, and the data are presented in Table 3. The values of C were higher in NiAl LDH/BC 1:1 revealed more surface adsorption than NiAl LDH, BC and NiAl LDH/BC 1:0.5, these finding reflects the boundary layer effect of the plot. Rates of diffusion were higher in NiAl LDH/BC 1:1, resulting in the high adsorption capacity of MG adsorption. From the results, it can be concluded that all adsorbents followed both surface adsorption and intraparticle diffusion mechanism.

The adsorption isotherm of MG is shown in Fig. 6. The increase of adsorption capacity can be related to the increase in temperature. The isotherm parameters were calculated according to the Langmuir and Freundlich isotherm model formulated by the previous report [47].

Table 4 represents the calculation results of the coefficient correlation, which identifies that Langmuir was the best fitted for NiAl LDH/BC composites. These results exhibited that the surface of adsorbents was uniform, with the mechanism of the adsorption process is a monolayer. The maximum adsorption capacity obtained by NiAl LDH/BC composite 1:1 and 1:0.5 was 185.1 and 142.8 mg/g, respectively, higher than NiAl LDH (94.9 mg/g) and BC (57.0 mg/g). These findings showed that the prepared materials have good properties as adsorbent than other materials for MG removal, as reported by Bagheri et al. [48]. The activated carbon (AC) as adsorbent was prepared from *Amygdalus scoparia* and was studied to remove MG from an aqueous solution. The adsorption process was obtained a maximum adsorption capacity of 144.3 mg/g of MG at 0.01 g of the adsorbent. Jiang et al. [49] reported ultra-light aerogels as MG adsorbent, with an equilibrium adsorption capacity of 53.0 mg/g. Rajabi et al. [49] reported that poly(methyl methacrylate)/graphene oxide-Fe_3O_4 (PMMA/GO-Fe_3O_4) was studied for MG removal with adsorption capacity 11.0 mg/g at 298 K after 35 min adsorption process. Graphene oxide/Fe_3O_4 was applied as an adsorbent of MG in an aqueous solution with an adsorption capacity of 179.0 mg/g [50]. Abukhadra et al. [47] was prepared Ni/NiO nanoparticles modified by diatomite skeletons and obtained an experimental equilibrium time of 660 min with an adsorption capacity of 161 mg/g. CuAl LDH and CuAl LDH intercalated using $SiW_{12}O_{40}$ Keggin anion was prepared and applied as an MG removal agent. The adsorption process was obtained adsorption capacity 55.8 mg/g and 149.2 mg/g for CuAl LDH and CuAl-$SiW_{12}O_{40}$, respectively [29]. CuCr LDH intercalated

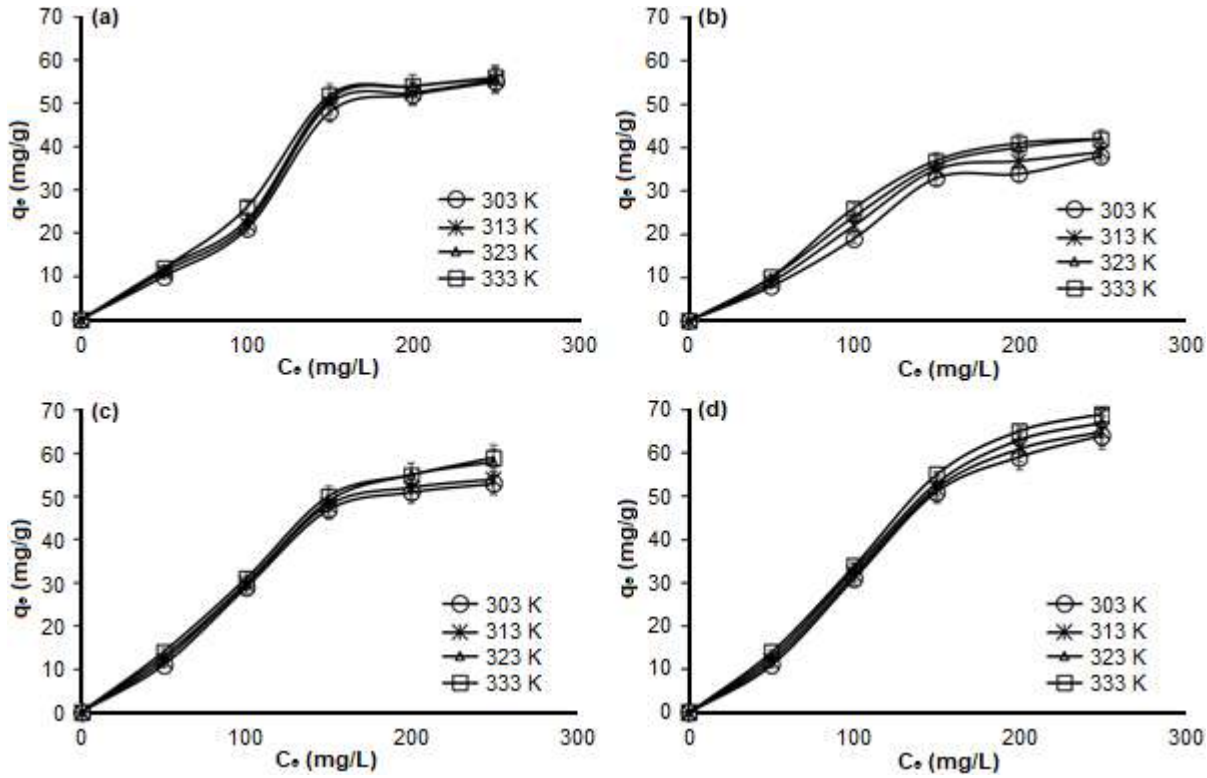

Fig 6. Effect of temperature and initial concentration of MG adsorption using NiAl LDH (a), BC (b), NiAl LDH/BC composites material 1:0.5 (c) and 1:1 (d)

Table 4. Isotherm adsorption parameters of MG adsorption using NiAl, BC, and NiAl LDH/BC composites

Adsorbent	Adsorption Isotherm	Adsorption Constant	T (K)			
			303	313	323	333
NiAl	Langmuir	q_{max}	56.2	88.3	88.2	94.9
		k_L	0.005	0.011	0.036	0.366
		R^2	0.999	0.813	0.9459	0.975
	Freundlich	n	0.5	0.6	0.7	1.1
		k_F	18.523	6.806	1.587	3.807
		R^2	0.993	0.9731	0.975	0.9483
BC	Langmuir	q_{max}	44.4	52.0	53.8	57.0
		k_L	0.014	0.014	0.029	0.039
		R^2	0.9263	0.8962	0.8917	0.9411
	Freundlich	n	0.4	0.5	0.5	0.6
		k_F	38.318	22.398	5.861	2.456
		R^2	0.997	0.993	0.986	0.969
NiAl LDH/BC 1:0.5	Langmuir	q_{max}	147.0	144.9	142.8	142.8
		k_L	0.073	0.108	0.163	0.249
		R^2	0.999	0.991	0.997	0.999
	Freundlich	n	14.6	15.4	16.6	3.1
		k_F	91.369	96.139	101.321	46.548
		R^2	0.921	0.977	0.989	0.992

Table 4. Isotherm adsorption parameters of MG adsorption using NiAl, BC, and NiAl LDH/BC composites (*Continued*)

Adsorbent	Adsorption Isotherm	Adsorption Constant	T (K)			
			303	313	323	333
NiAl LDH/BC 1:1	Langmuir	q_{max}	168.9	174.9	182.9	185.1
		k_L	0.011	0.031	0.049	0.067
		R^2	0.962	0.907	0.957	0.978
	Freundlich	n	0.5	0.6	0.8	0.9
		k_F	9.883	1.112	1.286	1.969
		R^2	0.999	0.992	0.987	0.954

using $SiW_{12}O_{40}$, also reported by Palapa et al. [51], was obtained adsorption capacity reached 55.322 mg/g at 323 K after 100 min adsorption time. According to all kinds of literature and compared by Table 4, the obtained q_{max} of this research has good performance than others with q_{max} of NiAl LDH/BC 1:1 was 185.1 mg/g. These findings showed the efficiency NiAl LDH/BC for the removal of MG dye in aqueous samples.

Table 5 presents the value of the thermodynamic parameters. The ΔH and ΔS were calculated from the slope and intercept of van't Hoff plots (ln Kd versus 1/T, as shown as Fig. 7). From Fig. 7, the ΔH and ΔS values were 7.292 kJ/mol and 0.024 J/K mol, respectively. The positive value of ΔS of MG adsorption was indicated to the randomness of adsorbent-adsorbate interaction from the adsorption process [52]. The positive value of ΔH indicated that the adsorption reaction became endothermic because the MG adsorbed increased with increasing temperature. The negative value of ΔG at various temperatures denotes the spontaneity adsorption process, and it is more favorable in high temperatures.

Fig. 8 shows the illustration of MG adsorption onto NiAl LDH/BC composite. The adsorption mechanism of adsorption parameter data, i.e., kinetic, isotherm, and thermodynamic data, in the present study, suggested that not only physisorption but also chemisorption can be indicated of MG adsorption onto the adsorbent [53]. In this research, the chemisorption occurs by electrostatic interactions, for example, the interaction of the polar NiAl LDH/BC charged surface with positively charged MG molecule. For supporting phenomena, the increase of the surface area of NiAl LDH/BC indicated that the active sites become more which could contribute to diffuse dye molecules [54]. The large specific surface area and high pore diameter are significant features for the diffusion of dye molecules, increasing MG adsorption [55]. The adsorption interaction between NiAl LDH/BC 1:1 and MG was also confirmed by FTIR

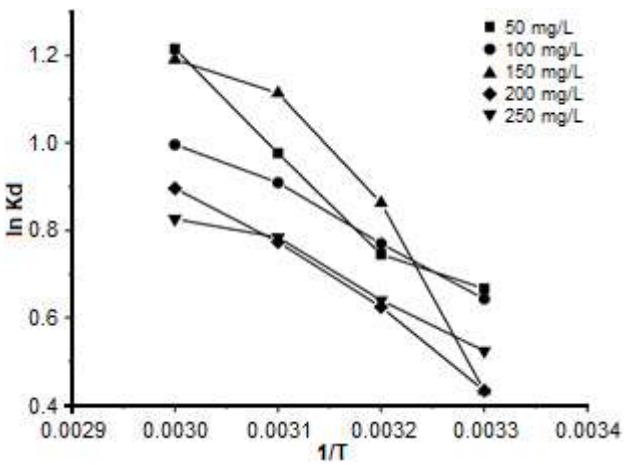

Fig 7. Van't Hoff linearity equation of MG adsorption using NiAl LDH/BC 1:1

Table 5. Thermodynamic study of MG adsorption onto NiAl, BC and NiAl LDH/BC composites

Adsorbent	T (K)	q_e (mg/g)	ΔH (kJ/mol)	ΔS (J/K mol)	ΔG (kJ/mol)
NiAl LDH/BC 1:1	303	101.164	7.292	0.024	-0.048
	313	106.164			-0.291
	323	110.45			-0.533
	333	114.164			-0.775

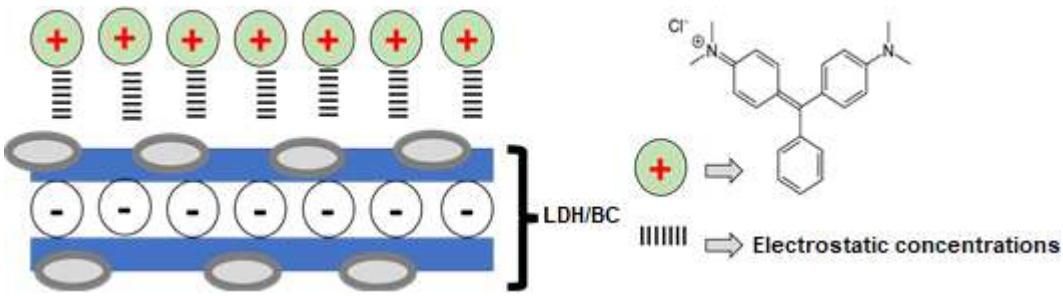

Fig 8. Illustration of MG adsorption onto NiAl LDH/BC composites

characterization. The FTIR spectrum is a useful tool to identify hydrogen bonding (500–4000 cm^{-1}) of the NiAl LDH/BC 1:1 before and after adsorption are shown in Fig. 9. Fig. 9(b), showed exhibited characteristic changes of the hydroxyl groups and nitrate band, which shifted from 3448 (OH), 1635 (OH), and 1381 cm^{-1} (N–O) before malachite green adsorption to 3289, 1660, 1560, and 1388 cm^{-1} after adsorption, as the evidence for the interaction between NiAl LDH/BC 1:1 and MG. Furthermore, to support the assumption in Fig. 8, the effect of the initial pH of the solution was determined.

The removal percentage of MG by NiAl LDH/BC 1:1 at different pH values was then studied (as shown in Fig. 10), while keeping the other parameters at constant values (m = 0.002 g; V = 0.05 L; Co = 50 mg/L; T = 303 K). Results showed that the highest removal efficiency of MG was 48% observed in the pH range of 7. This efficiency decreased to 39% at pH ranging 9–10. Meanwhile, the pHpzc of NiAl LDH/BC 1:1 is equal to 5.8. As the initial pH value of pH ranging from 3–4 solution decreased, the number of the negatively charged groups at the surface of the adsorbent decreased, while the positively charged groups increased. This behavior does not favor the adsorption due to the presence of electrostatic repulsion. Consequently, the removal percentage of MG increased proportionally to the pH values, mainly when pH > pHpzc. Indeed, at pH > pHpzc, charges at the surface of NiAl LDH/BC 1:1 are mainly negatives, and these charges increase proportionally to the pH. Therefore, the removal efficiency increases when the pH is in the range of 7–9 due to attractive forces that occur between MG and the negatively charged surface of NiAl LDH/BC 1:1. Therefore, the optimum pH value that maximizes MG removal from aqueous solution was fixed to 7.

Fig. 11(a) shows the desorption study by various reagents to obtain the suitable reagent for the desorption process. The desorption process was carried out using organic and inorganic solvents such as diethyl ether, water,

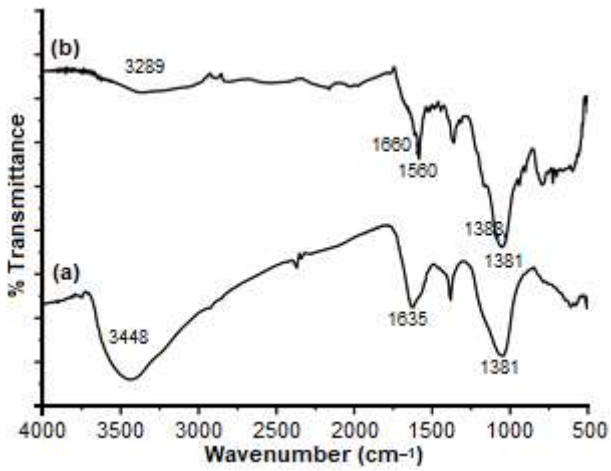

Fig 9. FTIR spectra of NiAl LDH/BC 1:1 before (a) and after (b) adsorption of MG

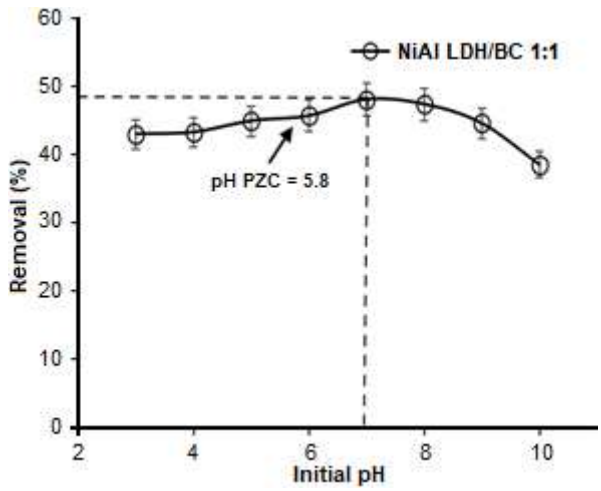

Fig 10. Effect of pH on MG adsorption

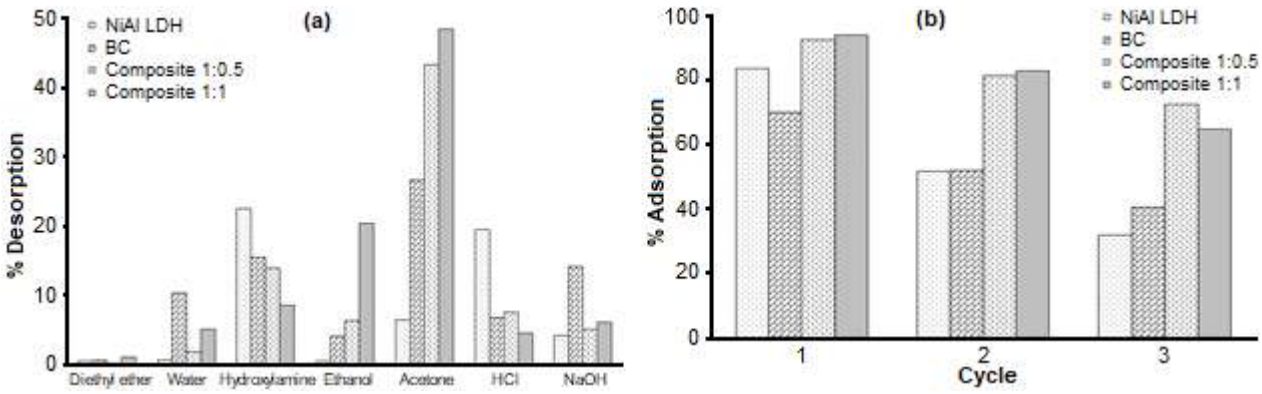

Fig 11. Desorption and reusability study of NiAl, BC, NiAl LDH/BC composite 1:0.5 and 1:1

hydroxylamine, ethanol, acetone, HCl, and NaOH. The higher desorption percentage was achieved by acetone, 48.2% for NiAl LDH/BC 1:1 and 43.8% for NiAl LDH/BC 1:0.5. Thus, the desorption process was conducted using acetone as a suitable solvent. According to previous research, the desorption process can be affected by hydrophobicity desorbed, molecule weight, and hydroxyl presence. This finding indicated that MG is more soluble in the organic polar solvent because of forming a hydrogen bond.

Fig. 11(b) shows present the regeneration experiment after three cycles of adsorption-desorption. The efficiency of MG removal was shown to decrease after three cycles slightly. According to Nishimura et al. [56], adsorbents treated in regeneration might damage their structure due to exfoliated included LDH. However, the NiAl LDH/BC composites material prepared in this work can be reused, although the adsorption capacity is slightly reduced.

■ CONCLUSION

The NiAl LDH/BC composite has been successfully synthesized, characterized, and applied as an adsorbent to remove MG. The adsorption parameters were determined using kinetic, isotherm, and thermodynamic parameters with various adsorption times, concentrations, and temperatures. MG removal on NiAl LDH/BC composite increased rapidly, and adsorption equilibrium was achieved after 120 min with kinetic parameter follow PSO. The adsorption isotherms could be effectively matched with the Langmuir isotherm model. The maximum adsorption capacity obtained by NiAl LDH/BC composite 1:1 and 1:0.5 was 185.1 mg/g and 142.8 mg/g, respectively, higher than NiAl LDH (94.9 mg/g) and BC (57.0 mg/g). The thermodynamic analysis indicates the spontaneous adsorption process, endothermic and the randomness of adsorbent-adsorbate interaction. Furthermore, NiAl LDH/BC composites exhibited good recycling performance. Finally, the utilization of the NiAl LDH/BC composite shows the material is a potential material as a removal agent.

■ ACKNOWLEDGMENTS

The authors would like to thank the Research Centre of Inorganic Materials and Complexes Universitas Sriwijaya for supporting instrumentation and analysis.

■ AUTHOR CONTRIBUTIONS

NRP and N experimented, collecting and assembling the data, AL wrote the manuscript and planning the research, TT and NRP analysis and interpretation the data. All authors agreed to the final version of this manuscript.

■ REFERENCES

[1] Srivastava, S., Sinha, R., and Roy, D., 2004, Toxicological effects of malachite green, *Aquat. Toxicol.*, 66 (3), 319–329.

[2] Bielska, M., Sobczyńska, A., and Prochaska, K., 2009, Dye-surfactant interaction in aqueous solutions, *Dyes Pigm.*, 80 (2), 201–205.

[3] Bekçi, Z., Özveri, C., Seki, Y., and Yurdakoç, K., 2008, Sorption of malachite green on chitosan bead, *J. Hazard. Mater.*, 154 (1-3), 254–261.

[4] Weber, E.J., and Adams, R.L., 1995, Chemical- and sediment-mediated reduction of the azo dye Disperse Blue 79, *Environ. Sci. Technol.*, 29 (5), 1163–1170.

[5] Ratna, and Padhi, B.S., 2012, Pollution due to synthetic dyes toxicity & carcinogenicity studies and remediation, *Int. J. Environ. Sci.*, 3 (3), 940–955.

[6] Panswad, T., and Luangdilok, W., 2000, Decolorization of reactive dyes with different molecular structures under different environmental conditions, *Water Res.*, 34 (17), 4177–4184.

[7] Siregar, P.M.S.B.N., Palapa, N.R., Wijaya, A., Fitri, E.S., and Lesbani, A., 2021, Structural stability of Ni/Al layered double hydroxide supported on graphite and biochar toward adsorption of Congo red, *Sci. Technol. Indones.*, 6 (2), 85–95.

[8] Boutemak, K., Taoualit, N., Cheknane, B., Laslouni, O., Djeddou, S., Medaoud, K., Mazouni, I., and Aoudj, S., 2019, Equilibrium, kinetic and thermodynamic study of green malachite and rhodamine-B dyes sorption on olive pomace, *Chem. Eng. Trans.*, 73, 277–282.

[9] Esan, O.S., Kolawole, A.O., and Olumuyiwa, A.C., 2019, The removal of single and binary basic dyes from synthetic wastewater using bentonite clay adsorbent, *Am. J. Polym. Sci. Technol.*, 5 (1), 16–28.

[10] Matpang, P., Sriuttha, M., and Piwpuan, N., 2017, Effects of malachite green on growth and tissue accumulation in pak choy (*Brassica chinensis* Tsen & Lee), *Agric. Nat. Resour.*, 51 (2), 96–102.

[11] Li, J., Fan, Q., Wu, Y., Wang, X., Chen, C., Tang, Z., and Wang, X., 2016, Magnetic polydopamine decorated with Mg-Al LDH nanoflakes as a novel bio-based adsorbent for simultaneous removal of potentially toxic metals and anionic dyes, *J. Mater. Chem. A*, 4 (5), 1737–1746.

[12] Oldring, P.K.T., and Nehring, U., 2007, *Packing Materials - 7. Metal Packing for Foodstuffs*, ILSI Europe Report Series, ILSI Europe Packaging Materials Task Force, Washington, DC, US.

[13] Krishna Murthy, T.P., Gowrishankar, B.S., Chandra Prabha, M.N., Kruthi, M., and Hari Krishna, R., 2019, Studies on batch adsorptive removal of malachite green from synthetic wastewater using acid treated coffee husk: Equilibrium, kinetics and thermodynamic studies, *Microchem. J.*, 146 192–201.

[14] Qu, W., Yuan, T., Yin, G., Xu, S., Zhang, Q., and Su, H., 2019, Effect of properties of activated carbon on malachite green adsorption, *Fuel*, 249, 45–53.

[15] Nidheesh, P.V., Zhou, M., and Oturan, M.A., 2018, An overview on the removal of synthetic dyes from water by electrochemical advanced oxidation processes, *Chemosphere*, 197, 210–227.

[16] Shankar, Y.S., Ankur, K., Bhushan, P., and Mohan, D., 2019, "Utilization of Water Treatment Plant (WTP) Sludge for Pretreatment of Dye Wastewater Using Coagulation/Flocculation" in *Advances in Waste Management*, Eds. Kalamdhad, A., Singh, J., and Dhamodharan, K., Springer Singapore, 107–121.

[17] Dahri, M.K., Kooh, M.R.R., and Lim, L.B.L., 2014, Water remediation using low cost adsorbent walnut shell for removal of malachite green: Equilibrium, kinetics, thermodynamic and regeneration studies, *J. Environ. Chem. Eng.*, 2 (3), 1434–1444.

[18] Robinson, T., McMullan, G., Marchant, R., and Nigam, P., 2001, Remediation of dyes in textile effluent: A critical review on current treatment technologies with a proposed alternative, *Bioresour. Technol.*, 77 (3), 247–255.

[19] Dai, L., Zhu, W., He, L., Tan, F., Zhu, N., Zhou, Q., He, M., and Hu, G., 2018, Calcium-rich biochar from crab shell: An unexpected super adsorbent for dye removal, *Bioresour. Technol.*, 267, 510–516.

[20] Fil, BA, 2016, Isotherm, kinetic, and thermodynamic studies on the adsorption behavior of malachite green dye onto montmorillonite clay, *Part. Sci. Technol.*, 34 (1), 118–126.

[21] Abdelrahman, E.A., 2018, Synthesis of zeolite nanostructures from waste aluminum cans for efficient removal of malachite green dye from aqueous media, *J. Mol. Liq.*, 253, 72–82.

[22] Chen, Y., Lin, Y.C., Ho, S.H., Zhou, Y., and Ren, N., 2018, Highly efficient adsorption of dyes by biochar derived from pigments-extracted macroalgae pyrolyzed at different temperature, *Bioresour. Technol.*, 259, 104–110.

[23] Palapa, N.R., Juleanti, N., Mohadi, R., Taher, T., Rachmat, A., and Lesbani, A., 2020, Copper aluminum layered double hydroxide modified by biochar and its application as an adsorbent for procion red, *J. Water Environ. Technol.*, 18 (6), 359–371.

[24] Blaisi, N.I., Zubair, M., Ihsanullah, I., Ali, S., Kazeem, T.S., Manzar, M.S., Al-Kutti, W., and Al Harthi, M.A., 2018, Date palm ash-MgAl-layered double hydroxide composite: Sustainable adsorbent for effective removal of methyl orange and eriochrome black-T from aqueous phase, *Environ. Sci. Pollut. Res.*, 25 (34), 34319–34331.

[25] Chen, J., 2011, "Chapter 18 - Host-Guest Functional Materials" in *Modern Inorganic Synthetic Chemistry*, Eds. Xu. R., Pang, W., and Huo, Q., Elsevier, Amsterdam, 405–428.

[26] Shan, R., Yan, L., Yang, Y., Yang, K., Yu, S., Yu, H., Zhu, B., and Du, B., 2015, Highly efficient removal of three red dyes by adsorption onto Mg-Al-layered double hydroxide, *J. Ind. Eng. Chem.*, 21, 561–568.

[27] Zhu, Z., Ouyang, S., Li, P., Shan, L., Ma, R., and Zhang, P., 2020, Persistent organic pollutants removal via hierarchical flower-like layered double hydroxide: Adsorption behaviors and mechanism investigation, *Appl. Clay Sci.*, 188, 105500.

[28] Starukh, H., and Levytska, S., 2019, The simultaneous anionic and cationic dyes removal with Zn–Al layered double hydroxides, *Appl. Clay Sci.*, 180, 105183.

[29] Palapa, N.R., Juleanti, N., Normah, N., Taher, T., and Lesbani, A., 2020, Unique adsorption properties of malachite green on interlayer space of Cu-Al and Cu-Al-$SiW_{12}O_{40}$ layered double hydroxides, *Bull. Chem. React. Eng. Catal.*, 15 (3), 653–661.

[30] Wang, T., Li, C., Wang, C., and Wang, H., 2018, Biochar/MnAl-LDH composites for Cu(II) removal from aqueous solution, *Colloids Surf., A*, 538, 443–450.

[31] Lestari, N.A., 2019, Reduction of CO_2 emission by integrated biomass gasification-solid oxide fuel cell combined with heat recovery and in-situ CO_2 utilization, *Evergreen*, 6 (3), 254–261.

[32] Tareq, R., Akter, N., and Azam, M.S., 2019, "Chapter 10 - Biochars and Biochar Composites: Low-Cost Adsorbents for Environmental Remediationin" in *Biochar from Biomass and Waste*, Eds., Ok, Y.S., Tsang, D.C.W., Bolan, N., and Novak, J.M., Elsevier Inc., Amsterdam, Netherland, 169–209.

[33] Jerai, F., Miyazaki, T., Saha, B.B., and Koyama, S., 2015, Overview of adsorption cooling system based on activated carbon: Alcohol Pair, *Evergreen*, 2 (1), 30–40.

[34] Huang, D., Liu, C., Zhang, C., Deng, R., Wang, R., Xue, W., Luo, H., Zeng, G., Zhang, Q., and Guo, X., 2019, Cr(VI) removal from aqueous solution using biochar modified with Mg/Al-layered double hydroxide intercalated with ethylenediaminetetraacetic acid, *Bioresour. Technol.*, 276, 127–132.

[35] Meili, L., Lins, P.V., Zanta, C.L.P.S., Soletti, J.I., Ribeiro, L.M.O., Dornelas, C.B., Silva, T.L., and Vieira, M.G.A., 2019, MgAl-LDH/biochar composites for methylene blue removal by adsorption, *Appl. Clay Sci.*, 168, 11–20.

[36] Wan, S., Wang, S., Li, Y., and Gao, B., 2017, Functionalizing biochar with Mg–Al and Mg–Fe layered double hydroxides for removal of phosphate from aqueous solutions, *J. Ind. Eng. Chem.*, 47, 246–253.

[37] Ravuru, S.S., Jana, A., and De, S., 2019, Synthesis of NiAl-layered double hydroxide with nitrate intercalation: Application in cyanide removal from steel industry effluent, *J. Hazard. Mater.*, 373, 791–800.

[38] Kajjumba, G.W., Emik, S., Öngen, A., Özcan, H.K., and Ayd, S., 2019, "Modelling of Adsorption Kinetic Processes—Errors, Theory and Application" in *Modelling of Adsorption Kinetic Processes — Errors, Theory and Application*, Eds. Edebali, S., IntechOpen, Rijeka, Croatia.

[39] Aljeboree, A.M., Alkaim, A.F., and Al-Dujaili, A.H., 2015, Adsorption isotherm, kinetic modeling and thermodynamics of crystal violet dye on coconut

husk-based activated carbon, *Desalin. Water Treat.*, 53 (13), 3656–3667.

[40] Shaji, A., and Zachariah, A.K., 2017, "Chapter 9 - Surface Area Analysis of Nanomaterials" in *Thermal and Rheological Measurement Techniques for Nanomaterials Characterization*, Eds. Thomas, S., Thomas, R., Zachariah, A.K., and Mishra, R.K., Elsevier Inc., Amsterdam, Netherlands, 197–231.

[41] Parida, K.M., and Mohapatra, L., 2012, Carbonate intercalated Zn/Fe layered double hydroxide: A novel photocatalyst for the enhanced photo degradation of azo dyes, *Chem. Eng. J.*, 179 131–139.

[42] James, J., and Rao, M.S., 1986, Silica from rice husk through thermal decomposition, *Thermochim. Acta*, 97, 329–336.

[43] Mohapatra, S., Sakthivel, R., Roy, G.S., Varma, S., Singh, S.K., and Mishra, D.K., 2011, Synthesis of β-SiC powder from bamboo leaf in a DC extended thermal plasma reactor, *Mater. Manuf. Processes*, 26 (11), 1362–1368.

[44] Gholami, P., Khataee, A., Soltani, R.D.C., Dinpazhoh, L., and Bhatnagar, A., 2020, Photocatalytic degradation of gemifloxacin antibiotic using Zn-Co-LDH@biochar nanocomposite, *J. Hazard. Mater.*, 382, 121070.

[45] Lesbani, A., Asri, F., Palapa, N.R., Taher, T., and Rachmat, A., 2020, Efficient removal of methylene blue by adsorption using composite based Ca/Al layered double hydroxide-biochar, *Global NEST J.*, 22 (2), 250–257.

[46] Harizi, I., Chebli, D., Bouguettoucha, A., Rohani, S., and Amrane, A., 2019, A new Mg–Al–Cu–Fe-LDH composite to enhance the adsorption of acid red 66 dye: characterization, kinetics and isotherm analysis, *Arabian J. Sci. Eng.*, 44 (6), 5245–5261.

[47] Abukhadra, M.R., Sayed, M.A., Rabie, A.M., and Ahmed, S.A., 2019, Surface decoration of diatomite by Ni/NiO nanoparticles as hybrid composite of enhanced adsorption properties for malachite green dye and hexavalent chromium, *Colloids Surf., A*, 577, 583–593.

[48] Bagheri, R., Ghaedi, M., Asfaram, A., Alipanahpour Dil, E., and Javadian, H., 2019, RSM-CCD design of malachite green adsorption onto activated carbon with multimodal pore size distribution prepared from *Amygdalus scoparia*: Kinetic and isotherm studies, *Polyhedron*, 171, 464–472.

[49] Jiang, F., Dinh, D.M., and Hsieh, Y.L., 2017, Adsorption and desorption of cationic malachite green dye on cellulose nanofibril aerogels, *Carbohydr. Polym.*, 173, 286–294.

[50] Rajabi, M., Mahanpoor, K., and Moradi, O., 2019, Preparation of PMMA/GO and PMMA/GO-Fe_3O_4 nanocomposites for malachite green dye adsorption: Kinetic and thermodynamic studies, *Composites, Part B*, 167, 544–555.

[51] Raghu, M.S., Kumar, K.Y., Prashanth, M.K., Prasanna, B.P., Vinuth, R., and Pradeep Kumar, C.B., 2017, Adsorption and antimicrobial studies of chemically bonded magnetic graphene oxide-Fe3O4 nanocomposite for water purification, *J. Water Process Eng.*, 17, 22–31.

[52] Palapa, N.R., Taher, T., Wijaya, A., and Lesbani, A., 2021, Modification of Cu/Cr layered double hydroxide by Keggin type polyoxometalate as adsorbent of malachite green from aqueous solution, *Sci. Technol. Indones.*, 6 (3), 209–217.

[53] Zhang, J., Liu, M., Yang, T., Yang, K., and Wang, H., 2016, A novel magnetic biochar from sewage sludge: Synthesis and its application for the removal of malachite green from wastewater, *Water Sci. Technol.*, 74 (8), 1971–1979.

[54] Sharifpour, E., Alipanahpour Dil, E., Asfaram, A., Ghaedi, M., and Goudarzi, A., 2019, Optimizing adsorptive removal of malachite green and methyl orange dyes from simulated wastewater by Mn-doped CuO-nanoparticles loaded on activated carbon using CCD-RSM: Mechanism, regeneration, isotherm, kinetic, and thermodynamic studies, *Appl. Organomet. Chem.*, 33 (3), e4768.

[55] Normah, N., Palapa, N.R., Taher, T., Mohadi, R., Utami, H.P., and Lesbani, A., 2021, The ability of composite Ni/Al-carbon based material toward readsorption of iron(II) in aqueous solution, *Sci. Technol. Indones.*, 6 (3), 156–165.

[56] Naushad, M., Alqadami, A.A., AlOthman, Z.A., Alsohaimi, I.H., Algamdi, M.S., and Aldawsari, A.M., 2019, Adsorption kinetics, isotherm and reusability studies for the removal of cationic dye from aqueous medium using arginine modified activated carbon, *J. Mol. Liq.*, 293, 111442.

[57] Nishimura, S., Takagaki, A., and Ebitani, K., 2010, Monodisperse iron oxide nanoparticles embedded in Mg-Al hydrotalcite as a highly active, magnetically separable, and recyclable solid base catalyst, *Bull. Chem. Soc. Jpn.*, 83 (7), 846–851.

Simple One-Pot Synthesis of Sulfonic-Acid-Functionalized Silica for Effective Catalytic Esterification of Levulinic Acid

Desinta Dwi Ristiana, Suyanta Suyanta, and Nuryono Nuryono*

Department of Chemistry, Faculty Mathematics and Natural Sciences, Universitas Gadjah Mada, Sekip Utara, PO BOX BLS 21, Yogyakarta 55281, Indonesia

** **Corresponding author:***

tel: +62-8156800908
email: nuryono_mipa@ugm.ac.id

Received: August 9, 2021
Accepted: September 24, 2021

DOI: 10.22146/ijc.68301

Abstract: *Silica functionalized with sulfonic acid catalyst (SiO_2–SO_3H) was synthesized through a one-pot method and evaluated as the catalyst material for esterification of levulinic acid in an excess amount of ethanol. Sodium silicate solution was used as the silica source, and then a silane coupling agent, namely GPTMS, was used to incorporate the sulfonic group of 2-aminoethanesulfonic acid (AS) into the silica. Functionalization of AS using GPTMS in the slightly acidic condition has been successfully carried out based on the characterization with FTIR, SEM-EDX, and TGA measurements. Catalyst with the AS to SiO_2 molar ratio of 5:6 (SiO_2–SO_3H(5)) showed the highest acid content (1.02 mmol g^{-1}) and the highest conversion of levulinic acid (70%). The reaction followed pseudo-first-order with the rate constant of 0.00414 min^{-1}. Catalyst material was regenerated by washing with alcohol and water, and the catalyst material can be reused at least for 3 cycles. From this study, the SiO_2–SO_3H produced from a green process is an effective catalyst to produce esters used in fuel additives.*

Keywords: *silica acid catalyst; coupling agent; one-pot method; esterification; levulinic acid*

INTRODUCTION

Liquid acid catalysts are widely used in industrial processes because of their high activity and selectivity [1]. However, these catalysts are avoided because of the toxicity, separation difficulty, and waste production. Solid acid catalysts then become the solution to overcome drawbacks in the liquid acid catalyst. The silica-based catalyst has been developed among many solid acid catalysts because it is widely abundant, biocompatible, non-toxic, thermally stable, and easy to synthesize in mild conditions [2]. Silica-based material has been highly explored because it can easily be modified with other molecules or materials because of its surface silanol (Si–OH) groups. Silanol groups themselves are weak acid sites that cannot be used directly without modification. Silica was compatible with organic substances and was often modified with organic compounds for different purposes such as adsorbent, catalyst, and ion-exchanger [3-5]. A silica network can be formed via a sol-gel process consisting of hydrolysis and condensation silica precursors such as silica alkoxides or silica salts with acid or base catalyst.

One particular challenge in synthesizing acid catalysts is incorporating acid sites onto weak acid, an inorganic material such as silica. Several reports have been demonstrated to increase its acidity. Xiong et al. [6] incorporated HSO_3Cl directly onto the surface of silica materials to form a SiO_2–SO_3H acid catalyst. However, –SO_3H groups were not firmly attached to SiO_2 and were accessible to leach. Berbar et al. [4] used sulfonated polyethersulfone membrane (PES) to increase the acidity of silica materials. However, the sulfonation degree of PES was limited only up to 27%. Ziarani et al. [5] used organosilane 3-mercaptopropyltrimethoxysilane (MPTMS) as –SO_3H groups precursor whereas –SH groups were oxidized with strong oxidants such as H_2O_2 and HNO_3. This research seems promising mainly because of the strong covalent bond formed between acid sites and silica surfaces. Amidst its advantage, the synthesis method needs to use a very toxic oxidizing

agent that was not safe for the environment. New approaches need to be developed to form silica acid catalysts without harming the environment.

Silica modification with organosilane seems pretty interesting with the advantages to adding organic moieties that already bonded in organosilane onto silica by strong covalent bonding [7]. Organosilane consists of an organic functional group and three alkoxy groups. Similar to the silica alkoxides, it can undergo hydrolysis and condensation, leaving organic moiety on the external sites [8]. The organic moiety of organosilane can be used directly, and it can also be used as a coupling agent to bridge other organic substances onto silica materials. The organic sites of organosilane can be further modified with another organic substance to change the functional groups as desired [3]. Through this crosslinking, the preferred organic groups can form strong covalent bonds with silanols from silica materials. One of the silane coupling agents often used is 3-glycidoxypropyltrimethoxysilane (GPTMS). GPTMS is often labeled as "network former" because it has an epoxy ring that is reactive with nucleophile groups [7,9-10]. Several experiments have been reported using GPTMS as a coupling agent between silica and many organic substances such as chitosan [9], alginate [11], ethylenediamine, and diethylenetriamine [12-13]. Most of them take advantage of epoxy ring-opening of GPTMS through nucleophilic substitution with nucleophilic groups. However, none of these experiments was conducted to obtain silica acid catalysts. Previously, Palla-Rubio et al. [7] incorporated chitosan onto GPTMS and caused crosslinking through condensation with silanol groups. Amine groups of chitosan act as a nucleophile to encourage ring-opening of the epoxide group in GPTMS.

Various studies have shown that the ring-opening of epoxide groups could happen in acid solutions such as acetic acid [7] and formic acid [14]. Gabrielli et al. [15] reported that ring-opening of epoxide group in GPTMS could be conducted at slightly acidic conditions to undergo nucleophilic attack. In neutral pH, the catalysis will be too slow. Meanwhile, it can cause hydrolysis of epoxide ring to form diol group that hinders the nucleophilic reaction in the too acidic condition. In basic conditions, polymerization of silanol groups will dominate the ring-opening reaction. Incorporating an organic substance containing nucleophilic group onto GPTMS might cause another challenge because it requires appropriate conditions to maximize nucleophilic attack and maintain the polymerization of silanol groups.

In silica modified with organic substance with the presences of GPTMS, generally, silica is first isolated and functionalized with GPTMS using grafting method and then reacted with an organic molecule to form crosslinking between silica and organic molecules [9]. However, this method is limited by multi-step processes, high cost, strict preparation conditions, and often uses many additional reagents, which are not environmentally friendly [16]. In addition, the surface of pre-synthesized silica may have different reactivity towards modifier molecules. Silane groups of modifier molecules may also undergo self-condensation before reacting with silica surfaces resulting in non-uniform particles [17].

In contrast with the grafting method, the one-pot synthesis method offers many advantages, such as reducing synthesis steps and using additional reagents [18]. This method reduces the total synthesis time, which is more economical and efficient. Moreover, more organic moieties can be bonded onto silica using the one-pot co-condensation method [19]. Epoxide group of GPTMS can undergo nucleophilic attack by the amine group in slightly acidic conditions. The sulfonic acid group is at the end of the structure and acts as the acid site for catalysis. By crosslinking with GPTMS, the sulfonic group can bond tightly onto the silica surface.

In the present study, we develop a new strategy that is simple, non-toxic, and environmentally friendly to synthesize silica-based acid catalysts with covalent bonds between the epoxy group in GPTMS and the amine group in 2-aminoethanesulfonic acid. Another objective of this study is to examine the catalyst activity in the esterification of levulinic acid with ethanol, including the evaluation of the reaction kinetics. Levulinic esters are often used as an additive to blend with diesel or biodiesel fuel where they can give great

performances such as high lubricity, low toxicity, flash point stability, and good cold flow properties [20]. Fernandes et al. [21] reported that levulinic acid could be used up to 5 wt.% in biodiesel engines without further modification.

■ EXPERIMENTAL SECTION

Materials

The chemicals used for the synthesis of catalysts included sodium silicate (Na_2SiO_3) solution (SiO_2 25.5–28.5%, Na_2O 7.5–8.5%, Aldrich) as a silica source, 3-glycidoxypropyltrimethoxysilane (GPTMS, 98.0%, Aldrich), and 2-aminoethanesulfonic acid (99.4% Focus Herb). Levulinic acid (98.0%, Aldrich) and ethanol (99.8%, Aldrich) were used to evaluate the activity of catalysts.

Instrumentation

The characterization of functional groups in the materials was performed by FTIR spectrometer using Shimadzu Prestige 21 (4000–400 cm^{-1}) with the KBr pellet method. The thermogravimetric analysis (TGA) was performed on Mettler Toledo by measuring the weight loss materials in increasing temperature of 303–973 K at a rate of 10 K min^{-1} under N_2 atmosphere. The morphology and the elemental composition were analyzed with the scanning electron microscopy (SEM) images (JEOL JSM-6510LA) equipped with an energy dispersive X-ray spectrometer (EDX). Gas Chromatography-Mass Spectroscopy (Thermo scientific Trace 1310 Gas Chromatograph-ISQ LT Single Quadrupole Mass Spectrometer) was used to confirm the presence of ethyl levulinate.

Procedure

Synthesis of catalyst

The synthesis was carried out by varying the amount of GPTMS-AS from 3 to 6 mmol. First, 3–6 mmol (0.38–0.76 g) of 2-aminoethanesulfonic acid (AS) was dissolved in 10 mL of 0.05 M formic acid. Afterward, the GPTMS of the same amount (3–6 mmol, 0.71–1.42 g) was added, and the reaction was allowed to proceed for 2 h at room temperature to form GPTMS-AS. This step was done to form a covalent bond between two structures. Then, a solution of Na_2SiO_3 (2 mL, 6 mmol SiO_2) and GPTMS-AS was reacted under a magnetic stirrer with the addition of 5 M HCl solution dropwise until the gel was formed. The gel was left for 24 h at room temperature to strengthen the bond, and the resulting gel was dried at 60 °C for 24 h and named as SiO_2–SO_3H. The dried gel was ground and washed with alcohol to remove residues. The composition of precursors and code of the resulted products are summarized in Table 1. The obtained materials were characterized to identify the functional groups with FTIR, morphology and chemical composition with SEM-EDX, and the acidity with volumetry.

Determination of SiO_2–SiO_3H acidity

Acidity was determined with a volumetric method. Excess of NaOH solution was used to measure the total of acidic groups in catalysts [22]. After equilibrium was reached, the solution was back titrated with HCl solution. A small number of catalysts (0.1 g) were reacted with 10 mL NaOH solution 0.05 M for 60 min. Non-adsorbed NaOH was determined using the back titration method with 0.05 M HCl solution and phenolphthalein as the indicator.

Esterification of levulinic acid

The catalytic performance of various catalysts was tested on levulinic esterification with excess ethanol, as shown in Fig. 1. The optimum condition of esterification was first determined using a catalyst with the highest acid content. As much as 1 g (8.4 mmol) of levulinic acid and 2.5 mL (84 mmol) ethanol (the molar ratio of 1:10) were mixed with 50 mg (5 wt.%) of catalyst. The reaction was performed by heating the mixture of levulinic acid, ethanol, and the catalyst at 70 °C in a three-necked flask equipped with a stirrer and a condenser for 6 h. After the reaction, the catalysts were separated from liquid mixtures

Table 1. Composition and code of catalysts produced

AS (g; mmol)	GPTMS (g; mmol)	Na_2SiO_3 (mL; mmol SiO_2)	Product code
0.38; 3	0.71; 3	2; 6	SiO_2–SO_3H(3)
0.50; 4	0.95; 4	2; 6	SiO_2–SO_3H(4)
0.63; 5	1.18; 5	2; 6	SiO_2–SO_3H(5)
0.76; 6	1.42; 6	2; 6	SiO_2–SO_3H(6)

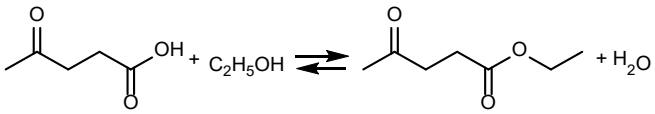

Fig 1. Esterification reaction of levulinic acid

with the filtration. The liquid mixtures of product and unreacted levulinic acid were collected and titrated with KOH and phenolphthalein as the indicator. The conversion was calculated according to Eq. (1). GC-MS confirmed the presence of ethyl levulinate product.

$$\text{Conversion}(\%) = 1 - \frac{(\text{M} \times \text{V}) \text{ of KOH}}{\text{mol of acid total}} \times 100 \quad (1)$$

Different levulinic acid:ethanol molar ratios (1:10 and 1:15) and percentage of the catalyst (10 wt.%) were tested as the comparison. The esterification conditions with the highest conversion were then used to determine the catalysts' optimum reaction time and reusability. The levulinic acid:ethanol molar ratio of 1:10 gave the highest conversion (~32%) when the reaction used 5 wt.% of catalyst for 3 h, and this condition was then used for further experiments.

A reusability test was also performed using the used catalysts that have been washed with alcohol and water. Esterification of levulinic acid with regenerated catalyst was performed at the same condition for 4 h. With the same proportion (molar ratio 1:10 and 5 wt.% catalyst), the composition of levulinic acid, ethanol, and catalyst used for the reusability test was 4 times higher because of its possible mass decrease of the catalyst after reaction and washing treatment.

Kinetic study

The kinetics of levulinic acid esterification were evaluated based on the levulinic acid conversion at various times (1, 2, 4, 5, and 6 h). Esterification of levulinic acid and ethanol is a reversible reaction with the reaction rate presented in Eq. (2).

$$\text{Levulinic acid } (C_A) + \text{Ethanol } (C_B) \rightleftarrows \text{Ethyl Levulinate } (C_C) + \text{Water } (C_D)$$

$$-r_A = \frac{-dC_A}{d_t} = k_1 C_A^{\alpha} C_B^{\beta} - k_2 C_C^{\gamma} C_D^{\delta} \quad (2)$$

where C_A, C_B, C_c, and C_D are the concentrations of levulinic acid, ethanol, ethyl levulinate, and water, with the reaction orders of α, β, γ, and δ, respectively. k_1 is the kinetic constant of ethyl levulinate formation, and k_2 is the kinetic constant of its reverse reaction.

The kinetic model could be simplified based on the following assumption [23]: The initial ethanol concentration was much higher than the initial concentration of levulinic acid; thus, C_B could be assumed constant through the reaction; The excess ethanol could push forward the equilibrium reaction and was considered an irreversible reaction as $k_1 >>> k_2$.

Thus, the kinetic model was simplified as Eq. (3) and (4), where $k = k_1 C_B^{\beta}$.

$$-\frac{dC_A}{dt} = k_1 C_A^{\alpha} C_B^{\beta} \quad (3)$$

$$-\frac{dC_A}{dt} = k C_A^{\alpha} \quad (4)$$

When levulinic acid conversion was assumed as x, the concentration of levulinic acid can be written as $C_A = C_{A_0}(1 - x)$, where C_{A0} was referred to as the initial concentration of levulinic acid. Then Eq. (4) can be transformed to Eq. (5) and (6).

$$-\frac{d(1-x)}{dt} = \frac{k}{C_{A_0}} \left[C_{A_0} (1-x) \right]^{\alpha} \quad (5)$$

$$\frac{dx}{dt} = \frac{k}{C_{A_0}} \left[C_{A_0} (1-x) \right]^{\alpha} \quad (6)$$

Using the integration method, the equation can be solved for different order reactions (α = 0, 1, 2) based on the experimental results.

■ RESULTS AND DISCUSSION

FTIR analysis was conducted to ensure the successful reaction of GPTMS and AS and the success of SiO_2 and GPTMS-AS polymerization. Fig. 2 shows absorption spectra of precursors (GPTMS and AS) and synthesized SiO_2–SO_3H. FTIR spectra of GPTMS shown at 2900 and 2800 cm^{-1} are due to asymmetric and symmetric stretching of C–H composed from the organic side of GPTMS. The broad peak at 1090 cm^{-1} corresponds to the stretching vibration of Si–O–CH_3 [24]. The characteristic of the epoxide group can be observed from the sharp peak at 850 cm^{-1} that corresponds to asymmetric C–O–C vibration [25]. The C–O stretching vibrations were observed at 1400 cm^{-1} [26]. The presence of the sulfonic group in AS is

observed at 1200 and 1050 cm^{-1}, representing stretching asymmetric and symmetric of S=O, respectively [27].

The success of GPTMS functionalization with AS can be observed from the FTIR spectra of synthesized SiO_2–SO_3H catalysts. It is indicated by the absence of a prominent peak at 850 cm^{-1}, which represents asymmetric C–O–C stretching vibrations. The peaks corresponding to the epoxide ring and sulfonic group are not observed mainly due to the complete ring-opening or the overlapping band with the strong Si–O–Si absorption band at 1200–1050 cm^{-1}. However, it can be observed that the band around 1200–1050 cm^{-1} in the spectra of SiO_2–SO_3H catalyst appears very sharp, indicating the character of the S=O band. The character of the N–H bond also appears slightly around 3200–3000 cm^{-1}.

Fig. 3 shows FTIR spectra of SiO_2–SO_3H materials prepared using various concentrations of GPTMS-AS. The small shoulder at 950 cm^{-1} is due to Si–OH groups [25], the peak at 1200–1050 cm^{-1} corresponds to Si–O–Si stretching vibration, and the broad absorption around 3500 cm^{-1} is due to O–H stretching vibrations from hydroxyl groups. This peak overlapped with secondary amines (–NH–), which appear at 3350–3310 cm^{-1} after the reaction of GPTMS and AS [7,26]. The absorption of Si–O–Si at 750 cm^{-1} [25] increased when more GPTMS functionalized sulfonic acid was added. Increased sharpness around 1250–1200 cm^{-1} indicates S=O bands overlapped with broad Si–O–Si in the same area. Even though S=O bands overlapped with Si–O–Si vibration, we can assume that the appearance of sharp peaks in the catalysts with more GPTMS-AS content indicates the presence of sulfonic acid groups in the catalysts. SiO_2–SO_3H(5) shows the sharpest peak in this area, indicating the highest value of sulfonic acid groups.

Hydrolyzed methoxy groups of GPTMS can react with silanol groups of silica while the epoxy ring reacts with organic molecules giving hybrid organic-inorganic networks. The epoxy ring can easily be opened with a nucleophile group such as an amine group at room temperature. The amine group of an organic substance was acidified with formic acid to promote the epoxy ring-opening and provide suitable pH for hydrolysis and condensation with silicate [14]. The reaction of GPTMS and AS are shown in Fig. 4(a). Hydrolysis of silicate produces silanol groups (Fig. 4(b)) at the same time as hydrolysis of GPTMS-AS (Fig. 4(c)) produced from the previous reaction. Silanols from silicate and GPTMS-AS can undergo condensation to form a silica network (Fig. 4(d)).

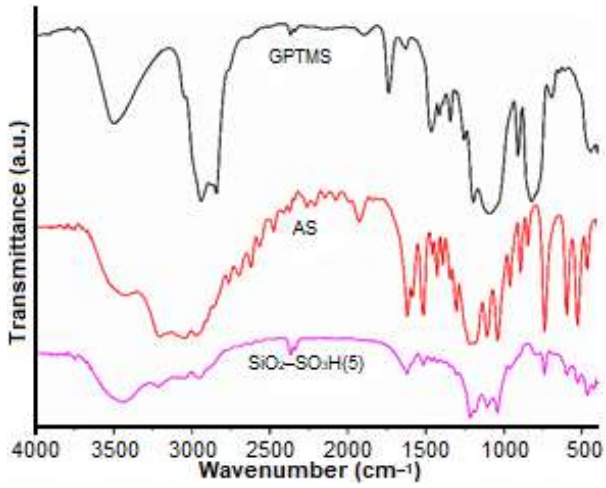

Fig 2. FTIR spectra of GPTMS, AS, and SiO_2–SO_3H(5)

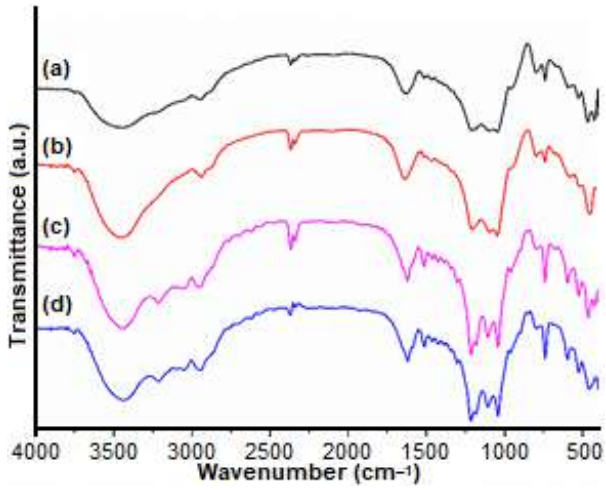

Fig 3. FTIR spectra of (a) SiO_2–SO_3H(3), (b) SiO_2–SO_3H(4); (c) SiO_2–SO_3H(5); and (d) SiO_2–SO_3H(6)

A scanning electron microscope (SEM) was used to characterize the particles' morphology, shape, and size. Fig. 5 and 6 show SEM images and particle size distribution of catalysts. The surface of the particles was not smooth because of the presence of organic moieties. GPTMS-AS addition will loosen the gel network and

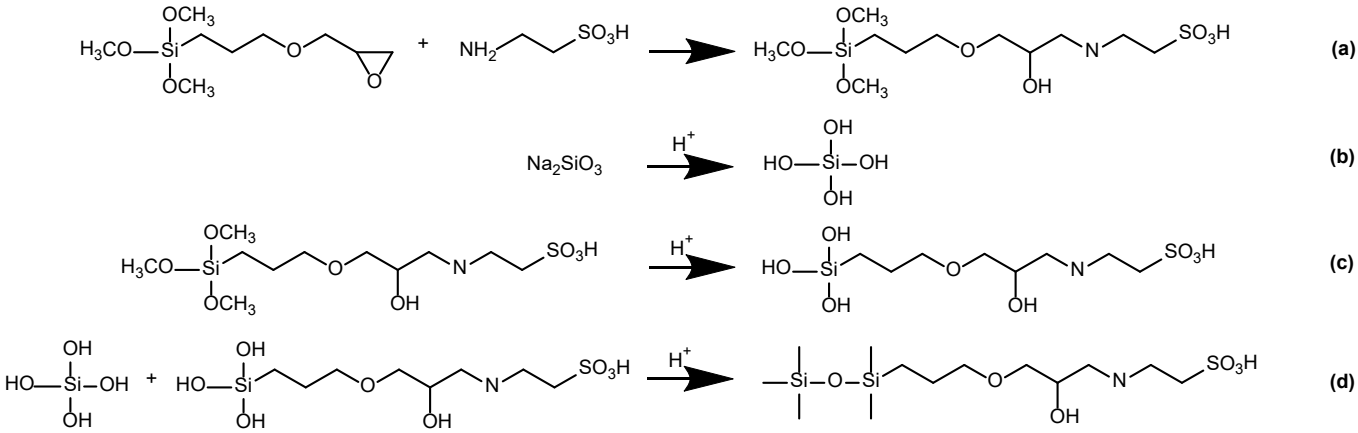

Fig 4. Reaction model of catalyst synthesis

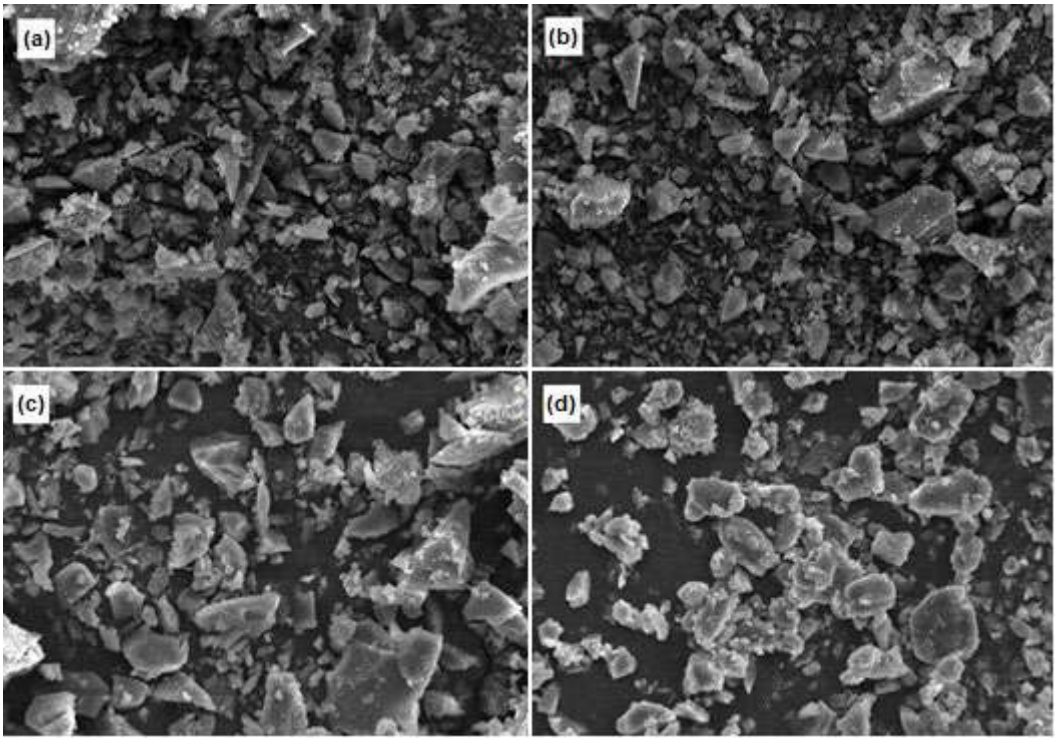

Fig 5. SEM images of (a) SiO_2–SO_3H(3), (b) SiO_2–SO_3H(4); (c) SiO_2–SO_3H(5); and (d) SiO_2–SO_3H(6)

increase the particle size because of the organic sites in the significant difference between all catalysts. The particles are spheres, and the size distribution with increasing GPTMS-AS is around 3.66, 4.10, 4.36, and 4.40 μm. Catalyst with more organic content (SiO_2–SO_3H(6)) showed a larger particle size than catalysts with less organic content (SiO_2–SO_3H(3)).

EDX analysis of catalysts showed the presence of S and N elements which is part of AS. The existence of these elements indicates the successful reaction of GPTMS and AS. N and S elements observed from the surface of particles were found around 5–7% and 5–8%, respectively. The highest amount of N and S elements was found in SiO_2–SO_3H(5), suggesting high acid sites. From the mapping images of the SiO_2–SO_3H(6) catalyst in Fig. 7, it can be observed that all compounds were fairly distributed around silica particles. The acid content of catalysts was also determined using the titration method. Excess of NaOH solution was used to measure the total of acidic groups in catalysts. After equilibrium

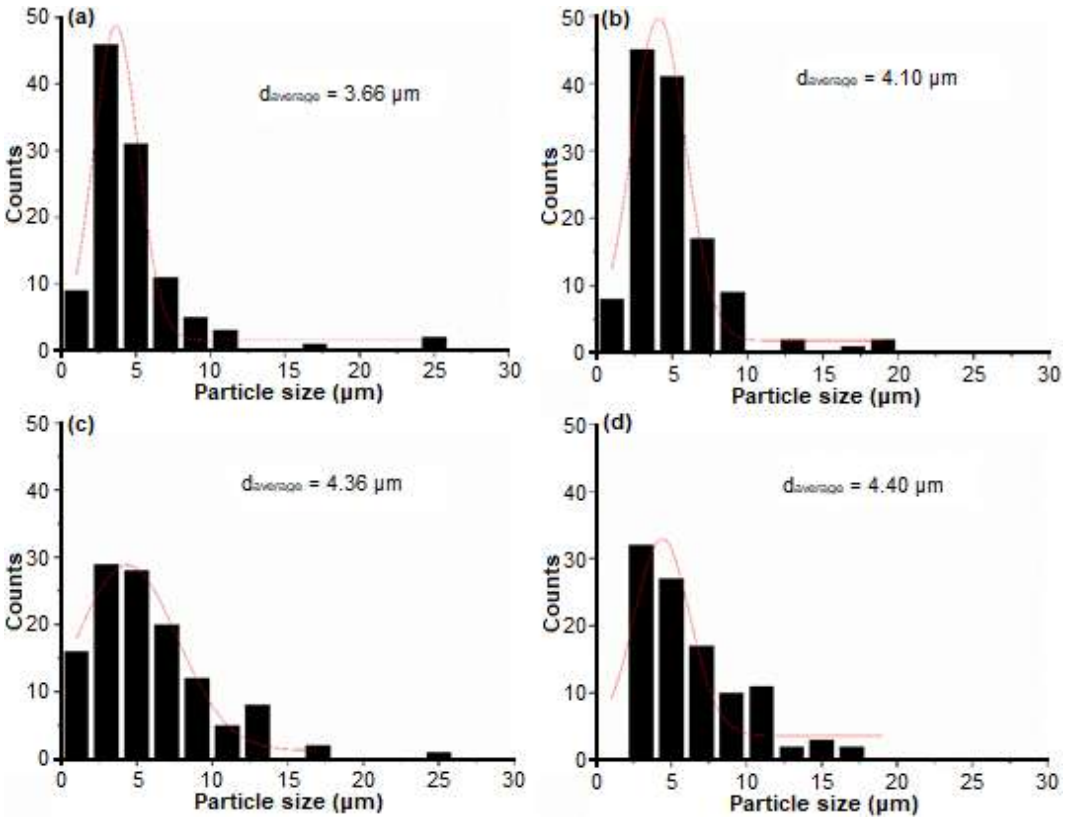

Fig 6. Particle size distribution of (a) SiO_2–SO_3H(3), (b) SiO_2–SO_3H(4); (c) SiO_2–SO_3H(5); and (d) SiO_2–SO_3H(6)

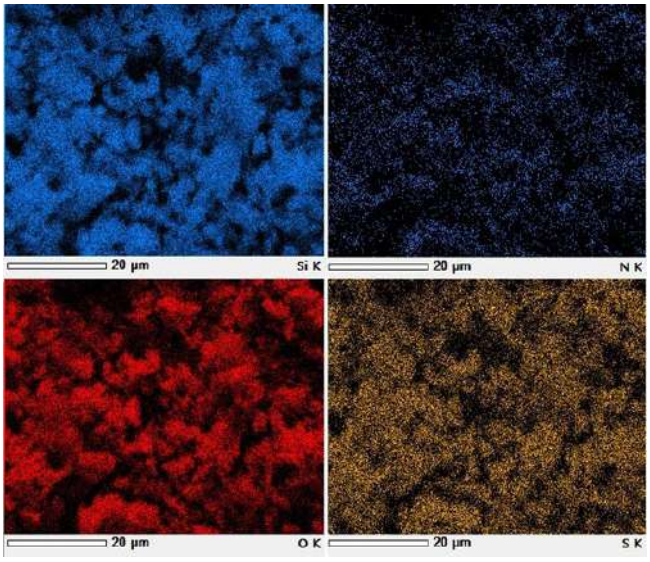

Fig 7. Mapping images of SiO_2–SO_3H(6)

was reached, the solution was back titrated with HCl solution. Table 2 shows that SiO_2–SO_3H(5) has the highest acid content (1.02 mmol g^{-1}) even though the GPTMS-AS added was less than on SiO_2–SO_3H(6). Excessive content of organic network might cause steric hindrance that blocks the accessibility of acid sites to react with incoming molecules. The high content of GPTMS-AS might also cause insufficient polymerization ability of silane sides in GPTMS-AS with silanols of silica precursors. This result agrees with FTIR analysis, showing that SiO_2–SO_3H(5) has the sharpest peak at 1200 and 1050 cm^{-1}, representing stretching of S=O bonds, indicating the highest content of sulfonic acid groups. From EDX results, SiO_2–SO_3H(5) also has the highest S element content, further confirming the high amount of sulfonic acid groups as acid sites in catalysts.

The thermogravimetric analysis is provided in Fig. 8. TG analysis was performed to quantify organic moiety to understand the functionalization and analyze catalysts' stability. The total weight loss depended on the amount of organic network. The pattern is similar for all catalysts. The decrease in weight before 100 °C was caused by removing small organic molecules and adsorbed water from the samples [29]. The weight loss of around 250 °C was assigned to an organic network

Table 2. N and S elements content by EDX analysis and acid content by titration method

Catalyst	Element content (%) by EDX analysis		Acid content (mmol g^{-1}) by titration method
	N	S	
$SiO_2–SO_3H(3)$	6.42	6.66	0.56
$SiO_2–SO_3H(4)$	5.16	5.27	0.86
$SiO_2–SO_3H(5)$	7.18	8.15	1.02
$SiO_2–SO_3H(6)$	5.79	7.75	0.66

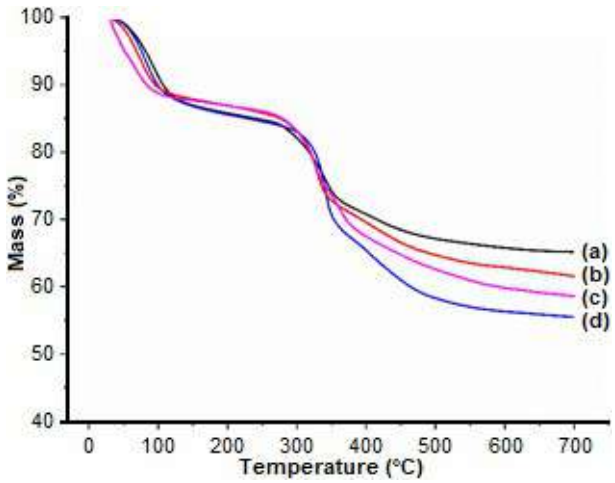

Fig 8. TGA curve of (a) $SiO_2–SO_3H(3)$, (b) $SiO_2–SO_3H(4)$; (c) $SiO_2–SO_3H(5)$; and (d) $SiO_2–SO_3H(6)$

that undergoes evaporation [30-31]. At those temperatures, organic networks, including acid sites from GPTMS-AS, may be evaporated. The difference in weight loss was due to the amount of GPTMS-AS on the catalyst surface. The weight loss observed for all catalysts from 250-500 °C increased with GPTMS-AS content. $SiO_2–SO_3H(3)$ showed 16.94% weight loss at those temperatures, while $SiO_2–SO_3H(4)$, $SiO_2–SO_3H(5)$, and $SiO_2–SO_3H(6)$ showed 20.70, 22.75, and 25.95% weight loss, respectively. $SiO_2–SO_3H(6)$ showed the highest weight loss even though the N and S content were not the highest. This result may be due to the incomplete reaction of GPTMS and AS, resulting in bond formation between silica and GPTMS, leaving AS out of the framework. Organic decomposition continues slightly till temperature 500 °C indicating the complete decomposition of the organic network. There is no weight loss observed above 500 °C for all materials indicating the presence of stable silica.

Esterification of Levulinic Acid

Catalytic performance of $SiO_2–SO_3H$ catalysts was evaluated for esterification of levulinic acid with excess ethanol. The acidity of the catalyst is the main factor determining the catalyst activity for esterification reaction; thus, the catalyst with the highest acid content ($SiO_2–SO_3H(5)$) was first used to determine the optimum conditions. Different reaction parameters such as levulinic acid:ethanol molar ratio and amount of catalyst were examined to optimize the esterification reaction conditions. Fig. 9 shows conversion of levulinic acid esterification with 1:5, 1:10, and 1:15 levulinic acid:ethanol molar ratio, over 5 and 10 wt.% catalysts $SiO_2–SO_3H(5)$.

As more catalyst was used, the conversion increased progressively, except for the 1:10 molar ratio of levulinic acid to ethanol, where the conversion only slightly increased. Increasing the catalyst amount will supply

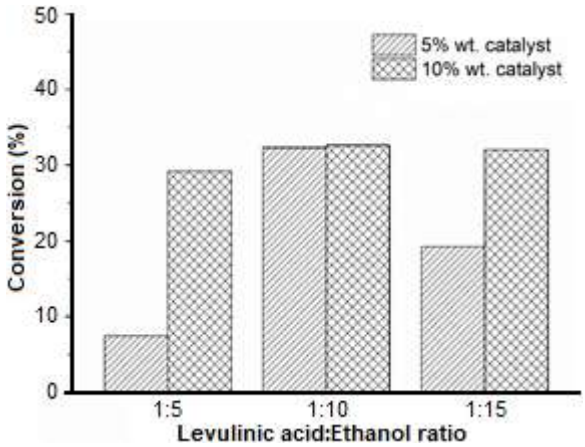

Fig 9. Determination of optimum condition for esterification of levulinic acid using a catalyst with highest acid content ($SiO_2–SO_3H(5)$)

enough acid sites to improve the esterification of levulinic acid and ethanol. The levulinic acid conversion at varied ethanol amounts increased at 1:10 and decreased at 1:15 molar ratios. As esterification is a reversible reaction, excess alcohol needs to be added to drive the forward reaction. However, too many alcohol supplies could reduce the conversion. Alcohol exists as a reactant and co-solvent to dilute levulinic acid. The redundant alcohol content can shield levulinic acid molecules from reacting with acid sites of catalysts [32]. As a result, a suitable condition is needed to keep the esterification going and optimize the blending condition to minimize the viscosity and limitation of mass transfer in the reaction system [33]. The molar ratio of 1:10 might be the optimum condition for esterification of levulinic acid because it produces the highest conversion for both amounts of catalysts (5 and 10 wt.%). As the conversion in 5 and 10 wt.% was only slightly different, 5 wt.% catalysts were chosen as the optimum catalyst amount.

The total conversion of levulinic acid over time is shown in Fig. 10. All catalysts have the same pattern for conversion at different times of reaction. The highest conversions are reached only after 5 h. The use of catalysts with the highest acid content can accelerate product formation. The SiO_2–SO_3H(5) catalyst gives the highest conversion (70%), while SiO_2–SO_3H(3) and SiO_2–SO_3H(4) only give 46% and 65% conversion. A decrease in conversion (59%) can be observed in SiO_2–SO_3H(6) catalyst. This result followed the amount of acid sites, where the highest conversion was achieved from catalyst with highest acid sites. More acid sites give more available sites for levulinic acid and ethanol to interact. Hence, there are more molecules reacted to form ethyl levulinate products. According to the previous report [34], the production of esters is limited by the reversibility and water by-product formation. After some time of reactions, water by-product is accumulated, encouraging the back reaction of esterification, and at 5 h of reaction, all catalysts exhibit the highest conversion. However, at 6 h of reaction, the conversion of levulinic acid decreased. This phenomenon might happen because of the occurrence of back-reaction and also the blocking of acid sites by water by-products. The accumulation of levulinic acid and its intermediate on acid sites and the entanglement of organic chains can also cause the decrease of conversion at 6 h [35].

Compared to previous literature presented in Table 3, this result was higher than the commercial catalyst reported by Fernandes et al. [21]. For the same reaction

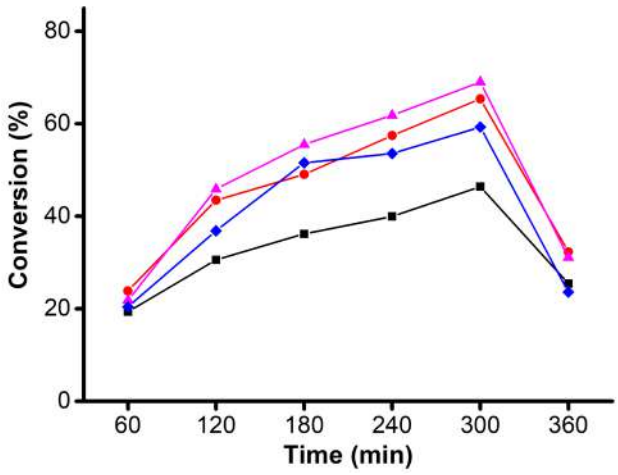

Fig 10. Conversion of levulinic acid over (□) SiO_2–SO_3H(3), (○) SiO_2–SO_3H(4), (△) SiO_2–SO_3H(5), and (◊) SiO_2–SO_3H(6)

Table 3. Conversion of levulinic acid esterification over various catalysts from previous reports

Catalyst	Levulinic acid:Ethanol	Catalyst amount (%)	Temp (°C)	Time (h)	Conversion (%)	Ref.
Amberlyst-15	1:5	2.5	70	5	54	[21]
Sulfonated CNT	1:5	2.5	70	5	20–55	[40]
Sulfonated carbon	1:5	5.0	80	9	58	[37]
Sulfated SnO_2	1:5	2.5	70	7	75	[36]
Carbon cryogel	1:20	5.0	78	6	52	[39]
ZSM-12	1:1	13.1	100	24	56	[41]
SiO_2–SO_3H(5)	1:10	5.0	70	5	70	this work

time, Amberlyst-15 generates 54% conversion. On the other hand, sulfated SnO_2 showed higher conversion (75%) in 7 h, mainly due to a higher acid site [36]. Moreover, the synthesis of the catalyst requires a toxic H_2SO_4 solution and a longer esterification reaction time. With the same amount of catalyst, sulfonated carbon gives 58% conversion only after 9 h of reaction at 80 °C [37].

The used catalyst was washed with alcohol and water to remove adsorbed organic species to examine the reusability of the catalysts. Under the optimum condition, three cycles of esterification were conducted. As shown in Fig. 11, all catalysts showed a decrease in conversion after the third circle. Conversion of SiO_2–SO_3H(4) decreases from 65 to 51% after the third cycle, while SiO_2–SO_3H(5) and SiO_2–SO_3H(6) decrease from 70 to 50% and 59 to 50%, respectively. In addition, SiO_2–SO_3H(3) shows a recognizable reduction in conversion after the third cycle (from 46 to 13%). These decreases in conversions are attributed to the loss of acid sites into the alcohol media during repeated use, as previously reported by Kuwahara et al. [38].

Kinetic Study

The reaction order and rate constants were determined by integration of Eq. (6) for pseudo-zeroth order (α = 0), pseudo-first-order (α = 1), and pseudo-second-order (α = 2). The equations are shown in Eq. (7), (8), and (9), respectively.

$$xC_{A_0} = kt \quad (7)$$

$$-\ln(1-x) = kt \quad (8)$$

$$\frac{1}{(1-x)} = C_{A_0}kt \quad (9)$$

The rate constant (k) for the pseudo-zeroth-order reaction was determined as the slope in the plot of x vs. t, and the rate constant (k) for the pseudo-first-order reaction was determined as the slope of the -ln(1-x) vs. t plot. For pseudo-second-order reaction, the rate constant (k) was calculated from the slope of 1/(1-x) vs. t.

Experimental data was used to calculate the rate constant and determine the reaction order by linear fitting. Zainol et al. [39] determined the kinetic model of levulinic acid using a carbon catalyst. The observed data were directly fitted with a pseudo-first-order kinetic model. For better determination, other kinetic models were also fitted. The kinetic model could be determined by comparing observed and predicted data accuracy for three kinetic models. Fig. 12 shows the kinetic plots obtained from levulinic acid esterification using SiO_2–SO_3H catalysts. Based on the data shown in Table 4, all catalysts fitted the best with a pseudo-first-order kinetic plot with the highest R^2 value compared to other kinetic plots. The predicted and observed data showed a small deviation in pseudo-first-order than pseudo-zeroth and pseudo-second-order. Therefore, the kinetic models of levulinic acid esterification with SiO_2–SO_3H catalyst could be classified as pseudo-first-order reactions.

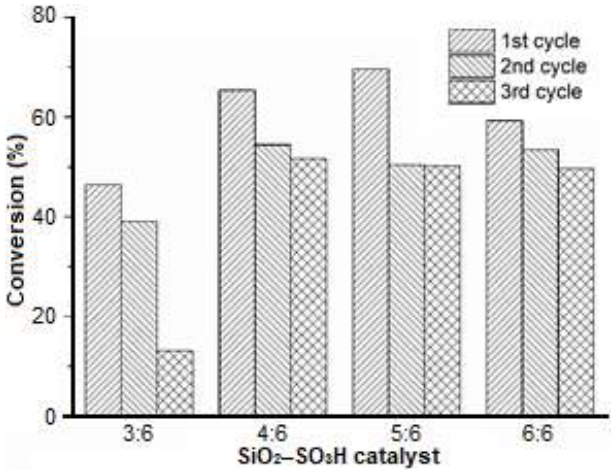

Fig 11. Reusability of SiO_2–SO_3H catalysts

Table 4. Kinetic parameters of levulinic acid esterification over SiO_2–SO_3H catalysts

Catalysts	Pseudo-Zeroth-Order	Pseudo-First-Order	Pseudo-Second-Order	Pseudo-First-Order
	R^2	R^2	R^2	k (10^{-3} min^{-1})
SiO_2–SO_3H(3)	0.83	0.92	0.50	2.36
SiO_2–SO_3H(4)	0.88	0.97	0.83	3.78
SiO_2–SO_3H(5)	0.88	0.98	0.90	4.14
SiO_2–SO_3H(6)	0.87	0.95	0.75	3.36

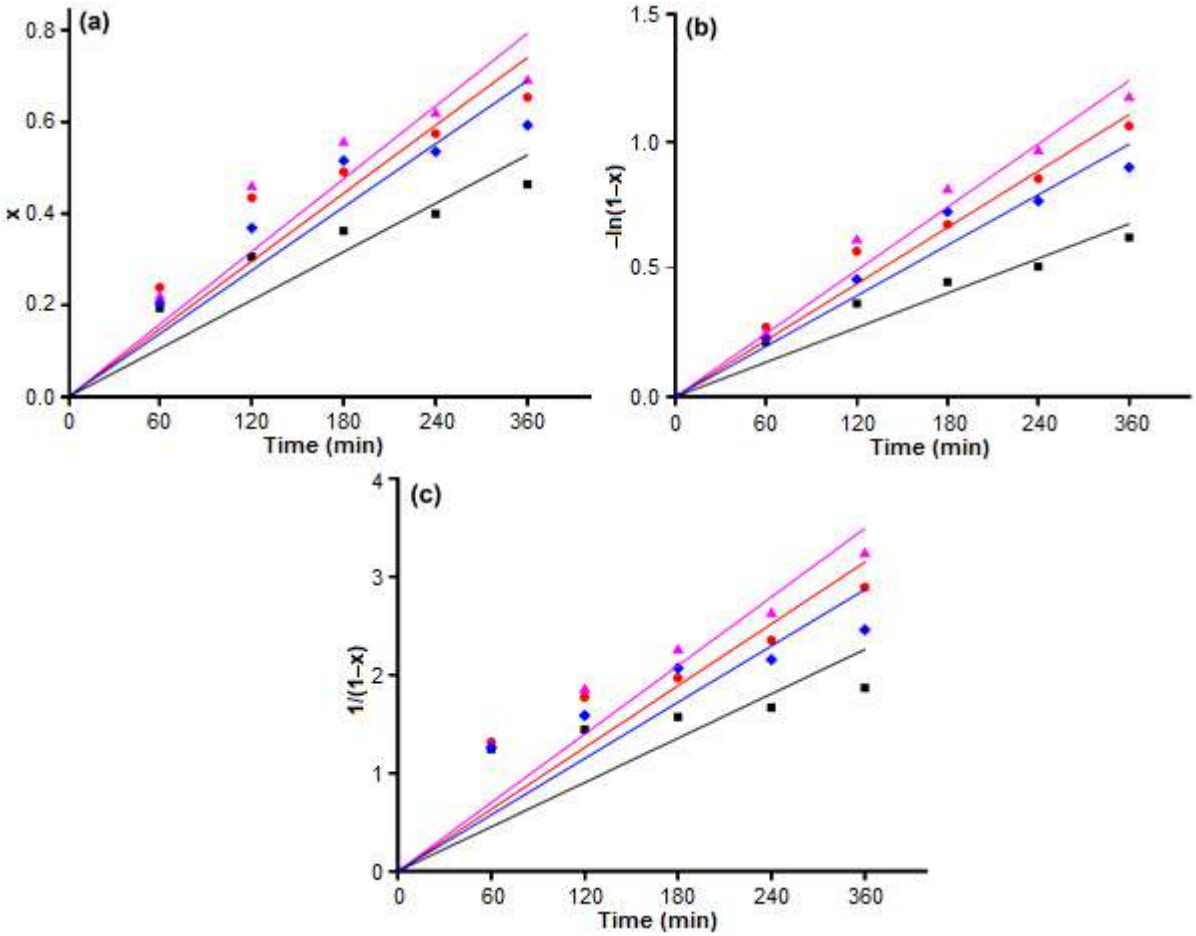

Fig 12. Kinetic plots for (a) pseudo-zeroth-order, (b) pseudo-first-order, and (c) and pseudo-second-order of (□) SiO_2–SO_3H(3), (○) SiO_2–SO_3H(4), (△) SiO_2–SO_3H(5), and (◊) SiO_2–SO_3H(6)

The slope acquired from the pseudo-first-order linear equation determined the rate constant (k) for each catalyst. As expected, the catalyst with the highest acidity has a higher rate constant.

CONCLUSION

In summary, we have shown that sulfonate functionalized silicas (SiO_2-SO_3H) have been successfully synthesized with a simple one-pot and green process using the solution of Na_2SiO_3, 3-glycidoxypropyltrimethoxysilane (GPTMS), and 2-aminoethanesulfonic acid (AS) as the silica source, the coupling agent, and sulfonic acid group source, respectively. The epoxide groups of GPTMS react with amine groups from AS by a ring-opening reaction. The SiO_2–SiO_3H produced is a prospective solid acid catalyst to any reaction for producing renewable fuels. SiO_2–SO_3H(5) is the most effective catalyst for esterification of levulinic acid with 70% conversion and high reusability; three cycles of reuse did not give a significant conversion decrease.

ACKNOWLEDGMENTS

We acknowledge the Universitas Gadjah Mada and PMDSU scholarship by the Ministry of the Higher Education Republic of Indonesia under grant No. 6314/UN1/DITLIT/DIT-LIT/LT/2019.

REFERENCES

[1] Malins, K., Kampars, V., Kampare, R., Prilucka, J., Brinks, J., Murnieks, R., and Apseniece, L., 2014, Properties of rapeseed oil fatty acid alkyl esters derived from different alcohols, *Fuel*, 137, 28–35.

[2] Liu, Y., Huo, P., Ren, J., and Wang, G., 2017, Organic–inorganic hybrid proton-conducting

electrolyte membranes based on sulfonated poly(arylene ether sulfone) and SiO_2–SO_3H network for fuel cells, *High Perform. Polym.*, 29 (9), 1037–1048.

[3] Diagboya, P.N.E., and Dikio, E.D., 2018, Silica-based mesoporous materials; emerging designer adsorbents for aqueous pollutants removal and water treatment, *Microporous Mesoporous Mater.*, 266, 252–267.

[4] Berbar, Y., Hammache, Z.E., Bensaadi, S., Soukeur, R., Amara, M., and Van der Bruggen, B., 2019, Effect of functionalized silica nanoparticles on sulfonated polyethersulfone ion exchange membrane for removal of lead and cadmium ions from aqueous solutions, *J. Water Process Eng.*, 32, 100953.

[5] Ziarani, G.M., Badiei, A., Hassanzadeh, M., and Mousavi, S., 2014, Synthesis of 1,8-dioxo-decahydroacridine derivatives using sulfonic acid functionalized silica (SiO_2-Pr-SO_3H) under solvent free conditions, *Arabian J. Chem.*, 7 (3), 335–339.

[6] Xiong, Y., Zhang, Z., Wang, X., Liu, B., and Lin, J., 2014, Hydrolysis of cellulose in ionic liquids catalyzed by a magnetically-recoverable solid acid catalyst, *Chem. Eng. J.*, 235, 349–355.

[7] Palla-Rubio, B., Araújo-Gomes, N., Fernández-Gutiérrez, M., Rojo, L., Suay, J., Gurruchaga, M., and Goñi, I., 2019, Synthesis and characterization of silica-chitosan hybrid materials as antibacterial coatings for titanium implants, *Carbohydr. Polym.*, 203, 331–341.

[8] Rahman, I.A., and Padavettan, V., 2012, Synthesis of silica nanoparticles by sol-gel: Size-dependent properties, surface modification, and applications in silica-polymer nanocomposites-A review, *J. Nanomater.*, 2012, 132424.

[9] Nhavene, E.P.F., da Silva, W.M., Trivelato Junior, R.R., Gastelois, P.L., Venâncio, T., Nascimento, R., Batista, R.J.C., Machado, C.R., Macedo, W.A.A., and de Sousa, E.M.B., 2018, Chitosan grafted into mesoporous silica nanoparticles as benznidazol carrier for Chagas diseases treatment, *Microporous Mesoporous Mater.*, 272, 265–275.

[10] Parale, V.G., Kim, T., Lee, K.Y., Phadtare, V.D., Dhavale, R.P., Jung, H.N.R., and Park, H.H., 2019, Hydrophobic TiO_2–SiO_2 composite aerogels synthesized via in situ epoxy-ring opening polymerization and sol-gel process for enhanced degradation activity, *Ceram. Int.*, 46 (4), 4939–4946.

[11] Vueva, Y., Connell, L.S., Chayanun, S., Wang, D., McPhail, D.S., Romer, F., Hanna, J.V., and Jones, J.R., 2018, Silica/alginate hybrid biomaterials and assessment of their covalent coupling, *Appl. Mater. Today*, 11, 1–12.

[12] Shao, Z., Wu, G., Cheng, X., and Zhang, Y., 2012, Rapid synthesis of amine cross-linked epoxy and methyl co-modified silica aerogels by ambient pressure drying, *J. Non-Cryst. Solids*, 358 (18-19), 2612–2615.

[13] Vreugdenhil, A.J., Gelling, V.J., Woods, M.E., Schmelz, J.R., and Enderson, B.P., 2008, The role of crosslinkers in epoxy-amine crosslinked silicon sol-gel barrier protection coatings, *Thin Solid Films*, 517 (2), 538–543.

[14] de Luca, M.A., Martinelli, M., and Barbieri, C.C.T., 2009, Hybrid films synthesised from epoxidised castor oil, γ-glycidoxypropyltrimethoxysilane and tetraethoxysilane, *Prog. Org. Coat.*, 65 (3), 375–380.

[15] Gabrielli, L., Russo, L., Poveda, A., Jones, J.R., Nicotra, F., Jiménez-Barbero, J., and Cipolla, L., 2013, Epoxide opening versus silica condensation during sol-gel hybrid biomaterial synthesis, *Chem. Eur. J.*, 19 (24), 7856–7864.

[16] An, S., Sun, Y., Song, D., Zhang, Q., Guo, Y., and Shang, Q., 2016, Arenesulfonic acid-functionalized alkyl-bridged organosilica hollow nanospheres for selective esterification of glycerol with lauric acid to glycerol mono- and dilaurate, *J. Catal.*, 342, 40–54.

[17] Sierra, I., and Pérez-Quintanilla, D., 2013, Heavy metal complexation on hybrid mesoporous silicas: An approach to analytical applications, *Chem. Soc. Rev.*, 42 (9), 3792–3807.

[18] Da'na, E., 2017, Adsorption of heavy metals on functionalized-mesoporous silica: A review, *Microporous Mesoporous Mater.*, 247, 145–157.

[19] Chen, J., Chen, J., Zhang, X., Gao, J., and Yang, Q., 2016, Efficient and stable PS-SO_3H/SiO_2 hollow

nanospheres with tunable surface properties for acid catalyzed reactions, *Appl. Catal., A*, 516, 1–8.

[20] Hayes, D.J., Ross, J., Hayes, H.B., and Fitzpatrick, S., 2005, "The Biofine Process – Production of Levulinic Acid, Furfural, and Formic Acid from Lignocellulosic Feedstocks" in *Biorefineries-Industrial Processes and Products: Status Quo and Future Directions*, Eds. Kamm, B., Gruber, P.R., and Kamm, M., Wiley-VCH Verlag GmbH & Co. KGaA, Weinheim, 139–164.

[21] Fernandes, D.R., Rocha, A.S., Mai, E.F., Mota, C.J.A., and da Silva, V.T., 2012, Levulinic acid esterification with ethanol to ethyl levulinate production over solid acid catalysts, *Appl. Catal., A*, 425-426, 199–204.

[22] Benak, K.R., Dominguez, L., Economy, J., and Mangun, C.L., 2002, Sulfonation of pyropolymeric fibers derived from phenol-formaldehyde resins, *Carbon*, 40 (13), 2323–2332.

[23] Trinh, B.M., and Mekonnen, T., 2018, Hydrophobic esterification of cellulose nanocrystals for epoxy reinforcement, *Polymer*, 155, 64–74.

[24] Gupta, G., Pathak, S.S., and Khanna, A.S., 2012, Anticorrosion performance of eco-friendly silane primer for coil coating applications, *Prog. Org. Coat.*, 74 (1), 106–114.

[25] Shajesh, P., Smitha, S., Aravind, P.R., and Warrier, K.G.K., 2009, Synthesis, structure and properties of cross-linked $R(SiO_{1.5})/SiO_2$ (R = 3-glycidoxypropyl) porous organic inorganic hybrid networks dried at ambient pressure, *J. Colloid Interface Sci.*, 336 (2), 691–697.

[26] Heo, J.H., Lee, J.W., Lee, B., Cho, H.H., Lim, B., and Lee, J.H., 2017, Chemical effects of organo-silanized SiO_2 nanofillers on epoxy adhesives, *J. Ind. Eng. Chem.*, 54, 184–189.

[27] Elsayed, I., Mashaly, M., Eltaweel, F., Jackson, M.A., and Hassan, E.B., 2018, Dehydration of glucose to 5-hydroxymethylfurfural by a core-shell $Fe_3O_4@SiO_2$-SO_3H magnetic nanoparticle catalyst, *Fuel*, 221, 407–416.

[28] Ambrożewicz, D., Ciesielczyk, F., Nowacka, M., Karasiewicz, J., Piasecki, A., MacIejewski, H., and Jesionowski, T., 2013, Fluoroalkylsilane versus alkylsilane as hydrophobic agents for silica and silicates, *J. Nanomater.*, 2013, 631938.

[29] Han, X., Zhu, G., Ding, Y., Miao, Y., Wang, K., Zhang, H., Wang, Y., and Liu, S.B., 2019, Selective catalytic synthesis of glycerol monolaurate over silica gel-based sulfonic acid functionalized ionic liquid catalysts, *Chem. Eng. J.*, 359, 733–745.

[30] González, M.D., Salagre, P., Taboada, E., Llorca, J., Molins, E., and Cesteros, Y., 2013, Sulfonic acid-functionalized aerogels as high resistant to deactivation catalysts for the etherification of glycerol with isobutene, *Appl. Catal., B*, 136-137, 287–293.

[31] de Oliveira, F.M., Segatelli, M.G., and Tarley, C.R.T., 2016, Hybrid molecularly imprinted poly(methacrylic acid-TRIM)-silica chemically modified with (3-glycidyloxypropyl)trimethoxysilane for the extraction of folic acid in aqueous medium, *Mater. Sci. Eng., C*, 59, 643–651.

[32] Niu, S., Ning, Y., Lu, C., Han, K., Yu, H., and Zhou, Y., 2018, Esterification of oleic acid to produce biodiesel catalyzed by sulfonated activated carbon from bamboo, *Energy Convers. Manage.*, 163, 59–65.

[33] Mahmoud, H.R., 2019, Bismuth silicate ($Bi_4Si_3O_{12}$ and Bi_2SiO_5) prepared by ultrasonic-assisted hydrothermal method as novel catalysts for biodiesel production via oleic acid esterification with methanol, *Fuel*, 256, 115979.

[34] Cannilla, C., Bonura, G., Costa, F., and Frusteri, F., 2018, Biofuels production by esterification of oleic acid with ethanol using a membrane assisted reactor in vapour permeation configuration, *Appl. Catal., A*, 566, 121–129.

[35] Liu, Y., Lotero, E., and Goodwin, J.G., 2006, Effect of carbon chain length on esterification of carboxylic acids with methanol using acid catalysis, *J. Catal.*, 243 (2), 221–228.

[36] Popova, M., Shestakova, P., Lazarova, H., Dimitrov, M., Kovacheva, D., Szegedi, A., Mali, G., Dasireddy, V., Likozar, B., Wilde, N., and Gläser, R., 2018, Efficient solid acid catalysts based on sulfated tin oxides for liquid phase esterification of levulinic

acid with ethanol, *Appl. Catal., A*, 560, 119–131.

[37] Li, N., Wang, Q., Ullah, S., Zheng, X.C., Peng, Z.K., and Zheng, G.P., 2019, Esterification of levulinic acid in the production of fuel additives catalyzed by porous sulfonated carbon derived from pine needle, *Catal. Commun.*, 129, 105755.

[38] Kuwahara, Y., Kaburagi, W., Nemoto, K., and Fujitani, T., 2014, Esterification of levulinic acid with ethanol over sulfated Si-doped ZrO_2 solid acid catalyst: Study of the structure-activity relationships, *Appl. Catal., A*, 476, 186–196.

[39] Zainol, M.M., Amin, N.A.S., and Asmadi, M., 2019, Kinetics and thermodynamic analysis of levulinic acid esterification using lignin-furfural carbon cryogel catalyst, *Renewable Energy*, 130, 547–557.

[40] Oliveira, B.L., and da Silva, V.T., 2014, Sulfonated carbon nanotubes as catalysts for the conversion of levulinic acid into ethyl levulinate, *Catal. Today*, 234, 257–263.

[41] Imyen, T., Saenluang, K., Dugkhuntod, P., and Wattanakit, C., 2021, Investigation of ZSM-12 nanocrystals evolution derived from aluminosilicate nanobeads for sustainable production of ethyl levulinate from levulinic acid esterification with ethanol, *Microporous Mesoporous Mater.*, 312, 110768.

Influence of LLDPE-g-MA on Mechanical Properties, Degradation Performance, and Water Absorption of Thermoplastic Sago Starch Blends

Denny Akbar Tanjung[1,2], Novesar Jamarun[1*], Syukri Arief[1], Hermansyah Aziz[1], Ahmad Hafizullah Ritonga[1,3], and Boy Isfa[1]

[1]*Department of Chemistry, University of Andalas, Limau Manis, Padang 25163, West Sumatera, Indonesia*

[2]*Department of Agrotechnology, Faculty Agriculture, Universitas Medan Area, Medan-20223, North Sumatera, Indonesia*

[3]*Department of Chemistry, Faculty of Science, Technology, and Information, University of Sari Mutiara Indonesia, Medan 20123, North Sumatera, Indonesia*

* ***Corresponding author:***

email: novesarjamarun@sci.unand.ac.id

Received: August 20, 2021
Accepted: November 11, 2021

DOI: 10.22146/ijc.68558

Abstract: *The addition of LLDPE-g-MA into the compound of sago starch/LLDPE was studied to improve its mechanical, morphology, degradation performance, and water absorption properties. Thermoplastic Sago Starch was composed of a mixture of sago starch and glycerol. LLDPE-g-MA was prepared in varied concentrations based on the weight of TPSS (0, 6, 8, 10, and 14 wt.%) by reacting LLDPE, maleic anhydride, and benzoyl peroxide using an internal mixer. The results showed an increase in values obtained from mechanical tests, i.e., tensile strength was improved from 0.6902 to 3.6187 N/mm^2 with the addition of LLDPE-g-MA at 10 wt.%. The addition also resulted in a 1.44% increment in elongation at break and 251 N/mm^2 for Young's Modulus. The surface morphology of the sample demonstrated an excellent interfacial adhesion reaction or LLDPE dispersion over the entire surface of the matrix (starch). The water absorption test continued to decrease with the increase in the LLDPE-g-MA concentration from 53 wt.% (without LLDPE-g-MA) to 14 wt.% at 10 wt.% LLDPE-g-MA concentration. The degradation performance showed that the sample could be degraded under all three conditions for up to 30 days.*

Keywords: *bioplastic; compatibilizer; coupling agent; LLDPE-g-MA; thermoplastic*

INTRODUCTION

Several ways that can be done in handling plastic waste are recycling, incineration, and burial. However, burning plastic waste can produce toxic substances that are harmful to living things and the environment. Meanwhile, planting waste has been found ineffective because plastic is difficult to degrade. Another way that has been developed to overcome the problem of plastic waste is the use of biodegradable plastics. Biodegradable plastics can be decomposed by microorganisms such as fungi, algae, and bacteria [1-2]. Unfortunately, the use of biodegradable plastics has yet to be perceived as impactful in saving the environment.

The advantages of using natural materials to make biodegradable plastics include their natural abundance, economical price, ease of accessibility, and degradability in the natural environment [3-4]. Some natural materials used as basic materials for making bioplastics are starch, cellulose, protein, and fat. However, biodegradable plastic materials have several weaknesses, including poor mechanical properties, susceptibility to high temperatures, brittleness, very low flow indices, and hydrophilicity [5-9].

The weakness of the natural material can be overcome by mixing it with synthetic materials such as Linear Low-Density Polyethylene (LLDPE), High-Density Polyethylene (HDPE), Polypropylene (PP), and others. The advantages of these synthetic materials include resistance to high temperatures, good mechanical properties, high flow indices, elasticity, and

hydrophobicity. However, mixing the materials can be challenging as it is difficult for the mixture of natural and synthetic materials to be homogeneous (incompatible) due to their hydrophilicity and hydrophobicity, respectively. The compatibility between the two mixtures can be improved by adding a compatibilizer, a compound capable of increasing the homogeneity of a mixture and improving the adhesion between different phases [10-13].

The most widely used compatibilizer is anhydrous maleic acid. The addition of anhydrous maleic acid is widely used because of its economic cost, low toxicity, and ease of grafting the anhydrous maleic acid onto polymers at normal melting temperatures without significant homo-polymerization. Anhydride reaction with starch hydroxyl forms esters that do not produce water during the reaction [11].

Several studies have used anhydrous maleic acid as a compatibilizer [14-15] and sago starch as a matrix [16-18]. This study aimed to determine the effect of the compatibilizer (LLDPE-g-MA) on the mechanical properties, degradation performance, and water absorption of the thermoplastic mixture of sago starch. The addition of LLDPE-g-MA (LLDPE grafting anhydrous maleic acid) at varying concentrations into the thermoplastic mixture of sago starch (sago starch + glycerol) and LLDPE was expected to improve the mechanical properties of the composite, inhibit the rate of water absorption by the composite and allow for degradation of the composite under three environmental conditions.

■ EXPERIMENTAL SECTION

Materials

The materials used in this study were commercial sago starch from the Parang brand of PT Warna Jaya Indonesia, anhydrous maleic acid (p.a) and benzoyl peroxide (p.a) from MERCK-Germany, glycerol (p.a), and Low Linear Density of Polyethylene (LLDPE) UF 1810S1 pellet (density: 0.922 g/m^3, melt Index (190 °C/2.16 kg) of 1.0 g/10 min, melt point of 122 °C) from PT Chandra Asri- Indonesia, and distilled water.

Procedure

Preparation of TPSS

TPSS was made by reacting sago starch with glycerol plus water as a solvent. The ratio of sago starch and glycerol was 65:35 wt.% [19]. Therefore, the amount of water added was 250% of the total mixture. First, the mixture was heated at 100 °C until it formed gelatin. Then, the water content of the gelatin was reduced by drying for 24 h at 80 °C, which could reduce the water content to 5%.

Preparation of compatibilizer

The compounds were mixed using an internal mixer (Haake Polydrive Thermo). LLDPE was firstly added into the mixing chamber, followed by anhydrous maleic acid after 5 min of mixing, before finally being added with BPO. The mixture was incubated at 150 °C and shaken at 100 rpm, for 13 min. The composition of the mixture with added compatibilizer was 88 wt.% LLDPE, 9 wt.% anhydrous maleic acid, and 3 wt.% benzoyl peroxide. The mixture was cooled down and cut into pellets with 3 mm × 2 mm × 2 mm.

Preparation of TPSS/LLDPE/PE-g-MA blends

The final phase of this research involved the preparation of TPSS/LLDPE/PE-g-MA blends made of TPSS, LLDPE, and compatibilizer, with the ratio of TPSS to LLDPE, 80:20 wt.%. In addition, the concentration of compatibilizer was varied from 0, 6, 8, 10, 12 to14 wt.% based on TPSS weight.

Characterization

Compression molding. The Thermoplastic Sago Starch (TPSS)/LLDPE blends were molded via electric heating hydraulic compression. The procedures involved melting by preheating at 150 °C for 5 min, followed by compression at maximum pressure for 10 min at 150 °C. The mixture was molded according to the specimen of ASTM D638.

Spectroscopy Fourier Transform Infra-Red (FTIR). Spectroscopy Fourier Transform Infra-Red (FTIR; Perkin Elmer System 2000) was used to obtain qualitative information of the groups and chemical

characteristics of the TPSS/LLDPE blends. For each spectrum, 32 scans were consecutively recorded at a resolution of 16 cm^{-1}. The samples were measured in a layer with a thickness of 1 mm, prepared via hot press molding.

Tensile properties. Testing the mechanical properties of biodegradable plastics is necessary to determine the homogeneity of the mixture or interactions between polymers. Therefore, a tensile test was carried out using the Universal Band Tensilon with the specimen of ASTM D638 Type 1. The chamber temperature was set at 25 °C, with humidity of 60% RH and 10 mm speed/min. Three specimens were used to obtain the average value of tensile strength, elongation at break, and Young's modulus.

Test of morphology. Scanning Electron Microscopy (SEM) test was performed to evaluate the surface morphology of the TPSS/LLDPE mixture. Samples were dried in an oven to reduce moisture content and avoid electrostatic charging and poor resolution. Before the surface inspection, the sample was mounted on a piece of aluminum and a sputter, coated with a thin layer of gold.

Water absorption test. The water absorption test was carried out to investigate the ability of the TPSS/LLDPE compatibilizer mixture to absorb water. First, the sampling sheet was cut into a dimension of 20 mm × 20 mm [15] with a thickness of 3 mm. Next, the sheet was washed with distilled water, dried up to 80 wt.% for 12 h, then cooled down in a desiccator and weighed to gain initial weight. It was then immersed into aquadest for 10 days in the chamber at 28–30 °C and reweighed.

Biodegradability test. The compatible blend of TPSS/LLDPE with a dimension of 20 mm × 20 mm and a thickness of 3 mm was examined under different controlled conditions [20]. The sample was immersed in freshwater in the first condition and seawater in the second condition. The weight loss was measured every 10, 20, and 30 days. The hollow container was filled with soil, and the sample was buried 10 mm deep from the surface of the alluvial soil [15]. The soil was regularly wet to keep the humidity. The weight loss in the sample was monitored regularly every 10, 20, and 30 days. The test was carried out by washing the sample with distilled water, drying it in the chamber, and weighing until the measured weight was constant. The degradation test in the three environmental conditions was carried out indoors, with the humidity kept at 45–65% RH.

Thermogravimetric Analysis (TGA). The Thermogravimetric was carried out according to the STA module with a channel TGDTA 7,300. The sample used in this test was 7.73 mg with a heating rate of 10 °C/min, increasing from 30 to 650 °C. The flow rate of nitrogen gas was set at 50 mL/min.

■ RESULTS AND DISCUSSION

In Fig. 1, the spectrum of all mixtures with and without the compatibilizer shows characteristic peaks at 970–1080 and 3000–3650 cm^{-1}, indicating the presence of COO and hydroxyl, respectively. The new peak at 1707 cm^{-1} observed in each spectrum of the sago starch/LLDPE mixture with added compatibilizer was identified as an ester group formed from a hydroxyl reaction (3265 cm^{-1}) with an anhydride functional group in the TPSS. The formation of an ester group was also reported in previous studies [19]. It was also observed that the same peaks are present in all graphs, except those without the compatibilizer. Such difference was due to the small amount of compatibilizer (%) present in the mixture as determined based on the TPSS weight.

Fig. 2 shows that the values measured for tensile strength, Young's Modulus, and elongation at break

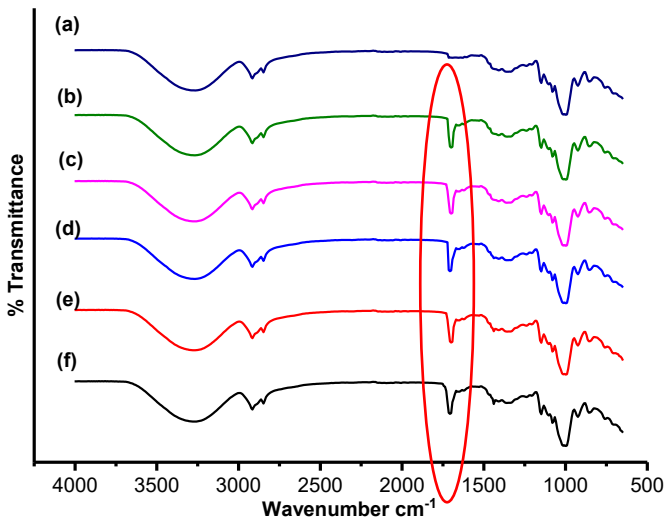

Fig 1. FTIR spectra of TPSS/LLDPE (a) 0%, (b) 4%, (c) 6%, (d) 8%, (e) 10%, (d) 12%, and (f) Compatibilizer 14%

significantly increased after adding a compatibilizer. The maximum peak was obtained with the addition of 10 wt.% LLDPE, resulting in values of 3.6187 N/mm^2 for tensile strength, 1.44% for Young's Modulus, and 251 N/mm^2 for elongation at break. The complete data are presented in Table 1.

The addition of a compatibilizer tends to increase the tensile strength by facilitating the interaction between starch (matrix) and LLDPE to make the mixture more homogeneous or compatible [19]. This study reported an increase in the tensile strength of the mixture from 0.6902 N/mm^2 (without compatibilizer) to 3.6187 N/mm^2 (with compatibilizer at 10 wt.%).

Compatibility has also been associated with the increase in flexibility or decrease in stiffness, as the compatibilizer acts as a bridge between hydrophobic (LLDPE) and hydrophilic (TPSS) components [21-22]. However, under certain conditions, increasing the compatibilizer's concentration may weaken the mixture's mechanical properties. It is safe to deduce that the interaction between the TPSS and LLDPE is only physical, which reduces the adhesion force between the surfaces of the hydrophilic and hydrophobic polymer groups, despite being connected by a coupling agent. Previous studies have reported that the decrease in tensile strength was due to homopolymerization that caused the maleic anhydride monomers to bind themselves instead of binding to the LLDPE chain [7].

Fig. 3(a) shows a TPSS/LLDPE blend without compatibilizer at a 1:500 scale. The image shows that the LLDPE polymer was not evenly distributed in the starch

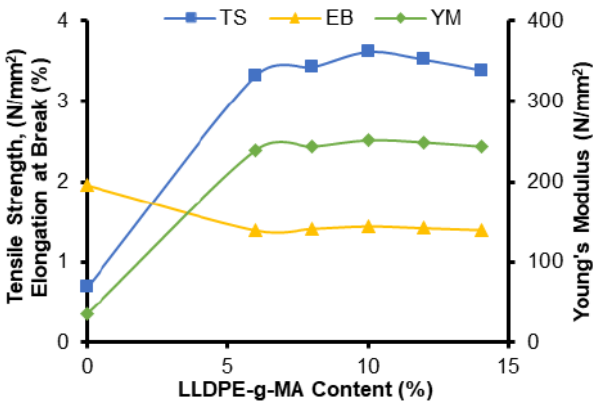

Fig 2. Tensile strength (TS), elongation at breaks (EB) and Young's Modulus (YM) test of TPSS/LLDPE blends

Table 1. Data of mechanical properties

No.	Compatibilizer content (%)	Density g/mm^3	Tensile strength (N/mm^2)	Elongation at breaks (%)	Young's Modulus (N/mm^2)
1	0	1.2612	0.6902	1.96	35
2	6	1.2635	3.3256	1.39	239
3	8	1.2606	3.4273	1.41	243
4	10	1.2620	3.6187	1.44	251
5	12	1.2618	3.5243	1.42	248
6	14	1.2631	3.3930	1.39	243

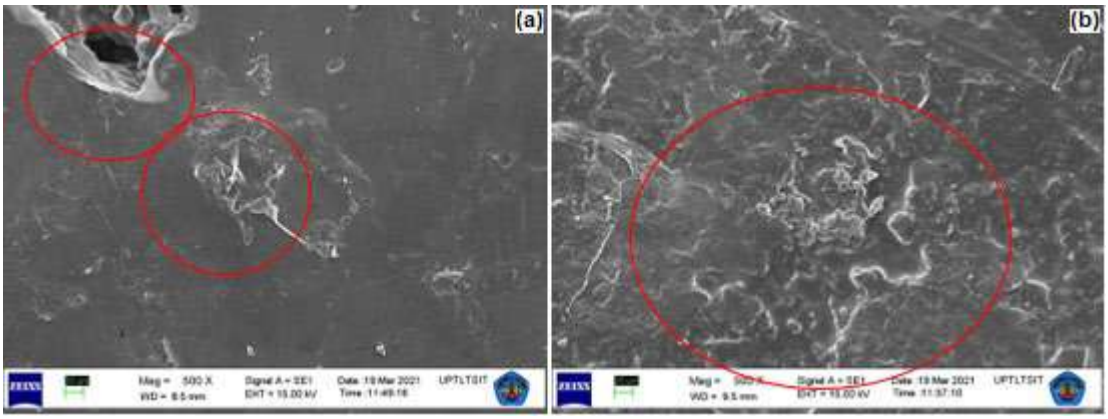

Fig 3. SEM image of (a) Uncompatibilizer, (b) Compatibilizer content 10 wt.%)

matrix. The difference in polarity between the two polymers was the cause of non-homogeneity in the mixture (incompatibility). Fig. 3(b) shows the surface morphology of TPSS/LLDPE with added compatibilizer, which demonstrated an even distribution of LLDPE in the starch matrix as the compatibilizer acted as a coupling agent. The use of a compatibilizer improved the surface adhesion between LLDPE and starch. This data was supported by the mechanical test results, which showed that the addition of a 10% compatibilizer increased the tensile strength compared to that without a compatibilizer.

One of the disadvantages of using starch as a basic material for making bioplastics is its high capacity to absorb water. This study found that without the addition of a compatibilizer, the TPSS/LLDPE mixture could absorb water up to 54% (see Fig. 4) due to the large number of starch hydroxyl groups that were not bound to the synthetic polymers (LLDPE) as the latter exhibited hydrophobicity in the presence of water. The minimal water absorption (14%) was achieved with the addition of a compatibilizer at 10 wt.%. Further increase in the compatibilizer concentration only resulted in an insignificant increase in the water absorption curve.

The advantage of using bioplastics includes their ability to degrade rapidly in the environment. The degradation tests were carried out under several conditions, i.e., in freshwater, seawater, and soil. Degradation in freshwater, the mixture with a compatibilizer of 10% achieved a mass loss of 47%, compared to the uncompatibilzer mixture (14%) (Fig. 5). In seawater, a mass loss of 44% was recorded with the addition of 10 wt.% compatibilizers compared to that without a compatibilizer (14%). Such observation was due to the high molecular weight of seawater that made it difficult for the hydroxyl groups in starch to react with seawater molecules.

In the soil, the degradation was measured with a mass loss of 30% in the mixture added with 10 wt.% compatibilizers as compared to that without a compatibilizer (28%). It can be deduced that the compatibilizer exhibited maximum effectiveness as a coupling agent between starch (hydrophilic) and LLDPE (hydrophobic) at a concentration of 10 wt.%. This finding

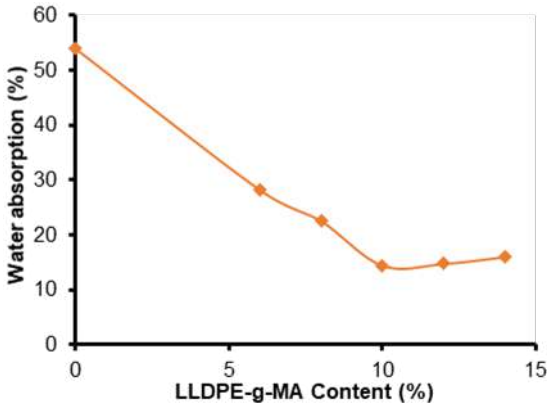

Fig 4. Water absorption of TPSS/LLDPE/compatibilizer blends

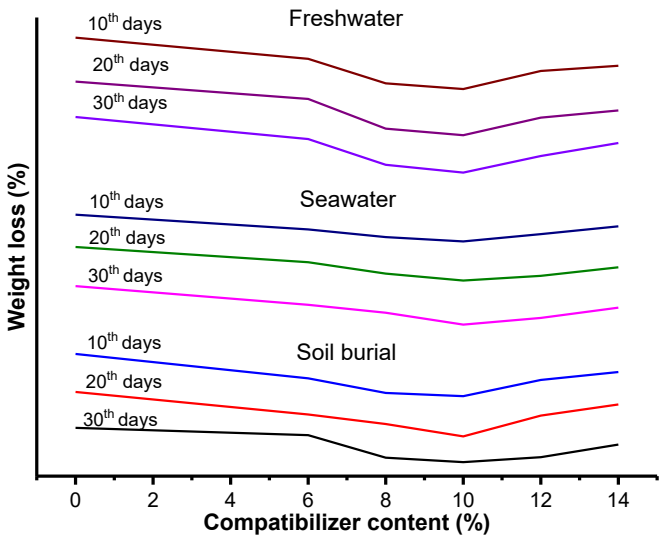

Fig 5. Degradation test in freshwater, seawater, and soil burial

was supported by results obtained in mechanical and water absorption tests, which showed that the maximum values were obtained with the addition of 10 wt.% compatibilizers. Meanwhile, the degradability test showed that the highest degradation rate in freshwater, followed by seawater and soil. The compatibilizer (LLDPE-g-MA) has an inhibitory effect on the biodegradation of the mixture in the soil due to PP-g-MA interactions. The chemical bond between the anhydride group of PP-g-MA and the hydride group of starch could prevent the absorption of starch by microorganisms in the soil [23-24].

The thermal-gravimetric analysis technique was performed to determine the thermal decomposition and

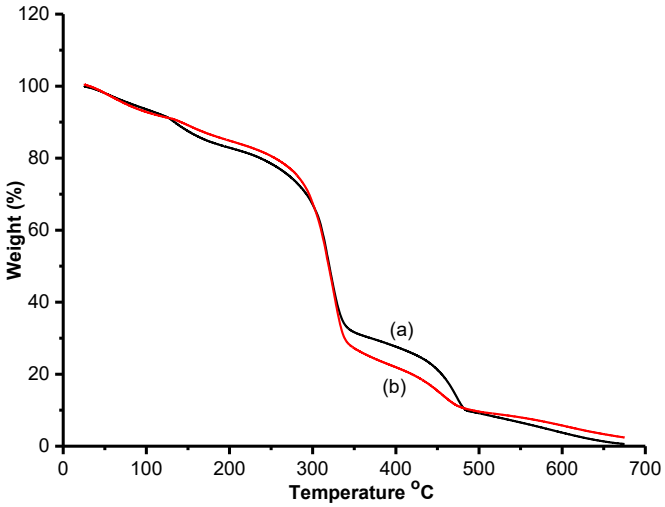

Fig 6. TGA curve of (a) Compatibilizer 10wt.%, (b) Uncompatibilizer

stability of TPSS/LLDPE blends. Fig. 6 shows no difference between the spectra of samples with and without the addition of compatibilizer, except in stage 3. Based on the spectrum in Fig. 6, it can be observed that there is no difference between the two spectra. However, in Stage 3, the percentage of weight degradation with the compatibilizer is slightly higher because the compatibilizer contains LLDPE, which is degraded at this stage.

The thermogravimetric analysis confirmed that the degradation occurred in stage 4. In the first stage, which was carried out at 201 °C, only water and glycerol were degraded. Evaporation (up to 6%) occurred in stage 1 as water decomposed into O_2 and H_2 at 100 °C. In stage 2, which was carried out at 125–290 °C, plasticizer compounds (glycerol) degradation [25-26] continued as the temperature increased, forming simpler compounds. The initial thermal degradation of starch occurred at 300 °C, and LLDPE started to degrade into gas and hydrocarbon oil at 400 °C in stage 3 [27-28]. The process of thermal degradation of LLDPE continued as the temperature increased, forming simpler compounds.

CONCLUSION

The addition of a compatibilizer as a coupling agent into the Sago Starch/LLDPE blends can improve the interface and adhesion properties of the mixture, as proven in the improved mechanical properties reported in this study. The tensile test value increased from 0.6902 N/mm^2 (without a compatibilizer) to 3.6187 N/mm^2 (with 10 wt.% compatibilizer). However, up to a certain concentration, the addition of the compatibilizer reached its saturation point that further increase in concentration did not affect its mechanical properties. The FTIR spectrum showed the formation of an ester group from the reaction of a hydroxyl group with an anhydrous group. The surface morphology of the samples showed that LLDPE was evenly distributed in the starch matrix. The degradation test in three environmental conditions demonstrated that the mixture of Sago starch and LLDPE could be degraded within 30 days. Results from TGA analysis indicated that thermal degradation occurred stably as no significant degradation was observed.

ACKNOWLEDGMENTS

The author would thank the Education Funding Management Institute (LPDP) for funding this doctoral dissertation research.

REFERENCES

[1] Kumar, M., Mohanty, S., Nayak, S.K., and Parvaiz, M.R., 2010, Effect of glycidyl methacrylate (GMA) on the thermal, mechanical and morphological property of biodegradable PLA/PBAT blend and its nanocomposites, *Bioresour. Technol.*, 101 (21), 8406–8415.

[2] Zoungranan, Y., Lynda, E., Dobi-Brice, K.K., Tchirioua, E., Bakary, C., and Yannick, D.D., 2020, Influence of natural factors on the biodegradation of simple and composite bioplastics based on cassava starch and corn starch, *J. Environ. Chem. Eng.*, 8 (5), 104396.

[3] Amin, M.R., Chowdhury, M.A., and Kowser, M.A., 2019, Characterization and performance analysis of composite bioplastics synthesized using titanium dioxide nanoparticles with corn starch, *Heliyon*, 5 (8), e02009.

[4] Thiruchelvi, R., Das, A., and Sikdar, E., 2020, Bioplastics as better alternative to petro plastic, *Mater. Today: Proc.*, 37, 1634–1639.

[5] Méité, N., Konan, L.K., Tognonvi, M.T., Doubi, B.I.H.G., Gomina, M., and Oyetola, S., 2021,

Properties of hydric and biodegradability of cassava starch-based bioplastics reinforced with thermally modified kaolin, *Carbohydr. Polym.*, 254, 117322.

[6] Ezeoha, S.L., and Ezenwanne, J.N., 2013, Production of biodegradable plastic packaging film from cassava starch, *IOSR J. Eng.*, 3 (10), 14–20.

[7] Ashok, A., Abhijith, R., and Rejeesh, C.R., 2018, Material characterization of starch derived biodegradable plastics and its mechanical property estimation, *Mater. Today: Proc.*, 5 (1), 2163–2170.

[8] Garg, S., and Jana, A.K., 2014, Preparation of LDPE-acetylated/butyrylated starch blend blow films and characterization, *Chin. J. Polym. Sci.*, 32 (3), 268–279.

[9] Zárate-Ramírez, L.S., Romero, A., Bengoechea, C., Partal, P., and Guerrero, A., 2014, Thermo-mechanical and hydrophilic properties of polysaccharide/gluten-based bioplastics, *Carbohydr. Polym.*, 112, 16–23.

[10] Imre, B., and Pukánszky, B., 2013, Compatibilization in bio-based and biodegradable polymer blends, *Eur. Polym. J.*, 49 (6), 1215–1233.

[11] Mengual, A., Juárez, D., Balart, R., and Ferrándiz, S., 2017, PE-g-MA, PP-g-MA and SEBS-g-MA compatibilizers used in material blends, *Procedia Manuf.*, 13, 321–326.

[12] Panrong, T., Karbowiak, T., and Harnkarnsujarit, N., 2020, Effects of acetylated and octenyl-succinated starch on properties and release of green tea compounded starch/LLDPE blend films, *J. Food Eng.*, 284, 110057.

[13] Pavlík, Z., Pavlíková, M., and Záleská, M., 2019, "Properties of Concrete with Plastic Polypropylene Aggregates" in *Use of Recycled Plastics in Eco-efficient Concrete*, Eds. Pacheco-Torgal, F., Khatib, J., Colangelo, F., and Tuladhar, R., Woodhead Publishing, UK, 189–213.

[14] Obasi, H.C., Egeolu, F.C., and Oparaji, O.D., 2015, Comparative analysis of the tensile and biodegradable performances of some selected modified starch filled polypropylene blends, *Am. J. Chem. Mater. Sci.*, 2 (2), 6–13.

[15] Obasi, H.C., and Igwe, I.O., 2014, Cassava starch-mixed polypropylene biodegradable polymer: Preparation, characterization and effects of biodegradation products on growth of plants, *Int. J. Sci. Res.*, 3 (7), 802–807.

[16] Abdorreza, M.N., Cheng, L.H., and Karim, A.A., 2011, Effects of plasticizers on thermal properties and heat sealability of sago starch films, *Food Hydrocolloids*, 25 (1), 56–60.

[17] Zaman, H.U., and Beg, M.D.H., 2021, Study on binary low-density polyethylene (LDPE)/ thermoplastic sago starch (TPS) blend composites, *Prog. Appl. Sci. Technol.*, 11 (1), 53–65.

[18] Ramírez-Hernández, A., Hernández-Mota, C.E., Páramo-Calderón, D.E., González-García, G., Báez-García, E., Rangel-Porras, G., Vargas-Torres, A., and Aparicio-Saguilán, A., 2020, Thermal, morphological and structural characterization of a copolymer of starch and polyethylene, *Carbohydr. Res.*, 488, 107907.

[19] Abdul Majid, R., Ismail, H., and Mat Taib, R., 2009, Effects of PE-g-MA on tensile properties, morphology and water absorption of LDPE/ thermoplastic sago starch blends, *Polym.-Plast. Technol. Eng.*, 48 (9), 919–924.

[20] Maran, J.P., Sivakumar, V., Thirugnanasambandham, K., and Sridhar, R., 2014, Degradation behavior of biocomposites based on cassava starch buried under indoor soil conditions, *Carbohydr. Polym.*, 101 (1), 20–28.

[21] Mayasari, H.E., Setyorini, I., and Yuniari, A., 2019, The blending of EPDM/NR with maleic anhydride as compatibilizer: Comparing the effect of accelerators on cure characteristic and mechanical properties, *Indones. J. Chem.*, 19 (1), 106–114.

[22] Islam, H.B.M.Z., Susan, M.A.B.H., and Imran, A.B., 2020, Effects of plasticizers and clays on the physical, chemical, mechanical, thermal, and morphological properties of potato starch-based nanocomposite films, *ACS Omega*, 5 (28), 17543–17552.

[23] Changwichan, K., Silalertruksa, T., and Gheewala, S.H., 2018, Eco-efficiency assessment of bioplastics production systems and end-of-life options, *Sustainability*, 10 (4), 1–15.

[24] Polman, E.M.N., Gruter, G.J.M., Parsons, J.R., and

Tietema, A., 2021, Comparison of the aerobic biodegradation of biopolymers and the corresponding bioplastics: A review, *Sci. Total Environ.*, 753, 141953.

[25] Wang, Y.G., Nie, X.A., and Liu, Z.X., 2014, Biodiesel synthesis from styrax tonkinensis catalyzed by $S_2O_8^{2-}$/ZrO_2-TiO_2-Fe_3O_4, *Appl. Mech. Mater.*, 521, 621–625.

[26] Sahari, J., Sapuan, S.M., Zainudin, E.S., and Maleque, M.A., 2013, Thermo-mechanical behaviors of thermoplastic starch derived from sugar palm tree (*Arenga pinnata*), *Carbohydr. Polym.*, 92 (2), 1711–1716.

[27] Nascimento, T.A., Calado, V., and Carvalho, C.W.P., 2012, Development and characterization of flexible film based on starch and passion fruit mesocarp flour with nanoparticles, *Food Res. Int.*, 49 (1), 588–595.

[28] Bagri, R., and Williams, P.T., 2002, Catalytic pyrolysis of polyethylene, *J. Anal. Appl. Pyrolysis*, 63 (1), 29–41.

Supplementary Data

This supplementary data is a part of paper entitled "Rotational Barrier and Bond Dissociation Energy and Enthalpy: Computational Study of the Substituent Effects in Para-Substituted Anilines and Phenols".

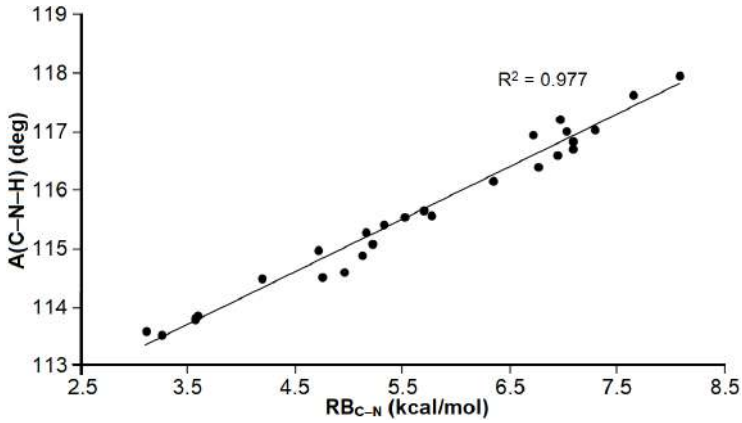

Fig S1. Phenyl–N–H bond angle vs rotational barrier around pheny–NH_2 bond in *para*-substituted anilines

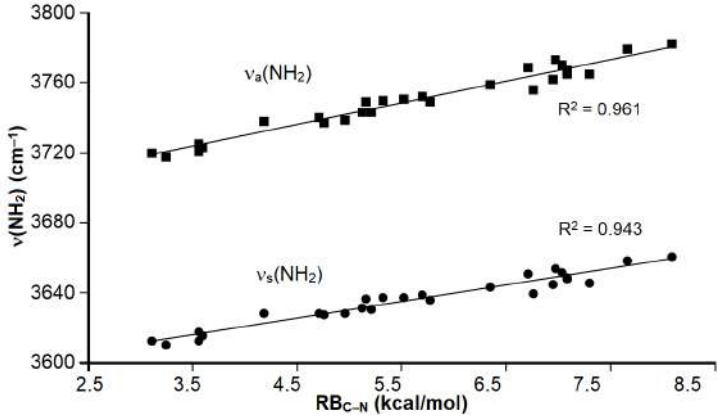

Fig S2. Symmetric and asymmetric NH_2 stretching frequencies vs rotational barrier around pheny–NH_2 bond in *para*-substituted anilines

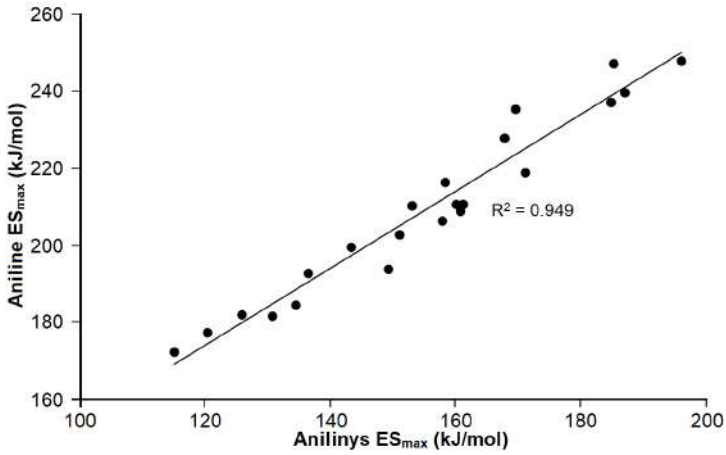

Fig S3. Maximum electrostatic potential around the amino H atom in *para*-substituted anilinic compounds vs that in *para*-substituted anilinyl radicals

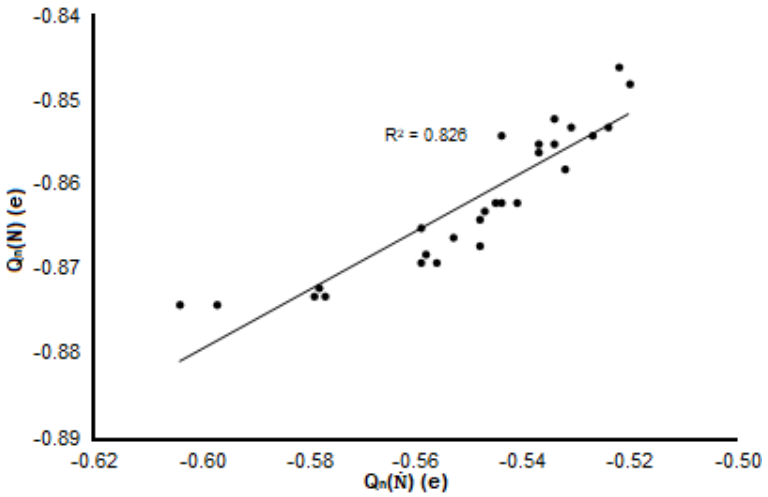

Fig S4. Natural partial charge on amino N atom of *para*-substituted anilines vs that in *para*-substituted anilinyl radicals

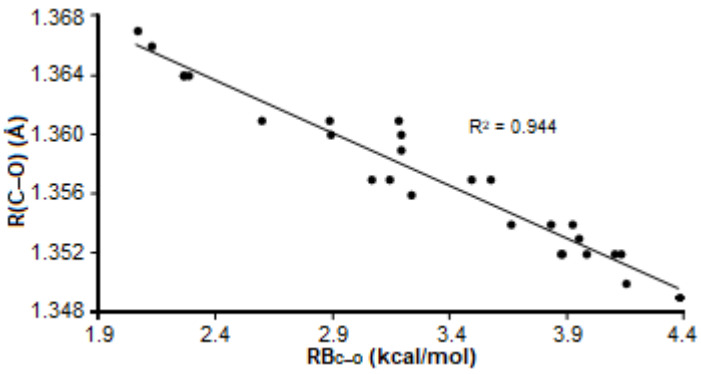

Fig S5. Phenyl–OH bond distance vs rotational barrier around phenyl–OH bond in *para*-substituted phenols

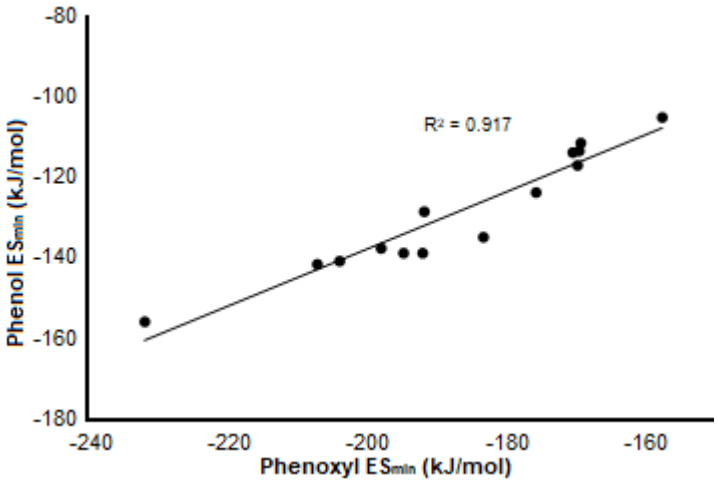

Fig S6. Minimum electrostatic potential around the hydroxyl O atom in *para*-substituted phenolic compounds vs that in *para*-substituted phenoxyl radicals

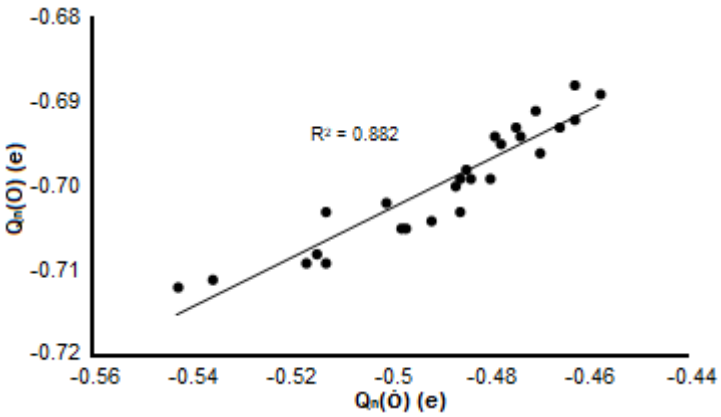

Fig S7. Natural partial charge on hydroxyl O atom of *para*-substituted phenols vs that in *para*-substituted phenoxyl radicals

Table S1. Symmetric and asymmetric NH_2 stretching frequencies, $\nu_s(NH_2)$ and $\nu_a(NH_2)$, respectively, for neutral anilinic compounds and the $\dot{N}H$ stretching frequency, $\nu(\dot{N}H)$, of the corresponding anilinyl radicals

Substituent	Anilines		Anilinyls
	$\nu_s(NH_2)$ (cm^{-1})	$\nu_a(NH_2)$ (cm^{-1})	$\nu(\dot{N}H)$
COCl	3661	3782	3487
NO_2	3659	3779	3493
CHO	3646	3765	3492
COOH	3648	3765	3491
SiF_3	3649	3767	3489
CN	3652	3770	3493
SO_2CH_3	3654	3773	3491
$COCH_3$	3645	3762	3491
CO_2CH_3	3640	3756	3486
SCN	3651	3769	3494
CF_3	3644	3759	3490
SCH_3	3636	3749	3489
SH	3639	3752	3489
I	3638	3751	3491
Br	3638	3750	3491
Phenyl	3631	3743	3483
Cl	3637	3749	3491
H	3632	3743	3484
$C(CH_3)_3$	3629	3739	3485
CH_3	3628	3737	3486
OPhenyl	3629	3740	3490
F	3629	3738	3491
OCH_3	3616	3723	3490
OH	3618	3725	3490
OCH_2CH_3	3613	3721	3491
$N(CH_3)_2$	3611	3718	3488
NH_2	3613	3720	3489

Rotational Barrier and Bond Dissociation Energy and Enthalpy: Computational Study of the Substituent Effects in *Para*-Substituted Anilines and Phenols

Ali Hussain Yateem*

Department of Chemistry, College of Science, University of Bahrain, P. O. Box 32038, Sakhir, Kingdom of Bahrain

** Corresponding author:*

email: alihali222@gmail.com

Received: August 26, 2021
Accepted: September 28, 2021

DOI: 10.22146/ijc.68687

Abstract: *This report presents the N–H and O–H bond dissociation energies (BDEs) and enthalpies (BDEts) of 27* para*-substituted anilines and phenols using Density Functional Theory (DFT) with functional ωB97X-D and basis set 6-31G**. The computed BDEs/BDEts show a strong correlation with the calculated rotational barrier (RB) around phenyl–NH_2 and phenyl–OH bonds of the parent neutral molecules. Electron-withdrawing (EW) substituents increased RB and BDEs/BDEts, while electron-donating (ED) substituents caused opposite behavior. Geometric, atomic, molecular, and spectroscopic properties of NH_2 and OH groups in neutral anilinic and phenolic molecules exhibited excellent correlations with RB and BDEs/BDEts. The geometry around heteroatoms of the radicals displayed constant geometrical changes for all substituents. Spin density maps confirmed that the unpaired electrons in radicals are delocalized in heteroatoms and phenyl rings for all the* para*-substituents. Spin delocalization in both types of radicals was further enhanced in the presence of* para*-ED substituents. The increase in electronic density around heteroatoms of radicals with the strength of ED substituents was found proportional to that in neutral molecules. Therefore, the N–H and O–H BDE/BDEt are mainly governed by the stabilization/destabilization of the neutral molecules and, to a significantly lower extent, the stabilization of radicals in the case of strong ED groups.*

Keywords: *rotational barrier; bond dissociation energy; bond dissociation enthalpy; electron-donating/electron-withdrawing groups; substituent effect*

INTRODUCTION

Antioxidants such as phenolic compounds and aromatic amines protect free radical intermediates and reactive oxygen/nitrogen species in biological systems and synthetic products [1-9]. The radical scavenging mechanism is initiated by abstracting a hydrogen atom from the antioxidants [10-17]. The energy calculation for the breakage of a hydrogen bond is essential for understanding the antioxidant scavenging mechanism and is also fundamental for various chemical and biochemical transformations [10-11,18-20]. The bond dissociation energies (BDEs) and bond dissociation enthalpies (BDEts) are the most critical factors for the estimation of hydrogen atom abstraction and stability of the parent molecules as well as the radical products [3,10,18,21-23].

BDEs and BDEts have been calculated experimentally and theoretically for *para*-substituted anilines and phenols with a very close agreement between the two approaches [2,24-31]. In almost all theoretical studies, the DFT functional has successfully reproduced the experimental BDEs [24-25,28,30]. It was concluded from the experimental and theoretical studies that EW groups in para position to phenols and anilines increase the N–H and O–H BDE/BDEt, while the opposite is true for ED groups [2,27-29,31]. Several studies also show good correlation with Hammett parameters [2,27-29,32]. Despite many studies on BDE/BDEt, the origin of the substituent effects on BDE/BDEt in *para*-substituted anilines and phenols is not clearly elaborated.

Some studies suggest that *para*-electron-

withdrawing (EW) groups in anilines and phenols stabilize the neutral molecules and destabilize the resulting radicals [28-29]. The converse holds good for electron-donating (ED) groups. Wu and Lai [33] proposed that stabilization of the phenoxyl radicals is more important than the neutral parent molecules in determining the O–H BDEs. In their study, the stabilization of neutral *para*-substituted phenols in the presence of EW groups originates from the increase in π-delocalization throughout the whole molecule. The destabilization in the presence of ED groups occurs due to the repulsive π-saturation effect. Wu and Lai further suggested that spin delocalization stabilizes phenoxyl radicals in the case of both ED and EW substituents. Song et al. [32] indicated that the substituent effects on N–H BDE/BDEt are attributed mainly to the stabilization/destabilization of the neutral *para*-substituted anilines and not to their corresponding radicals. The EW groups can interact with lone pair of electrons in NH_2 more significantly than electron-donating groups due to the presence of low-lying unoccupied molecular orbitals in the formers. It was demonstrated by Zhang et al. [34] that stabilization of parent *para*-substituted phenols and the corresponding phenoxyl radicals is determined mainly by the resonance effect due to correlation of O–H BDE with resonance parameter R^+. The resonance effect causes a reduction of O–H BDE in the case of ED groups and increases O–H BDE with EW groups.

It is clear from the above discussion that BDEs/BDEts values depend on stabilization/destabilization effects of substituent on both neutral parent molecules and their corresponding anilinyl and phenoxyl radicals. However, the origin of substituent effects is not yet fully clarified, especially for radicals. Some essential structural, atomic, molecular, and spectroscopic properties of neutral molecules and radicals have been neglected or considered incomprehensively in investigating the substituent effect. Moreover, BDEs and BDEts have been studied for typical substituents and correlated mainly to traditional Hammett parameters [2,27-29,32]. A clear distinction has not been made between the effect of substituent on neutral molecules and radicals. The current work bridges this literature gap to present BDEs/BDEts of 27 *para*-substituted anilines and phenols and their correlation to the rotational barrier (RB) around phenyl–NH_2 and phenyl–OH bonds. Some geometric, atomic, and molecular parameters have been calculated in this study to investigate further the governing reason behind the trend of BDE/BDEt with the nature of the substituent. Previous studies have reported that RB is a valid and valuable measure for the stability in *para*-substituted anilines [35], *para*-substituted benzaldehydes [36], as well as in disubstituted 1,3-butadienes [37] through resonance or inductive effects. Hence, the correlation of the BDEs/BDEts of 27 *para*-substituted anilines and phenols with RB is a particular focus of interest in the current work. The para position was selected since RBs were calculated before for para-substituted anilines and benzaldehydes [35-36]. Moreover, substituents in para position exhibit a more reliable trend in terms of the effect of substituents on BDE/BDEt compared to other positions [24,26]. Also, the available experimental data for N-H and O-H BDEs of *para*-substituted anilines and phenols are noticeably more than those of different positions [26-31].

■ COMPUTATIONAL METHODS

All calculations were carried out using DFT level of theory with exchange-correlation functional of ωB97X-D [38-39] and 6-31G**. The computational calculations were executed using Spartan 14 (v. 1.1.4) [40]. The same method was used to calculate rotational barrier in para-substituted anilines and benzaldehydes [35-36].

Bond dissociation energy, BDE, was calculated according to Eq. (1)

$$BDE = E_o(\dot{R}) + E_o(\dot{H}) - E_o(R–H) \quad (1)$$

where $E_o(\dot{R})$, $E_o(\dot{H})$, and $E_o(R–H)$ are the total electronic energy of the radical, the hydrogen atom, and the neutral molecule, respectively.

Bond dissociation enthalpy, BDEt, was calculated using Eq. (2)

$$BDEt = H°(\dot{R}) + H°(\dot{H}) - H°(R–H) \quad (2)$$

where $H°(\dot{R})$, $H°(\dot{H})$, and $H°(R–H)$ are the total enthalpy of the radical, the hydrogen atom, and the neutral

molecule, respectively. The electronic energies and enthalpies of all species were obtained directly from this software.

The internal rotation potential energy curves were obtained by performing geometry optimization calculations at a set of CCNH (for anilines) and CCOH (for phenols) dihedral angles ranging from 0 to 130° with an increment of 10°. Close to the maximum state, the increment was decreased to 1° and then to 0.1°. The minimum equilibrium states were optimized separately. The internal RB around the phenyl–NH_2 and phenyl–OH single bonds was considered between the minimum (equilibrium) and maximum conditions. The minimum states appear at dihedral angles between 18.50° and 28.38° for anilinyl compounds and between -0.87° and 0.43° for phenolic compounds. The maximum conditions appear at dihedral angles between 120.50° and 122.10° for anilinyl compounds and between 90.70° and 92.40° for phenolic compounds. Energies of the minimum and maximum states were corrected for zero-point energies, and transition states were confirmed using frequency analysis.

The minimum ionization potential was calculated on the lone pair of the amino nitrogen region in the equilibrium states of neutral anilinyl molecules and their corresponding radicals. The maximum (positive) electrostatic potential was calculated if it occupied amino hydrogens in the equilibrium states of neutral anilinyl molecules and their corresponding radicals. The minimum (negative) electrostatic potential was calculated using hydroxyl oxygen in equilibrium states of neutral phenolic molecules and their corresponding radicals.

Substituents considered here are all neutral, and they are ranged from weakly to strongly electron-withdrawing/donating substituents. The ED substituents include amino, alkoxy, and alkyl groups. The EW substituents include nitro, cyano, carbonyl, and sulfonyl groups and groups such as SiF_3 and CF_3. Other substituents like halides are considered borderline groups. In the case of more than one conformer for a molecule, the conformer with the lowest energy was chosen after performing conformers distribution analysis.

■ RESULTS AND DISCUSSION

Para-Substituted Anilines

Table 1 shows calculated RB around phenyl–NH_2 bond, RB_{C-N}, calculated N–H BDE and BDEt, and experimental BDE [28,30] of 27 *para*-substituted anilines. The substituents are arranged in terms of decreasing values of RBs_{C-N}. It can be seen from Table 1 that calculated BDEts are well consistent with the experimental values. An observation of the table further shows that with the increase in RB_{C-N}, the values of both N–H BDE and BDEt increase, and the EW character of *para*-substituent gets enhanced. It has been established previously that EW groups in the para position of aniline increase the N–H BDE/BDEt, and the opposite is true for ED groups [28-29,31]. It has also been shown previously that RBs_{C-N} increases with the strength of EW properties of *para*-substituents in anilines [35]. Fig. 1 shows that N–H BDE/BDEt correlates well with the RB_{C-N} around phenyl–NH_2 bond. Since BDEs are strongly correlated with BDEts (R^2 = 0.999), the data for BDEt were used in most of the graphs presented in this work.

Table 2 shows phenyl–NH_2 bond length, *R*(C–N), and phenyl-N–H bond angle, *A*(C–N–H), of *para*-substituted anilines and their corresponding radicals. The decrease in C–N bond length and the increase of C–N–H bond angle of neutral molecules from the bottom to the top of the table are the outcomes of increased π-delocalization corresponding to the strength of EW

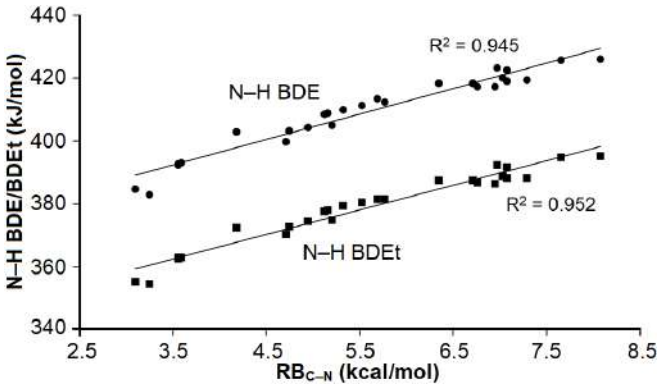

Fig 1. N–H bond dissociation energy (BDE) and enthalpy (BDEt) vs. rotational barrier around the phenyl–NH_2 bond of para-substituted anilines

Table 1. The calculated rotational barrier around phenyl–NH_2 bond (RB_{C-N}), calculated bond dissociation energy (BDE) and enthalpy (BDEt), and experimental BDE of *para*-substituted anilines

Substituent	RB_{C-N} (kcal/mol)	BDE (kJ/mol)	BDEt (kJ/mol)	Expt BDE[a] (kJ/mol)
COCl	8.08	426.09	395.09	
NO_2	7.65	425.68	394.91	405
CHO	7.29	419.30	388.31	
COOH	7.08	418.95	388.09	
SiF_3	7.08	422.49	391.83	
CN	7.03	420.00	388.97	398, 384
SO_2CH_3	6.97	423.17	392.33	
$COCH_3$	6.94	417.25	386.28	394, 379
CO_2CH_3	6.76	417.30	386.82	
SCN	6.71	418.28	387.50	
CF_3	6.34	418.30	387.55	404, 385
SCH_3	5.77	412.36	381.37	
SH	5.69	413.47	381.62	
I	5.52	411.36	380.58	373
Br	5.32	409.96	379.31	386
Phenyl	5.21	405.17	374.76	
Cl	5.16	408.80	378.13	387
H	5.12	408.36	377.63	386, 373, 375
$C(CH_3)_3$	4.95	404.17	374.56	372
CH_3	4.75	403.11	372.59	385, 371, 366
OPhenyl	4.71	399.90	370.15	
F	4.18	402.92	372.41	372
OCH_3	3.59	393.12	362.94	378, 365
OH	3.56	392.56	362.83	
OCH_2CH_3	3.56	392.66	362.51	
$N(CH_3)_2$	3.25	382.84	354.63	
NH_2	3.10	384.80	355.30	360

[a] from ref. [28, 30]

groups [35]. The increase of double bond character of C–N bond and the decrease of pyramidization of NH_2 group reflect the involvement of lone pair of amino nitrogen in π-electron resonance stabilization [35]. Fig. 2 and S1 show that C–N bond lengths and C-N-H bond angles strongly correlate with RB_{C-N}. On the other hand, the phenyl–ṄH bond distances and phenyl–Ṅ–H bond angles of the anilinyl radicals are almost constant at 1.332 Å and 109.10°, respectively, for *para* substituents. The Ṅ-H bond distance is also stable at 1.024 Å for all substituents versus

Table 2. Phenyl–NH_2 bond length, R(C–N), phenyl–N–H bond angle, A(C–N–H), para-substituted anilines, and corresponding aniline radicals

Substituent	Anilines		Anilinyls	
	R(C–N) (Å)	A(C–N–H) (deg)	R(C–Ṅ) (Å)	A(C–N–H) (deg)
COCl	1.373	117.97	1.330	109.34
NO_2	1.375	117.64	1.332	109.38
CHO	1.379	117.05	1.329	109.30
COOH	1.381	116.72	1.332	109.16
SiF_3	1.380	116.84	1.334	109.16
CN	1.379	117.02	1.330	109.36
SO_2CH_3	1.379	117.22	1.335	109.23
$COCH_3$	1.382	116.60	1.330	109.20
CO_2CH_3	1.383	116.42	1.332	109.12
SCN	1.380	116.97	1.331	109.25
CF_3	1.385	116.18	1.335	109.12
SCH_3	1.389	115.58	1.334	109.06
SH	1.388	115.66	1.334	109.07
I	1.389	115.56	1.333	109.16
Br	1.390	115.42	1.332	109.15
Phenyl	1.392	115.10	1.33	109.00
Cl	1.391	115.30	1.332	109.15
H	1.394	114.91	1.336	108.94
$C(CH_3)_3$	1.396	114.61	1.334	108.86
CH_3	1.397	114.54	1.333	108.92
OPhenyl	1.394	114.99	1.334	109.06
F	1.397	114.51	1.334	109.07
OCH_3	1.402	113.87	1.332	108.96
OH	1.403	113.82	1.332	108.98
OCH_2CH_3	1.402	113.80	1.332	108.94
$N(CH_3)_2$	1.404	113.55	1.328	108.83
NH_2	1.405	113.60	1.329	108.92

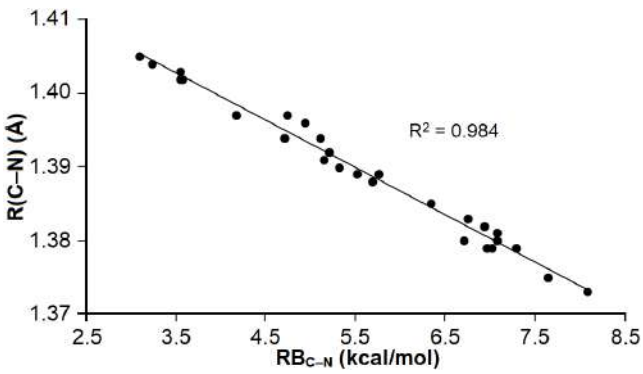

Fig 2. Phenyl–NH_2 bond distance vs. rotational barrier around phenyl–NH_2 bond in *para*-substituted anilines

a slight decrease with RB in neutral molecules from 1.010–1.006 Å. The C–Ṅ and Ṅ–H bond distances and C–Ṅ–H bond angles in anilinyl radicals are close to those calculated for 2-propanimine (1.273 Å, 1.023 Å, and 110.14°, respectively) using the ωB97X-D/6-31G**.

The spin density map representing unpaired electron location [41-42] is shown for unsubstituted and *para-N*, *N*-dimethylamino anilinyl radicals in Fig. 3. The blue color on the spin density map indicates a high spin density area, and the electron density decreases from blue to red. It can be seen that the unpaired electron (blue color) is located mainly in the vicinity of Ṅ atom and the ortho and para positions. The spin density is more intense on Ṅ atom than the phenyl positions, especially in the case of strong donor $N(CH_3)_2$ at the *para* position. The fraction of spin density on Ṅ was found to increase with the strength of the ED group. The spin density maps of anilinyl radicals with *para*-EW groups and borderline substituents are similar to that of unsubstituted anilinyl radicals.

Table S2 shows the NH_2 symmetric and asymmetric stretching frequencies, $\nu_s(NH_2)$ and $\nu_a(NH_2)$, respectively, for neutral anilinic compounds [35] and the ṄH stretching frequency, ν(ṄH), of the corresponding anilinyl radicals. It is observable from the table that both $\nu_s(NH_2)$ and $\nu_a(NH_2)$ increase with the strength of EW character of the *para*-substituent and hence with RB_{C-N}, the ν(ṄH) is roughly constant at an average value of 3489 cm^{-1}. Fig. S2 shows that $\nu_s(NH_2)$ and $\nu_a(NH_2)$ are linearly proportional to RB_{C-N}.

Table 3 shows calculated minimum ionization potential around amino N atom, IP_{min}, maximum (positive) electrostatic potential around the amino H atom, ES_{max}, and the natural partial charge on amino N atom, $Q_n(N)$, of neutral and corresponding radicals of para-substituted anilines. Tabulated data for both neutral molecules and radicals reveal that as the strength of the EW substituent increases, minimum IP increases, ES_{max} increases, and $Q_n(N)$ becomes less negative. However, the opposite trend is actual for ED substituents. For neutral molecules, strengthening the electron-acceptor *para*-substituent leads to a decrease in electronic density

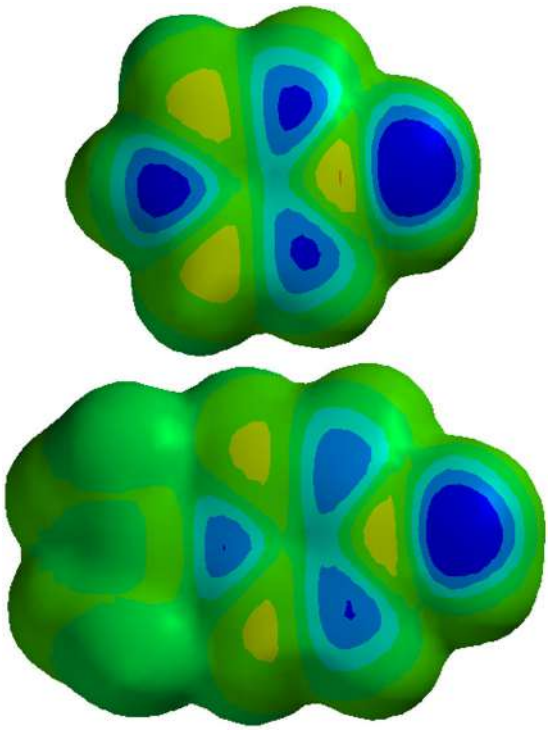

Fig 3. Spin density map for unsubstituted anilinyl (top) and *para-N, N*-dimethylamino anilinyl (bottom) radicals

Table 3. Minimum ionization potential around amino N atom, IP_{min}, maximum (positive) electrostatic potential around the amino H atom, ES_{max}, and the natural partial charge on amino N atom, $Q_n(N)$, of *para*-substituted anilines and the corresponding anilinyl radicals

Substituent	Anilines			Anilinyls		
	IP_{min} (eV)	ES_{max} (kJ/mol)	$Q_n(N)$ (e)	IP_{min} (eV)	ES_{max} (kJ/mol)	$Q_n(Ṅ)$ (e)
COCl	11.41	247.48	-0.846	11.09	185.12	-0.522
NO_2	11.39	248.19	-0.848	11.16	196.11	-0.520
CHO	11.07	227.97	-0.852	10.88	167.80	-0.534
COOH	10.94		-0.855	10.76		-0.534
SiF_3	11.11	228.98	-0.854	10.94		-0.527
CN	11.22	239.89	-0.853	11.03	187.05	-0.531

Table 3. Minimum ionization potential around amino N atom, IP_{min}, maximum (positive) electrostatic potential around the amino H atom, ES_{max}, and the natural partial charge on amino N atom, $Q_n(N)$, of *para*-substituted anilines and the corresponding anilinyl radicals (*Continued*)

Substituent	Anilines			Anilinyls		
	IP_{min} (eV)	ES_{max} (kJ/mol)	$Q_n(N)$ (e)	IP_{min} (eV)	ES_{max} (kJ/mol)	$Q_n(\dot{N})$ (e)
SO_2CH_3	11.20	237.49	-0.853	11.00	184.64	-0.524
$COCH_3$	10.91	216.62	-0.855	10.75	158.30	-0.537
CO_2CH_3	10.84	210.43	-0.856	10.71	152.94	-0.537
SCN		235.57	-0.854		169.57	-0.544
CF_3	10.92	219.22	-0.858	10.84	170.96	-0.532
SCH_3		203.00	-0.862		151.03	-0.544
SH		206.54	-0.862		157.74	-0.541
I		210.75	-0.862		159.99	-0.545
Br	10.73	210.73	-0.863	10.69	161.18	-0.547
Phenyl	10.48	192.83	-0.865	10.40	136.38	-0.559
Cl	10.70	209.12	-0.864	10.66	160.63	-0.548
H	10.39	184.66	-0.867	10.45	134.43	-0.548
$C(CH_3)_3$	10.32	182.06	-0.868	10.31	125.71	-0.558
CH_3	10.30	181.73	-0.869	10.30	130.54	-0.559
OPhenyl	10.54	199.61	-0.866	10.53	143.17	-0.553
F	10.46	193.89	-0.869	10.54	149.28	-0.556
OCH_3	10.17	177.42	-0.872	10.16	120.34	-0.578
OH	10.20		-0.873	10.22		-0.577
OCH_2CH_3	10.16	172.64	-0.873	10.14	114.96	-0.579
$N(CH_3)_2$	10.01		-0.874	9.79		-0.604
NH_2	10.04	167.84	-0.874	9.93		-0.597

around the amino group as the lone pair on nitrogen atom becomes more involved in π-delocalization that extends throughout the whole molecules [33,35]. This phenomenon implies more energy required to remove lone pair electrons on the nitrogen atom, an increase in acidity of amino hydrogen, and a less negative charge on amino N [35]. While for radicals, the data clearly show an increase in electron density around ṄH moiety with increasing ED ability of the *para*-substituent. However, the change in electronic density around the radical NH group is almost parallel to that around the amino group in neutral molecules, as shown in Fig. 4, S3, and S4. Therefore, the effect of substituents on radicals correlates with neutral molecules in terms of a shift in electronic density.

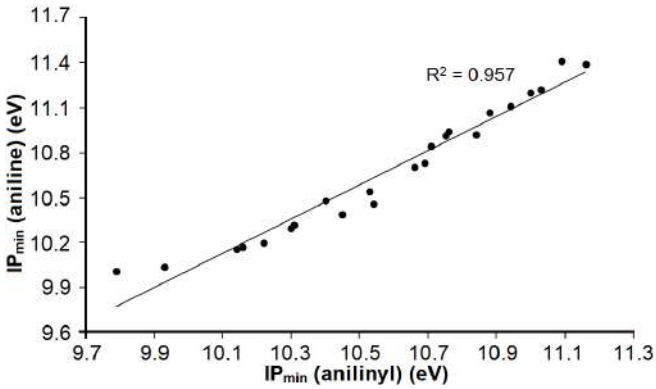

Fig 4. The minimum ionization potential of neutral *para*-substituted anilines vs. minimum ionization potential of the corresponding anilinyl radicals

Para-Substituted Phenols

Table 4 shows calculated rotational barrier around phenyl–OH bond, RB_{C-O}, calculated O–H BDE and BDEt, and experimental BDE [12,16] for all selected 27 *para*-substituted phenols. Unfortunately, the experimental BDEs fall in a rather broad range for most substituents,

Table 4. The calculated rotational barrier around phenyl–OH bond (RB_{C-O}), calculated bond dissociation energy (BDE) and enthalpy (BDEt), and experimental BDE of *para*-substituted phenols

Substituent	RB_{C-O} (kcal/mol)	BDE (kJ/mol)	BDEt (kJ/mol)	Expt BDE[a] (kJ/mol)	Expt BDE[b] (kJ/mol)
COCl	4.38	403.40	372.48		
NO_2	4.15	403.94	373.32	394–399	373–399
CHO	4.13	395.50	364.96		
SO_2CH_3	4.10	402.25	371.20	397	
SiF_3	3.98	401.09	370.75		
COOH	3.95	395.74	364.64		372
CO_2CH_3	3.92	393.74	363.72		
CN	3.88	396.27	365.48	388–397	370–397
SCN	3.87	401.13	370.09		
$COCH_3$	3.83	392.66	362.16	370–391	366–391
CF_3	3.66	396.57	366.02	398, 401	382–401
SCH_3	3.57	388.49	358.12		
SH	3.49	390.13	358.84		
I	3.23	386.49	356.34		
H	3.19	385.44	355.23	367–379	368, 369
Phenyl	3.19	378.34	349.43	366	355–369
$C(CH_3)_3$	3.18	382.20	352.55	357–374	357–374
Br	3.14	384.82	354.93	368–382	356–382
Cl	3.06	383.47	353.56	366–381	267–391
Ophenyl	2.89	369.01	340.16		
CH_3	2.88	377.71	347.68	360–374	360–374
F	2.59	376.89	347.37	365	354–382
OH	2.28	362.96	334.44	335, 341	336–354
OCH_2CH_3	2.26	362.26	333.33		
OCH_3	2.26	362.99	334.14	341–356	346–361
NH_2	2.12	350.35	321.87	316–355	316–357
$N(CH_3)_2$	2.06	346.77	320.20	310–338	310–336

[a] from ref. [27], [b] from ref. [24]

so a direct comparison with calculated BDE/BDEt is troublesome. Still, most of the calculated O–H BDE and BDEt are within the range of experimental data.

The data of *para*-substituted anilines listed in Table 4 show that as RB_{C-O} increases, the values of both O–H BDE and BDEt increase, and this increase in RB_{C-O} and BDE/BDEt is proportional to the strength of EW *para*-substituent. Fig. 5 demonstrates a strong correlation between RB_{C-O} and O–H BDE/BDEt.

Table 5 shows calculated RB_{C-O}, phenyl–OH bond length, R(C–O), a natural partial charge on O of hydroxyl group, $Q_n(O)$, and minimum (negative) electrostatic potential in the vicinity of lone pair of hydroxyl O, ES_{min},

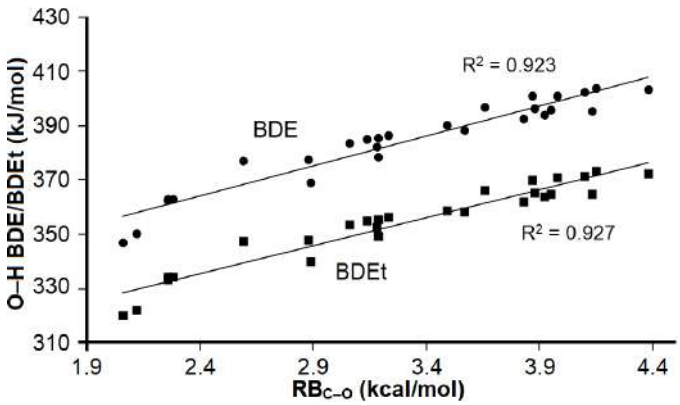

Fig 5. O–H bond dissociation energy (BDE) and enthalpy (BDEt) vs. rotational barrier around the phenyl–OH bond of *para*-substituted phenols

Table 5. Phenyl–OH bond length, R(C–O, minimum (negative) electrostatic potential around lone pair of hydroxyl O, ES_{min}, and natural partial charge on hydroxyl O atom, $Q_n(O)$, of *para*-substituted phenols and the corresponding radicals

Substituent	Phenols			Phenoxyls		
	R(C–O) (Å)	ES_{min} (kJ/mol)	$Q_n(O)$ (e)	R(C–Ȯ) (Å)	ES_{min} (kJ/mol)	$Q_n(\dot{O})$ (e)
COCl	1.349		-0.688	1.244		-0.463
NO_2	1.350		-0.689	1.245		-0.458
CHO	1.352		-0.693	1.244		-0.475
SO_2CH_3	1.352		-0.692	1.248		-0.463
SiF_3	1.352		-0.693	1.248		-0.466
COOH	1.353		-0.694	1.246		-0.474
CO_2CH_3	1.354		-0.695	1.246		-0.478
CN	1.352		-0.691	1.244		-0.471
SCN	1.352		-0.692	1.247		
$COCH_3$	1.354		-0.694	1.245		-0.479
CF_3	1.354	-104.65	-0.696	1.248	-157.27	-0.470
SCH_3	1.357		-0.699	1.247		-0.484
SH	1.357	-116.54	-0.699	1.247	-169.42	-0.480
I	1.356	-110.87	-0.698	1.246	-169.14	-0.485
H	1.360	-134.26	-0.703	1.249	-183.05	-0.486
Phenyl	1.359	-128.06	-0.702	1.246	-191.51	-0.501
$C(CH_3)_3$	1.361	-138.25	-0.705	1.249	-194.66	-0.497
Br	1.357	-113.32	-0.699	1.246	-170.17	-0.486
Cl	1.357	-112.88	-0.700	1.246	-169.23	-0.487
Ophenyl	1.360		-0.703	1.247		-0.513
CH_3	1.361	-138.19	-0.705	1.248	-191.80	-0.498
F	1.361	-123.27	-0.704	1.248	-175.53	-0.492
OH	1.364	-137.19	-0.709	1.247	-197.81	-0.513
OCH_2CH_3	1.364	-140.90	-0.709	1.248	-207.11	-0.517
OCH_3	1.364	-140.06	-0.708	1.248	-203.92	-0.515
NH_2	1.366		-0.711	1.247	-221.16	-0.536
$N(CH_3)_2$	1.367	-155.28	-0.712	1.247	-231.90	-0.543

of *para*-substituted phenols and their corresponding radicals. The decrease in C–O bond length for neutral phenol molecules from bottom to top of the table indicates the increase of π-delocalization with the strength of the EW group, as was seen for anilines. Furthermore, the C–O bond length in neutral phenolic compounds is correlated with RB_{C-O} (S5). The C–O bond in phenoxyl radicals, on the other hand, is almost constant at 1.247 Å for all *para*-substituents. Moreover, this C–O bond length in phenoxyl radicals is closer to C=O bond distance in aldehydes (1.210 Å) than C–O bond distance in phenols (1.360 Å), as calculated with ωB97X-D level of theory.

Spin density map for unsubstituted phenoxyl and *para-N*, *N*-dimethylamino phenoxyl radicals is shown in Fig. 6. As with anilinyl radicals, the unpaired electron is located mainly in the vicinity of Ȯ atom and the ortho and para positions. However, spin density is less intense on Ȯ than the ring positions. In the presence of strong electron-donor $N(CH_3)_2$, the spin intensity is less than that of unsubstituted phenoxyl radical. Only in the case of *para*-amino phenoxyl radical, a tiny fraction of

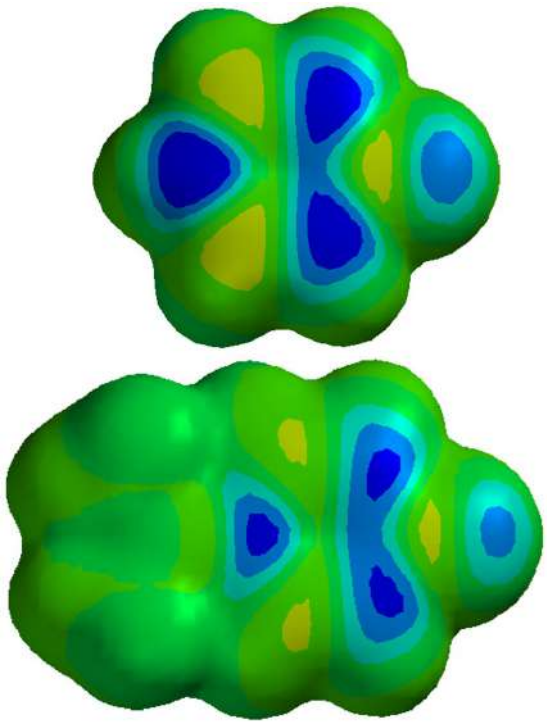

Fig 6. Spin density map for unsubstituted phenoxyl (top) and *para-N*, *N*-dimethylamino phenoxyl (bottom) radicals

spin density was observed on the amino Ṅ as well. The spin density maps of phenoxyl radicals with EW groups and borderline substituents are similar to that of unsubstituted phenoxyl radicals.

An examination of Table 5 further reveals an increase in negative natural charge on hydroxyl O and the minimum electrostatic potential around O with the rise in the electron-donating ability of *para*-substituent in both neutral phenols and their radicals.

The role of ED groups in increasing the negative charge on Ȯ of phenoxyl radical has also been reported in the literature [33]. Therefore, in *para*-substituted anilines, the electronic density around the vicinity of O and Ȯ atoms is enhanced with the increase of the electron-donating power of the *para*-substituent. Moreover, the change in electronic density around hydroxyl O in neutral molecules is linearly proportional to that on Ȯ in phenoxyl (Figs. S6 and S7).

Origin of Substituent Effect

The RB was confirmed as a measure of stability in neutral systems similar to the documented literature [35-37] regarding the extent of resonance and inductive effects. Here it is demonstrated clearly that N–H and O–H BDEs/BDEts correlate well with RB in neutral *para*-substituted phenolic and anilinic compounds. Moreover, geometrical and spectroscopic parameters that are also expected to change with resonance or inductive stabilization power of the *para*-substituents in the neutral molecules are also shown to correlate well with BDE/BDEt and RB. On the contrary, such geometric parameters are independent of the nature of the *para*-substituent in the formed phenoxyl and anilinyl radicals.

It is shown that there is a noticeable interaction of ṄH and Ȯ unpaired electrons with phenyl carbons regardless of the nature of the para-substituent in both *para*-substituted anilinyl and phenoxyl radicals. There is a significant increase in the double-bond character of the radical C–Ṅ and C–Ȯ bonds with all substituents. Since the geometry around the heteroatoms is fixed and not affected by substituent identity, it can be suggested that there is resonance stabilization of the unpaired electron with the phenyl ring but not with the *para*-substituent for both types of radicals and with all substituents. This resonance phenomenon is further validated by the spin density maps for the phenoxyl and anilinyl radicals, where no spin fraction is observed at the *para*-substituent region and by N–H stretching vibrations that are almost constant with the variously *para*-substituents. By comparing the spin density distribution for anilinyl and phenoxyl radicals in Fig. 3 and 6, it can be concluded that Ȯ group is a better electron acceptor than the ṄH group. This fact was observed before and attributed to shorter C–O bonds than N–H bonds [29].

It is observable from the spin density maps that there is a decrease in spin density in the phenyl ring in the presence of electron-donors in anilinyl and phenoxyl radicals. Furthermore, spin delocalization in radicals in strong *para*-ED groups is further stabilized by increasing electronic density around ṄH and·O moieties induced by these groups. Therefore, it can be assumed that there is some extra stabilization of radicals in the case of strong electron-donors, and this is expected to decrease the BDEs/BDEts further. It was suggested before that ED

groups in *para*-substituted anilines and phenols stabilize the formed radicals by delocalizing the unpaired electron [31], especially $N(CH_3)_2$ and NH_2 groups [22]. In this work, the data for $N(CH_3)_2$ and NH_2 groups are outliners toward lower N–H and O–H BDEs/BDEts in Fig. 1 and 5. However, the stabilization of radicals by ED para-substituents plays a small effect in determining BDE/BDEt for anilines and phenols, especially since the shift of electronic density toward the heteroatoms of the radicals is proportional to the increase in electronic density they induce on neutral molecules. Also, spin delocalization is observed by all substituents in anilinyl and phenoxyl radicals.

This work shows that the effect of *para*-EW-substituents on BDE/BDEt due to π-delocalization and inductive effects in the parent neutral molecules is significantly more important than their effect on the corresponding radicals. Furthermore, it is also confirmed by the similarity of spin density distribution between unsubstituted and *para*-EW-substituted anilines and phenols. Therefore, the unpaired electron delocalization in radicals with EW groups [33] does not seem to add extra stabilization compared to unsubstituted compounds. The decrease in electronic density opposes the effect of spin delocalization observed with the electron-acceptors.

From above, it can be suggested that N–H and O–H BDEs/BDEts are determined primarily by the stabilization/destabilization of the parent neutral molecules than the formed radicals. This study used several structural, atomic, and molecular properties to decide on the effect of substituent on both neutral molecules and radicals. In addition, the study provides, for the first time, the correlation between BDE/BDEt and several geometrical, atomic, molecular, and spectroscopic descriptors with RB to confirm that stabilization/destabilization of the parent molecules is the main factor in the evaluation of BDE/BDEt values.

The calculated RB_{C-O} in *para*-substituted phenols fall in a narrower range than those of *para*-substituted anilines for all substituents, and the content of RB_{C-O} values of phenolic compounds is only 2.26 kcal/mol compared to 4.98 kcal/mol of anilinic compounds. This data trend can be understood by noting that the change of C–N bond length is almost double that of C–O length compared to unsubstituted aniline and phenol, as shown in Tables 2 and 5. Also, the N–H BDEs/BDEts of anilines are more significant than the O–H BDEs/BDEts of phenols because NH_2 is a more robust π-electron donor than OH [29] in the neutral compounds.

From the present study results, it can also be concluded that both BDE and BDEt are valid for investigating the substituent effect in molecules similar to those studied in this work. However, calculated BDEts reproduce better the experimental N–H BDE. Finally, The exchange-correlation functional ωB97X-D used in this work produces the measured BDE for both anilinic and phenolic compounds.

■ CONCLUSION

The calculated N–H and O–H BDE/BDEt of *para*-substituted anilines and phenols showed a strong correlation with RB around phenyl–NH_2 and phenyl–OH bonds of neutral anilinic and phenolic compounds. The *para*-EW groups were found to cause an increase in N–H and OH BDEs/BDEts, while results revealed the opposite behavior for ED groups. Geometric, atomic, and molecular properties of the NH_2 and OH groups correlated well with the RB and BDE/BDEt. In the case of radicals, the geometrical changes around $\dot{N}H$ and $\dot{O}$ moieties remained constant for all substituents. Spin delocalization that involves the heteroatoms and the phenyl ring was observed for all substituents in anilinyl and phenoxyl radicals. The increase in electronic density around $\dot{N}H$ and $\dot{O}$ moieties of the radicals was proportional to that in neutral molecules. Based on the obtained results, N–H and OH BDE/BDEt are determined mainly by stabilization/destabilization of neutral molecules except in the case of strong ED groups where minimal reduction in values of N–H and O–H BDE/BDEt occurs.

■ REFERENCES

[1] Horton, W., Peerannawar, S., Török, B., and Török, M., 2019, Theoretical and experimental analysis of the antioxidant features of substituted phenol and

aniline model compounds, *Struct. Chem.*, 30 (1), 23–35.

[2] Biela, M., Pelikánová, B., and Michalík, M., 2019, Antioxidant action of phenols: Revisiting theoretical calculations of their thermodynamics, *Acta Chim. Slovaca*, 12 (2), 212–217.

[3] Poliak, P., Vagánek, A., Lukeš, V., and Klein, E., 2015, Substitution and torsional effects on the energetics of homolytic N–H bond cleavage in diphenylamines, *Polym. Degrad. Stab.*, 114, 37–44.

[4] Ali, H.M., Abo-Shady, A., Eldeen, H.A.S., Soror, H.A., Shousha, W.G., Abdel-Barry, O.A., and Saleh, A.M., 2013, Structural features, kinetics and SAR study of radical scavenging and antioxidant activities of phenolic and anilinic compounds, *Chem. Cent. J.*, 7 (1), 53.

[5] Parcheta, M., Świsłocka, R., Orzechowska, S., Akimowicz, M., Choińska, R., and Lewandowski, W., 2021, Recent developments in effective antioxidants: The structure and antioxidant properties, *Materials*, 14 (8), 1984.

[6] Khalil, I., Yehye, W.A., Etxeberria, A.E., Alhadi, A.A., Dezfooli, S.M., Julkapli, N.B.M., Basirun, W.J., and Seyfoddin, A., 2020, Nanoantioxidants: Recent trends in antioxidant delivery applications, *Antioxidants*, 9 (1), 24.

[7] Maraveas, C., Bayer, I.S., and Bartzanas, T., 2021, Recent advances in antioxidant polymers: From sustainable and natural monomers to synthesis and applications, *Polymers*, 13 (15), 2465.

[8] Vo, Q.V., Nam, P.C., Thong, N.M., Trung, N.T., Phan, C.T.D. and Mechler, A., 2019, Antioxidant motifs in flavonoids: O–H versus C–H bond dissociation, *ACS Omega*, 4 (5), 8935–8942.

[9] Thong, N.M., Duong, T., Pham, L.T., and Nam, P.C., 2014, Theoretical investigation on the bond dissociation enthalpies of phenolic compounds extracted from *Artocarpus altilis* using ONIOM (ROB3LYP/6-311++G(2df,2p):PM6) method, *Chem. Phys. Lett.*, 613, 139–145.

[10] Alisi, I.O., Uzairu, A., and Abechi, S.E., 2020, Free radical scavenging mechanism of 1,3,4-oxadiazole derivatives: Thermodynamics of O–H and N–H bond cleavage, *Heliyon*, 6 (3), e03683.

[11] Boli, L.S.P., Rusydi, F., Khoirunisa, V., Puspitasari, I., Rachmawati, H., and Dipojono, H.K., 2021, O–H and C–H bond dissociations in non-phenyl and phenyl groups: A DFT study with dispersion and long-range corrections, *Theor. Chem. Acc.*, 140 (7), 94.

[12] Beya, M.M., Netzel, M.E., Sultanbawa, Y., Smyth, H., and Hoffman, L.C., 2021, Plant-based phenolic molecules as natural preservatives in comminuted meats: A review, *Antioxidants*, 10 (2), 263.

[13] Ali, H.M., and Ali, I.H., 2015, QSAR and mechanisms of radical scavenging activity of phenolic and anilinic compounds using structural, electronic, kinetic, and thermodynamic parameters, *Med. Chem. Res.*, 24 (3), 987–998.

[14] Sharopov, F.S., Wink, M., and Setzer, W.N., 2015, Radical scavenging and antioxidant activities of essential oil components–An experimental and computational investigation, *Nat. Prod. Commun.*, 10 (1), 153–156.

[15] Stepanić, V., Trošelj, K.G., Lučić, B., Marković, Z., and Amić, D., 2013, Bond dissociation free energy as a general parameter for flavonoid radical scavenging activity, *Food Chem.*, 141 (2), 1562–1570.

[16] Saqib, M., Mahmood, A., Akram, R., Khalid, B., Afzal, S., and Kamal, G.M., 2015, Density functional theory for exploring the structural characteristics and their effects on the antioxidant properties, *J. Pharm. Appl. Chem.*, 1 (2), 65–71.

[17] Bendary, E., Francis, R.R., Ali, H.M.G., Sarwat, M.I., and El Hady, S., 2013, Antioxidant and structure–activity relationships (SARs) of some phenolic and anilines compounds, *Ann. Agric. Sci.*, 58 (2), 173–181.

[18] John, P.C.S., Guan, Y., Kim, Y., Kim, S., and Paton, R.S., 2020, Prediction of organic homolytic bond dissociation enthalpies at near chemical accuracy with sub-second computational cost, *Nat. Commun.*, 11 (1), 2328.

[19] Galano, A., Muñoz-Rugeles, L., Alvarez-Idaboy, J.R., Bao, J.L., and Truhlar, D.G., 2016, Hydrogen abstraction reactions from phenolic compounds by peroxyl radicals: Multireference character and density functional theory rate constants, *J. Phys. Chem. A*, 120 (27), 4634–4642.

[20] Liu, M., Zhang, Z., Chen, B., Meng, Q., Zhang, P., Song, J., and Han, B., 2020, Synthesis of thioethers, arenes and arylated benzoxazoles by transformation of the C (aryl)–C bond of aryl alcohols, *Chem. Sci.*, 11 (29), 7634–7640.

[21] Lai, W., Li, C., Chen, H., and Shaik, S., 2012, Hydrogen-abstraction reactivity patterns from A to Y: The valence bond way, *Angew. Chem. Int. Ed.*, 51 (23), 5556–5578.

[22] Garrett, G.E., Pratt, D.A., and Parent, J.S., 2020, Hydrogen atom abstraction from polyolefins: Experimental and computational studies of model systems, *Macromolecules*, 53 (8), 2793–2800.

[23] Aliaga, C., Almodovar, I., and Rezende, M.C., 2015, A single theoretical descriptor for the bond-dissociation energy of substituted phenols, *J. Mol. Model.*, 21 (1), 12.

[24] Khursan, S.L., 2016, Homodesmotic method of determining the O–H bond dissociation energies in phenols, *Kinet. Catal.*, 57 (2), 159–169.

[25] Denisov, E.T., and Denisova, T.G., 2015, Dissociation energies of NH bonds in aromatic amines, *Pet. Chem.*, 55 (2), 85–103.

[26] Vagánek, A., Rimarčík, J., Ilčin, M., Škorňa, P., Lukeš, V., and Klein, E., 2013, Homolytic N–H bond cleavage in anilines: Energetics and substituent effect, *Comput. Theor. Chem.*, 1014, 60–67.

[27] Klein, E., and Lukeš, V., 2006, Study of gas-phase O–H bond dissociation enthalpies and ionization potentials of substituted phenols–applicability of *ab initio* and DFT/B3LYP methods, *Chem. Phys.*, 330 (3), 515–525.

[28] Li, Z., and Cheng, J.P., 2003, A detailed investigation of subsituent effects on N–H bond enthalpies in aniline derivatives and on the stability of corresponding N-centered radicals, *J. Org. Chem.*, 68 (19), 7350–7360.

[29] Pratt, D.A., DiLabio, G.A., Valgimigli, L., Pedulli, G.F., and Ingold, K.U., 2002, Substituent effects on the bond dissociation enthalpies of aromatic amines, *J. Am. Chem. Soc.*, 124 (37), 11085–11092.

[30] Jonsson, M., Lind, J., Merényi, G., and Eriksen, T.E., 1995, N–H bond dissociation energies, reduction potentials and pK_as of multisubstituted anilines and aniline radical cations, *J. Chem. Soc., Perkin Trans.*, 2 (1), 61–65.

[31] Bordwell, F.G., Zhang, X.M., and Cheng, J.P., 1993, Bond dissociation energies of the nitrogen-hydrogen bonds in anilines and in the corresponding radical anions. Equilibrium acidities of aniline radical cations, *J. Org. Chem.*, 58 (23), 6410–6416.

[32] Song, K.S., Liu, L., and Guo, Q.X., 2003, Remote Substituent effects on N–X (X = H, F, Cl, CH_3, Li) bond dissociation energies in *para*-substituted anilines, *J. Org. Chem.*, 68 (2), 262–266.

[33] Wu, Y.D., and Lai, D.K.W., 1996, A density functional study of substituent effects on the O–H and O–CH_3 bond dissociation energies in phenol and anisole, *J. Org. Chem.*, 61 (22), 7904–7910.

[34] Zhang, H.Y., Sun, YM., and Chen, D.Z., 2001, O–H bond dissociation energies of phenolic compounds are determined by field/inductive effect or resonance effect? A DFT study and its implication, *Quant. Struct.-Act. Relat.*, 20 (2), 148–152.

[35] Yateem, A.H., 2020, Rotational barrier and electron-withdrawing substituent effects: Theoretical study of π-conjugation in *para*-substituted anilines, *Mediterr. J. Chem.*, 10 (4), 319–334.

[36] Yateem, A.H., 2020, Rotational barrier and quantification of electron-donating substituent effects: A computational study of *para*-substituted benzaldehydes, *Croat. Chem. Acta*, 93 (2), 85–96.

[37] Yateem, A.H., 2019, Rotational barrier and conjugation: Theoretical study of resonance stabilization of various substituents for the donors NH_2 and OCH_3 in substituted 1,3-butadienes, *Indones. J. Chem.*, 19 (4), 1055–1065.

[38] Jacobsen, H., and Cavallo, L., 2017, "Directions for Use of Density Functional Theory: A Short

Instruction Manual for Chemists" in *Handbook of Computational Chemistry*, Eds., Leszczynski, J., Kaczmarek-Kedziera, A., Puzyn, T., Papadopoulos, M.G., Reis H., Shukla M.K., Springer, Cham, 225–267.

[39] Mardirossian, N., and Head-Gordon, M., 2017, Thirty years of density functional theory in computational chemistry: an overview and extensive assessment of 200 density functionals, *Mol. Phys.*, 115 (19), 2315–2372.

[40] *SPARTAN'14*, 2014, Wavefunction, Irvine, CA, USA.

[41] Bruno, G., Macetti, G., Lo Presti, L., and Gatti, C., 2020, Spin density topology, *Molecules*, 25 (15), 3537.

[42] Grozav, A., Porumb, I.D., Găină, L.I., Filip, L., and Hanganu, D., 2017, Cytotoxicity and antioxidant potential of novel 2-(2-((1*H*-indol-5yl) methylene)-hydrazinyl)-thiazole derivatives, *Molecules*, 22 (2), 260.

Comparison of the Adsorption Ability of MgAl-HC, CaAl-HC, and ZaAl-HC Composite Materials Based on Duku Peel Hydrochar in Adsorption of Direct Green Anionic Dyes

Novie Juleanti[1], Normah Normah[1], Patimah Mega Syah Bahar Nur Siregar[1], Alfan Wijaya[1], Neza Rahayu Palapa[2], Tarmizi Taher[3,4], Nurlisa Hidayati[4], Risfidian Mohadi[4], and Aldes Lesbani[2,4*]

[1]*Magister Program, Faculty of Mathematics and Natural Sciences, Sriwijaya University, Jl. Padang Selasa No. 524, Ilir Barat 1, Palembang 30139, South Sumatra, Indonesia*

[2]*Graduate School, Faculty of Mathematics and Natural Sciences, Sriwijaya University, Jl. Palembang-Prabumulih Km. 90-32, Ogan Ilir 30862, South Sumatra, Indonesia*

[3]*Department of Environmental Engineering, Faculty of Mathematics and Natural Sciences, Institut Teknologi Sumatera, Jl. Terusan Ryacudu, Way Hui, Jati Agung, Lampung 35365, Indonesia*

[4]*Research Center of Inorganic Materials and Complexes, Faculty of Mathematics and Natural Sciences, Sriwijaya University, Jl. Padang Selasa, Bukit Besar, Palembang 30139, South Sumatera, Indonesia*

* ***Corresponding author:***

email: aldeslesbani@pps.unsri.ac.id

Received: August 27, 2021
Accepted: November 14, 2021

DOI: 10.22146/ijc.68719

Abstract: *Preparation of composite material from layered double hydroxide (LDH) with hydrochar (HC) from duku peel produces CaAl-HC, MgAl-HC, and ZnAl-HC have shown the success of the preparation process as evidenced by characterizations such as XRD and FT-IR. The XRD characterization data evidenced the typical diffraction of the hydrochar around 2θ = 20° in the composite material. FTIR analysis is a characterization that supports the success of composite materials, which showed the presence of typical vibrations of HC at 3245, 2931, and 1635 cm^{-1} contained in the composite spectrum. The application of MgAl-HC, CaAl-HC, and ZnAl-HC composites as adsorbents showed Q_{max} (adsorption ability) values of 94.340 mg/g, 128.205 mg/g, and 89.286 mg/g. Overall the adsorption process is endothermic with a positive enthalpy value, and a negative Gibbs free energy value indicates a spontaneous adsorption process. The isotherm model of MgAl-HC, CaAl-HC, and ZnAl-HC show that the Langmuir isotherm model is more dominant, as indicated by the R^2 value closer to 1 which indicates that the adsorption process takes place in a monolayer.*

Keywords: *duku peel; hydrochar; adsorption; regeneration; dyes*

■ INTRODUCTION

Lately, synthetic dyes have been in great demand in textiles, printing, paper, food, and pharmaceuticals. Synthetic dyes consist of cationic and anionic dyes, but most industries prefer the use of anionic dyes. Synthetic dyes are widely used as a substitute for natural dyes, which are unstable, and quickly decompose under sunlight, and the storage process must be precise. Synthetic dyes are the right choice because they are stable, do not break down quickly, and have many color variations [1].

Some of the advantages obtained from dyes can lead to uncontrolled use. Excessive use of dyes will harm the environment. Synthetic textile dyes have a complex aromatic molecular structure that makes them difficult to break down when disposed of in the ecosystem [2], which makes necessary efforts to overcome these harmful effects. Many methods can be used, such as ion exchange [3], biodegradation [4], chemical coagulation [5], catalytic reduction [6], and adsorption [7].

According to Milagres et al., adsorption is the most promising method for dealing with contamination, with an economic value, easy to do, and very efficient, making adsorption the suitable method for dealing with contamination [8]. Adsorption is an effective and

practical method for treating polluted water dyes due to its high efficiency, simplicity, and availability of many adsorbents [2]. Some adsorbents widely used for adsorption include activated carbon, graphene, zeolites, polymers, clays, and layered double hydroxides.

Layered double hydroxide is a natural inorganic lamellar compound that can be easily synthesized. Some of the advantages of layered double hydroxide that are the current attraction, such as large surface area [9], ion exchangeability [10], and can be regenerated [11], make this material continues to be developed. Layered double hydroxide has the general formula $[M^{2+}_{1-x}M^{3+}_{x}(OH)_2]^{x+}[(A^{m-})_{x/m}.nH_2O]^{x}$, where M^{2+} and M^{3+} are divalent and trivalent cations, and A^{m-} is charge balancing interlayer anion [9].

Layered double hydroxide (LDH) is a material that can be modified by intercalation and composite. The use of LDH as a composite can increase the Q_{max} of the material. This ability makes LDH-based composite materials an effective adsorbent to overcome contamination [13]. The adsorption ability of MgAl composites has been demonstrated in several studies. Badri et al. [12] studied rhodamine-B and methylene blue adsorption using MgAl-Biochar. The Q_{max} obtained from the adsorption process was 38.49 and 91.44 mg/g, respectively. Another study conducted by He et al. [13] using the MgAl-HC composite as a phosphate adsorbent resulted in a Q_{max} of 41.16 mg/g.

In this study, the direct green (DG) dye adsorption process was carried out using MgAl-HC, CaAl-HC, and ZnAl-HC. The success of material preparation is proven through XRD, FT-IR, and SEM characterization data. The adsorption ability of MgAl-HC, CaAl-HC, and ZnAl-HC composites was confirmed by several parameters: regeneration, selectivity, kinetics, isotherm, and thermodynamics.

■ EXPERIMENTAL SECTION

Materials

The chemicals used in this experiment were $Mg(NO_3)_2{\cdot}6H_2O$ (Merck, 256.41 g/mol), $Ca(NO_3)_2{\cdot}4H_2O$ (Merck, 236.15 g/mol), $Al(NO_3)_2{\cdot}9H_2O$ (Merck, 375.13 g/mol), Na_2CO_3 (Merck, 105.88 g/mol), NaOH (Merck, 40.00 g/mol), HCl 37% by MallinckrodtAR®, C_2H_5OH (Avantor, 99%). Hydrochar prepared from duku peel, anionic dyes direct green (DG), procion red (PR), methyl orange (MO). Water was obtained using a Purite® water purification system from the Research Center of Inorganic Materials and Complexes.

Instrumentation

The material characterization was performed using XRD Rigaku mini flex-6000. The concentration of the dye was analyzed using spectrophotometer UV-Visible Biobase BK-UV 1800PC.

Procedure

Duku peel preparation

As much as 1 kg duku peel that has been prepared is washed and cleaned and dried for 3 h in the sun. The dried duku peel was cut into several pieces and then baked for 8 h at a temperature of 100 °C. Then the resulting duku peel is left at room temperature, then mashed and filtered with a size of 40 mesh.

Hydrochar preparation

A total of 2.5 g of duku peel and 50 mL of water were put into a 100 mL Hydrothermal Stainless-steel Autoclave, then baked at 200 °C for 12 h. After that, the hydrochar was cooled at room temperature and then washed with distilled water. Drying was carried out in an oven at a temperature of 100 °C for 24 h to obtain a hydrochar product which was further characterized using FT-IR, XRD, BET, and SEM analysis.

Composite material preparation

Composite materials were prepared using the coprecipitation method. As much as 100 mL of M^{2+} (Ca, Mg, and Zn) 0.75 M solution was mixed with 100 mL of Al^{3+} 0.25 M solution. The mixture was stirred for 1 h and then added 2.5 g of hydrochar. The mixture was adjusted to pH 10 using 2 M NaOH to form a gel. Then continued stirring for 10 h for MgAl-HC (85 °C), 4 h for ZnAl-HC (60 °C), and 6 h for CaAl-HC (85 °C) to form a precipitate. The precipitation obtained was dried at 100 °C and then characterized using XRD, FT-IR, BET, and SEM.

Adsorption studies

Adsorption studies were carried out to determine selectivity, regeneration, isotherm, and thermodynamic

parameters. The selectivity process was carried out by mixing 25 mg/L of MO (methyl orange), PR (procion red), and DG (direct green) dye as much as 10 mL each. Then, the dye mixture was adsorbed with 0.02 g duku peel, HC, MgAl-HC, CaAl-HC, and ZnAl-HC with time variations (0, 30, 60, 90, 120, and 150) min. After the adsorption process, the separation was carried out to obtain the filtrate. Then a scan was carried out and measured the wavelength using a UV-Vis spectrophotometer. After obtaining a selective dye, proceed to the adsorbent regeneration stage. The regeneration process was carried out to determine the ability of the adsorbent when used repeatedly by adsorption of 1000 mg/L DG. After the dye is absorbed in the adsorbent, the desorption process is done using ultrasonic water. This adsorption-desorption process is repeated for up to five cycles. Kinetic studies were carried out by varying the time 0, 10, 30, 60, 90, 120, 150, and 180 min, then measured the absorbance using a UV-Vis spectrophotometer to determine the tendency of the pseudo-first-order (PFO) and pseudo-second-order (PSO) kinetic models. The adsorption isotherm model that has been determined includes Langmuir and Freundlich. The Langmuir isotherm model can determine the parameter kL, which is the adsorption affinity constant (L/mg), and Q_{max}, which indicates the adsorption ability of the adsorbent. At the same time, the Freundlich isotherm model can determine the parameter Kf which states the level of adsorption (mg/g), and 1/n, which is the Freundlich constant which states the heterogeneity factor. While thermodynamics was carried out to determine the adsorption energy, which includes enthalpy (ΔH), entropy (ΔS), and Gibbs free energy (ΔG). A total of 50 mL of DG 1000 mg/L was adsorbed using duku peel, HC, MgAl-HC, CaAl-HC, and ZnAl-HC varied the concentration (50, 75, 100, 125, and 150) mg/L and temperature (30, 40, 50, and 60) °C. Then the absorbance was measured using a UV-Vis spectrophotometer.

■ RESULTS AND DISCUSSION

The success of preparing composite materials consisting of layered double hydroxide as a precursor and hydrochar as a support material is proven by characterization data such as XRD, FT-IR, and SEM. Fig. 1(a) presents a peel duku XRD diffractogram with two specific peaks appearing at diffraction angles of 16.9° and 21.8°. Duku peel treated through hydrothermal carbonization produces HC with almost the same diffraction pattern as Fig. 1(b). XRD characterization was carried out to confirm the presence of typical diffraction peaks of the layered double hydroxide according to JCPDS data No. 87.0493 for Ca/Al, No. 20-0658 for Mg/Al (Balcomb et al. 2015) [14] and No. 48.2023 for Zn/Al (Liu et al. 2019) [6]. The diffraction patterns of the MgAl-HC, CaAl-HC, and ZnAl-HC composites are presented in Fig. 1.

Based on Fig. 1, the appearance of the MgAl-HC diffraction peaks at 11.47°(003), 22.86°(006), 61.62°(113), 65.50°(116) has been confirmed as typical diffraction peaks of layered double hydroxide. These data follow JCPDS 20-0658, where the LDH diffraction peaks are around 11.8°(003), 62.3°(113), and 66.3°(116). In addition, there is a confirmed diffraction peak of HC around 22 (002), which indicates the characteristics of cellulose (Castro et al thermal decomposition). The diffraction of the CaAl-HC composite (Fig. 1(b)) at 10.16°(003), 18.0°(002), and 20.25°(006) confirmed the diffraction of the layered double hydroxide according to JCPDS No. 87-0493. Fig. 1 shows the diffraction of ZnAl-HC at 10.05°(003), 19.92°(002), 34.10°(006), and

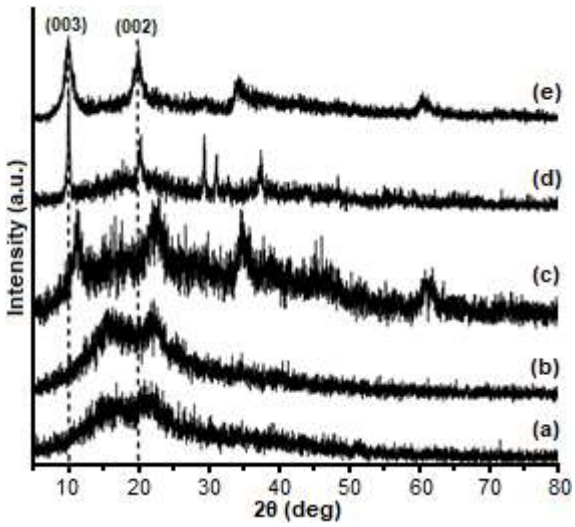

Fig 1. Diffraction pattern of (a) duku peel, (b) HC, (c) MgAl-HC, (d) CaAl-HC, and (e) ZnAl-HC

60.22°(110). Based on JCPDS data No. 48.2023 confirmed the successful preparation of ZnAl-HC composites. The diffraction pattern in Fig. 1 shows the presence of diffraction at 2θ around 19°, approved as a diffraction peak from hydrochar. Based on these data, the preparation of composite material in the form of Zn/Al-Hc has been successfully carried out, judging from the diffraction peaks of the supporting material, which are within the characteristics of the composite.

The success of composite preparation using HC is also supported by the FT-IR analysis presented in Fig. 2. The composite spectra of MgAl-HC, CaAl-HC, and ZnAl-HC have the characteristics of HC found at 3425 and 1627 cm^{-1} which were confirmed as vibrations of the hydroxyl and carbonyl OH groups [15]. There is also a C–H vibration of the cellulose at 2931 cm^{-1} [16]. The primary amide content in the duku peel indicated the presence of a C=O group seen at 1635 cm^{-1}. Another vibration at 1442 cm^{-1} revealed the C=C strain of the aromatic compounds, and there is a characteristic vibration of the layered double hydroxide (M–O), which is below 1000 cm^{-1}.

Determine the morphological characteristics of the material conducted by SEM analysis. The SEM's characterization results presented in Fig. 3 show the morphology of the duku peel adsorbent particles, which tend to agglomerate in the same phase or are commonly referred to as aggregation. While Fig. 3(b) shows the particle morphology pattern of the hydrochar adsorbent at a temperature of 200 °C, which tends to be heterogeneous and has an irregular shape, this is due to the hydrothermal carbonization treatment given, causing the particles to undergo splitting or commonly referred to as deaggregation. The morphology of MgAl-HC in Fig. 3(c) shows the presence of agglomerates with large and irregular pore sizes. While CaAl-HC has a small pore size with a smooth surface. On the other hand, ZnAl-HC has a heterogeneous pore size, with a lower agglomeration rate than MgAl-HC.

The large surface area is one of the advantages of the prepared composite material. The characterization evidences the increase in surface area in N_2 adsorption-desorption, whose profile can be seen in Fig. 4 and Table 1.

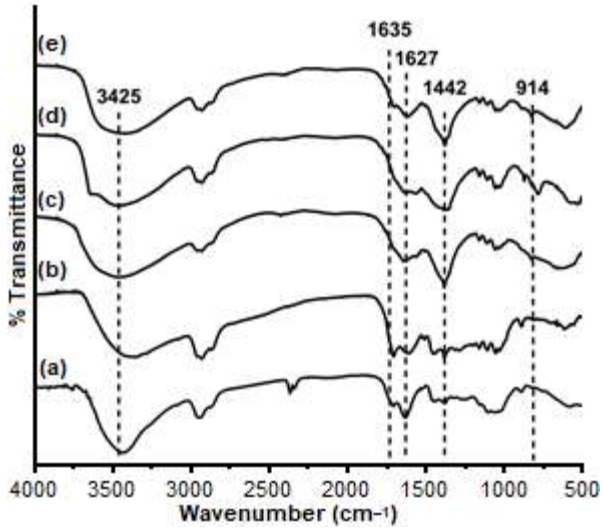

Fig 2. FT-IR spectra of (a) duku peel, (b) HC, composite materials (c) MgAl-HC, (d) CaAl-HC, dan (e) ZnAl-HC

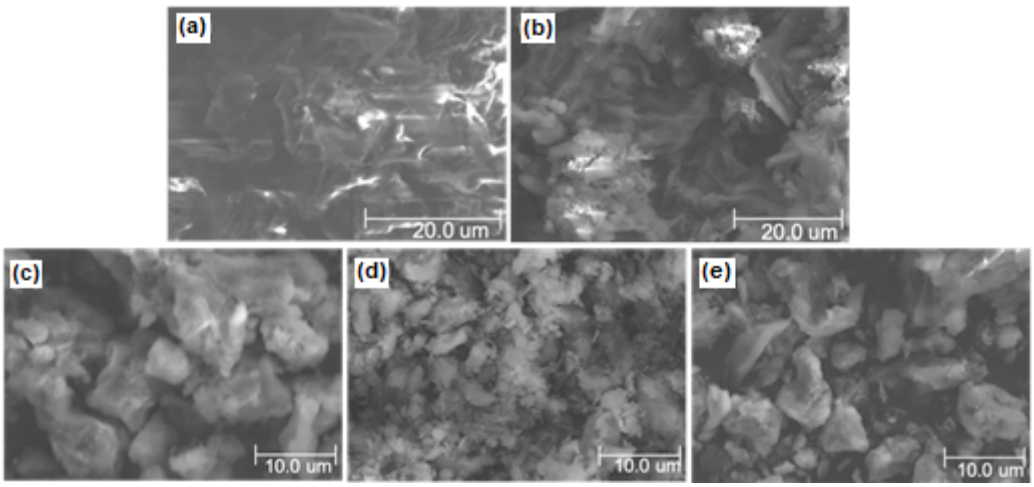

Fig 3. Surface morphology of (a) duku peel, (b) HC, (c) MgAl-HC, (d) CaAl-HC, and (e) ZnAl-HC

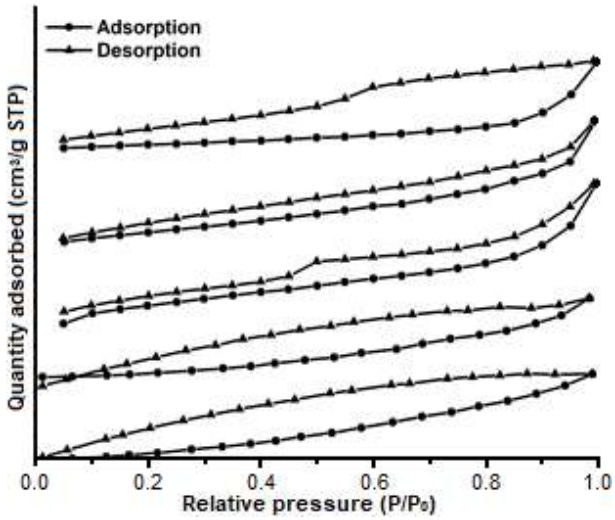

Fig 4. N_2 Adsorption-desorption profile of (a) duku peel, (b) HC, (c) MgAl-HC, (d) CaAl-HC, and (e) ZnAl-HC

Table 1. BET surface area analysis

Material	Surface area (m^2/g)	Pore volume (cm^3/g)	Pore diameter (nm)
Duku peel	12.34	0.02	2.65
HC	22.63	0.04	2.77
MgAl-HC	11.84	0.03	17.06
CaAl-HC	74.21	0.15	19.10
ZnAl-HC	29.87	0.04	24.42

The N_2 adsorption-desorption process produces a profile that describes the pore of the material. Fig. 4 shows the change in profile shape from LDH to composite.

According to Alsamman [17], the isotherm pattern (Fig. 4) of duku peel, HC, and composites (MgAl-HC, CaAl-HC, and ZnAl-HC) resembled type IV. The type IV isotherm pattern indicates a mesoporous material that shows non-overlapping adsorption and desorption patterns. The adsorption-desorption profile of N_2 on MgAl-HC, CaAl-HC, and ZnAl-HC composites stated the occurrence of H4 hysteresis. The hysteresis occurs in the adsorption-desorption process with a different mechanism on the adsorbent with pores that form gaps and is indicated by the adsorbent having a mesoporous size.

The surface area of MgAl-HC is 11.84 m^2/g, CaAl/Hc is 74.21 m^2/g, and ZnAl-HC is 29.87 m^2/g. Based on the data in Table 1, the value of the pore volume is proportional to the surface area. The large surface area results in a comparable pore volume. The pore diameter size shows a tendency inversely proportional to the surface area and pore volume values. The increase in surface area and the pore volume is inversely proportional to the small pore diameter size.

Based on the described characterization data, MgAl-HC, CaAl-HC, ZnAl-HC composites have been successfully prepared as adsorbents. Proving the ability of MgAl-HC, CaAl-HC, ZnAl-HC composites was determined through several parameters. The determination of selectivity is the first parameter that is carried out to see the ability of the adsorbent in the adsorption of mixed dyes. The adsorption process carried out selectivity on mixed dyes consisting of PR, MO, and DG. Results of the selectivity process presented in Fig. 5 show the change in absorbance before and after the adsorption process to the effect of time. Overall, the absorbance decreased with increasing time.

The spectrum in Fig. 5 shows that PR is at 544 nm, MO is 504 nm, and DG is at 623 nm. Before the adsorption process occurs, each dye is mixed with the same concentration, 25 mg/g. The adsorption process of mixed dyes was carried out with time variations of 0, 30, 60, 90, 120, and 150 min. After the adsorption process was carried out, there was a decrease in the concentration of each dye. The decrease in concentration in MO reached 12.49 mg/g in duku peel, 12.05 mg/g in HC, 0.558 in MgAl/HC, 3.32 mg/g in CaAl/HC, and 9.95 mg/g in ZnAl/HC. The decrease in concentration in PR reached 7.94 mg/g in duku peel, 8.77 mg/g in HC, 7.40 mg/g in MgAl/HC, 7.23 mg/g in CaAl/HC, and 7.22 mg/g in ZnAl/HC. While the spectrum in Fig. 5 shows a decrease in concentration in DG reaching 23.32 mg/g in duku peel, 10.65 in HC, 0.32 mg/g in MgAl/HC, 0.76 mg/g in CaAl/HC, and 1.26 mg/g in ZnAl/HC. Based on these data, DG showed a significant decrease compared to MO and PR. The duku peel adsorbents, HC, MgAl-HC, CaAl-HC, and ZnAl-HC, showed a selective adsorption tendency towards DG. Based on these results, the next adsorption process was carried out with a DG selective dye.

Furthermore, the regeneration process is carried out to determine the ability of the adsorbent during

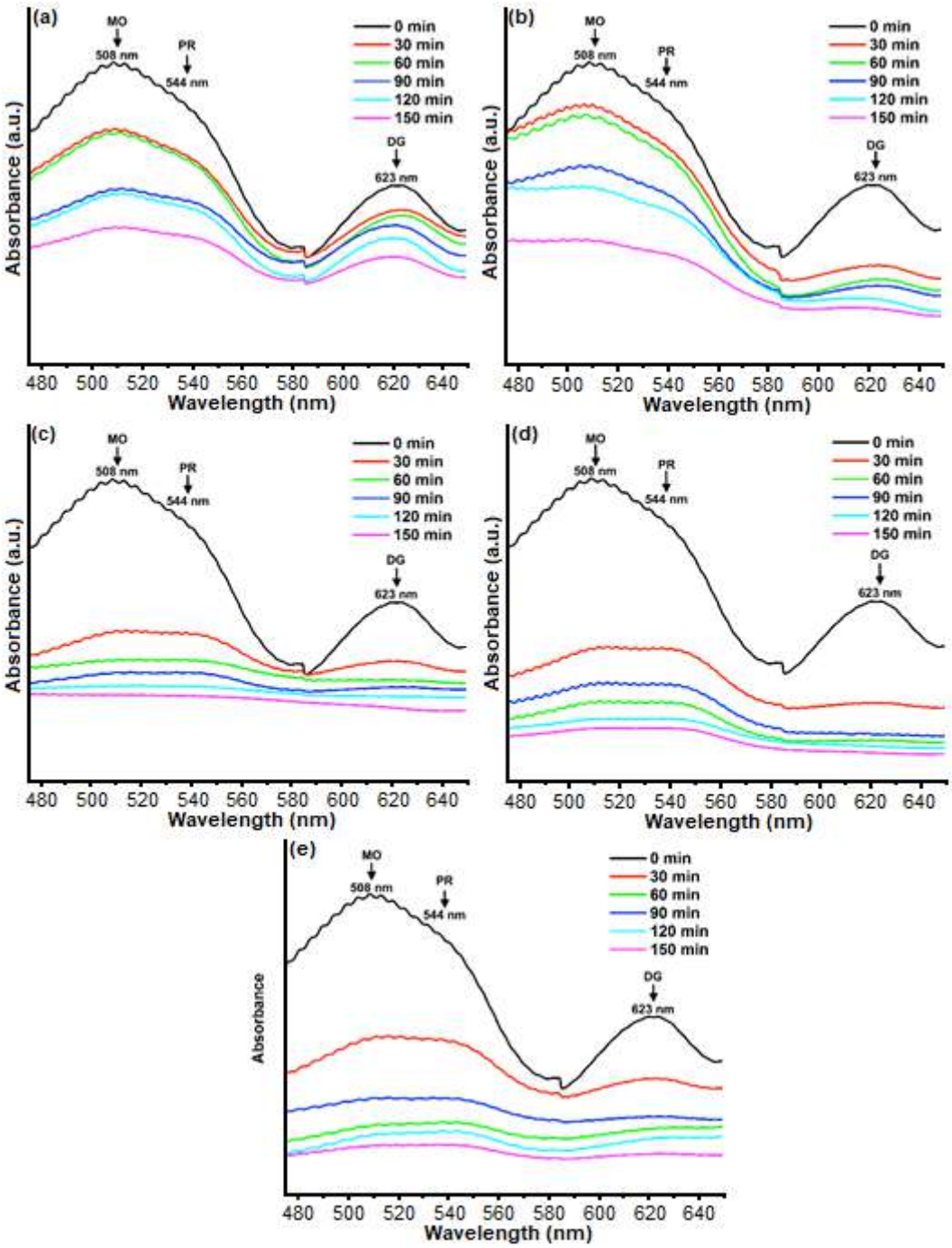

Fig 5. UV-Visible spectra of mixture anionic dyes (PR, MO, and DG) using (a) duku peel, (b) HC, (c) MgAl-HC, (d) CaAl-HC, dan (e) ZnAl-HC

repeated use. The duku peel regeneration process results, HC, MgAl-HC, CaAl-HC, and ZnAl-HC, are presented in Fig. 6. duku peel and HC show a decrease in the adsorption ability of the regeneration product. The first cycle of duku peel was 54.54% which decreased to 2.04% in the last cycle. The regeneration results on HC showed a more excellent value than duku peel. The first cycle showed an HC adsorption ability of 70.31%, but its ability also decreased to 8.41% at the last cycle.

The results of composite regeneration showed a

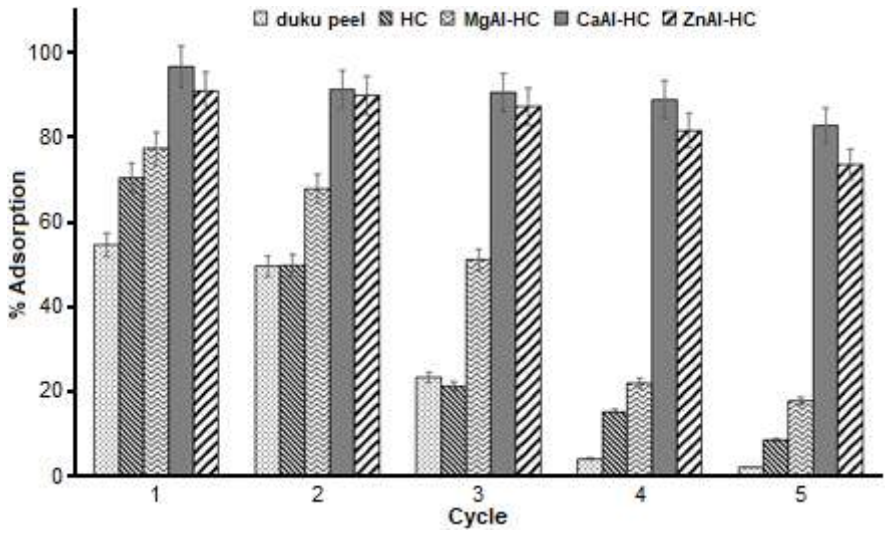

Fig 6. Regeneration process of duku peel, HC, MgAl-HC, CaAl-HC, and ZnAl-HC

stable curve, where the change in adsorption ability was not so significant from the first to the last cycle. The first cycle in MgAl-HC reached 77.27%, then became 51.02% in the third cycle to 17.57% in the previous cycle. CaAl-HC showed the first regeneration yield of 96.66% and remained 90.555% in the third cycle until it decreased to 82.70% in the last cycle. ZnAl-HC regeneration in the first cycle reached 90.91% and fell to 73.52% in the previous cycle. Based on these data, CaAl-HC achieved the best regeneration ability compared to MgAl-HC and ZnAl-HC.

The adsorption ability of MgAl-HC, CaAl-HC, ZnAl-HC composite adsorbents was determined by isotherm parameters which can be seen in Table 2. Q_{max} in Table 2 shows the Q_{max} that the adsorbent can do. MgAl-HC, CaAl-HC, and ZnAl-HC composites showed a higher Q_{max} than duku peel and HC. The Q_{max} of MgAl-HC, CaAl-HC, and ZnAl-HC composites, respectively 94.34 mg/g, 128.20 mg/g, and 89.28 mg/g, show that CaAl-HC has the best ability in the DG adsorption process. The ability of CaAl-HC is supported by surface area data from CaAl-HC in Table 1, which has the largest surface area compared to MgAl-HC and ZnAl-HC, where surface area is one of the parameters that most affect the adsorption capacity of the adsorbent. Several other studies have also carried out the adsorption process on DG, the results of which are presented in Table 3.

In addition to the Q_{max} value, Table 2 also shows the trend of the Langmuir and Freundlich isotherm models. The isotherm model is determined based on the linear regression value (R^2) closer to 1. Table 2 shows that the MgAl-HC, CaAl-HC, and ZnAl-HC composites have an R^2 value in the Langmuir isotherm model, which is more dominant close to 1 than the Freundlich isotherm model. Based on these data, the DG adsorption process using MgAl-HC, CaAl-HC, and ZnAl-HC occurs monolayer. Furthermore, determine the thermodynamic parameters consisting of Gibbs free energy (ΔG), enthalpy (ΔH), and entropy (ΔS) which are presented in Table 3. Overall, ΔG in Table 3 shows negative values.

Table 2. Isotherm parameters

Materials	Langmuir			Freundlich		
	k_L	Q_{max} (mg/g)	R^2	k_F	1/n	R^2
Duku peel	0.76	46.99	0.99	1.36	0.61	0.97
HC	0.10	48.78	0.98	11.26	0.84	0.98
MgAl-HC	1.12	94.34	0.99	1.09	0.52	0.96
CaAl-HC	0.09	128.20	0.96	4.99	1.20	0.69
ZnAl-HC	0.04	89.29	0.91	2.56	0.91	0.64

Table 3. Thermodynamic parameters

Adsorbent	T (K)	ΔH (kJ/mol)	ΔS (J/mol.K)	ΔG (kJ/mol)
Duku peel	303	41.75	0.14	-0.34
	313			-1.73
	323			-3.12
	333			-4.51
Hc	303	20.13	0.07	-0.83
	313			-1.52
	323			-2.21
	333			-2.91
MgAl-Hc	303	20.68	0.07	0.78
	313			0.13
	323			-0.53
	333			-1.19
CaAl-Hc	303	26.13	0.09	-1.12
	313			-2.02
	323			-2.92
	333			-3.82
ZnAl-Hc	303	65.65	0.22	-0.48
	313			-2.67
	323			-4.85
	333			-7.03

According to Siregar et al., a negative ΔG delta value indicates a spontaneous adsorption process [18]. The positive enthalpy in Table 3 shows the adsorption process that takes place endothermic. The enthalpy value in the 20.13–65.65 kJ/mol range indicates the physical and chemical adsorption process. According to Ngah et al., the range of enthalpy values at 40–120 kJ/mol is a chemisorption process [19]. However, if the enthalpy has a value below that range, the adsorption process takes place physisorption [20]. The entropy value, which tends to be minor, close to zero, indicates increased randomness at the solid/solution interface [21]. Table 4 present the adsorption capacity of several adsorbents for DG.

The Van't Hoff equation is used to determine the change in the equilibrium constant concerning temperature variations (Fig. 7). Based on some literature, the Van't Hoff equation in linear form is most widely used by applying Ln.

$$\ln K_e^{\circ} = \frac{\Delta S^{\circ}}{R} - \left(\frac{\Delta H^{\circ}}{R}\right)\frac{1}{T} \quad (1)$$

The equation is used to calculate the entropy and enthalpy changes in the adsorption process, where the Ke constant is obtained from the adsorption isotherm.

Table 4. comparison of sorption capacities of various adsorbents for DG, MO, and PR

Adsorbent	Maximum Capacity ($mg.g^{-1}$)	Ref
ZFN-CTAB	64.10	[22]
Cationized sawdust	35.70	[23]
Natural sawdust	9.30	[23]
Biochar-CMC	39.47	[24]
Fe_3O_4@C	38.03	[25]
CoAl-LDH	32.27	[26]
Magnetic geopolymer	25.46	[27]
Corncob	2.86	[28]
Duku peel	46.99	
HC	48.78	
MgAl-HC	94.34	This work
CaAl-HC	128.20	
ZnAl-HC	89.28	

The kinetic parameters determined in the DG adsorption process using duku peel, HC, MgAl-HC, CaAl-HC, and ZnAl-HC include pseudo-first-order (PFO) and pseudo-second-order (PSO). Determination

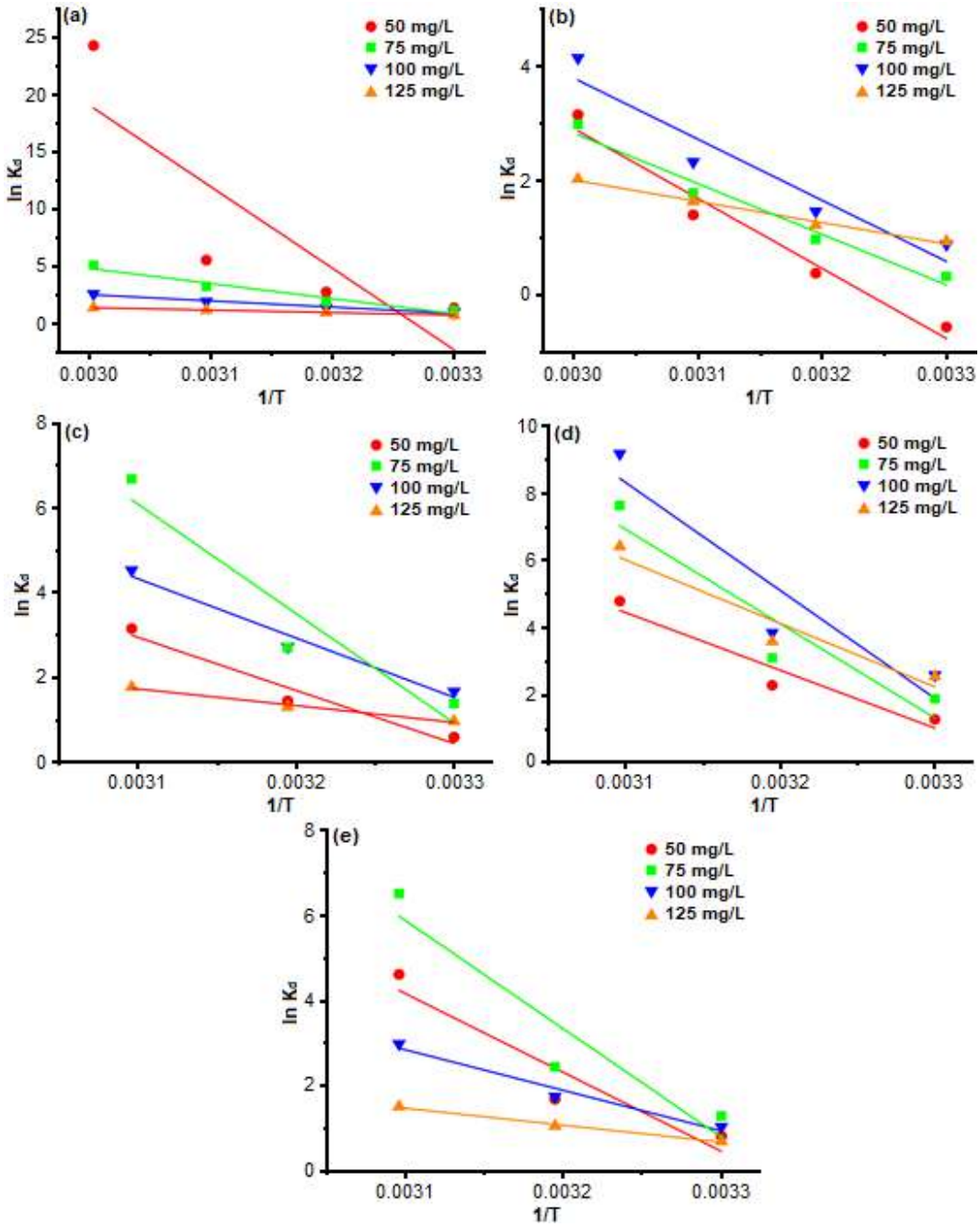

Fig 7. Van't Hoff linear plot for DG adsorption on (a) duku peel, (b) HC, (c) MgAl-HC, (d) CaAl-HC, and (e) ZnAl-HC

of kinetic parameters is done by varying the adsorption contact time from 0–150 min, presented in Fig. 8. Variations in contact time are carried out until the adsorption process reaches equilibrium time. Overall, the DG adsorption process got an equilibrium time of 90 min, indicating that the adsorption process after that minute has been saturated.

In addition, variations in adsorption time are also used to determine the adsorption kinetics model, which is presented in Table 5. The PFO kinetics model explains that the adsorption process is influenced by one of the components between the adsorbent or only the adsorbate. The PSO kinetic model demonstrates that the adsorption process occurs under the influence of both the adsorbent and the adsorbate components. The linear regression value (R^2), which tends to be closer to 1, as

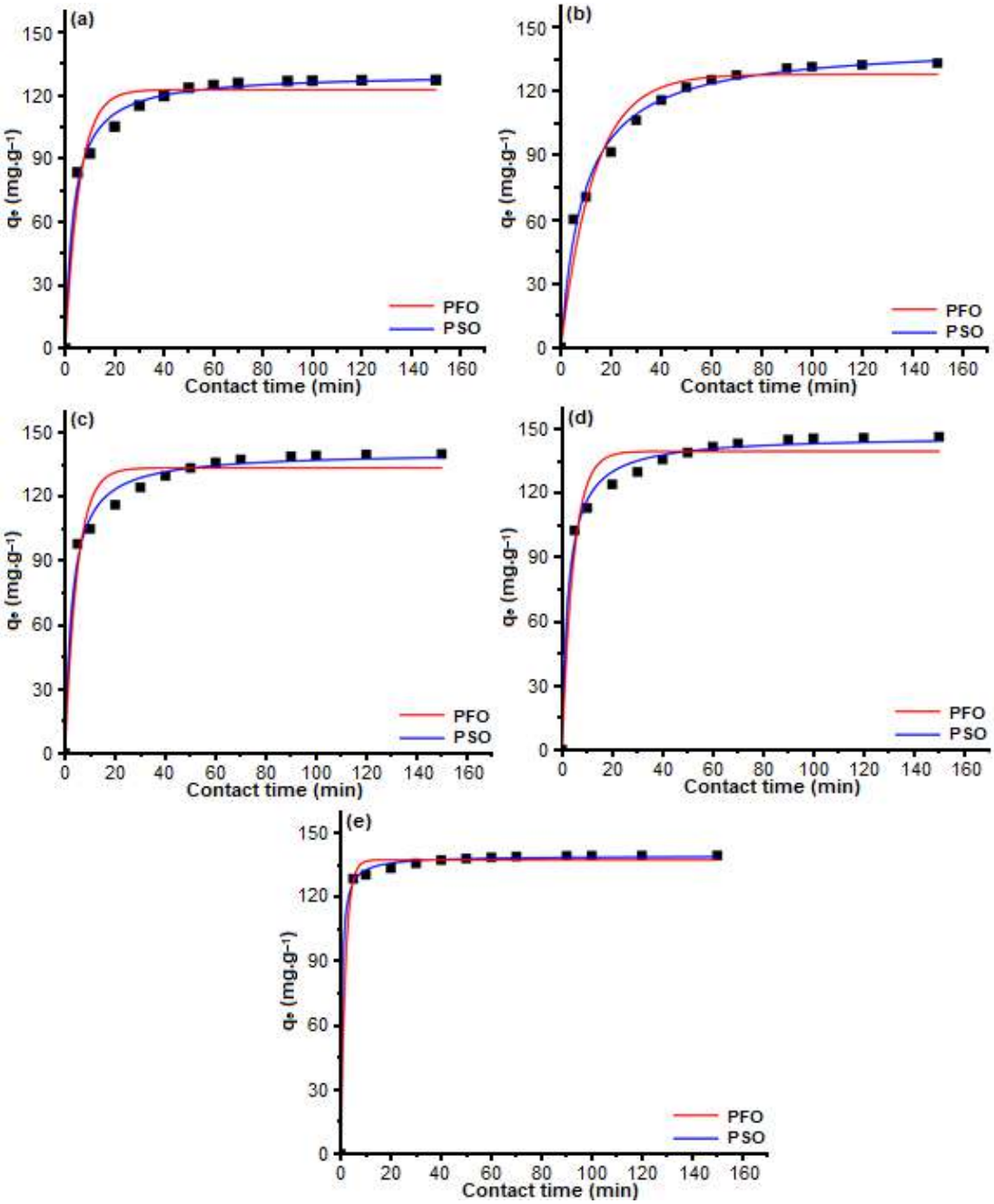

Fig 8. Variations in adsorption time of DG on (a) duku peel, (b) HC, (c) MgAl-HC, (d) CaAl-HC, dan (e) ZnAl-HC

Table 5. Adsorption kinetic models of DG on duku peel, HC, MgAl-HC, CaAl-HC, and ZnAl-HC

Adsorbent	Qe_{exp} (mg/g)	PFO			PSO		
		Qe_{Calc} (mg/g)	R^2	k_1	Qe_{Calc} (mg/g)	R^2	k_2
Duku peel	127.22	69.21	0.99	0.05	131.58	0.99	0.002
HC	133.13	96.94	0.99	0.04	142.86	0.99	0.0007
MgAl-HC	139.96	70.39	0.98	0.05	144.93	0.99	0.001
CaAl-HC	146.39	67.20	0.97	0.04	149.25	0.99	0.001
ZnAl-HC	139.50	24.02	0.92	0.05	140.84	0.99	0.008

shown in Table 5, determined the adsorption kinetics model.

In addition, variations in adsorption time are also used to determine the adsorption kinetics model, which is presented in Table 5. The PFO kinetics model explains that the adsorption process is influenced by one of the components between the adsorbent or only the adsorbate. The PSO kinetic model demonstrates that the adsorption process occurs under the influence of both the adsorbent and the adsorbate components. The linear regression value (R^2), which tends to be closer to 1, as shown in Table 5, determined the adsorption kinetics model.

Duku peel shows the tendency of the PSO kinetic model as seen from the R^2 value in the kinetic model, which is closer to 1. The same thing also happened to the DG adsorption process using HC, MgAl-HC, CaAl-HC, and ZnAl-HC. The R^2 value from Table 5 of the adsorbent shows a tendency to the PSO kinetic model so that the overall adsorption process tends to follow the PSO kinetic model.

CONCLUSION

Composite materials have proven adsorption capabilities, as evidenced by the Q_{max} value. CaAl-HC has the highest Q_{max} among other composites, which reach 128.205 mg/g, while MgAl-HC has a Q_{max} of 94.34 mg/g and ZnAl-HC 89.286 mg/g. The adsorption ability of CaAl-HC was also proven by the regeneration process which lasted until the fifth cycle. The first cycle in the regeneration process showed 96.658% and in the last cycle 82.697%. This shows that CaAl-HC has potential as a superior adsorbent with good adsorption ability and is effective for regeneration.

ACKNOWLEDGMENTS

We wish to express our gratitude to the research center Inorganic Materials and Complexes, Sriwijaya University, for instrument analysis.

REFERENCES

[1] Behbahani, E.S., Dashtian, K., and Ghaedi, M., 2020, Fe/Co-chalcogenide-stabilized Fe_3O_4 nanoparticles supported MgAl-layered double hydroxide as a new magnetically separable sorbent for the simultaneous spectrophotometric determination of anionic dyes, *Microchem. J.*, 152, 104431.

[2] Starukh, H., and Levytska, S., 2019, The simultaneous anionic and cationic dyes removal with Zn e Al layered double hydroxides, *Appl. Clay Sci.*, 180, 105183.

[3] Lim, S.J., and Kim, T.H., 2015, Combined treatment of swine wastewater by electron beam irradiation and ion-exchange biological reactor system, *Sep. Purif. Technol.*, 146, 42–49.

[4] Zhuang, H., Han, H., Ma, W., Hou, B., Jia, S., and Zhao, Q., 2015, Advanced treatment of biologically pretreated coal gasification wastewater by a novel heterogeneous Fenton oxidation process, *J. Environ. Sci.*, 33, 12–20.

[5] Mólgora, C.C., Domínguez, A.M., Avila, E.M., Drogui, P., and Buelna, G., 2013, Removal of arsenic from drinking water: A comparative study between electrocoagulation-microfiltration and chemical coagulation-microfiltration processes, *Sep. Purif. Technol.*, 118, 645–651.

[6] Liu, H., Zhou, H., Li, H., Liu, X., Ren, C., Liu, Y., Li, W., and Zhang, M., 2019, Fabrication of Bi_2S_3@Bi_2WO_6/WO_3 ternary photocatalyst with enhanced photocatalytic performance: Synergistic effect of Z-scheme/traditional heterojunction and oxygen vacancy, *J. Taiwan Inst. Chem. Eng.*, 95, 94–102.

[7] Liu, X., Zhou, Z., Yin, J., He, C., Zhao, W., and Zhao, C., 2020, Fast and environmental-friendly approach towards uniform hydrogel particles with ultrahigh and selective removal of anionic dyes, *J. Environ. Chem. Eng.*, 8 (5), 104352.

[8] Milagres, J.L., Bellato, C.R., Ferreira, S.O., de M. Guimarães, L., de P. Tonon, G.J., and Bolandini, A., 2019, Simultaneous removal process of divalent metal and anionic and cationic dyes by layered reconstruction with hydrocalumite intercalated with dodecyl sulfate, *Colloids Surf., A*, 582, 123890.

[9] Meng, Z., Wu, M., Zhao, S., Jing, R., Li, S., Shao, Y., Liu, X., Lv, F., Liu, A., and Zhang, Q., 2019, Removing anionic dyes from wastewater based on in-situ formation of Fe_3O_4@Zn-Al layered double

hydroxides by self-assembly, *Appl. Clay Sci.*, 170, 41–45.

[10] Li, N., Chang, Z., Dang, H., Zhan, Y., Lou, J., Wang, S., Attique, S., Li, W., Zhou, H., and Sun, C., 2020, Deep eutectic solvents assisted synthesis of MgAl layered double hydroxide with enhanced adsorption toward anionic dyes, *Colloids Surf., A*, 591, 124507.

[11] Daud, M., Hai, A., Banat, F., Wazir, M.B., Habib, M., Bharath, G., and Al-Harthi, M.A., 2019, A review on the recent advances, challenges and future aspect of layered double hydroxides (LDH) – Containing hybrids as promising adsorbents for dyes removal, *J. Mol. Liq.*, 288, 110989.

[12] Badri, A.F., Palapa, N.R., Mohadi, R., and Lesbani, A., 2020, Cationic dye removal by magnesium aluminum-biochar composite from aqueous solution, *Int. J. Sci. Technol. Res.*, 9 (7), 186–190.

[13] He, H., Zhang, N., Chen, N., Lei, Z., Shimizu, K., and Zhang, Z., 2019, Efficient phosphate removal from wastewater by MgAl-LDHs modified hydrochar derived from tobacco stalk, *Bioresour. Technol. Rep.*, 8, 100348.

[14] Balcomb, B., Singh, M., and Singh, S., 2015, Synthesis and characterization of layered double hydroxides and their potential as nonviral gene delivery vehicles, *ChemistryOpen*, 4 (2), 137–145.

[15] Palapa, N.R., Juleanti, N., Normah, N., Taher, T., and Lesbani, A., 2020, Unique Adsorption properties of malachite green on interlayer space of Cu-Al and Cu-Al-$SiW_{12}O_{40}$ layered double hydroxides, *Bull. Chem. React. Eng. Catal.*, 15 (3), 653–661.

[16] Bamroongwongdee, C., Suwannee, S., and Kongsomsaksiri, M., 2019, Adsorption of Congo red from aqueous solution by surfactant-modified rice husk: Kinetic, isotherm and thermodynamic analysis, *Songklanakarin J. Sci. Technol.*, 41 (5), 1076–1083.

[17] Alsamman, L., 2017, Development of Modified Layered Silicates with Superior Adsorption Properties for Uptake of Pollutants from Air and Water, *Dissertation*, RWTH Aachen University, Aachen, Germany.

[18] Siregar, P.M.S.B.N., Palapa, N.R., Wijaya, A., Fitri, E.S., and Lesbani, A., 2021, Structural stability of Ni/Al layered double hydroxide supported on graphite and biochar toward adorption of Congo red, *Sci. Technol. Indones.*, 6 (2), 85–95.

[19] Wan Ngah, W.S., and Hanafiah, M.A.K.M., 2008, Adsorption of copper on rubber (*Hevea brasiliensis*) leaf powder: Kinetic, equilibrium and thermodynamic studies, *Biochem. Eng. J.*, 39 (3), 521–530.

[20] Palapa, N.R., Taher, T., Wijaya, A., and Lesbani, A., 2021, Modification of Cu/Cr layered double hydroxide by Keggin type polyoxometalate as adsorbent of malachite green from aqueous solution, *Sci. Technol. Indones.*, 6 (3), 209–217.

[21] Sahmoune, M.N., 2019, Evaluation of thermodynamic parameters for adsorption of heavy metals by green adsorbents, *Environ. Chem. Lett.*, 17 (2), 697–704.

[22] Mahmoodi, N.M., Abdi, J., and Bastani, D., 2014, Direct dyes removal using modified magnetic ferrite nanoparticle, *J. Environ. Health Sci. Eng.*, 12 (1), 96.

[23] Hashem, A., Ahmad, F., and Badawy, S.M., 2016, Adsorption of direct green 26 onto fix 3500 treated sawdust: Equilibrium, kinetic and isotherms, *Desalin. Water Treat.*, 57 (28), 13334–13346.

[24] Yu, J., Zhang, X., Wang, D., and Li, P., 2018, Adsorption of methyl orange dye onto biochar adsorbent prepared from chicken manure, *Water Sci. Technol.*, 77 (5), 1303–1312.

[25] Tran, T.V., Phan, T.Q.T., Nguyen, D.T.C., Nguyen, T.T., Nguyen, D.H., Vo, D.V.N., Bach, L.G., and Nguyen, T.D., 2020, Recyclable Fe_3O_4@C nanocomposite as potential adsorbent for a wide range of organic dyes and simulated hospital effluents, *Environ. Technol. Innovation*, 20, 101122.

[26] Nazir, M.A., Khan, N.A., Cheng, C., Shah, S.S.A., Najam, T., Arshad, M., Sharif, A., Akhtar, S., and Ur Rehman, A., 2020, Surface induced growth of ZIF-67 at Co-layered double hydroxide: Removal of methylene blue and methyl orange from water, *Appl. Clay Sci.*, 190, 105564.

[27] Hua, P., Sellaoui, L., Franco, D., Netto, M.S., Luiz Dotto, G., Bajahzar, A., Belmabrouk, H., Bonilla-Petriciolet, A., and Li, Z., 2020, Adsorption of acid green and procion red on a magnetic geopolymer based adsorbent: Experiments, characterization and theoretical treatment, *Chem. Eng. J.*, 383, 123113.

[28] Nazifa, T.H., Habba, N., Salmiati, S., Aris, A., and Hadibarata, T., 2018, Adsorption of procion red MX-5B and crystal violet dyes from aqueous solution onto corncob activated carbon, *J. Chin. Chem. Soc.*, 65 (2), 259–270.

Preparation and Photoluminescence Spectra of Organometallic Complexes Containing Nanoparticles as Random Gain Media

Atheer Abdulraheem Mahmood[1*], Oday Atta Hammadi[2], and Kais Rzaik Ibraheem[3]

[1]*Department of Chemistry, College of Education, Al-Iraqia University, Baghdad, Iraq*

[2]*Department of Physics, College of Education, Al-Iraqia University, Baghdad, Iraq*

[3]*Department of Chemistry, College of Science, University of Anbar, Ramadi, Iraq*

* ***Corresponding author:***

tel: +964-7813479524
email: atheerinchemistry@yahoo.com

Received: September 1, 2021
Accepted: November 20, 2021

DOI: 10.22146/ijc.68822

Abstract: *This work prepared organometallic complexes from the 8-hydroxyquinoline ligand linked to metal ions such as Ba^{2+}, Ca^{2+}, and Zn^{2+}. The effects of metal ion type and adding nanoparticles to the complex solution on the absorption and photoluminescence characteristics of the prepared complexes were introduced. These nanoparticles were added to the prepared complex solutions to act as scattering centers to form random gain media with emission in the visible region of the electromagnetic spectrum. The random gain media made from the Znq_2 complex with nanoparticles showed the best characteristics with good chemical and spectroscopic stabilities, high reliability, and reproducibility in addition to the low production cost and reasonably simple requirements.*

Keywords: *photoluminescence; organometallic complex; nanoparticles; random gain medium*

INTRODUCTION

As of late, different interchanges, natural, biomedical, and space applications have been created by using irregular addition media as laser sources known as "random lasers" [1]. Additionally, the continuous and extraordinary improvements in nanotechnology have prompted uncommon advancements in the plan and manufacture of irregular increase media [2-3]. 8-Hydroxyquinoline zinc has many advantages, such as simple synthesis conditions [4]. In general, the random gain medium can be fabricated by adding nanoparticles to a laser dye solution to play the role of scatters within the dye solution to amplify the generated laser signal [5]. However, the spectroscopic characteristics of both dye solution and nanoparticles must be precisely determined as a requirement for successful gain amplification.

As the power of the random lasing activity is amazingly high, then, at that point, the population inversion is reached so rapidly, bringing about a short peak in the fluorescence spectrum. The population inversion is effectively achieved and consumed with continuous excitation of the added particles, prompting a progression of peaks in the emission range. The emission range of a random laser is high in intensity and narrow in width.

The host or gain media used to fabricate random laser systems are laser dyes like xanthene and coumarin. These dyes are characterized by high gain, high fluorescence efficiency, and extremely broad energy bands allowing both absorption and emission over a wide range of wavelengths. Also, the emission of laser dye can be controlled by several parameters, mainly dye-solution concentration, and solvent type. Therefore, the search for new organic complexes with featured spectroscopic and chemical characteristics continuously replaces common laser dyes and explores new dye laser physics and technology [6]. Znq_2 has many advantages, such as high luminous efficiency [6]. Many scholars have done in-depth research focused on extending application potential of MQ_2 [7]. At present, liquid-phase method is the main method to synthesize MQ_2 [8].

The 8-hydroxyquinoline (H.Q.) ligand is impressively used in coordination science for the extraction and goal of component particles [9-10].

Chelato-aromaticity can happen in metallo-cyclic rings shaped during metal particle complexation or in rings of the ligand that do not connect straightforwardly with metal particles [11]. The 8-hydroxyquinoline can arrange with different particles as bidentate through nitrogen iota of quinolone ring and oxygen molecule after deprotonation of hydroxyl group [12]. The 8-hydroxyquinoline (oxine) acts as a bidentate (N,O^-) univalent ligand to frame chelates with a few metal particles [13]. The zinc(II) buildings of amide and urea subbed of 8-hydroxyquinoline have shown superb photoluminescence and fluorescence qualities compared to their friend metalorganic edifices [14].

This work synthesized new organometallic complexes by connecting some metal ions to the 8-hydroxyquinoline ligand. The photoluminescence of the incorporated complexes was estimated before and after adding metal oxide nanoparticles to introduce their effects and form a random gain media to produce a random laser.

EXPERIMENTAL SECTION

Materials

Three different solvents, dimethyl sulfoxide (DMSO), N,N-dimethylformamide (DMF), and ethanol, were used in this work, while the 8-Hydroxyquinoline (8-HQ) was used as a ligand and barium(II) chloride dihydrate, calcium(II) chloride and zinc (II) chloride were used as metal salts to synthesize the required complexes.

Instrumentation

The precursors, ligands, and synthesized complexes were characterized as follows. The Fourier-transform infrared (FTIR) spectra were recorded using the Nicolet Impact 410 spectrophotometer using KBr disk in the range 400–4000 cm^{-1}. The absorption spectra were recorded using a UV-Visible SPEKOL 2000 double-beam spectrophotometer supplied by P.G. Instruments (U.K.), which has a slit width in a spectral range of 190–1100 nm. Both FTIR and UV-visible measurements were performed on the samples in ethanol. The field-effect scanning electron microscopy (FE-SEM) was used to study the effect of nanoparticle size and distribution on the characteristics of the prepared samples.

Procedure

Synthesis of bis(8-hydroxyquinolato) zinc (Znq_2) complex

A sample of 1.83 g (10 mmol) $Zn(CH_3COO)_2$ was dissolved in 10 mL of distilled water. Then this solution was added as drops to another solution of 2.9 g (2 mmol) 8-hydroxyquinoline ligand was dissolved in a mixture of 0.11 g potassium hydroxide (KOH) in 6 mL of distilled water. The first solution prepared in the first step was added to the second solution, and then the reaction mixture was stirred as the complex was prepared by filtration, washed by absolute ethanol, dried at room temperature for 24 h. The result is a white-green solid with a yield of 3.26 g (92.35%).

Synthesis of bis(8-hydroxyquinolato) barium (Baq_2) complex

A 2.44 g (10 mmol) of $BaCl_2{\cdot}2H_2O$ was dissolved in 10 mL distilled water, then the prepared solution was added to a solution of 2.9 g (2 mmol) 8-HQ dissolved in a solution of 0.11g KOH in 6 mL of distilled water. The first solution was added to the second solution, and the mixture was stirred until the complex was prepared by filtration, washed by absolute ethanol, dried at room temperature for 24 h to get a white green solid with a yield of 4.08 g (81.6%).

Synthesis of bis(8-hydroxyquinolato) calcium (Caq_2) complex

A solution was prepared by dissolving 1.11g (10 mmol) $CaCl_2$ in 10 mL distilled water, then added to a solution of 2.9 g (2 mmol) 8-HQ ligand dissolved in the same mixture (0.11g KOH in 6 mL of distilled water). The first solution was added to the second one, and the produced mixture was stirred until the complex was prepared by filtration, washed by absolute ethanol, dried at room temperature for 24 h. The final sample was a white-yellow solid with a yield of 1.82 g (98.7 %).

Adding nanoparticles

In order to form the random gain media, highly-pure titanium dioxide nanoparticles with an average particle size of 25 nm were added to the complex solution, and the absorption and photoluminescence spectra were recorded and compared before and after

adding these nanoparticles. The minimum amount of added nanoparticles was 0.5 mg for 5 mL of a complex solution of 10^{-5} M concentration. Many experiments were carried out to determine these preparation conditions.

■ RESULTS AND DISCUSSION

To affirm the arrangement of organometallic linkage, the FTIR spectra of the free 8-hydroxyquinoline ligand and all edifices arranged in this work were recorded in the wavenumber scope of 400–4000 cm^{-1} as displayed in Fig. 1. The range of the 8-Hq ligand shows two groups at 3161 cm^{-1} because of the O–H extending group and at 3049 cm^{-1} to C-Hst, group aromatic vibration. The main band was not found in the FTIR spectra of the three complexes, which affirms the coordination through the oxygen atom of the hydroxyl group. The subsequent band was seen inside the reach 3040–3055 cm^{-1}.

One more band at 1576 cm^{-1} attributed to the C=N group was marginally moved to various positions, which affirms the coordination through the nitrogen iota of the C=N group [15]. The groups were seen at 1500 and 1466 cm^{-1} are ascribed to the vibrations of the benzene ring. These bands were seen in all spectra of the prepared complexes with a slight shift, as shown in Table 1. The bands are seen within the range 1366–1386 cm^{-1} are ascribed to the vibration of C=N. The bands seen in the range 1274–1281 cm^{-1} are attributed to O–H's bend vibrations [16-17]. The bands observed at 1217 and 1203 cm^{-1} are ascribed to the stretch vibration modes of C–O.

Nonetheless, these groups were seen in the FTIR spectra of the Baq_2 complex and disappeared in the Caq_2 and Znq_2. Therefore, the new groups have seen inside 570–591 cm^{-1} and 475–504 cm^{-1} are ascribed to the arrangement of metal-nitrogen (M–N) metal-oxygen (M–O) bonds, separately, because of the coordination with metal particles in the buildings (Baq_2, Caq_2, and Znq_2) [18-20].

Fig. 2 shows the absorption spectra of the three complexes prepared in this work before and after adding

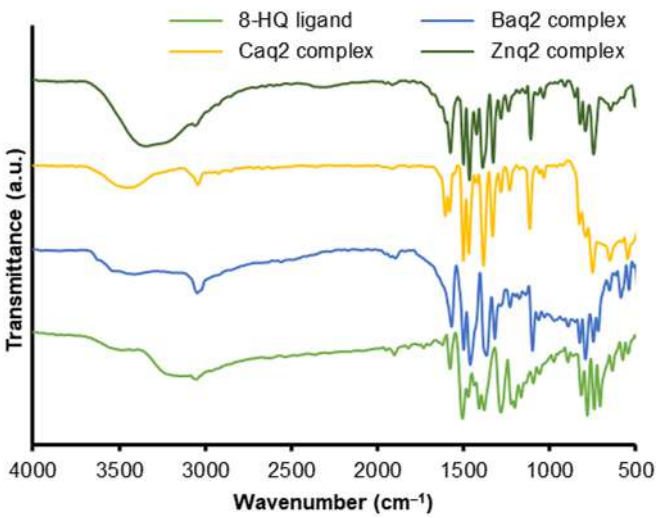

Fig 1. FTIR spectra of free 8-Hq ligand, Baq_2, Caq_2, and Znq_2 complexes prepared in this work

Table 1. Vibration modes of the free ligand and complexes prepared in this work

Vibration mode	8-Hq (cm^{-1})	Baq_2 (cm^{-1})	Caq_2 (cm^{-1})	Znq_2 (cm^{-1})
M–O vibration	475	478	492	504
M–N vibration	577	584	591	570
In-plane ring deformation	642	645	648	644
In-plane deformation	743	740	748	742
C–O stretching	1203	1198	1171	1175
O–H bending	1281	1281	1274	1280
C=N vibration	1375	1366	1375	1386
Phenyl group	1466	1460	1459	1466
Pyridyl group	1500	1497	1497	1500
C=N coordination	1576	1567	1569	1577
C-$H_{st.}$ aromatic vibration	3049	3044	3040	3054
OH stretching	3161	-	-	-

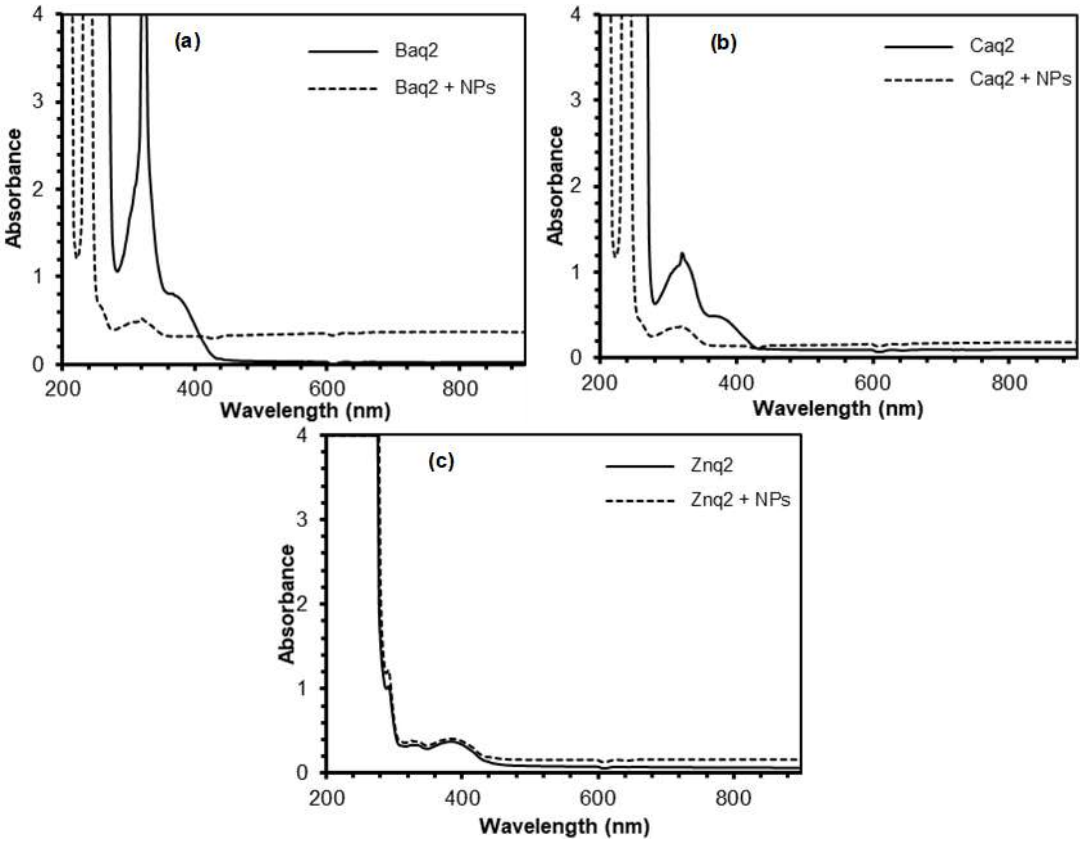

Fig 2. Absorption spectra of Baq_2 complex (a), Caq_2 complex (b), and Znq_2 complex (c) prepared in this work before and after adding nanoparticles

nanoparticles to the complex solution in ethanol solvent. It is clear that the absorption peak for Baq_2 and Caq_2 complexes at 326 and 330 nm, respectively, was suppressed after adding the nanoparticles, while no similar effect was observed for the Znq_2 complex. However, after adding the nanoparticles, all complexes showed high absorbance in the ultraviolet region (< 300 nm). As well, the Baq_2 complex showed higher absorbance in the spectral range 500–800 nm after adding the nanoparticles, while the difference in absorbance for both Caq_2 and Znq_2 complexes was very small.

As the aimed application of the organometallic complexes prepared in this work is the random gain media, then the photoluminescence intensities were compared before and after adding the nanoparticles, as shown in Fig. 3. All complexes showed two distinct peaks; the first in the blue region (450–470 nm) and the second in the green region (510–515 nm). In the Baq_2 and Caq_2 complexes, the intensity of the first peak was higher than that of the second one. In contrast, the second peak of the Znq_2 was higher than that of the first one.

After adding the nanoparticles, the Caq_2 complex showed a slight decrease in the photoluminescence intensity, whereas both Baq_2 and Znq_2 complexes showed higher photoluminescence intensities. The increase for the Znq_2 complex was 25% and 20% for both peaks, while it was more than 2% and 9% for the Baq_2 complex.

The FE-SEMs (Fig. 4) for both samples before nanoparticles addition were measured to attribute the different increases in photoluminescence for Baq_2 and Znq_2 complexes. The SEM was not performed on the synthesized samples after adding TiO_2 nanoparticles as no reaction is expected between the complex and nanoparticles. Instead, the SEM result of TiO_2 nanoparticles was inserted to confirm their formation. As a result, it was confirmed that the metal ions linked to the ligand form nanoparticles. As shown, the Baq_2 sample

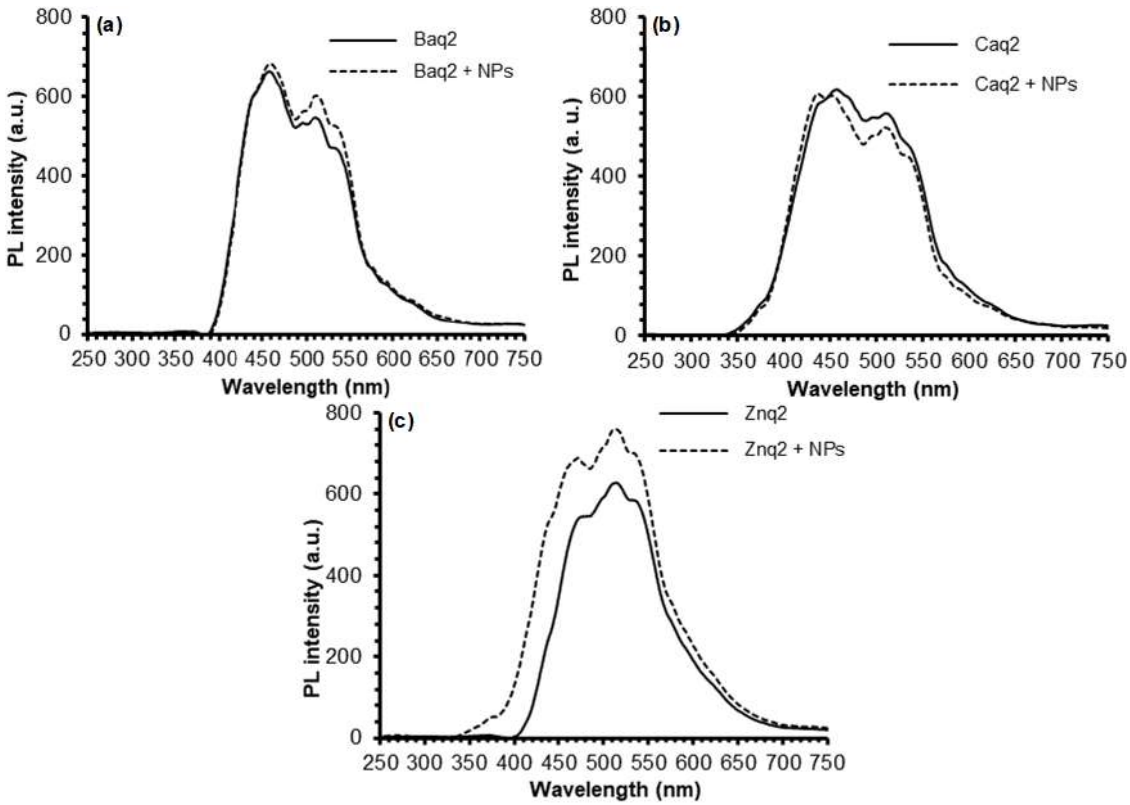

Fig 3. Photoluminescence spectra of Baq_2 complex (a), Caq_2 complex (b), and Znq_2 complex (c) prepared in this work before and after adding nanoparticles

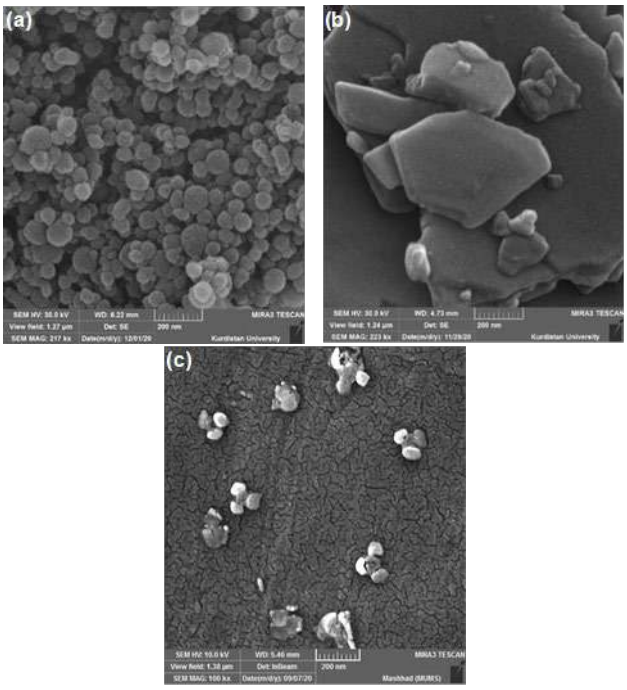

Fig 4. FE-SEM results of Baq_2 complex (a) and Znq_2 complex (b) prepared in this work before adding nanoparticles (c) SEM result of TiO_2 nanoparticles

exhibited a highly uniform distribution, spherical-shaped, and smaller particles when compared to the Znq_2 sample, which exhibited larger sizes and reasonable aggregation. The homogeneous distribution of nanoparticles may cause a homogeneous response to the incident radiation, and hence the average increase is smaller than that in the case of the inhomogeneous distribution of the Znq_2 sample.

Accordingly, the Znq_2 complex can be a good candidate for a random gain medium to produce a random laser. Furthermore, with further optimization of preparation conditions, mainly the concentrations of complex solution and nanoparticles added to the complex solution, the photoluminescence characteristics can be sufficiently enhanced to fabricate the final sample as a solid rod by embedding the sample in a transparent host.

■ CONCLUSION

In concluding remarks, organometallic complexes containing nanoparticles were prepared from the 8-

hydroxyquinoline ligand linked to metal ions such as Ba^{2+}, Ca^{2+}, and Zn^{2+}. The Znq_2 complex showed constant absorbance after adding the nanoparticles but higher photoluminescence intensity in the visible region. The random gain media made from the Znq_2 complex with nanoparticles showed the best characteristics with good chemical and spectroscopic stabilities, high reliability, and reproducibility in addition to the low production cost and reasonably simple requirements.

AUTHOR CONTRIBUTIONS

All authors agreed to the final version of this manuscript.

REFERENCES

[1] Nasser, B.K., and Hameed, M.A., 2020, Narrow emission linewidth of highly-pure silicon nitride nanoparticles in different dye solutions as random gain media, *Nonlinear Opt., Quantum Opt.*, 53 (1-2), 99–105.

[2] Chiad, B.T., Latif, K.H., Kadhim, F.J., and Hameed, M.A., 2011, Random laser of R6G dye and TiO_2 nanoparticles doped in PMMA polymer, *Adv. Mater. Phys. Chem.*, 1, 20–25.

[3] Chiad, B.T., Hameed, M.A., Latif, K.H., and Al-Maliki, F.J., 2011, Transition from amplified spontaneous emission to laser action in disordered media of R6G dye and TiO_2 nanoparticles doped with PMMA polymer, *J. Eur. Opt. Soc.-Rapid Publ.*, 6, 11049.

[4] Liu, J., Zhong, X., Xu, Y., and Li, Y., 2019, Green synthesis of 8-hydroxyquinoline barium as visible-light-excited luminescent material using mechanochemical activation method, *Global Challenges*, 3 (12), 1900052.

[5] Dai, G., Wang, L., and Deng, L., 2020, Flexible random laser from dye doped stretchable polymer film containing nematic liquid crystal, *Opt. Mater. Express*, 10 (1), 68–75.

[6] Liu, J., Zhang, H., Dong, H., Meng, L., Jiang, L., Wang, Y., Yu, J., Sun, Y., Hu,W., and Heeger, A.J., 2015, High mobility emissive organic semiconductor, *Nat. Commun.*, 6 (1), 10032.

[7] Wang, W., Marshall, M., Collins, E., Marquez, S., Mu, C., Bowen, K.H., and Zhang X., 2019, Intramolecular electron-induced proton transfer and its correlation with excited-state intramolecular proton transfer, *Nat. Commun.*, 10 (1), 1170.

[8] Wu, S., Zhong, X., Zeng, H., You, W., and Zhou, W., 2018, Study on green synthesis and properties of luminescent material bis(8-hydroxyquinoline) calcium (CaQ_2), *J. Lumin.*, 195, 120–125.

[9] Prachayasittikul, V., Prachayasittikul, S., Ruchirawat, S., and Prachayasittikul V., 2013, 8-Hydroxyquinolines: A review of their metal chelating properties and medicinal applications, *Drug Des., Dev. Ther.*, 7, 1157–1178.

[10] Albrecht, M, Fiege, M., and Osetska, O., 2008, 8-Hydroxyquinolines in metallosupramolecular chemistry, *Coord. Chem. Rev.*, 252 (8-9), 812–824.

[11] El-Wakiel, N.A., Rizk, H.F., and Ibrahim, S.A., 2017, Synthesis and characterization of metal complexes of azo dye based on 5-nitro-8-hydroxyquinoline and their applications in dyeing polyester fabrics, *Appl. Organometal. Chem.*, 31 (10), e3723.

[12] Vashi, R.T., Patel, S.B., and Kadiya, H.K., 2012, Synthesis, characterization and antimicrobial activity of metal chelates of 2-[(8-hydroxyquinolinyl)-5-aminomethyl]-3-(4-bromophenyl)-3(H)-quinazolin -4-one, *Pharma Chem.*, 4 (4), 1506–1511.

[13] Mahmood, A.A., Hammadi, O.A., and Ibraheem, K.R., 2021, Some physical properties of metal-hydroxyquinoline complexes in different solvents, *Iraqi J. Appl. Phys.*, 17 (1), 9–16.

[14] Lima, C.F.R.A.C., Taveira, R.J.S., Costa, J.C.S., Fernandes, A.M., Melo, A., Silva, A.M.S., and Santos, L.M.N.B.F., 2016, Understanding M–ligand bonding and *mer-/fac*-isomerism in tris(8-hydroxyquinolinate) metallic complexes, *Phys. Chem. Chem. Phys.*, 18 (24), 16555-16565.

[15] Podunavac-Kuzmanovic, S.O., Cvetkovic, D.M., and Vojinovic, L.S., 2004, Synthesis, physico-chemical characterization and biological activity of 2-aminobenzimidazole complexes with different metal ions, *Acta Period. Technol.*, 35, 239–246.

[16] Han, Y.K., and Lee, S.U., 2002, Molecular orbital study on the ground and excited states of methyl substituted tris(8-hydroxyquinoline) aluminum(III), *Chem. Phys. Lett.*, 366 (1-2), 9–16.

[17] Wagenknecht, P.S., and Ford, P.C., 2011, Metal centered ligand field excited states: Their roles in the design and performance of transition metal based photochemical molecular devices, *Coord. Chem. Rev.*, 255 (5-6), 591–616.

[18] Pimchan, P., Khaorapapong, N., and Ogawa, M., 2014, The effect of acetyl trimethyl ammonium ion and type of smectites on the luminescence efficiency of bis(8-hydroxyquinoline)zinc(II) complex, *Appl. Clay Sci.*, 101, 223–228.

[19] Tsuboi, T., Nakai, Y., and Torii, Y., 2012, Photoluminescence of bis(8-hydroxyquinoline) zinc (Znq_2) and magnesium (Mgq_2), *Cent. Eur. J. Phys.*, 10 (2), 524–528.

[20] Patel, K.D., and Patel, H.S., 2017, Synthesis, spectroscopic characterization and thermal studies of some divalent transition metal complexes of 8-hydroxyquinoline, *Arabian J. Chem.,* 10, S1328–S1335.

In Vitro Alpha-Amylase Inhibitory Activity of Microencapsulated *Cosmos caudatus* Kunth Extracts

Anna Safitri[1,2*], Anna Roosdiana[1], Ellysia Hitdatania[1], and Savira Ayu Damayanti[1]

[1]*Department of Chemistry, Faculty of Mathematics and Natural Sciences, Brawijaya University, Jl. Veteran, Malang, 65145, Indonesia*

[2]*Research Centre of SMONAGENES (Smart Molecules of Natural Genetic Resources), Brawijaya University, Indonesia*

* ***Corresponding author:***

email: a.safitri@ub.ac.id

Received: September 22, 2021
Accepted: November 3, 2021

DOI: 10.22146/ijc.68844

Abstract: *The existence of phytochemicals in* Cosmos caudatus *Kunth, predominantly phenolic compounds, offers several health benefits. Nevertheless, the bioactive compounds are usually susceptible to degradation, and therefore may reduce their biological activity. This work aims to carry out microencapsulation of* C. caudatus *K. extracts by spray drying technique. The* in vitro *alpha-amylase inhibitory activity of the microencapsulated product is also investigated. The effect of manufacturing conditions, including pH, the concentration of wall materials, and stirring time, was evaluated. The optimal conditions for microcapsules formation were selected based on the activity of microcapsules as inhibitors for the alpha-amylase enzyme, pointing out by the lowest number of IC_{50}. Results showed that microcapsules prepared in pH 4, 0.05% of chitosan, and 90 min stirring time had optimum efficiency, with the IC_{50} value of 92.85 ± 1.21 µg/mL. The FTIR (Fourier-Transform infrared) analysis showed that the –C–N stretching amine functional group appeared at wavenumber 1285 cm^{-1}, and the –P=O phosphate bending appeared at 1206 cm^{-1}. Characterization with PSA (particle size analyzer) and SEM (scanning electron microscope) indicated that microcapsules had predominantly spherical forms with a mean diameter of 38.92 µm. This work confirms the important role of microencapsulation in developing plant extracts with retained biological functionalities.*

Keywords: *chitosan;* Cosmos caudatus *Kunth; microencapsulation; spray-drying*

INTRODUCTION

Diabetes mellitus (DM) is a metabolism disorder caused by increased blood sugar levels due to a lack of insulin or insulin resistance [1]. Diabetes can cause various complications, both acute and chronic, if not adequately controlled. Data from the World Health Organization (WHO) shows that 8.5% of adults aged 18 years and over were suffering from diabetes in 2014. In 2016, diabetes was the direct cause of 1.6 million deaths; and in 2012, high blood glucose was the cause of 2.2 million other deaths [2]. Diabetes mellitus generally can be classified into DM type 1 and DM type 2 [3].

The present treatment of diabetes mellitus is focused on controlling and lowering the blood glucose levels to a normal level. However, most modern drugs have many side effects causing some serious medical problems during treatment. In addition, mild to severe adverse effects have been reported for some chemical-based drugs [4-5]. For example, metformin has been reported to have a few side effects, including gastrointestinal symptoms, nausea, and vomiting [6]. In addition to modern therapies, traditional medicines have been used for a long time and play an important role as alternative medicines [7-8]. According to the WHO (world health organization), a plant-based traditional system of medicine is still the dominant support of about 75–80% of the world's population, mainly in developing countries having a variety of plants [9].

Cosmos caudatus Kunth is an edible plant that is commonly used as an additive and flavor enhancer [10-11]. This plant contains bioactive compounds, including phenolic compounds, flavonoids, flavanones,

polyphenols, saponins, tannins, alkaloids, and essential oils [12]. The flavonoids contained in *C. caudatus* K. leaves, such as myricetin, quercetin, kaempferol, luteolin, and apigenin, have been proposed to have anti-diabetic activity [10].

The stability of natural bioactive compounds, *i.e.,* preservation of their functional properties, could be improved using encapsulation techniques, such as spray drying, spray cooling, coacervation, extrusion, and polymerization [13]. Microencapsulation is a technique that can be used to control a drug or bioactive compound release [14]. In addition, this technique also increases the absorption of active substances when they enter the human body, maximizing the functions of active substances [14]. A microencapsulation delivery system is described as the formulation of a particle dispersed at diameters ranging from 1 to 1000 μm [13,15]. Microencapsulation is increasingly in demand in controlled release because it is relatively at ease in the delivery system. The use of this technique, among others, is to control the release of active compounds from medicinal ingredients; thus, the active compounds are protected from their environment or unwanted effects such as the influence of light, humidity, and oxygen [14-15].

In the food industry, spray drying is one of the oldest and most widespread drying technologies used for microencapsulation of natural products because of its flexibility, good quality powder particles, rapid solubility of the capsules, and affordability [15-16]. In a spray drying process, the encapsulation structures are comprised of two components, the core (bioactive compounds) and the wall materials. The bioactive materials are dissolved in a polymer solution and subsequently atomized into a hot chamber, resulting in the rapid removal of the solvent [9]. The wall material used in this study is chitosan.

Chitosan is one of the natural biodegradable groups of polymers that have been extensively used for microencapsulation [17]. This natural polysaccharide has many pharmaceutical applications, such as oral and parenteral delivery of drugs. As a natural product, chitosan is a renewable pharmaceutic adjunct with good biocompatibility [18-19]. One of the methods used in the preparation of spray-drying microencapsulation is ionic gelation. The benefits of ionic gelation when using chitosan as wall materials include simple procedures, flexibility to produce particles in a wide range of sizes, and more stable particles in suspension [20-21]. The principle of ionic gelation is the electrostatic interaction between the amine groups on the positively charged biopolymer, i.e., chitosan that binds to the negatively charged polyanions cross-linker [22].

In the manufacture of chitosan-*C. caudatus* K. microcapsules, polyanions cross-linker are needed. The addition of sodium tripolyphosphate (Na-TPP) in the manufacture of chitosan microcapsules strengthens chitosan matrices [17]. Chitosan mechanical properties were improved by chitosan cross-linking with Na-TPP [22]. The preparation of microcapsules is influenced by several factors, including pH, chitosan concentration, and stirring time [23-25]. Chitosan dissolves easily in weak acid solution; hence, selecting the correct pH will produce the finest microcapsules. The concentration of coating material dramatically affects the particle size and the efficiency of the microencapsulation. The stirring time also influences the shapes and sizes of the microcapsules produced [26].

One method to determine the anti-diabetic activity of the natural product is by in vitro analysis, by investigating the inhibitory activity against alpha-amylase enzyme [27]. The inhibition of the enzyme involved in the hydrolyzing carbohydrates such as alpha-amylase is significant for lessening hyperglycemia [28]. In humans, alpha-amylase is an important enzyme that hydrolyzes the alpha glycosidic bonds, alpha-linked polysaccharides, like starch and glycogen, producing glucose and maltose [29]. The inhibition of alpha-amylase has reduced glucose absorption into the blood by postponing the digestion of carbohydrates. Therefore, this work aimed to study the encapsulation process of *C. caudatus* K. extracts by spray drying, using chitosan-Na-TPP as wall materials, proposing to assess concurrently the effect of pH, the concentration of wall materials, and stirring time. The determination of the alpha-amylase activity in each condition on

microcapsules preparations is designed to examine that the bioactive compounds can be released from the microcapsules. As a result, have biological activity as an alpha-amylase inhibitor.

■ EXPERIMENTAL SECTION

Materials

The research materials used were purchased from Merck: soluble starch (from potato, ACS grade), 3,5-dinitrosalicylic acid (DNS) reagent (≥ 98%, HPLC grade), acarbose (≥ 95%), glacial acetic acid (pharmaceutical primary standard), alpha-amylase from *Aspergillus* oryzae (≥ 150 units/mg protein), chitosan (low molecular weight, 50,000–190,000 Da), sodium tripolyphosphate (Na-TPP, technical grade, 85%), D-(+) glucose (analytical standard). The *C. caudatus* K. leaves powder was obtained from UPT (*Unit Pelaksana Teknis*) Materia Medica Batu, East Java, accompanied with a determination letter of species.

Instrumentation

Instruments used in this study were an FTIR spectrometer from Shimadzu Prestige 21 and a Shimadzu UV-Vis spectrophotometer. The size and distribution of the microcapsules particles were determined using a CILAS 1090 PSA. The shape and morphology of microcapsules were observed using an SEM TM 3000 Hitachi, with 5000× magnification.

Procedure

Extract preparation

Cosmos caudatus K. leaves powder was extracted using the maceration technique, with ethyl alcohol, in the volume of 4× dried weight, for 3 × 24 h. The resulted extracts were collected through filtration, and a rotary evaporator vacuum was used with a slow speed at 110 rpm, at 70 °C to obtain the concentrated extracts. The concentrated extracts were kept at 4 °C for subsequent analysis.

Microencapsulation procedures

The *C. caudatus* K. extract (0.5 g) was dissolved with 17.5 mL of distilled water. Then, 50 mL of 1% chitosan solution (w/v) in 2% acetic acid (v/v, pH variations of 4, 5, and 6) were added slowly to the extracts solution and stirred with a magnetic stirrer for 60 min at a speed of 500 rpm. After that, 175 mL of 0.3% Na-TPP solution (w/v) was added slowly and stirred again with a magnetic stirrer for 60 min. The colloid microcapsules in chitosan and Na-TPP were then dried using a spray dryer with an inlet temperature of 105 °C, an outlet temperature of 85 °C, and an air pressure of 1 bar. The process was repeated under the influence of different concentration of chitosan solution at: 0.05%; 0.1%, and 0.2% (w/v). The initial pH contributing to the optimum inhibition of alpha-amylase activity was used, whereas other conditions were the same. Finally, the effect of stirring time was determined by repeating the process using different stirring times at 30, 60, and 90 min. The optimum conditions were determined based on the activity of microcapsules as inhibitors for the alpha-amylase enzyme, indicated by the lowest value of IC_{50}.

Alpha-amylase inhibition assay

All samples (extracts, microcapsules, or acarbose) were prepared in various concentrations (10 to 100 µg/mL for *C. caudatus* K. extracts, 10 to 200 µg/mL for microcapsules, and 1–10 µg/mL for acarbose). Next, 250 µL of samples were added to 250 µL of the alpha-amylase enzyme solution (10 U/mL). The mixture was incubated for 10 min at 25 °C. Then, 250 µL of 1% soluble starch solution (w/v) was added to the mixture and incubated for 25 °C for another 10 min. Finally, 500 µL of DNS reagent was added, and all the mixture was incubated in boiling water for 5 min until the color of the solution changed to brownish red. The solution was cooled under running water. The solution mixture was diluted with 5 mL of distilled water, and the absorbance was measured at 490 nm using a UV-Vis spectrophotometer. Experiments were conducted in triplicates. Percentage of inhibition activity of the alpha-amylase enzyme was calculated using the following equation:

$$\text{Percentage of enzyme inhibition} = \frac{\text{Absorbance control} - \text{Absorbance sample}}{\text{Absorbance control}} \times 100\%$$

The IC_{50} value was calculated to determine the 50% inhibitory capacity of the reaction at a certain concentration.

Data analysis

Results were expressed as mean ± standard error of the mean. Statistical analyses were conducted using Statistical Package for The Social Science (SPSS) v.16 software. The one-way analysis of variance (ANOVA) followed by Tukey's HSD test was used to determine the real difference from each variation. The differences at $p<0.05$ were considered statistically significant.

■ RESULTS AND DISCUSSION

In this study, the spray drying process was used to produce microcapsules from *C. caudatus* K. extract. This process is the most common drying method used to prepare microparticles based on chitosan. The addition of cross-linking agents like Na-TPP improves the biocompatibility and performance of drugs [22]. In the microcapsules' formulation, various aspects, including pH, the concentration of the core material, or stirring time, play a role in the microcapsules' properties. The optimal conditions were chosen based on the biological activity of microcapsules acting as alpha-amylase inhibitors, indicated by the smallest number of IC_{50}.

The inhibitory activity test of the alpha-amylase enzyme was conducted first to the *C. caudatus* K. extract and acarbose. Results are shown in Fig. 1 and Table 1.

The *C. caudatus* K. extract had an IC_{50} value of 73.07 ± 0.39 μg/mL against alpha-amylase, whereas acarbose as a reference had a lower IC_{50} value of 4.83 ± 0.08 μg/mL. These results are understandable since acarbose is a known oral anti-hyperglycemic drug acting as alpha-amylase competitive inhibitor [30]. Furthermore, the *C. caudatus* K. extracts contain a mixture of various secondary metabolites [12], and not all these compounds have activity as an inhibitor for alpha-amylase. Compounds that are active as alpha-amylase inhibitors are phenolic compounds. They can bind covalently to alpha-amylase and alter their activity due to the ability to form quinones or lactones that react with nucleophilic groups on the active sites in the enzyme [27,31].

The inhibitory activity assay of the alpha-amylase enzyme against the microcapsules of *C. caudatus* K. extract in different pH variations, chitosan concentrations, and stirring times are presented in Fig. 2 and Table 2. The IC_{50} values obtained in the microcapsules with pH variations of 4, 5, and 6 were 132.22 ± 0.30, 150.40 ± 0.77, and 169.84 ± 0.77 μg/mL, respectively (Table 2). From these, the increase in pH will increase the IC_{50} value, which means that the inhibitory activity for the microcapsules against alpha-amylase enzyme was lower than those in the non-encapsulated *C. caudatus* K. extracts. These may be caused by the bioactive compounds contained in the microcapsules that cannot be released thoroughly and some retained in the microcapsules.

Nevertheless, microcapsules of the *C. caudatus* K are still active as an inhibitor for alpha-amylase. Microencapsulation's main purpose is not to increase biological activity but to protect and control the release of the active compounds [14-15]. Therefore, microcapsules

Table 1. The IC_{50} of the *C. caudatus* K. extract and acarbose on alpha-amylase inhibition

Sample	IC_{50} (μg/mL)*
C. caudatus Kunth extracts	73.07 ± 0.39[b]
Acarbose	4.83 ± 0.08[a]

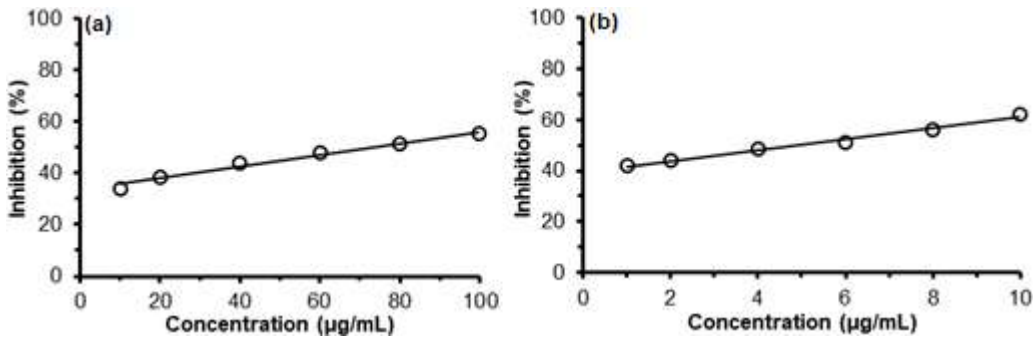

Fig 1. The inhibitory potency of (a) *C. caudatus* K. extracts; (b) acarbose, against alpha-amylase activity

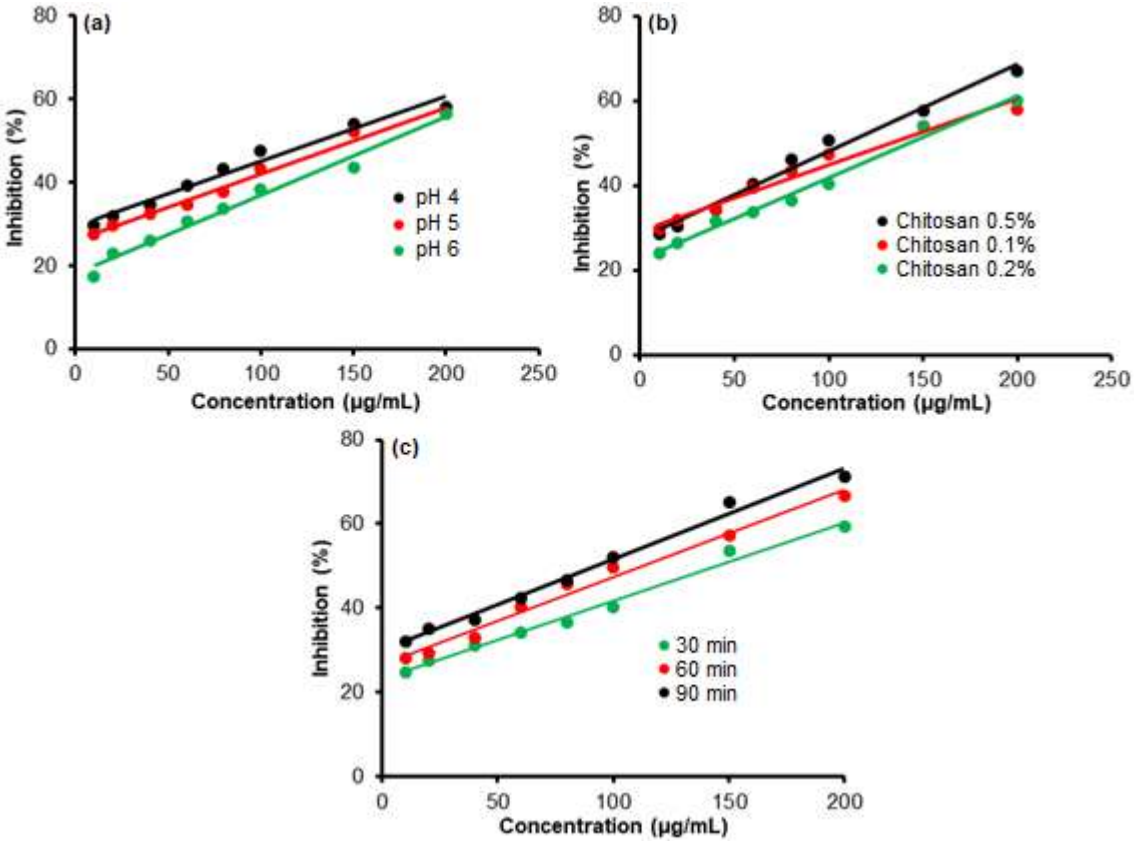

Fig 2. The inhibitory potency of microcapsules of *C. caudatus* K. prepared in (a) different pHs; (b) different chitosan concentrations (w/v); and (c) different stirring times against alpha-amylase activity

Table 2. The IC_{50} values of microcapsules of *C. caudatus* K. with pH, chitosan concentration, and stirring time variations

Sample	IC_{50} (µg/mL)*	Sample	IC_{50} (µg/mL)*	Sample	IC_{50} (µg/mL)*
Microcapsules pH 4	132.22 ± 0.30[a]	Microcapsules with 0.05% (w/v) chitosan	109.88 ± 0.46[a]	Microcapsules with 30 min stirring time	144.70 ± 2.15[c]
Microcapsules pH 5	150.40 ± 0.77b	Microcapsules with 0.1% (w/v) chitosan	132.22 ± 0.30[b]	Microcapsules with 60 min stirring time	112.37 ± 2.09[b]
Microcapsules pH 6	169.84 ± 0.48[c]	Microcapsules with 0.2% (w/v) chitosan	142.96 ± 0.86[c]	Microcapsules with 90 min stirring time	92.85 ± 1.2[a]

prepared in pH 4 were the optimum conditions with the lowest IC_{50} toward alpha-amylase enzyme.

The increase in pH increases the IC_{50} value. It means that the inhibitory activity of the alpha-amylase decreased. Microcapsules prepared in pH 4 resulted in the highest inhibitory activity for the enzyme. The protonation process in an acid environment to neutral solution occurs due to the pKa value of the amino group in chitosan (~6.5) [32]. An increase in solubility of chitosan can be made despite the protonation of the amino group in an acidic solution. The practice of this property has great importance on biomedical applications when chitosan is used to deliver drugs to acidic environment targets. In pH 4, chitosan received more proton donors; as a result, more amine groups (NH_2) will be protonated to NH_3^+ ions which will ionically cross-link with $P_3O_{10}^{5-}$ ions from Na-TPP, forming microcapsules. A large number of protonated chitosan will further increase chitosan's ability to absorb the bioactive compounds from the extracts; and, as a

result, increase the inhibitory activity for the alpha-amylase enzyme. A large number of protonated chitosan will further increase chitosan's ability to absorb the bioactive compounds from the extracts and increase the alpha-amylase enzyme's inhibitory activity.

This observation was similar to a previous report that demonstrated pH 4 was the most effective pH for designing chitosan-containing microparticles [32]. At pH 4, biopolymers' charge densities of opposing signs were stoichiometrically balanced. If the pH was too low, the ionization degree of amine groups on the chitosan molecular chain did not assist the formation of a homogeneous particle in the system. When pH values were higher than 4, both ionization degree and solubility of chitosan reduced, which perhaps stimulated the discrepancy in size distribution [33].

The resulting IC_{50} values on the microcapsules with a variation of the chitosan concentration of 0.05%, 0.1%, and 0.2% (w/v) were 109.88 ± 0.46, 132.22 ± 0.30, and 142.96 ± 0.86 μg/mL, respectively. Increasing the chitosan concentration will increase the IC_{50} value, which means that the alpha-amylase inhibitory activity decreases. Microcapsules with the lowest chitosan concentration of 0.05% (w/v) resulted in the optimal inhibitory activity since this concentration had the lowest IC_{50} value.

The higher the concentration of chitosan, the inhibitory activity of the microcapsules about the alpha-amylase enzyme decreases. The optimum microcapsule condition was obtained at the lowest chitosan concentration of 0.05% (w/v), resulting in the best inhibitory activity seen from the lowest IC_{50} number. The greater the amount of chitosan, the more ammonium ions from chitosan can bind to the extract compounds; therefore, microcapsules provide the best inhibitory activity against the alpha-amylase. The higher the chitosan concentration, the smaller the space between the pores, preventing the active ingredients from diffusing from the microcapsules [34-35]. Previous research showed similar results [34]; optimal chitosan concentration in limonene essential oil microencapsulated in chitosan was not the highest concentration used.

The longer the stirring time to prepare microcapsules, the lower the IC_{50} values obtained. Microcapsules prepared in 30, 60, and 90 min stirring time had IC_{50} of 144.70 ± 2.15, 112.37 ± 2.09, and 92.85 ± 1.2 μg/mL, respectively. The longer the stirring time, the more homogeneous and the coating process on the microcapsules increases. The longer the stirring process, the longer it takes to break the particles into smaller pieces and have a longer dispersion of particles aggregates [26]. In this study, microcapsules with a stirring time of 90 min resulted in the highest inhibitory activity toward the alpha-amylase enzyme. This result agreed with an earlier study that increasing stirring time and stirring speed had better distribution and better structures of microparticles [23].

Fig. 3 displays the FTIR results of the Na-TPP, chitosan, *C. caudatus* K. extracts, and the microcapsules of the *C. caudatus* K extracts, and the assignment of the peaks of interest is tabulated in Table 3. All FTIR spectra, except for Na-TPP, exhibit a strong and broad antisymmetric band at about 3500–3400 cm^{-1} that results from overlapping of the O–H and N–H stretching vibrations of functional groups engaged in hydrogen bonds (peak 1). The Na-TPP FTIR spectrum showed their characteristic bands at the region of 1250–1150 cm^{-1} (peak 5) related to the phosphate group (P=O) and 980–960 cm^{-1} from symmetric and antisymmetric stretching vibrations in the PO_3 group (peak 6). The spectrum of chitosan exhibits characteristic absorption bands at 1650–1600 cm^{-1} (peak 2, C=O stretching in amide group, amide I vibration) and 1360–1150 cm^{-1} (peak 5, N–H bending in amide group, amide II vibration). The FTIR spectrum of *C. caudatus* K extracts shows that the extracts' secondary metabolites compounds were mostly flavonoid compounds [38-39]. These were deduced from the characteristic peaks seen in the spectra numbered 1 to 5. Number 1 to 5 peaks were as follows: 3500–3400 cm^{-1}; 3000–2850 cm^{-1}; 1650–1600 cm^{-1}; 1440–1430 cm^{-1}; and 1360–1250 cm^{-1}. Those peaks were identified as alcohol O–H stretching (peak 1), C–H alkanes (peak 2), C-H alkanes and C=C aromatics (peaks 3 and 4), and C-H alkanes from the

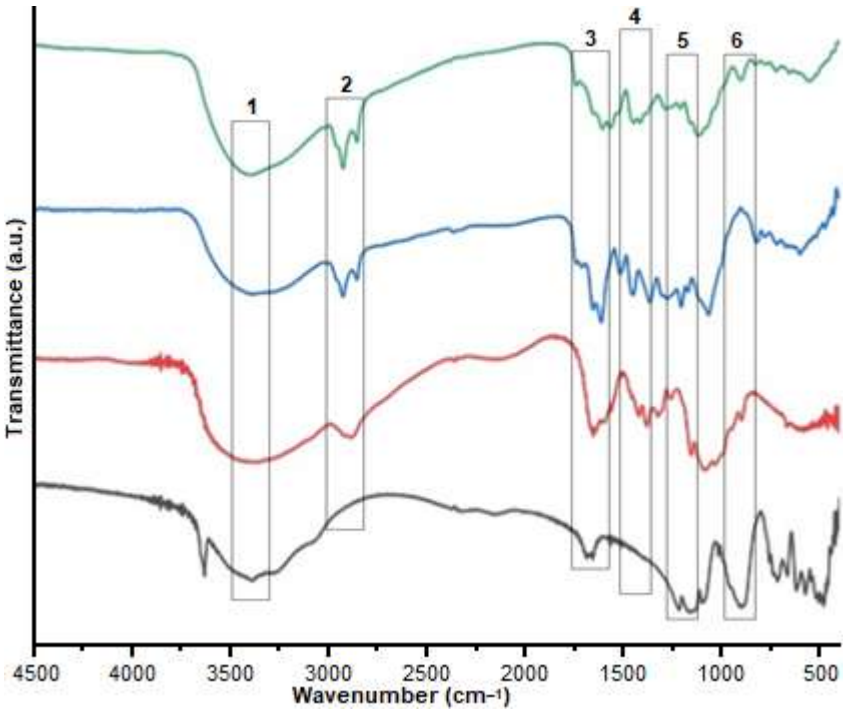

Fig 3. FTIR spectra of: (a) Na-TPP; (b) chitosan; (c) *C. caudatus* K. extract; and (d) microcapsules of *C. caudatus* K. extract

Table 3. Assignment of the FTIR spectra from Fig. 3

Peak number	Na-TPP [36-37]	Chitosan [36-37]	*C. caudatus* K. extract [38-39]	Microcapsules of *C. caudatus* K. extract [35-39]
1	3500–3400 cm^{-1} for O–H alcohol	3500–3400 cm^{-1} for O–H alcohol	3500–3400 cm^{-1} for O–H alcohol	3500–3400 cm^{-1} for O–H alcohol
2	(undetected)	3000–2900 cm^{-1} for C–H alkanes	3000–2850 cm^{-1} for C–H alkanes	2970–2850 cm^{-1} for C–C alkanes
3	(undetected)	1650–1600 cm^{-1} for C–H alkanes and C=C aromatics	1650–1600 cm^{-1} for C–H alkanes and C=C aromatics	1600–1650 cm^{-1} for C–H alkanes and C=C aromatics
4	(undetected)	1440–1430 cm^{-1} for C–H alkanes and C=C aromatics	1440–1430 cm^{-1} for C–H alkanes and C=C aromatics	1440–1430 cm^{-1} for C–H alkanes and C=C aromatics
5	1250–1150 cm^{-1} for P=O stretching	1360–1150 cm^{-1} for C–N stretching	1360–1250 cm^{-1} for C–H alkanes	1360–1150 cm^{-1} for C–N stretching
6	980–960 cm^{-1} for P–O stretching in PO_3 group	(undetected)	(undetected)	980–960 cm^{-1} for P–O stretching in PO_3 group

aromatics nucleus (peak 5).

The FTIR spectra of the extracts and microcapsules of *C. caudatus* K. exhibit some similarities with some distinct features in the spectrum of microcapsules. The similarities indicate that microcapsules were loaded with the bioactive compounds from the *C. caudatus* K. extracts, whereas the differences propose that the microencapsulation is conducted successfully. As shown in Fig. 3, a new absorption peak in the microcapsules spectrum at 1360–1150 cm^{-1} indicates a C–N functional group from amines, which may derive from chitosan as coating materials microcapsules. In addition, in the microcapsules spectrum, new absorption also appeared at a wavenumber of 980–960 cm^{-1}, suggesting a P=O functional group that possibly originated from Na-TPP used as a cross-linker agent in microencapsulation.

The obtained microparticles were then characterized with their size and surface structure. Particles size distribution analysis can be useful to analyze the microparticles' properties and deduce their stability. The mean average size of the particles was 38.92 µm, as shown in Fig. 4. Considering the SEM images (Fig. 5), the microcapsules formulated in optimum conditions, pH 4, 0.05% (w/v) chitosan concentration, and 90 min stirring time present more spherical and regular shapes than the morphological shapes of the *C. caudatus* K. extract, even though the surface of the microcapsules was partially rough. In this work, the sizes and the microcapsules surfaces containing *C. caudatus* K. extracts appear similar to those of the common microparticles. Other authors obtained similar results that displayed small and spherical microparticles with some variabilities and roughness from the spray drying process [16-17,19]. Nonetheless, the microcapsules product was already in the range of microparticles sizes, with a mean diameter of 38.92 µm.

The optimal IC_{50} value from all optimal pH, chitosan concentration, and stirring time was 92.85 ± 1.2 µm. This number is comparable with the IC_{50} value of *C. caudatus* K. extract with the IC_{50} of 73.07 ± 0.39 µm. Therefore, *C. caudatus* K. extract's microcapsules also have a high capacity for alpha-amylase enzyme inhibitors.

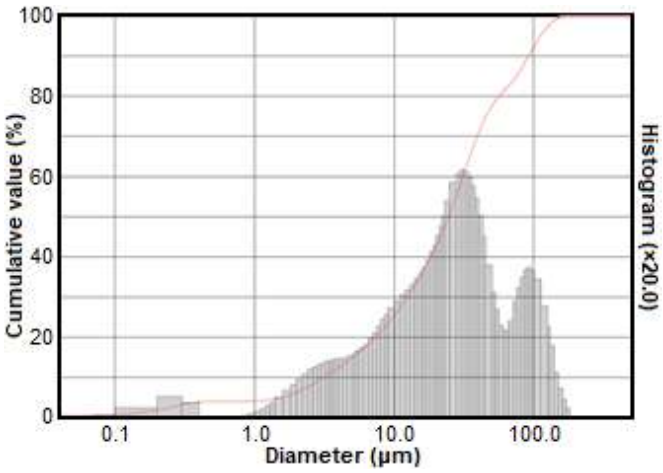

Fig 4. Particle size distribution from microcapsules of *C. caudatus* K. extracts prepared in pH 4, 0.05% (w/v) chitosan concentration, and 90 min stirring time. The mean diameter was 38.92 µm

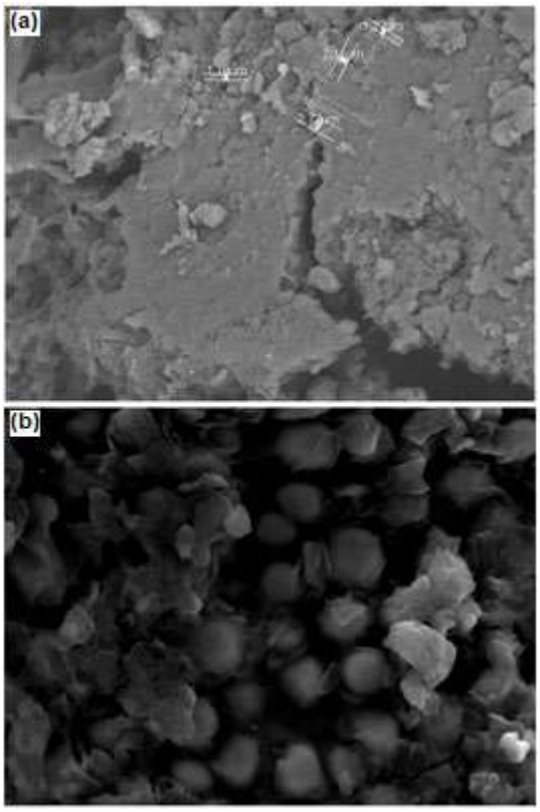

Fig 5. SEM images of the (a) *C. caudatus* K. extracts; microcapsules of *C. caudatus* K. extracts prepared in pH 4, 0.05% (w/v) chitosan, and 90 min stirring time. The magnification was 5000×

■ CONCLUSION

This study has successfully developed microencapsulation of *C. caudatus* K. extracts under variation of pH, chitosan concentration, and stirring time; and determined theirs in vitro biological activity. The activity of microencapsulated *C. caudatus* K. extracts increased by increasing stirring time and chitosan concentration and decreasing pH. The microencapsulated products resulted in high in vitro alpha-amylase inhibition with the IC_{50} value of 92.85 ± 1.2 µg/mL. The FTIR analysis showed that cross-linking was developed between chitosan and Na-TPP. The morphological analysis by SEM indicated that the surface of encapsulated extracts was rough and mostly spherical; nevertheless, PSA analysis showed that the micro-sized particles were achieved at a mean diameter of 38.92 µm.

The obtained results suggest that microencapsulation of *C. caudatus* K. extracts allow a new approach in utilizing bioactive compounds from plant nutraceuticals.

ACKNOWLEDGMENTS

The financial aid for this study was provided by Hibah Doktor Grant, Brawijaya University, Indonesia, in the year 2021, grant number 1612/UN10.F09/PN/2021.

AUTHOR CONTRIBUTIONS

EH and SAD conducted the experiment, AS and AR conducted the analysis, wrote, and revised the manuscript. All authors agreed to the final version of this manuscript.

REFERENCES

[1] Zimmet, P.Z., 2017, Diabetes and its drivers: the largest epidemic in human history?, *Clin. Diabetes Endocrinol.*, 3 (1), 1.

[2] Zimmet, P.Z., Alberti, K.G., Magliano, D.J., and Bennet, P.H., 2016, Diabetes mellitus statistics on prevalence and mortality: Facts and fallacies, *Nat. Rev. Endocrinol.*, 12 (10), 616–622.

[3] Kerner, W. and Brückel, J., 2014, Definition, classification and diagnosis of diabetes mellitus, *Exp. Clin. Endocrinol. Diabetes*, 122 (7), 384–386.

[4] Filippatos, T.D., Panagiotopoulou, T.V., and Elisaf, M.S., 2014, Adverse effects of GLP-1 receptor agonists, *Rev. Diabet. Stud.*, 11 (3-4), 202–230.

[5] Nesti, L. and Natali, A., 2017, Metformin effects on the heart and the cardiovascular system: A review of experimental and clinical data, *Nutr., Metab. Cardiovasc. Dis.*, 27 (8), 657–669.

[6] Wang, Y.W., He, S.J., Feng, X., Cheng, J., Luo, Y.T., Tian, L., Huang, Q., 2017, Metformin: a review of its potential indications, *Drug Des., Dev. Ther.*, 11, 2421–2429.

[7] Safitri, A., Srihardyastutie, A., Roosdiana, A., Aulanni'am, A., and Octaviana, E.N.L., 2019, Effects of root extract of Ruellia tuberosa L. on kidneys of diabetic rats, *J. Math. Fundam. Sci.*, 51 (2), 127–137.

[8] Roosdiana, A., Permata, F.S., Fitriani, R.I., Umam, K., and Safitri, A., 2020, *Ruellia tuberosa* L. extract improves histopathology and lowers malondialdehyde levels and TNF alpha expression in the kidney of streptozotocin-induced diabetic rats, *Vet. Med. Int.*, 2020, 8812758.

[9] Siahaan, P., Mentari, N.C., Wiedyanto, U.O., Hudiyanti, D., Hildayani, S.Z., and Laksitorini, M.D., 2017, The optimum conditions of carboxymethyl chitosan synthesis on drug delivery application and its release of kinetics study, *Indones. J. Chem.*, 17 (2), 291–300.

[10] Bunawan, H., Baharum, S.N., Bunawan, S.N., Mat Amin, N., and Noor, N.M., 2014, *Cosmos caudatus* Kunth: A traditional medicinal herb, *Global J. Pharmacol.*, 8 (3), 420–426.

[11] Abdullah, A., Dhaliwal, K.K., Roslan, N.N.F., Lee, C.H., Kalaiselvam, M., Radman, H.M., Haji Mohd Saad, Q., Yusof, K., and Jaarin, K., 2015, The effects of *Cosmos caudatus* (ulam raja) on detoxifying enzymes in extrahepatic organs in mice, *J. Appl. Pharm. Sci.*, 5 (1), 82–88.

[12] Safitri, A., Putri, A.S., Octavianty, T.D., and Sari, D.R.T., 2020, Metabolomic profiles of *Curcuma longa* L and *Cosmos caudatus* extracts and their in-silico anti-cancer activity, *J. Phys.: Conf. Ser.*, 1665, 012022.

[13] Chen, L., Gnanaraj, C., Arulselvan, P., El-Seedi, H., and Teng, H., 2019, A review on advanced microencapsulation technology to enhance bioavailability of phenolic compounds: Based on its activity in the treatment of type 2 diabetes, *Trends Food Sci. Technol.*, 85, 149–162.

[14] Suratman, A., Purwaningsih, D.R., Kunarti, E.S., and Kuncaka, A., 2020, Controlled release fertilizer encapsulated by glutaraldehyde-crosslinked chitosan using freeze-drying method, *Indones. J. Chem.*, 20 (6), 1414–1421.

[15] Ćujić-Nikolić, N., Stanisavljević, N., Šavikin, K., Kalušević, A., Nedović, V., Samardžić, J., and Janković, T., 2019, Chokeberry polyphenols preservation using spray drying: Effect of encapsulation using maltodextrin and skimmed milk on their recovery following *in vitro* digestion, *J. Microencapsulation*, 36 (8), 693–703.

[16] Lucas, J., Ralaivao, M., Estevinho, B.N., and Rocha, F., 2020, A new approach for the microencapsulation of curcumin by a spray drying method, in order to

value food products, *Powder Technol.*, 362, 428–435.

[17] Lestari, A.D.N, Siswanta, D., Martien, R., and Mudasir, M., 2020, Synthesis, characterization, and stability evaluation of β-carotene encapsulated in starch-chitosan/tripolyphosphate matrices, *Indones. J. Chem.*, 20 (4), 929–940.

[18] Abdelkader, H., Hussain, S.A., Abdullah, N., and Kmaruddin, S., 2018, Review on micro-encapsulation with chitosan for pharmaceuticals applications, *MOJ Curr. Res. Rev.*, 1 (2), 77–84.

[19] Jayanudin, J, Fahrurrozi, M., Wirawan, S.K., and Rochmadi, R., 2019, Preparation of chitosan microcapsules containing red ginger oleoresin using emulsion crosslinking method, *J. Appl. Biomater. Funct. Mater.*, 17 (1), 1–9.

[20] Sacco, P., Paoletti, S., Cok, M., Asaro, F., Abrami, M., Grassi, M., and Donati, I., 2016, Insight into the ionotropic gelation of chitosan using tripolyphosphate and pyrophosphate as cross-linkers, *Int. J. Biol. Macromol.*, 92, 476–483.

[21] Sacco, P., Pedroso-Santana, S., Kumar, Y., Joly, N., Martin, P., and Bocchetta, P., 2021, Ionotropic gelation of chitosan flat structures and potential applications, *Molecules*, 26 (3), 660.

[22] Goh, C.Y., Lim, S.S., Tshai, K.Y., El Azab, A.W.Z.Z., and Loh, H. S., 2019, Fabrication and in vitro biocompatibility of sodium tripolyphosphate-crosslinked chitosan–hydroxyapatite scaffolds for bone regeneration, *J. Mater. Sci.*, 54 (4), 3403–3420.

[23] Ang, L.F., Darwis, Y., Por, L.Y., and Yam, M.F., 2019, Microencapsulation curcuminoids for effective delivery in pharmaceutical application, *Pharmaceutics*, 11 (9), 451.

[24] Singh, M.N., Hemant, K.S.Y., Ram, M., and Shivakumar, H.G., 2010, Microencapsulation: A promising technique for controlled drug delivery, *Res. Pharm. Sci.*, 5 (2), 65–77.

[25] Özkan, G. and Bilek, S.E., 2014, Microencapsulation of natural food colourants, *Int. J. Nutr. Food Sci.*, 3 (3), 145–156.

[26] Kashif, P.M., Madni, A., Ashfaq, M., Rehman, M., Mahmood, M.A., Khan, M.I., and Tahir, N., 2017, Development of Eudragit RS 100 microparticles loaded with ropinirole: Optimization and *in vitro* evaluation studies, *AAPS PharmSciTech*, 18 (5), 1810–1822.

[27] Oyedemi, S.O., Oyedemi, B.O., Ijeh, I.I., Ohanyerem, P.E., Coopoosamy, R.M., and Aiyegoro, O.A., 2017, Alpha-amylase inhibition and antioxidative capacity of some anti-diabetic plants used by the traditional healers in Southeastern Nigeria, *Sci. World J.*, 2017, 3592491.

[28] Safitri, A., Fatchiyah, F., Sari, D.R.T., and Roosdiana, 2020, Phytochemical screening, *in vitro* anti-oxidant activity, and *in silico* anti-diabetic activity of aqueous extracts of *Ruellia tuberosa* L, *J. Appl. Pharm. Sci.*, 10 (3), 101–108.

[29] Prasad, B.J., Sharavanan, P.S., and Sivaraj, R., 2019, Efficiency of *Oryza punctata* extract on glucose regulation: Inhibition of α-amylase and α-glucosidase activities, *Grain Oil Sci. Technol.*, 2 (2), 44–48.

[30] DiNicolantonio, J.J., Bhutani, J., and O'Keefe, J.H., 2015, Acarbose: Safe and effective for lowering postprandial hyperglycaemia and improving cardiovascular outcomes, *Open Heart*, 2 (1), e000327.

[31] Oyedemi, S., Koekemoer, T., Bradley, G., Van De Venter, M., and Afolayan, A., 2013, In vitro anti-hyperglycemia properties of the aqueous stem bark extract from *Strychnos henningsii* (Gilg), *Int. J. Diabetes Dev. Countries*, 33 (2), 120–127.

[32] Tan, C., Xie, J., Zhang, X., Cai, J., and Xia, S., 2016, Polysaccharide-based nanoparticles by chitosan and gum Arabic polyelectrolyte complexation as carriers for curcumin, *Food Hydrocolloids*, 57, 236–245.

[33] Sharpe, L.A., Vela Ramirez, J.E., Haddadin, O.M., Ross, K.A., Narasimhan, B., and Peppas, N.A., 2018, pH-Responsive microencapsulation systems for the oral delivery of polyanhydride nanoparticles, *Biomacromolecules*, 19 (3), 793–802.

[34] Suzery, M., Hadiyanto, Majid, D., Setyawan, D., and Sutanto, H., 2017, Improvement of stability and antioxidant activities by using phycocyanin-chitosan encapsulation technique, *IOP Conf. Ser.: Earth Environ. Sci.*, 55, 012052.

[35] Souza, J.M., Caldas, A.L., Tohidi, S.D., Molina, J., Souto, A.P., Fangueiro, R., Zille, A., 2014, Properties and controlled release of chitosan microencapsulated limonene oil, *Rev. Bras. Farmacogn.*, 24 (6), 691–698.

[36] Gierszewska-Drużyńska, M., and Ostrowska-Czubenko, J., 2010, The effect of ionic crosslinking on thermal properties of hydrogel chitosan membrane, *Prog. Chem. Appl. Chitin Its Deriv.*, 15, 25–32.

[37] Azevedo, J.R., Sizilio, R.H., Brito, M.B., Costa, A.M.B., Serafini, M.R., Araujo, A.A.S., Santos, M.R.V., Lira, A.A.M., and Nunes, R.S., 2011, Physical and chemical characterization insulin-loaded chitosan-TPP nanoparticles, *J. Therm. Anal. Calorim.*, 106, 685–689.

[38] Kartini K., Putri, L.A.D., and Hadiyat, M.A., 2020, FTIR-based fingerprinting and discriminant analysis of *Apium graveolens* from different locations, *J. Appl. Pharm. Sci.*, 10 (12), 62–67.

[39] Patle, T.K., Shrivas, K., Kurrey, R., Upadhyay, S., Jangde, R., and Chauhan, R., 2020. Phytochemical screening and determination of phenolics and flavonoids in *Dillenia pentagyna* using UV–vis and FTIR spectroscopy, *Spectrochim. Acta, Part A*, 242, 118717.

Synthesis, Structural Analysis and Thermal Behavior of New 1,2,4-Triazole Derivative and Its Transition Metal Complexes

Ali Talib Bader[1*], Nada Ahmed Rasheed Al-qasii[2], Ahmed Hassen Shntaif[1], Maryam El Marouani[3], Mohammed Idaan Hassan AL Majidi[1,4], László Trif[5], and Mohammed Boulhaoua[4]

[1]*Department of Chemistry, College of Sciences for Woman, University of Babylon, Hilla, Iraq*

[2]*Department of Chemistry, College of Science, University of Baghdad, Baghdad, Iraq*

[3]*Department of Chemistry, College of Sciences, University of Hafr Al Batin, Hafr Al Batin, Kingdom of Saudi Arabia*

[4]*Institute of Chemistry, ELTE Eötvös Loránd University, Pázmány Péter sétány 1/A, H-1117, Budapest, Hungary*

[5]*Institute of Materials and Environmental Chemistry, Research Centre for Natural Sciences, Budapest, Hungary*

* ***Corresponding author:***

tel: +964-7710783571
email: wsc.ali.taleb@uobabylon.edu.iq

Received: September 3, 2021
Accepted: November 3, 2021

DOI: 10.22146/ijc.68859

Abstract: *Cobalt(II), nickel(II), and copper(II) complexes containing bidentate ligands (5-(4-nitrophenyl)-4-((4-phenoxybenzylidene)amino)-4H-1,2,4-triazole-3-thiol) could be synthesized by the condensation reaction between 1,2,4-triazole derivative and p-phenoxy benzaldehyde. The ligand and its complexes were characterized by various spectroscopic techniques such as FTIR, UV-visible, ^{1}H and ^{13}C-NMR, element analysis, molar conductance, and magnetic susceptibility test. The new ligand was exploited as a ligand to coordinate with Co(II), Ni(II), and Cu(II) by a molar ratio of 1:2 (metal:ligand). The prepared complexes (C_1, C_2, and C_3) were exposed to thermo-gravimetric analysis (TGA/DTG) under an inert atmosphere to investigate their thermal stability. The ligand (L) degradation was also investigated as a reference. The results indicated that the complexes proposed structures had an octahedral geometry.*

Keywords: *1,2,4-triazole; Schiff base; thermal analysis; metal complexes*

INTRODUCTION

Heterocyclic compounds are organic molecules that contain a minimum of two different atom types in the ring [1]. Heterocyclic compounds with different donor atoms, like S, N, or O, tend to form metal chelates or coordination compounds utilized as active antibacterial agents [2]. 1,2,4-triazole is one of the most important aromatic heterocyclic nitrogen-rich molecules [3-4]. There is increasing attention to the triazole substructure's potential application as urease and lipase enzyme inhibitors [5]. Linking the triazole moiety to a reasonably selected and different biologically active agent fragment would form new complexes that might have better biological activity because of the synergistic effects [6-7].

Furthermore, these compounds have multiple sites for metal atoms to coordinate with, forming more stable transition metal complexes that are bioactive triazole-based. Recently, significant effort has been devoted to studying the thermal degradation characteristics under inert and oxidative atmospheres. In this work, we determined the first synthesis and characterization of a new Schiff base triazole derivative and its cobalt(II), nickel(II), and copper(II) complexes. Common spectroscopic techniques such as ^{1}H-NMR, ^{13}C-NMR, FTIR, UV–Vis, elemental analysis, and thermal analysis were used to characterize the synthesized compounds. We have examined the thermal degradation profile of the prepared complexes to highlight their energy potential and the far-reaching possibilities of their use.

EXPERIMENTAL SECTION

Materials

The 4-nitro benzoic acid, absolute ethanol, hydrazine hydrate 80%, acetic acid, carbon disulfide,

potassium hydroxide, and 4-phenoxy benzaldehyde were supplied by Sigma-Aldrich (Germany), and the metal salt $CoCl_2{\cdot}6H_2O$, $NiCl_2{\cdot}6H_2O$, and $CuCl_2{\cdot}6H_2O$ were supplied by Fluka (Germany). All chemicals were used without further purification.

Instrumentation

The Nuclear magnetic resonance (NMR) measurements of the synthesized compounds were performed at 500 MHz in DMSO-d6 at 25 °C on Bruker DRX-500 spectrometer using the deuterium signal of the solvent as the lock and tetramethylsilane (TMS) as the internal standard. Varian 2000 (Scimitar Series) FTIR spectrometer with MCT (mercury–cadmium–telluride) detector and single reflection diamond ATR unit (Varian Inc., US) (Specac Ltd, UK) was used to record infrared (IR) spectra. For a single spectrum, 32 individual scans were averaged at a resolution of 4 cm^{-1}, and the instrument's data acquisition software (ResPro 4.0) was used to ATR-correct all the spectra. A PerkinElmer UV/Vis Lambda 35 spectrometer was used to conduct the spectrophotometric measurements by applying acetonitrile as a solvent and a slit width of 1 nm.

Procedure

Synthesizes of ethyl 4-nitrobenzoate

Dropwise additions of H_2SO_4 (3 mL) to a mixture of 5 g (0.025 mol) of 4-nitrobenzoic acid in 50 mL ethanol were heated under reflux for 6 h. The precipitate formed after cooling, and the excess ethanol was evaporated. The solid product was washed with a sodium bicarbonate solution, filtered, rinsed with cold water, dried, and recrystallized from ethanol to yield, as shown in Scheme 1.

Synthesizes of 4-nitrobenzohydrazide

Hydrazine hydrate (80%, 20 mL) was added to a solution of ethyl 4-nitrobenzoate by dissolving (5 g, 0.027 mol) in 50 mL of absolute ethanol, and then the mixture was heated under reflux for 8 h. Finally, the mixture was allowed to cool, and a solid product was filtered, washed with cold water, dried, and recrystallized from ethanol to produce 4-nitrobenzohydrazide, as shown in Scheme 1.

Synthesized of potassium 2-(4-nitrobenzoyl)hydrazine-1-carbodithioate

The 4-nitrobenzohydrazide (4 g, 0.022 mol) was treated at 0 °C with stirring in a solution of 2.5 g (0.044 mol) potassium hydroxide in 40 mL ethanol. Dropwise additions of 7 mL (0.2 mol) carbon disulfide were made to the reaction mixture, agitated overnight at room temperature. The reaction was then cooled with 200 mL diethyl ether, which was agitated for 10 min. The solid result was then filtered, washed with cold ethanol, and dried to yield potassium 2-(4-nitrobenzoyl)hydrazine-1-carbodithioate, as shown in Scheme 1.

Synthesis of 4-amino-5-(4-nitrophenyl)-4H-1,2,4-triazole-3-thiol

The synthesis used a reported procedure in the literatures [8-9]. Potassium 2-(4-nitrobenzoyl)hydrazine-1-carbodithioate (3.5 g, 0.011 mol) was heated under reflux for 6 h in excess of hydrazine hydrate (approximately 30 mL). The color of the lead acetate sheet changed from black to white to release hydrogen sulfide gas by changing the color of the mixture from black-green to light yellow. The chilled mixture was put into 30 mL of ice water and acidified with concentrated hydrochloric acid (pH 2–3). To get 4-amino-5-(4-nitrophenyl)-4*H*-1,2,4-triazole-3-thiol, the precipitate was filtered, rinsed with cold water, dried, and recrystallized from ethanol.

Synthesis of Schiff base (ligand L)

A hot solution of 4-amino-5-(4-nitrophenyl)-4*H*-1,2,4-triazole-3-thiol (0.237 g, 1 mmol) in 15 mL of EtOH was added dropwise to a solution of *p*-phenoxybenzaldehyde (0.198 g, 0.001 mol) in the presence of three drops of glacial acetic acid (AcOH), The reaction mixture was refluxed for 4 h. The resulting yellow compound was filtered and then dried in air to yield the required Schiff base ligand (L) as a yellow solid (yield: 78%, MP: 270−272 °C) (Scheme 1).

Synthesis of metal ions complexes

The complexes (C_1, C_2, C_3) were synthesized as shown in Scheme 1 by adding the hot ethanolic solution of the metal ions ($CoCl_2{\cdot}6H_2O$, $NiCl_2{\cdot}6H_2O$, and $CuCl_2{\cdot}2H_2O$) to the hot ligand (L) (0.834 g, 2 mmol)

ethanolic solution in 1:2 (metal: ligand) molar ratio. The reaction mixture was refluxed for 1 h, and colored precipitates were formed. Then, the obtained complexes were filtered and recrystallized from ethanol. Table 1 shows the number of metal salts in the complexes [10].

■ RESULTS AND DISCUSSION

Table 2 shows the results of metal content determination by atomic absorption, chloride content, CHNS elemental analysis, and the physical features of the ligand and its metal complexes. The suggestion of the molecular formula of the studied compounds was made relying on spectral data, atomic absorption analysis, chloride content, CHNS, and conductivity measurements. Table 2 shows the metal complexes' analytical data. The complexes formation was revealed by these data having a 1:2 (ligand:metal ion) ratio, showing that the Schiff base ligand was a chelating agent.

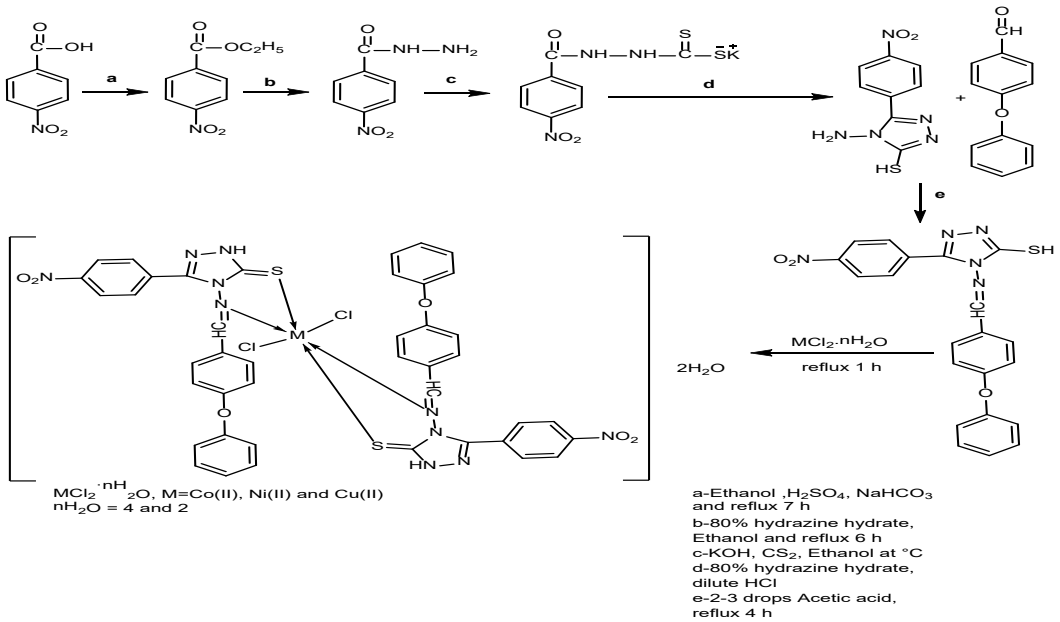

Scheme 1. Synthesis pathway of Schiff base (ligand L) and their metal complex

Table 1. Amount of metal salts in the complexes

Complex symbol	Complexes formal	Metal salts	Weight metal salts (g)
C1	$[Co(L)_2Cl_2]\cdot 2H_2O$	$CoCl_2\cdot 6H_2O$	0.237
C2	$[Ni(L)_2Cl_2]\ 2H_2O$	$NiCl_2\cdot 6H_2O$	0.237
C3	$[Cu(L)_2Cl_2]\ 2H_2O$	$CuCl_2\cdot 2H_2O$	0.170

Table 2. Physical properties and analytical data for synthesized ligand and its metal ion complexes

Product	Color	Yield	Molar mass (g mol)	Micro elemental analysis found (calc.) % C	% H	% N	% S	% Metal content found (calc.)	% Chloride content found (calc.)
(L)	Yellow	70	417.44	59.90 (60.42)	3.44 (3.62)	3.44 (3.62)	7.20 (7.68)	--	--
C_1	Brown	65	998.73	51.90 (52.05)	2.60 (2.91)	2.60 (2.91)	6.02 (6.62)	6.12 (6.75)	6.96 (7.32)
C_2	Green	70	988.73	44.66 (44.87)	3.11 (3.59)	3.11 (3.59)	5.20 (5.70)	7.80 (7.50)	5.97 (6.31)
C_3	Yellow	70	1033	45.01 (45.68)	2.12 (2.56)	2.12 (2.56)	5.81 (5.44)	6.12 (6.33)	6.42 (7.81)

FTIR Spectrometric Analysis

Compared to the spectrum shown in Fig. 1, the FTIR spectra of the ligand (L) showed various alterations of 4-amino-5-(4-nitrophenyl)-4*H*-1,2,4-triazole-3-thiol. At 3160 cm^{-1}, there was a medium intensity band associated with the ν(NH) group. The disappearance of a band at 3890 and 3400 cm^{-1} was due to the stretch of ν(NH_2) (asymmetry and symmetry). The appearance of a new set of sharp stretching vibration bands at the frequency that is identical to the ν(C=N) imine group confirmed the formation of Schiff base at 1568 cm^{-1}, and ν(S–H) appeared as a weak band at 2550 cm^{-1}. In all the complexes, the (C=N) imine group in the ligand (L) was moved to a lower wavenumber, indicating that the (C=N) imine group was coordinated with the metal via the N atom. However, in the spectra of prepared micro complexes, the (C=S) stretching vibration shifted to higher frequencies or appeared as multiple bands with different shapes and reduced intensity. This frequency shift, change in form, and location for the stretching vibrations of the (C=N) imine and (C=S) group showed the coordination of metal ion with (N) atom of imine group and (S) atom of thiol group. Table 3 lists the important stretching vibrations of ligands and their complexes [11].

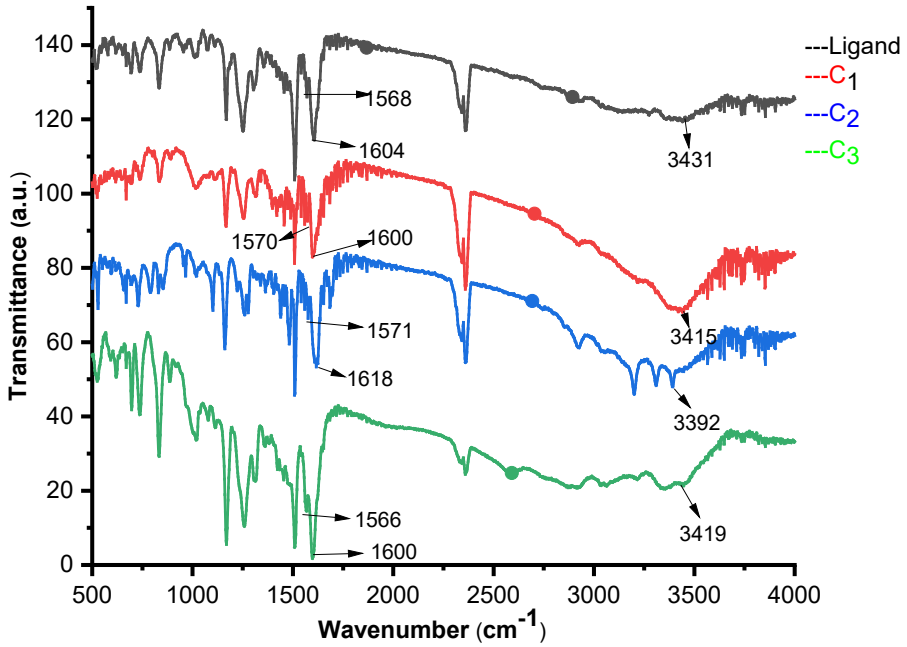

Fig 1. FTIR spectra of the Schiff base (ligand L) and its metal ion complexes (C_1 to C_3)

Table 3. FTIR spectral data of Schiff base (Ligand) and its complexes

Bond	Wavenumber (cm^{-1})			
	Ligand (L)	Complex (C_1)	Complex (C_2)	Complex (C_3)
N–H	3431	3415	3392	3419
C=N (imine)	1568	1571	1577	1566
C=N (triazole)	1604	1600	1618	1598
$C=S_{st}$	1167	1167	1162	1169
N–O	1510	1510	1510	1510
C–O–C	1249	1253	1276	1257
=C–H (aromatic)	3033	3033	3043	3033
C–H (aromatic)	694–835	698–835	698–831	696–831
C=C (aromatic)	1681	1679	1689	1685

Electronic Spectra, Magnetic Susceptibility and Molar Conductance

In a DMF solution, the UV-visible absorption spectra of ligand L are shown in Fig. 2 and summarized in Table 4. Two bands at 265 nm and 318 nm were assigned to the (π–π*) transition while a band at 318 nm was assigned to the (n–π*) transition. In the visible region, the electronic spectra of C_1 complex in DMF solvent showed two spin-allowed bands at 435 nm and 622 nm, which could be associated with the transitions of the $^4T_1g \rightarrow {}^4T_2g$ (f) (ν_2) and $^4T_1g \rightarrow {}^4T_1g$ (p) (ν_3), respectively. The C_1 complex was paramagnetic, as indicated by its magnetic

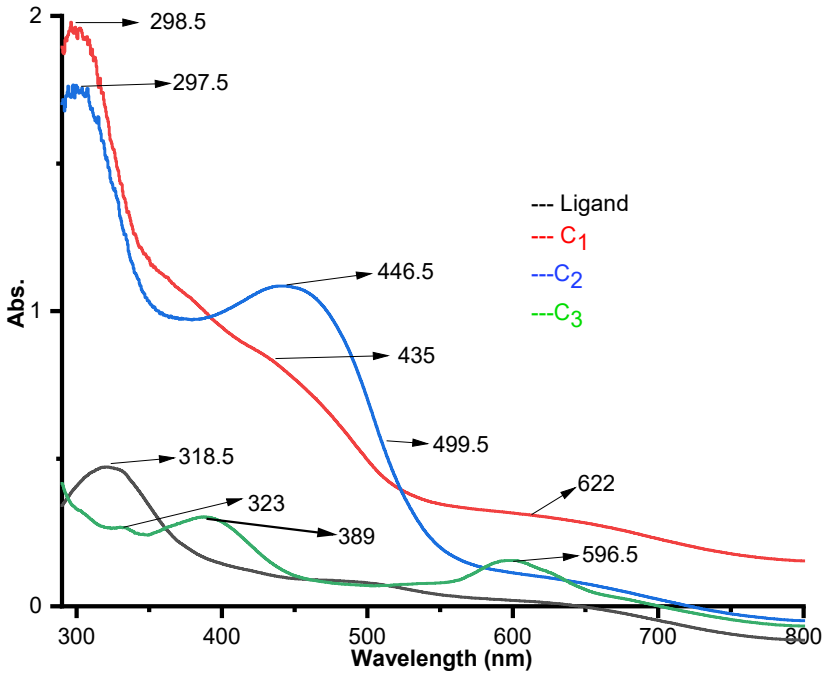

Fig 2. Electronic spectra of the ligand and its metal complexes

Table 4. Magnetic susceptibility, molar conductivity, and electronic spectral data of ligand(L)

Compound	λ_{max} nm (υ cm^{-1})	Assignment	Molar conductivity ohm^{-1} cm^2 mol^{-1}	Magnetic susceptibility (BM) found (calc.)	Suggested geometry
Ligand	265 (37735.84)	(π–π*)	-	-	Octahedral geometry
	318 (31446.54)	(n–π*)			
C_1	435 (22988.50)	$^4T_1g \rightarrow {}^4T_2g$ (f)	39.00	3.9 (3.87)	Octahedral geometry
	622 (16077.17)	$^4T_1g \rightarrow {}^4T_1g$ (p)			
C_2	499.5 (20020.02)	$^3A_2g \rightarrow {}^3T_1g$ (f)	50.2	3.10 (2.8)	Octahedral geometry
	446 (22421.52)	$^3A_2g \rightarrow {}^3T_1g$			
C_3	596.5 (16764.45)	$^2B_1g \rightarrow {}^2B_2g + {}^2Eg$	1.63	1.63	Octahedral geometry
	398 (25125.62)	$^2B_1g \rightarrow {}^2A_1g$			

susceptibility of 3.9 BM, and the complex had a molar conductivity of 39.00 ohm^{-1} cm^2 mol^{-1} indicating that it was non-conductive as indicated in Table 4. In addition to this information, the results of elemental (CHNS) analysis, flame atomic absorption, and FTIR spectrum supported this hypothesis, and implied an octahedral structure for the C_1 complex as shown in Fig. 3 [12]. The C_2 complex's electronic spectra in DMSO solution revealed two spin-allowed bands of 499.5 nm and 446 nm, which corresponded to the $^3A_2g \rightarrow {}^3T_1g$ (f) and $^3A_2g \rightarrow {}^3T_1g$ (p) transitions, respectively. Around the Ni(II) ion, these bands indicated an octahedral shape. The magnetic moment value for Ni(II) in Table 3 was 3.10 BM, which was within the range of 2.8–3.5 BM for Ni(II) ion with octahedral geometry. The conductivity of this compound referred to its non-ionic performance. Thus, based on the information presented above, as well as those derived from FTIR spectra and flame atomic absorption, an octahedral geometry around the Ni(II) ion can be proposed as shown in Fig. 3 [13-14]. The d^9 ion was characterized by a large distortion from the octahedral symmetry, and the band was asymmetrical. Several transformations have occurred, and these transitions have emerged, which cannot be easily set without ambiguity. The free ion ^2D term was expected to split in a crystal field in the same way as the ^5D term of the d^4 ion, and a similar interpretation of the spectra was likewise expected. The spectrum of Cu(II) complex in the DMF solution showed one broadband at 596.5 nm which agreed with $^2B_1g \rightarrow {}^2B_2g + {}^2Eg$ ($\nu_2 + \nu_3$) transition, and shoulder band at 398 nm allocated to $^2B_1g \rightarrow {}^2A_1g$ (ν_1) transitions. The purpose of these bands was to approve extremely warped octahedral geometry with their configuration. At room temperature, the magnetic moment was 1.80 BM. The complex's conductivity in DMF revealed that it was non electrolytic. As shown in Fig. 2 the octahedral geometry around the Cu(II) ion might be inferred from the electronic spectra, FTIR spectroscopy data, and flame atomic absorption Fig. 3 [15].

NMR Studies

^{1}H-NMR of Schiff base (ligand L)

Fig. 4 displays the signal assignments for the ^{1}H-NMR spectrum of Schiff base (ligand L) in DMSO-d^6. A key singlet 8.51 ppm (1H) was observed corresponding to the Schiff base proton [13]. The chemical shifts of aromatic and triazole ring protons were exhibited at 6.3–8.08 ppm, respectively. The spectrum showed a strong peak of thiol proton singlet at 13.10 ppm (1H) [16-17].

^{13}C-NMR of Schiff base (ligand L)

The ^{13}C-NMR spectra of the ligand is depicted in Fig. 5. The presence of the (N=CH) azomethine group in the ligand's spectra, which occurred at 158 ppm, was a distinguishing feature. Aromatic carbons shifted

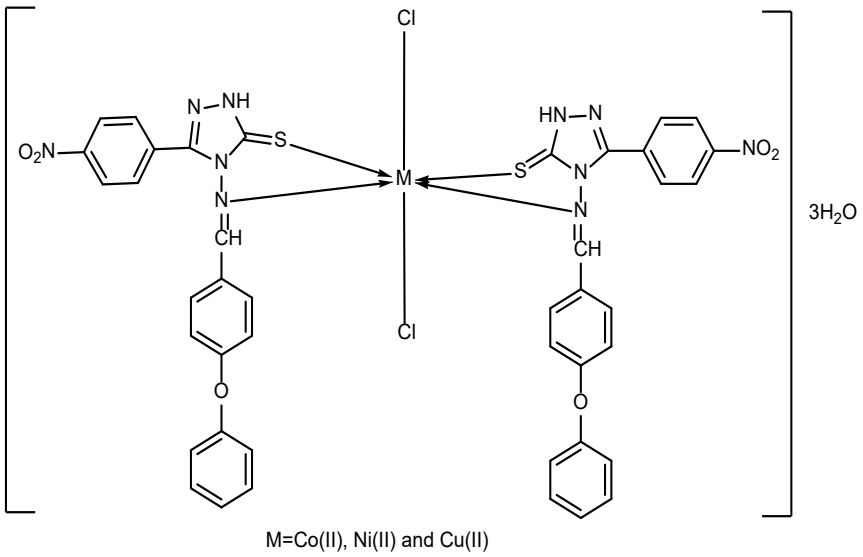

Fig 3. Suggestion of metal complexes

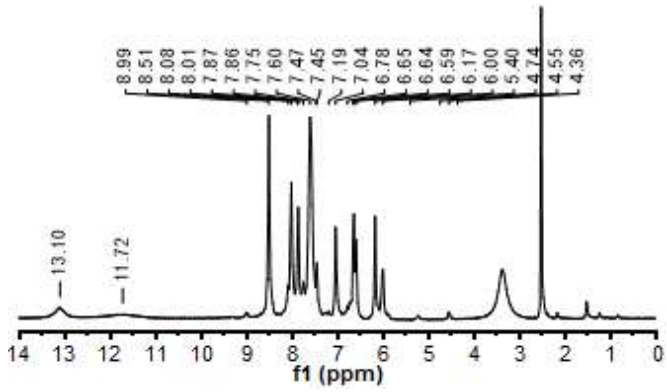

Fig 4. ^{1}H-NMR spectrum of Schiff base (Ligand L)

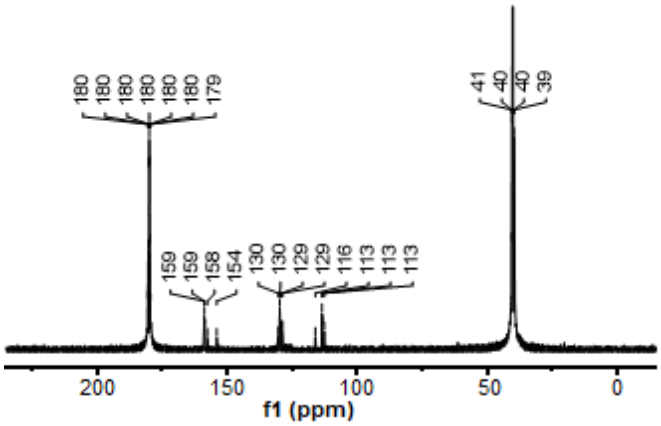

Fig 5. ^{13}C-NMR Spectrum of Schiff base (Ligand L)

chemically between 112 ppm and 130 ppm [17].

Thermal Analysis

Thermogravimetric analysis

Fig. 6 and 7 show indicative TG and DTG curves for the Schiff base ligand and its complexes of a metal ion [18] under the nitrogen atmosphere at a rate of 20 °C/min. Table 5 shows the function of the temperature. Overall, the TG curves of the C_1, C_2, and C_3 complexes displayed an early loss of weight due to evaporation of moisture, followed by a degradation step up to 200 °C, and an extended degradation up to almost 900 °C for C_1 and C_2 complexes, and 600 °C for C_3 complex. The latter decomposition was where the majority of the weight loss occurred, with a final degradation that led to a total weight loss of over 80%. Thus, after the moisture evaporation, the first degradation step of complexes was attributed to the thermal vaporization of volatile compounds. The second degradation step was most probably due to the loss of molecules from the complexes. Similarly, the Schiff base ligand (L) showed two degradation steps after dehydration [19-20]. Furthermore, the DTG curves had a small peak related to moisture loss; a steep top, which maximum temperature values were also recorded in Table 5; as well

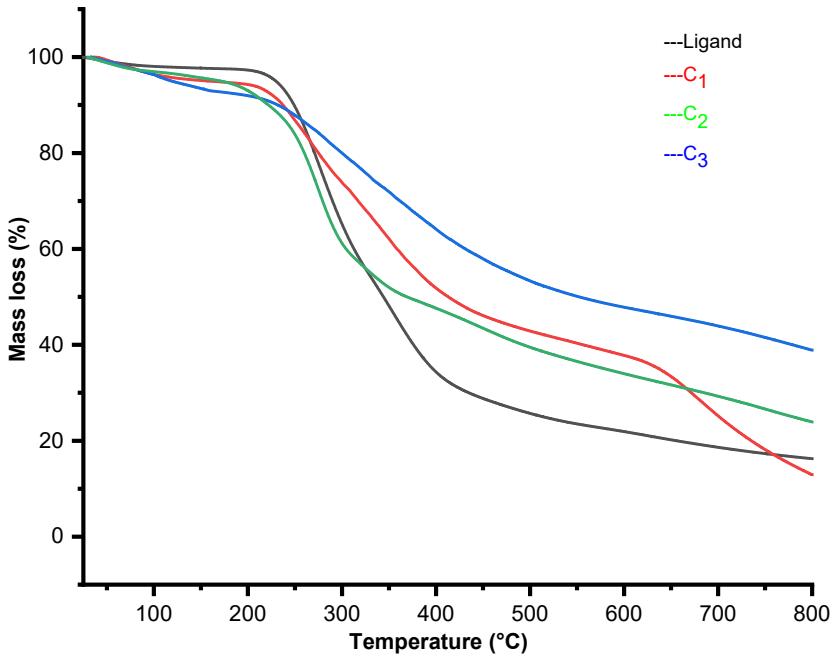

Fig 6. TG curves of the ligand and its metal ion complexes under nitrogen atmosphere at a heating rate of 20 °C/min

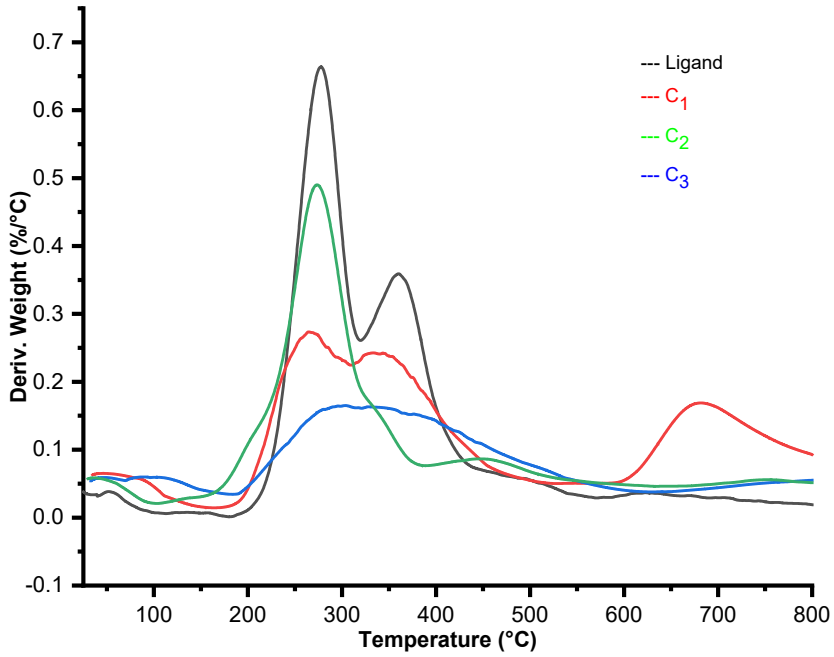

Fig 7. DTG curves of the ligand and its metal ion complexes under nitrogen atmosphere at a heating rate of 20 °C/min

Table 5. Thermal decomposition data of TG/DTG curves for the ligand and its metal ion complexes under nitrogen atmosphere

Compound	Molecular formula	Molecular weight (g/mol)	Step	Temperature range of the decomposition (°C)	Mass (%)	DTG maxima (°C)
Ligand L	$C_{21}H_{15}O_3N_5S$	417	1	0–175	2.469	275 362
			2	175–340	40.63	
			3	340–560	33.59	
			4	560–1000	12.55	
			5	> 1000	10.761	
C_1	$[Co(L)_2Cl_2]\cdot 2H_2O$	1072	1	0–160	7.556	290
			2	160–620	45.08	
			3	620–1000	19.89	
			4	> 1000	27.474	
C_2	$[Ni(L)_2Cl_2]\cdot 2H_2O$	998.73	1	0–95	3.071	273
			2	95–390	48.33	
			3	390–635	16.06	
			4	635–1000	17.32	
			5	> 1000	15.219	
C_3	$[Cu(L)_2Cl_2]\cdot 2H_2O$	988.73	1	0–180	4.997	267
			2	180–360	23.12	339
			3	360–540	30.68	677
			4	540–1000	38.47	
			5	> 1000	2.733	

as a slight minimum owing to moisture loss, except for C1 that had a large and broad peak located between 600–900 °C. More interestingly, all of the complexes had virtually the same breakdown temperature, which was in the range of 180 °C to 400 °C, indicating that they were thermally stable. The temperature at which degradation

began has been suggested to confirm the comparative stability of the complexes. Unlike C_3 complex, C_1 and C_2 degradation continued at temperatures higher than 600 °C [20-21].

CONCLUSION

Based on the process described in the literature, 2-amino-triazole derivative and 4-phenoxybenzaldehyde produced the Schiff bases (ligand L). The new ligands exhibited bidentate behavior in all metal complexes, with at least one of the nitrogen of azomethine and thiol groups being used as a chelate to coordinate with copper(II), nickel(II), and cobalt(II) metal ions. The complexes were synthesized with the new ligand according to 1:2 molar ratio of the complexes and were characterized using FTIR, ^{13}C-NMR, and ^{1}H-NMR to confirm the structures. Other analyses, such as magnetic property measurements, molar conductance, elemental analysis (CHNS), thermal analysis (TG, DTG), and atomic absorption were also performed. The results indicated that the complexes' proposed structures had an octahedral geometry. Thermogravimetric analyses of metal complexes were carried out in an inert atmosphere from room temperature to 1000 °C at 20 °C/min of heating rate. We were able to investigate their thermal deterioration profile using TGA/DTG. Thus, the degradation of the major components occurred in two steps for C_1 and C_2 complexes, and one step for C_3 complexes. These results could be used to predict the study biology activities behavior of these complex and could help in the evaluation of the could become a basis for further studies and at in-vitro and in-vivo levels experimental and this excellent performance would encourage us to develop more triazole derivative.

REFERENCES

[1] Al-Khazraji, A.M.A., and Al Hassani, R.A.M., 2020, Synthesis, characterization and spectroscopic study of new metal complexes form heterocyclic compounds for photostability study, *Sys Rev Pharm.*, 11 (5), 535–555.

[2] Sumrra, S.H., Sahrish, I., Raza, M.A., Ahmad, Z., Zafar, M.N., Chohan, Z.H., Khalid, M., and Ahmed, S., 2020, Efficient synthesis, characterization, and in vitro bactericidal studies of unsymmetrically substituted triazole-derived Schiff base ligand and its transition metal complexes, *Monatsh. Chem.*, 151 (4), 549–557.

[3] Bennion, J.C., McBain, A., Son, S.F., and Matzger, A.J., 2015, Design and synthesis of a series of nitrogen-rich energetic cocrystals of 5,5′-dinitro-2*H*,2*H*′-3,3′-bi-1,2,4-triazole (DNBT), *Cryst. Growth Des.*, 15 (5), 2545–2549.

[4] Peng, Z., Wang, G., Zeng, Q.H., Li, Y., Wu, Y., Liu, H., Wang, J.J., and Zhao, Y., 2021, Synthesis, antioxidant and anti-tyrosinase activity of 1,2,4-triazole hydrazones as antibrowning agents, *Food Chem.*, 341, 128265.

[5] Menteşe, E., Akyüz, G., Emirik, M., and Baltaş, N., 2019, Synthesis, *in vitro* urease inhibition and molecular docking studies of some novel quinazolin-4(3*H*)-one derivatives containing triazole, thiadiazole and thiosemicarbazide functionalities, *Bioorg. Chem.*, 83, 289–296.

[6] Dalloul, H.M., El-nwairy, K., Shorafa, A.Z., and Samaha, A.A., 2017, Synthesis and biological activities of some new spiro 1,2,4-triazole derivatives having sulfonamide moiety, *Org. Commun.*, 10 (4), 280–287.

[7] Jin, R., Wang, Y., Guo, H., Long, X., Li, J., Yue, S., Zhang, S., Zhang, G., Meng, Q., Wang, C., Yan, H., Tang, Y., and Zhou, S., 2020, Design, synthesis, biological activity, crystal structure and theoretical calculations of novel 1,2,4-triazole derivatives, *J. Mol. Struct.*, 1202, 127234.

[8] Sahoo, P.K., Sharma, R., and Pattanayak, P., 2010, Synthesis and evaluation of 4-amino-5-phenyl-4*H*-[1,2,4]-triazole-3-thiol derivatives as antimicrobial agents, *Med. Chem. Res.*, 19 (2), 127–135.

[9] Bader, A.T., Rasheed, N.A., Aljeboree, M., and Alkaiml, A.F., 2020, Synthesis, characterization of new 5-(4-nitrophenyl)-4-((4 phenoxybenzylidene) amino)-4*H*-1,2,4-triazole-3-thiol metal complexes and study of the antibacterial activity, *J. Phys. Conf. Ser.*, 1664, 012100.

[10] Emam, S.M., Tolan, D.A., and El-Nahas, A.M., 2020, Synthesis, structural, spectroscopic, and thermal studies of some transition-metal complexes of a ligand containing the amino mercapto triazole moiety, *Appl. Organomet. Chem.*, 34 (5), e5591.

[11] Venugopala, K.N., Kandeel, M., Pillay, M., Deb, P.K., Abdallah, H.H., Mahomoodally, M.F., and Chopra, D., 2020, Anti-tubercular properties of 4-amino-5-(4-fluoro-3-phenoxyphenyl)-4*H*-1,2,4-triazole-3-thiol and its Schiff bases: Computational input and molecular dynamics, *Antibiotics*, 9 (9), 559.

[12] Rapheal, P., Manoj, E., Kurup, M.R.P., and Fun, H.K., 2021, Nickel(II) complexes of N(4)-substituted thiosemicarbazones derived from pyridine-2-carbaldehyde: Crystal structures, spectral aspects and Hirshfeld surface analysis, *J. Mol. Struct.*, 1237, 130362.

[13] Hamil, A., Khalifa, K.M., Almutaleb, A.A., and Nouradean, M.Q., 2020, Synthesis, characterization and antibacterial activity studies of some transition metal chelates of Mn(II), Ni(II) and Cu(II) with Schiff base derived from diacetylmonoxime with O-phenylenediamine, *Adv. J. Chem. A*, 3 (4), 524–533.

[14] Kargar, H., Torabi, V., Akbari, A., Behjatmanesh-Ardakani, R., Sahraei, A., and Tahir, M.N., 2020, Pd(II) and Ni(II) complexes containing an asymmetric Schiff base ligand: Synthesis, X-ray crystal structure, spectroscopic investigations and computational studies, *J. Mol. Struct.*, 1205, 127642.

[15] Mahmoud, N.F., Abbas, A.A., and Mohamed, G.G., 2021, Synthesis, characterization, antimicrobial, and MOE evaluation of nano 1,2,4-triazole-based Schiff base ligand with some d-block metal ions, *Appl. Organomet. Chem.*, 35 (6), e6219.

[16] Silverstein, R., Webster, F.X., and Kiemle, D., 2005, *Spectrometric Identification of Organic Compounds*, 7th Ed., John Wiley & Sons, Inc., Hoboken, New Jersey, USA.

[17] Amer, S., El-Wakiel, N., and El-Ghamry, H., 2013, Synthesis, spectral, antitumor and antimicrobial studies on Cu(II) complexes of purine and triazole Schiff base derivatives, *J. Mol. Struct.*, 1049, 326–335.

[18] Magyari, J., Holló, B.B., Rodić, M.V., Jovanović, L.S., Szécsényi, K.M., Ferenc, W., Osypiuk, D., Mosolygó, T., Kincses, A., and Spengler, G., 2020, Synthesis, characterization, thermal properties and biological activity of diazine-ring containing hydrazones and their metal complexes, *J. Therm. Anal. Calorim.*, 2020, 1–14.

[19] Abid, M.N., Hafith, F.R., Musa, T.M., and Abbas, B.F., 2021, Synthesis, characterization and biological activity study of cobalt(II), nickel(II) and copper(II) complexes derived from mixed bidentate ligands of oxime and phenanthroline, *Egypt. J. Chem.*, 64 (11), 6487–6492.

[20] Chaurasia, M., Tomar, D., and Chandra, S., 2019, Synthesis, spectral characterization, and DNA binding studies of Co(II), Ni(II), Cu(II) and Zn(II) complexes of Schiff base 2-((1*H*-1,2,4-triazol-3-ylimino)methyl)-5-methoxyphenol, *J. Mol. Struct.*, 1179, 431–442.

[21] Gaber, M., El-Ghamry, H.A., and Fathalla, S.K., 2020, Synthesis, structural identification, DNA interaction and biological studies of divalent Mn, Co and Ni chelates of 3-amino-5-mercapto-1,2,4-triazole azo ligand, *Appl. Organomet. Chem.*, 34 (8), e5678.

Improvement of Mechanical, Thermal, and Morphological Properties of Organo-Precipitated Calcium Carbonate Filled LLDPE/Cyclic Natural Rubber Composites

Ahmad Hafizullah Ritonga[1,2], Novesar Jamarun[1*], Syukri Arief[1], Hermansyah Aziz[1], Denny Akbar Tanjung[1,3], and Boy Isfa[1]

[1]*Department of Chemistry, University of Andalas, Limau Manis, Padang 25163, West Sumatera, Indonesia*

[2]*Department of Chemistry, University of Sari Mutiara Indonesia, Medan 20123, North Sumatera, Indonesia*

[3]*Department of Agrotechnology, University of Medan Area, Medan 20223, North Sumatera, Indonesia*

* ***Corresponding author:***

email: novesarjamarun@sci.unand.ac.id

Received: September 3, 2021
Accepted: November 1, 2021

DOI: 10.22146/ijc.68888

Abstract: *This study investigates the improvement of the mechanical, thermal, and morphological properties of linear low-density polyethylene (LLDPE)/cyclic natural rubber (CNR) after the addition of organo-precipitated calcium carbonate (O-PCC). The impact on the properties of the LLDPE/CNR/LLDPE-g-OA/O-PCC composites was investigated by a series of empirical experiments. First, the polymer composite was blended in the molten state using an internal mixer with a heating temperature of 160 °C and a rotation speed of 100 rpm. The LLDPE was placed in a chamber of internal mixer until melted, followed by CNR, LLDPE-g-OA, and O-PCC. The polymer composites with an O-PCC concentration of 5% obtained the optimal mechanical properties compared to other variations, with a tensile strength of 17.17 MPa and Young's modulus of 252.68 MPa. The presence of O-PCC resulted in better thermal stability and a change in the melting point temperature of 124 °C. The FTIR spectra of the polymer composite showed the specific characteristics of O-PCC at 872.1 cm^{-1}. The morphology of the polymer composite indicates that the O-PCC is evenly dispersed in the polymer composite.*

Keywords: *O-PCC; LLDPE; CNR; LLDPE-g-OA; filler*

INTRODUCTION

Increasing awareness of the environment encourages both researchers and manufacturers to create environmentally-friendly products. For example, cyclic natural rubber (CNR) is a natural rubber derivative in the form of a granular solid and is known as resiprene-35 (CAS Reg. no: 68441-13-4). CNR is an environmentally-friendly and non-volatile resin used as a coating or paint binder on glass, metal, paper, and wood surfaces [1]. However, the application of CNR on the surface of polyolefin substrates, such as Linear Low-Density Polyethylene (LLDPE), is not suitable since LLDPE is semi-crystalline and has low surface energy [2]. Therefore, there is an opportunity to develop LLDPE/CNR-based polymer blend products and then be used as a reference in developing CNR as a paint binder for polyolefin surfaces, especially LLDPE.

The compatibility of polymer blends between polyolefin and CNR can be improved by the presence of a compatibilizer or coupling agent from one of the parts of the polymer blends. Mahendra et al. [3] reported the improvement of polymer blends between polypropylene (PP) and CNR using PP-g-MA and CNR-g-MA as compatibilizers. The oleic acid-grafted linear low-density polyethylene (LLDPE-g-OA) can also be used as compatibilizers to reduce the interfacial tension between the two polymer phases by increasing the interfacial adhesion of the two phases.

The presence of fillers in the polymer blends is needed to improve its mechanical and thermal properties. Pang et al. [4] mentioned that using kenaf fibers filler treated with amino acid lysine improved the mechanical, thermal, and morphological properties of LLDPE/PVOH/kenaf composites. Moreover, the

chemical treatment of kenaf fibers using hydrated chromium(III) sulfate ($[Cr(H_2O)_6]_2(SO_4)_3{\cdot}6(H_2O)$) can also improve the mechanical, thermal, and morphological properties of LLDPE/PVOH/kenaf composites [5]. The use of precipitated calcium carbonate (PCC) as a filler in polymer materials has been widely developing because it includes natural materials that are abundant and easy to obtain [6-10]. PCC is calcite with an amorphous crystal structure and low hardness [11-13]. The addition of PCC in the polyolefin matrix improved the mechanical and physical properties of the composite in several ways: increased thermal conductivity, stiffness, dimensional stability, reduced injection molding cycle time, lowered shrinkage, relaxation of internal stresses, and increased anti-blocking [14].

Furthermore, the particle size in the nanometer scale makes this filler more easily dispersed than the micro or ordinary scale [15]. According to Zapata et al. [7], it is necessary to modify $CaCO_3$ with oleic acid (OA) as a surfactant to obtain O–$CaCO_3$, which is more hydrophobic on the surface, so that the O–$CaCO_3$ can be evenly dispersed with no agglomeration on the composite. The O-$CaCO_3$ does not only function as fillers but also as a co-compatibilizer in non-polar polymer composites. de Oliveira et al. [16] reported that PCC in HDPE/PLA blends in the presence of a PE-g-MA compatibilizer and has shown the role of PCC as a co-compatibility since it can adsorb one of the blends. This study investigates the improvement of the mechanical, thermal, and morphological properties of organo-precipitated calcium carbonate (O-PCC) filled LLDPE/CNR composites with the presence of LLDPE-g-OA compatibilizer.

■ EXPERIMENTAL SECTION

Materials

Linear low-density polyethylene (LLDPE) Asrene UF-1810 with a density of 0.918 g/cm^3 and melt flow index (MFI) of 1.0 g/10 min (190 °C/2.16 kg) was supplied by *PT. Chandra Asri* Petrochemical Tbk. (Jakarta, Indonesia). Cyclic natural rubber (CNR) Resiprene-35 with a density of 0.91 g/mL and MFI of 36.37 g/10 min (190 °C/2.16 kg) was obtained from *PT. Industri Karet Nusantara* (Deli Serdang, Indonesia). Precipitated calcium carbonate (PCC) Schaefer Precarb 100 with a density of 0.0027-0.00295 g/cm^3 was supplied by Schaefer Kalk (Kuala Lumpur, Malaysia). Oleic acid (OA) with a density of 0.895 g/mL was obtained from *Subur Kimia Jaya* Chemical Company (Bandung, Indonesia). Benzoyl peroxide, xylene, ethanol, acetone, and methanol were obtained from Merck (Darmstadt, Germany). Oleic acid-grafted linear low-density polyethylene (LLDPE-g-OA) was prepared based on the methods conducted in prior work [17-18].

Instrumentation

The PCC and O-PCC nanoparticles' crystallite size was analyzed using an X-ray diffractometer (Shimadzu 6100). The mechanical properties (i.e., tensile strength, elongation at break, and Young's modulus) on polymer composites were determined using the Ultimate Testing Machine (GoTech AI-7000) with a maximum load cell capacity of 20 KN at a speed of 10 mm/min. The test specimen was according to ASTM D638-14 (type I). The stability and thermal properties of the polymer composites were analyzed using the TGA/DTA (Hitachi STA-7300), with a heating rate of 10 °C/min and a temperature range of 30 to 600 °C. The functional groups of the PCC, O-PCC, OA, and polymer composites were analyzed using an FTIR spectrometer (Agilent Cary 630) at the wavenumbers of 650–4000 cm^{-1}. The morphologies of the polymer composites were observed on the surface structure using a Scanning Electron Microscope (ZEISS EVO@MA10).

Procedure

Organic modification of precipitated calcium carbonate (O-PCC)

One mL of oleic acid (OA) was added into a beaker glass containing 100 mL of *n*-hexane and then stirred. One gram of PCC was added into the solution during stirring and then heated at 60 °C for 6 h. The blends were filtered, washed with ethanol, and dried at 100 °C for 24 h. The obtained results were in the form of O-PCC powder [7].

Preparation of LLDPE/CNR/LLDPE-g-OA/O-PCC composites

The LLDPE pellets were slowly placed into a chamber on the internal mixer (Thermo HAAKE Polydrive) at 160 °C with a rotation speed of 100 rpm for 5 min. After the LLDPE melted, CNR was added into the chamber, followed by LLDPE-g-OA as a compatibilizer in the polymer blend. It was then stirred and left for 5 min. Next, the O-PCC was added into the polymer blends according to the variations in Table 1 and left for 10 min until the blending process was finished. The composites were then removed from the internal mixer, left at room temperature, and cut into small pieces [3,19]. The results obtained were LLDPE/CNR/LLDPE-g-OA/O-PCC composites. The same treatment of neat PCC was required for result comparison. Henceforth, LLDPE/CNR/LLDPE-g-OA blends were referred to as LCC, LLDPE/CNR/ LLDPE-g-OA/O-PCC composites as LCCO, and LLDPE/CNR/LLDPE-g-OA/PCC composites as LCCP.

■ RESULTS AND DISCUSSION

X-Ray Diffraction Analysis

The XRD analysis was carried out on PCC and O-PCC nanofillers to identify crystallite size and crystalline phase of filler. The XRD patterns obtained from PCC and O-PCC nanofillers are presented in Fig. 1. The characteristic peaks of PCC are at 2θ of 23.09°, 29.46°, 35.97°, 39.43°, 43.16°, 47.60°, 48.55°, 57.35°, 60.64°, and 64.68°, corresponding to the $CaCO_3$ phase, indicating the presence of $CaCO_3$ in the PCC filler with a crystal size of 44.00 nm and a degree of crystallinity of 60.49%. The characteristic peaks of O-PCC are at 2θ of 23.40°, 29.76°, 36.27°, 39.71°, 43.46°, 47.88°, 48.83°, 57.63°, 60.91°, and 64.84° also attributable to the $CaCO_3$ phase, which indicates the presence of $CaCO_3$ in the O-PCC filler with a crystal size of 48.47 nm and a degree of crystallinity of 61.48% [12,20]. Organic modification of PCC with OA caused a slight shift in the characteristic peaks of $CaCO_3$ and a decrease in intensity. The presence of oleic compounds on the PCC surface caused an increase in the PCC crystallite size of 10.16% and crystallinity degree of 1.65%.

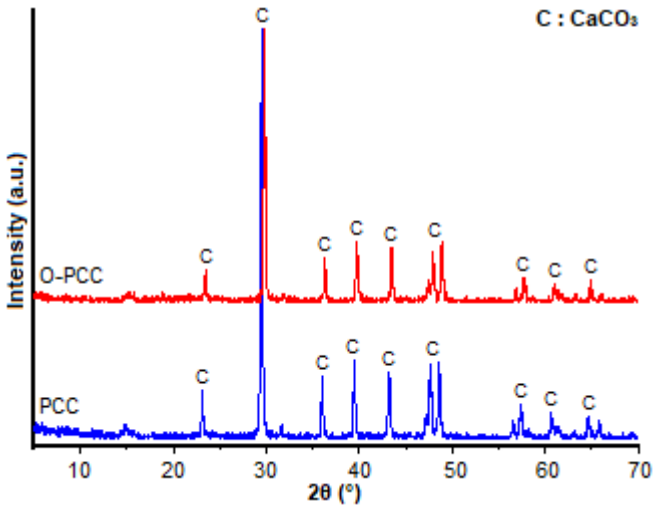

Fig 1. X-ray diffraction analysis of nanofillers

Table 1. Composition of polymer composites

Sample code	LLDPE (wt.%)	CNR (wt.%)	LLDPE-g-OA (wt.%)	O-PCC (wt.%)	PCC (wt.%)
LCC	67.5	27.5	5.0	-	-
LCCO-1	67.0	27.0	5.0	1.0	-
LCCO-2	66.5	26.5	5.0	2.0	-
LCCO-3	66.0	26.0	5.0	3.0	-
LCCO-4	65.5	25.5	5.0	4.0	-
LCCO-5	65.0	25.0	5.0	5.0	-
LCCP-1	67.0	27.0	5.0	-	1.0
LCCP-2	66.5	26.5	5.0	-	2.0
LCCP-3	66.0	26.0	5.0	-	3.0
LCCP-4	65.5	25.5	5.0	-	4.0
LCCP-5	65.0	25.0	5.0	-	5.0

Mechanical Properties

The mechanical properties of the composites, including tensile strength, elongation at break, and Young's modulus, are shown in Fig. 2. Compared to the LCC blends, the LCCO composites showed better mechanical properties (higher tensile strength and Young's modulus) and decreased elongation at break. The improvement in mechanical properties was caused by the addition of O-PCC concentration into the LCCO composite. These results can be associated with the even dispersion quality of the fillers in the composite matrix and the potential interaction between the coupling agent and the polymer. The strong interfacial adhesion between the O-PCC particles with the polymer composites matrix macromolecular chains through the compatibilizer, and coupling agent resulted in load sharing and effective stress transfer on the interfacial zone between LLDPE/CNR with O-PCC [4-5,21]. In the LCCP composites, PCC addition did not significantly improve the mechanical properties because the unmodified PCC had poor dispersion quality and formed agglomerations when fillers were added continuously. In addition, the weak interfacial adhesion between the fillers and polymer composites matrix limited the load transfer, causing the material to be damaged due to particle de-cohesion and the formation of cavities around the fillers [21].

The value of Young's modulus on LCCO composites also showed a significant increase with the addition concentration of the O-PCC filler. The improvement in stiffness is associated with the strong interfacial adhesion between the filler and the compatible material and between the polymer and the compatible material [21]. The presence of O-PCC in polymer composites acts as fillers and as co-compatibilizers [7]. Meanwhile, there was no significant increase in LCCP composites due to the potential agglomeration and the cavities around the fillers [21]. The elongation at the break of the LCCO and LCCP composites shows a decrease along with the addition in fillers concentration. This decrease is related to the ductile

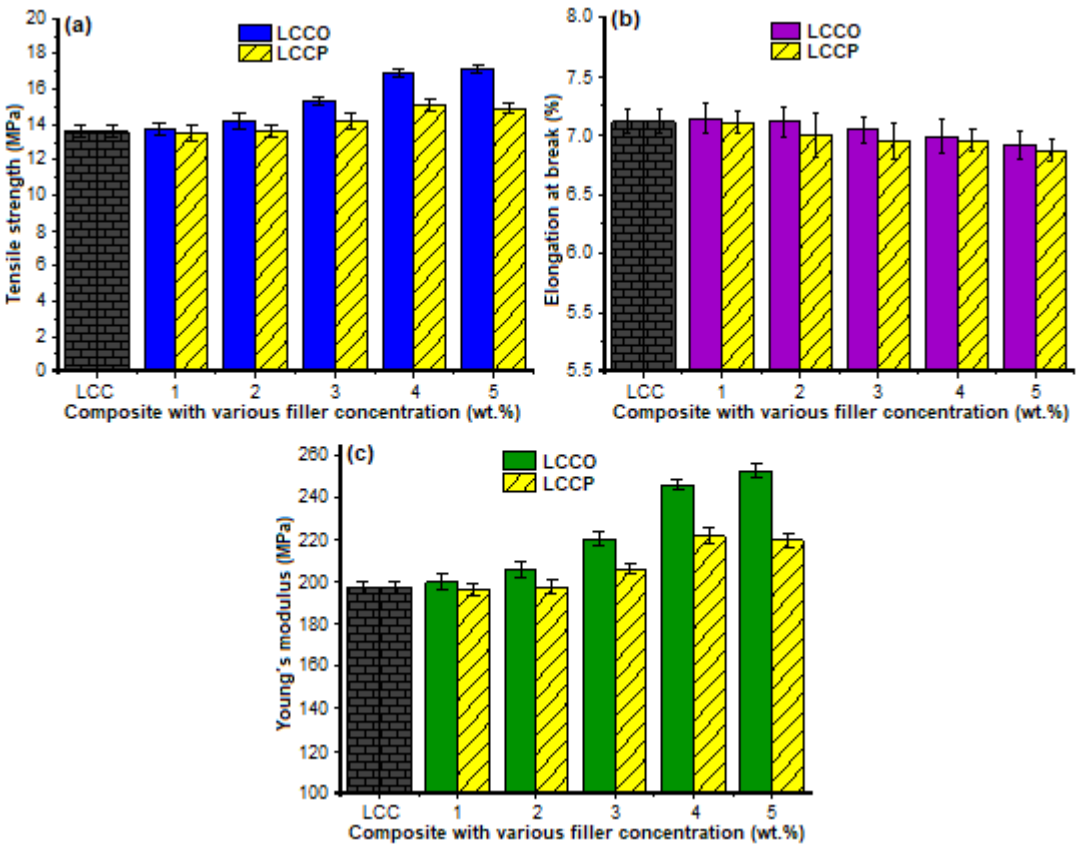

Fig 2. Tensile strength, elongation at break, and Young's modulus of polymer composites

to brittle transition in the behavior of the polymer composites [21]. The increase in interfacial adhesion causes a decrease in the flexibility of the polymer composite [5].

Thermal Analysis

Based on the TGA (Fig. 3(a)) and DTG (Fig. 3(b)) curves, the initial degradation temperature at a 5% weight loss and the maximum degradation temperature of the polymer composite were represented by $T_{5\%}$ and T_{max}, respectively. The existence of fillers has increased the initial degradation temperature of both LCCO and LCCP, which can be seen at $T_{5\%}$. In addition, the presence of inorganic materials in the polymer composites with a certain amount has also increased the degradation temperature since PCC decomposes at high temperatures.

Meanwhile, LCC blends started to degrade at the temperature of 319 °C. The thermal stability of the polymer composites increased after the addition of inorganic materials. The maximum degradation temperature of LCCO composites is higher than LCCP and LCC. These results illustrate that polymer composites treated with O-PCC fillers have higher thermal stability due to the increased interfacial adhesion between the polymer composite matrix and O-PCC fillers. Therefore, the addition of the modified PCC fillers increased the thermal stability of the LCCO composite [4-5].

T_m and T_d respectively represented the melting point temperature and the decomposition temperature of the polymer composite. The decomposition temperature of all samples showed endothermic peak phenomena (Fig. 3(c)) and did not show any significant difference at T_{max} of the TGA curve. The first endothermic peak indicates the melting point temperature of each sample. The LCCO and LCCP composites showed a T_m of 124 °C. The LCC blends showed a T_m of 123 °C, which indicates that the addition of OPCC/PCC fillers resulted in a higher T_m than those without fillers. All samples are semi-crystalline because endothermic peaks have formed, and no transitions occur before the T_m [18]. Data analysis of the TGA and DTG curves is summarized in Table 2.

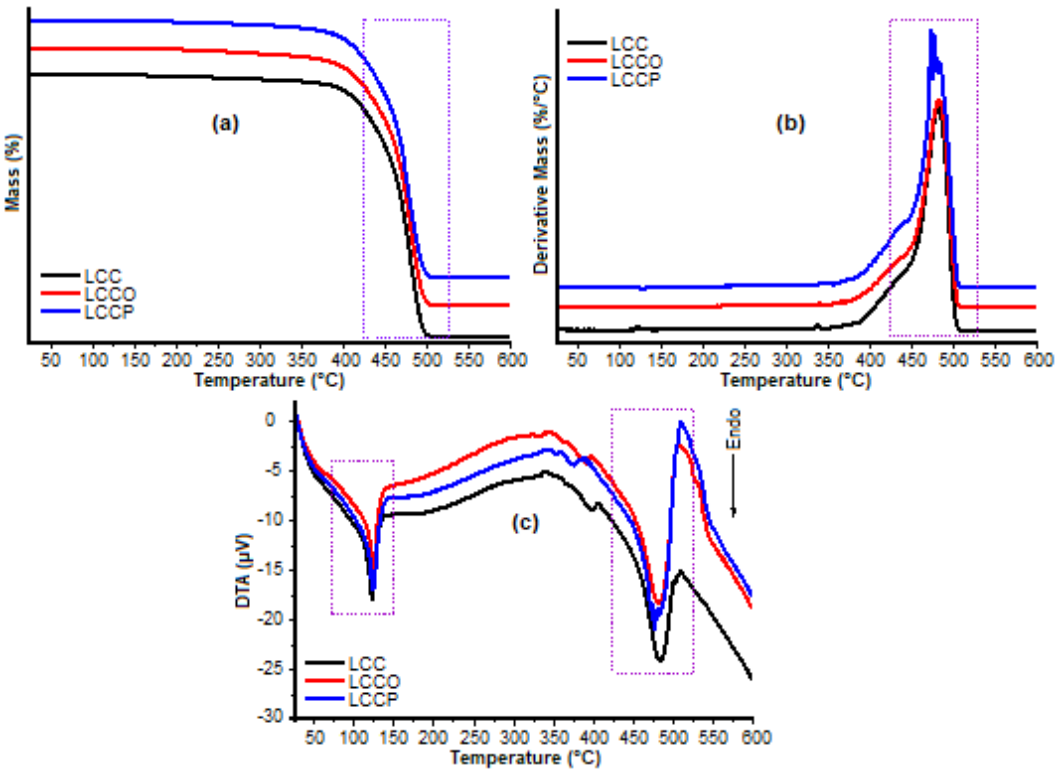

Fig 3. (a) TGA, (b) DTG, (c) DTA curves of the polymer composites

Table 2. Thermal analysis data of LCC, LCCO, and LCCP

Sample	$T_{5\%}$ (°C)	T_{max} (°C)	T_m (°C)	T_d (°C)
LCC	319	480	123	480
LCCO	382	481	124	481
LCCP	389	471	124	476

FTIR Analysis

The FTIR spectra of OA, PCC, and O-PCC are presented in Fig. 4(a). The absorption at 2922.2–2855.1 cm^{-1} indicates stretching vibrations of methyl and methylene groups of oleic acid, suggesting that it has been adsorbed on the PCC surface. The band at 1701.1 cm^{-1} indicates the presence of carbonyl (C=O) stretching vibrations of $CaCO_3$. A strong band at 1394.0 cm^{-1} indicates carbonate stretching vibrations. The absorptions at 872.1 and 723.1 cm^{-1} correspond to the typical vibrational bands of calcite [7].

The FTIR spectra of the LCC, LCCO, and LCCP are presented in Fig. 4(b). The band at 2914.7–2847.6 cm^{-1} indicates stretching vibrations in methyl and methylene from organic polymer compounds. The bands at 1461.1 and 1371.6 cm^{-1} indicate the presence of $-CH_2$ and $-CH_3$ bending vibrations. An absorption at 723.1 cm^{-1} indicates the stretching vibrations of C–H [4-5,22]. The small band at 1654.9 cm^{-1}, which shows C=C double bond originating from the CNR, is visible in the LCC spectrum but not in the LCCO and LCCP since it is possibly overlapped with the absorption at 1701.1 cm^{-1} at the same intensity, which indicates the presence of oleic groups on the surface of the O-PCC. In LCCP composites, the absorption intensity at 1701.1 cm^{-1} appears to be reduced due to the absence of oleic groups on the PCC surface. The difference in the spectrum of LCCO and LCCP is observed from the absorption at 872.1 cm^{-1}, where the intensity of O-PCC is found to be weaker than PCC [7,18,21].

Morphological Analysis

Analysis of surface morphology of the composites was carried out to observe the surface structure of LCC, LCCO, and LCCP (see Fig. 5). The surface morphology of LCC shows a slightly rough surface structure and appears to achieve homogeneous blends. LCCO composites show a surface structure that is not much different from LCC, where a surface structure is slightly rough and seems to have homogeneous composites because the O-PCC was evenly distributed on the surface of the polymer composites. LCCP shows a rough surface structure and appears non-homogeneous composites because PCC is not unevenly dispersed or agglomerates on the surface of the polymer composites. PCC has modified with oleic acid and clearly showed its role as a dispersing agent in LCCO composites, which causes the surface structure of the LCCO not to be significantly different from the LCC blends since the O-PCC was evenly

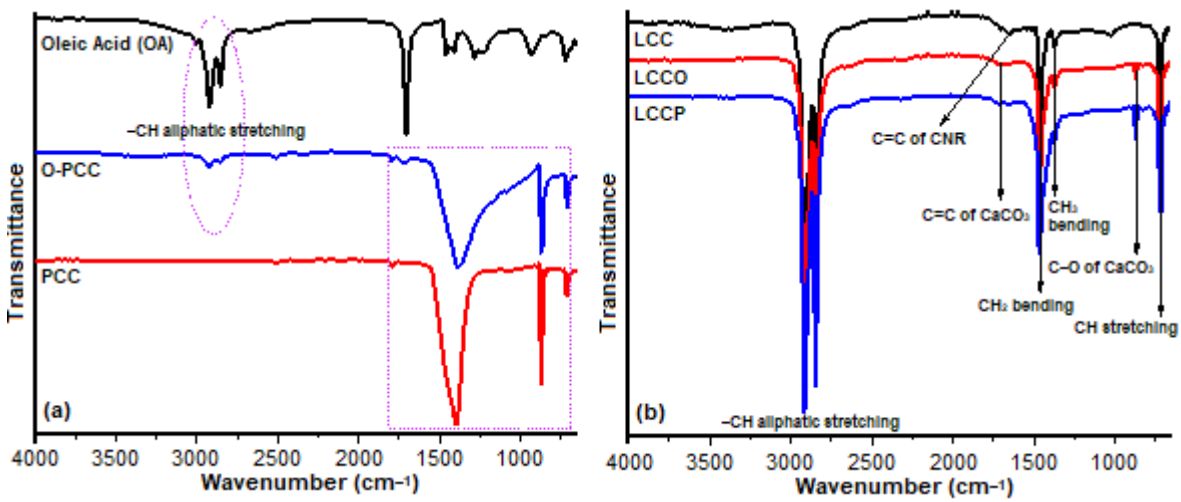

Fig 4. FTIR spectra of (a) nanofillers, (b) polymer composites

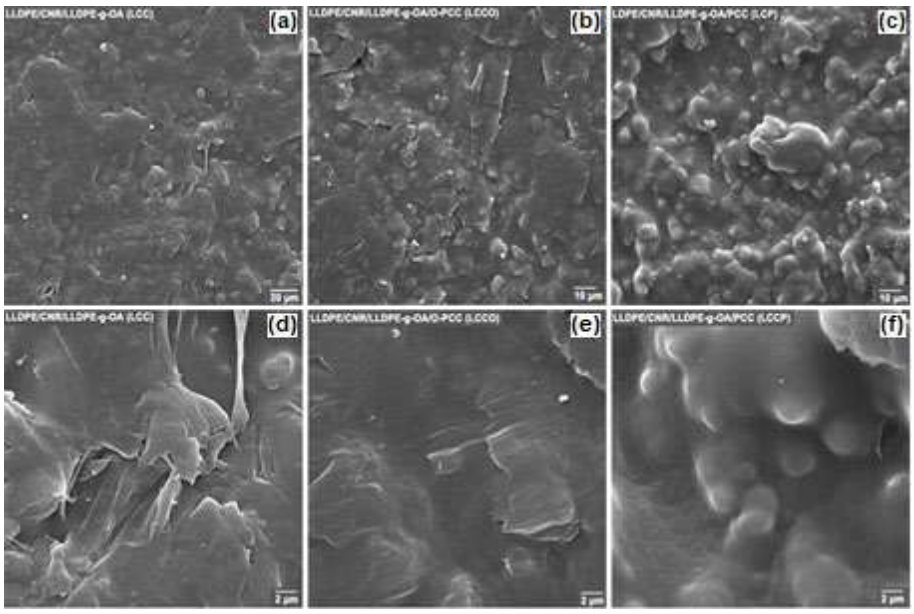

Fig 5. SEM micrographs of (a) LCC, (b) LCCO, (c) LCCP at 1000× magnification, and (d) LCC, (e) LCCO, (f) LCCP at 5000× magnification

dispersed on the LCCO composite. The presence of O-PCC is not only a filler but also acts as a co-compatibilizer that makes the composite more compatible with the ingredients [7].

CONCLUSION

The presence of O-PCC nanoparticles (crystal size of 48.4 nm and crystallinity of 61.48%) as a filler has affected the mechanical properties of the LCCO composites. An O-PCC concentration of 5% has resulted in tensile strength of 17.17 MPa, increasing 26.2% compared to the unfilled LCC blends. The Young's modulus was 252.68 MPa, about 28.1% higher than the unfilled one. The presence of O-PCC in LCCO composites has achieved better thermal stability than LCC blends and LCCP composites, with a maximum mass degradation temperature of 481 °C. The FTIR spectra of LCCO composites showed the characteristic absorption of $CaCO_3$ at 872.1 and 1701.1 cm^{-1}, indicating the presence of O-PCC in LCCO composites. The morphology of the LCCO composite resulted in a slightly rough and homogeneous surface structure with the homogenously dispersed O-PCC in the composite.

ACKNOWLEDGEMENTS

The author would like to thank the Ministry of Education, Culture, Research, and Technology of the Republic of Indonesia for the BPPDN scholarship program and funding for doctoral dissertation research grants in 2021, with the main contract number is 104/E4.1/AK.04.PT/2021 and derivative contract number is contract/6.17/PT.01.03/PDD-Material Maju/2021.

AUTHOR CONTRIBUTIONS

AHR conducted the experiment. AHR, DAT, and BI conducted the calculations and analysis. AHR wrote the manuscript. NJ, SA, HA, and AHR revised the manuscript. All authors agreed to the final version of this manuscript.

REFERENCES

[1] Aritonang, B., Tamrin, T., Wirjosentono, B., and Eddiyanto, E., 2019, Grafting of oleic acid on cyclic natural rubber resiprene-35 using dicumyl peroxide initiator and divinylbenzene compatibilizers for paint binder in polyamide thermoplastics, *Orient. J. Chem.*, 35 (1), 173–179.

[2] Rahayu, I., Zainuddin, A., and Hendrana, S., 2020, Improved maleic anhydride grafting to linear low density polyethylene by microencapsulation method, *Indones. J. Chem.*, 20 (5), 1110–1118.

[3] Mahendra, I.P., Wirjosentono, B., Tamrin, T., Ismail, H., Mendez, J.A., and Causin, V., 2019, The influence of maleic anhydride-grafted polymers as compatibilizer on the properties of polypropylene and cyclic natural rubber blends, *J. Polym. Res.*, 26 (9), 215.

[4] Pang, A.L., Ismail, H., and Abu Bakar, A., 2020, Effect of lysine treatment on the properties of linear low-density polyethylene/poly(vinyl alcohol)/kenaf composites, *BioResources*, 15 (1), 1915–1926.

[5] Pang, A.L., Ismail, H., and Abu Bakar, A., 2018, Mechanical, morphological, and thermal properties of kenaf filled linear low-density polyethylene/ poly(vinyl alcohol) composites: Effect of chemical treatment, *J. Vinyl Addit. Technol.*, 24, E164–E171.

[6] Fernando, N.A.S., and Thomas, N.L., 2012, Investigation of precipitated calcium carbonate as a processing aid and impact modifier in poly(vinyl chloride), *Polym. Eng. Sci.*, 52 (11), 2369–2374.

[7] Zapata, P.A., Palza, H., Díaz, B., Armijo, A., Sepúlveda, F., Ortiz, J.A., Ramírez, M.P., and Oyarzún, C., 2019, Effect of $CaCO_3$ nanoparticles on the mechanical and photo-degradation properties of LDPE, *Molecules*, 24 (1), 126.

[8] Lourenço, A.F., Gamelas, J.A.F., and Ferreira, P.J., 2015, Precipitated calcium carbonate modified by the layer-by-layer deposition method–Its potential as papermaking filler, *Chem. Eng. Res. Des.*, 104, 807–813.

[9] Declet, A., Reyes, E., and Suárez, O.M., 2016, Calcium carbonate precipitation: A review of the carbonate crystallization process and applications in bioinspired composites, *Rev. Adv. Mater. Sci.*, 44, 87–107.

[10] Wardhani, S., Prasetia, F., Khunur, M.M., Purwonugroho, D., and Prananto, Y.P., 2018, Effect of CO_2 flow rate and carbonation temperature in the synthesis of crystalline precipitated calcium carbonate (PCC) from limestone, *Indones. J. Chem.*, 18 (4), 573–579.

[11] Piskin, S., and Dere Özdemir, O., 2012, Effect of process conditions on crystal structure of precipitated calcium carbonate ($CaCO_3$) from fly ash: Na_2CO_3 preparation conditions, *Int. J. Biol. Ecol. Environ. Sci.*, 1 (6), 2277–4394.

[12] Erdogan, N., and Eken, H.A., 2017, Precipitated calcium carbonate production, synthesis and properties, *Physicochem. Probl. Miner. Process.*, 53 (1), 57–68.

[13] Sisca, V., Deska, A., Syukri, S., Zilfa, Z., and Jamarun, N., 2021, Synthesis and characterization of CaO limestone from Lintau Buo supported by TiO_2 as a heterogeneous catalyst in the production of biodiesel, *Indones. J. Chem.*, 21 (4), 979–989.

[14] Lin, Y., and Chan, C.M., 2012, "Calcium Carbonate Nanocomposites" in *Advances in Polymer Nanocomposites*, Woodhead Publishing, Cambridge, UK, 55–90.

[15] Ouarhim, W., Semlali Aouragh Hassani, F.Z., Bouhfid, R., Thomas, S., Sarathchandran, C., and Chandran, N., 2020, "Rheology of Polymer Nanocomposites" in *Rheology of Polymer Blends and Nanocomposites*, Elsevier, Amsterdam, Netherlands, 73–96.

[16] de Oliveira, A.G., Moreno, J.F., de Sousa, A.M.F., Escócio, V.A., de Oliveira Cavalcanti Guimarães, M.J., and da Silva, A.L.N., 2019, Composites based on high-density polyethylene, polylactide and calcium carbonate: Effect of calcium carbonate nanoparticles as co-compatibilizers, *Polym. Bull.*, 77 (6), 2889–2904.

[17] Liu, M., Liu, Z., Ding, S., Li, S., and Zhang, L., 2003, Graft copolymerization of oleic acid onto low-density polyethylene in the molten state, *J. Appl. Polym. Sci.*, 90 (12), 3299–3304.

[18] Aritonang, B., Tamrin, T., Wirjosentono, B., and Eddiyanto, E., 2020, Effect of graft copolymerization of oleic acid on to cyclic natural rubber in polyamide, *Case Stud. Therm. Eng.*, 21, 100690.

[19] dos Anjos, E.G.R., Backes, E.H., Marini, J., Pessan,

L.A., Montagna, L.S., and Passador, F.R., 2019, Effect of LLDPE-g-MA on the rheological, thermal, mechanical properties and morphological characteristic of PA6/LLDPE blends, *J. Polym. Res.*, 26 (6), 134.

[20] Sisca, V., Tanjung, D.A., Syukri, S., Zilfa, Z., and Jamarun, N., 2021, Catalytic activity of precipitated calcium carbonate for biodiesel production, *Rasayan J. Chem.*, 14 (3), 1587–1593.

[21] Doufnoune, R., Haddaoui, N., and Riahi, F., 2008, Effects of coupling agents on the tensile properties of calcium carbonate filled LDPE compatibilized with maleic anhydride-g-LDPE (Part I), *Int. J. Polym. Mater. Polym. Biomater.*, 57 (4), 295–318.

[22] Pang, A.L., Ismail, H., and Bakar, A.A., 2018, Linear low density polyethylene/poly(vinyl alcohol)/kenaf composites: Effect of natural weathering on functional group, weight loss characteristics, tensile, morphological and thermal properties, *Sains Malays.*, 47 (3), 571–580.

Supplementary Data

This supplementary data is a part of paper entitled "Growth, Electronic Structure, and Electrochemical Properties of Cubic $BaTiO_3$ Synthesized by Low-Pressure Hydrothermal-Assisted Sintering".

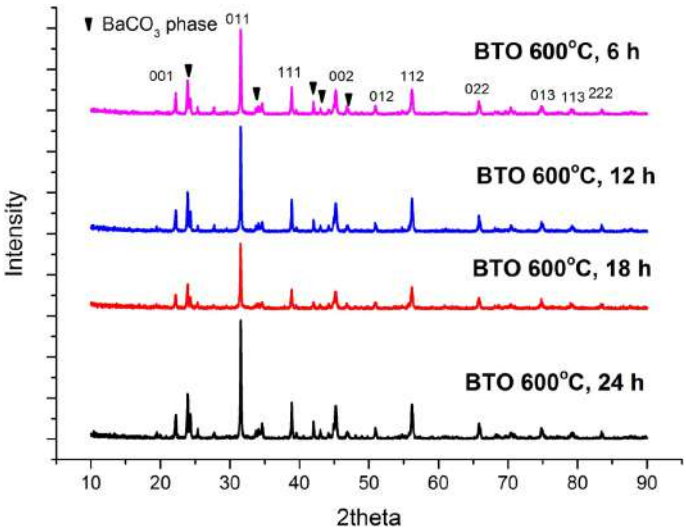

Fig S1. XRD pattern of cubic $BaTiO_3$ that resulted from sintering at 600 °C

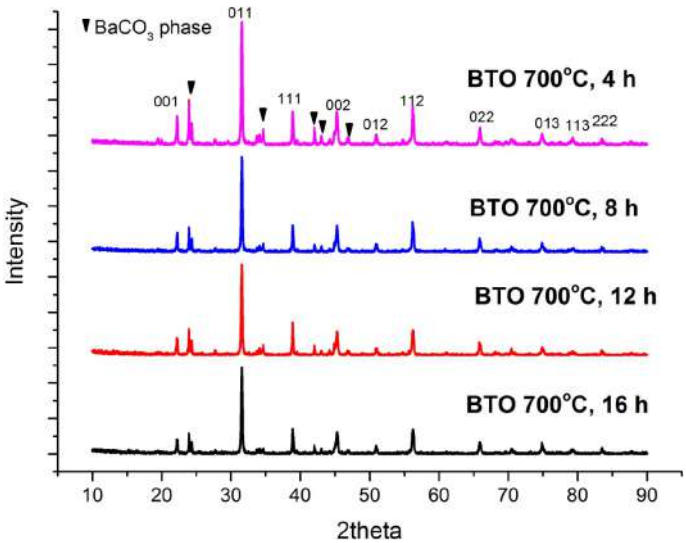

Fig S2. XRD pattern of cubic $BaTiO_3$ that resulted from sintering at 700 °C

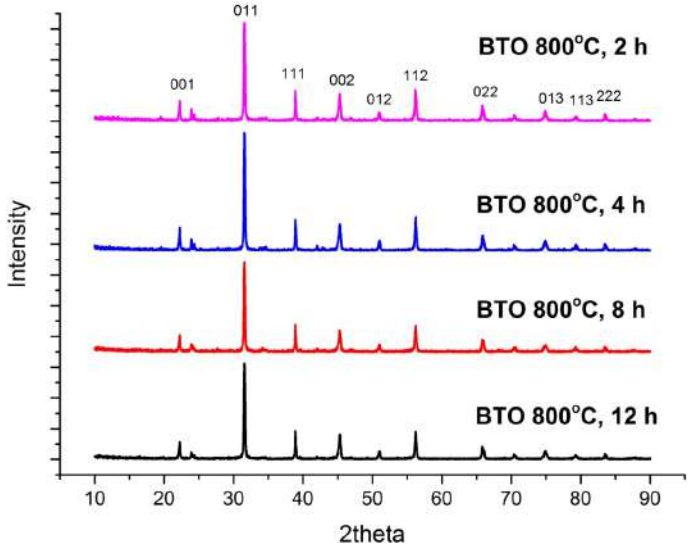

Fig S3. XRD pattern of cubic $BaTiO_3$ that resulted from sintering at 800 °C

Growth, Electronic Structure, and Electrochemical Properties of Cubic $BaTiO_3$ Synthesized by Low-Pressure Hydrothermal-Assisted Sintering

Mohammad Khotib[1,2*], Bambang Soegijono[3], Zainal Alim Mas'ud[1,2], and Gina Libria Nadjamoeddin[2]

[1]*Department of Chemistry, Bogor Agricultural University, Chemistry Building, Wing 1, 3rd Floor, Jl. Tanjung, IPB Darmaga Campus, Bogor 16680, Indonesia*

[2]*Laboratory for Testing, Calibration and Certification Services, Bogor Agricultural University, Baranangsiang Campus, Jl. Padjajaran, Bogor 16129, Indonesia*

[3]*Department of Physics, Faculty of Mathematics and Natural Sciences, Universitas Indonesia, Kampus Baru UI, Depok 16424, Indonesia*

* ***Corresponding author:***

email: mohammadkh@apps.ipb.ac.id

Received: September 7, 2021
Accepted: November 9, 2021

DOI: 10.22146/ijc.68978

Abstract: *Cubic $BaTiO_3$ was synthesized through low-pressure hydrothermal-assisted sintering using $Ba(OH)_2$ and TiO_2 as precursors with a mol ratio of Ba:Ti = 1.4:1. The single phase of cubic $BaTiO_3$ was produced at a sintering temperature of 800 °C for 2, 4, 8, and 12 h. The absence of diffraction peak splitting at 2θ of 45° was indicated cubic $BaTiO_3$. The crystallite size of $BaTiO_3$ ranged from 80–200 nm, and its size increased with increasing temperatures and sintering times. The micro-strain of the $BaTiO_3$ crystal lattice had a range between 0.27 and 0.68%. The minimum bandgap on the indirect bandgap was about 1.75 eV from point M to Γ, while the direct bandgap was about 1.95 eV from Γ to Γ. Ti–O's interaction had a covalent character, while that of Ba–O had an ionic character based on the density of state (DOS) calculation. The characteristics of the $BaTiO_3$ voltammogram show an irreversible redox mechanism with a more observable reduction peak in Ti^{4+}/Ti^{3+}. Higher current density at over potential indicated greater $BaTiO_3$ capabilities in Oxygen Evolution Reaction (OER)-Oxygen Reduction Reaction (ORR) electrocatalysis. For that, purified cubic $BaTiO_3$ offers potential application as an electrode for batteries, water splitting systems, and regenerative fuel cells.*

Keywords: *cubic $BaTiO_3$; bandgap; the density of state; oxygen evolution-reduction; electrocatalyst*

■ INTRODUCTION

Barium titanate ($BaTiO_3$) is widely used as the main material for multilayer capacitors, thermistors, high-density data storage, and electro-optical equipment due to its dielectric and ferroelectric properties as well as environmentally friendly materials. The application of $BaTiO_3$ to electronic materials is closely related to the character of its microstructures. The nano-size of $BaTiO_3$ also exhibits better performance than other sizes. $BaTiO_3$ is also known to have abilities in the electrolysis of oxygen evolution reaction (OER), oxygen reduction reaction (ORR), and hydrogen evolution reaction (HER) [1-2]. Furthermore, it is well-known that a high specific area could increase its catalytic activity by enabling a shorter diffusion distance of its electrons and holes, facilitating the surface redox reaction. Therefore, many studies have been developed to obtain $BaTiO_3$ with microstructure and morphology matching application requirements.

The conventional technique of $BaTiO_3$ synthesis requires high temperatures (~1200 °C) followed by grinding or milling its precursors such as BaO and TiO_2 [3]. A disadvantage of this solid technique is the presence of contamination and crystal growth problems during milling and calcination. New techniques are thus being continuously developed, such as sol-gel [4-5], the Pechini process [6], hydrothermal [7], and precipitation [8-9]. These techniques can be categorized as wet techniques that facilitate the crystallization of nano-size

particles at low temperatures. A synthesis technique for $BaTiO_3$ is required to produce nano-sized particles free of impurities and damage.

The main advantages of low-pressure hydrothermal techniques over solid-phase techniques include lower reaction temperatures and higher product purity. In addition, hydrothermal techniques no longer require thermal treatment for crystallization [10-11], so it is possible to obtain sub-micro or nano-sized materials of $BaTiO_3$. Crystallization via the hydrothermal technique also provides advantages over sol-gel and co-precipitation, such as shorter crystallization times with good control over crystallization, crystallite size, purity, and morphology [12].

Based on the above explanation of the many benefits of $BaTiO_3$ as a ferroelectric material and the advantages of the hydrothermal technique, a study was conducted to obtain cubic $BaTiO_3$ using a low-pressure hydrothermal technique and identify its crystal growth.

■ EXPERIMENTAL SECTION

Materials

All the reagents were obtained from PT Merck Indonesia Tbk, analytical grade, and used without further purification, i.e., $Ba(OH)_2{\cdot}8H_2O$ (for an analysis-ensure grade, Merck, Germany), TiO_2 (for an analysis-ensure grade, Merck, Germany), and HNO_3 (for analysis-65% purity, Merck, Germany).

Instrumentation

The equipment for synthesis and characterization were oven (Memmert UN55), XRD (Shimadzu XRD-7000), TG/DTA (LINSEISS STA PT 1600), and Potentiostat (Digi-Ivy).

Procedure

Synthesis of cubic barium titanate (Cubic $BaTiO_3$)

Cubic $BaTiO_3$ was synthesized using barium hydroxide ($Ba(OH)_2{\cdot}8H_2O$), titanium oxide (TiO_2), and distilled water as precursors. $BaTiO_3$ was synthesized via a low-pressure system hydrothermal method using the mole ratio of Ba:Ti = 1.4:1. The suspension was prepared by mixing 9 g (0.12 mol) of TiO_2 and 45 g (0.14 mol) of $Ba(OH)_2{\cdot}8H_2O$ in 250 mL of CO_2-free-distilled water in a Teflon container. The mixture was stirred evenly and heated in an oven at 150 °C until the water evaporated entirely. Then, the solid was heated at temperatures of 600, 700, and 800 °C for the following durations: (a) for 600 °C = 6, 12, 18, and 24 h, (b) for 700 °C = 4, 8, 12, and 16 h, (c) for 800 °C = 2, 4, 8, 12 h.

The purification of $BaTiO_3$ was conducted by immersing it in 100 mL of 1 N HNO_3 solution followed by heating at 60 °C for one hour. Next, the solid was separated, washed with distilled water until being acid-free, and dried at 105 °C for 3 h.

Phase identification using XRD

Each product was identified for phase and crystallite size using XRD GBC EMMA software Traces 28 mA, 35 kV with Cu Kθ = 1.54056 A in the 2θ range of 10 to 90°, step size = 0.02°, and scan rate= 2°/min. An analysis of the XRD data in phase identification and refinement was conducted using HighScore Plus and FullProf software using COD and the ICDD database. The $BaTiO_3$ crystallite size was determined by Scherrer and Williamson-Hall equations using XRD measurement data. The equations are:

$$\text{Scherrer: } B = \frac{K\lambda}{D\cos\theta}$$

$$\text{Williamson-Hall: } B = \frac{K\lambda}{D\cos\theta} + \eta\tan\theta$$

then rearranged to $B.\cos\theta = \frac{K\lambda}{D} + \eta\,\mathrm{Sin}\,\theta$

where B = FWHM peaks after correction by instrumental broadening, $B = \sqrt{{B_0}^2 - {B_i}^2}$; B_0 = FWHM sample, B_i = FWHM standard (silicon), D = crystallite size, K = constant Scherrer (0.94 for cubic system), and η=strain. The sizes of the crystallite and strain were determined by making the linear equation between B*cos θ and sin θ. The intercept and slope of the linear equations were used to determine the size of the crystal (D) and the strain of a micro-crystal lattice, respectively. The determination of crystal size through the Scherrer equation used FWHM from peaks 111 and 200 because it was close to the standard of the silicon peak [13].

Study of crystal growth

The kinetics of $BaTiO_3$crystal growth was determined using a Burke-Turnbull equation modification based on an isothermal reaction model:

$D_t^n - D_0^n = Ate^{-\frac{Ea}{RT}}$; this equation was rearranged to: $\ln D_t = \frac{1}{n}\ln t + \frac{1}{n}(\ln A - \frac{Ea}{RT})$ and then rearranged to: $\ln\frac{D_t^n}{t} = \ln A - \frac{Ea}{RT}$

D_t and D_0 are average grain sizes at time t and original grain size, n is the grain growth exponent, t is the sintering time, E_a is the grain growth activation energy, and A is the pre-exponential, and R is the general gas constant.

Thermal and electrochemical characteristics

The thermal properties of a low-pressure hydrothermal product prior to sintering were monitored using a TG-DTA pattern in air and oxygen atmospheric with a flow rate of 10 °C/min. In addition, the electrochemical properties of $BaTiO_3$ were obtained from cyclic voltammetry (CV) and linear sweep voltammetry (LSV). CV was performed using potentiostat DY 2300 digi-ivy, SPCE DS-110 as substrate of $BaTiO_3$, potential range (-1)–(1) V, scan rate 0.05 V/sec, and sensitivity 10^{-3} A/V in a 1 M NaOH solution.

■ RESULTS AND DISCUSSION

Cubic Barium Titanate

The single-phase was successfully synthesized through low-pressure hydrothermal at 150 °C and sintering at 800 °C for 2, 4, 8, and 12 h based on the XRD measurements (Suppl. 1–3). The $BaTiO_3$ diffractions show peaks at 2θ close to $BaTiO_3$ in the COD database No. 96-210-0863 (Fig. 1). The temperatures of the sintering and distilled water purity could affect the purity of $BaTiO_3$. The impurities of $BaTiO_3$ formed at sintering temperatures of between 600 and 700 °C. The impurities were caused by the reaction between $Ba(OH)_2$ and dissolved CO_2 in distilled water. The use of free-CO_2 distilled water, cleaning with Nitrogen/Argon, or washing with organic acids like formic acid can reduce impurities [7]. In this study, the purification of $BaTiO_3$ was successfully performed using nitric acid to remove $BaCO_3$, which was characterized by the absence of $BaCO_3$ peaks at 23.939, 24.335, 34.143, 42.045, and 43.035° after treatment with nitric acid (Fig. 1). The formation of $BaCO_3$ impurities indicates the weakness of the synthesis of $BaTiO_3$ through wet techniques performed at low sintering temperatures [14-15]. Inhibition of $BaCO_3$ formation is important for

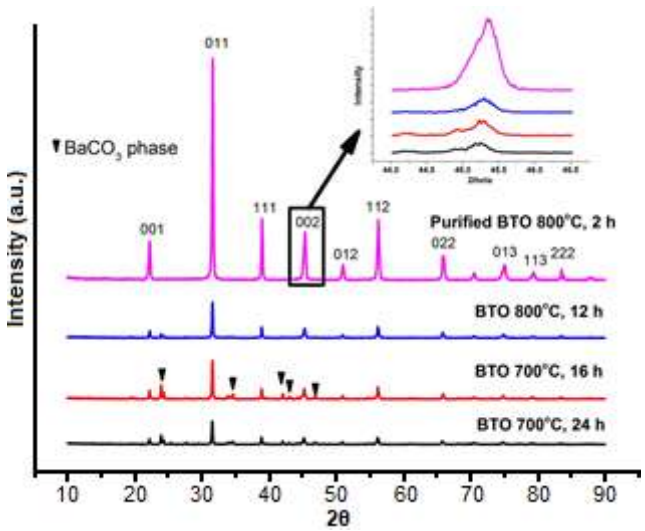

Fig 1. The XRD diffraction patterns of resulted $BaTiO_3$ using low-pressure hydrothermal assisted sintering. The black rectangular and insert shows absence splitting peak at 2θ = 45°

obtaining $BaTiO_3$ with high purity. Small amounts of $BaCO_3$ impurities were also identified in the hydrothermal synthesis of $BaTiO_3$ at 200 °C with $Ba(OH)_2$ and $TiO_2/TiCl_4$ as precursors [16].

$BaCO_3$ was also produced in synthesizing hydrothermal $BaTiO_3$, with Ba $(OH)_2$ and TiO_2 as precursors at 220 °C for three days. The impurities of the $BaCO_3$ phase decreased at the sintering temperature of 800 °C. Based on the Rietveld refinement result, the composition of $BaCO_3$ was not significantly different at 600 and 700 °C for all durations of sintering (Table 1). Moreover, the sintering temperature of 800 °C caused $BaCO_3$ to turn into BaO and CO_2.

The synthesized $BaTiO_3$ had a cubic crystal system based on the XRD diffractogram (Fig. 2), which was indicated by the absence of splitting at the diffraction peak of 2θ = 45°, the {200} plane into two peaks (i.e., {200} and {002} planes) (Fig. 1) [17-19]. Sintering at 600, 700, and 800 °C was predicted to be caused by the crystal structure change from tetragonal to cubic. Thermodynamically, $BaTiO_3$ will form a cubic crystal structure at temperatures above 130 °C.

The reaction equation and mechanism were proposed to explain the formation of $BaTiO_3$ from $Ba(OH)_2$ and TiO_2 via the hydrothermal technique.

Table 1. Phase composition in barium titanate synthesis after refinement

Treatment		Phase composition (%)		Rietveld refinement (FullProf)	
Temperature (°C)	Times (h)	$BaTiO_3$	$BaCO_3$	Chi^2	Weighted average R-Bragg
600	6	61.4	38.6	1.8	20.3
	12	64.2	35.8	1.9	21.1
	18	61.4	38.6	2.0	26.8
	24	60.1	39.9	1.9	17.7
700	4	63.2	36.8	1.9	16.7
	8	65.0	35.0	1.9	21.6
	12	70.5	29.6	1.9	20.6
	16	74.4	25.6	1.7	21.1
800	2	100		1.2	15.6
	4	100		1.4	14.4
	6	100		1.3	15.4
	8	100		1.1	12.5

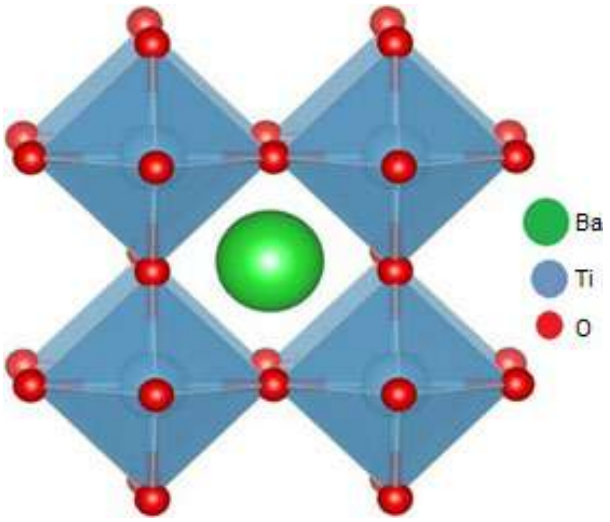

Fig 2. Crystal structure of purified cubic $BaTiO_3$

$BaTiO_3$ formation with $Ba(OH)_2$ and TiO_2 as precursors could be due to the dissolution-precipitation mechanism. In this mechanism, two-step reactions for $BaTiO_3$ formation were proposed [18,20]:

Dissolution: $TiO_2 + H_2O \rightarrow [Ti(OH)_{4-x}]^{x+}$

Precipitation: $[Ti(OH)_{4-x}]^{x+} + Ba^{2+} + 2\ OH^- \rightarrow BaTiO_3 + 2H_2O$

The rate of nucleation and the growth of $BaTiO_3$ were influenced by the dissolution rate of TiO_2, which is indicated by the surface area dependence of the resulting $BaTiO_3$ on the size of the TiO_2 precursor [21]. Therefore, the rate of $BaTiO_3$ formation could be increased by adding KOH or NaOH since the formation of $[Ti(OH)_{4-x}]^{x+}$ ions were accelerated in the alkaline medium. Other explanations for the formation process of $BaTiO_3$ include the condensation reaction occurring between $[Ti(OH)_6]^{2-}$ and Ba^{2+}; the migration of the Ba^{2+} ion into the TiO_2 structure, resulting in the breaking of Ti–O–Ti bonds; and the hydrolysis of Ti–O–Ti in an alkaline medium following the migration of the Ba^{2+} ion [22]. Thermodynamically, hydroxide ions play a role in the nucleation of $BaTiO_3$ and its function as a catalyst through the transition acceleration of Ba^{2+} ions during the dynamic point of crystallization to form $BaTiO_3$ crystals. Therefore, increasing the nucleation of $BaTiO_3$ could increase its growth and cause larger particle size.

Size and Kinetics of Crystal Growth

The crystallite size of the synthesized $BaTiO_3$ was measured using the Scherrer equation. The size of the obtained crystals ranged from 82 to 169 nm, 100 to198 nm, and 82 to149 nm for sintering temperatures of 600, 700, and 800 °C (Table 2). The crystallite size increased in line with the duration of sintering time. The crystallite size and structure of the crystal were also influenced by the particle size and TiO_2 precursor type, with a smaller particle size of the TiO_2 precursor resulting in smaller-sized $BaTiO_3$ as well. Other studies were conducted for $BaTiO_3$ hydrothermal synthesis at 96 °C with Ba $(OH)_2$ and TiO_2 precursors obtaining a crystallite size of 70 nm [23]. Additives, such as Polyacrylate, PVA, and fructose

Table 2. Crystallite size, rate parameter, and E_a crystal growth of cubic $BaTiO_3$

Treatments		Crystallite size (nm)	Micro-strain (η, %)	Crystal growth exponent (n)	Ea (kJ/mol)
Temperature (°C)	Time (h)				
600	6	82	0.27	2.0	119.3
	12	118	0.64		
	18	131	0.58		
	24	169	0.53		
700	4	100	0.51	2.2	
	8	134	0.59		
	12	148	0.63		
	16	198	0.53		
800	2	82	0.31	2.5	
	4	110	0.50		
	6	126	0.68		
	8	149	0.65		

to the hydrothermal process, could reduce particle size [23]. $BaTiO_3$ with a crystallite size of 75 nm (48 h of treatment) and 130 nm (72 h of treatment) were obtained using hydrothermal techniques followed by plasma spark sintering [24].

The XRD pattern could be used to calculate micro strains from the crystal lattice. One of the top causes of expansion at peak X-ray diffraction is the microstrain. $BaTiO_3$, obtained with low hydrothermal pressure at 150 °C, a sintering temperature between 600 to 800 °C, and a sintering time of 2 to 24 h has a microstrain of 0.27 to 0.68% (Table 2). Microstrains can occur due to the uniform distortion of the crystal lattice, dislocation, anti-phase domain boundaries, or deformation faulting.

The size of the crystallite material is closely related to its chemical and physical properties, so it needs to be studied to identify its crystal growth. Information on crystal growth kinetics can be used to control the desired crystal size of the material. The crystals/grains from $BaTiO_3$ growth via low-pressure hydrothermal methods were studied at sintering temperatures of 600, 700, 800 °C for different time durations. Based on the linear plot between ln (D) and ln (t) of the Burke-Turnbull equation changes, n values were 2.0, 2.2, and 2.5, respectively, for sintering temperatures 600, 700, and 800 °C. In general, the value of n ranged from 2 to 6, but there were up to 10 [24]. The exponent of crystallite growth was obtained at n = 3.4 (matrix) and n = 9.7 (template) for the growth kinetics of the ceramic-textured $BaTiO_3$ through template techniques [25]. The greater value of n indicates the crystal growth is constrained, resulting in the slower growth of the crystal.

A correlation between the crystal growth exponent and the grain mechanism was proposed (i.e., $n \leq 3$ due to pore controlled lattice diffusion, pore controlled vapor transport with constant vapor pressure, boundary controlled coalescence of the second phase particles for a system containing second phase particles, and boundary controlled solute drag for the doped system. Based on the value of the grain growth exponent, the growth mechanism of $BaTiO_3$ synthesized with low-pressure hydrothermal-assisted sintering was due to poorly controlled lattice diffusion. On the other hand, the sintering temperature change did not affect the grain growth exponent, which means that temperature changes do not affect the diffusion mechanism [26].

Crystal growth is influenced by the crystal-boundary curvature mechanism, lattice diffusion, crystal-bound diffusion, interfacial diffusion, evaporative agglomeration, the dissolving-settling mechanism, and super-saturation (concentrations of reactant, temperature, and mixing conditions) [25]. The size of the initial crystal affects the crystal formation process and its growth rate. In this research, $BaTiO_3$ had

an initial crystallite size that did not differ significantly among the materials (82 and 100 nm) and grew to 198 nm during sintering, with an activation energy of 119.8 kJ/mol (Table 2). This activation energy was in line with the growth rate. Based on our references, activation energies of 190, 202, and 196 kJ/mol for $BaTiO_3$ were produced using the milling technique for $BaCO_3$ and TiO_2 [27]. Activation energies of 364 kJ/mol (matrix) and 918 kJ/mol (template) for $BaTiO_3$ produced by the template method [25].

Electronic Structure of $BaTiO_3$

The bandgap and density of state (DOS) of the cubic $BaTiO_3$, calculated using quantum espresso with Burai as the graphical user interface (GUI), are shown in Fig. 3 and 4. For band structure, the maximum of the valence band and the minimum of the conduction band are located at the M and Γ band, respectively, with the smallest value of the direct bandgap about 1.9 eV at the Γ to Γ band and the indirect bandgap from M to Γ band being about 1.75 eV. This result was in line with Rohj et al. [28], who used DFT+U approximations for $BaTiO_3$ with values of 1.67 eV at the Γ'G band, and Taib et al. [29], who used the using LDA+U method for $BaTiO_3$ with a value of about 1.778 eV for the indirect bandgap. Orbital O 2p dominated the highest valence band (VB), while orbital Ti 3d dominated the lowest conduction band. Details on the electron density of cubic $BaTiO_3$ were explained using the DOS data.

The DOS of cubic $BaTiO_3$ exhibited a symmetric type (Fig. 4). The valence band (VB) from -6 to 0 eV consisted of an O 2p state with a small contribution from the Ti 3d and Ba 5p states. The conduction band minimum from 0 to 5 eV was dominated by the Ti 3d state, with a small contribution from the O 2p state, which

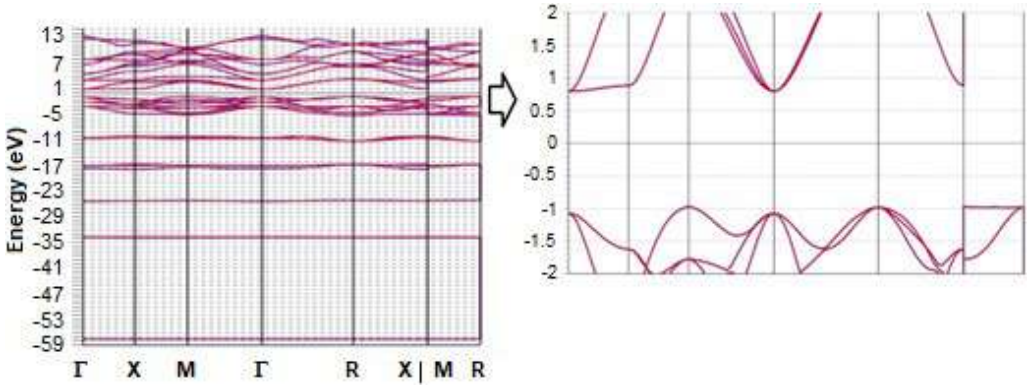

Fig 3. Band structure of cubic $BaTiO_3$

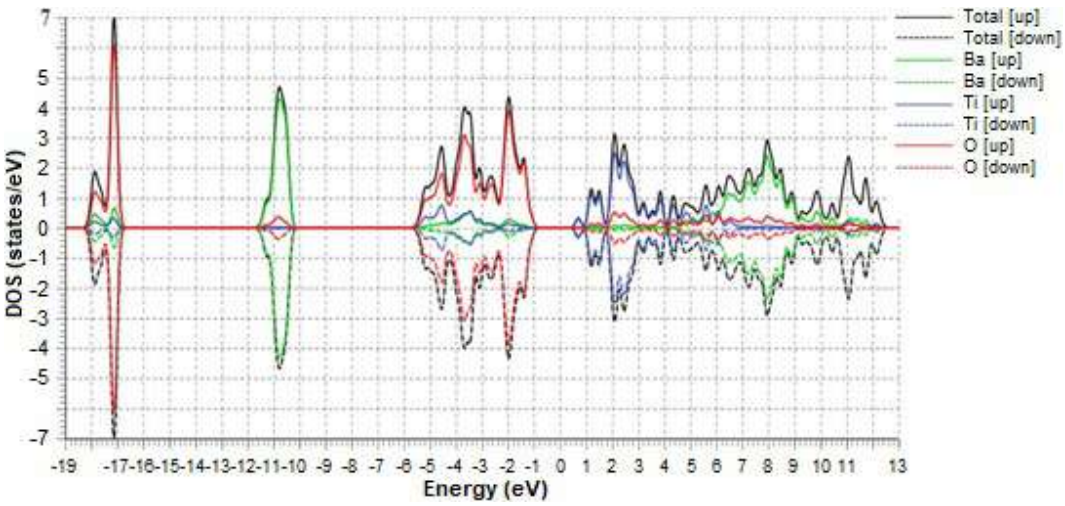

Fig 4. The total density of state (DOS) for cubic $BaTiO_3$

indicates that some electrons moved from the valence band of the O 2p orbital to the conduction band of Ti 3d and hybridized to form a covalent bond. The Ba state was not influenced by the valence band even when separated from the other bands. The Ba and O states were much larger than the O and Ti states in DOS, which indicates that the Ba–O interaction takes on an ionic character, while the Ti–O interaction takes on a covalent character.

Thermal Characteristics and Electrochemical Properties

Thermal analysis can be used to explain the process of forming barium titanate from its precursors. Theoretically, the formation of $BaTiO_3$ from $Ba(OH)_2$ and TiO_2 precursors will release 7.17% w/w H_2O molecules so that the $BaTiO_3$ material quantity after a water loss is 92.83% w/w. The study of thermal analysis using TG/DTA showed that the percentage loss of weight at 1000 °C by 8% (airflow) and 6.7% (oxygen flow) were in line with theoretical calculations (Fig. 5(a) and 5(b)). The weight loss occurred slowly until reaching a temperature of 650 °C and then increased sharply until reaching the temperature of 950 °C.

The temperature achieved for weight loss acceleration in the airflow was lower than that of the oxygen flow, indicating that airflow can accelerate $BaTiO_3$ formation. This phenomenon followed the TG-DTA pattern of BTO from $BaCO_3$ and TiO_2 and exhibited that the phase transition temperature during $BaTiO_3$ formation will be from 650 °C to 950 °C [30]. Endothermic peaks appeared in a TG-DTA pattern, which indicates a phase change during the formation of $BaTiO_3$. In the airflow, phase transition more frequently occurs, which is possible due to the effects of the chemical components contained in the air, such as N_2, O_2, CO_2, and CO. Ba_2TiO_4 is a possible phase, which occurs due to the reaction between $BaTiO_3$ and $BaCO_3$. This phase will react again with TiO_2 to form $BaTiO_3$ [30]. Endothermic peaks in oxygen flow occur at 750 °C and 900 °C, with sharper characters than airflow. An endothermic DTA peak above 800 °C was associated with CO_2 release due to a reaction between $BaCO_3$ and $BaTiO_3$ to form Ba_2TiO_4. On the other hand, water released in the formation of $BaTiO_3$ from the $Ba(OH)_2$ and TiO_2 precursors requires high temperatures, indicating a strong OH chemisorption in the lattice perovskite [31].

The voltammogram of $BaTiO_3$ indicated an irreversible redox system in the alkaline medium (Fig. 6(a)). A reduction peak appeared at -0.4 V vs. Ag/AgCl, and an oxidation peak appeared at 0.6 V vs. Ag/AgCl, indicating the behavior of Ti^{3+}/Ti^{4+} redox on an electrode surface. On the other hand, the redox system of the $BaTiO_3$ electrode surface caused an oxygen evolution/reduction reaction (OER/ORR) and a hydrogen evolution reaction (HER). Positive potential is the OER/ORR region, while the negative potential is the HER region. The current at a positive potential is higher than negative potential indicating that $BaTiO_3$ is more active as an OER/ORR electrocatalyst. The OER/ORR

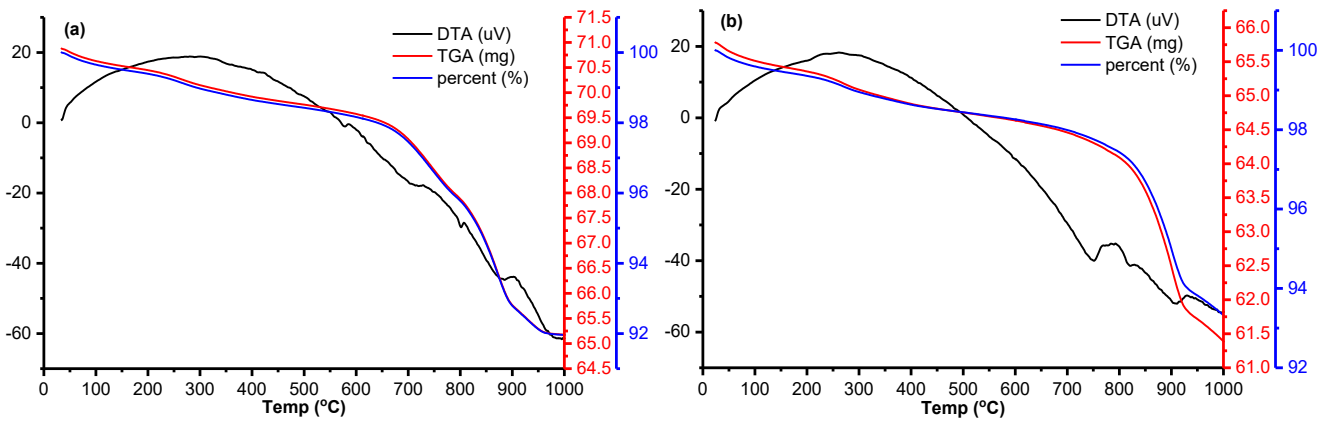

Fig 5. The TG-DTA pattern of the product resulted from low pressure hydrothermal from $Ba(OH)_2$ and TiO_2 before sintering using (A) airflow and (B) oxygen flow

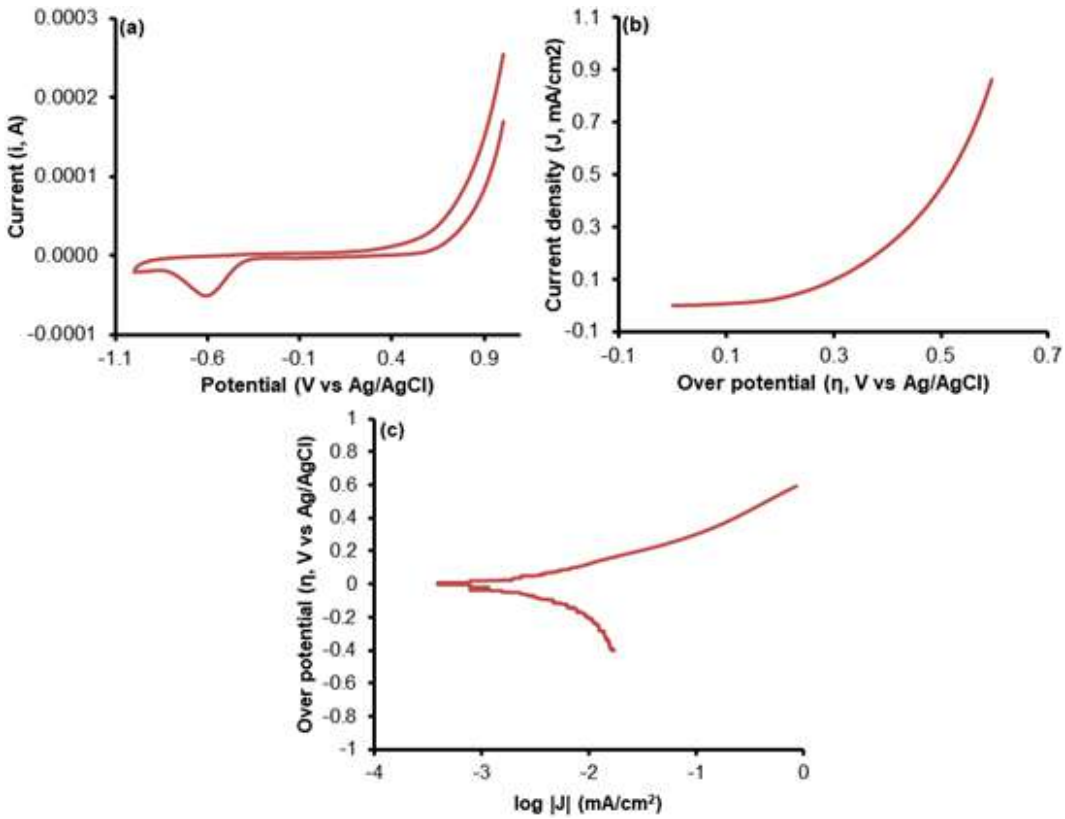

Fig 6. Cyclic voltammogram (a), Polarization plot (b), and Tafel plot (c) of $BaTiO_3$ was produced through sintering at 800 °C during 4 h in 1 M NaOH solution

bifunctional electrocatalyst of $BaTiO_3$ has been studied previously [32] due to the oxygen vacancy of $BaTiO_3$ that changes its crystal structure from cubic to hexagonal. Mechanistic of OER, ORR, and HER are initiated via OH adsorption on the Ti atom, the formation of the O-O bond, and $O_2^{2-}/^{-}OH$ exchange. The OER/ORR mechanism of the perovskite has also been previously studied, and a proposed mechanism of OER in an alkaline medium is as follows:

$M + {}^{-}OH \rightarrow MOH$

$MOH + {}^{-}OH \rightarrow MO + H_2O_{(l)}$

$2MO \rightarrow 2M + O_{2(g)}$

$MO + {}^{-}OH \rightarrow MOOH + e^{-}$

$MOOH + {}^{-}OH \rightarrow M + O_{2(g)} + H_2O_{(l)}$

Good electrocatalyst was indicated by Tafel slope value and also may provide insightful information about the OER mechanism. Suen et al. [33] was reviewed various OER mechanisms that correlated with Tafel slope value. Tafel slope value can be linked to the rate-determining step and implicates to some pattern may exist. The same rate-determining steps could have several values of Tafel slope, dependent on different coverage degree of intermediate. OER mechanism included intermediate such oxo, peroxide and superoxide group on surface electrocatalyst.

The OER ability of $BaTiO_3$ can be attributed to the electron configuration system of the Ti atom, in which the d orbitals of Ti are not filled (d^0), so it is possible to interact with more reactive ligands, such as ${}^{-}OH$ at the initial stage. Based on Hard-Soft Acid Base (HSAB) theory, The Ti ion is categorized as a hard acid, while O^{2-} and ${}^{-}OH$ are categorized as hard bases. ${}^{-}OH$ ions are preferred for interacting with Ti compared to O_2 ions due to their having a larger degree of basicity. To study the OER mechanism of $BaTiO_3$, the calculation of reaction Gibbs free energy using MMFF-based molecular mechanics was calculated (Fig. 7). The energy profile showed that the OOH stage is the rate

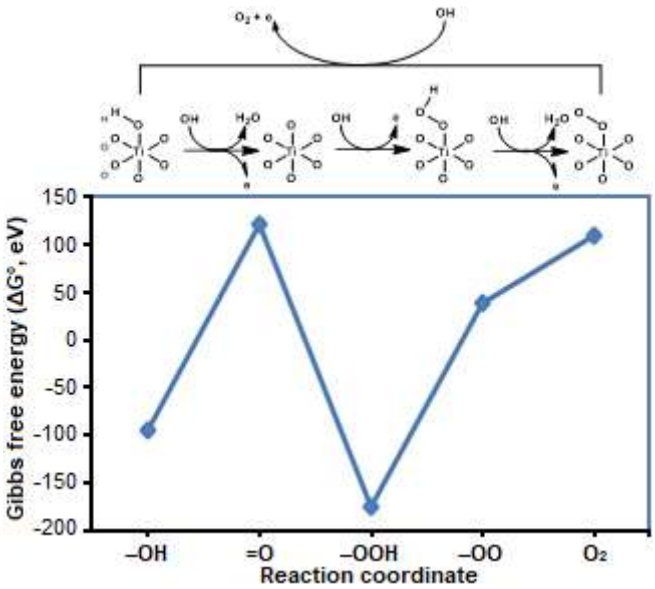

Fig 7. Profile of Gibbs Free Energy in oxygen evolution reaction

determining step, allowing for oxygen evolution in the base medium. The calculation of Gibbs free energy in Fig. 7 was used a mechanism of OER proposed by Hong et al. [34] for perovskite surface.

CONCLUSION

The hydrothermal technique of low-pressure systems followed by sintering at 600, 700, and 800 °C can be used to synthesize $BaTiO_3$ with $Ba(OH)_2$ and TiO_2 precursors. Sintering temperatures of 600 and 700 °C still contain $BaCO_3$ impurities sourced from distilled water and air. The crystal size of $BaTiO_3$ ranged from 82 to 198 nm based on the Williamson-Hall equation with strains from 0.27 to 0.68%. $BaTiO_3$ crystal growth following lattice diffusion is controlled by pore size based on the exponent value of 2-2.5. The band structure of cubic $BaTiO_3$ exhibited an indirect band from the M to Γ band of about 1.75 eV and a direct bandgap of about 1.9 eV at Γ to Γ. The density of state (DOS) indicated the covalent character on the Ti-O interaction and the ionic character on the Ba-O interaction. Electrochemical measurements indicated that $BaTiO_3$ has OER electrocatalytic capabilities in an alkaline medium. The purified cubic $BaTiO_3$ offers potential application in electrocatalyst for energy storage and conversion as an electrode for batteries, water splitting systems, and regenerative fuel cells.

ACKNOWLEDGMENTS

This work was supported and funded by the Laboratory of Testing and Certification Services, IPB University.

REFERENCES

[1] Chen, T., Meng, J., Wu, S., Pei, J., Lin, Q., Wei, X., Li, J., and Zhang, Z., 2018, Room temperature synthesized $BaTiO_3$ for photocatalytic hydrogen evolution, *J. Alloys Compd.*, 754, 184–189.

[2] Artrith, N., Sailuam, W., Limpijumnong, S., and Kolpak, A.M., 2016, Reduced overpotentials for electrocatalytic water splitting over Fe-and Ni-modified $BaTiO_3$, *Phys. Chem. Chem. Phys.*, 18 (42), 29561–29570.

[3] Kudłacik-Kramarczyk, S., Drabczyk, A., Głąb, M., Dulian, P., Bogucki, R., Miernik, K., Sobczak-Kupiec, A., and Tyliszczak, B., 2020, Mechanochemical synthesis of $BaTiO_3$ powders and evaluation of their acrylic dispersions, *Materials*, 13 (15), 3275.

[4] Gaikwad, A.S., More, S.S., Kathare, R.V., Mane, M.L., Borade, R.B., Vijapure, Y.A., and Kadam, A.B., 2018, Barium titanate ($BaTiO_3$) synthesized by sol-gel auto-combustion method, *Int. Res. J. Sci. Eng.*, A5, 41–44.

[5] Wang, W., Cao, L., Liu, W., Su, G., and Zhang, W., 2013, Low-temperature synthesis of $BaTiO_3$ powders by the sol–gel-hydrothermal method, *Ceram. Int.*, 39 (6), 7127–7134.

[6] Wu, Y.T., Wang, X.F., Yu, C.L., and Li, E.Y., 2012, Preparation and characterization of barium titanate ($BaTiO_3$) nano-powders by pechini sol-gel method, *Mater. Manuf. Processes*, 27 (12), 1329–1333.

[7] Zanfir, A.V., Voicu, G., Jinga, S.I., Vasile, E., and Ionita, V., 2016, Low-temperature synthesis of $BaTiO_3$ nanopowders, *Ceram. Int.*, 42 (1), 1672–1678.

[8] Zhang, B., Jin, H., Liu, X., Guo, X., He, G., and Yang, S., 2019, The formation and application of submicron spherical $BaTiO_3$ particles for the diffusion layer of medical dry films, *Crystals*, 9 (11), 594.

[9] Gao, Y., Shvartsman, V.V., Elsukova, A., and Lupascu, D.C., 2012, Low-temperature synthesis of

crystalline $BaTiO_3$ nanoparticles by one-step "organosol"-precipitation, *J. Mater. Chem.*, 22 (34), 17573–17583.

[10] Bowland, C.C., and Sodano, H.A., 2017, Hydrothermal synthesis of tetragonal phase $BaTiO_3$ on carbon fiber with enhanced electromechanical coupling, *J. Mater. Sci.*, 52 (13), 7893–7906.

[11] Li, J., Inukai, K., Tsuruta, A., Takahashi, Y., and Shin, W., 2017, synthesis of highly disperse tetragonal $BaTiO_3$ nanoparticles with core–shell by a hydrothermal method, *J. Asian Ceram. Soc.*, 5 (4), 444–451.

[12] Yan, C., Zou, L., Xue, D., Xu, J., and Liu, M., 2008, Chemical tuning polymorphology of functional materials by hydrothermal and solvothermal reactions, *J. Mater. Sci.*, 43 (7), 2263–2269.

[13] Khan, M., Mishra, A., Shukla, J., and Sharma, P., 2019, X-ray analysis of $BaTiO_3$ ceramics by Williamson-Hall and size strain plot methods, *AIP Conf. Proc.*, 2100, 020138.

[14] Yun, H.S., Yun, B.G., Shin, S.Y., Jeong, D.Y., and Cho, N.H., 2021, Crystallization kinetics in $BaTiO_3$ synthesis from hydrate precursors via microwave-assisted heat treatment, *Nanomaterials*, 11 (3), 754.

[15] Usher, T.M., Kavey, B., Caruntu, G., and Page, K., 2020, Effect of $BaCO_3$ impurities on the structure of $BaTiO_3$ nanocrystals: Implications for multilayer ceramic capacitors, *ACS Appl. Nano Mater.*, 3 (10), 9715–9723.

[16] Viviani, M., Buscaglia, M.T., Testino, A., Buscaglia, V., Bowen, P., and Nanni, P., 2003, The influence of concentration on the formation of $BaTiO_3$ by direct reaction of $TiCl_4$ with $Ba(OH)_2$ in aqueous solution, *J. Eur. Ceram. Soc.*, 23 (9), 1383–1390.

[17] Pasuk, I., Neațu, F., Neațu, Ș., Florea, M., Istrate, C.M., Pintilie, I., and Pintilie, L., 2021, Structural details of $BaTiO_3$ nano-powders deduced from the anisotropic XRD peak broadening, *Nanomaterials*, 11 (5), 1121.

[18] Lee, H.W., Moon, S., Choi, C.H., and Kim, D.K., 2012, Synthesis and size control of tetragonal barium titanate nanopowders by facile solvothermal method, *J. Am. Ceram. Soc.*, 95 (8), 2429–2434.

[19] Li, M., Gu, L., Li, T., Hao, S., Tan, F., Chen, D., Zhu, D., Xu, Y., Sun, C., and Yang, Z., 2020, TiO_2-seeded hydrothermal growth of spherical $BaTiO_3$ nanocrystals for capacitor energy-storage application, *Crystals*, 10 (3), 202.

[20] Ahn, K.H., Lee, Y.H., Kim, M., Lee, H.S., Youn, Y.S., Kim, J., and Lee, Y.W., 2013, Effects of surface area of titanium dioxide precursors on the hydrothermal synthesis of barium titanate by dissolution–precipitation, *Ind. Eng. Chem. Res.*, 52 (37), 13370–13376.

[21] Habib, A., Stelzer, N., Angerer, P., and Haubner, R., 2011, Effect of temperature and time on solvothermal synthesis of tetragonal $BaTiO_3$, *Bull. Mater. Sci.*, 34 (1), 19–23.

[22] Wu, M., Long, J., Wang, G., Huang, A., Luo, Y., Feng, S., and Xu, R., 1999, Hydrothermal synthesis of tetragonal barium titanate from barium hydroxide and titanium dioxide under moderate conditions, *J. Am. Ceram. Soc.*, 82 (11), 3254–3256.

[23] Maxim, F., Ferreira, P., Vilarinho, P.M., Aimable, A., and Bowen, P., 2010, Additive-assisted aqueous synthesis of $BaTiO_3$ nanopowders, *Cryst. Growth Des.*, 10 (9), 3996–4004.

[24] Ortiz-Landeros, J., Gómez-Yáñez, C., López-Juárez, R., Dávalos-Velasco, I., and Pfeiffer, H., 2012, Synthesis of advanced ceramics by hydrothermal crystallization and modified related methods, *J. Adv. Ceram.*, 1 (3), 204–220.

[25] Fu, F., Zhai, J., Xu, Z., Shen, B., and Yao, X., 2014, Grain growth kinetics of textured-$BaTiO_3$ ceramics, *Bull. Mater. Sci.*, 37 (4), 779–787.

[26] Kambale, K.R., Kulkarni, A.R., and Venkataramani, N., 2014, Grain growth kinetics of barium titanate synthesized using conventional solid state reaction route, *Ceram. Int.*, 40 (1), 667–673.

[27] Osman, K.I., 2011, Synthesis and Characterization of $BaTiO_3$ Ferroelectric Material, *Dissertation*, Faculty of Engineering, Cairo University.

[28] Rohj, R.K., Hossain, A., Mahadevan, P., and Sarma, D.D., 2021, Band gap reduction in ferroelectric $BaTiO_3$ through heterovalent Cu-Te co-doping for visible-light photocatalysis, *Front. Chem.*, 9, 682979.

[29] Taib, M.F.M., Hussin, N.H., Samat, M.H., Hassan, O.H., and Yahya, M.Z.A., 2016, Structural, electronic and optical properties of $BaTiO_3$ and $BaFeO_3$ from first principles LDA+U study, *Int. J. Electroact. Mater,* 4, 14–17.

[30] Gomez-Yañez, C., Benitez, C., and Balmori-Ramirez, H., 2000, Mechanical activation of the synthesis reaction of $BaTiO_3$ from a mixture of $BaCO_3$ and TiO_2 powders, *Ceram. Int.*, 26 (3), 271–277.

[31] Hennings, D., and Schreinemacher, S., 1992, characterization of hydrothermal barium titanate, *J. Eur. Ceram. Soc.*, 9 (1), 41–46.

[32] Chen, C.F., King, G., Dickerson, R.M., Papin, P.A., Gupta, S., Kellogg, W.R., and Wu, G., 2015, Oxygen-deficient $BaTiO_{3-x}$ perovskite as an efficient bifunctional oxygen electrocatalyst, *Nano Energy*, 13, 423–432.

[33] Suen, N.T., Hung, S.F., Quan, Q., Zhang, N., Xu, Y.J., and Chen, H.M., 2017, Electrocatalysis for the oxygen evolution reaction: recent development and future perspectives, *Chem. Soc. Rev.*, 46 (2), 337–365.

[34] Hong, W.T., Risch, M., Stoerzinger, K.A., Grimaud, A., Suntivich, J., and Shao-Horn, Y., 2015, Toward the rational design of non-precious transition metal oxides for oxygen electrocatalysis, *Energy Environ. Sci.*, 8 (5), 1404–1427.

Supplementary Data

This supplementary data is a part of paper entitled "Density Functional Theory Study of Intermolecular Interactions between Amylum and Cellulose".

Table S1. Topological parameters of the complex cellulose-amylum

BCP	Point	ρ(BCP)	λ1	λ2	λ3	$\nabla^2\rho$	G(BCP)	V(BCP)	H(BCP)	|V/G|	ε (BCP)	EHB (kcal/mol)
Amylum-Cellulose												
143	H29...O60	0.008	-0.006	0.038	-0.003	0.029	0.006	-0.006	0.001	0.858	0.296	-1.079
125	H95...O2	0.024	0.013	0.073	-0.015	0.07	0.018	-0.019	-0.001	1.051	0.019	-4.560
174	H94...O8	0.017	0.08	-0.008	-0.019	0.053	0.013	-0.014	0.000	1.011	0.059	-3.008
134	H84...H29	0.007	0.008	0.024	-0.005	0.027	0.005	-0.004	0.001	0.724	0.770	-0.882
138	O61...H37	0.012	0.052	-0.005	-0.011	0.036	0.009	-0.009	0.000	0.968	0.065	-1.985
220	O62...H50	0.005	0.008	-0.002	0.012	0.018	0.004	-0.003	0.001	0.758	0.625	-0.310
227	H82...C25	0.005	0.021	-0.002	0.000	0.018	0.003	-0.002	0.001	0.656	1.895	-0.324
233	H88...H50	0.005	0.004	0.012	0.002	0.019	0.003	-0.002	0.001	0.641	0.374	-0.326
246	O58...H49	0.016	0.018	0.044	-0.018	0.044	0.011	-0.012	0.000	1.034	0.040	-2.825
177	O54...H30	0.015	0.072	-0.014	-0.012	0.047	0.011	-0.011	0.000	0.976	0.125	-2.569
181	H78...O10	0.015	0.053	-0.015	0.003	0.041	0.011	-0.011	0.000	1.034	0.051	-2.579
206	O62...H47	0.017	-0.016	0.091	-0.018	0.057	0.014	-0.014	0.000	0.992	0.120	-3.038
154	H94...O1	0.014	0.007	0.007	0.031	0.045	0.011	-0.011	0.000	0.988	0.096	-2.361
120	O61...H48	0.034	-0.026	0.163	-0.045	0.092	0.024	-0.025	-0.001	1.047	0.042	-6.791
153	O54...O1	0.011	0.022	0.022	-0.008	0.036	0.009	-0.009	0.000	0.980	0.064	-1.636

CP: critical point; BCP: Bond critical point; ρ: Electron density (a.u.); $\nabla^2\rho$: Laplacian of electron density (a.u.); G: Lagrangian kinetic energy (a.u.); H: Hamiltonian kinetic energy or electronic energy density (a.u.); V: Potential energy density (a.u.); ε: Ellipticity of electron density (a.u.); λ_1, λ_2, λ_3: Components of Laplacian in x/y/z (a.u.); E_{HB}: Hydrogen bond energy (kcal/mol)

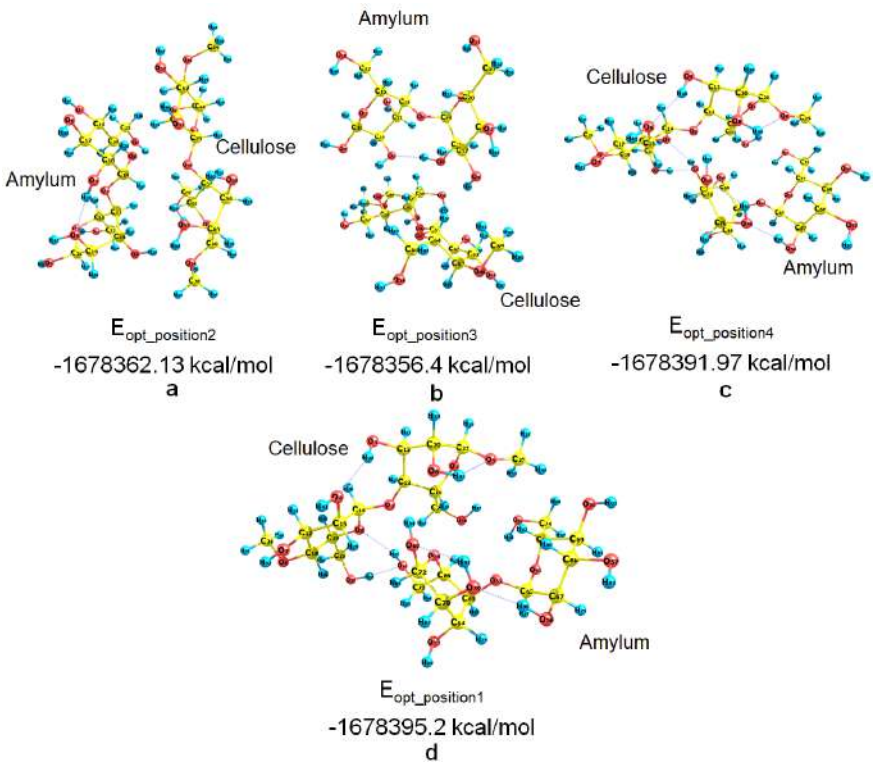

Fig S1. Energy optimization of various positions of cellulose-amylum complexes: (a) position2, (b) position3, (c) position4, (d) position1